RUSSIAN JOURNAL of EARTH SCIENCES

Vol. 23
Issue 5

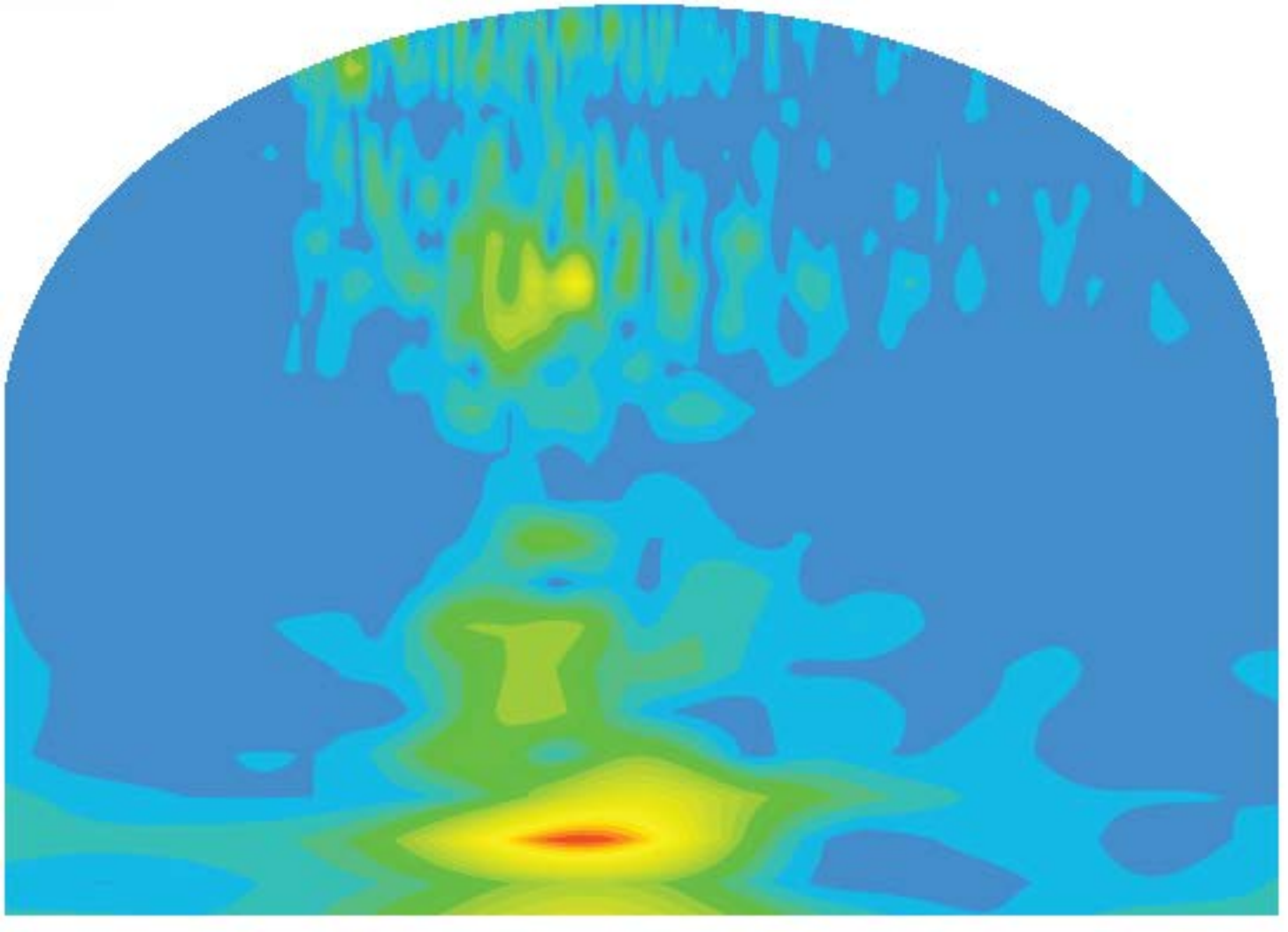

Russian Journal of Earth Sciences

# Microwave Radar Sensing of Sea Waves: An Effective Reflection Coefficient

**V. Karaev*[,1], M. Panfilova[1], Yu. Titchenko[1], E. Meshkov[1], D. Kovaldov[1], X. Li[2], and Y. He[2]**

[1]Institute of Applied Physics RAS, N. Novgorod, Russia
[2]School of Marine Sciences, Nanjing University of Information Science and Technology, Nanjing, China
* **Correspondence to:** V. Karaev, volody@ipfran.ru

**Abstract:** At the small incidence angles, the dominant backscattering mechanism for sea waves is the quasi-specular backscattering mechanism. The power of the reflected signal depends on the distribution function of the slopes of large-scale waves (in comparison with radar wavelength) and on the effective reflection coefficient, which is introduced instead of the Fresnel coefficient. In this paper, we discussed a new method for calculating the effective reflection coefficient from the wave scatterometer SWIM data. For the first time, measurements are performed by a radar at different azimuth angles at small incidence angles. This makes it possible to measure the effective reflection coefficient. An original algorithm was developed for data processing and determination of the total mean square slopes of large-scale sea waves and the azimuth dependence of the backscattering radar cross section at zero incidence angle. In the result of subsequent processing, the azimuth dependence of the effective reflection coefficient is retrieved. SWIM data were used to evaluate the developed algorithm. Processing of the test data set confirmed the efficiency of the algorithm. The azimuth anisotropy coefficients for the mean square slopes of large-scale waves and the effective reflection coefficient are calculated.

**Keywords:** microwaves, small incidence angles, Fresnel coefficient, effective reflection coefficient

**Citation:** Karaev, V., M. Panfilova, Yu. Titchenko, E. Meshkov, D. Kovaldov, X. Li, and Y. He (2023), Microwave Radar Sensing of Sea Waves: An Effective Reflection Coefficient, *Russian Journal of Earth Sciences*, 23, ES5001, EDN: TURMEQ, https://doi.org/10.2205/2023es000850

## Introduction

To describe the backscattering of microwaves by the sea surface at small incidence angles the concept of a two-scale model (TSM) of the scattering surface was introduced. In accordance with it, the sea surface is represented as large-scale waves (in comparison with the radar wavelength), covered with small ripples. Thus, the concept of a boundary (so-called cut off) wave number is introduced, which divides the sea wave spectrum into large-scale waves, in comparison with radar wavelength, and small ripples.

Within the framework of the Kirchhoff's approximation, the mechanism of electromagnetic waves backscattering from the sea surface at small incidence angles is quasi-specular. Reflection occurs from facets of the wave profile oriented perpendicular to the incident radiation, and the backscattering radar cross section (RCS) depends on the mean square slopes (MSS) of large-scale wave. Small ripples located on the "large" wave lead to the appearance of diffuse (resonant) scattering, which reduces the power of the backscattering signal. To take this effect into account, the concept of the effective reflection coefficient (ERC) is introduced, which is used instead of the Fresnel coefficient in the formula for the RCS [*Bass and Fuks*, 1979; *Valenzuela*, 1978].

The complicated task of measuring the ERC has attracted attention for a long time. The first paper devoted to experiment was published in 1986 [*Masuko et al.*, 1986]. The most detailed analysis of the dependence of the ERC on the wind speed was made in [*Freilich and Vanhoff*, 2003], where data from the precipitation radar (Ku-band) of the TRMM satellite were used. While moving, the precipitation radar scans by the incidence

Research Article

Received: 30 March 2023
Accepted: 6 July 2023
Published: 13 December 2023

**Copyright:** © 2023. The Authors. This article is an open access article distributed under the terms and conditions of the Creative Commons Attribution (CC BY) license (https://creativecommons.org/licenses/by/4.0/).

angle in a direction perpendicular to the flight track. As a result, the dependence of the RCS on the incidence angle is measured, and it can be used to retrieve the MSS along the scanning direction.

Since the MSS was calculated only along one azimuthal angle, the ERC was calculated using the assumption that large-scale waves are isotropic [*Freilich and Vanhoff*, 2003]. The use of this incorrect assumption is due to the lack of measurements of MSS at different azimuth angles. As a result, the ERC was calculated with an error.

The wave scatterometer SWIM, installed on the CFOSAT satellite, for the first time performs measurements at 24 azimuth angles, so the anisotropy of sea waves can be taken into account when calculating the ERC.

**Discussion of the Retrieval Algorithm**

At the small incidence angles, the backscattering radar cross section is given by the following formula [*Bass and Fuks*, 1979]:

$$\sigma_0(\theta_0,\varphi_{az}) = \frac{|R_{eff}(U_{10},\varphi_{az},\theta_0)|^2}{2\cos^4\theta_0\sqrt{mss_{xx}mss_{yy}-mss_{xy}^2}}\exp\left[-\frac{\tan^2\theta_0}{2\left(mss_{xx}mss_{yy}-mss_{xy}^2\right)}mss_{yy}\right], \quad (1)$$

where $mss_{xx}$ and $mss_{yy}$ – mean square slopes along $X$ and $Y$ axis respectively; $mss_{xy}$ – the coefficient of cross-correlation of the slopes of large-scale waves $mss_{xx}$ and $mss_{yy}$; $\theta_0$ – incidence angle; $U_{10}$ – wind speed at the 10 m height; $\varphi_{az}$ – wind direction; $R_{eff}$ – effective reflection coefficient and ERC = $|R_{eff}|^2$. We assume that the sounding is carried out along the $X$ axis and then the azimuth angle is equal to the angle between the wind direction and the sounding direction.

With an increase in wind speed, an increase in the MSS of large-scale waves and an increase in the spectral density of small ripples (variance of height) occur. As a result, the combined action of these factors leads to a decrease in the backscattering RCS at small incidence angles.

At a zero incidence angle, the formula (1) is simplified and takes the following form:

$$\sigma_0(0^\circ,\varphi_{az}) = \frac{|R_{eff}(U_{10},\varphi_{az},0)|^2}{2\sqrt{mss_{xx}mss_{yy}-mss_{xy}^2}}. \quad (2)$$

The effective reflection coefficient depends on the wind speed and the azimuth angle. The most important factor is the near-water wind speed, which has a significant effect on the amplitude of the ripple (the small-scale part of the sea wave spectrum). This can be seen from the dependence of resonant scattering at the middle incidence angles, when a change in wind speed leads to a change in the backscattering RCS by tens of decibels [*Li et al.*, 2022b; *Lin et al.*, 2012].

The next factor affecting the effective reflection coefficient is related to the azimuth dependence of the ripple spectral density. A change in wind direction will lead to a change in the spectral density along the sounding direction, which will change the effective reflection coefficient and, accordingly, the backscattering RCS.

To study the dependence of the effective reflection coefficient on the azimuth angle, the following approach is proposed.

The measurement of the backscattering RCS at small incidence angles at different azimuth angles is performed by the wave scatterometer SWIM installed on the Chinese-French CFOSAT satellite [*Hauser et al.*, 2017, 2021].

For the first time radar performs measurements at 24 azimuth angles, so the anisotropy of sea waves can be taken into account when calculating the effective reflection coefficient. To calculate the effective reflection coefficient, the following method was used, which includes three stages.

At the first stage, using the well-known algorithm and the dependence of the RCS on the incidence angle is used to calculate the MSS of large-scale waves along the sensing direction (azimuth angle) [*Chen et al.*, 2018; *Chu et al.*, 2012; *Freilich and Vanhoff*, 2003; *Hauser et al.*, 2008; *Panfilova et al.*, 2020]. When retrieving the MSS, the RCS at zero incidence angle was also determined, which will be used further.

At the second stage the large-scale MSS calculated at the 12 or 24 azimuthal angles (after the first stage) are used for calculation of the azimuth dependence of large-scale slopes [*Karaev et al.*, 2021; *Li et al.*, 2022a]:

$$mss_{xx} = 0.5mss_{total} + 0.5\Delta mss \cdot \cos(2\varphi_0 - 2\varphi_{az}), \tag{3}$$

$$mss_{yy} = 0.5mss_{total} - 0.5\Delta mss \cdot \cos(2\varphi_0 - 2\varphi_{az}), \tag{4}$$

where $mss_{total} = mss_{xx} + mss_{yy}$, $\Delta mss = mss_{xx} - mss_{yy}$, and $\varphi_0$ direction of radar sensing.

Before processing, the preparation of SWIM data is performed so that the azimuth angle is measured from the expected (according to the numerical wind field model) wind direction. This data is made available to users. However, the real wind direction may not coincide with the estimates from the model, so the angle $\varphi_0$ is left in formulas (**??**) and (3) and it will be calculated. Thus, the direction of the wind may be clarified.

To estimate the coefficient of azimuth anisotropy of the MSS of large-scale waves, the following formula is used:

$$A_{az} = \frac{mss_{xx}}{mss_{yy}}. \tag{5}$$

At the third stage of processing, the model is used for calculation of $mss_{xx}$ for azimuth angles of 0° and 90° relative to the direction of wave propagation. Here the real wind direction is used, which was determined in the second stage. Only in this case, the RCS at zero incidence angle (the result of the first stage) and the MSS are related by a simple analytical formula.

As a result, the ERC is calculated for two azimuth angles: 0° and 90°, for example.

$$|R_{eff}(0°, 90°)|^2 = \frac{\sigma_0(0°, 90°)}{2\sqrt{mss_{xx}mss_{yy}}} = \text{ERC}, \tag{6}$$

$$|R_{eff}(0°, 0°)|^2 = \frac{\sigma_0(0°, 0°)}{2\sqrt{mss_{xx}mss_{yy}}} = \text{ERC}. \tag{7}$$

In this case, the coefficient of azimuth asymmetry of the *mss* of large-scale waves $K_{az}$ will be equal to

$$K_{az} = \frac{|R_{eff}(0°, 0°)|}{|R_{eff}(0°, 90°)|}.$$

The value of the cross-correlation coefficient is much less than the MSS of large-scale waves; therefore, it can be neglected in formula (2) and this formula can be tried to use for all azimuth angles. As a result, an estimate of the azimuth dependence of the effective reflection coefficient will be obtained.

### Example of Data Processing

Let us illustrate the operation of the proposed processing method on SWIM data. The input data are the backscattering RCS measured at different incidence angles and different azimuth angles. Data are analyzed that refer to a section of the sea surface measuring $70 \times 180$ km (24 azimuth angles) or $70 \times 90$ km (12 azimuth angles).

At the first stage, the dependence of the backscattering RCS on the incidence angle is analyzed and the MSS of large-scale wave are calculated for 24 (or 12) azimuth angles. The result is shown in Figure 1 by stars. In addition, the backscattering RCS for a zero incidence angle is retrieved.

The retrieved MSS are the input parameters for the second processing stage. Regression is performed and the coefficients of the model are found (see formula (3)). For this example, $mss_{\text{total}} = 0.0319$; $\Delta mss = 0.0016$ and $\varphi_0 = 5°$. On Figure 1 this dependence is shown by a solid curve.

The azimuth asymmetry coefficient for slopes is $A_{\text{az}} = 1.11$.

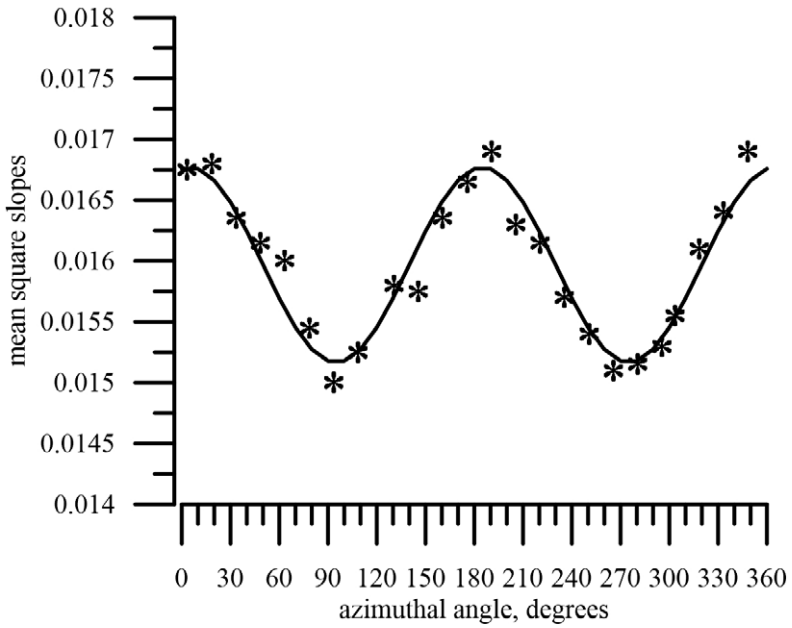


**Figure 1.** Azimuth dependence of the $mss_{\text{xx}}$ of large-scale waves: asterisks – retrieved values, curve – model.

Simultaneously with the MSS of the large-scale waves, the RCS for a zero incidence angle were retrieved, and the result is shown in Figure 2. The asterisks show the RCS retrieved in the course of processing. The curve shows the result of the regression.

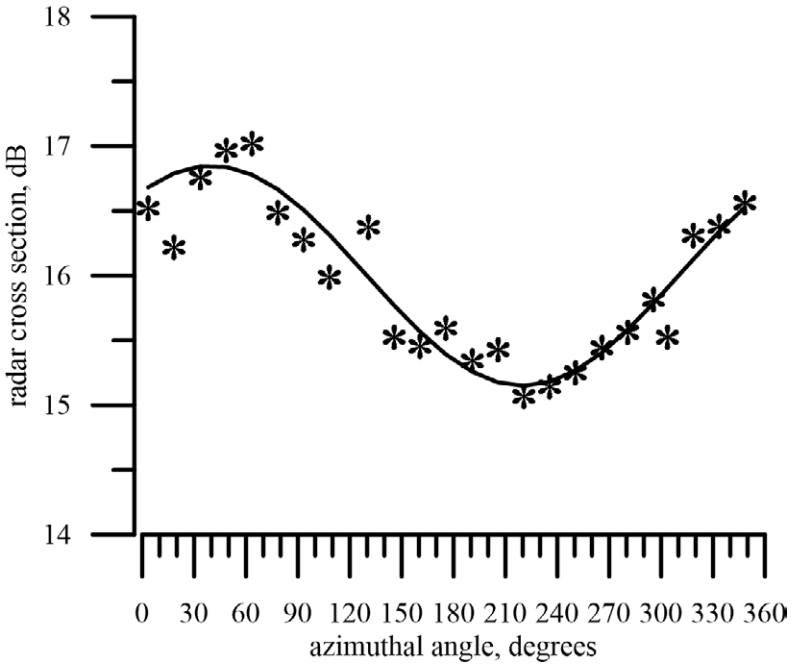


**Figure 2.** Azimuth dependence of the RCS at zero incidence angle: asterisks – retrieved values, curve – result of the regression.

The observed fluctuations of the initial data in Figures 1 and 2 can be caused by different reasons, in particular, due to insufficient averaging or wave variability in a $70 \times 180$ km area. It is impossible to make the right choice without additional analysis; therefore, when performing calculations at the third stage, we will consider both options: calculated data and a model data.

In the first case, we use the data that were obtained during processing and are shown in the figures with asterisks. In the second variant, we use the model data (result of the regression analysis) that were obtained during processing (curves in the figures).

To calculate the effective reflection coefficient, formula (6) is used and Figure 3 shows the results of the calculations. Here the input parameters from Figure 1 and Figure 2 were used.

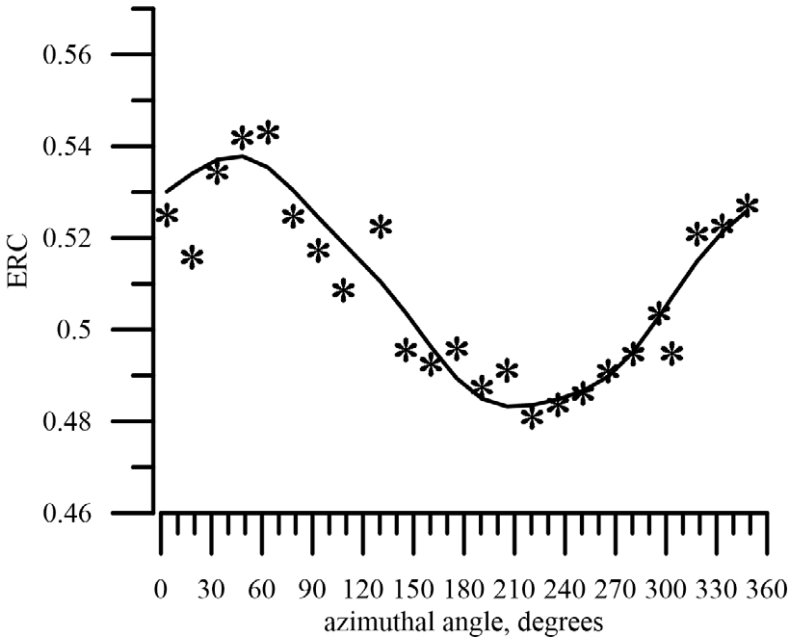


**Figure 3.** Azimuth dependence of the ERC: asterisks – according to experimental data and curve – according to formula (6) with input parameters from Figure 1 and Figure 2.

It can be seen from the figure that the dependences obtained by both methods are similar and, therefore, can be used to study the effective reflection coefficient.

In this case, the asymmetry coefficient is equal to $K_{az} = 1.11$.

The next step is the evaluation of the retrieval precision of the ERC (5). To do this, it is necessary to have data from independent contact measurements, but such measurements are unknown to us. To obtain a rough estimate, we use the following approach.

Let us represent the azimuthal dependence of the MSS of large-scale waves, taking into account the $\Delta mss$ error, in the following form

$$mss_{xx} mss_{yy} = mss_{xx} mss_{yy} + \Delta mss.$$

The results of numerical simulation showed that the relative error $\varepsilon_{mss}$ according to numerical simulation does not exceed 15–20%. The calculations were performed under the assumption of a known value of the ERC.

Measurements of the RCS are also performed with an error of no more than $\Delta\sigma$:

$$\sigma_0 = \sigma_0 + \Delta\sigma.$$

It is known from the requirements for orbital radars that the absolute error in measuring the RCS does not exceed 2 dB.

**Table 1.** Relative measurement error of the RCS

| RCS, dB | Relative error, % | Intensity of sea waves |
|---|---|---|
| 8 | 25 | high |
| 14 | 6 | medium |
| 20 | 2 | low |

Formulas (6) and (7) are used to calculate ERC, so the relative error in determining ERC does not exceed the following value

$$\varepsilon_{\mathrm{ERC}} < \varepsilon_{\mathrm{RCS}} + 0.5\varepsilon_{mss},$$

where $\varepsilon_{\mathrm{RCS}}$ is the relative measurement error of the RCS. Table 1 shows the relative errors for typical RCS, assuming that the absolute error does not exceed 2 dB for all values of RCS.

Thus, the relative error in determining the effective reflection coefficient is less than 10–12% for low intensity of sea waves and less 33–35% for high intensity of sea waves.

## Conclusions

The original method for calculating the effective reflection coefficient from the wave scatterometer SWIM data is developed. The algorithm consists of three stages. Firstly, in data processing the total MSS of large-scale wave slopes is calculated, the azimuth anisotropy is determined, and the wind direction is refined. At the second stage the azimuth dependence of the backscattering RCS at a zero incidence angle is also determined. And at the third stage in the course of subsequent processing, the azimuth dependence of the effective reflection coefficient is retrieved.

SWIM data can be used to evaluate the performance of the developed algorithm. Processing of the test data set confirmed the efficiency of the algorithm. The azimuth anisotropy coefficients for the MSS of large-scale waves and the effective reflection coefficient are calculated.

It is planned to process the SWIM data and calculate the dependence of the effective reflection coefficient on the wind speed.

**Acknowledgement.** The study was carried out at the expense of a grant from the Russian Science Foundation (project No. 20-77-10089).

## References

Bass, F. G., and I. M. Fuks (1979), *Wave Scattering from Statistically Rough Surfaces*, 528 pp., Elsevier, https://doi.org/10.1016/c2013-0-05724-6.

Chen, P., G. Zheng, D. Hauser, and F. Xu (2018), Quasi-Gaussian probability density function of sea wave slopes from near nadir Ku-band radar observations, *Remote Sensing of Environment*, *217*, 86–100, https://doi.org/10.1016/j.rse.2018.07.027.

Chu, X., Y. He, and G. Chen (2012), Asymmetry and Anisotropy of Microwave Backscatter at Low Incidence Angles, *IEEE Transactions on Geoscience and Remote Sensing*, *50*(10), 4014–4024, https://doi.org/10.1109/tgrs.2012.2189010.

Freilich, M. H., and B. A. Vanhoff (2003), The Relationship between Winds, Surface Roughness, and Radar Backscatter at Low Incidence Angles from TRMM Precipitation Radar Measurements, *Journal of Atmospheric and Oceanic Technology*, *20*(4), 549–562, https://doi.org/10.1175/1520-0426(2003)20<549:trbwsr>2.0.co;2.

Hauser, D., G. Caudal, S. Guimbard, and A. A. Mouche (2008), A study of the slope probability density function of the ocean waves from radar observations, *Journal of Geophysical Research*, *113*(C2), https://doi.org/10.1029/2007jc004264.

Hauser, D., C. Tison, T. Amiot, L. Delaye, N. Corcoral, and P. Castillan (2017), SWIM: The First Spaceborne Wave Scatterometer, *IEEE Transactions on Geoscience and Remote Sensing*, *55*(5), 3000–3014, https://doi.org/10.1109/tgrs.2017.2658672.

Hauser, D., C. Tourain, L. Hermozo, D. Alraddawi, L. Aouf, B. Chapron, A. Dalphinet, L. Delaye, M. Dalila, E. Dormy, F. Gouillon, V. Gressani, A. Grouazel, G. Guitton, R. Husson, A. Mironov, A. Mouche, A. Ollivier, L. Oruba, F. Piras, R. R. Suquet, P. Schippers, C. Tison, and N. Tran (2021), New Observations From the SWIM Radar On-Board CFOSAT: Instrument Validation and Ocean Wave Measurement Assessment, *IEEE Transactions on Geoscience and Remote Sensing*, *59*(1), 5–26, https://doi.org/10.1109/tgrs.2020.2994372.

Karaev, V. Y., M. A. Panfilova, M. S. Ryabkova, Y. A. Titchenko, E. M. Meshkov, and X. Li (2021), Retrieval of the two-dimensional slope field by the SWIM spectrometer of the CFOSAT satellite: discussion of the algorithm, *Russian Journal of Earth Sciences*, *21*(6), 1–9, https://doi.org/10.2205/2021es000784.

Li, X., V. Karaev, M. Panfilova, B. Liu, Z. Wang, Y. Xu, J. Liu, and Y. He (2022a), Measurements of Total Sea Surface Mean Square Slope Field Based on SWIM Data, *IEEE Transactions on Geoscience and Remote Sensing*, *60*, 1–9, https://doi.org/10.1109/tgrs.2022.3174392.

Li, X., W. Lin, B. Liu, Z. Wang, B. Zhang, and Y. He (2022b), Sea Surface Wind Retrieval Using the Combined Scatterometer and Altimeter Backscatter Measurements of the HY-2B Satellite, *IEEE Transactions on Geoscience and Remote Sensing*, *60*, 1–12, https://doi.org/10.1109/tgrs.2021.3065663.

Lin, C.-C., M. Betto, M. B. Rivas, A. Stoffelen, and J. de Kloe (2012), EPS-SG Windscatterometer Concept Tradeoffs and Wind Retrieval Performance Assessment, *IEEE Transactions on Geoscience and Remote Sensing*, *50*(7), 2458–2472, https://doi.org/10.1109/tgrs.2011.2180393.

Masuko, H., K. Okamoto, M. Shimada, and S. Niwa (1986), Measurement of microwave backscattering signatures of the ocean surface using X-band and Ka-band airborne scatterometers, *Journal of Geophysical Research*, *91*(C11), 13,065, https://doi.org/10.1029/jc091ic11p13065.

Panfilova, M., V. Karaev, L. Mitnik, Y. Titchenko, M. Ryabkova, and E. Meshkov (2020), Advanced View at the Ocean Surface, *Journal of Geophysical Research: Oceans*, *125*(11), https://doi.org/10.1029/2020jc016531.

Valenzuela, G. R. (1978), Theories for the interaction of electromagnetic and oceanic waves – A review, *Boundary-Layer Meteorology*, *13*(1-4), 61–85, https://doi.org/10.1007/bf00913863.

Russian Journal of Earth Sciences

# Результаты совместной интерпретации гравитационного и теплового полей Уральского региона

**П. С. Мартышко*,[1], И. В. Ладовский[1], Д. Д. Бызов[1]**

[1]Институт геофизики им. Ю. П. Булашевича УрО РАН, Екатеринбург, Россия
* **Контакт:** П. С. Мартышко, pmart3@mail.ru

Реализован метод решения задач сопряжения для уравнения Пуассона, позволяющий интерпретировать потенциальные поля (гравитационное и стационарное тепловое) на основе унифицированных сеточных алгоритмов. Разработан численный алгоритм пересчета мантийной составляющей теплового потока от уровня земной поверхности к границе «кора–мантия» через неоднородную по теплопроводности слоистую среду. В измеренные значения градиента температуры и теплового потока для северных территорий введены палеоклиматические поправки. В осевой части Уральской геосинклинали удалось исключить отрицательную депрессию мантийной составляющей теплового потока, полученную по результатам геотермического моделирования; учет плейстоцен-голоценового потепления предшествующего межледникового палеоклиматического цикла приводит к положительным значениям теплового потока, пересчитанного на границу «кора–мантия». Показано, что использование данных о тепловом потоке позволяет значительно повысить геологическую информативность гравитационного моделирования.

**Ключевые слова:** Стационарный тепловой поток, кусочно-однородная слоистая среда, условия теплового сопряжения, интегральная формула Грина, разделение потока на составляющие от источников земной коры и верхней мантии

**Цитирование:** Мартышко, П. С., Ладовский И. В., Бызов Д. Д. Результаты совместной интерпретации гравитационного и теплового полей Уральского региона // Russian Journal of Earth Sciences. — 2023. — Т. 23. — ES5002. — DOI: 10.2205/2023es000855 — EDN: HEETEZ

## Введение

Интерпретация тепловых полей и ее геолого-геофизическая информативность проявляется в сопоставлении расчетных и «наблюденных» значений тепловых потоков, редуцированных на верхнюю изотермическую граничную плоскость «нейтрального» слоя. Накопленный массив данных о поверхностных тепловых потоках и сопутствующий им картографический материал находятся в открытом доступе и могут использоваться для всестороннего геотермического анализа, с возможностью виртуальной корректировки при сопоставлении с результатами математического моделирования.

Методическая часть настоящей работы подразумевает совместную количественную интерпретацию тепловых и гравитационных полей с практической целью: рассчитать для территории Полярного и Приполярного Урала мантийную составляющую глубинного теплового потока и увязать характер ее распределения с особенностями тектонического строения нижних горизонтов земной коры.

Геотермическая модель верхней части неоднородной литосферы рассчитывается на сеточном шаблоне трехмерного распределения плотности [*Martyshko et al.*, 2019]. Ее размеры соответствуют трехмерной плотностной модели, построенной в пределах градусной трапеции 60°–68° с.ш., 48°–72° в.д. до глубины 80 км. Трехмерные распределения теплофизических параметров (теплогенерации и теплопроводности) пересчитываются по базе послойных сеточных матриц плотности $\rho_k(x,y)$ и данных

https://elibrary.ru/heetez

Получено: 19 апреля 2023 г.
Принято: 3 июля 2023 г.
Опубликовано: 25 декабря 2023 г.

© 2023. Коллектив авторов.

статистической зависимости «плотность – теплогенерация» и «плотность – теплопроводность». Их конфигурация образует пространственные формы, соответствующие блочной структуре распределения источников теплогенерации $Q_k(x,y)$ в земной коре и послойному распределению коэффициента теплопроводности $\lambda_k(x,y)$ в коре и мантии [*Ladovskii et al.*, 2020].

**Основные формулы аналитического алгоритма**

Методы количественной интерпретации стационарных тепловых и гравитационных полей, которые описываются уравнением Пуассона, очень близки. Коэффициенты (и свободные члены) соответствующих уравнений аппроксимируются распределением плотностных и теплофизических параметров неоднородной среды. В задаче гравиметрии не предусмотрена явная постановка граничных условий, кроме асимптотических. В связи с чем, ее решение записывается напрямую в виде интеграла Пуассона по области сосредоточения аномальных масс.

В геотермических моделях стационарных температур в решении необходимо учитывать два типа граничных условий. Это односторонние условия Дирихле–Неймана на внешних границах слоисто-неоднородного пласта и двусторонние условия теплового сопряжения на его внутренних границах. В практике применения мы разделили внутренние и внешние граничные условия и разработали новый аналитический метод решения задачи теплового сопряжения, как граничной задачи теории потенциала. В результате был построен алгоритм расчетов, близкий по технологии к вычислительным схемам количественной интерпретации гравитационных аномалий.

*Геометрия математической модели*

Определим метрические и теплофизические параметры геотермической модели слоистой среды с кусочно-однородным распределением коэффициента теплопроводности $\lambda$ и интегрируемой функцией тепловых источников $Q$. Модельная (расчетная) область $D$ представляет собой пласт бесконечного простирания мощности $H$ с горизонтальными границами внешнего обрамления. В системе прямоугольных координат $(X) = (x,y,z)$ горизонтальная плоскость $(x,0,y)$ совпадает с верхней граничной плоскостью, ось $(0,z)$ направлена вертикально вниз по глубине пласта. Верхняя граница $S_0 : (z = 0)$ условно принята за уровень земной поверхности, точнее за изотермическую граничную плоскость в «нейтральном» слое; нижняя граница $S_H : (\ z = H)$ – вспомогательная адиабатическая плоскость задания внешней (восходящей) составляющей глубинного теплового потока. Внутренние граничные поверхности $S_k : (z = z_k(x,y))$; $(k = 1\ \ldots\ M)$ разделяют область $D$ на $(M+1)$ криволинейных слоев. Выше границы $S_k$ теплопроводность постоянна и равна $\lambda_k$; ниже равна $\lambda_{k+1}$. Из семейства внутренних контактных границ особо выделена граница $S_M : (z = z_M(x,y))$ – граница раздела «кора–мантия» («$M$», или поверхность Мохо). Выше границы «$M$», т.е. только в земной коре, сосредоточены эндогенные источники тепла $Q_k$; их плотность $Q(X) = \bigcup_{(k)} Q_k$ предполагается интегрируемой.

*Редукция условий теплового сопряжения*

Принцип редукции Дюамеля предписывает включение граничных условий в операторную часть дифференциального уравнения [*Тихонов и Самарский*, 1999]. В его основе лежит функциональное представление разрывного коэффициента обратной теплопроводности слоистой среды с последующим переходом к дифференциальным операциям в континуальном пространстве обобщенных функций.

Обобщенно-непрерывный оператор для уравнения теплопроводности с разрывными коэффициентами порождает уравнение Пуассона с двумя типами источников в его правой части:

$$\nabla^2 T = -\nabla\left(\frac{1}{\hat{\lambda}}\right)\cdot \boldsymbol{q} - \left(\frac{1}{\hat{\lambda}}\cdot Q\right). \qquad (1)$$

Объемные источники $\left[Q(X)/\hat{\lambda}(X)\right]$ – источники первичного поля для модели слоисто-неоднородного пласта; поверхностные источники $\left[\nabla\left(1/\hat{\lambda}\right)\cdot\boldsymbol{q}\right]$ – это вторичные источники эквивалентного простого слоя, с подлежащей определению поверхностной плотностью.

Разрыв функции обратной теплопроводности слоистой среды преобразует градиентный член в уравнении (1) в формат источников эквивалентного простого слоя:

$$\nu_k(S_k) = -\boldsymbol{N}_k\cdot\left(\frac{\boldsymbol{q}}{\lambda_{k+1}} - \frac{\boldsymbol{q}}{\lambda_k}\right) = \boldsymbol{N}_k\cdot(\nabla T_{k+1} - \nabla T_k) = 2\varepsilon_k(\boldsymbol{N}_k\cdot\nabla T). \tag{2}$$

Здесь $(\boldsymbol{N}_k\cdot\nabla T)$ – прямое значение нормальной составляющей градиента температуры на поверхности $S_k$, равное полусумме Дирихле его лево- и правосторонних значений; $\varepsilon_k$ –параметр теплопроводной контрастности $k$-го и $(k+1)$-го сопредельных слоев:

$$2\boldsymbol{N}_k\cdot\nabla T = \boldsymbol{N}_k(\nabla T_{k+1} + \nabla T_k); \qquad \varepsilon_k = (\lambda_k - \lambda_{k+1})/(\lambda_k + \lambda_{k+1}).$$

Двусторонние условия теплового сопряжения в формате простого слоя (2) заложены в обобщенно непрерывный оператор редуцированного уравнения теплопроводности (1):

$$\nabla^2 T - \sum_{k=1}^{M}\nu_k(S_k)\cdot\|\nabla\Phi_k\|\cdot\delta(\Phi_k) + \frac{Q(X)}{\lambda(X)} = 0, \tag{3}$$

где $\nabla\Phi_k$ – градиент уравнения границы. Для замыкания области решения уравнения (3) достаточно постановки односторонних условий на внешних границах $S_0$ и $S_H$ неоднородного пласта:

$$T(X)\Big|_{X\in S_0} = \theta(S_0);\ \left(\boldsymbol{N}_{S_H}\cdot\nabla T\right)\Big|_{X\in S_H} = \mu(S_H). \tag{4}$$

Здесь $\theta(S_0) = \theta_0$ – постоянная температура на верхней границе пласта $(S_0 : z = 0)$; $\mu(S_H)$ – геотермический градиент на его нижней границе $(S_H : z = H)$.

Стационарность краевого режима обеспечивает верхнее граничное условие постоянства температуры (внутренняя задача Дирихле) и нижнее – по восходящему глубинному тепловому потоку (внутренняя задача Неймана). Условие Неймана опосредованно учитывает стационарный теплообмен на границе «кора–мантия». Если температура в «нейтральном слое» равна нулю, а поток тепла через нижнюю границу пласта отсутствует, то смешанные условия внутренней краевой задачи становятся однородными.

*Интегральная формула задачи сопряжения для слоистого пласта*

Совокупность интегральных преобразований свертки редуцированного уравнения (3) образует линейное подпространство обобщенных функций. Ядром преобразования является функция Грина, структура и вид которой находятся из граничных условий (4) однородной задачи Дирихле–Неймана.

Пусть $A(X)$ – параметрическая точка вычисления поля внутри пласта, $C(X)$– точка локализации источников и $P_k(X)$ – точка на контактной поверхности $S_k$. Функция Грина $G(A,C)$ приравнивается к потенциалу точечного источника внутри однородного пласта с однородными граничными условиями Дирихле–Неймана на его замкнутой внешней поверхности $S_0\cup S_H$. Выполнив преобразования, предписанные интегральной формулой Грина [*Владимиров и Жаринов*, 2000; *Тихонов и Самарский*, 1999], выделим из общего решения две составляющие для температуры. Это потенциал первичного поля тепловых источников и вторичный потенциал источников простого слоя [*Ladovskii et al.*, 2020]:

$$T(A) = W(A) - \frac{1}{4\pi}\sum_{k=1}^{M}\iint_{S_k}\nu_k(S_k)G(A,P_k)dS_k. \tag{5}$$

Здесь $W(A)$ – аддитивное решение для температуры в «грави-термическом» приближении, заданное суммой внутренних $Q/\lambda$ (коровых) и внешних $\mu(H)$ (мантийных) источников теплового поля:

$$W(A) = \theta_0 + \frac{1}{4\pi}\iiint\limits_D \frac{Q(C)}{\lambda(C)} G(A,C)d\tau_C + \frac{1}{4\pi}\iint\limits_{S_H} \mu(P_H)G(A,\ P_H)dS_H. \tag{6}$$

Неизвестные плотности простых слоев $\nu_k(S_k)$ для вторичной составляющей потенциала (5) можно найти из системы интегральных уравнений (2). В приближении малого контраста теплопроводностей сопредельных слоев систему уравнений (2) заменяет список интегральных формул:

$$\nu_k(S_k) = 2\varepsilon_k\left(\boldsymbol{N}_k \cdot \nabla_{P_k}\right)W(P_k). \tag{7}$$

Неявное решение для температуры (5) в линейном по $\epsilon$ приближении (7) принимает тот же вид интегральной свертки с аддитивной структурой, что и первичный потенциал (6):

$$T(A) = \frac{1}{4\pi}\iiint\limits_D \frac{Q(\tau_C)}{\lambda(\tau_C)} K(A,C)dV_C + \frac{1}{4\pi}\iint\limits_{S_H} \mu(P_H)K(A,P_H)dS_H. \tag{8}$$

Но в отличие от функции Грина $G(A,C)$ для однородного пласта, ядро $k(A,C)$ преобразующего оператора (10) учитывает рефракцию теплового поля на всех внутренних границах слоистого пласта:

$$K(A,C) = G(A,C) - \frac{1}{2\pi}\sum_{k=1}^{M}\varepsilon_k \iint\limits_{S_k} G(A,P_k)\cdot\left(\boldsymbol{N}_k \cdot \nabla_{P_k}\right)G(P_k,C)dS_{P_k}. \tag{9}$$

При небольших контрастах теплопроводности слоев (для литологических разностей горных пород относительная теплопроводность не более 1,1–1,5 ед.) модельные тепловые поля, как и гравитационные, удовлетворяют общему принципу суперпозиции. Это позволяет из общего решения задачи для температур и тепловых потоков выделить эндогенные аномалии от тепловых источников в земной коре и рефрагированные аномалии глубинного (мантийного) теплового потока.

*Модельный тепловой поток*

В работе [*Ladovskii et al.*, 2020] предложен детерминированный и наглядный способ вычисления глубинной составляющей теплового потока на границе «кора–мантия». Способ основан на решении обратной задачи аналитического продолжения тепловых полей с граничного уровня земной поверхности на требуемую глубину. Тепловой поток, вычисленный на земной поверхности (в плоскости «нейтрального слоя»), служит искомой функцией в прямой задаче геотермии; с ней сопоставляется вертикальная составляющая наблюденного потока.

Восходящая составляющая теплового потока на поверхности $S_i$ анти направлена к оси глубин; ее знак считается положительным:

$$q(A_i) = -(\boldsymbol{N}_i \cdot \boldsymbol{q}(A_i)) = +\lambda_i\left(\boldsymbol{N}_i \cdot \nabla_{A_i}\right)T(A_i).$$

На земной поверхности $S_0 : A_i = A_0(x,y,0)$. При этом оператор поверхностного градиента температуры вычисляется из предельного соотношения:

$$\left(\boldsymbol{N}_i \cdot \nabla_{A_i}\right)T(A_i)\Big|_{z_{Ai} \to 0} = \left(\boldsymbol{N}_0 \cdot \nabla_{A_0}\right)T(A_0).$$

Как и в формуле для температуры (8), суммарный тепловой поток разделяется на составляющие от источников радиогенной теплогенерации $Q$ в земной коре и от поверхностных источников $\mu$ с подошвы мантийного слоя, $q(A_0) = q_Q(A_0) + q_\mu(A_0)$:

$$q_Q(A_0) = \frac{\lambda_1}{4\pi}\left(\boldsymbol{N}_0 \cdot \nabla_{A_0}\right) \iiint\limits_D \frac{Q(C)}{\lambda(C)} K(A_0, C) dV_C, \tag{10}$$

$$q_\mu(A_0) = \frac{\lambda_1}{4\pi}\left(\boldsymbol{N}_0 \cdot \nabla_{A_0}\right) \iint\limits_{S_H} \mu(P_H) K(A_0, P_H) dS_H. \tag{11}$$

Вертикальная производная контактной функции Грина $K'_z(A_0, C) = K'_z(0, C)$ является ядром интегральной формулы прямой задачи для расчета поверхностного теплового потока (10) от источников земной коры; примем ее за коровую составляющую потока. Производная $K'_z(A_0, P_H) = K'_z(0, H)$ входит в ядро интегрального оператора (11) для вычисления мантийной составляющей поверхностного потока на верхней граничной плоскости. На нижней граничной плоскости $z = H$ восходящий тепловой поток $q_\mu(H) = \lambda_{M+1} \cdot \mu(P_H)$ не является известной функцией. Но «след» этой функции однозначно проявляется в решении для верхней границы пласта – плоскости, на которой заданы редуцированные значения «наблюденного» теплового потока. Разность между «наблюденным» и модельным тепловым потоком от источников теплогенерации в земной коре приравнена к целевой функции подбора обратной задачи аналитического продолжения гармонических функций. Полагая $q_Q(A_0) + q_\mu(A_0) = q_{\text{observ}}$, получаем интегральное уравнение относительно граничной составляющей глубинного теплового потока:

$$q_\mu(A_0) = q_{\text{observ}} - q_Q(A_0) = \frac{1}{4\pi} \cdot \frac{\lambda_1}{\lambda_{M+1}}\left(\boldsymbol{N}_0 \cdot \nabla_{A_0}\right) \iint\limits_{S_H} K(A_0, P_H)\ q_\mu(P_H) dS_H. \tag{12}$$

Правая часть выражения (12) является интегральным оператором типа свертки прямого пересчета поля $q_\mu(P_H)$ с уровня $z = H$ «на высоту» $z = 0$. Инверсия интегрального оператора (12) дает решение обратной задачи аналитического продолжения мантийной составляющей теплового потока через слоисто-неоднородную среду с уровня земной поверхности на нижнюю граничную плоскость $z = H$. Последующий пересчет поля $q_\mu(P_H)$ вверх на криволинейную границу $z = z_M(x, y)$, $A_M = A(x, y, z_M)$, реализуется (как решение прямой задачи) по аналогу интегральной формулы (11):

$$q_\mu(A_M) = = \frac{1}{4\pi} \cdot \frac{\lambda_M}{\lambda_{M+1}}\left(\boldsymbol{N}_M \cdot \nabla_{A_M}\right) \iint\limits_{S_H} K(A_M, P_H) q_\mu(P_H) dS_H. \tag{13}$$

Формулы пересчета (11)–(13) позволяют исключить граничное условие Неймана по тепловому потоку из решения прямой задачи и выразить поток $q_\mu(A_M)$ на кровле верхней мантии через его значение $q_\mu(A_0)$ на поверхности Земли.

**Выбор соотношения плотность–теплогенерация**

Как правило, в литературе эмпирическое соотношение между плотностью и теплогенерацией задано в виде таблиц (или графиков) с указанием пределов возможных погрешностей. Маркеры точек представляют из себя «крест» интервальных погрешностей. Средняя точка интервалов принимается за интерпретируемые значения. Вариация обоих параметров значительная (по факту, она может достигать 50%). Соответственно, вычисленные значения потоков по «облаку» исходных данных могут отличаться более чем в два раза. Это объективная информация, и без предварительной фильтрации эмпирических значений плотности и теплогенерации нельзя подходить к практическим задачам «термо-плотностного» моделирования.

Для различных геологических провинций и тектонических структур (на континентах) облако точек физических параметров и их статистические зависимости будут разные. В качестве демонстрационного примера мы привели данные ВСЕГЕИ по Балтийскому щиту (см. рис. 1). Этот графический материал приводится без ссылки на источник, так как получен нами из устного сообщения в середине 90-х годов прошлого века.

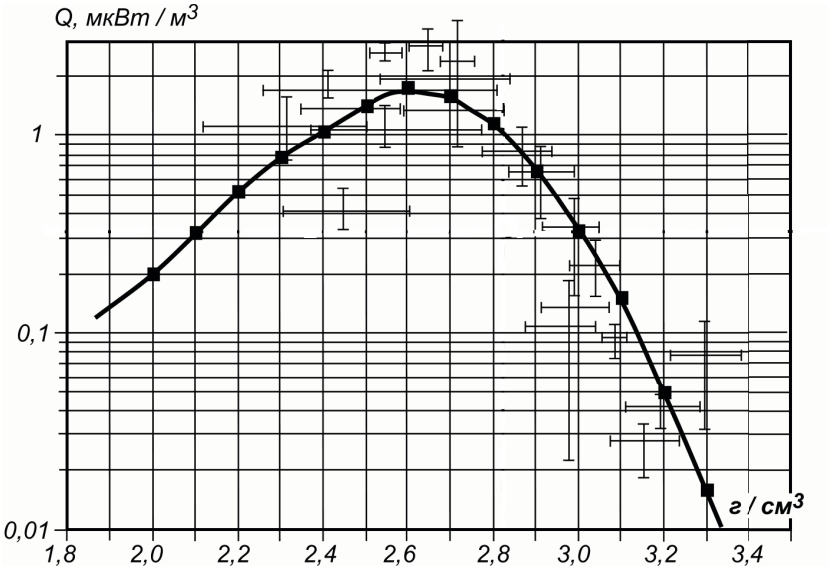


**Рис. 1.** Сглаженное распределение «плотность–теплогенерация» с указанием интервала абсолютных погрешностей в некоторых точках.

Аналогичные, в том числе и мировые, данные можно найти в работах Артемьевой [*Artemieva*, 2009; *Artemieva and Mooney*, 2001], Хуторского [*Khutorskoi and Polyak*, 2016], Гордиенко и Павленковой [*Gordienko and Pavlenkova*, 1985], Кутаса [*Кутас*, 2014; *Кутас и Гордиенко*, 1971], Хачая [*Хачай и Дружинин*, 1996], Кукконена [*Kukkonen et al.*, 1997], Сальникова [*Сальников*, 1984] Голованової [*Голованова*, 2005], Щапова [*Щапов*, 2000; *Щапов и др.*, 2004], Дучкова [*Дучков и Соколова*, 1997], Crough и Thompson [*Crough and Thompson*, 1976] и многих других. Самые ценные данные, на наш взгляд, получены «in situ» по результатам плотностного и спектрометрического каротажа скважин и на образцах горных пород. Данные получены при перекрестной компиляции материалов из указанных статей.

Другой путь – поиск опосредованных связей между теплофизическими параметрами и скоростью распространения сейсмических волн. Здесь следует обратить внимание на пионерские работы Гордиенко и Павленковой [*Gordienko and Pavlenkova*, 1985]. Модельная плотность верифицируется по гравитационному полю; скорости распространения продольных и поперечных волн берутся с разрезов по профилям ГСЗ. Связь «скорость–плотность» аппроксимируется кусочно-линейной функцией. Ее параметры определяются из уравнений регрессии по скоростным интервалам.

Первоначально необходимый этап – построение объемной плотностной модели с использованием сейсмических профилей. Мы использовали данные по Уральскому региону, ориентируясь на работы Кашубина и Дружинина. Использовались данные Баженовской геофизической экспедиции и, частично, фрагменты геотраверсов центра «ГЕОН». По каждому из разрезов решалась линейная обратная задача гравиметрии с целью уточнения величин регрессионных коэффициентов. После чего моделировалось трехмерное распределение плотности в земной коре и верхней мантии. По алгоритму нашей методики [*Martyshko et al.*, 2021] сеточное решение обратной задачи гравиметрии будет единственным. При этом есть основание предполагать, что суммарные погрешности в массиве данных «скорость–плотность» для промежуточной плотностной модели можно не учитывать, поскольку расчетное гравитационное поле совпадает

с наблюденным. Этот умозрительный критерий тестового примера вполне достаточен с физической точки зрения.

Подобранное трехмерное распределение плотности было использовано для пересчета в теплофизические параметры и построения стационарной тепловой модели земной коры. По возможности данные выборки следует приурочить к региону исследований. Для Урала мы использовали обобщающее распределение Ю. П. Булашевича [*Булашевич*, 1983; *Булашевич и Щапов*, 1983], с ориентировкой на фактические данные Щапова [*Щапов*, 2000; *Щапов и др.*, 2004] и Голованової [*Голованова*, 2005]. Отдельные элементы выборки теплофизических параметров и фрагменты трехмерной тепловой модели были сопоставлены с результатами геотермического моделирования по южным уральским профилям «Гранит» и «Троицкий» [*Хачай и Дружинин*, 1996; *Kukkonen et al.*, 1997].

Последовательная связь «теплогенерация–плотность–скорость» применяется в теоретических расчетах при построении региональных геотермических моделей по сейсмическим профилям. Обычно сравниваются две зависимости, принятые для вулканогенных и метаморфических пород [*Cermak et al.*, 1990; *Gordienko and Pavlenkova*, 1985]. Первая – это зависимость Рибаха, составленная по мировым данным [*Rybach and Buntebarth*, 1982]; вторая – зависимость Гордиенко для Украинского щита [*Гордиенко*, 1980]. Они изменяются от наибольших значений, характерных для пород гранитного состава, до минимальных величин, отличающих ультраосновные породы. Нисходящий тренд этих зависимостей разный, и, если допустить, что они построены по выборкам стохастических переменных, то тогда наиболее вероятной оценкой этих распределений будет «среднее». Такое среднее мы выбрали для пород Уральского региона [*Булашевич*, 1983]. На рис. 2 нанесены три рассмотренных типа теоретических зависимостей «теплогенерация–плотность» в сопоставлении со сглаженными экспериментальными данными ВСЕГЕИ.

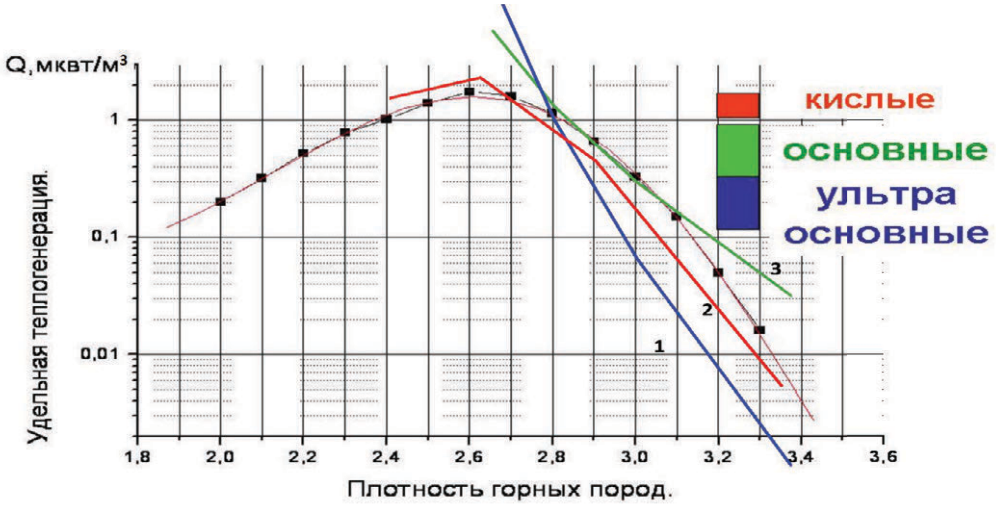


**Рис. 2.** Модельные зависимости «теплогенерация–плотность»: 1 – зависимость Рибаха по мировым данным; 2 – зависимость Булашевича для уральских пород; 3 – зависимость Гордиенко для Украинского щита. Для сравнения квадратными маркерами обозначены данные ВСЕГЕИ для Балтийского щита.

По петрологической коллекции горных пород различной основности и вещественного состава были проанализированы интервальные значения теплогенерации и их абсолютные погрешности (относительные – не менее 50%). Сводные данные по образцам пород Южно-Уральского региона приведены в работе [*Голованова*, 2005] и изображены на рис. 3 (логарифмический масштаб).

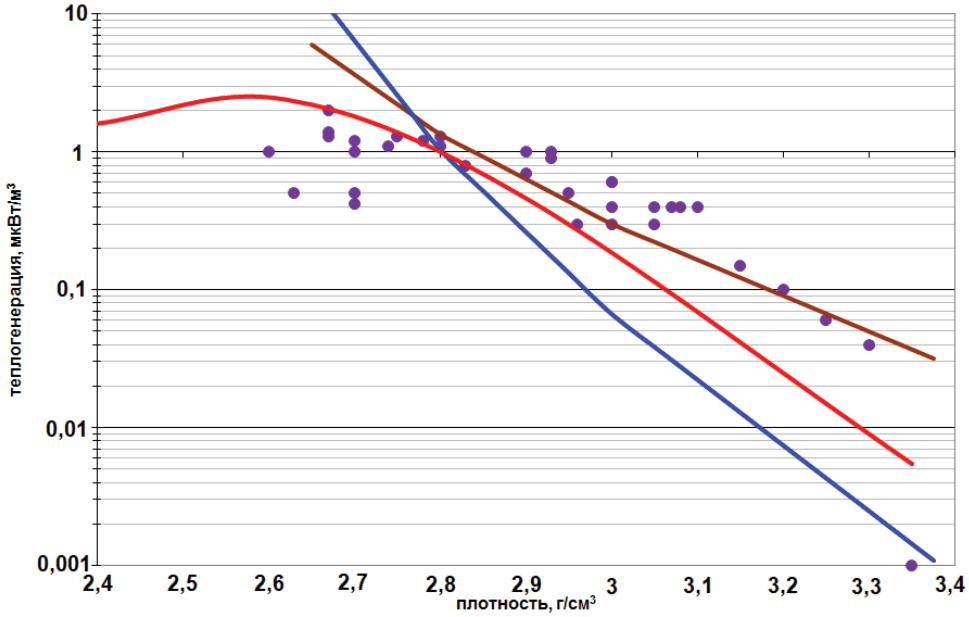


**Рис. 3.** Модельные зависимости «теплогенерация–плотность»: 1 – зависимость Рибаха по мировым данным; 2 – зависимость Булашевича для уральских пород; 3 – зависимость Гордиенко для Украинского щита. Здесь же круглыми маркерами обозначены данные фактических измерений для Южно-Уральского региона [*Голованова*, 2005].

Для выборки на рис. 3 выбран постоянный 50% интервал относительной погрешности. В том же интервале будет меняться коровый тепловой поток. Например, при постоянной погрешности Δ см. формулу (10):

$$\frac{\lambda_1}{4\pi}\iiint\limits_D \frac{Q(C)(1+\Delta)}{\lambda(C)} K'_z(A_0, C)dV_C = (1+\Delta)q_Q(A_0).$$

Мы не располагаем образцом трехмерной геотермической модели, относительно которой могли бы верифицировать наши вычисления. Относительная погрешность в измеренной теплогенерации 50% дает либо «горячую», либо «холодную» кору. При этом есть два ограничивающих момента: коровый тепловой поток не может превышать наблюденный («горячая» кора); для всех геологических провинций в пределах указанной территории соотношение между коровым и мантийным потоком («холодная» кора) должно соответствовать оценкам потоков в простейшем случае одномерной модели. В процессе наших вычислений мы строго придерживались этих двух принципов.

**Поверхностный тепловой поток. Палеоклиматическая редукция**

Приповерхностный тепловой поток вычислен авторами по результатам измерений температуры и теплопроводности в параметрических (или разведочных) скважинах глубокого бурения и привязан к разреженной градусной сети геотермических пикетов. Выборка экспериментальных данных для Северного и Приполярного Урала получена по результатам скважинных геотермических исследований В. А. Щапова и существенно дополнена сходными данными И. В. Головановой и А. Д. Дучкова [*Голованова*, 2005; *Дучков и др.*, 1997; *Щапов*, 2000]. «Наблюдённые» 234 значения теплового потока (точнее, вычисленные по значениям поинтервально-усредненных геотермических градиентов и теплопроводностей образцов керна) пересчитаны на регулярную сетку 11 зоны картографической проекции Гаусса – Крюгера с шагом $(10\times10)$ км$^2$. Соответствующая карта в изолиниях, скомпонованная в виде трехмерной поверхности, изображена на рис. 4а.

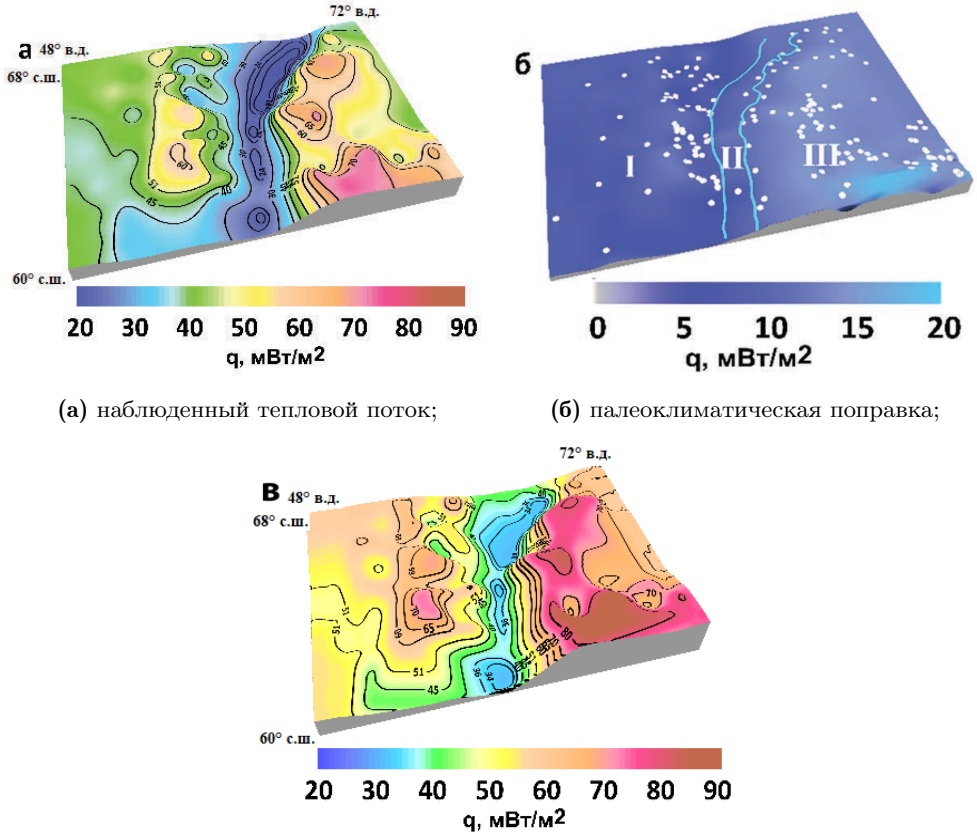


**(а)** наблюденный тепловой поток; **(б)** палеоклиматическая поправка;

**(в)** редуцированный тепловой поток.

**Рис. 4.** Карта редуцированных значений теплового потока для северных территорий.

Изменение температуры земной поверхности в процессе чередования палеоклиматических циклов искажают геотермический градиент (и тепловой поток) по стволу скважины [*Голованова и др.*, 2008]. Вековые колебания температуры проникают ниже «нейтрального слоя» и захватывают типичные по глубине области геотермического каротажа. Наиболее значительные вариации температурного градиента вызваны вюрм-голоценовым потеплением (около 10 000 лет назад), его влияние распространяется до первых километров по глубине. Малый ледниковый период (150–600 лет назад) оказывает влияние на распределение градиента в верхних 400–500 м. В результате геотермический градиент, следовательно, и тепловой поток в этом интервале оказываются пониженными [*Голованова и др.*, 2014]. Поправки за влияние палеоклимата в измеренный тепловой поток в изучаемом регионе введены на основе «Каталога данных по тепловому потоку Урала» [*Голованова*, 2005]. Все результаты объединены в три группы с учетом геолого-тектонического строения региона; по ним рассчитывались поправки в градиенты температуры, и (с учетом теплопроводности приповерхностного слоя) в тепловой поток (см. рис. 4б). Поправочные коэффициенты для Среднего Урала (отношение исправленного к измеренному потоку) мы сохранили и применили к геотермическим материалам для территории Северного и Приполярного Урала (трапеция 60°–68° с.ш., 48°–72° в.д.), по которым был составлен новый вариант карты теплового потока, исправленного за влияние палеоклимата (см. рис. 4в):

*Тепловой поток от источников в земной коре*

Прямая задача (10) вычисления поверхностной составляющей теплового потока при $z = 0$ исходит из распределения приведенной мощности $Q$: трехмерного распределения источников теплогенерации $Q$ и коэффициента теплопроводности $\lambda$ в земной коре. Производная контактной функции Грина $K'_z(0, C)$ полностью учитывает рефракцию теплового потока на всех внутренних границах неоднородного пласта. Поправки

в поток вводились в рамках модели трехслойной среды [*Martyshko et al.*, 2019]: чехол ($\lambda \approx 2$ Вт/(м·К)), кора ($\lambda \approx 2,6$ Вт/(м·К)), мантия ($\lambda \approx 4,2$ Вт/(м·К)).

В работе [*Ladovskii et al.*, 2020] приведен подробный алгоритм расчета интеграла (10) для прямой задачи посредством представления производной контактной функции $K'_z(0,C)$ в виде двойного ряда. Данный алгоритм был реализован авторами в программном обеспечении, позволяющем вести параллельные вычисления с использованием графических ускорителей NVidia. При выбранном числе элементов разбиения модели среды $256 \times 256 \times 50$ и с числом членов ряда $K'_z(0,C)$ $10 \times 10$ решение прямой задачи с использованием одного ускорителя NVidia Titan Black заняло чуть больше 4 часов.

Замена в интеграле (10) производной контактной функции $K'_z(0,C)$ на производную $G'_z(0,C)$ для однородного пласта соответствует решению задачи в гравитермическом приближении. В этом случае расчетный тепловой поток от источников в земной коре будет ниже, а время вычисления составит около 20 минут. На рис. 5 приведены оба варианта решения задачи.

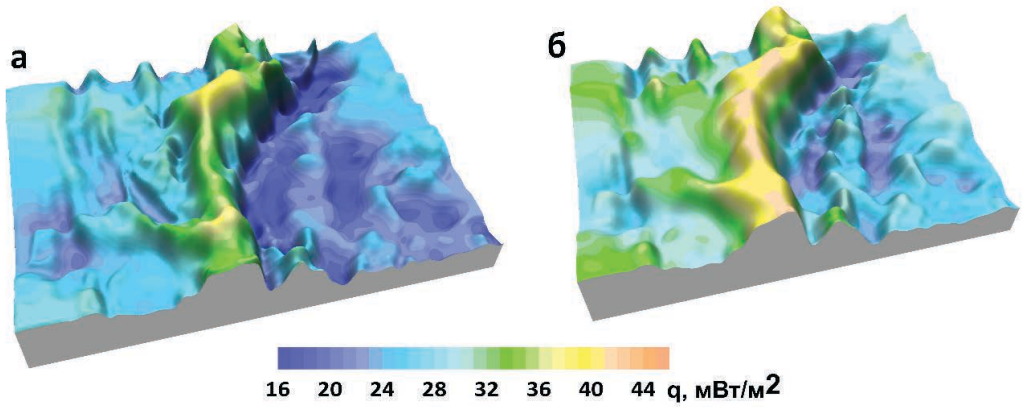


**Рис. 5.** Расчётные значения теплового потока для кристаллической коры и осадочного чехла в плоскости $z = 0$: а) – гравитермическое приближение для однородной модели; б) – то же, но для трёхслойной среды с учетом теплопроводной рефракции.

Поскольку границы раздела трехслойной среды заданы горизонтальными, то мы не наблюдаем значимого изменения морфологии расчетного теплового поля в варианте (б); меняется (увеличивается) только амплитуда рефрагированных аномалий.

Вклад мантийной составляющей (11) в поверхностный поток (12) равняется разности между редуцированными наблюденными (см. рис. 4в) и вычисленными значениями теплового потока (см. рис. 5). Эта разность показана на рис. 6, где светлыми полутонами выделена меридиональная зона отрицательных значений мантийной составляющей теплового потока.

Отношение мантийной составляющей и полного теплового потока на уровне верхней граничной плоскости ($z = 0$) можно интерпретировать как тектонический индикатор геотермического режима [*Gordienko and Pavlenkova*, 1985]. Для Восточно-Европейской и Тимано-Печерской платформ, Предуралья и западной части Уральской складчатой системы отношение потоков близко к нормальным значениям $\sim (30 \div 50)\%$. Для зоны Восточного Зауралья и примыкающей к ней части Западно-Сибирской плиты тектонический индикатор увеличивается до (50÷70)%, а для областей с аномально высокими значениями полного потока достигает $(80 \div 90)\%$. Как правило, это наблюдается в палеозойских обнажениях, перспективных на нефть и газ, постсинклинальных складчатых орогенах или по окраинам рифтовых зон, где восходящее течение флюидов привносит дополнительный вклад в суммарный тепловой поток.

Главный Уральский разлом приурочен к западному борту Уральской геосинклинали. Здесь низкий измеренный (и редуцированный) тепловой поток, малы коровая и мантийная составляющие, а тектонический фактор не превышает 20%. Как уникальная тектоническая провинция Уральская геосинклиналь разделяет западные и более

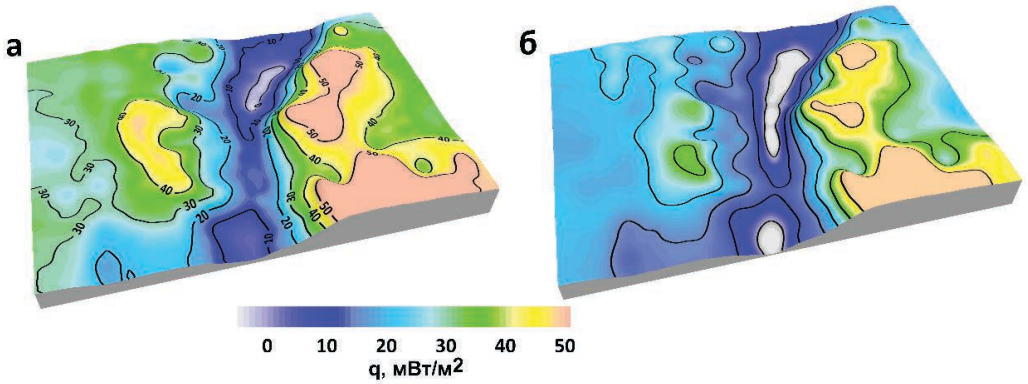


**Рис. 6.** Разностный тепловой поток в плоскости $z = 0$ (мантийная составляющая): а) – гравитермическое приближение для однородной модели; б) – то же, но для трёхслойной среды (чехол, кора, мантия) с учетом теплопроводной рефракции.

молодые восточные области по мантийному и суммарному тепловому потоку или же по их отношению. Депрессивная зона тепловых потоков четко выявляется в поле измеренных значений и при внесении поправок за влияние палеоклимата. Ее возникновение невозможно объяснить только изменением температуры поверхности Земли. Скорее всего, низкий редуцированный тепловой поток и незначительный вклад его составляющих (радиогенной + мантийной) связаны с особенностями глубинного строения и геологического развития региона, а основной причиной его аномальности служит низкая теплогенерация в Приуральском прогибе (Тагило-Магнитогорской зоне) [*Булашевич*, 1983; *Булашевич и Щапов*, 1978].

*Мантийная составляющая теплового потока*

Разделение общего теплового потока на коровую (см. рис. 5) и мантийную составляющие на верхней граничной плоскости (см. рис. 6) позволяет восстановить тепловой поток на глубинной границе «кора–мантия» и сопоставить его величину с распределением плотностных и сейсмических параметров в низах коры и верхней мантии.

Модельный тепловой поток (10) (прямая задача) от источников в земной коре вычислен в плоскости «нейтрального слоя» ($z = 0$); мантийная составляющая поверхностного потока (12) (обратная задача) приравнена к разности между наблюденным (редуцированным) полем и полем тепловых источников в земной коре. Инверсия интегрального оператора (12) дает решение обратной задачи аналитического продолжения для мантийной составляющей теплового потока через слоисто-неоднородную среду с уровня земной поверхности на глубину в направлении источников поля. Ядром преобразования пересчетов служит функция-отклик $K'_z(0,H)$ для модели трёхслойной среды, которая, по нашим оценкам, в полтора раза больше обычного ядра Пуассона $G'_z(0,H)$, включенного в модели пересчетов гравитационных полей (или тепловых потоков в «гравитермическом» приближении).

Аналитическое продолжение мантийной составляющей теплового потока на границу «кора–мантия» выполняется двумя этапами: сначала решается интегральное уравнение (12) обратной задачи относительно неизвестной составляющей потока на нижней граничной плоскости, а затем найденный глубинный поток пересчитывается по прямой интегральной формуле (13) на любую вышележащую поверхность. Последовательность пересчетов соответствует схеме $z = 0 \underset{\text{вниз}}{\longrightarrow} z = H \underset{\text{вверх}}{\longrightarrow} z_M(x,y)$. Оптимальный параметр регуляризации в задаче численного аналитического продолжения выбирается по критерию стационарности пересчета гармонических функций; он соответствует минимуму невязки исходного и пересчитанного поля с глубины $H$ на земную поверхность. Детали сеточного алгоритма последовательных пересчетов гравитационного поля «вверх–вниз» изложены в [*Martyshko et al.*, 2021]. Для теплового потока алгоритм

пересчета «вниз–вверх» (12)–(13) будет аналогичным. Мантийная составляющая теплового потока на верхней граничной плоскости и на глубинной границе «кора–мантия» показана на рис. 7:

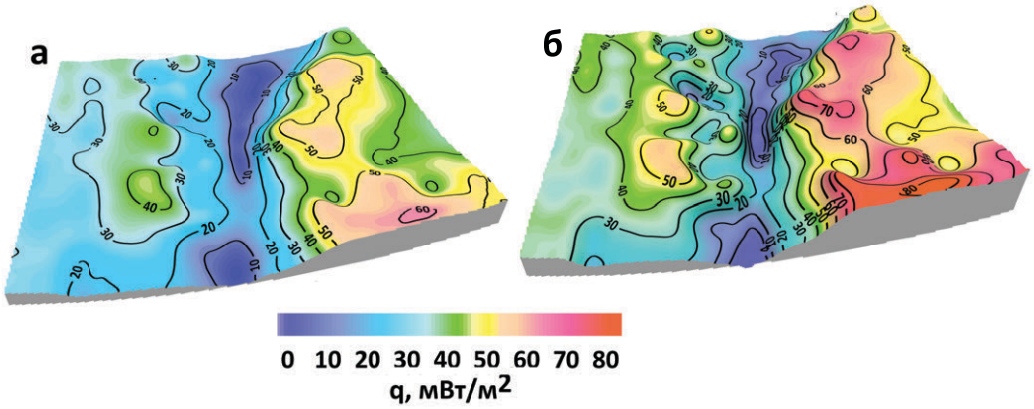


**Рис. 7.** Продолжение мантийной составляющей теплового потока с уровня земной поверхности на глубину границы «кора–мантия» при оптимальном параметре регуляризации: а) – мантийная составляющая потока на уровне верхней граничной плоскости $z = 0$; б) – то же на уровне границы раздела «кора–мантия» $z = z_M(x, y)$.

Для горизонтально-слоистой среды рельеф поля мантийного теплового потока на границе «кора–мантия» практически воспроизводит таковой на верхней граничной плоскости, но с большей амплитудой. Мантийная составляющая потока на верхней граничной плоскости при среднем значении 37,4 мВт/м$^2$ меняется в пределах от 5,5 мВт/м$^2$ в осевой части Уральской геосинклинали до 65,6 мВт/м$^2$ в полосе Широтного Приобья Западно-Сибирской плиты. Разброс значений теплового потока на границе Мохо шире. При среднем значении 40,44 мВт/м$^2$ диапазон изменений составляет от 0,5 мВт/м$^2$ до 82,2 мВт/м$^2$. Заметим, что повышенные значения расчётных тепловых потоков в мантии связаны с введением положительной поправки за палеоклиматическую редукцию (в среднем 24%) в наблюденное тепловое поле.

**Комплексирование геофизических полей**

Для осевой части геосинклинали Среднеуральского сегмента (Приуральский краевой прогиб) установлена тесная отрицательная (обратная) корреляционная связь между аномалиями гравитационного поля (Уральский супермаксимум) и экстремально низкими значениями измеренного теплового потока [*Булашевич*, 1983; *Булашевич и Щапов*, 1978; 1986]. Это следует из обратной зависимости между плотностью (основностью) пород кристаллического фундамента и их эндогенной теплогенерацией. При этом мантийная составляющая глубинного теплового потока исключается из схемы количественной интерпретации тепловых полей.

Подобная связь между аномалиями физических полей и вещественным составом горных пород установлена лишь для осевой части Приуральского краевого прогиба и не может рассматриваться как универсальная характеристика других геологических провинций. Например, для Приполярного и Северного сегментов складчатого Урала и его платформенного обрамления не обнаружена даже тенденция к обратной зависимости тепловых и гравитационных полей (см. рис. 8).

Плотностная модель литосферы северной части Уральской провинции построена до глубины 80 км – первого регионального уровня изостатической компенсации [*Martyshko et al.*, 2019]. Та же глубина принята и для геотермической модели стационарных тепловых полей. Интенсивные гравитационные аномалии в большей степени связаны с большим перепадом плотностей в осадочных отложениях и в верхней кристаллической коре до глубины 10–15 км. Аномалии теплового потока носят интегральный характер и создаются всей толщей земной коры и верхней мантии. Поэтому на поверхности Земли

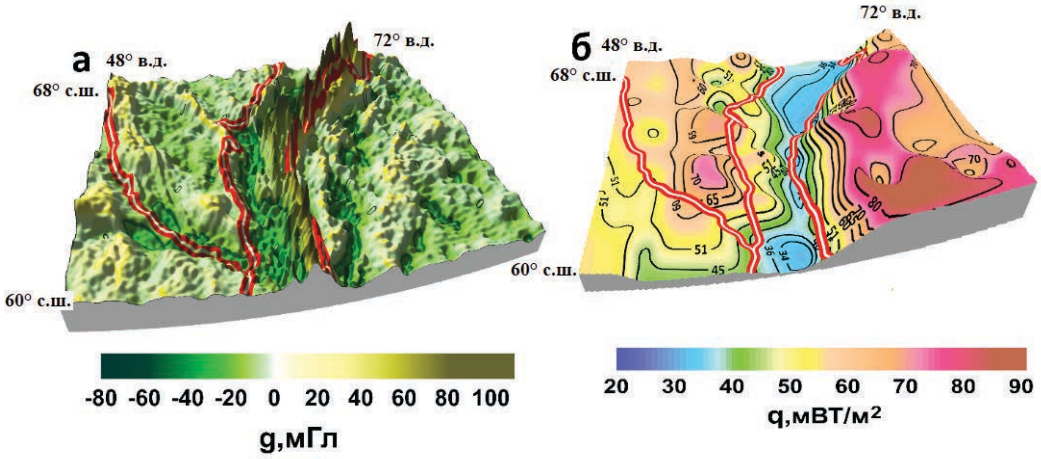


**Рис. 8.** Карта наблюденных аномалий гравитационного поля и редуцированного теплового потока для Северного и Приполярного Урала. Двойная красно-белая линия позиционирует тектонические границы надпорядковых структур [*Тектоническая карта России, сопредельных территорий и акваторий*, 2006]. Приуральский краевой прогиб приурочен к восточной части Уральской мегазоны ($\approx 60°$ в.д.).

практически не наблюдается какой-либо закономерной связи между гравитационными и тепловыми аномалиями. Облако точек стохастической зависимости, построенное по выборке исходных данных на сетке $10 \times 10$ км$^2$, не имеет явно выраженного тренда; коэффициент линейной обратной корреляции $r = -0{,}30$ не является значимым.

Коровая составляющая теплового потока рассчитывается по формуле (10) прямой задачи геотермии. Разность между наблюденными и коровыми значениями потока приравнивается к его мантийной составляющей на уровне дневной поверхности – поверхности «нейтрального слоя» (см. рис. 6). Аналитическое продолжение мантийной составляющей через слоисто-неоднородную среду с уровня земной поверхности на границу «кора–мантия» показано на (см. рис. 7).

Аномалии гравитационного и теплового поля, рассчитанные по отдельным слоям плотностной и геотермической моделей, имеют более тесную стохастическую зависимость. Так, для земной коры коэффициент обратной корреляции между тепловым потоком и гравитационным полем составляет $r = -0{,}69$ (см. рис. 9).

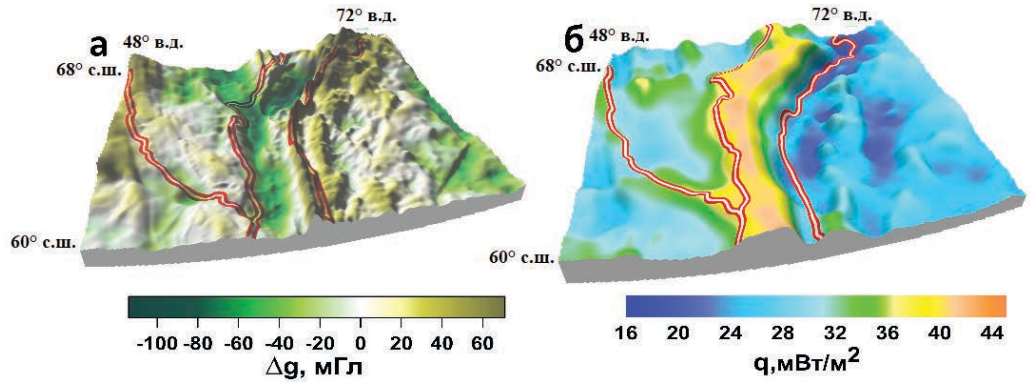


**Рис. 9.** Расчетные гравитационные аномалии (а) и величина теплового потока (б) для консолидированной коры и осадочного чехла палеозоя – мезокайнозоя.

Для мантии – коэффициент прямой корреляции мантийного потока с рельефом границы Мохо $r = +0{,}71$ (см. рис. 10).

Мантийная составляющая теплового потока по границе $M(x, y)$воспроизводит распределение граничных мантийных скоростей и по характеру своего изменения

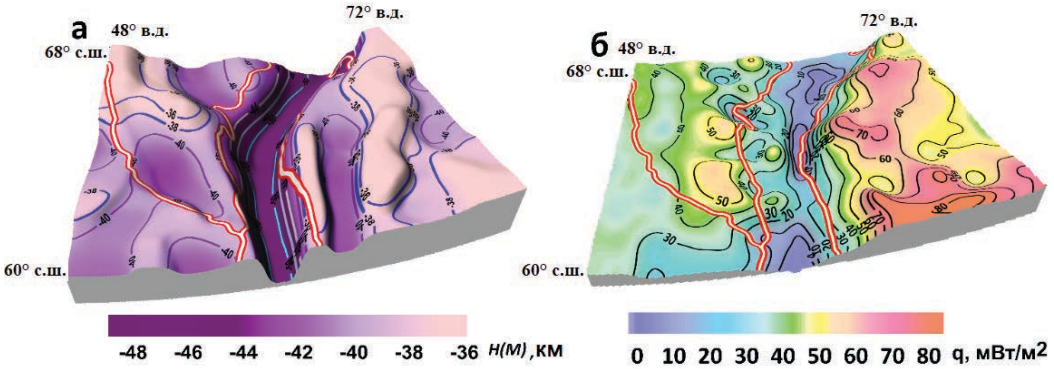


**Рис. 10.** Распределение граничных скоростей и рельеф кровли верхней мантии по данным ГСЗ – МОВЗ (а) и расчетное значение мантийной составляющей теплового потока (б). Теплопроводность мантии принята постоянной $\lambda = 4$ Вт/(м · К).

хорошо согласуется с формой рельефа мантийных структур. Коровая составляющая потока эндогенных тепловых источников, в общих чертах, повторяет морфологию гравитационных аномалий; мантийный тепловой поток хорошо согласуется с формой рельефа мантийных структур.

Гравитационные аномалии заданы с точностью до некоторой постоянной (или слабо переменной) составляющей регионального поля. По этой причине из решения обратной задачи гравиметрии находится лишь избыточная плотность. Плотность относимости региональной геофизической модели остается вариативным параметром. Использование данных о тепловом потоке может существенно повысить геологическую информативность гравитационного моделирования. Резко градиентная зависимость между плотностью пород земной коры (2,6–2,9 г/см$^3$) и их эффективной теплогенерацией (2,4–0,004 мкВт/м$^3$) позволяет уверенно разделить подобранную плотностную модель на структурные этажи различной тепловой активности и сопоставить послойные аномалии гравитационного поля с расчетными значениями теплового потока до глубины региональной границы Мохо.

Стохастическая связь тепловых, плотностных и сейсмических параметров позволяет сопоставлять поля различной эндогенной природы и верифицировать распределение порождающих их источников в земной коре и верхней мантии.

## Заключение

Предложен метод решения задач сопряжения для уравнения Пуассона, позволяющий интерпретировать на основе единых сеточных алгоритмов потенциальные поля (гравитационное и стационарное тепловое поле). На основе 3D подобранной плотностной модели было построено слоисто-блочное распределение теплофизических параметров земной коры по статистическим выборкам «плотность–теплопроводность» и «плотность–теплогенерация». Реализован сеточный параллельный алгоритм решения прямых и обратных задач стационарной теплопроводности для геотермических моделей слоисто-неоднородных сред. Проанализирована возможность применения аддитивных схем количественной интерпретации тепловых полей. Дана оценка вклада корового и мантийного теплового потока в общий энергетический баланс литосферы Уральского региона. Измеренный тепловой поток разделен на коровую и мантийную составляющие с последующим аналитическим продолжением последней на кровлю верхней мантии. В результате установлено, что коровая составляющая потока эндогенных тепловых источников в общих чертах повторяет морфологию гравитационных аномалий; мантийный тепловой поток хорошо согласуется с формой рельефа мантийных структур.

Уральская геосинклиналь характеризуется чрезвычайно низкими значениями наблюденного теплового потока. Теплопроводность геотермического разреза возрастает с глубиной, в силу чего рефракция теплового поля на внутренних границах разнотеплопроводных сред (земная кора + мантия) увеличивает расчетную величину коровой

составляющей потока и уменьшает величину мантийной составляющей вплоть до отрицательных значений. Показано, что учет плейстоцен-голоценового потепления предшествующего межледникового палеоклиматического цикла приводит к положительным значениям теплового потока, пересчитанного на границу «кора–мантия». На примере Урала показано, что использование результатов интерпретации тепловых данных позволяет более четко определять тектонические границы надпорядковых структур.

**Благодарности.** Работа выполнена в рамках государственного задания Института геофизики имени Ю. П. Булашевича УрО РАН.

**Список литературы**

Булашевич Ю. П. Информативность геотермии при изучении земной коры Уральской эвгеосинклинали // Известия Академии наук СССР. Серия Физика Земли. — 1983. — № 8. — С. 76—83.

Булашевич Ю. П., Щапов В. А. Геотермические особенности уральской геосинклинали // Доклады Академии наук СССР. — 1978. — Т. 243, № 3. — С. 715—718.

Булашевич Ю. П., Щапов В. А. Геотермическая характеристика Урала // Применение геотермии в региональных и поисково-разведочных исследованиях. — Свердловск : Академия наук СССР. Уральский научный центр, 1983. — С. 3—17.

Булашевич Ю. П., Щапов В. А. Геотермические особенности уральской геосинклинали // Доклады Академии наук СССР. — 1986. — Т. 290, № 1. — С. 173—176.

Владимиров В. С., Жаринов В. В. Уравнения математической физики. — Москва : Физматлит, 2000. — С. 400.

Голованова И. В. Тепловое поле Южного Урала. — Москва : Наука, 2005. — С. 190.

Голованова И. В., Пучков В. Н., Сальманова Р. Ю. *и др.* Новый вариант карты теплового потока Урала, построенный с учетом влияния палеоклимата // Доклады Академии наук. — 2008. — Т. 422, № 3. — С. 394—397. — DOI: 10.1134/S1028334X08070350.

Голованова И. В., Сальманова Р. Ю., Тагирова Ч. Д. Методика расчета глубинных температур с учетом исправленных на влияние палеоклимата значений теплового потока // Геология и геофизика. — 2014. — Т. 55, № 9. — С. 1426—1435. — DOI: 10.1016/j.rgg.2014.08.008.

Гордиенко В. В. Радиогенная теплогенерация в земной коре и тепловой поток из мантии древних платформ // Геофизический журнал. — 1980. — Т. 2, № 3. — С. 29—34.

Дучков А. Д., Соколова Л. С. Термическая структура литосферы Сибирской платформы // Геология и геофизика. — 1997. — Т. 38, № 2. — С. 494—503.

Дучков А. Д., Соколова Л. С., Аюнов Д. Е. Электронный геотермический атлас Сибири и Дальнего Востока // Интерэкспо ГЕО-СИБИРЬ. — 1997. — Т. 2, № 3. — С. 153—157.

Кутас Р. И. Тепловой поток и геотермические модели земной коры Украинских Карпат // Геофизический журнал. — 2014. — Т. 36, № 6. — С. 3—27.

Кутас Р. И., Гордиенко В. В. Тепловое поле Украины. — Киев : Наукова Думка, 1971.

Сальников В. Е. Геотермический режим Южного Урала. — Москва : Наука, 1984. — С. 88.

Тектоническая карта России, сопредельных территорий и акваторий / под ред. Е. Е. Милановского. — Москва : МГУ, 2006.

Тихонов А. Н., Самарский А. А. Уравнения математической физики. — Москва : Наука, 1999. — С. 979.

Хачай Ю. В., Дружинин В. С. Возможности применения геотермии для восстановления динамики переходной зоны мантии Урала // Глубинное строение и развитие Урала. — Екатеринбург : Наука, 1996. — С. 298—306.

Щапов В. А. Тепловое поле Урала // Уральский геофизический вестник. — 2000. — Т. 1. — С. 126—130.

Щапов В. А., Бурдин Ю. Б., Больщиков В. А. *и др.* Радиогенная теплогенерация пород Уральской эвгеосинклинали // Уральский геофизический вестник. — 2004. — № 6. — С. 116—121.

Artemieva I. M. The continental lithosphere: Reconciling thermal, seismic, and petrologic data // Lithos. — 2009. — Vol. 109, no. 1/2. — P. 23–46. — DOI: 10.1016/j.lithos.2008.09.015.

Artemieva I. M., Mooney W. D. Thermal thickness and evolution of Precambrian lithosphere: A global study // Journal of Geophysical Research: Solid Earth. — 2001. — Vol. 106, B8. — P. 16387–16414. — DOI: 10.1029/2000jb900439.

Cermak V., Bodri L., Rybach L., *et al.* Relationship between seismic velocity and heat production: comparison of two sets of data and test of validity // Earth and Planetary Science Letters. — 1990. — Vol. 99, no. 1/2. — P. 48–57. — DOI: 10.1016/0012-821x(90)90069-a.

Crough S. T., Thompson G. A. Thermal model of continental lithosphere // Journal of Geophysical Research. — 1976. — Vol. 81, no. 26. — P. 4857–4862. — DOI: 10.1029/jb081i026p04857.

Gordienko V. V., Pavlenkova N. I. Combined geothermal-geophysical models of the earth's crust and upper mantle for the European continent // Journal of Geodynamics. — 1985. — Vol. 4, no. 1–4. — P. 75–90. — DOI: 10.1016/0264-3707(85)90053-5.

Khutorskoi M. D., Polyak B. G. Role of radiogenic heat generation in surface heat flow formation // Geotectonics. — 2016. — Vol. 50, no. 2. — P. 179–195. — DOI: 10.1134/s0016852116020047.

Kukkonen I. T., Golovanova I. V., Khachay Y. V., *et al.* Low geothermal heat flow of the Urals fold belt - implication of low heat production, fluid circulation or palaeoclimate? // Tectonophysics. — 1997. — Vol. 276, no. 1–4. — P. 63–85. — DOI: 10.1016/s0040-1951(97)00048-6.

Ladovskii I. V., Martyshko P. S., Tsidaev A. G., *et al.* A Method for Quantitative Interpretation of Stationary Thermal Fields for Layered Media // Geosciences. — 2020. — Vol. 10, no. 5. — P. 199. — DOI: 10.3390/geosciences10050199.

Martyshko P., Ladovskii I., Byzov D. Parallel Algorithms for Solving Inverse Gravimetry Problems: Application for Earth's Crust Density Models Creation // Mathematics. — 2021. — Vol. 9, no. 22. — P. 2966. — DOI: 10.3390/math9222966.

Martyshko P. S., Ladovskii I. V., Byzov D. D., *et al.* On solutions of forward and inverse problem for potential geophysical fields: Gravity inversion for Urals region // Application of Mathematics in Technical and Natural Sciences: 11th International Conference for Promoting the Application of Mathematics in Technical and Natural Sciences - AMiTaNS'19. — AIP Publishing, 2019. — DOI: 10.1063/1.5130870.

Rybach L., Buntebarth G. Relationships between the petrophysical properties density, seismic velocity, heat generation, and mineralogical constitution // Earth and Planetary Science Letters. — 1982. — Vol. 57, no. 2. — P. 367–376. — DOI: 10.1016/0012-821x(82)90157-1.

Russian Journal of Earth Sciences

# Joint Interpretation Results of Gravitational and Thermal Fields for the Ural Region

**P. S. Martyshko**[**,1], **I. V. Ladovskii**[1], and **D. D. Byzov**[1]

[1]Institute of Geophysics named after Yu. P. Bulashevich Ural Branch of the Russian Academy of Sciences, Yekaterinburg, Russia
****Correspondence to:** P. S. Martyshko, pmart3@mail.ru

A method for solving conjugation problems for the Poisson equation is implemented, which makes it possible to interpret potential fields (gravitational and stationary thermal fields) based on unified grid algorithms. A numerical algorithm has been developed for recalculating the mantle component of the heat flow from the level of the earth's surface to the "crust–mantle" boundary through a layered medium inhomogeneous in thermal conductivity. Paleoclimate corrections were introduced into the measured values of the temperature gradient and heat flux for the northern territories. In the axial part of the Ural geosyncline, it was possible to exclude the negative depression of the mantle component of the heat flow, obtained from the results of geothermal modeling; taking into account the Pleistocene-Holocene warming of the preceding interglacial paleoclimate cycle leads to positive values of the heat flow recalculated to the "crust–mantle" boundary. It is shown that the use of heat flow data can significantly increase the geological information content of gravity modeling.

**Keywords:** Stationary heat flow, piecewise homogeneous layered medium, thermal conjugation conditions, Green's integral formula, separation of the flow into components from sources of the earth's crust and upper mantle

Recieved: 19 April 2022
Accepted: 3 July 2023
Published: 25 December 2023

**Citation:** Martyshko, P. S., I. V. Ladovskii, and D. D. Byzov (2023), Joint Interpretation Results of Gravitational and Thermal Fields for the Ural Region, *Russian Journal of Earth Sciences*, 23, ES5002, https://doi.org/10.2205/2023ES000855 EDN: HEETEZ

© 2023. The Authors.

## References

Artemieva I. M. The continental lithosphere: Reconciling thermal, seismic, and petrologic data // Lithos. — 2009. — Vol. 109, no. 1/2. — P. 23–46. — DOI: 10.1016/j.lithos.2008.09.015.

Artemieva I. M., Mooney W. D. Thermal thickness and evolution of Precambrian lithosphere: A global study // Journal of Geophysical Research: Solid Earth. — 2001. — Vol. 106, B8. — P. 16387–16414. — DOI: 10.1029/2000jb900439.

Bulashevich Y. P. Informativeness of geothermy in the study of the earth's crust of the Ural eugeosyncline // Proceedings of the Academy of Sciences of the USSR. Series Physics of the Earth. — 1983. — No. 8. — P. 76–83.

Bulashevich Y. P., Shchapov V. A. Geothermal features of the Ural geosyncline // Doklady Akademii nauk SSSR. — 1978. — Vol. 243, no. 3. — P. 715–718.

Bulashevich Y. P., Shchapov V. A. Geothermal characteristics of the Urals // Use of geothermy in regional and exploration research. — Sverdlovsk : Academy of Sciences of the USSR. Ural Scientific Center, 1983. — P. 3–17.

Bulashevich Y. P., Shchapov V. A. Geothermal features of the Ural geosyncline // Doklady Akademii nauk SSSR. — 1986. — Vol. 290, no. 1. — P. 173–176.

Cermak V., Bodri L., Rybach L., *et al.* Relationship between seismic velocity and heat production: comparison of two sets of data and test of validity // Earth and Planetary Science Letters. — 1990. — Vol. 99, no. 1/2. — P. 48–57. — DOI: 10.1016/0012-821x(90)90069-a.

Crough S. T., Thompson G. A. Thermal model of continental lithosphere // Journal of Geophysical Research. — 1976. — Vol. 81, no. 26. — P. 4857–4862. — DOI: 10.1029/jb081i026p04857.

Duchkov A. D., Sokolova L. S. Thermal structure of the lithosphere of the Siberian platform // Russian geology and geophysics. — 1997. — Vol. 38, no. 2. — P. 494–503.

Duchkov A. D., Sokolova L. S., Ayunov D. E. Electronic geothermal atlas of Siberia and the Far East // Interexpo GEO-SIBERIA. — 1997. — Vol. 2, no. 3. — P. 153–157.

Golovanova I. V. The thermal field of the Southern Urals. — Moscow : Science, 2005. — P. 190.

Golovanova I. V., Puchkov V. N., Sal'manova R. Y., *et al.* A new version of the heat flow map of the Urals with paleoclimatic corrections // Doklady Earth Sciences. — 2008. — Vol. 422, no. 1. — P. 1153–1156. — DOI: 10.1134/s1028334x08070350.

Golovanova I. V., Salmanova R. Y., Tagirova C. D. Method for deep temperature estimation with regard to the paleoclimate influence on heat flow // Russian geology and geophysics. — 2014. — Vol. 55, no. 9. — P. 1130–1137. — DOI: 10.1016/j.rgg.2014.08.008.

Gordienko V. V. Radiogenic heat generation in the Earth's crust and heat flow from the mantle of ancient platforms // Geophysical journal. — 1980. — Vol. 2, no. 3. — P. 29–34.

Gordienko V. V., Pavlenkova N. I. Combined geothermal-geophysical models of the earth's crust and upper mantle for the European continent // Journal of Geodynamics. — 1985. — Vol. 4, no. 1–4. — P. 75–90. — DOI: 10.1016/0264-3707(85)90053-5.

Khachai Y. V., Druzhinin V. S. Possibilities of applying geothermal to restore the dynamics of the transitional zone of the Ural mantle // Deep structure and development of the Urals. — Yekaterinburg : Science, 1996. — P. 298–306.

Khutorskoi M. D., Polyak B. G. Role of radiogenic heat generation in surface heat flow formation // Geotectonics. — 2016. — Vol. 50, no. 2. — P. 179–195. — DOI: 10.1134/s0016852116020047.

Kukkonen I. T., Golovanova I. V., Khachay Y. V., *et al.* Low geothermal heat flow of the Urals fold belt - implication of low heat production, fluid circulation or palaeoclimate? // Tectonophysics. — 1997. — Vol. 276, no. 1–4. — P. 63–85. — DOI: 10.1016/s0040-1951(97)00048-6.

Kutas R. I. Heat flow and geothermal models of the earth's crust of the Ukrainian Carpathians // Geophysical journal. — 2014. — Vol. 36, no. 6. — P. 3–27.

Kutas R. I., Gordienko V. V. Heat field of Ukraine. — Kyiv : Naukova Dumka, 1971.

Ladovskii I. V., Martyshko P. S., Tsidaev A. G., *et al.* A Method for Quantitative Interpretation of Stationary Thermal Fields for Layered Media // Geosciences. — 2020. — Vol. 10, no. 5. — P. 199. — DOI: 10.3390/geosciences10050199.

Martyshko P., Ladovskii I., Byzov D. Parallel Algorithms for Solving Inverse Gravimetry Problems: Application for Earth's Crust Density Models Creation // Mathematics. — 2021. — Vol. 9, no. 22. — P. 2966. — DOI: 10.3390/math9222966.

Martyshko P. S., Ladovskii I. V., Byzov D. D., *et al.* On solutions of forward and inverse problem for potential geophysical fields: Gravity inversion for Urals region // Application of Mathematics in Technical and Natural Sciences: 11th International Conference for Promoting the Application of Mathematics in Technical and Natural Sciences - AMiTaNS'19. — AIP Publishing, 2019. — DOI: 10.1063/1.5130870.

Rybach L., Buntebarth G. Relationships between the petrophysical properties density, seismic velocity, heat generation, and mineralogical constitution // Earth and Planetary Science Letters. — 1982. — Vol. 57, no. 2. — P. 367–376. — DOI: 10.1016/0012-821x(82)90157-1.

Salnikov V. E. Geothermal regime of the Southern Urals. — Moscow : Science, 1984. — P. 88.

Shchapov V. A. The thermal field of the Urals // Ural Geophysical Bulletin. — 2000. — Vol. 1. — P. 126–130.

Shchapov V. A., Burdin Y. B., Bolshchikov V. A., *et al.* Radiogenic heat generation of Ural eugeosyncline rocks // Ural Geophysical Bulletin. — 2004. — No. 6. — P. 116–121.

Tectonic map of Russia, adjacent territories and water areas / ed. by E. E. Milanovsky. — Moscow : MSU, 2006.

Tikhonov A. N., Samarsky A. A. Equations of Mathematical Physics. — Moscow : Science, 1999. — P. 979.

Vladimirov V. S., Zharinov V. V. Equations of Mathematical Physics. — Moscow : Fizmatlit, 2000. — P. 400.

Russian Journal of Earth Sciences

# Оценка геомеханических свойств карбонатных пород башкирского яруса Республики Татарстан с целью оптимизации гидроразрыва пласта

**Э. Р. Зиганшин*,[1], А. Н. Кольчугин[1], А. Н. Даутов[1], и Е. М. Нуриева[1]**

[1]Казанский федеральный университет, Казань, Россия
* **Контакт:** Эдуард Ришадович Зиганшин, erziganshin@kpfu.ru

С каждым годом процент разработки сложных коллекторов углеводородов увеличивается, что связано с истощением традиционных запасов нефти и газа. Карбонатные отложения относятся к сложным породам-коллекторам ввиду высокой степени неоднородности внутреннего строения скелета породы и порового пространства. Более подробное изучение литологических особенностей и физических свойств карбонатных пород является важной и неотъемлемой частью освоения данных объектов. В настоящей работе проведен комплексный анализ литологических и геомеханических характеристик отложений среднекаменноугольных толщ Дачного месторождения нефти, расположенного на юго-востоке Республики Татарстан. Основное внимание при исследованиях было сосредоточено на оценке хрупкости горных пород. Этот параметр является одним из необходимых для корректного прогнозирования операций гидроразрыва пласта. Результатом исследований является выделение карбонатных фаций и литологических типов согласно классификации Данхема, слагающих разрез, и их геомеханическая характеристика, а также оценка хрупкости горных пород различными методами.

**Ключевые слова:** геомеханика, литология, геология, лабораторное исследование, карбонатная порода, хрупкость горных пород, гидроразрыв пласта

**Цитирование:** Зиганшин, Э. Р., Кольчугин А. Н., Даутов А. Н., и Нуриева Е. М. Оценка геомеханических свойств карбонатных пород башкирского яруса Республики Татарстан с целью оптимизации гидроразрыва пласта // Russian Journal of Earth Sciences. — 2023. — Т. 23. — ES5003. — DOI: 10.2205/2023es000886 — EDN: VJOAVB

## Введение

Отложения башкирского яруса среднего карбона Волго-Уральского региона относятся к регионально нефтеносным [*Нефтегазоносность Республики Татарстан. Геология и разработка нефтяных месторождений*, 2007]. Эти отложения уже много лет активно разрабатываются и с ними связаны определенные перспективы устойчивой нефтедобычи в регионе в целом. Одной из главных проблем освоения башкирских отложений является их высокая степень вертикальной и латеральной изменчивости по площади, что значительно усложняет прогноз распространения зон потенциальных пород-коллекторов [*Kolchugin et al.*, 2020]. С другой стороны, разработку таких объектов усложняет высокая естественная трещиноватость пород. Так, выявлено, что помимо тектонической трещиноватости пород отложения яруса характеризуются и высокой плотностью трещин растворения, часто осложненных раздувами в виде цепочек каверн и каналов выщелачивания [*Хисамов и др.*, 2010].

В последние годы для эффективного освоения среднекаменноугольных толщ региона применяют метод гидроразрыва пласта (ГРП), в том числе метод солянокислотного ГРП. При этом традиционно основные объемы работ по ГРП проводятся на вышележащих отложениях московского яруса, в составе верейского горизонта [*Кольчугин*

https://elibrary.ru/vjoavb

Получено: 11 сентября 2023 г.
Принято: 14 декабря 2023 г.
Опубликовано: 25 декабря 2023 г.

© 2023. Коллектив авторов.

*и др.*, 2022]. Тогда как к отложениям башкирского яруса относятся с опасением в силу вышеперечисленных причин высокой трещиноватости пород, их низкой изученности геомеханическими методами и опасности появления протяженных сквозных трещин в водоносную зону залежи.

Объектом настоящего исследования был керн Дачного месторождения нефти, административно расположенного в Черемшанском районе Республики Татарстан, тектонически приуроченного к западному склону Южно-Татарского свода. Керн отложений яруса представлен карбонатными породами, главным образом, известняками, сформированными в различных обстановках мелководного шельфа. Верхняя граница отложений надежно выделяется как по керну, по смене карбонатных отложений терригенными и смешанными карбонатно-терригенными московского яруса, так и по данным ГИС, по резкой смене значений гамма-каротажа. Нижняя граница отложений яруса отбивается лишь по данным палеонтологического изучения и сложно определяется по данным макроскопического изучения керна [*Хворова*, 1958]. Средняя мощность отложений башкирского яруса составляет 40 м. Подробное комплексное изучение литологических и геомеханических характеристик пород яруса позволит прогнозировать проведение ГРП, в том числе моделировать успешность проводимых мероприятий на конкретных объектах. Фокус внимания в данной работе направлен на оценку хрупкости горных пород, потому что хрупкость и пластичность напрямую влияют на возможность распространения трещины в породе и удержание трещины, открытой при помощи проппанта.

**Описание методов исследований**

*Изучение литологического строения разрезов.* Выделение литологических типов отложений осуществлялось на основе детального послойного описания керна, а также изучения петрографических шлифов. Для определения литологических типов известняков, слагающих разрезы, использовалась классификация Данхема [*Dunham*, 1962]. На основе подробного описания керна совместно с анализом данных ГИС был построен разрез скважины, наиболее полно отражающий геологическое строение Дачного месторождения в составе башкирского яруса (рис. 1). Помимо литологического строения на разрезе указаны характер нефтенасыщения пород и фациальная приуроченность различных участков разреза к той или иной зоне осадконакопления. Расшифровка фаций дана в условных обозначениях к разрезу, а также подробно изложена в работе Кольчугина и соавторов [*Kolchugin et al.*, 2020].

*Лабораторные геомеханические исследования* состояли из определения упругих и прочностных параметров. Испытания проводились на цилиндрических образцах диаметром 30 мм и полудисках с надрезом. Определение упругих, деформационных и прочностных свойств в условиях трехосного сжатия выполнялось согласно требованиям (ASTM D7012-14, ГОСТ 21153.7-75, ГОСТ 21153.2-84, ГОСТ 21153.8-88, ГОСТ 28985-91, ГОСТ 21153.3-85). Испытания проводились в состоянии естественного насыщения при эффективном давлении 5, 10, 15, 20 МПа для трехосных испытаний. Определение предела прочности на растяжение при раскалывании методом приложения сжимающей нагрузки вдоль диаметра образца выполнялось согласно требованиям (ASTM D3967-08). Значения коэффициента трещиностойкости $K_{IC}$ определялись на образцах-полудисках с диаметром 62 мм. Процедура пробоподготовки образца к испытаниям подробно описана в методике (ISRM 2014).

*Методы определения хрупкости горных пород.* Распространенным методом увеличения нефтеотдачи на исследуемом месторождении, как упоминалось ранее, является операция по гидроразрыву горных пород. Процесс образования и распространения трещины во многом зависит от полноты знаний о напряженно-деформированном состоянии горных массивов в околоскважинной зоне и от достоверных данных об упругих и прочностных параметрах горных пород. Возможность создания эффективной сети трещин зависит от многих факторов, среди которых немаловажную роль играет хрупкость породы. Коэффициент хрупкости успешно изучался и использовался при

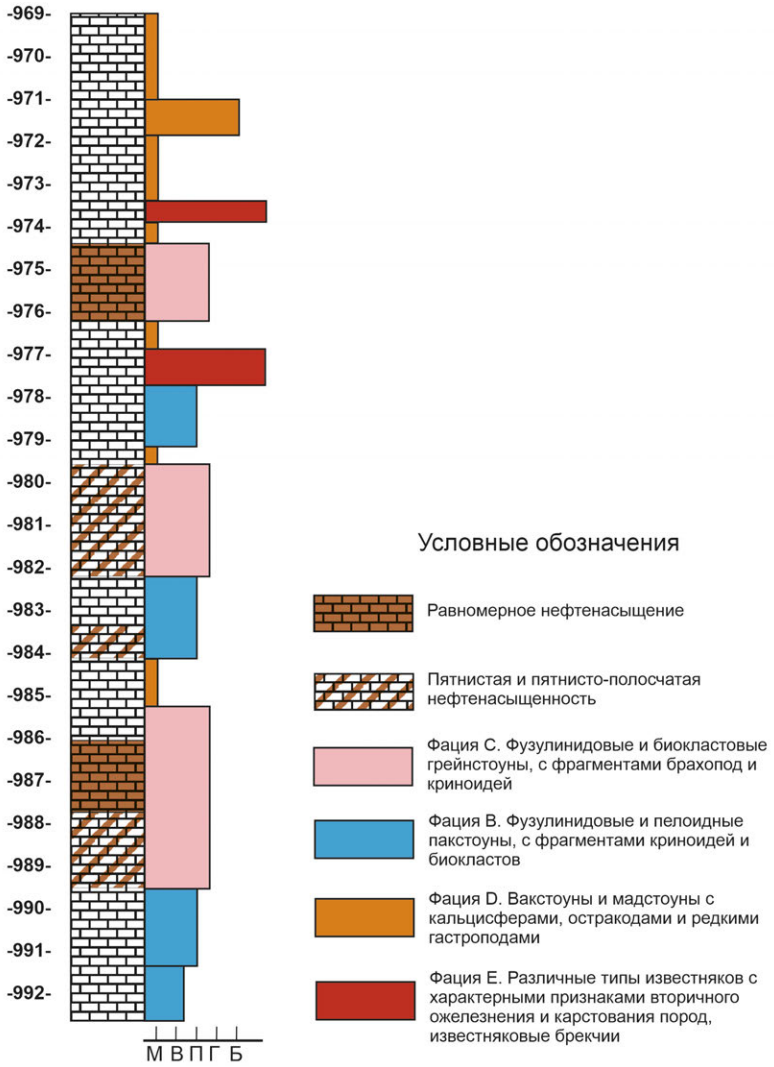


**Рис. 1.** Сводный литологический разрез Дачного месторождения нефти.

оптимизации ГРП в сланцах Барнет [*Wood*, 2021]. Это связано с тем, что хрупкие породы легче подвергаются хрупкому разрушению и способны лучше удерживаться раскрытыми при помощи проппантов. Этого не происходит в пластичных породах из-за преобладающей пластической деформации, которая вызывает залечивание трещин после сброса давления. Особое внимание в данной работе уделено оценке хрупкости пород различными методами.

Для количественной оценки хрупкости горных пород рекомендуется использовать совместно как лабораторные данные, так и результаты геофизических исследований скважин (ГИС). На сегодняшний день существует множество методов для количественной оценки хрупкости горных пород, основанных на различных концепциях. При этом учитываются различные факторы, включая минеральный состав, напряженное состояние и прочностные параметры. В разных исследованиях понятие хрупкости определяется по-разному. Это может быть отсутствие пластичности [*Hetényi*, 1950; *Morley*, 1944], нарушение внутреннего сцепления [*Ramsey*, 1968], разрушение материала с небольшим пластическим течением или полным отсутствием пластического течения [*Howell*, 1960].

Как правило, хрупкие породы разрушаются при небольшой неупругой деформации. Пластичные же породы, наоборот, до разрушения претерпевают значительную неупругую деформацию. Согласно существующим исследованиям, хрупкие породы обладают следующими свойствами [*Hajiabdolmajid et al.*, 2003; *Hucka and Das*, 1974;

*Jarvie et al.*, 2007; *Jin et al.*, 2014; 2015; *Nygård et al.*, 2006; *Rickman et al.*, 2008; *Tarasov and Potvin*, 2013]:

- относительно низкая деформация породы при приложении нагрузки;
- во время хрупкого разрушения наблюдается отчетливая поверхность разрыва, в отличие от пластичного разрушения;
- образование большого числа мелких трещин при приложении нагрузки;
- более высокое отношение прочности на сжатие к прочности на растяжение;
- относительно высокие значения угла внутреннего трения;
- содержание большего числа хрупких минералов, таких как кварц, и меньшего числа пластичных минералов, таких как глина;
- более высокие значения модуля Юнга и более низкие значения коэффициента Пуассона.

Существует множество различных способов определения коэффициента хрупкости пород [*Altindag*, 2002; *Hajiabdolmajid et al.*, 2003; *Holt et al.*, 2011; *Hucka and Das*, 1974; *Jin et al.*, 2014; 2015; *Nygård et al.*, 2006; *Rickman et al.*, 2008; *Tarasov and Potvin*, 2013; *Yagiz*, 2009]. Все предложенные методы условно можно разделить на несколько групп, исходя из способов их оценки: из кривых напряжение–деформация; из упругих параметров (модуля Юнга и коэффициента Пуассона); из значений прочности пород на одноосное сжатие и прочности на раскалывание; из значений твердости породы; из данных минерального состава, пористости и размеров зерен; из сейсмических данных; из данных об условиях осадконакопления. С учетом имеющихся материалов в рамках данной работы коэффициент хрупкости горной породы был оценен по упругим свойствам, по прочностным характеристикам и по данным об осадконакоплении. Анализ данных по кривым напряжение–деформация не проводился из-за того, что кривые записывались только до момента разрушения породы. Для оценки же хрупкости необходимы кривые и после разрушения. Значения твердости пород не определялись, сейсмические данные отсутствуют, поэтому эти способы оценки не применялись.

*Коэффициент хрупкости по упругим параметрам*

Согласно исследованиям Рикмана и соавторов [*Rickman et al.*, 2008] модуль Юнга и коэффициент Пуассона тесно связаны с хрупкостью горной породы. Чем выше модуль Юнга и ниже коэффициент Пуассона, тем выше хрупкость горных пород (1):

$$BI_{1,1} = \frac{1}{2}\left[\frac{E - E_{\min}}{E_{\max} - E_{\min}} + \frac{\nu_{\max} - \nu}{\nu_{\max} - \nu_{\min}}\right], \quad (1)$$

где $BI$ – коэффициент хрупкости, $E$, $E_{\min}$, $E_{\max}$ – модуль Юнга, минимальное значение и максимальное значение модуля Юнга соответственно, $\nu$, $\nu_{\min}$, $\nu_{\max}$ – коэффициент Пуассона, минимальное значение и максимальное значение коэффициента Пуассона соответственно. В данном уравнении происходит нормирование коэффициента хрупкости, чтобы диапазон значений менялся от 0 до 1. По мнению многих авторов, такой подход является корректным, однако возникает вопрос, какие значения должны соответствовать минимальным и максимальным параметрам [*Dubinya et al.*, 2022]? Либо необходимо брать эти значения из всей выборки, либо использовать существующие предельные значения для рассматриваемых типов горных пород. В данном случае было принято решение использовать крайние значения модулей из имеющейся выборки образцов.

В работе [*Luan et al.*, 2014] коэффициент хрупкости был рассчитан следующим способом (2):

$$BI_{1,2} = \frac{E}{\nu}, \quad (2)$$

где $BI$ – коэффициент хрупкости, $E$ – модуль Юнга, $\nu$ – коэффициент Пуассона.

*Sun et al.* [2013] добавили в оценку хрупкости значения объемной плотности (3):

$$BI_{1,3} = \frac{E\rho}{\nu}, \tag{3}$$

где $BI$ – коэффициент хрупкости, $E$ – модуль Юнга, $\rho$ – объемная плотность, $\nu$ – коэффициент Пуассона.

Преимуществом методов, основанных на упругих параметрах, является доступность данных. Упругие свойства могут быть легко определены по данным каротажа скважин, что позволит рассчитать коэффициент хрупкости породы вдоль всего разреза скважины. Однако есть ряд работ, указывающих на то, что определение хрупкости породы с использованием только модуля Юнга и коэффициента Пуассона является неточным, поскольку хрупкость породы зависит от многих других параметров, таких как объемный модуль упругости, поровое давление, напряженное состояние породы и пр. [*Cho and Perez*, 2014; *Holt et al.*, 2011; *Nasehi and Mortazavi*, 2013]. Несмотря на имеющиеся недостатки, данный метод широко используется на практике [*Yagiz*, 2009].

*Коэффициент хрупкости по прочностным параметрам*

Предел прочности при одноосном сжатии и предел прочности при раскалывании являются двумя основными параметрами, характеризующими прочность горных пород, которые можно получить путем лабораторных геомеханических испытаний. Предел прочности при одноосном сжатии характеризует сжимаемость горной породы, а прочность на раскалывание – сцепление между зернами при растяжении. В хрупких породах наблюдается высокая разница между этими двумя параметрами [*Hucka and Das*, 1974]. Порода с низкой прочностью на раскалывание легче подвергается образованию и распространению трещины, при этом высокие значения $UCS$ способствуют большему сопротивлению закрытия трещин [*Gong and Zhao*, 2007]. Основываясь на этих постулатах, существует несколько основных уравнений для коэффициента хрупкости породы (4)–(6):

$$BI_{2,1} = \frac{UCS}{P_b}, \tag{4}$$

$$BI_{2,2} = \frac{UCS - P_b}{UCS + P_b}, \tag{5}$$

$$BI_{2,3} = \frac{UCS \cdot P_b}{2}, \tag{6}$$

где $BI$ – коэффициент хрупкости, $UCS$ – предел прочности при одноосном сжатии, $P_\mathrm{b}$ – прочность породы при раскалывании.

*Коэффициент хрупкости по минеральному составу и пористости*

Хрупкость или пластичность породы во многом обусловлена минеральным составом пород. Установлено, что наличие кварца увеличивает хрупкость пород, тогда как наличие глинистых минералов увеличивает пластичность породы. Так как исследуемые образцы на 98–100% состоят из карбонатных минералов, то применение данной методики оказалось неэффективным.

Прочностные свойства также зависят от пористости. С увеличением пористости прочность породы снижается из-за снижения внутреннего сцепления частиц или когезии. Существует ряд эмпирических уравнений, описывающих зависимость предела прочности на сжатие от пористости породы [*Zhang et al.*, 2016]. Помимо этого, наличие пор способствует увеличению скорости деформации породы под напряжением. Это всё свидетельствует о том, что пористость влияет на хрупкость горных пород. В работе [*Jin et al.*, 2014; 2015] было выведено уравнение зависимости хрупкости пород от нейтронной пористости (7):

$$BI_{3,1} = -1{,}8748 \cdot \varphi + 0{,}9679, \tag{7}$$

где $BI$ – коэффициент хрупкости, $\varphi$ – пористость, вычисленная по нейтронному каротажу.

Есть работы, которые ставят под сомнение корректность использования пористости при вычислении хрупкости [*Cho and Perez*, 2014], однако возможно данный метод способен оценить хрупкость в некоторых массивах пород. Учитывая, что пористость в данном методе определяется по каротажным данным, его можно использовать только для данных ГИС.

*Хрупкость породы по данным угла внутреннего трения*

Согласно [*Hucka and Das*, 1974], хрупкость породы зависит от угла внутреннего трения. Из данной работы следует, что в критерии разрушения Кулона – Мора, при увеличении нормального напряжения $\sigma_n$, диаграмма Мора обретает квадратичную форму, а угол внутреннего трения и хрупкость горной породы при этом уменьшаются. Зависимость хрупкости от угла внутреннего трения выглядит следующим образом (8):

$$BI_{4,1} = \sin\theta, \tag{8}$$

где $BI$ – коэффициент хрупкости, $\theta$ – угол внутреннего трения породы.

*Хрупкость на основе чрезмерной консолидации*

Физические свойства осадочных горных пород во многом обусловлены условиями осадконакопления и вторичными преобразованиями. Процессы осадконакопления, диагенеза, поднятия влияют на изменения напряженного состояния. Таким образом, история напряжений любого массива горных пород оказывает непосредственное влияние на его хрупкопластическое поведение [*Ingram and Urai*, 1999; *Nygård et al.*, 2006]. Историю напряженного состояния в массивах горных пород можно оценить при помощи коэффициента чрезмерной консолидации – отношение между максимальным эффективным вертикальным напряжением, когда-либо существовавшим, и текущим эффективным вертикальным напряжением (9):

$$OCR = \frac{\sigma'_{v\max}}{\sigma'_v} \tag{9}$$

где $OCR$ – коэффициент чрезмерной консолидации, $\sigma'_{v\max}$ – максимальное вертикальное напряжение за период образования осадков, $\sigma'_v$ – текущее вертикальное напряжение.

Максимальное вертикальное напряжение за период образования осадков можно оценить по уравнениям (10)–(11):

$$\sigma'_{v\max} = 8,6 \cdot (UCS)^{0,55}, \tag{10}$$

$$\sigma'_{v\max} = 1 \times 10^{-7} \cdot (V_p)^{2,5}. \tag{11}$$

Следует отметить, что данный метод применим только для горизонтально-слоистых пород. Породы с высокими значениями $OCR$ являются более хрупкими. То есть если порода ранее испытывала более высокие напряжения, чем в настоящий момент времени, то она становится более хрупкой. Эта взаимосвязь описана в работе [*Nygård et al.*, 2006] уравнением (12):

$$BI_{5,1} = OCR^b, \tag{12}$$

где $BI$ – коэффициент хрупкости, $OCR$ – коэффициент чрезмерной консолидации, $b$ – эмпирический коэффициент.

Данный метод оценки видится весьма полезным при оценке хрупкости пород на территориях больших, чем околоскважинное пространство.

## Обсуждение результатов

*Литологическая и геомеханическая характеристика разреза*

Традиционно в строении башкирского яруса на юго-востоке Татарстана выделяют три карбонатных пачки: нижняя пачка – бш-2, средняя – бш-3, верхняя – бш-4. Пачка бш-1 на изученной площади не встречается, а пачка бш-2 несогласно залегает на регионально размытых отложениях серпуховского яруса. В строении разреза выделяются как участки пород-коллекторов, представленных известняками с пятнисто-полосчатым и равномерным нефтенасыщением, мощностью до 3 метров, так и интервалы плотных известняков без признаков нефтенасыщения пород, мощностью до 5 метров. Основными типами известняков, участвующих в строении разреза, являются грейнстоуны, пакстоуны и мадстоуны, другие типы встречаются заметно реже (рис. 2). При этом пакстоуны и грейнстоуны преобладают в нижней части разреза и маркируют обстановки открытого морского мелководья, тогда как в верхней части разреза они сменяются лагунными типами мадустоунов, с признаками периодических субаэральных событий. Высокая литологическая пестрота разрезов, а именно частая сменяемость типов известняков, вызвана глобальными эвстатическими колебаниями положения уровня моря, характерными для всего каменноугольного времени [*Bishop et al.*, 2009; *Mii et al.*, 2001].

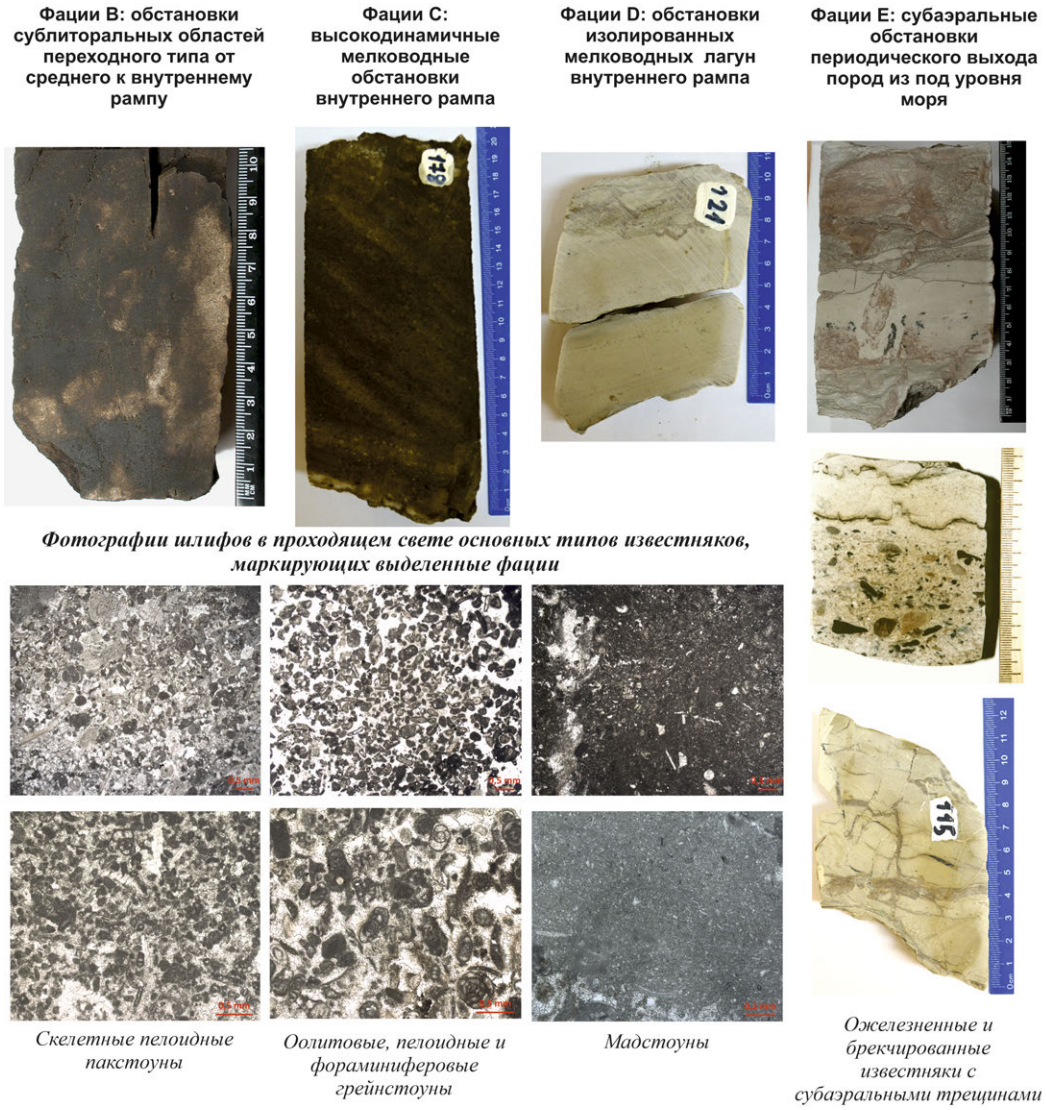


**Рис. 2.** Основные типы фаций башкирского яруса и типы известняков их слагающих.

Постседиментационная история пород башкирского яруса определяется как диа-, катагенетическими изменениями, выражающимися, главным образом, в уплотнении пород, так и наложенными вторичными процессами. Вторичные процессы чаще проявляются в виде кальцитизации, сульфатизации и окремнения пород, а также вторичного выщелачивания. Конкретно для изученного разреза проявление названных вторичных процессов, за исключением выщелачивания, определяющего значительный прирост пустотно-порового пространства в резервуаре, крайне несущественно. В данном случае можно говорить, что геомеханические свойства пород в большей степени зависят от первичных условий их седиментации, а также диа- , катагенетических преобразований. В случае вторично пористых известняков, которыми чаще всего выступают пелоидные пакстоуны, характерные для фаций B, геомеханические свойства определенно будут зависеть от процесса выщелачивания пород.

По результатам лабораторных геомеханических исследований была получена обобщенная характеристика механических и упругих свойств различных фаций, слагающих башкирский ярус. Нижняя часть башкирского яруса (фация B) характеризуется относительно высокими упруго-прочностными параметрами. Предел прочности на одноосное сжатие составляет около 100 МПа, модуль Юнга 24 ГПа, коэффициент Пуассона 0,178 д. ед., предел прочности на раскалывание 8 МПа, коэффициент трещиностойкости 0,61 МПа·м$^{1/2}$.

Равномерно-нефтенасыщенный интервал (фация C) обладает относительно низкими геомеханическими характеристиками. Предел прочности на одноосное сжатие составляет от 20 до 60 МПа, модуль Юнга 6–12 ГПа, коэффициент Пуассона 0,1–0,137 д. ед., предел прочности на раскалывание от 2,4 до 4,7 МПа, коэффициент трещиностойкости 0,26–0,36. Породы фации C с пятнисто-полосчатым нефтенасыщением, встречающиеся в верхней половине разреза башкирского яруса, обладают следующими геомеханическими свойствами. Предел прочности на одноосное сжатие составляет от 20 до 85 МПа, модуль Юнга 12–16,5 ГПа, коэффициент Пуассона 0,127–0,25 д. ед., предел прочности на раскалывание от 2,4 до 6 МПа, коэффициент трещиностойкости 0,19–0,8 МПа·м$^{1/2}$.

Плотные породы без нефтенасыщения (фации D), разделяющие нефтенасыщенные интервалы, обладают относительно повышенными упруго-прочностными свойствами. Предел прочности на одноосное сжатие составляет от 65 до 125 МПа, модуль Юнга 13,5–28,7 ГПа, коэффициент Пуассона 0,11–0,269 д. ед., предел прочности на раскалывание от 3 до 11 МПа, коэффициент трещиностойкости 0,33–1,23 МПа·м$^{1/2}$.

Таким образом, из всех изученных интервалов, самыми низкими упруго-прочностными характеристиками обладают равномерно нефтенасыщенные грейнстоуны. Самыми высокими значениями прочности и упругих свойств обладают мадстоуны, несколько в меньшей степени пакстоуны. Установлено, что среди выявленных типов фаций наименее прочными оказались наиболее пористые известняки, обладающие самыми высокими фильтрационно-емкостными свойствами, объединяющиеся в фации типа C. Структура пустотного пространства может являться одной из основных причин различий в геомеханических свойствах пород. Форма пор может как завышать (если поры близки к сферичной изолированной форме), так и занижать (наличие вытянутых пор, микротрещины) упругие и прочностные характеристики пород. В данном случае породы фации C обладают относительно низкими упругими и прочностными свойствами, что в первую очередь обусловлено повышенной пористостью и нефтенасыщенностью. Также низкое содержание цементирующего материала способствует понижению прочности породы. Напротив, наиболее устойчивыми к разрушению оказались плотные типы известняков с низкими исходными емкостно-фильтрационными свойствами, объединяющиеся в фации типа B и D. Относительно высокая прочность достигается благодаря высокому содержанию микрита, низкой пористости и более плотной упаковке зерен. Результаты лабораторных геомеханических исследований были также использованы для построения непрерывной геомеханической модели вдоль всего разреза. Помимо значений хрупкости горных пород были вычислены значения упругих и прочностных параметров для всего изучаемого интервала. Это позволяет

сопоставить механические свойства пород башкирского яруса с остальными породами, слагающими разрез (рис. 3).

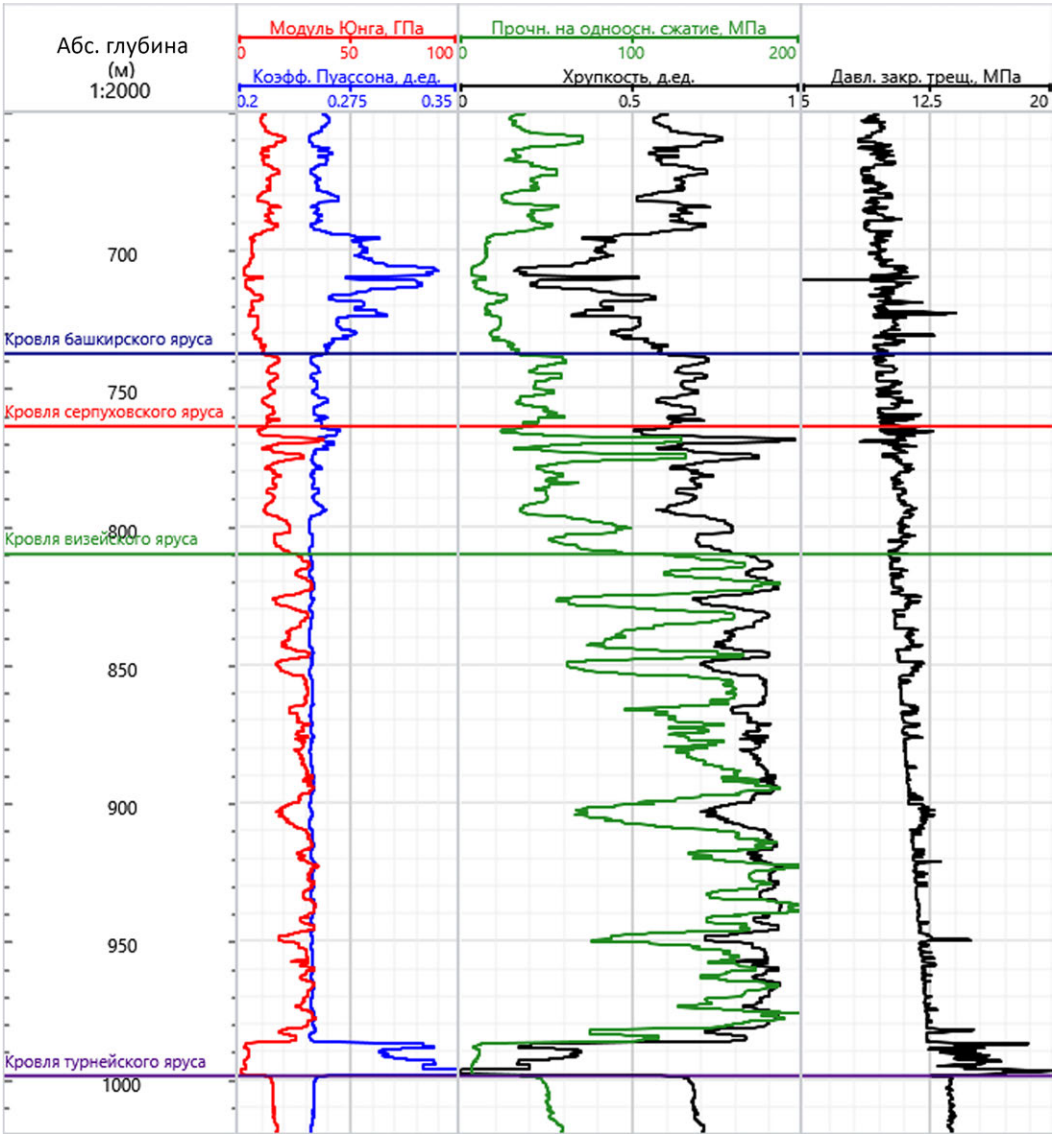


**Рис. 3.** Общий планшет геомеханических свойств.

Башкирский ярус обладает относительно повышенными значениями упругих и прочностных параметров по сравнению с вышележащими верейскими отложениями. Есть небольшие колебания механических свойств, что вероятнее всего вызвано сменой фаций. Породы башкирского яруса являются более хрупкими по сравнению с вышележащими породами и обладают схожей хрупкостью с нижележащими породами протвинского возраста. Вполне вероятно, что условия осадконакопления и вторичные преобразования пород башкирского и серпуховского ярусов схожи и отличаются от пород верейского возраста. Как следствие, отличается структура порового пространства, процентное содержание органических остатков и цементного материала.

Следует также отметить, что на данном месторождении были оценены величины главных напряжений. По полученным данным следует, что Дачное месторождение находится в области тектонического режима сброс – максимальным является вертикальное напряжение. Азимут максимального горизонтального напряжения равен 125 градусам. По данным напряжений и механических свойств пород был рассчитан профиль смыкающего напряжения. Напряжение закрытия трещины в башкирском

ярусе не отличается от напряжений в выше- и нижележащих породах (рис. 3, крайний правый график).

*Хрупкость пород*

Все вышеописанные способы оценки коэффициента хрупкости горных пород были применены для исследуемого интервала, результаты представлены в табл. 1.

**Таблица 1**

| № | Фация | Глубина | $BI_{1,1}$ | $BI_{1,2}$ | $BI_{1,3}$ | $BI_{2,1}$ | $BI_{2,2}$ | $BI_{2,3}$ | $BI_{4,1}$ | $BI_{5,1}$ |
|---|---|---|---|---|---|---|---|---|---|---|
| 1 | С | 974,48 | 0,48 | 183 | 482 | 5,5 | 0,69 | 97 | 0,61 | 1,29 |
| 2 | В | 977,71 | 0,55 | 210 | 562 | 8,9 | 0,80 | 254 | 0,58 | 1,44 |
| 3 | С | 979,66 | 0,40 | 126 | 280 | 8,5 | 0,79 | 24 | 0,33 | 1,25 |
| 4 | В | 983,72 | 0,86 | 254 | 652 | 15,6 | 0,88 | 230 | 0,63 | 1,51 |
| 5 | С | 986,73 | 0,12 | 128 | 330 | 10,3 | 0,82 | 34 | 0,25 | 1,25 |
| 6 | В | 990,79 | 0,73 | 248 | 668 | 12,1 | 0,85 | 380 | 0,62 | 1,52 |

Условно было принято разделить все данные на четыре группы, исходя из методов, на которых они основаны: упругие свойства ($BI_{1,1}$, $BI_{1,2}$, $BI_{1,3}$), прочностные параметры ($BI_{2,1}$, $BI_{2,2}$, $BI_{2,3}$), угол внутреннего трения ($BI_{4,1}$) и коэффициент чрезмерного уплотнения ($BI_{5,1}$). Для возможности сопоставления данных из каждой группы были выбраны данные с близкой размерностью: $BI_{1,1}$, $BI_{2,2}$, $BI_{4,1}$, $BI_{5,1}$ и нанесены на один график (рис. 4).

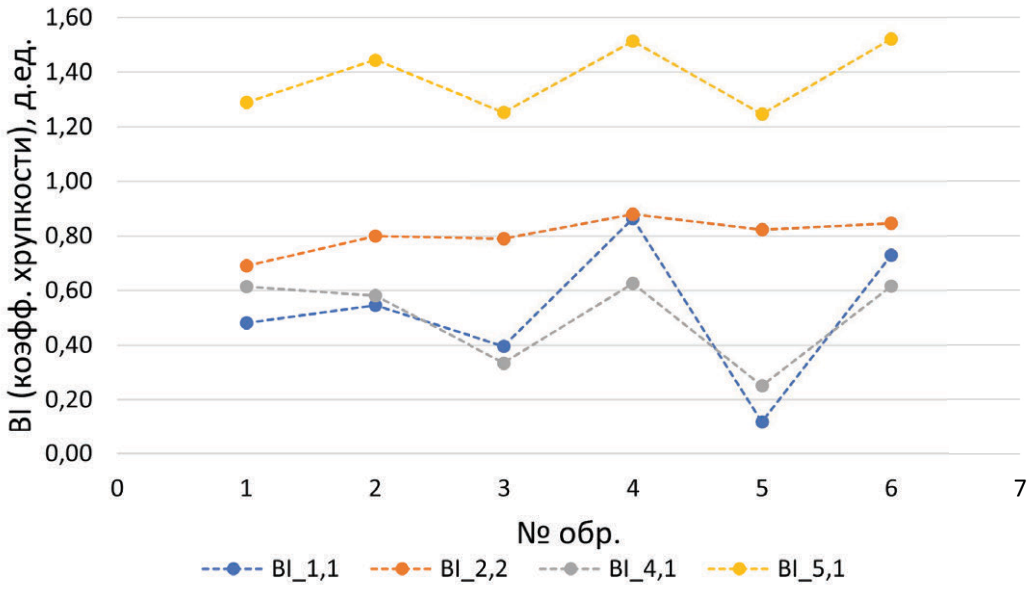


**Рис. 4.** Коэффициент хрупкости для разных образцов.

Несмотря на то, что полученные коэффициенты отличаются по величине, очевидно, что на качественном уровне они одинаково описывают хрупкость образцов. Пакстоуны, отобранные из плотных интервалов, обладают повышенной хрупкостью. Нефтенасыщенные породы, наоборот, обладают высокой пластичностью. При этом коэффициенты $BI_{1,1}$ и $BI_{4,1}$ имеют более высокую вариативность и показывают явное различие образцов 4, 5 и 6.

Есть ещё один важный параметр, описывающий способность трещины распространяться в горной породе – трещиностойкость. Его можно измерить в лабораторных условиях. Этот параметр используется для оценки благоприятности проведения гидроразрыва пласта. Его зачастую используют совместно с хрупкостью породы для

оценки успешности ГРП [*Салимов и др.*, 2017]. Данный параметр был сопоставлен с вычисленными коэффициентами хрупкости (рис. 5).

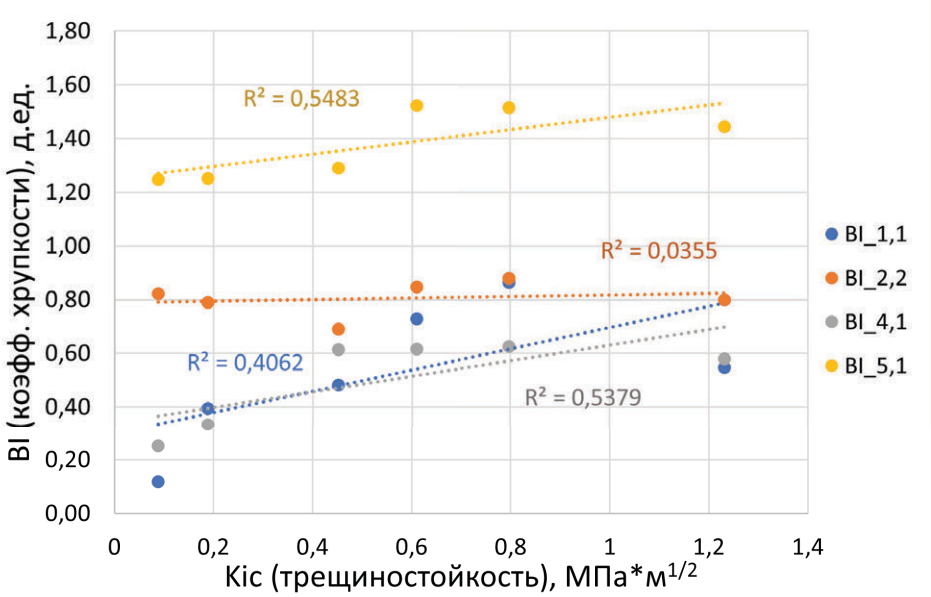


**Рис. 5.** Зависимость коэффициента хрупкости и трещиностойкости.

Коэффициент хрупкости, определенный из прочностных параметров, показал самый низкий коэффициент корреляции. Остальные три коэффициента обладают хорошей корреляционной зависимостью. Из всех рассмотренных способов определения хрупкости, только способ, основанный на упругих параметрах (модуль Юнга, коэффициент Пуассона) позволяет определить хрупкость пород для всего разреза.

Существует проблема выбора метода, при помощи которого следует определять хрупкость горных пород. Очень важным фактором является масштаб исследования: размер керна, околоскважинное пространство или куб сейсморазведки. Если на уровне керна можно использовать прямой метод лабораторных испытаний (тест на разрушение), то на скважинном и сейсмическом уровне возможно использование только данных об упругих параметрах. Чтобы корректно вычислить коэффициент хрупкости в масштабах скважины, необходимо понимание взаимосвязи между внутренним строением породы и его хрупкостью. Этот вопрос подробно рассматривался в работе [*Dubinya et al.*, 2022]. На исследуемом месторождении метод оценки хрупкости, основанный на упругих параметрах, показал хорошую сходимость с лабораторными методами, а также неплохую корреляцию с трещиностойкостью. Из этого следует, что для исследуемых карбонатов можно использовать вычисление хрупкости по упругим параметрам: модулю Юнга и коэффициенту Пуассона.

## Заключение

По результатам лабораторных геомеханических и литологических исследований была получена общая характеристика карбонатных пород башкирского яруса. В данном интервале выделяются несколько фаций, представленных грейнстоунами, пакстоунами и мадстоунами с разной степенью нефтенасыщенности. Для каждого интервала даны характеристики упруго-прочностных свойств. Грейнстоуны в этом ряду обладают наименьшими прочностными характеристиками, мадстоуны – наибольшими.

Среди выявленных типов фаций наименее прочными оказались нефтенасыщенные известняки (фации типа C), что вероятнее всего обусловлено повышенной пористостью и низким содержанием цементирующего материала. Наиболее прочными оказались плотные типы известняков с низкими емкостно-фильтрационными свойствами (фации типа B и D). Относительно высокая прочность достигается благодаря высокому содержанию микрита, низкой пористости и более плотной упаковке зерен.

Помимо стандартных геомеханических параметров, была определена хрупкость пород различными методами. Выявлено, что оптимальным методом оценки хрупкости пород на данном месторождении является метод, основанный на упругих свойствах (модуль Юнга и коэффициент Пуассона). В то же время следует верифицировать коэффициент хрупкости, определенный по упругим свойствам, с хрупкостью, определенной по прочностным параметрам лабораторными методами.

Породы башкирского яруса оказались более хрупкими по сравнению с вышележащими породами верейского возраста, однако со схожими геомеханическими свойствами нижележащих пород серпуховского яруса, что может объясняться особенностями условий осадконакопления и вторичных преобразований.

Было установлено, что рассматриваемое месторождение залегает в области тектонического режима типа сброс. Был также построен профиль смыкающего напряжения вдоль всего ствола скважины.

Таким образом, башкирский ярус по геомеханическим параметрам является благоприятным для создания трещин ГРП и закрепления в них проппанта. Однако отсутствие контраста смыкающих напряжений по разрезу может вызвать неконтролируемый рост высоты трещины. Это может повлечь за собой обводнение пласта. Перед проведением гидроразрыва важно правильно оценить профиль смыкающего напряжения. Желательно определять давления закрытия трещины прямым методом: мини-ГРП или тест на утечку.

Полученные результаты можно использовать и для других месторождений с одновозрастными отложениями, если при этом на других месторождениях наблюдается схожий тектонический режим (сброс). Также следует учитывать глубину залегания, потому что величина тектонических напряжений может внести изменения в геомеханические свойства пород: создать зоны уплотнения или трещиноватости.

**Благодарности.** Работа выполнена за счет средств субсидии, выделенной Казанскому федеральному университету для выполнения государственного задания в сфере научной деятельности, проект №FZSM-2023–0014.

**Список литературы**

Кольчугин А. Н., Зиганшин Э. Р., Морозов В. П. *и др.* Геомеханические и литологические характеристики отложений верейского горизонта среднего карбона в связи с прогнозированием применения технологии гидроразрыва пласта, на примере Ивинского месторождения юго-востока Татарстана // Георесурсы. — 2022. — Т. 24, № 4. — С. 65—74. — DOI: 10.18599/grs.2022.4.5.

Нефтегазоносность Республики Татарстан. Геология и разработка нефтяных месторождений. Т. 1 / под ред. Р. Х. Муслимов. — Казань : «Фэн», 2007. — 316 с.

Салимов О. В., Насыбуллин А. В., Сахабутдинов Р. З. *и др.* О критериях подбора скважин для гидроразрыва пласта // Георесурсы. — 2017. — Т. 19, № 4. — С. 368—373. — DOI: 10.18599/grs.19.4.10.

Хворова И. В. Атлас карбонатных пород среднего и верхнего карбона Русской платформы. — АН СССР, 1958. — 170 с.

Хисамов Р. С., Губайдуллин А. А., Базаревская В. Г. *и др.* Геология карбонатных сложнопостроенных коллекторов девона и карбона Татарстана. — Казань : «Фэн», 2010. — 283 с.

Altindag R. The evaluation of rock brittleness concept on rotary blast hole drills // The Journal of The South African Institute of Mining and Metallurgy. — 2002. — Vol. 102, no. 1. — P. 61–66.

Bishop J. W., Montañez I. P., Gulbranson E. L., *et al.* The onset of mid-Carboniferous glacio-eustasy: Sedimentologic and diagenetic constraints, Arrow Canyon, Nevada // Palaeogeography, Palaeoclimatology, Palaeoecology. — 2009. — Vol. 276, no. 1–4. — P. 217–243. — DOI: 10.1016/j.palaeo.2009.02.019.

Cho D., Perez M. Rock quality assessment for hydraulic fracturing: A rock physics perspective // SEG Technical Program Expanded Abstracts 2014. — Society of Exploration Geophysicists, 2014. — DOI: 10.1190/segam2014-1624.1.

Dubinya N., Bayuk I., Bakhmach M. Problems of Multiscale Brittleness Estimation for Hydrocarbon Reservoir Exploration and Development // Applied Sciences. — 2022. — Vol. 12, no. 3. — P. 1134. — DOI: 10.3390/app12031134.

Dunham R. J. Classification of Carbonate Rocks According to Depositional Texture // Classification of Carbonate Rocks-A Symposium. Vol. 1 / ed. by W. E. Ham. — American Association of Petroleum Geologists, 1962. — P. 108–121. — DOI: 10.1306/m1357.

Gong Q. M., Zhao J. Influence of rock brittleness on TBM penetration rate in Singapore granite // Tunnelling and Underground Space Technology. — 2007. — Vol. 22, no. 3. — P. 317–324. — DOI: 10.1016/j.tust.2006.07.004.

Hajiabdolmajid V., Kaiser P., Martin C. Mobilised strength components in brittle failure of rock // Géotechnique. — 2003. — Vol. 53, no. 3. — P. 327–336. — DOI: 10.1680/geot.2003.53.3.327.

Hetényi M. Handbook of Experimental Stress Analysis. — New York (USA) : Wiley, 1950. — 1077 p.

Holt R., Fjaer E., Nes O. M., *et al.* A Shaly Look at Brittleness // 45th US Rock Mechanics/Geomechanics Symposium. — San Francisco, California : American Rock Mechanics Association, 2011.

Howell J. V. Glossary of Geology and Related Sciences. — American Geological Institute, 1960. — Washington, D. C.

Hucka V., Das B. Brittleness determination of rocks by different methods // International Journal of Rock Mechanics and Mining Sciences & Geomechanics Abstracts. — 1974. — Vol. 11, no. 10. — P. 389–392. — DOI: 10.1016/0148-9062(74)91109-7.

Ingram G. M., Urai J. L. Top-seal leakage through faults and fractures: the role of mudrock properties // Geological Society, London, Special Publications. — 1999. — Vol. 158, no. 1. — P. 125–135. — DOI: 10.1144/gsl.sp.1999.158.01.10.

Jarvie D. M., Hill R. J., Ruble T. E., *et al.* Unconventional shale-gas systems: The Mississippian Barnett Shale of north-central Texas as one model for thermogenic shale-gas assessment // AAPG Bulletin. — 2007. — Vol. 91, no. 4. — P. 475–499. — DOI: 10.1306/12190606068.

Jin X., Shah S., Truax J., *et al.* A Practical Petrophysical Approach for Brittleness Prediction from Porosity and Sonic Logging in Shale Reservoirs // All Days. — SPE, 2014. — DOI: 10.2118/170972-ms.

Jin X., Shah S. N., Roegiers J.-C., *et al.* An Integrated Petrophysics and Geomechanics Approach for Fracability Evaluation in Shale Reservoirs // SPE Journal. — 2015. — Vol. 20, no. 03. — P. 518–526. — DOI: 10.2118/168589-pa.

Kolchugin A. N., Porta G. D., Morozov V. P., *et al.* Facies variability of pennsylvanian oil-saturated carbonate rocks (constraints from Bashkirian reservoirs of the south-east Tatarstan) // Georesursy. — 2020. — Vol. 22, no. 2. — P. 29–36. — DOI: 10.18599/grs.2020.2.29-36.

Luan X., Di B., Wei J., *et al.* Laboratory measurements of brittleness anisotropy in synthetic shale with different cementation // SEG Technical Program Expanded Abstracts 2014. — Society of Exploration Geophysicists, 2014. — DOI: 10.1190/segam2014-0432.1.

Mii H.-S., Grossman E. L., Yancey T. E., *et al.* Isotopic records of brachiopod shells from the Russian Platform — evidence for the onset of mid-Carboniferous glaciation // Chemical Geology. — 2001. — Vol. 175, no. 1/2. — P. 133–147. — DOI: 10.1016/s0009-2541(00)00366-1.

Morley A. Strength of Materials: with 260 Diagrams and Numerous Examples. — New York : Longmans, Green, Company, 1944.

Nasehi M. J., Mortazavi A. Effects of in-situ stress regime and intact rock strength parameters on the hydraulic fracturing // Journal of Petroleum Science and Engineering. — 2013. — Vol. 108. — P. 211–221. — DOI: 10.1016/j.petrol.2013.04.001.

Nygård R., Gutierrez M., Bratli R. K., *et al.* Brittle–ductile transition, shear failure and leakage in shales and mudrocks // Marine and Petroleum Geology. — 2006. — Vol. 23, no. 2. — P. 201–212. — DOI: 10.1016/j.marpetgeo.2005.10.001.

Ramsey J. Folding and Fracturing of Rock. — New York (USA) : McGraw-Hill, 1968.

Rickman R., Mullen M., Petre E., *et al.* A Practical Use of Shale Petrophysics for Stimulation Design Optimization: All Shale Plays Are Not Clones of the Barnett Shale // All Days. — SPE, 2008. — DOI: 10.2118/115258-ms.

Sun S. Z., Wang K. N., Yang P., *et al.* Integrated Prediction of Shale Oil Reservoir Using Pre-Stack Algorithms for Brittleness and Fracture Detection // International Petroleum Technology Conference. — International Petroleum Technology Conference, 2013. — DOI: 10.2523/17048-ms.

Tarasov B., Potvin Y. Universal criteria for rock brittleness estimation under triaxial compression // International Journal of Rock Mechanics and Mining Sciences. — 2013. — Vol. 59. — P. 57–69. — DOI: 10.1016/j.ijrmms.2012.12.011.

Wood D. A. Brittleness index predictions from Lower Barnett Shale well-log data applying an optimized data matching algorithm at various sampling densities // Geoscience Frontiers. — 2021. — Vol. 12, no. 6. — P. 101087. — DOI: 10.1016/j.gsf.2020.09.016.

Yagiz S. Assessment of brittleness using rock strength and density with punch penetration test // Tunnelling and Underground Space Technology. — 2009. — Vol. 24, no. 1. — P. 66–74. — DOI: 10.1016/j.tust.2008.04.002.

Zhang D., Ranjith P. G., Perera M. S. A. The brittleness indices used in rock mechanics and their application in shale hydraulic fracturing: A review // Journal of Petroleum Science and Engineering. — 2016. — Vol. 143. — P. 158–170. — DOI: 10.1016/j.petrol.2016.02.011.

Russian Journal of Earth Sciences

# Evaluation of the Geomechanical Properties of Bashkirian Carbonate Rocks at the Tatarstan Republic for Optimization of Hydraulic Fracturing

**E. Ziganshin**[**,1], **A. Kolchugin**[1], **A. Dautov**[1] **and E. Nurieva**[1]

[1]Kazan Federal University, Kazan, Russia
****Correspondence to:** Eduard Ziganshin, erziganshin@kpfu.ru

Every year, the percentage of development of complex and unconventional hydrocarbon reservoirs is increasing, which is associated with the depletion of traditional oil and gas reserves. Carbonate reservoirs are hard-to-recover reservoir rocks due to the high degree of heterogeneity. A more detailed study of the lithological features and physical properties of carbonate rocks is an important and integral part of the complex reservoirs development. In the present work has done a comprehensive analysis of the lithological and geomechanical properties of the Middle Carboniferous strata deposits of the Dachnoye oil field, located in the southeast of the Republic of Tatarstan. The main attention in the research was focused on the estimation of the britleness of rocks. Britleness index is necessary for correct prediction of hydraulic fracturing. The result of the research is the identification of carbonate facies and their geomechanical characteristics, as well as the estimation of the britleness of rocks by various methods.

**Keywords:** geomechanics, lithology, geology, laboratory study, carbonate rock, rock britleness, hydraulic fracturing

Recieved: 11 September 2022
Accepted: 14 December 2023
Published: 25 December 2023

**Citation:** Ziganshin, E., A. Kolchugin, A. Dautov, and E. Nurieva (2023), Evaluation of the Geomechanical Properties of Bashkirian Carbonate Rocks at the Tatarstan Republic for Optimization of Hydraulic Fracturing, *Russian Journal of Earth Sciences*, 23, ES5003, https://doi.org/10.2205/2023ES000886 EDN: VJOAVB

© 2023. The Authors.

## References

Altindag R. The evaluation of rock brittleness concept on rotary blast hole drills // The Journal of The South African Institute of Mining and Metallurgy. — 2002. — Vol. 102, no. 1. — P. 61–66.

Bishop J. W., Montañez I. P., Gulbranson E. L., *et al.* The onset of mid-Carboniferous glacio-eustasy: Sedimentologic and diagenetic constraints, Arrow Canyon, Nevada // Palaeogeography, Palaeoclimatology, Palaeoecology. — 2009. — Vol. 276, no. 1–4. — P. 217–243. — DOI: 10.1016/j.palaeo.2009.02.019.

Cho D., Perez M. Rock quality assessment for hydraulic fracturing: A rock physics perspective // SEG Technical Program Expanded Abstracts 2014. — Society of Exploration Geophysicists, 2014. — DOI: 10.1190/segam2014-1624.1.

Dubinya N., Bayuk I., Bakhmach M. Problems of Multiscale Brittleness Estimation for Hydrocarbon Reservoir Exploration and Development // Applied Sciences. — 2022. — Vol. 12, no. 3. — P. 1134. — DOI: 10.3390/app12031134.

Dunham R. J. Classification of Carbonate Rocks According to Depositional Texture // Classification of Carbonate Rocks-A Symposium. Vol. 1 / ed. by W. E. Ham. — American Association of Petroleum Geologists, 1962. — P. 108–121. — DOI: 10.1306/m1357.

Gong Q. M., Zhao J. Influence of rock brittleness on TBM penetration rate in Singapore granite // Tunnelling and Underground Space Technology. — 2007. — Vol. 22, no. 3. — P. 317–324. — DOI: 10.1016/j.tust.2006.07.004.

Hajiabdolmajid V., Kaiser P., Martin C. Mobilised strength components in brittle failure of rock // Géotechnique. — 2003. — Vol. 53, no. 3. — P. 327–336. — DOI: 10.1680/geot.2003.53.3.327.

Hetényi M. Handbook of Experimental Stress Analysis. — New York (USA) : Wiley, 1950. — P. 1077.

Holt R., Fjaer E., Nes O. M., *et al.* A Shaly Look at Brittleness // 45th US Rock Mechanics/Geomechanics Symposium. — San Francisco, California : American Rock Mechanics Association, 2011.

Howell J. V. Glossary of Geology and Related Sciences. — Washington, D. C. : American Geological Institute, 1960.

Hucka V., Das B. Brittleness determination of rocks by different methods // International Journal of Rock Mechanics and Mining Sciences & Geomechanics Abstracts. — 1974. — Vol. 11, no. 10. — P. 389–392. — DOI: 10.1016/0148-9062(74)91109-7.

Ingram G. M., Urai J. L. Top-seal leakage through faults and fractures: the role of mudrock properties // Geological Society, London, Special Publications. — 1999. — Vol. 158, no. 1. — P. 125–135. — DOI: 10.1144/gsl.sp.1999.158.01.10.

Jarvie D. M., Hill R. J., Ruble T. E., *et al.* Unconventional shale-gas systems: The Mississippian Barnett Shale of north-central Texas as one model for thermogenic shale-gas assessment // AAPG Bulletin. — 2007. — Vol. 91, no. 4. — P. 475–499. — DOI: 10.1306/12190606068.

Jin X., Shah S., Truax J., *et al.* A Practical Petrophysical Approach for Brittleness Prediction from Porosity and Sonic Logging in Shale Reservoirs // All Days. — SPE, 2014. — DOI: 10.2118/170972-ms.

Jin X., Shah S. N., Roegiers J.-C., *et al.* An Integrated Petrophysics and Geomechanics Approach for Fracability Evaluation in Shale Reservoirs // SPE Journal. — 2015. — Vol. 20, no. 03. — P. 518–526. — DOI: 10.2118/168589-pa.

Khisamov R. S., Gubaidullin A. A., Bazarevskaya V. G., *et al.* Geology of carbonate complex reservoirs of the Devonian and Carboniferous of Tatarstan. — Kazan : "Fen", 2010. — P. 283.

Khvorova I. V. Atlas of carbonate rocks of the Middle and Upper Carboniferous of the Russian Platform. — USSR Academy of Sciences, 1958. — P. 170.

Kolchugin A. N., Porta G. D., Morozov V. P., *et al.* Facies variability of pennsylvanian oil-saturated carbonate rocks (constraints from Bashkirian reservoirs of the south-east Tatarstan) // Georesursy. — 2020. — Vol. 22, no. 2. — P. 29–36. — DOI: 10.18599/grs.2020.2.29-36.

Kolchugin A. N., Ziganshin E. R., Morozov V. P., *et al.* Geomechanical and lithological characteristics of the Vereysky horizon in the Middle Carboniferous for prediction of hydraulic fracturing technology, on the example of the Ivinskoye field in the South-East of Tatarstan // Georesursy. — 2022. — Vol. 24, no. 4. — P. 65–74. — DOI: 10.18599/grs.2022.4.5.

Luan X., Di B., Wei J., *et al.* Laboratory measurements of brittleness anisotropy in synthetic shale with different cementation // SEG Technical Program Expanded Abstracts 2014. — Society of Exploration Geophysicists, 2014. — DOI: 10.1190/segam2014-0432.1.

Mii H.-S., Grossman E. L., Yancey T. E., *et al.* Isotopic records of brachiopod shells from the Russian Platform — evidence for the onset of mid-Carboniferous glaciation // Chemical Geology. — 2001. — Vol. 175, no. 1/2. — P. 133–147. — DOI: 10.1016/s0009-2541(00)00366-1.

Morley A. Strength of Materials: with 260 Diagrams and Numerous Examples. — New York : Longmans, Green, Company, 1944.

Nasehi M. J., Mortazavi A. Effects of in-situ stress regime and intact rock strength parameters on the hydraulic fracturing // Journal of Petroleum Science and Engineering. — 2013. — Vol. 108. — P. 211–221. — DOI: 10.1016/j.petrol.2013.04.001.

Nygård R., Gutierrez M., Bratli R. K., *et al.* Brittle–ductile transition, shear failure and leakage in shales and mudrocks // Marine and Petroleum Geology. — 2006. — Vol. 23, no. 2. — P. 201–212. — DOI: 10.1016/j.marpetgeo.2005.10.001.

Oil and gas potential of the Republic of Tatarstan. Geology and oil field development. Vol. 1 / ed. by R. K. Muslimov. — Kazan : "Fen", 2007. — P. 316.

Ramsey J. Folding and Fracturing of Rock. — New York (USA) : McGraw-Hill, 1968.

Rickman R., Mullen M., Petre E., *et al.* A Practical Use of Shale Petrophysics for Stimulation Design Optimization: All Shale Plays Are Not Clones of the Barnett Shale // All Days. — SPE, 2008. — DOI: 10.2118/115258-ms.

Salimov O. V., Nasybullin A. V., Sakhabutdinov R. Z., *et al.* The Criteria for the Selection of Wells for Hydraulic Fracturing // Georesursy. — 2017. — Vol. 19, no. 4. — P. 368–373. — DOI: 10.18599/grs.19.4.10.

Sun S. Z., Wang K. N., Yang P., *et al.* Integrated Prediction of Shale Oil Reservoir Using Pre-Stack Algorithms for Brittleness and Fracture Detection // International Petroleum Technology Conference. — International Petroleum Technology Conference, 2013. — DOI: 10.2523/17048-ms.

Tarasov B., Potvin Y. Universal criteria for rock brittleness estimation under triaxial compression // International Journal of Rock Mechanics and Mining Sciences. — 2013. — Vol. 59. — P. 57–69. — DOI: 10.1016/j.ijrmms.2012.12.011.

Wood D. A. Brittleness index predictions from Lower Barnett Shale well-log data applying an optimized data matching algorithm at various sampling densities // Geoscience Frontiers. — 2021. — Vol. 12, no. 6. — P. 101087. — DOI: 10.1016/j.gsf.2020.09.016.

Yagiz S. Assessment of brittleness using rock strength and density with punch penetration test // Tunnelling and Underground Space Technology. — 2009. — Vol. 24, no. 1. — P. 66–74. — DOI: 10.1016/j.tust.2008.04.002.

Zhang D., Ranjith P. G., Perera M. S. A. The brittleness indices used in rock mechanics and their application in shale hydraulic fracturing: A review // Journal of Petroleum Science and Engineering. — 2016. — Vol. 143. — P. 158–170. — DOI: 10.1016/j.petrol.2016.02.011.

Russian Journal of Earth Sciences

# Linear perturbations of the Bloch type of space-periodic magnetohydrodynamic steady states. III. Asymptotics of branching

**R. Chertovskih**[1] **and V. Zheligovsky***,[2]

[1]SYSTEC, ARISE, Faculty of Engineering, University of Porto, Porto, Portugal
[2]Institute of Earthquake Prediction Theory and Mathematical Geophysics RAS, Moscow, Russian Federation
* **Correspondence to:** V. Zheligovsky, vlad@mitp.ru

**Abstract:** The previous paper of this series presented the results of a numerical investigation of the dependence of the dominant growth rates of Bloch eigenmodes on the diffusivity parameters (the molecular viscosity $\nu$ and molecular magnetic diffusivity $\eta$) in three linear stability problems: the kinematic dynamo problem, and the hydrodynamic and MHD stability problems for steady space-periodic flows and MHD states. The dominant eigenmodes (i.e., the stability modes, whose growth rates are maximum over the wave vector $\mathbf{q}$ of the planar wave involved in the Bloch modes) comprise branches. In some branches, the dominant growth rates are attained for constant half-integer $\mathbf{q}$. In all the three stability problems for parity-invariant steady states, offshoot branches, stemming from the branches of this type, were found, in which the dominant growth rates are attained for $\mathbf{q}$ depending on $\nu$ and/or $\eta$. We consider now such a branching of the dominant magnetic modes in the kinematic dynamo problem, where an offshoot stems from a branch of neutral eigenmodes for $\mathbf{q} = 0$, and construct power series expansions for the offshoots and the associated eigenvalues of the magnetic induction operator near the point of bifurcation. We show that the branching occurs for the molecular magnetic diffusivities, for which the two eigenvalues of the eddy diffusivity operator become imaginary, and magnetic field generation by the mechanism of the negative eddy diffusivity ceases. The details of branching in the other linear stability problems under consideration are distinct.

**Keywords:** Power series expansion, asymptotics, kinematic dynamo problem, Bloch magnetic mode, branching, neutral eigenmodes, magnetic eddy diffusivity, scale separation.

**Citation:** Chertovskih, R., and V. Zheligovsky (2023), Linear perturbations of the Bloch type of space-periodic magnetohydrodynamic steady states. III. Asymptotics of branching, *Russ. J. Earth. Sci.*, 23, ES5004, https://doi.org/10.2205/2023es000841

## 1. Introduction

Bloch eigenmodes of three linear stability problems: the kinematic dynamo problem, the hydrodynamic and MHD stability problem for steady space-periodic flows and MHD states were considered in the previous papers [*Chertovskih and Zheligovsky*, 2023a,b] of this series. A Bloch mode is a product of a three-dimensional vector field of the same periodicity as the perturbed state and an amplitude-modulating planar wave $e^{i\mathbf{q}\cdot\mathbf{x}}$.

We have studied the dependence of the dominant growth rates of the Bloch modes on the diffusivity parameters, the molecular magnetic diffusivity $\eta$ and the molecular viscosity $\nu$. Computations [*Chertovskih and Zheligovsky*, 2023b] have revealed that the Bloch modes, maximizing growth rates $\gamma(\mathbf{q})$ over the Bloch wave vectors $\mathbf{q}$, constitute branches, in which the dependence of the dominant growth rates on the diffusivity parameter is smooth. It was demonstrated in [*Chertovskih and Zheligovsky*, 2023a] that half-integer $\mathbf{q}$ (whose all components are integer or half-integer) satisfy the necessary condition for the maximum, $\partial\gamma/\partial q_m = 0$. In agreement with this, branches of the dominant eigenmodes were found [*Chertovskih and Zheligovsky*, 2023a], that are comprised of the eigenmodes for constant

Research Article

Received: 22 November 2022
Accepted: 7 March 2023
Published: 28 December 2023

**Copyright:** © 2023. The Authors. This article is an open access article distributed under the terms and conditions of the Creative Commons Attribution (CC BY) license (https://creativecommons.org/licenses/by/4.0/).

half-integer $\mathbf{q}$. Furthermore, in all the three stability problems for parity-invariant steady states, instances of branches (which we call offshoots) stemming from branches of this type (we call them main branches) were detected; the dominant growth rates in the offshoots are attained for $\mathbf{q}$ depending on $\nu$ and/or $\eta$.

The phenomenon is very common. It is observed in 9 problems out of the 18 ones which were solved in [*Chertovskih and Zheligovsky*, 2023b], see figs. 6, 9, 10, 13–15, 21–23 *ibid.* (there are two instances of branching in figs. 9, 22 and 23, and three in fig. 6). Moreover, continuation of the plots "by eye" suggests, that the branch of neutral modes for $\mathbf{q} = 0$ perhaps experiences similar branching, that we have not detected (although some of the offshoots can consist of modes that have just the locally and not globally maximum growth rates). For $\nu$ or $\eta$ larger than 0.3 for which computations were performed, branching can happen in fig. 15, as well as (probably with a different asymptotics of the approach of the Bloch wave vector in the offshoots to $\mathbf{q} = 0$ in the main branch) in figs. 1, 2, 4, 6, 10, 12, 13, 18 and 20. Potential offshoots stemming from the branch of neutral modes for $\mathbf{q} = 0$ at the diffusivities below this upper bound can be observed in figs. 1 (perhaps one or two more possible branchings), 2, 12, 14, 15, 20 (the second possible branching in each of the four figures). This scenario seems impossible only for figs. 7, 16 and 19.

Consequently, questions arise: At which points (i.e., molecular diffusivities) does the branching occurs? What is the asymptotics of the offshoot near the point of bifurcation? How general is the behavior: does the asymptotics of branching coincide in the context of the three stability problems under consideration? Can offshoots stem similarly from branches of $\nu$- and/or $\eta$-dependent eigenmodes?

In order to answer some of these questions, we consider in the present paper the problem for Bloch magnetic modes kinematically generated by a parity-invariant flow $\mathbf{V}(\mathbf{x}) = -\mathbf{V}(-\mathbf{x})$. The precise statement of this problem is outlined in the next section. We expand all the quantities involved in power series in $\vartheta = (\eta_0 - \eta)^{1/2}$, where $\eta_0$ is the magnetic diffusivity, for which branching occurs. The eigenvalue equations for the modified magnetic induction operator and its adjoint (see [*Chertovskih and Zheligovsky*, 2023a] for derivation),

$$\mathscr{D}_{\mathbf{q}} : \mathbf{b} \mapsto \eta\Delta_{\mathbf{q}}\mathbf{b} + \nabla\times(\mathbf{V}\times\mathbf{b}) + \mathrm{i}\mathbf{q}\times(\mathbf{V}\times\mathbf{b}),$$
$$\mathscr{D}^*_{\mathbf{q}} : \mathbf{b} \mapsto \eta\Delta_{\mathbf{q}}\mathbf{b} - \mathbf{V}\times(\nabla\times\mathbf{b} + \mathrm{i}\mathbf{q}\times\mathbf{b}),$$

where

$$\Delta_{\mathbf{q}} : \mathbf{f} \mapsto \nabla^2\mathbf{f} + 2\mathrm{i}(\mathbf{q}\cdot\nabla)\mathbf{f} - |\mathbf{q}|^2\mathbf{f}$$

is the modified Laplacian, give rise to a hierarchy of equations emerging at different orders of $\vartheta$. In sections 3–7 we consider the equations of the hierarchy at orders $\vartheta^0$ to $\vartheta^4$, respectively. At order $\vartheta^4$ we obtain the leading-order expression for the growth rate. In principle, we could also solve the equations at higher orders and obtain all terms of the expansions. The concluding remarks are summarized in the last section.

## 2. Statement of the problem

We consider here kinematic generation of magnetic Bloch modes by a parity-invariant flow $\mathbf{V}(\mathbf{x}) = -\mathbf{V}(-\mathbf{x})$ and investigate branching of modes featuring locally maximum growth rates from a branch of minimum-periodicity modes for $\mathbf{q} = 0$. This bifurcation is illustrated, e.g., by Fig. 14(a),(b) [*Chertovskih and Zheligovsky*, 2023b], where branch II bifurcates from branch III comprised of neutral (stationary) magnetic modes for $\mathbf{q} = 0$. We observe that at the point of bifurcation the graph of growth rates is tangent to the zero eigenvalue for $\mathbf{q} = 0$, and the locally maximum growth rates in branch II are attained for the optimal $\mathbf{q}$ that are order $\vartheta = (\eta_0 - \eta)^{1/2}$. This suggests to study the bifurcation by expanding the magnetic modes, $\mathbf{b}(\mathbf{x})$, and the associated eigenvalue, $\lambda$,

$$\mathscr{D}_{\mathbf{q}}\mathbf{b} = \lambda\mathbf{b}, \tag{1}$$

the respective eigenfunctions of the adjoint operator, $\mathbf{b}^*(\mathbf{x})$,

$$\mathscr{D}_{\mathbf{q}}^*\mathbf{b}^* = \overline{\lambda}\mathbf{b}^*, \tag{2}$$

and the optimal $\mathbf{q}$ in power series in $\vartheta$:

$$\mathbf{b} = \sum_{j=0}^{\infty}\mathbf{b}_j\vartheta^j, \qquad \mathbf{b}^* = \sum_{j=0}^{\infty}\mathbf{b}_j^*\vartheta^j, \qquad \lambda = \sum_{j=1}^{\infty}\lambda_j\vartheta^j, \qquad \mathbf{q} = \sum_{j=1}^{\infty}\mathbf{q}_j\vartheta^j. \tag{3}$$

The modes are normalized by the condition

$$\langle\langle\mathbf{b},\mathbf{b}^*\rangle\rangle = 1 \tag{4}$$

(the individual normalization of each mode is irrelevant). Here the angle brackets $\langle\langle\cdot,\cdot\rangle\rangle$ denote the scalar product

$$\langle\langle\mathbf{f}_1,\mathbf{f}_2\rangle\rangle = \left\langle\mathbf{f}_1\cdot\overline{\mathbf{f}_2}\right\rangle \equiv (2\pi)^{-3}\int_{\mathbb{T}^3}\mathbf{f}_1(\mathbf{x})\cdot\overline{\mathbf{f}_2(\mathbf{x})}\,\mathrm{d}\mathbf{x}$$

in the Lebesgue space $\mathbb{L}_2(\mathbb{T}^3)$ of three-dimensional complex-valued vector fields, and the angle brackets $\langle\cdot\rangle$ denote the spatial averaging

$$\langle\mathbf{b}(\mathbf{x})\rangle = (2\pi)^{-3}\int_{\mathbb{T}^3}\mathbf{b}(\mathbf{x})\,\mathrm{d}\mathbf{x}.$$

An eigenfunction of $\mathscr{D}_{\mathbf{q}}$, whose growth rate $\gamma = \mathrm{Re}\,\lambda$ is positive, automatically gives rise to a solenoidal Bloch mode. Nevertheless, it is useful to specialize the condition of solenoidality of the Bloch field $\mathrm{e}^{\mathrm{i}\mathbf{q}\cdot\mathbf{x}}\mathbf{b}(\mathbf{x})$ for eigenfunctions of the form of the series (3). We obtain at order $\vartheta^j$

$$\nabla\cdot\mathbf{b}_j + \mathrm{i}\sum_{k=1}^{j}\mathbf{q}_k\cdot\mathbf{b}_{j-k} = 0.$$

In particular, $\mathbf{b}_0$ (but not $\mathbf{b}_0^*$) must be solenoidal. Averaging this equation yields

$$\sum_{k=1}^{j}\mathbf{q}_k\cdot\left\langle\mathbf{b}_{j-k}\right\rangle = 0. \tag{5}$$

We substitute the series (3) into the eigenvalue equations (1) and (2), and the conditions

$$\frac{\partial\gamma}{\partial q_m} = 0 \quad\Leftrightarrow\quad -2\eta q_m\mathrm{Re}\langle\langle\mathbf{b},\mathbf{b}^*\rangle\rangle - \mathrm{Im}\left\langle\!\!\left\langle 2\eta\,\frac{\partial\mathbf{b}}{\partial x_m} + \mathbf{e}_m\times(\mathbf{V}\times\mathbf{b}),\mathbf{b}^*\right\rangle\!\!\right\rangle = 0$$

$$\Leftrightarrow\quad 2\eta\left(\mathbf{q} + \sum_m \mathrm{Im}\left\langle\frac{\partial\mathbf{b}}{\partial x_m}\cdot\overline{\mathbf{b}^*}\right\rangle\mathbf{e}_m\right) + \mathrm{Im}\left\langle(\mathbf{V}\times\mathbf{b})\times\overline{\mathbf{b}^*}\right\rangle = 0 \tag{6}$$

for the local maximum of the growth rate $\gamma$ (derived from the general expression for the gradient, see (14) in [*Chertovskih and Zheligovsky*, 2023a]).

### 3. Order $\vartheta^0$ equations

Substituting $\eta = \eta_0 - \vartheta^2$ and the series (3) into (1), (2), (6) and the normalization condition (4) we obtain at order $\vartheta^0$, respectively, the equations

$$\mathscr{D}\mathbf{b}_0 = 0, \tag{7.1}$$
$$\mathscr{D}^*\mathbf{b}_0^* = 0, \tag{7.2}$$
$$\mathrm{Im}\left\langle\!\!\left\langle 2\eta_0 \frac{\partial \mathbf{b}_0}{\partial x_m} + \mathbf{e}_m \times (\mathbf{V}\times\mathbf{b}_0), \mathbf{b}_0^*\right\rangle\!\!\right\rangle = 0, \tag{7.3}$$
$$\langle\langle \mathbf{b}_0, \mathbf{b}_0^*\rangle\rangle = 1, \tag{7.4}$$

where

$$\mathscr{D} : \mathbf{b} \mapsto \eta_0\nabla^2\mathbf{b} + \nabla\times(\mathbf{V}\times\mathbf{b}), \qquad \mathscr{D}^* : \mathbf{b} \mapsto \eta_0\nabla^2\mathbf{b} - \mathbf{V}\times(\nabla\times\mathbf{b}). \tag{8}$$

For a space-periodic flow, the magnetic induction operator $\mathscr{D}$ has at least a three-dimensional kernel of neutral modes of the same periodicity (*Arnol'd et al.* [1982], see also *Zheligovsky* [2011]). Generically, the dimension of the kernel is 3, and we assume that this holds for $\eta = \eta_0$. Then, for a parity-invariant flow $\mathbf{V}$, (7.1) implies that $\mathbf{b}_0$ is a parity-antiinvariant solenoidal field (i.e., $\mathbf{b}_0(\mathbf{x}) = \mathbf{b}_0(-\mathbf{x})$), the set of all possible $\langle\mathbf{b}_0\rangle$ spans $\mathbb{R}^3$, and

$$\mathbf{b}_0(\mathbf{x}) = \sum_{k=1}^{3} \langle\mathbf{b}_0\rangle_k \mathbf{S}_k, \quad \text{where} \quad \mathscr{D}\mathbf{S}_k = 0, \ \langle\mathbf{S}_k\rangle = \mathbf{e}_k. \tag{9}$$

Here $\langle\cdot\rangle_k$ denotes averaging of the $k$th component of a vector field: $\langle\mathbf{f}\rangle = \sum_{k=1}^{3}\langle\mathbf{f}\rangle_k\mathbf{e}_k$. Neutral modes $\mathbf{S}_k$ are real, solenoidal and parity-antiinvariant. From (7.2),

$$\mathbf{b}_0^* = \sum_k b_{0k}^*\mathbf{e}_k \tag{10}$$

is a constant vector. Consequently, (7.3) is satisfied identically (which agrees with the statement that half-integer $\mathbf{q}$ are stationary points of the growth rate regarded as a function of $\mathbf{q}$; it was proven in section 4 of [*Chertovskih and Zheligovsky*, 2023a]). $\{\mathbf{S}_k\}$ constitute the basis in the kernel of $\mathscr{D}$, biorthogonal to $\{\mathbf{e}_k\}$ that are the basis in the kernel of $\mathscr{D}^*$. By the Fredholm alternative theorem, the equations $\mathscr{D}\mathbf{b} = \mathbf{f}$ and $\mathscr{D}^*\mathbf{b}^* = \mathbf{f}^*$ have solutions if and only if, respectively,

$$\langle\mathbf{f}\rangle = 0, \tag{11.1}$$
$$\langle\langle\mathbf{f}^*, \mathbf{S}_k\rangle\rangle = 0 \quad \text{for all } \mathbf{S}_k \in \ker\mathscr{D}. \tag{11.2}$$

### 4. Order $\vartheta^1$ equations

At order $\vartheta^1$ we obtain from (1), (2), (6) and (4), respectively,

$$\mathscr{D}\mathbf{b}_1 + 2\mathrm{i}\eta_0(\mathbf{q}_1\cdot\nabla)\mathbf{b}_0 + \mathrm{i}\mathbf{q}_1\times(\mathbf{V}\times\mathbf{b}_0) = \lambda_1\mathbf{b}_0, \tag{12.1}$$
$$\mathscr{D}^*\mathbf{b}_1^* - \mathbf{V}\times(\mathrm{i}\mathbf{q}_1\times\mathbf{b}_0^*) = \overline{\lambda}_1\mathbf{b}_0^*, \tag{12.2}$$
$$2\eta_0\left(\mathbf{q}_1 + \sum_m \mathrm{Im}\left\langle\frac{\partial\mathbf{b}_0}{\partial x_m}\cdot\overline{\mathbf{b}_1^*}\right\rangle\mathbf{e}_m\right) + \mathrm{Im}\left\langle(\mathbf{V}\times\mathbf{b}_0)\times\overline{\mathbf{b}_1^*} + (\mathbf{V}\times\mathbf{b}_1)\times\overline{\mathbf{b}_0^*}\right\rangle = 0, \tag{12.3}$$
$$\langle\langle\mathbf{b}_0, \mathbf{b}_1^*\rangle\rangle + \langle\langle\mathbf{b}_1, \mathbf{b}_0^*\rangle\rangle = 0. \tag{12.4}$$

Averaging (12.1) yields $\lambda_1\langle\mathbf{b}_0\rangle = 0$, whereby $\lambda_1 = 0$. The conditions (11) for solvability of equations (12.1) and (12.2) are satisfied ((11.2) holds because all $\mathbf{S}_k \in \ker\mathscr{D}$ are parity-antiinvariant). The solutions are

$$\mathbf{b}_1 = \sum_k \langle\mathbf{b}_1\rangle_k\mathbf{S}_k + \mathbf{b}_{1\mathrm{p}}, \qquad \mathbf{b}_1^* = \langle\mathbf{b}_1^*\rangle + \mathbf{b}_{1\mathrm{p}}^*. \tag{13}$$

Here

$$\mathbf{b}_{1\mathrm{p}} = \mathrm{i}\sum_{k,m} q_{1m}\langle \mathbf{b}_0\rangle_k \mathbf{G}_{mk}(\mathbf{x}), \qquad \mathscr{D}\mathbf{G}_{mk} + 2\eta_0\frac{\partial \mathbf{S}_k}{\partial x_m} + \mathbf{e}_m\times(\mathbf{V}\times\mathbf{S}_k) = 0, \tag{14.1}$$

$$\mathbf{b}^*_{1\mathrm{p}} = \mathrm{i}\sum_{m,k,n} \epsilon_{mkn} q_{1m} b^*_{0k}\mathbf{Z}_n(\mathbf{x}), \qquad \mathscr{D}^*\mathbf{Z}_n - \mathbf{V}\times\mathbf{e}_n = 0, \tag{14.2}$$

$q_{1k}$ are the Cartesian components of $\mathbf{q}_1 = \sum_k q_{1k}\mathbf{e}_k$ and $\epsilon_{mkn}$ is the unit antisymmetric tensor. $\mathbf{G}_{mk}(\mathbf{x})$ and $\mathbf{Z}_n(\mathbf{x})$ are real-valued parity-invariant zero-mean vector fields (since parity-invariant and parity-antiinvariant fields constitute invariant subspaces of the operators $\mathscr{D}$ and $\mathscr{D}^*$).

In the equations for $\mathbf{G}_{mk}$ and $\mathbf{Z}_n$ we recognize auxiliary problems for the magnetic induction operator (cf. section 5.2 in [*Chertovskih and Zheligovsky*, 2023a], equations (39)) and the adjoint operator (cf. section 5.3 *ibid.*) arising in the standard formalism of the analysis of magnetic eddy diffusivity in small-scale flows of electrically conducting fluid (see *Andrievsky et al.* [2015], *Rasskazov et al.* [2018], *Zheligovsky* [2011]). In fact, so far the expansion followed (except for the new condition (6) of local extremality of the growth rate) that formalism, but in the present context we have to consider the problems emerging at further levels of the asymptotic expansion.

We substitute (9), (10) and (13) into (12.3), use the identity

$$\Big\langle(\mathbf{V}\times\mathbf{S}_j)\times\mathbf{Z}_n\Big\rangle_l + 2\eta_0\Big\langle\frac{\partial\mathbf{S}_j}{\partial x_l}\cdot\mathbf{Z}_n\Big\rangle = \Big\langle\mathbf{V}\times\mathbf{G}_{lj}\Big\rangle_n \tag{15}$$

and obtain

$$\mathscr{E}\mathbf{q}_1 = 0, \tag{16}$$

where

$$\mathscr{E}:\mathbf{c}\mapsto 2\eta_0\,\mathbf{c} - \sum_{k,m}\Big(\Big(\mathbf{c}\times\mathrm{Re}\,(\langle\mathbf{b}_0\rangle_k\overline{\mathbf{b}^*_0})\Big)\cdot\langle\mathbf{V}\times\mathbf{G}_{mk}\rangle\Big)\,\mathbf{e}_m - \sum_{k,m} c_m\,\mathrm{Re}\Big(\langle\mathbf{b}_0\rangle_k\overline{\mathbf{b}^*_0}\Big)\times\langle\mathbf{V}\times\mathbf{G}_{mk}\rangle.$$

The linear operator $\mathscr{E}:\mathbb{R}^3\to\mathbb{R}^3$ is self-adjoint. By (16), the vector $\mathbf{q}_1$ belongs to its kernel. Generically, the kernel is one-dimensional, and then the solvability condition for the equation $\mathscr{E}\mathbf{c} = \mathbf{f}$ is the orthogonality $\mathbf{f}\cdot\mathbf{q}_1 = 0$.

### 5. Order $\vartheta^2$ equations

At order $\vartheta^2$, (1), (2), (6) and (4) give rise, respectively, to the equations

$$\begin{aligned}&\mathscr{D}\mathbf{b}_2 + 2\mathrm{i}\eta_0((\mathbf{q}_1\cdot\nabla)\mathbf{b}_1 + (\mathbf{q}_2\cdot\nabla)\mathbf{b}_0) - \nabla^2\mathbf{b}_0 + \mathrm{i}\mathbf{q}_1\times(\mathbf{V}\times\mathbf{b}_1) + \mathrm{i}\mathbf{q}_2\times(\mathbf{V}\times\mathbf{b}_0)\\ &\quad = (\lambda_2 + \eta_0|\mathbf{q}_1|^2)\mathbf{b}_0,\end{aligned} \tag{17.1}$$

$$\mathscr{D}^*\mathbf{b}^*_2 + 2\mathrm{i}\eta_0(\mathbf{q}_1\cdot\nabla)\mathbf{b}^*_1 - \mathrm{i}\mathbf{V}\times(\mathbf{q}_1\times\mathbf{b}^*_1 + \mathbf{q}_2\times\mathbf{b}^*_0) = (\overline{\lambda}_2 + \eta_0|\mathbf{q}_1|^2)\mathbf{b}^*_0, \tag{17.2}$$

$$\begin{aligned}&2\eta_0\Big(\mathbf{q}_2 + \sum_m \mathrm{Im}\left\langle\frac{\partial\mathbf{b}_0}{\partial x_m}\cdot\overline{\mathbf{b}^*_2} + \frac{\partial\mathbf{b}_1}{\partial x_m}\cdot\overline{\mathbf{b}^*_1}\right\rangle\mathbf{e}_m\Big)\\ &\quad + \mathrm{Im}\left\langle(\mathbf{V}\times\mathbf{b}_0)\times\overline{\mathbf{b}^*_2} + (\mathbf{V}\times\mathbf{b}_1)\times\overline{\mathbf{b}^*_1} + (\mathbf{V}\times\mathbf{b}_2)\times\overline{\mathbf{b}^*_0}\right\rangle = 0,\end{aligned} \tag{17.3}$$

$$\langle\langle\mathbf{b}_0,\mathbf{b}^*_2\rangle\rangle + \langle\langle\mathbf{b}_1,\mathbf{b}^*_1\rangle\rangle + \langle\langle\mathbf{b}_2,\mathbf{b}^*_0\rangle\rangle = 0. \tag{17.4}$$

The solvability condition for (17.1) is obtained by averaging (see (11.1)):

$$\mathrm{i}\,\langle\mathbf{q}_1\times(\mathbf{V}\times\mathbf{b}_1)\rangle = (\lambda_2 + \eta_0|\mathbf{q}_1|^2)\langle\mathbf{b}_0\rangle.$$

Substituting here (13) and (14.1) yields an eigenvalue equation

$$\mathfrak{D}\,\langle\mathbf{b}_0\rangle = (\lambda_2 + \eta_0|\mathbf{q}_1|^2)\langle\mathbf{b}_0\rangle \tag{18.1}$$

for the $3\times 3$ real entry matrix $\mathfrak{D}$,

$$\mathfrak{D}\mathbf{c} = -\sum_{k,m} q_{1m}c_k \mathbf{q}_1 \times \langle \mathbf{V}\times\mathbf{G}_{mk}\rangle \tag{18.2}$$

($\mathfrak{D}$ is the symbol of the operator of eddy correction of magnetic eddy diffusivity). Upon substituting (13) and (14.2), the solvability condition (11.2) for (17.2) reduces to the eigenvalue equation

$$\mathfrak{D}^*\mathbf{b}_0^* = (\overline{\lambda}_2 + \eta_0|\mathbf{q}_1|^2)\mathbf{b}_0^* \tag{18.3}$$

for the $3\times 3$ matrix $\mathfrak{D}^*$ defined by the relation

$$\mathfrak{D}^*\mathbf{c} = -\sum_{k,m,n,j} \epsilon_{mkn} q_{1m}c_k \left\langle \Big(2\eta_0(\mathbf{q}_1\cdot\nabla)\mathbf{Z}_n - \mathbf{V}\times(\mathbf{q}_1\times\mathbf{Z}_n)\Big)\cdot\mathbf{S}_j\right\rangle \mathbf{e}_j. \tag{18.4}$$

Eigenvalues of the two matrices are complex conjugate, $\mathfrak{D}^*$ being equal to the transpose of the matrix $\mathfrak{D}$ since

$$\begin{aligned}
-\mathbf{q}_1\times\langle\mathbf{V}\times\mathbf{G}_{mk}\rangle &= \sum_n (\mathbf{q}_1\times\mathbf{e}_n)\langle(\mathbf{V}\times\mathbf{e}_n)\cdot\mathbf{G}_{mk}\rangle\\
&= \sum_n (\mathbf{q}_1\times\mathbf{e}_n)\langle(\mathscr{D}^*\mathbf{Z}_n\cdot\mathbf{G}_{mk}\rangle\\
&= \sum_n (\mathbf{q}_1\times\mathbf{e}_n)\langle\mathbf{Z}_n\cdot\mathscr{D}\mathbf{G}_{mk}\rangle\\
&= -\sum_n (\mathbf{q}_1\times\mathbf{e}_n)\langle\mathbf{Z}_n\cdot(2\eta_0\,\partial\mathbf{S}_k/\partial x_m + \mathbf{e}_m\times(\mathbf{V}\times\mathbf{S}_k))\rangle\\
&= \sum_{n,l,j} \epsilon_{jln}q_{1l}\langle\mathbf{S}_k\cdot(2\eta_0\,\partial\mathbf{Z}_n/\partial x_m - \mathbf{V}\times(\mathbf{e}_m\times\mathbf{Z}_n))\rangle\mathbf{e}_j.
\end{aligned}$$

Let us consider the component of (16) parallel to $\mathbf{q}_1$. In terms of the matrix $\mathfrak{D}$ (18.2), the scalar product of (16) and $\mathbf{q}_1$ takes the form

$$2\eta_0|\mathbf{q}_1|^2 - 2\mathrm{Re}\,\langle\langle\mathfrak{D}\langle\mathbf{b}_0\rangle,\mathbf{b}_0^*\rangle\rangle = 0.$$

Hence $\mathrm{Re}\,\lambda_2 = 0$ by virtue of (18.1) and normalization (7.4). We can now clarify the nature of the condition (16). Differentiating (18.1) in $q_{1n}$ yields

$$\Big(\mathfrak{D} - (\lambda_2+\eta_0|\mathbf{q}_1|^2)\Big)\frac{\partial\langle\mathbf{b}_0\rangle}{\partial q_{1n}} - \left(\frac{\partial\lambda_2}{\partial q_{1n}} + 2\eta_0\mathbf{q}_{1n}\right)\langle\mathbf{b}_0\rangle - \sum_{k,m}\langle\mathbf{b}_0\rangle_k(\mathbf{q}_1\delta_m^n + q_{1m}\mathbf{e}_n)\times\langle\mathbf{V}\times\mathbf{G}_{mk}\rangle = 0.$$

Scalar multiplying this equation by $\overline{\mathbf{b}_0^*}$, applying (7.4), taking the real part and noting that $n$ is an arbitrary index, we obtain $\nabla_{\mathbf{q}_1}\mathrm{Re}\,\lambda_2 = -\mathscr{E}\mathbf{q}_1$. Thus, the relation (16) is equivalent to the condition that 0 is an extreme (on varying $\mathbf{q}_1$) large-scale magnetic field growth rate – that is, an extreme real part of the eigenvalue of the operator of eddy diffusivity $\mathfrak{D} - \eta_0|\mathbf{q}_1|^2$. Of course, we choose the dominant eigenvalue, i.e., the maximum over $\mathbf{q}_1$ growth rate, and then $\eta_0$ is the molecular diffusivity for which the large-scale dynamo sets in on decreasing $\eta$.

For $j=1$, (5) amounts to the orthogonality condition $\mathbf{q}_1\cdot\langle\mathbf{b}_0\rangle = 0$. An immediate consequence of (18.4) is that $\mathfrak{D}^*$ has an eigenvalue zero associated with the eigenvector $\mathbf{q}_1$. It is spurious, being associated with an eigenvector of $\mathfrak{D}$ for which $\mathbf{q}_1\cdot\langle\mathbf{b}_0\rangle \neq 0$ (see *Rasskazov et al.* [2018], *Zheligovsky* [2011] for details of solving the eigenvalue problem for $\mathfrak{D}$). Consequently, the operator $\mathfrak{D}^*$ has eigenvalues $-\lambda_2+\eta_0|\mathbf{q}_1|^2$, $\lambda_2+\eta_0|\mathbf{q}_1|^2$ and 0 associated with eigenvectors $\mathbf{h}_1^* = \mathbf{b}_0^*$, $\mathbf{h}_2^* = \overline{\mathbf{b}_0^*}$ and $\mathbf{h}_3^* = \mathbf{q}_1$, respectively; the adjoint operator $\mathfrak{D}$ has eigenvalues $\lambda_2+\eta_0|\mathbf{q}_1|^2$, $-\lambda_2+\eta_0|\mathbf{q}_1|^2$ and 0 associated with eigenvectors $\mathbf{h}_1 = \langle\mathbf{b}_0\rangle$, $\mathbf{h}_2 = \left\langle\overline{\mathbf{b}_0}\right\rangle$ and a vector that we denote $\mathbf{h}_3$. The bases of the eigenvectors of $\mathfrak{D}$ and $\mathfrak{D}^*$ are

biorthogonal, i.e., $\mathbf{h}_k \cdot \overline{\mathbf{h}_j^*} = 0$ for $k \neq j$, and this scalar product is non-zero for $k = j$ (whereby the normalization (7.4) is always possible).

Equations (18.1), (18.3) and (16) are homogeneous in $\mathbf{q}_1$: upon dividing (18.1) and (18.3) by $|\mathbf{q}_1|^2$, and (16) by $|\mathbf{q}_1|$, none of them involves the length of $\mathbf{q}_1$ (except for in the product $|\mathbf{q}_1|^{-2}\lambda_2$). Therefore, at least in principle, this system can be solved as follows: $(i)$ we find eigenvectors $\langle \mathbf{b}_0 \rangle$ of $\mathfrak{D}$ and $\mathbf{b}_0^*$ of the transposed matrix $\mathfrak{D}^*$ associated with non-zero complex conjugate eigenvalues as functions of $\eta_0$ and $\mathbf{q}_1/|\mathbf{q}_1|$; $(ii)$ we find $\mathbf{q}_1/|\mathbf{q}_1|$ as a function of $\eta_0$ from (16); $(iii)$ we equate $\eta_0$ to the real part of the eigenvalue of the matrix $|\mathbf{q}_1|^{-2}\mathfrak{D}$ obtained in step $(ii)$, and solve the resultant equation for $\eta_0$; $(iv)$ finally, $|\mathbf{q}_1|^{-2}\lambda_2$ is equal to the imaginary part of the eigenvalue of the matrix $|\mathbf{q}_1|^{-2}\mathfrak{D}$. At this stage we thus fully determine $\eta_0$, the eigenvectors $\langle \mathbf{b}_0 \rangle$ and $\mathbf{b}_0^*$ (up to arbitrary individual normalizations, that are irrelevant provided the condition (7.4), equivalent to $\langle \mathbf{b}_0 \rangle \cdot \overline{\mathbf{b}_0^*} = 1$, is imposed), the direction $\mathbf{q}_1/|\mathbf{q}_1|$, and the imaginary value $|\mathbf{q}_1|^{-2}\lambda_2$. We lack an equation for determining the length $|\mathbf{q}_1|$: this scaling is controlled by the term $-\vartheta^2\nabla^2\mathbf{b}$ in the original eigenvalue problem (1), but neither the solvability conditions at this order, nor (16) involve contributions from this term.

By (17.1) and (17.2),

$$\mathbf{b}_2 = \sum_k \Big( \langle \mathbf{b}_2 \rangle_k \mathbf{S}_k + \langle \mathbf{b}_0 \rangle_k \Big( (\lambda_2 + \eta_0 |\mathbf{q}_1|^2) \mathbf{S}_k^{(1)} + \mathbf{S}_k^{(2)} + \sum_{m,n} q_{1m} q_{1n} \mathbf{S}_{nmk}^{(3)} \Big) \Big) + \mathrm{i} \sum_{k,m} (q_{2m} \langle \mathbf{b}_0 \rangle_k + q_{1m} \langle \mathbf{b}_1 \rangle_k) \mathbf{G}_{mk}, \tag{19.1}$$

$$\mathbf{b}_2^* = \langle \mathbf{b}_2^* \rangle + \mathrm{i} \sum_{m,k,n} \epsilon_{mkn} (q_{1m} \langle \mathbf{b}_1^* \rangle_k + q_{2m} b_{0k}^*) \mathbf{Z}_n + \sum_{m,k,n,j} \epsilon_{mkn} q_{1m} q_{1j} b_{0k}^* \mathbf{Z}_{jn}^{(1)}, \tag{19.2}$$

where parity-antiinvariant zero-mean functions $\mathbf{S}_k^{(1)}(\mathbf{x})$, $\mathbf{S}_k^{(2)}(\mathbf{x})$, $\mathbf{S}_{nmk}^{(3)}(\mathbf{x})$ and $\mathbf{Z}_{jn}^{(1)}(\mathbf{x})$ solve the auxiliary problems

$$\begin{aligned}
\mathscr{D}\mathbf{S}_k^{(1)} &= \mathbf{S}_k - \mathbf{e}_k, \\
\mathscr{D}\mathbf{S}_k^{(2)} &= \nabla^2 \mathbf{S}_k, \\
\mathscr{D}\mathbf{S}_{nmk}^{(3)} &= 2\eta_0 \, \partial \mathbf{G}_{mk}/\partial x_n + \mathbf{e}_n \times (\mathbf{V} \times \mathbf{G}_{mk} - \langle \mathbf{V} \times \mathbf{G}_{mk} \rangle), \\
\mathscr{D}^* \mathbf{Z}_{jn}^{(1)} &= 2\eta_0 \, \partial \mathbf{Z}_n/\partial x_j - \mathbf{V} \times (\mathbf{e}_j \times \mathbf{Z}_n) + \sum_{l=1}^{3} \Big\langle \mathbf{V} \times \mathbf{G}_{jl} \Big\rangle_n \mathbf{e}_l.
\end{aligned}$$

Upon substituting (13), (14) and (19), and applying (15), the extremality condition (17.3) takes the form

$$\mathscr{E}\mathbf{q}_2 = \sum_{k,m} \Big( \Big( \mathbf{q}_1 \times \mathrm{Re}\,(\langle \mathbf{b}_0 \rangle_k \overline{\langle \mathbf{b}_1^* \rangle} + \langle \mathbf{b}_1 \rangle_k \overline{\mathbf{b}_0^*}) \Big) \cdot \langle \mathbf{V} \times \mathbf{G}_{mk} \rangle \, \mathbf{e}_m + q_{1m} \, \mathrm{Re}\,(\langle \mathbf{b}_0 \rangle_k \overline{\langle \mathbf{b}_1^* \rangle} + \langle \mathbf{b}_1 \rangle_k \overline{\mathbf{b}_0^*}) \times \langle \mathbf{V} \times \mathbf{G}_{mk} \rangle \Big). \tag{20}$$

## 6. Order $\vartheta^3$ equations

At order $\vartheta^3$, power series expansions of (1), (2), (6) and (4) yield, respectively, the equations

$$\mathscr{D}\mathbf{b}_3 + 2\mathrm{i}\eta_0((\mathbf{q}_1\cdot\nabla)\mathbf{b}_2 + (\mathbf{q}_2\cdot\nabla)\mathbf{b}_1 + (\mathbf{q}_3\cdot\nabla)\mathbf{b}_0) - \nabla^2\mathbf{b}_1 - 2\mathrm{i}(\mathbf{q}_1\cdot\nabla)\mathbf{b}_0 + \mathrm{i}\mathbf{q}_1\times(\mathbf{V}\times\mathbf{b}_2) + \mathrm{i}\mathbf{q}_2\times(\mathbf{V}\times\mathbf{b}_1) + \mathrm{i}\mathbf{q}_3\times(\mathbf{V}\times\mathbf{b}_0) = (\lambda_3 + 2\eta_0\mathbf{q}_1\cdot\mathbf{q}_2)\mathbf{b}_0 + (\lambda_2 + \eta_0|\mathbf{q}_1|^2)\mathbf{b}_1, \tag{21.1}$$

$$\mathscr{D}^*\mathbf{b}_3^* + 2\mathrm{i}\eta_0((\mathbf{q}_1\cdot\nabla)\mathbf{b}_2^* + (\mathbf{q}_2\cdot\nabla)\mathbf{b}_1^*) - \nabla^2\mathbf{b}_1^* - \mathrm{i}\mathbf{V}\times(\mathbf{q}_1\times\mathbf{b}_2^* + \mathbf{q}_2\times\mathbf{b}_1^* + \mathbf{q}_3\times\mathbf{b}_0^*) = (\overline{\lambda}_3 + 2\eta_0\mathbf{q}_1\cdot\mathbf{q}_2)\mathbf{b}_0^* + (\overline{\lambda}_2 + \eta_0|\mathbf{q}_1|^2)\mathbf{b}_1^*, \tag{21.2}$$

$$2\eta_0\left(\mathbf{q}_3 + \sum_m \mathrm{Im}\left\langle\frac{\partial\mathbf{b}_0}{\partial x_m}\cdot\overline{\mathbf{b}_3^*} + \frac{\partial\mathbf{b}_1}{\partial x_m}\cdot\overline{\mathbf{b}_2^*} + \frac{\partial\mathbf{b}_2}{\partial x_m}\cdot\overline{\mathbf{b}_1^*}\right\rangle\mathbf{e}_m\right) - 2\left(\mathbf{q}_1 + \sum_m \mathrm{Im}\left\langle\frac{\partial\mathbf{b}_0}{\partial x_m}\cdot\overline{\mathbf{b}_1^*}\right\rangle\mathbf{e}_m\right) + \mathrm{Im}\left\langle(\mathbf{V}\times\mathbf{b}_0)\times\overline{\mathbf{b}_3^*} + (\mathbf{V}\times\mathbf{b}_1)\times\overline{\mathbf{b}_2^*} + (\mathbf{V}\times\mathbf{b}_2)\times\overline{\mathbf{b}_1^*} + (\mathbf{V}\times\mathbf{b}_3)\times\overline{\mathbf{b}_0^*}\right\rangle = 0, \tag{21.3}$$

$$\langle\langle\mathbf{b}_0,\mathbf{b}_3^*\rangle\rangle + \langle\langle\mathbf{b}_2,\mathbf{b}_1^*\rangle\rangle + \langle\langle\mathbf{b}_1,\mathbf{b}_2^*\rangle\rangle + \langle\langle\mathbf{b}_3,\mathbf{b}_0^*\rangle\rangle = 0. \tag{21.4}$$

Again we use first the solvability conditions for (21.1) and (21.2). Averaging reduces (21.1) to

$$\mathrm{i}\langle\mathbf{q}_1\times(\mathbf{V}\times\mathbf{b}_2) + \mathbf{q}_2\times(\mathbf{V}\times\mathbf{b}_1)\rangle = (\lambda_3 + 2\eta_0\mathbf{q}_1\cdot\mathbf{q}_2)\langle\mathbf{b}_0\rangle + (\lambda_2 + \eta_0|\mathbf{q}_1|^2)\langle\mathbf{b}_1\rangle.$$

Upon substituting (13), (14) and (19), the solvability condition for (21.1) becomes

$$\mathfrak{D}\langle\mathbf{b}_1\rangle - \sum_{m,k}\langle\mathbf{b}_0\rangle_k(q_{1m}\mathbf{q}_2 + q_{2m}\mathbf{q}_1)\times\langle\mathbf{V}\times\mathbf{G}_{mk}\rangle = (\lambda_3 + 2\eta_0\mathbf{q}_1\cdot\mathbf{q}_2)\langle\mathbf{b}_0\rangle + (\lambda_2 + \eta_0|\mathbf{q}_1|^2)\langle\mathbf{b}_1\rangle. \tag{22}$$

Scalar multiplying it by $\overline{\mathbf{b}_0^*}$, we find

$$\lambda_3 = -2\eta_0\mathbf{q}_1\cdot\mathbf{q}_2 - \sum_{m,k}\langle\mathbf{b}_0\rangle_k\left((q_{1m}\mathbf{q}_2 + q_{2m}\mathbf{q}_1)\times\langle\mathbf{V}\times\mathbf{G}_{mk}\rangle\right)\cdot\overline{\mathbf{b}_0^*}. \tag{23}$$

Here the real part of the r.h.s. is equal to $-\mathbf{q}_2\cdot\mathscr{E}\mathbf{q}_1$, and thus $\mathrm{Re}\,\lambda_3 = 0$ by (16). Scalar multiplying (22) by $\mathbf{q}_1$ yields a relation equivalent to (5) for $j = 2$. To solve (22), we exploit the biorthogonality of the bases of the eigenvectors of $\mathfrak{D}$ and $\mathfrak{D}^*$, and find

$$\langle\mathbf{b}_1\rangle = \mu_1\langle\mathbf{b}_0\rangle - \sum_{m,k}\langle\mathbf{b}_0\rangle_k\frac{\left((q_{1m}\mathbf{q}_2 + q_{2m}\mathbf{q}_1)\times\langle\mathbf{V}\times\mathbf{G}_{mk}\rangle\right)\cdot\mathbf{b}_0^*}{2\lambda_2}\left\langle\overline{\mathbf{b}}_0\right\rangle - \frac{\langle\mathbf{b}_0\rangle\cdot\mathbf{q}_2}{\mathbf{h}_3\cdot\mathbf{q}_1}\mathbf{h}_3, \tag{24}$$

where $\mu_1$ is a constant. The solvability condition for (21.2) is

$$\sum_j\left\langle\left(2\mathrm{i}\eta_0((\mathbf{q}_2\cdot\nabla)\mathbf{b}_1^* + (\mathbf{q}_1\cdot\nabla)\mathbf{b}_2^*) - \mathrm{i}\mathbf{V}\times(\mathbf{q}_1\times\mathbf{b}_2^* + \mathbf{q}_2\times\mathbf{b}_1^*)\right)\cdot\mathbf{S}_j\right\rangle\mathbf{e}_j = (\overline{\lambda}_3 + 2\eta_0\mathbf{q}_1\cdot\mathbf{q}_2)\mathbf{b}_0^* + (\overline{\lambda}_2 + \eta_0|\mathbf{q}_1|^2)\langle\mathbf{b}_1^*\rangle,$$

or, upon substituting (13), (14) and (19), and using the identity (15)),

$$\mathfrak{D}^*\langle\mathbf{b}_1^*\rangle + \sum_{l,j}\left(\left((q_{1l}\mathbf{q}_2 + q_{2l}\mathbf{q}_1)\times\mathbf{b}_0^*\right)\cdot\left\langle\mathbf{V}\times\mathbf{G}_{lj}\right\rangle\right)\mathbf{e}_j = (\overline{\lambda}_3 + 2\eta_0\mathbf{q}_1\cdot\mathbf{q}_2)\mathbf{b}_0^* + (\overline{\lambda}_2 + \eta_0|\mathbf{q}_1|^2)\langle\mathbf{b}_1^*\rangle. \tag{25}$$

The scalar product of this equation with $\left\langle\overline{\mathbf{b}}_0\right\rangle$ is equivalent to (23). The solution to (25) is

$$\langle\mathbf{b}_1^*\rangle = \mu_1^*\mathbf{b}_0^* + \sum_{l,j}\left(\left((q_{1l}\mathbf{q}_2 + q_{2l}\mathbf{q}_1)\times\mathbf{b}_0^*\right)\cdot\left\langle\mathbf{V}\times\mathbf{G}_{lj}\right\rangle\right)\left(-\frac{\langle\mathbf{b}_0\rangle_j\overline{\mathbf{b}_0^*}}{2\lambda_2} + \frac{h_{3,j}\mathbf{q}_1}{(\overline{\lambda}_2 + \eta_0|\mathbf{q}_1|^2)\mathbf{h}_3\cdot\mathbf{q}_1}\right), \tag{26}$$

where $\mu_1^*$ is a constant. The eigenfunctions can be multiplied by any linear function of $\vartheta$; this changes arbitrarily the coefficients $\mu_1$ and $\mu_1^*$. In view of (9), (13) and (14), the normalization condition (12.4) reduces to $\langle \mathbf{b}_0\rangle\cdot\overline{\langle \mathbf{b}_1^*\rangle}+\langle \mathbf{b}_1\rangle\cdot\overline{\mathbf{b}_0^*}=0$. Substituting here the expressions (24) and (26), and employing the biorthogonality of the bases $\{\mathbf{h}_k\}$ and $\{\mathbf{h}_j^*\}$ transforms this equation into $\mu_1+\overline{\mu_1^*}=0$. Without any loss of generality we henceforth assume $\mu_1=\mu_1^*=0$.

The solvability condition for the problem (20) in $\mathbf{q}_2$ amounts to the orthogonality of the inhomogeneous term in (20) to $\mathbf{q}_1$ (as discussed at the end of section 4), which is equivalent to the equality

$$-2\mathrm{Re}\Big(\mathfrak{D}\langle \mathbf{b}_0\rangle\cdot\overline{\langle \mathbf{b}_1^*\rangle}+\mathfrak{D}\langle \mathbf{b}_1\rangle\cdot\overline{\mathbf{b}_0^*}\Big)=0.$$

Substituting here $\mathfrak{D}\langle \mathbf{b}_0\rangle$ (18.1) and $\mathfrak{D}\langle \mathbf{b}_1\rangle$ (22), using the normalization conditions (7.4) and (12.4), and relying on (23), we find that this equality holds true.

Upon dividing (22) and (25) by $|\mathbf{q}_1|^2$, and (20) by $|\mathbf{q}_1|$, we obtain equations that involve the direction $\mathbf{q}_1/|\mathbf{q}_1|$ and the vector $\mathbf{q}_2/|\mathbf{q}_1|$, but not the length $|\mathbf{q}_1|$. Hence, we solve this system of equations as follows: (*i*) We have expressed $\langle \mathbf{b}_1\rangle$ and $\langle \mathbf{b}_1^*\rangle$ as functions of $\mathbf{q}_2/|\mathbf{q}_1|$ and $\lambda_2/|\mathbf{q}_1|^2$. (*ii*) We find $\mathbf{q}_2/|\mathbf{q}_1|$ from the extremality condition (20) up to an unknown additive term $\beta_2\mathbf{q}_1/|\mathbf{q}_1|$ (cf. (16)). (*iii*) The imaginary value $\lambda_3/|\mathbf{q}_1|^2$ is determined by (23). We still lack an equation for determining the length $|\mathbf{q}_1|$.

Next we find solutions to equations the (21.1) and (21.2):

$$\begin{aligned}\mathbf{b}_3=&\sum_k\Big(\langle \mathbf{b}_3\rangle_k\mathbf{S}_k+\Big(\langle \mathbf{b}_0\rangle_k(\lambda_3+2\eta_0\mathbf{q}_1\cdot\mathbf{q}_2)+\langle \mathbf{b}_1\rangle_k(\lambda_2+\eta_0|\mathbf{q}_1|^2)\Big)\mathbf{S}_k^{(1)}+\langle \mathbf{b}_1\rangle_k\mathbf{S}_k^{(2)}\Big)\\&+\sum_{k,m,n}\Big(\langle \mathbf{b}_0\rangle_k(q_{1n}q_{2m}+q_{2n}q_{1m})+\langle \mathbf{b}_1\rangle_k q_{1n}q_{1m}\Big)\mathbf{S}_{nmk}^{(3)}\\&+\mathrm{i}\sum_{k,m}\Big((q_{3m}\langle \mathbf{b}_0\rangle_k+q_{2m}\langle \mathbf{b}_1\rangle_k+q_{1m}\langle \mathbf{b}_2\rangle_k)\mathbf{G}_{mk}\\&\qquad+q_{1m}\langle \mathbf{b}_0\rangle_k\Big((\lambda_2+\eta_0|\mathbf{q}_1|^2)\mathbf{G}_{mk}^{(1)}+\mathbf{G}_{mk}^{(2)}+\sum_{j,n}q_{1j}q_{1n}\mathbf{G}_{jnmk}^{(3)}\Big)\Big),\end{aligned}\tag{27.1}$$

$$\begin{aligned}\mathbf{b}_3^*=&\langle \mathbf{b}_3^*\rangle+\mathrm{i}\sum_{m,k,n}\epsilon_{mkn}(q_{1m}\langle \mathbf{b}_2^*\rangle_k+q_{2m}\langle \mathbf{b}_1^*\rangle_k+q_{3m}b_{0k}^*)\mathbf{Z}_n\\&+\sum_{m,k,n,j}\epsilon_{mkn}\Big(\Big(b_{0k}^*(q_{1m}q_{2j}+q_{2m}q_{1j})+\langle \mathbf{b}_1^*\rangle_k q_{1m}q_{1j}\Big)\mathbf{Z}_{jn}^{(1)}+\mathrm{i}\sum_p b_{0k}^*q_{1m}q_{1j}q_{1p}\mathbf{Z}_{jnp}^{(2)}\Big)\\&+\mathrm{i}\sum_{m,k,n}\epsilon_{mkn}q_{1m}b_{0k}^*\Big(\mathbf{Z}_n^{(3)}+(\overline{\lambda}_2+\eta_0|\mathbf{q}_1|^2)\mathbf{Z}_n^{(4)}\Big),\end{aligned}\tag{27.2}$$

where we refer to parity-invariant solutions to the following auxiliary problems:

$$\begin{aligned}\mathscr{D}\mathbf{G}_{mk}^{(1)}+2\eta_0\,\partial\mathbf{S}_k^{(1)}/\partial x_m+\mathbf{e}_m\times(\mathbf{V}\times\mathbf{S}_k^{(1)})-\mathbf{G}_{mk}&=0;\\\mathscr{D}\mathbf{G}_{mk}^{(2)}+2\eta_0\,\partial\mathbf{S}_k^{(2)}/\partial x_m+\mathbf{e}_m\times(\mathbf{V}\times\mathbf{S}_k^{(2)})-2\partial\mathbf{S}_k/\partial x_m-\nabla^2\mathbf{G}_{mk}&=0;\\\mathscr{D}\mathbf{G}_{jnmk}^{(3)}+2\eta_0\,\partial\mathbf{S}_{nmk}^{(3)}/\partial x_j+\mathbf{e}_j\times(\mathbf{V}\times\mathbf{S}_{nmk}^{(3)})&=0;\\\mathscr{D}^*\mathbf{Z}_{jnp}^{(2)}=2\eta_0\,\partial\mathbf{Z}_{jn}^{(1)}/\partial x_p-\mathbf{V}\times(\mathbf{e}_p\times\mathbf{Z}_{jn}^{(1)});&\\\mathscr{D}^*\mathbf{Z}_n^{(3)}=\nabla^2\mathbf{Z}_n;&\\\mathscr{D}^*\mathbf{Z}_n^{(4)}=\mathbf{Z}_n.&\end{aligned}$$

Upon substituting (13), (19) and (27), and applying (15), the extremality condition (21.3) reduces to

$$
\begin{aligned}
&\mathscr{E}\mathbf{q}_3 - \sum_{l,j}\Big\langle \mathbf{V}\times\mathbf{G}_{lj}\Big\rangle\cdot\mathrm{Re}\Big(\langle\mathbf{b}_0\rangle_j\overline{(\mathbf{q}_1\times\langle\mathbf{b}_2^*\rangle+\mathbf{q}_2\times\langle\mathbf{b}_1^*\rangle)}+\langle\mathbf{b}_1\rangle_j\overline{(\mathbf{q}_1\times\langle\mathbf{b}_1^*\rangle+\mathbf{q}_2\times\mathbf{b}_0^*)}+\langle\mathbf{b}_2\rangle_j\mathbf{q}_1\times\overline{\mathbf{b}_0^*}\Big)\,\mathbf{e}_l\\
&+\sum_{k,m}\langle\mathbf{V}\times\mathbf{G}_{mk}\rangle\times\mathrm{Re}\Big((q_{2m}\langle\mathbf{b}_1\rangle_k+q_{1m}\langle\mathbf{b}_2\rangle_k)\overline{\mathbf{b}_0^*}+(q_{2m}\langle\mathbf{b}_0\rangle_k+q_{1m}\langle\mathbf{b}_1\rangle_k)\overline{\langle\mathbf{b}_1^*\rangle}+q_{1m}\langle\mathbf{b}_0\rangle_k\overline{\langle\mathbf{b}_2^*\rangle}\Big)\\
&+2\eta_0\sum_l\mathrm{Re}\Big\langle-\sum_{j,m,k,n}\epsilon_{mkn}q_{1m}\overline{b_{0k}^*}\langle\mathbf{b}_0\rangle_j\frac{\partial\mathbf{S}_j}{\partial x_l}\cdot\Big(\mathbf{Z}_n^{(3)}+(\lambda_2+\eta_0|\mathbf{q}_1|^2)\mathbf{Z}_n^{(4)}+\sum_{p,r}q_{1r}q_{1p}\mathbf{Z}_{rnp}^{(2)}\Big)\\
&+\Big(\sum_{k,m}q_{1m}\langle\mathbf{b}_0\rangle_k\frac{\partial\mathbf{G}_{mk}}{\partial x_l}\Big)\cdot\sum_{m,k,n,r}\epsilon_{mkn}q_{1m}q_{1r}\overline{b_{0k}^*}\mathbf{Z}_{rn}^{(1)}\\
&-\Big(\frac{\partial}{\partial x_l}\sum_j\langle\mathbf{b}_0\rangle_j\Big((\lambda_2+\eta_0|\mathbf{q}_1|^2)\mathbf{S}_j^{(1)}+\mathbf{S}_j^{(2)}+\sum_{m,n}q_{1m}q_{1n}\mathbf{S}_{nmj}^{(3)}\Big)\Big)\cdot\sum_{m,k,n}\epsilon_{mkn}q_{1m}\overline{b_{0k}^*}\mathbf{Z}_n\Big\rangle\,\mathbf{e}_l\\
&-2\Big(\mathbf{q}_1-\sum_{l,j,m,k,n}\epsilon_{mkn}q_{1m}\mathrm{Re}\Big(\overline{b_{0k}^*}\langle\mathbf{b}_0\rangle_j\Big)\Big\langle\frac{\partial\mathbf{S}_j}{\partial x_l}\cdot\mathbf{Z}_n\Big\rangle\,\mathbf{e}_l\Big)\\
&+\mathrm{Re}\Big\langle-\Big(\mathbf{V}\times\sum_j\langle\mathbf{b}_0\rangle_j\mathbf{S}_j\Big)\times\sum_{m,k,n}\epsilon_{mkn}q_{1m}\overline{b_{0k}^*}\Big(\mathbf{Z}_n^{(3)}+(\lambda_2+\eta_0|\mathbf{q}_1|^2)\mathbf{Z}_n^{(4)}+\sum_{p,r}q_{1r}q_{1p}\mathbf{Z}_{rnp}^{(2)}\Big)\\
&+\Big(\mathbf{V}\times\sum_{k,m}q_{1m}\langle\mathbf{b}_0\rangle_k\mathbf{G}_{mk}\Big)\times\sum_{m,k,n,p}\epsilon_{mkn}q_{1m}q_{1p}\overline{b_{0k}^*}\mathbf{Z}_{pn}^{(1)}\\
&-\Big(\mathbf{V}\times\sum_j\langle\mathbf{b}_0\rangle_j\Big((\lambda_2+\eta_0|\mathbf{q}_1|^2)\mathbf{S}_j^{(1)}+\mathbf{S}_j^{(2)}+\sum_{m,n}q_{1m}q_{1n}\mathbf{S}_{nmj}^{(3)}\Big)\Big)\times\sum_{m,k,n}\epsilon_{mkn}q_{1m}\overline{b_{0k}^*}\mathbf{Z}_n\\
&+\Big(\mathbf{V}\times\sum_{k,m}q_{1m}\langle\mathbf{b}_0\rangle_k\Big((\lambda_2+\eta_0|\mathbf{q}_1|^2)\mathbf{G}_{mk}^{(1)}+\mathbf{G}_{mk}^{(2)}+\sum_{j,n}q_{1j}q_{1n}\mathbf{G}_{jnmk}^{(3)}\Big)\Big)\times\overline{\mathbf{b}_0^*}\Big\rangle=0.
\end{aligned}
\tag{28}
$$

Scalar multiplying (28) by $\mathbf{q}_1$ yields the solvability condition for (28):

$$
\begin{aligned}
&\sum_{l,j}\Big\langle\mathbf{V}\times\mathbf{G}_{lj}\Big\rangle\cdot\Big((q_{1l}\mathbf{q}_2+q_{2l}\mathbf{q}_1)\times\mathrm{Re}(\langle\mathbf{b}_1\rangle_j\overline{\mathbf{b}_0^*}-\langle\mathbf{b}_0\rangle_j\overline{\langle\mathbf{b}_1^*\rangle})\Big)\\
&+2\mathrm{Re}\Big((\lambda_2+\eta_0|\mathbf{q}_1|^2)\sum_{j,m,k,n,p}\epsilon_{mkn}q_{1m}q_{1j}\overline{b_{0k}^*}\langle\mathbf{b}_0\rangle_p\Big\langle\mathbf{S}_p\cdot\mathbf{Z}_{jn}^{(1)}+\mathbf{G}_{jp}^{(1)}\cdot\mathbf{Z}_n\Big\rangle-(\lambda_3+2\eta_0\,\mathbf{q}_1\cdot\mathbf{q}_2)\langle\mathbf{b}_1\rangle\cdot\overline{\mathbf{b}_0^*}\Big)\\
&+2\eta_0\sum_l\mathrm{Re}\Big\langle-\sum_{j,m,k,n}\epsilon_{mkn}q_{1m}\overline{b_{0k}^*}\langle\mathbf{b}_0\rangle_j\frac{\partial\mathbf{S}_j}{\partial x_l}\cdot\Big(\mathbf{Z}_n^{(3)}+(\lambda_2+\eta_0|\mathbf{q}_1|^2)\mathbf{Z}_n^{(4)}+\sum_{p,r}q_{1r}q_{1p}\mathbf{Z}_{rnp}^{(2)}\Big)\\
&+\Big(\sum_{k,m}q_{1m}\langle\mathbf{b}_0\rangle_k\frac{\partial\mathbf{G}_{mk}}{\partial x_l}\Big)\cdot\sum_{m,k,n,r}\epsilon_{mkn}q_{1m}q_{1r}\overline{b_{0k}^*}\mathbf{Z}_{rn}^{(1)}\\
&-\Big(\frac{\partial}{\partial x_l}\sum_j\langle\mathbf{b}_0\rangle_j\Big((\lambda_2+\eta_0|\mathbf{q}_1|^2)\mathbf{S}_j^{(1)}+\mathbf{S}_j^{(2)}+\sum_{m,n}q_{1m}q_{1n}\mathbf{S}_{nmj}^{(3)}\Big)\Big)\cdot\sum_{m,k,n}\epsilon_{mkn}q_{1m}\overline{b_{0k}^*}\mathbf{Z}_n\Big\rangle q_{1l}\\
&-2\Big(|\mathbf{q}_1|^2-\sum_{l,j,m,k,n}\epsilon_{mkn}q_{1m}\mathrm{Re}\Big(\overline{b_{0k}^*}\langle\mathbf{b}_0\rangle_j\Big)\Big\langle\frac{\partial\mathbf{S}_j}{\partial x_l}\cdot\mathbf{Z}_n\Big\rangle q_{1l}\Big)\\
&+\mathrm{Re}\Big\langle-\Big(\mathbf{V}\times\sum_j\langle\mathbf{b}_0\rangle_j\mathbf{S}_j\Big)\times\sum_{m,k,n}\epsilon_{mkn}q_{1m}\overline{b_{0k}^*}\Big(\mathbf{Z}_n^{(3)}+(\lambda_2+\eta_0|\mathbf{q}_1|^2)\mathbf{Z}_n^{(4)}+\sum_{p,r}q_{1r}q_{1p}\mathbf{Z}_{rnp}^{(2)}\Big)\\
&+\Big(\mathbf{V}\times\sum_{k,m}q_{1m}\langle\mathbf{b}_0\rangle_k\mathbf{G}_{mk}\Big)\times\sum_{m,k,n,p}\epsilon_{mkn}q_{1m}q_{1p}\overline{b_{0k}^*}\mathbf{Z}_{pn}^{(1)}
\end{aligned}
$$

$$-\left(\mathbf{V}\times\sum_j\langle\mathbf{b}_0\rangle_j\left((\lambda_2+\eta_0|\mathbf{q}_1|^2)\mathbf{S}_j^{(1)}+\mathbf{S}_j^{(2)}+\sum_{m,n}q_{1m}q_{1n}\mathbf{S}_{nmj}^{(3)}\right)\right)\times\sum_{m,k,n}\epsilon_{mkn}\,q_{1m}\,\overline{b_{0k}^*}\,\mathbf{Z}_n$$
$$+\left(\mathbf{V}\times\sum_{k,m}q_{1m}\langle\mathbf{b}_0\rangle_k\left((\lambda_2+\eta_0|\mathbf{q}_1|^2)\mathbf{G}_{mk}^{(1)}+\mathbf{G}_{mk}^{(2)}+\sum_{j,n}q_{1j}q_{1n}\mathbf{G}_{jnmk}^{(3)}\right)\right)\times\overline{\mathbf{b}_0^*}\Big\rangle\cdot\mathbf{q}_1=0. \tag{29}$$

At this stage $\mathbf{q}_2$ is known up to the factor $|\mathbf{q}_1|^{-1}$ and an additive term proportional to $\mathbf{q}_1$. Expressions (24) and (26) reveal that $\langle\mathbf{b}_1\rangle$ and $\left\langle\mathbf{b}_1^*\right\rangle$ depend on $\mathbf{q}_2$, but it is easy to check (relying on (18.1), (18.2) and the biorthogonality of the bases of the eigenvectors of the operators $\mathfrak{D}$ and $\mathfrak{D}^*$) that they are invariant under the transformation $\mathbf{q}_2\to\mathbf{q}_2+\beta\mathbf{q}_1$ for any $\beta$. The remaining potentially affected terms in (29) are the first term involving $\mathbf{q}_2$ explicitly, and, by virtue of (23), $\lambda_3+2\eta_0\,\mathbf{q}_1\cdot\mathbf{q}_2$. For a real $\beta$, the total change in the l.h.s. of (29) due to the transformation $\mathbf{q}_2\to\mathbf{q}_2+\beta\mathbf{q}_1$ is

$$2\beta\mathrm{Re}\left(\mathfrak{D}\langle\mathbf{b}_1\rangle\cdot\overline{\mathbf{b}_0^*}-\mathfrak{D}\langle\mathbf{b}_0\rangle\cdot\left\langle\overline{\mathbf{b}_1^*}\right\rangle-2(\mathfrak{D}\langle\mathbf{b}_0\rangle\cdot\overline{\mathbf{b}_0^*})\langle\mathbf{b}_1\rangle\cdot\overline{\mathbf{b}_0^*}\right)$$
$$=-2\beta\mathrm{Re}\left((\lambda_2+\eta_0|\mathbf{q}_1|^2)(\langle\mathbf{b}_1\rangle\cdot\overline{\mathbf{b}_0^*}+\langle\mathbf{b}_0\rangle\cdot\left\langle\overline{\mathbf{b}_1^*}\right\rangle)\right)=0$$

(we have employed relations (18.1)–(18.3), (23) and the normalization conditions at orders $\vartheta^0$ and $\vartheta^1$). Thus, the solvability condition (29) is not altered by the unknown additive component of $\mathbf{q}_2$, parallel to $\mathbf{q}_1$. All the quantities involved in (29) are known completely or up to factors that are powers of $|\mathbf{q}_1|$. Substituting the values of these quantities transforms (29) into an inhomogeneous equation in $|\mathbf{q}_1|$, involving terms proportional to $|\mathbf{q}_1|^2$ and $|\mathbf{q}_1|^4$. We determine from it the length $|\mathbf{q}_1|$. Now (28) yields $\mathbf{q}_3$ up to an additive term that is a multiple of $\mathbf{q}_1$.

## 7. Order $\vartheta^4$ equations

At order $\vartheta^4$, (1), (2), (6) and (4) yield, respectively, the equations

$$\mathscr{D}\mathbf{b}_4+2\mathrm{i}\eta_0((\mathbf{q}_1\cdot\nabla)\mathbf{b}_3+(\mathbf{q}_2\cdot\nabla)\mathbf{b}_2+(\mathbf{q}_3\cdot\nabla)\mathbf{b}_1+(\mathbf{q}_4\cdot\nabla)\mathbf{b}_0)-\nabla^2\mathbf{b}_2$$
$$-2\mathrm{i}((\mathbf{q}_2\cdot\nabla)\mathbf{b}_0+(\mathbf{q}_1\cdot\nabla)\mathbf{b}_1))+\mathrm{i}\mathbf{q}_1\times(\mathbf{V}\times\mathbf{b}_3)$$
$$+\mathrm{i}\mathbf{q}_2\times(\mathbf{V}\times\mathbf{b}_2)+\mathrm{i}\mathbf{q}_3\times(\mathbf{V}\times\mathbf{b}_1)+\mathrm{i}\mathbf{q}_4\times(\mathbf{V}\times\mathbf{b}_0)$$
$$=(\lambda_4+\eta_0(2\mathbf{q}_1\cdot\mathbf{q}_3+|\mathbf{q}_2|^2)-|\mathbf{q}_1|^2)\mathbf{b}_0+(\lambda_3+2\eta_0\,\mathbf{q}_1\cdot\mathbf{q}_2)\mathbf{b}_1+(\lambda_2+\eta_0|\mathbf{q}_1|^2)\mathbf{b}_2, \tag{30.1}$$
$$\mathscr{D}^*\mathbf{b}_4^*+2\mathrm{i}\eta_0((\mathbf{q}_1\cdot\nabla)\mathbf{b}_3^*+(\mathbf{q}_2\cdot\nabla)\mathbf{b}_2^*+(\mathbf{q}_3\cdot\nabla)\mathbf{b}_1^*)-\nabla^2\mathbf{b}_2^*-2\mathrm{i}(\mathbf{q}_1\cdot\nabla)\mathbf{b}_1^*$$
$$-\mathrm{i}\mathbf{V}\times(\mathbf{q}_1\times\mathbf{b}_3^*+\mathbf{q}_2\times\mathbf{b}_2^*+\mathbf{q}_3\times\mathbf{b}_1^*+\mathbf{q}_4\times\mathbf{b}_0^*)$$
$$=(\overline{\lambda}_4+\eta_0(2\mathbf{q}_1\cdot\mathbf{q}_3+|\mathbf{q}_2|^2)-|\mathbf{q}_1|^2)\mathbf{b}_0^*+(\overline{\lambda}_3+2\eta_0\,\mathbf{q}_1\cdot\mathbf{q}_2)\mathbf{b}_1^*+(\overline{\lambda}_2+\eta_0|\mathbf{q}_1|^2)\mathbf{b}_2^*, \tag{30.2}$$
$$2\eta_0\left(\mathbf{q}_4+\sum_m\mathrm{Im}\left\langle\frac{\partial\mathbf{b}_0}{\partial x_m}\cdot\overline{\mathbf{b}_4^*}+\frac{\partial\mathbf{b}_1}{\partial x_m}\cdot\overline{\mathbf{b}_3^*}+\frac{\partial\mathbf{b}_2}{\partial x_m}\cdot\overline{\mathbf{b}_2^*}+\frac{\partial\mathbf{b}_3}{\partial x_m}\cdot\overline{\mathbf{b}_1^*}\right\rangle\mathbf{e}_m\right)$$
$$-2\left(\mathbf{q}_2+\sum_m\mathrm{Im}\left\langle\frac{\partial\mathbf{b}_0}{\partial x_m}\cdot\overline{\mathbf{b}_2^*}+\frac{\partial\mathbf{b}_1}{\partial x_m}\cdot\overline{\mathbf{b}_1^*}\right\rangle\mathbf{e}_m\right)+\mathrm{Im}\left\langle(\mathbf{V}\times\mathbf{b}_0)\times\overline{\mathbf{b}_4^*}+(\mathbf{V}\times\mathbf{b}_1)\times\overline{\mathbf{b}_3^*}\right.$$
$$\left.+(\mathbf{V}\times\mathbf{b}_2)\times\overline{\mathbf{b}_2^*}+(\mathbf{V}\times\mathbf{b}_3)\times\overline{\mathbf{b}_1^*}+(\mathbf{V}\times\mathbf{b}_4)\times\overline{\mathbf{b}_0^*}\right\rangle=0, \tag{30.3}$$
$$\langle\langle\mathbf{b}_0,\mathbf{b}_4^*\rangle\rangle+\langle\langle\mathbf{b}_3,\mathbf{b}_1^*\rangle\rangle+\langle\langle\mathbf{b}_2,\mathbf{b}_2^*\rangle\rangle+\langle\langle\mathbf{b}_1,\mathbf{b}_3^*\rangle\rangle+\langle\langle\mathbf{b}_4,\mathbf{b}_0^*\rangle\rangle=0. \tag{30.4}$$

Averaging (30.1) yields its solvability condition

$$\mathrm{i}\langle\mathbf{q}_1\times(\mathbf{V}\times\mathbf{b}_3)+\mathbf{q}_2\times(\mathbf{V}\times\mathbf{b}_2)+\mathbf{q}_3\times(\mathbf{V}\times\mathbf{b}_1)\rangle$$
$$=(\lambda_4+\eta_0(2\mathbf{q}_1\cdot\mathbf{q}_3+|\mathbf{q}_2|^2)-|\mathbf{q}_1|^2)\langle\mathbf{b}_0\rangle+(\lambda_3+2\eta_0\,\mathbf{q}_1\cdot\mathbf{q}_2)\langle\mathbf{b}_1\rangle+(\lambda_2+\eta_0|\mathbf{q}_1|^2)\langle\mathbf{b}_2\rangle. \tag{31}$$

Upon substitution of the expressions (13), (14.1), (19.1) and (27.1) for $\mathbf{b}_i$, $i = 1,2,3$, this equation takes the form

$$\Big(\mathfrak{D} - (\lambda_2 + \eta_0|\mathbf{q}_1|^2)\Big)\langle\mathbf{b}_2\rangle = \mathbf{R}_2 + (\lambda_4 + \eta_0(2\mathbf{q}_1\cdot\mathbf{q}_3 + |\mathbf{q}_2|^2) - |\mathbf{q}_1|^2)\langle\mathbf{b}_0\rangle, \tag{32}$$

where

$$\begin{aligned}\mathbf{R}_2 = \sum_{k,m}\Bigg(&q_{1m}\langle\mathbf{b}_0\rangle_k\mathbf{q}_1\times\left\langle\mathbf{V}\times\left((\lambda_2+\eta_0|\mathbf{q}_1|^2)\mathbf{G}^{(1)}_{mk} + \mathbf{G}^{(2)}_{mk} + \sum_{j,n} q_{1j}q_{1n}\mathbf{G}^{(3)}_{jnmk}\right)\right\rangle\\ &+\Big(\mathbf{q}_1(q_{3m}\langle\mathbf{b}_0\rangle_k + q_{2m}\langle\mathbf{b}_1\rangle_k) + \mathbf{q}_2(q_{2m}\langle\mathbf{b}_0\rangle_k + q_{1m}\langle\mathbf{b}_1\rangle_k) + \mathbf{q}_3 q_{1m}\langle\mathbf{b}_0\rangle_k\Big)\times\langle\mathbf{V}\times\mathbf{G}_{mk}\rangle\Bigg)\\ &+(\lambda_3 + 2\eta_0\,\mathbf{q}_1\cdot\mathbf{q}_2)\langle\mathbf{b}_1\rangle.\end{aligned}$$

Scalar multiplying (32) by $\overline{\mathbf{b}^*_0}$, we find

$$\lambda_4 = -\eta_0(2\mathbf{q}_1\cdot\mathbf{q}_3 + |\mathbf{q}_2|^2) + |\mathbf{q}_1|^2 - \left\langle\overline{\mathbf{b}^*_0}\cdot\mathbf{R}_2\right\rangle. \tag{33}$$

Since $\mathbf{q}_1$ belongs to the kernel of the operator $\mathscr{E}$ (see (16)), the resultant expression for the growth rate does not involve $\mathbf{q}_3$:

$$\begin{aligned}\operatorname{Re}\lambda_4 = -\overline{\mathbf{b}^*_0}\cdot\Bigg(&\sum_{k,m}\Bigg(q_{1m}\langle\mathbf{b}_0\rangle_k\mathbf{q}_1\times\left\langle\mathbf{V}\times\left((\lambda_2+\eta_0|\mathbf{q}_1|^2)\mathbf{G}^{(1)}_{mk} + \mathbf{G}^{(2)}_{mk} + \sum_{j,n} q_{1j}q_{1n}\mathbf{G}^{(3)}_{jnmk}\right)\right\rangle\\ &+\Big(\mathbf{q}_1 q_{2m}\langle\mathbf{b}_1\rangle_k + \mathbf{q}_2(q_{2m}\langle\mathbf{b}_0\rangle_k + q_{1m}\langle\mathbf{b}_1\rangle_k)\Big)\times\langle\mathbf{V}\times\mathbf{G}_{mk}\rangle\Bigg)\\ &+(\lambda_3 + 2\eta_0\,\mathbf{q}_1\cdot\mathbf{q}_2)\langle\mathbf{b}_1\rangle\Bigg) - \eta_0|\mathbf{q}_2|^2 + |\mathbf{q}_1|^2.\end{aligned} \tag{34}$$

Furthermore, it is easy to check that this expression remains invariant under the transformation $\mathbf{q}_2 \to \mathbf{q}_2 + \beta\mathbf{q}_1$ for any real $\beta$. Thus, (34) uniquely determines the leading term of the expansion of the growth rate.

Scalar multiplying (31) by $\mathbf{q}_1$ yields (5) for $j = 3$ (given that (5) is satisfied for $j = 2$). We find $\langle\mathbf{b}_2\rangle$ exploiting the biorthogonality of the bases of the eigenvectors of $\mathfrak{D}$ and $\mathfrak{D}^*$:

$$\langle\mathbf{b}_2\rangle = \mu_2\langle\mathbf{b}_0\rangle - \frac{\mathbf{R}_2\cdot\mathbf{b}^*_0}{2\lambda_2}\left\langle\overline{\mathbf{b}}_0\right\rangle - \frac{\langle\mathbf{b}_0\rangle\cdot\mathbf{q}_3 + \langle\mathbf{b}_1\rangle\cdot\mathbf{q}_2}{\mathbf{h}_3\cdot\mathbf{q}_1}\mathbf{h}_3,$$

where $\mu_2$ is a constant.

The solvability condition for (30.2) amounts to the orthogonality of the non-homogeneous term in this equation to all $\mathbf{S}_l$:

$$\begin{aligned}&\sum_l\Big\langle\mathbf{S}_l\cdot\Big(2\mathrm{i}\eta_0((\mathbf{q}_1\cdot\nabla)\mathbf{b}^*_3 + (\mathbf{q}_2\cdot\nabla)\mathbf{b}^*_2 + (\mathbf{q}_3\cdot\nabla)\mathbf{b}^*_1) - \nabla^2\mathbf{b}^*_2 - 2\mathrm{i}(\mathbf{q}_1\cdot\nabla)\mathbf{b}^*_1\\ &-\mathrm{i}\mathbf{V}\times(\mathbf{q}_1\times\mathbf{b}^*_3 + \mathbf{q}_2\times\mathbf{b}^*_2 + \mathbf{q}_3\times\mathbf{b}^*_1) - (\overline{\lambda}_2 + \eta_0|\mathbf{q}_1|^2)\mathbf{b}^*_2\Big)\Big\rangle\,\mathbf{e}_l\\ &= (\overline{\lambda}_4 + \eta_0(2\mathbf{q}_1\cdot\mathbf{q}_3 + |\mathbf{q}_2|^2) - |\mathbf{q}_1|^2)\mathbf{b}^*_0 + (\overline{\lambda}_3 + 2\eta_0\,\mathbf{q}_1\cdot\mathbf{q}_2)\langle\mathbf{b}^*_1\rangle.\end{aligned}$$

Substituting the expressions (13), (14.2), (19.2) and (27.2) for $\mathbf{b}^*_i$, $i = 1,2,3$, transforms this equation into

$$\Big(\mathfrak{D}^* - (\overline{\lambda}_2 + \eta_0|\mathbf{q}_1|^2)\Big)\langle\mathbf{b}^*_2\rangle = \mathbf{R}^*_2, \tag{35}$$

where

$$\mathbf{R}_2^* = -\sum_{l,p}\left(\left(q_{1p}(\mathbf{q}_2\times\langle\mathbf{b}_1^*\rangle+\mathbf{q}_3\times\mathbf{b}_0^*)+q_{2p}(\mathbf{q}_1\times\langle\mathbf{b}_1^*\rangle+\mathbf{q}_2\times\mathbf{b}_0^*)+q_{3p}\mathbf{q}_1\times\mathbf{b}_0^*\right)\cdot\left\langle\mathbf{V}\times\mathbf{G}_{pl}\right\rangle\right)\mathbf{e}_l$$
$$-\sum_{m,k,n,l}\epsilon_{mkn}\left\langle\mathbf{S}_l\cdot\left(-2\eta_0\,b_{0k}^*q_{1m}(\mathbf{q}_1\cdot\nabla)\left(\sum_{j,p}q_{1j}q_{1p}\mathbf{Z}_{jnp}^{(2)}+\mathbf{Z}_n^{(3)}+(\overline{\lambda}_2+\eta_0|\mathbf{q}_1|^2)\mathbf{Z}_n^{(4)}\right)\right.\right.$$
$$-\sum_j\left(b_{0k}^*(q_{1m}q_{2j}+q_{2m}q_{1j})+\langle\mathbf{b}_1^*\rangle_k q_{1m}q_{1j}\right)\nabla^2\mathbf{Z}_{jn}^{(1)}+2b_{0k}^*q_{1m}(\mathbf{q}_1\cdot\nabla)\mathbf{Z}_n$$
$$+b_{0k}^*q_{1m}\mathbf{V}\times\left(\mathbf{q}_1\times\left(\sum_{j,p}q_{1j}q_{1p}\mathbf{Z}_{jnp}^{(2)}+\mathbf{Z}_n^{(3)}+(\overline{\lambda}_2+\eta_0|\mathbf{q}_1|^2)\mathbf{Z}_n^{(4)}\right)\right)$$
$$\left.\left.-(\overline{\lambda}_2+\eta_0|\mathbf{q}_1|^2)q_{1m}b_{0k}^*\sum_j q_{1j}\mathbf{Z}_{jn}^{(1)}\right)\right\rangle\mathbf{e}_l+(\overline{\lambda}_3+2\eta_0\,\mathbf{q}_1\cdot\mathbf{q}_2)\langle\mathbf{b}_1^*\rangle+\left(\overline{\lambda}_4+\eta_0(2\mathbf{q}_1\cdot\mathbf{q}_3+|\mathbf{q}_2|^2)-|\mathbf{q}_1|^2\right)\mathbf{b}$$

The solvability condition for (35), $\mathbf{R}_2^*\cdot\left\langle\overline{\mathbf{b}}_0\right\rangle=0$, is equivalent to (33). Due to the biorthogonality of the bases of the eigenvectors of $\mathfrak{D}$ and $\mathfrak{D}^*$, the solution to (35) is

$$\langle\mathbf{b}_2^*\rangle=\mu_2^*\mathbf{b}_0^*+\frac{\mathbf{R}_2^*\cdot\langle\mathbf{b}_0\rangle}{2\lambda_2}\overline{\mathbf{b}_0^*}-\frac{\mathbf{R}_2^*\cdot\mathbf{h}_3}{(\overline{\lambda}_2+\eta_0|\mathbf{q}_1|^2)\mathbf{h}_3\cdot\mathbf{q}_1}\mathbf{q}_1,$$

where $\mu_2^*$ is a constant. By multiplying the eigenfunctions $\mathbf{b}_2$ and $\mathbf{b}_2^*$ by linear functions of $\vartheta^2$, we can arbitrarily change $\mu_2$ and $\mu_2^*$. The value of the sum $\mu_2+\overline{\mu_2^*}=0$ is prescribed by the normalization condition (17.4), but no other constraints are imposed on the coefficients $\mu_2$ and $\mu_2^*$.

From equations (30.1) and (30.2), we now find the fluctuating parts of $\mathbf{b}_4$ and $\mathbf{b}_4^*$ and substitute the results into (30.3). The solvability condition for the resultant equation yields the unknown so far additive term proportional to $\mathbf{q}_1$ that is involved in $\mathbf{q}_2$. From the equation we obtain $\mathbf{q}_4$ up to an analogous additive term.

Reasoning similarly, we can solve successively the systems of equations at all higher orders and determine all terms in the series (3).

## 8. Concluding remarks

We have developed a power series asymptotic expansion in $\vartheta=(\eta_0-\eta)^{1/2}$ of magnetic Bloch modes, kinematically generated by a parity-invariant flow and featuring locally maximum growth rates, which stem from the branch of neutral (i.e., associated with the zero eigenvalue of the magnetic induction operator $\mathscr{D}$ (8)) space-periodic modes for $\mathbf{q}=0$ (see Fig. 14 in [*Chertovskih and Zheligovsky*, 2023b]). We have shown that branching occurs at a critical molecular diffusivity $\eta_0$ for which the two eigenvalues of the operator of eddy diffusivity are imaginary and complex-conjugate. The associated eigenvalues of the eigenmodes in the offshoot are order $\vartheta^2$ and the first two terms of their expansion (order $\vartheta^2$ and $\vartheta^3$) turn out to be imaginary. The locally maximum (over $\mathbf{q}$) growth rates in the offshoot are order $\vartheta^4$; they are attained for the optimal $\mathbf{q}=\mathrm{O}(\vartheta)$. Thus, the optimal $\mathbf{q}$ and the maximum growth rate are continuous in $\eta$, but $\mathbf{q}$ is not differentiable when passing through the critical point $\eta_0$ from the branch of the neutral magnetic modes ($\eta>\eta_0$) to the offshoot ($\eta<\eta_0$).

We have expected this instance of branching to be representative. Indeed, numerical estimates reveal that for all the offshoots found *ibid.* the deviations of the optimal wave vectors $\mathbf{q}$ from the constant half-integer $\mathbf{q}$ in the respective main branch are order $\vartheta$, and therefore expansions in power series in $\vartheta$ can be constructed for all offshoots. However, Table 1 reveals that the branchings differ in detail. (Recalling that the eigenvalues of the operators of linearization have period one in each component $q_m$ of the Bloch wave vector $\mathbf{q}$, we do not distinguish the component values $\pm1/2$ in the table and in the text that follows.) For instance, the kinematic dynamo problem for a parity-invariant flow, for which

**Table 1.** Instances of branching found numerically in [*Chertovskih and Zheligovsky*, 2023b]. F: figures *ibid.* showing the plots; P: the linear stability problem, HD hydrodynamic, MHD magnetohydrodynamic, KD kinematic dynamo; ES: type of the energy spectrum of the state subjected to perturbations; S: the symmetry of the state subjected to perturbations, PI parity-invariant, nPI non-symmetric; $\nu, \eta$: the molecular viscosity and/or diffusivity, at which branching occurs; $\boldsymbol{q}$: the Bloch wave vector in the main branch; $\gamma$: the growth rate of the instability at the branching point, common to both the main branch and offshoot; A: the order of the growth rates in the offshoot, or of the real and imaginary parts of the eigenvalue of the operator of linearisation, when two numbers are shown

| F | P | ES | S | $\nu, \eta$ | $\mathbf{q}$ | $\gamma$ | A |
|---|---|---|---|---|---|---|---|
| 6 | HD | exponential | PI | 0.0460 | (0,1/2,1/2) | 0.2593 | 2 |
| 6 | HD | exponential | PI | 0.1231 | (1/2,1/2,0) | 0.1049 | 2 |
| 6 | HD | exponential | PI | 0.1917 | (1/2,1/2,0) | 0.0401 | 2 |
| 9 | HD | large eddies | PI | 0.1046 | (1/2,1/2,0) | 0.1252 | 2 |
| 9 | HD | large eddies | PI | 0.2040 | 0 | 0 | 4 |
| 10 | KD | exponential | nPI | 0.0472 | (0,0,1/2) | 0.0711 | 2/2 |
| 13 | KD | large eddies | nPI | 0.0394 | (0,1/2,0) | 0.0868 | 2/2 |
| 14 | KD | exponential | PI | 0.1339 | 0 | 0 | 4/2 |
| 15 | KD | Kolmogorov | PI | 0.1491 | (1/2,1/2,0) | 0.0276 | 2 |
| 21 | MHD | exponential | PI | 0.1545 | (0,0,1/2) | 0.1353 | 2 |
| 22 | MHD | Kolmogorov | PI | 0.2483 | 0 | 0 | 4 |
| 22 | MHD | Kolmogorov | PI | 0.2710 | 0 | 0 | 4 |
| 23 | MHD | large eddies | PI | 0.0902 | 0 | 0.2618 | 2 |
| 23 | MHD | large eddies | PI | 0.2868 | 0 | 0 | 4 |

we have constructed the expansions here, is unique in that the dominant eigenvalues of the eddy diffusivity operator are imaginary at the bifurcation point. Clearly, for a parity-invariant steady state experiencing perturbation, the molecular diffusivity, for which the eddy diffusivity becomes positive, is necessarily a branching point of the branch of neutral modes for $\mathbf{q} = 0$, provided all short-scale zero-mean stability modes have negative growth rates at this critical point. The converse does not hold true: in all the 9 stability problems for parity-invariant steady states discussed *ibid.*, dominant eigenvalues of the eddy diffusivity operator pass at the branching point through zero only in the sample kinematic dynamo problem considered here. Expansions of the deviations of the growth rates, $\gamma(\eta) - \gamma(\eta_0)$, have the leading terms order $\vartheta^2$ or $\vartheta^4$ (the power is shown in the last column of the table); for the deviations of the imaginary parts (if applicable) of the eigenvalues of the operators of linearization, $\mathrm{Im}\lambda(\eta) - \mathrm{Im}\lambda(\eta_0) = \mathrm{O}(\vartheta^2)$. Here $\eta_0$ is the critical magnetic molecular diffusivity (in the hydrodynamic stability problem, the molecular viscosity substitutes the molecular diffusivity, and then $\vartheta = |\nu - \nu_0|^{1/2}$). The left branching in fig. 23b *ibid.* is unique in that the growth rates in the main branch also depend on molecular diffusivity, and upon branching the offshoot coexists with the main branch comprised of stability modes, which have locally, but not globally maximum growth rates (not shown in fig. 23a,b). By numerical estimations, for this branching $\gamma_m(\eta) - \gamma_o(\eta) = \mathrm{O}(\vartheta^4)$, where the subscripts $m$ and $o$ indicate the growth rates in the main branch and in the offshoot.

In the context of the hydrodynamic stability problem for a sample steady flow with an exponentially decaying energy spectrum (Fig. 6 *ibid.*), branch IV of stability modes of globally maximum growth rates for $\mathbf{q} = (1/2, -1/2, 0)$ terminates in bifurcations of branching at both ends. A similar bifurcation is observed in Fig. 15 *ibid.* for the dynamo problem for a flow with a Kolmogorov energy spectrum, where offshoot II stems from branch I comprised of eigenmodes for $\mathbf{q} = (1/2, -1/2, 0)$. The behavior looks more "canonical" in Fig. 9 *ibid.* for the stability problem for a steady flow comprised of large eddies of wave numbers 2 or less. The offshoot (branch III) of positive globally maximum growth rate modes stems

from branch IV of neutral stability modes, whose zero growth rates are globally maximum. The growth rates in the offshoot and in the main branch are equal at a branching; no other conditions for these bifurcations have been identified. Both eigenvalues of the eddy viscosity operator are real and negative, unlike in the considered here magnetic dynamo.

For the linear MHD stability of parity-invariant steady states, the behavior is more involved. A similar branching was detected for all the three sample MHD steady states. For the state with an exponential energy spectrum decay (see Fig. 21 in [*Chertovskih and Zheligovsky*, 2023b]), the branching point, $\eta_0 = \nu_0$, (the computations were performed for $\nu = \eta$) is the left terminal point of branch III, where growth rates admit the global maximum for $\mathbf{q} = (0, 0, 1/2)$. The adjacent branch is I; the growth rates of its eigenmodes cease to be globally maximum inside the interval of its existence, leaving room for branch II. Small-scale instability (for $\mathbf{q} = 0$) sets in near $\nu = \eta = 0.193$ (the eigenvalues of the operator of linearization being real and strictly positive in both branches, I and III), and the combined eddy diffusivity for smaller molecular diffusivities is irrelevant.

Two instances of offshoots, stemming from branch VI comprised of neutral eigenmodes for $\mathbf{q} = 0$, are observed in Fig. 22 *ibid.* for the sample MHD steady state with the Kolmogorov energy spectrum. The dominant eigenvalues of the linearization and all the four eigenvalues of the operator of the combined eddy diffusivity are real at both branching points, the latter ones are strictly negative (unlike in the dynamo problem considered in this paper) at the right critical point, and one eigenvalue passes through zero at the left one, $\eta_0$, (i.e., the large-scale instability is present for $\eta < \eta_0$, the combined eddy diffusivity becoming negative). Near the point of bifurcation, eigenmodes in the offshoot branch V have globally maximum growth rates. Growth rates of eigenmodes constituting the offshoot branch IV are only locally maximum near the point where it stems, becoming globally maximum in interval IV at a positive distance from this point.

The arrangement is again different for the sample MHD steady state built of short-scale Fourier harmonics of wave numbers not exceeding 2 (Fig. 23 in [*Chertovskih and Zheligovsky*, 2023b]). Two offshoots stem from branches II and V comprised of short-scale eigenmodes for $\mathbf{q} = 0$. Bifurcation of branch V is similar to how the offshoot branch V stems in Fig. 22: Branch V consists now of neutral stability modes, the eigenvalues of the linearization are real, all the four eigenvalues of the operator of the combined eddy diffusivity are real and strictly negative, and the eigenmodes comprising the offshoot branch III have globally maximum growth rates near the critical points (the growth rates of the eigenmodes in the offshoot branch III lose global maximality strictly inside the interval of its existence, becoming just locally maximum and surpassed by branch IV). Unlike branch V, branch II consists of zero-mean short-scale instability modes whose growth rates are strictly positive.

Similar bifurcations of branching for non-parity-invariant states were also detected. In the kinematic dynamo problem, offshoots stem from branch I of the eigenmodes for $\mathbf{q} = (0, 0, 1/2)$ for the sample flow with an exponentially decaying energy spectrum (Fig. 10 *ibid.*) and from branch I of the magnetic modes for $\mathbf{q} = (0, -1/2, 0)$ generated by the sample flow comprised of large short-scale eddies of wave numbers not exceeding 2 (Fig. 13 *ibid.*).

We can give the following physical interpretation of the results of this paper. We have considered magnetic field generation by parity-invariant flows, which lack magnetic $\alpha$-effect. On decreasing the molecular diffusivity $\eta$ towards the critical point $\eta_0$ of the onset of negative magnetic eddy diffusivity, generation of large-scale magnetic modes begins, while (typically) magnetic field that has the periodicity of the flow is not yet generated (because the action of molecular diffusivity on large scales is the least). When the molecular diffusivity is close to the critical value, the most unstable generated modes constituting an offshoot branch involve very large (order $(\eta_0 - \eta)^{-1/2}$) spatial scales, which decrease fast on decreasing the molecular diffusivity below $\eta_0$. By contrast, the growth rates of the modes are very small (order $(\eta_0 - \eta)^2$) in magnitude) and they evolve very slowly. The modes are oscillatory, the frequency of oscillations behaving as $\eta_0 - \eta$.

We plan to study the asymptotics in all variants of branching encountered or suspected in this work. Moreover, it is of interest to investigate the asymptotics of co-dimension 2

branching, which may take place in the MHD stability problem on varying both $\nu$ and $\eta$ independently.

**Acknowledgements**

The project was financed by the grant No. 22-17-00114 of the Russian Science Foundation, https://rscf.ru/project/22-17-00114/.

**References**

Andrievsky, A., A. Brandenburg, A. Noullez, and V. Zheligovsky (2015), Negative magnetic eddy diffusivities from the test-field method and multiscale stability theory, *The Astrophysical Journal*, *811*(2), 135, https://doi.org/10.1088/0004-637x/811/2/135.

Arnol'd, V., Y. Zel'dovich, A. Ruzmaikin, and D. Sokolov (1982), Steady-state magnetic field in a periodic flow, *Soviet Physics–Doklady*, *266*(6), 1357–1361 (in Russian).

Chertovskih, R., and V. Zheligovsky (2023a), Linear perturbations of the Bloch type of space-periodic magnetohydrodynamic steady states. I. Mathematical preliminaries, *Russian Journal of Earth Sciences*, *23*, ES3001, https://doi.org/10.2205/2023ES000834.

Chertovskih, R., and V. Zheligovsky (2023b), Linear perturbations of the Bloch type of space-periodic magnetohydrodynamic steady states. II. Numerical results, *Russian Journal of Earth Sciences*, *23*, ES4004, https://doi.org/10.2205/2023ES000838.

Rasskazov, A., R. Chertovskih, and V. Zheligovsky (2018), Magnetic field generation by pointwise zero-helicity three-dimensional steady flow of an incompressible electrically conducting fluid, *Physical Review E*, *97*(4), 043,201, https://doi.org/10.1103/PhysRevE.97.043201.

Zheligovsky, V. (2011), *Large-Scale Perturbations of Magnetohydrodynamic Regimes*, 330 pp., Springer Berlin Heidelberg, https://doi.org/10.1007/978-3-642-18170-2.

Russian Journal of Earth Sciences

# Co- and Pre-Seismic Crustal Deformations Related to Large Earthquakes Between Years of 2009 and 2023 Using Continuous CORS-TR GNSS Observations in the Anatolian Diagonal (Turkey)

**P. Dokukin[1], M. A. Güvenaltin[2], V. Kaftan[*,3], M. Toker[4],**

[1] People's Friendship University of Russia, Moscow, Russia
[2] Hacettepe University, Ankara, Turkey
[3] Geophysical Center RAS, Moscow, Russia
[4] Yuzuncu Yil University, Van, Turkey
* **Correspondence to:** Vladimir Kaftan, v.kaftan@gcras.ru.

**Abstract:** Synoptic animations of internal displacements and deformations of the earth's crust were obtained based on the results of continuous GNSS observations in Eastern Anatolia from 2009 to 2023. The spatiotemporal patterns of the seismic deformation process in connection with the tectonics of the region have been identified. It is shown that dilatation and total shear strains evolve in concert with the migration of the strongest earthquakes Elazig, Elazig-Malatya and devastate Karamanmaraş series. Two years before the occurrence of the devastating earthquakes of 2023, a deficit of internal displacements of GNSS stations developed in the area of their epicenters. The conducted research suggests that the strongest events of 2009–2023 are connected by a unitary seismic deformation process. The most important action in this case is the SW movement of the Anatolian block as monolithic element. In the development of movements and deformations, a flow of increasing stresses is observed in the direction from Karliova Triple Junction to the SW to the area of the strongest seismic events on February 2023. It originates east of the Karliova Triple Junction where the Arabian Plate encounters an obstacle. The role of mantle flows in the seismic process is assessed.

**Keywords:** GNSS, crustal deformation, displacement deficit, earthquake migration, seismo-deformation process, synoptic analysis.

**Citation:** Dokukin, P., M. A. Güvenaltin, V. Kaftan, and M. Toker (2023), Co- and Pre-Seismic Crustal Deformations Related to Large Earthquakes Between Years of 2009 and 2023 Using Continuous CORS-TR GNSS Observations in the Anatolian Diagonal (Turkey), *Russian Journal of Earth Sciences*, 23, ES5005, EDN: CJREIU, https://doi.org/10.2205/2023es000877

Research Article

Received: 21 September 2023
Accepted: 10 November 2023
Published: 29 December 2023

**Copyright:** © 2023. The Authors. This article is an open access article distributed under the terms and conditions of the Creative Commons Attribution (CC BY) license (https://creativecommons.org/licenses/by/4.0/).

## 1. Introduction

The territory of Eastern Anatolia (Turkey) is an area of intense movements and deformations of the earth's crust caused by active tectonic processes and seismic activity. The tectonics of this territory is represented by fault zones with a left-sided shear mechanism. This area is called the Anatolian neotectonic diagonal due to the spatial orientation of the main tectonic faults, extending in the SW–NE direction [*Seyitoğlu et al.*, 2022].

In recent years and decades, a network of continuous GNSS observations has been deployed in Turkey. This circumstance provided the opportunity for an experimental study of recent movements and deformations of the earth's crust in the specified territory for the interval 2009–2023. During this time, several destructive earthquakes occurred in the region. The purpose of this work was to study the spatiotemporal tendencies in the deformation of the earth's crust in connection with strong seismic events in accordance with the tectonic regime of the region.

The study consisted of two stages. The first and main stage was to study the evolution of movements and deformations of the region over the time interval from 2009–2021. About

a year after its completion, in February 2023, a series of destructive doublet earthquake sequences occurred in the SW-section of our study area; the 6th February 2023 ($M7.9$, $M7.6$) earthquake ruptures struck the region, triggering a second event and a cascade of strong aftershocks (~10,000 events) in the Maras Triple Junction (MTJ) [*Toker et al.*, 2023] region of SE-Anatolia. The circumstance associated with the 2023 catastrophic doublets, which redistributed and/or shifted the crustal stresses in the study area, led to further analysis in order to assess co- and pre-seismic displacements and related crustal deformations.

## 2. Tectonics and Seismicity of the Studied Region

The study region represents the area of interaction between the Nubian and Arabian tectonic plates with the Anatolian block and the Eurasian plate, respectively.

The tectonics of the studied region is represented by the following main tectonic elements (Figure 1). The main tectonic structure is the North Anatolian Fault Zone (NAFZ). This is the main fault zone marking the boundary of the main tectonic plates: the Eurasian and Arabian. This zone, along with the Varto Fault Zone (VFZ), creates an obstacle to the movement of the Arabian Plate to the North, reversing the movement of the lithosphere towards the west-southwest within the segment bounded by the NAFZ and East Anatolian Fault Zone (EAFZ).

The Karliova Triple Junction (KTJ) area is a key feature that determines the nature of tectonic movements in the study region. It is dissected by multiple local faults and includes the volcanic areas of Turnadag and Varto. The feeding of these volcanic centers, as the authors believe, is due to the outcrop of the Anatolian tectonic block to the west-southwest [*Karaoğlu et al.*, 2018]. There is a hypothesis about the existence of a mantle plume east of the KTJ [*Gök et al.*, 2007], the dynamics of which can form an asthenospheric flow that contributes to the removal of the Anatolian block to the west-southwest. The southern end of the East Anatolian Fault Zone from the east limits the area of hypothetical rise of warmer upper mantle, thereby leading to extensional deformation of the earth's crust in the southern part of the Anatolian block [*Gök et al.*, 2007].

Recent GNSS studies show that plate-pulling forces are also characteristic of Western Turkey [*Bartol and Govers*, 2014; *Kutoglu et al.*, 2016; *McClusky et al.*, 2000; *Reilinger et al.*, 2006; *Wei et al.*, 2019]. These studies also suggest that these forces play an important role in the westward movement of the Anatolian Plate.

The main tectonic element in the context of this study is the EAFZ. The EAFZ, one of the most active faults in Turkey, has a NE-SW direction and has a length of approximately 550 km [*Reilinger et al.*, 2006]. The first study on the slip rate of the fault was made by *Taymaz et al.* [1991]. *Taymaz et al.* [1991] determined the slip rate as 29 mm/year for the EAFZ zone. However, current GNSS studies show that the slip rate is around 8–11 mm/year [*Angus et al.*, 2006; *McClusky et al.*, 2000; *Reilinger et al.*, 2006] and our study. *Çetin et al.* [2003] used paleoseismological and historical earthquake records and suggest that there is strain accumulation on the EAFZ. Although the tectonic stress on the EAFZ is mostly accommodated by strike-slip faulting, moreover it is seen that small-medium earthquakes have different focal mechanisms.

The structure of the lithosphere of the studied region is represented by three different structures: the East Anatolian High plateau (further east of the KTJ), the Anatolian block and the northern part of the Arabian plate. The boundaries of the structures are consistent with the main tectonic boundaries. The authors of [*Gök et al.*, 2007] show that the area east of the KTJ is supported by doming hot asthenospheric material resulted from slab delamination and break off process (e.g., beneath Lake Van region in [*Toker and Şahin*, 2019, 2022]).

## 3. Data and Method

The study used three types of experimental data: faulting, earthquakes, and continuous GPS observations.

Digital data on the position of active faults in the study area were obtained from the source [*Emre et al.*, 2012].

The earthquake catalogue used in this study is retrieved from the Bogaziçi University, Kandilli Observatory and Earthquake Research Institute (KOERI) database [*KOERI, Boğaziçi University*, 2021] and contains instrumental period data (1900–2021). In the subsequent period 2022–2023, we limited ourselves to data on the strongest events, due to too many moderate and weak aftershocks, information about which is not so important for our specific study.

The most important earthquakes of the period under study are presented in the Table 1.

The most important component of experimental data is GNSS observation data. For this study, continuous measurements were used at stations of the Turkish continuously operating network. TUSAGA-Aktif (Continuously Operating Reference Stations-Turkey (CORS-TR) has been continuously measuring with its more than 150 stations since 2009 and obtaining daily observation files within Turkey's borders. Especially recent earthquakes have been monitored by near-area stations [*Irmak et al.*, 2021; *Konca et al.*, 2021; *Yalvac*, 2020].

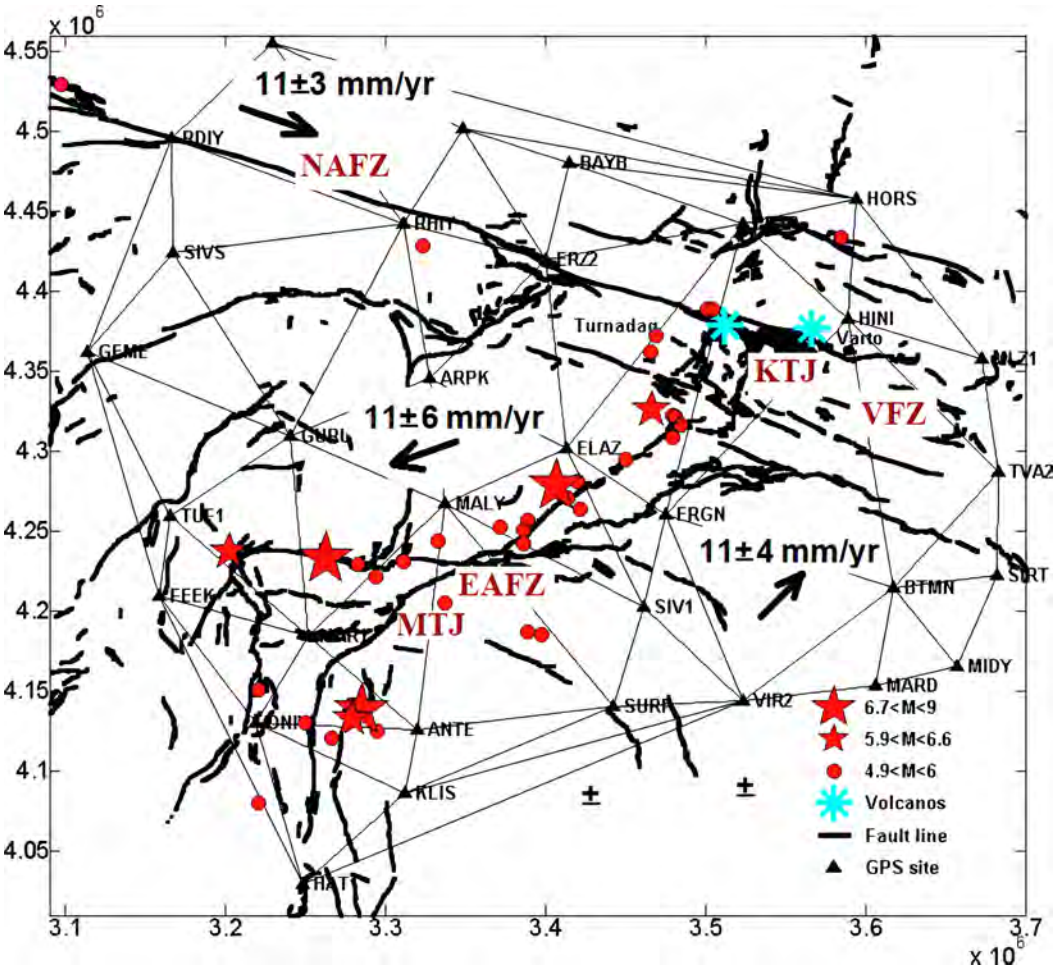


**Figure 1.** Fault tectonics, major earthquakes, and Delaunay triangulation from GNSS stations participating in the study. Black arrows are the directions of movement of the main tectonic blocks in the internal coordinate reference system. Average movement velocities are calculated for the period 2009–2023. EAFZ – East Anatolian Fault Zone. KTJ – Karliova Triple Junction. NAFZ – North Anatolian Fault Zone. MTJ – Maras Triple Junction. VFZ – Varto Fault Zone. The borders of the frames of the figures here and below indicate rectangular coordinates in the UTM projection, expressed in meters.

**Table 1.** The most important earthquakes of the period of between years of 2009 and 2023

| City | Date, (yyyy.mm.dd) | Time, (h:m:s) | Coordinates, (°C) | | Depth, (km) | $M_w$ |
|---|---|---|---|---|---|---|
| | | | Lat. | Long. | | |
| Elazığ | 2010.03.08 | 02:32:34.710 | 38.864 | 39.986 | 12 | 6.1 |
| Elazığ, Malatya | 2020.01.24 | 17:55:14.147 | 38.43120 | 39.06090 | 10 | 6.7 |
| Bingöl | 2020.06.14 | 14:24:29.501 | 39.42290 | 40.70730 | 10 | 5.9 |
| Bingöl | 2020.06.15 | 06:51:31.776 | 39.42260 | 40.74790 | 10 | 5.5 |
| Gaziantep | 2023.02.06 | 01:17:35 | 37.112 | 37.119 | 17.9 | 7.8 |
| Nuradagi | 2023.02.06 | 01:28:15 | 37.127 | 36.943 | 12.2 | 6.7 |
| Kahramanmaraş | 2023.02.06 | 10:24:49 | 38.024 | 37.203 | 10.0 | 7.5 |
| Dogansehir | 2023.02.06 | 10:35:38 | 38.008 | 37.751 | 8.1 | 6.0 |

In the first part of the study, 32 of these stations' time series have been examined. In order for the observation files to be interpreted geometrically, they must go through post-processing. From the beginning of 2022, the Turkish General Mapping Directorate started to share the daily results and time series obtained from observation files of these stations (https://www.harita.gov.tr/public/sunum/). The aforementioned post-processing was provided by this institution and it is known that the open-source GAMIT/GLOBK software is used [*Herring et al.*, 2018]. The final solution is computed in ITRF2014 datum. While processing daily observation files, IGS (International GNSS Service) stations have been used for regional stabilization [*Kurt et al.*, 2020].

The network used in the study is shown in Figure 1. An important circumstance is that before and after the catastrophic earthquakes in Eastern Anatolia, some GNSS stations were moved from their original locations. The following stations have been moved and renamed as BAYB-BYB1, GEME-GEM1, HAT1-HAT2, KLIS-KLS1, MALY-MLY1, SIRT-SRT1, SIVS-SVS1. To obtain a continuous history of movements and deformations of the earth's crust, the time series of the previous stations were extended by observations at their new analogues, taking into account the local mutual increments of coordinates obtained as soon as possible after the completion of the operation of these relocated stations. We allowed such laxity on the basis that all new analogues of GNSS stations are installed in the territories of the same consolidated blocks at a considerable distance from moving faults. Most stations are mutually distant by no more than km. BAYB and MALY stations have been moved by 5.5 and 8.6 km, respectively. However, they did not cease to be on the same consolidated block.

On dates of technical breaks in observations, in order to avoid irregularity of time series, the missing coordinates were determined by interpolation with Hermite splines.

## 4. Analysis of Internal Movements and Deformations of the Earth's Crust

Horizontal displacements of GNSS sites are calculated for the every daily coordinate solution. Time series of horizontal displacements $U_n$ and $U_e$ in a reference to the initial epoch $T_0$ as horizontal coordinate differences $n$ and $e$ in UTM projection were received by the formulas

$$U_{n_i} = n_i - n_0,\ U_{e_i} = e_i - e_0,$$

where index $i$ denotes the current epoch (day) of measurements.

Displacements of GNSS points, expressed in a global reference system, demonstrate first of all the trends in the movement of the global tectonic plate on which the observation point is located. This effect makes it difficult to track movements associated with local changes, such as the slow accumulation of elastic deformations in the Earth's crust near the epicenter of a future event. In this case, more indicative characteristics of the movements

are the displacements of points, presented in the local (internal) reference system, which well reflect the mutual multidirectional movements of the sides of local faults. The rationale for this approach is presented in [*Gvishiani et al.*, 2022]. Such a local (internal) displacement reference system can be easily obtained by subtracting from each displacement $U_j$ in the global reference system the average value $\overline{U}$, which characterizes the trend of global tectonics common to all network points, for each epoch measurements. Thus, we obtain a reference system for displacements (or displacement rates) according to the well-known no net translation principle

$$u_{n_j} = U_{n_j} - \overline{U_n},\ u_{e_j} = U_{e_j} - \overline{U_e},$$

where index $j$ is the current number of the GNSS observation point.

For each day of observation, based on the displacement values, we obtained digital models of the distribution of horizontal deformations of total shear and dilatation. These characteristics are invariant with respect to the choice of coordinate system. The spatial models were motion and deformation characteristics interpolated onto a regular 1 km grid using Hermite splines.

To calculate the deformations of the finite elements, the horizontal deformation tensor was used (the $n$ and $e$ axes are directed to the north and east)

$$T_\varepsilon = \begin{pmatrix} \varepsilon_n & \varepsilon_{ne} \\ \varepsilon_{en} & \varepsilon_e \end{pmatrix},$$

whose elements were equal $\varepsilon_n = \frac{\partial u_n}{\partial n}$ , $\varepsilon_e = \frac{\partial u_e}{\partial e}$ and $\varepsilon_{en} = \varepsilon_{ne} = \frac{1}{2}\left(\frac{\partial u_n}{\partial e} + \frac{\partial u_e}{\partial n}\right)$, correspondently, where $\left(\frac{\partial u_n}{\partial e} + \frac{\partial u_e}{\partial n}\right) = \gamma_{ne} = \gamma_{en}$ – relative shear.

Elements of the strain tensor are represented by the partial derivatives of the displacements $u_n$ and $u_e$ along the coordinate axes $n$ and $e$.

To study the spatiotemporal distribution of horizontal deformations, the following invariant characteristics were calculated.

1) Principal strains $\varepsilon_1$ and $\varepsilon_2$ $\varepsilon_{1,2} = \frac{1}{2}\left[\varepsilon_n + \varepsilon_e \pm \sqrt{(\varepsilon_n - \varepsilon_e)^2 + \gamma_{ne}^2}\right]$.
2) Total shear $\gamma = \left((\varepsilon_n - \varepsilon_e)^2 + \gamma_{ne}^2\right)^{1/2}$.
3) Dilatation $\Delta = \varepsilon_1 + \varepsilon_2$.

The strain components were calculated using the method described in [*Wu et al.*, 2006].

Due to the significant non-equivalence of the finite elements (see Figure 1), the deformation values were reduced to the average square of the network triangle [*Kaftan and Melnikov*, 2019].

Spatial models of movements and deformations obtained for each day were combined into evolutionary models – video animations of the seismic deformation process. All video images show active fault lines. The epicenters of earthquakes were plotted on the frames starting from the date of their occurrence. Thus, a basis was obtained for a heuristic analysis of the spatiotemporal relationship between fault tectonics, seismicity, movements and deformations of the study area.

## 5. Study of the Evolution of Seismotectonic Movements and Crustal Deformations

### 5.1. Horizontal Dilatation Strain

Analysis of the characteristics of areal extension and compression is aimed primarily at assessing the behavior of subcrustal currents and the temperature regime of the asthenosphere. But at the same time, significant dilatation anomalies are formed due to the release of accumulated seismic energy at the source of a strong earthquake. Long-term and continuous GNSS observations make it possible to test modern concepts in the field of tectonics and geodynamics. The evolution of dilatation strain from 2009 to 2023 can

be observed in video animation [*Kaftan et al.*, 2023a]. Selected key frames covering the catastrophic earthquakes of 2023 are presented in Figure 2.

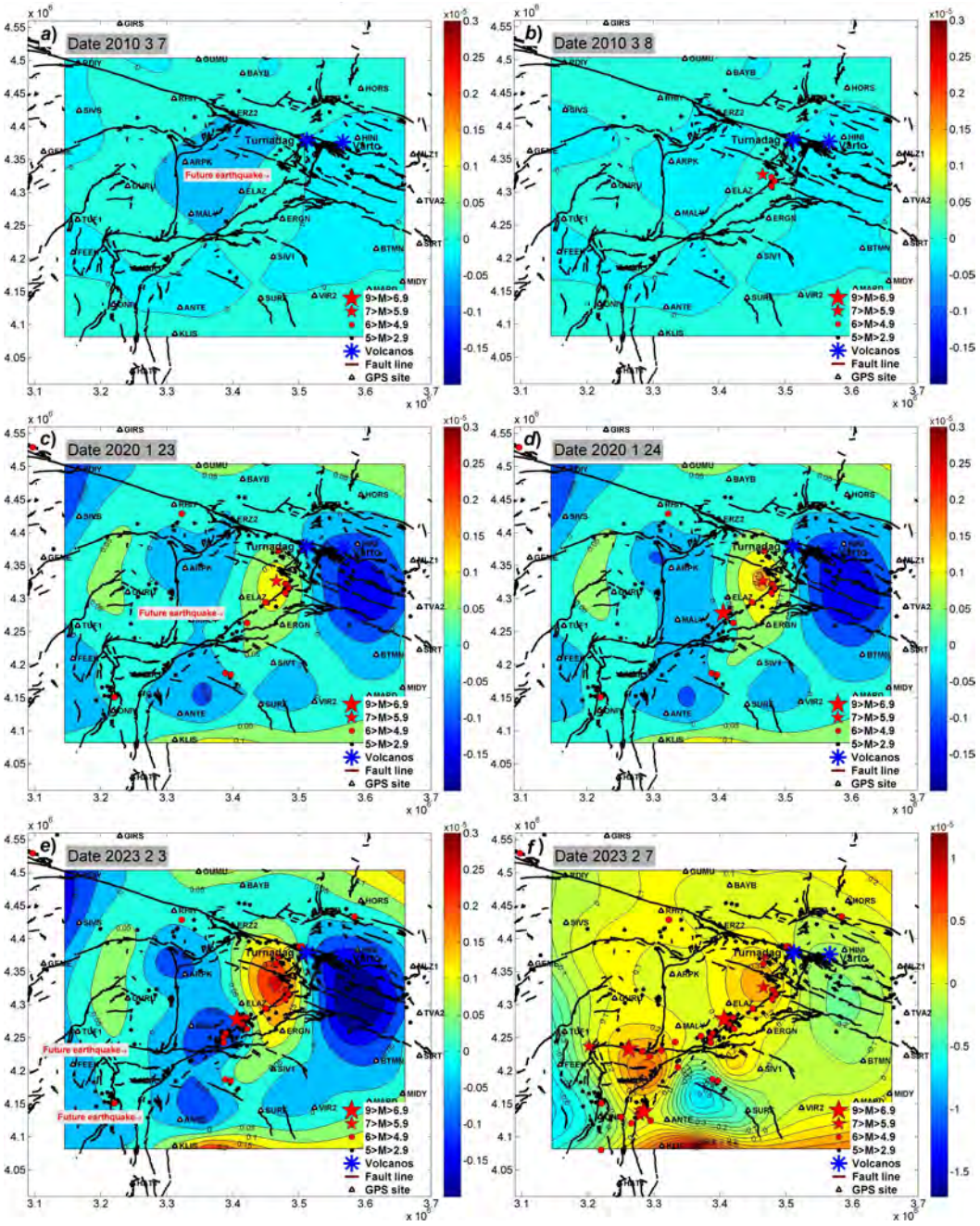


**Figure 2.** Evolution of dilatation deformation 2009–2023 in connection with the strongest seismic events.

Visual analysis shows that the first strong seismic event $M6.1$ in 2010 was not significantly manifested by changes in dilatational deformation. Approximately two years after this event, significant compressive strains began to develop in the VFZ region. Following this event, in the area of the epicenter, about a year later, an extreme areal extension formed, which began to develop without being accompanied by noticeable seismic activity. The area of horizontal extension expanded until the main seismic event $M6.7$ in 2020. This earthquake occurred at the boundary of the interaction of compression and extension areas, revealing the shear mechanism of seismic rupture. A destructive series of moderate Bingol earthquakes in the second half of 2020 also occurred at the boundary of the interaction

of the main extrema of extension and compression in the north of the KTJ. The main extremum of extension in the southwestern part of the KTJ fault series appears to be the main source of tectonic deformation that determines the spatiotemporal distribution of the stress pattern. The extremum of tensile stresses contributes to the movement of the Anatolian block in the earth's crust to the southwest. After the catastrophic earthquakes of Eastern Anatolia 2023, the entire territory of the Eastern Anatolian block between the main seismic ruptures experienced significant horizontal extension.

### 5.2. Total Shear Deformation Analysis

In regions with a predominant shear mechanism of movements along active faults, slow deformation shear waves are detected [*Kaftan and Melnikov*, 2019; *Kaftan and Tatarinov*, 2022]. This prompted the idea to investigate this phenomenon in the Eastern Anatolia region. Based on the results of processing GNSS observations, video animations of the full shear deformation were obtained [*Kaftan et al.*, 2023b]. Key frames are shown in Figure 3.

Visual synoptic analysis allows us to discover new patterns of seismicity and cause-and-effect relationships in the evolution of the seismic-deformation process. It can be seen that approximately a year before the strong earthquake $M6.1$ (August 3, 2010), a significant deformation extremum of $2.5 \times 10^{-6}$ was formed in the area of the future epicenter (Figure 3a). This indicates that a strong earthquake is caused by the accumulation of shear deformations that contribute to the release of stress within a mature seismic source. The subsequent development of the deformation process shows an increase and spread of deformation to the southwest along the EAFZ, as well as to the northwest along the NAFZ. At the same time, moderate seismic events with $M \sim 5$ occur in the area of deformation propagation. The main part of them migrates, following the deformation flow, to the epicenter of the future strong earthquake Elazig-Malatya on January 24, 2020 $M6.7$. This creates a trimodal region of extremes of the total shear strain. An earthquake occurs in a trough between two local maxima of deformation. The main shock promotes the merging of two local deformation extrema into a single region extended along the EAFZ. An interesting feature is the formation of a local maximum of deformation on the northwestern border of the study area, in which two moderate seismic events occurred. Visual analysis allows one to observe the seismic deformation process and draw conclusions about the mechanisms of stress accumulation and release during strong earthquakes, as well as the role of the Karliova Triple Junction as an intersection point of the study area. From this area, the propagation of total shear deformation continued directly towards the epicenter of the first devastate earthquake of Eastern Anatolia 2023 (Figure 3e). This circumstance suggests that the second strongest earthquake of the February 2023 series was a consequence of the first.

### 5.3. Deficit of Internal Movements Due to Strong Earthquakes

Having long-term data on the nature of crustal movements in the study area, we analyzed the accumulation trends of the module of vectors of internal movements of GPS points. The corresponding synoptic animation is presented in [*Dokukin et al.*, 2023; *Kaftan et al.*, 2023c]. Key frames of the animation are shown in Figure 4.

The experience of similar studies has shown that a minimum of internal displacements accumulates before strong earthquakes in the area of their epicenter [*Kaftan*, 2021; *Kaftan et al.*, 2022]. We consider this characteristic as a predictor of the location of a future earthquake as a place that impedes general movement.

The presented synoptic video demonstrates the evolution of the deficit of internal displacements in the area of occurrence of a set of strong earthquakes in Elazig (Turkey) in 2009–2021. It can be seen that the first strong seismic event of 2010 with $M6.1$ occurred in a zone of deficiency of internal displacements, expressed in dark brown. Subsequently, an increase in internal displacements occurred in this place, accompanying the release and relaxation of elastic stresses. The area of internal displacement deficit has shifted in two directions to the southwest and northwest along the distribution of the NAFZ and EAFZ.

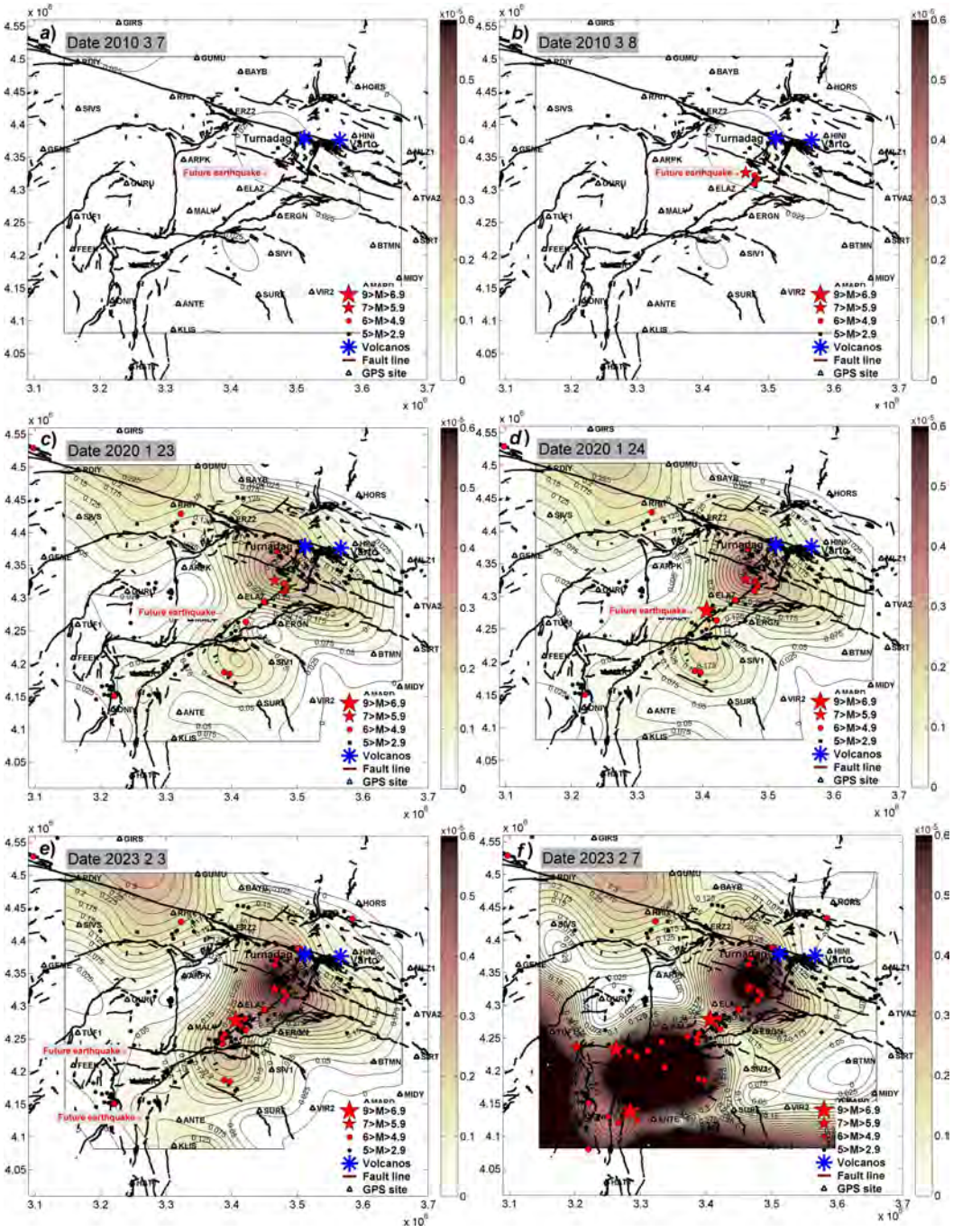


**Figure 3.** Evolution of the total shear deformation 2009–2023 in connection with the strongest seismic events.

Subsequently, four moderate earthquakes with $M \sim 5$ occurred in these areas. Two of them, located to the southeast of the EAFZ, caused increased mobility of the earth's crust at the epicenter of the strongest earthquake of 2020 with $M6.7$. The 2020 Elazig earthquake occurred in a zone of accumulated displacements at a level of 5–6 cm and was accompanied by a co-seismic displacement of more than 10 cm, which subsequently increased to 13 cm. A series of destructive Bingol earthquakes in 2020 also occurred in the mobile zone. In the subsequent period, the entire study area was subjected to accumulated displacements of at least 5 cm. This indicates a release of elastic pre-seismic stresses throughout this area.

Starting from 2020, a minimum of local internal displacements has formed in the southwestern territory of the region. It existed until the occurrence of a series of strong

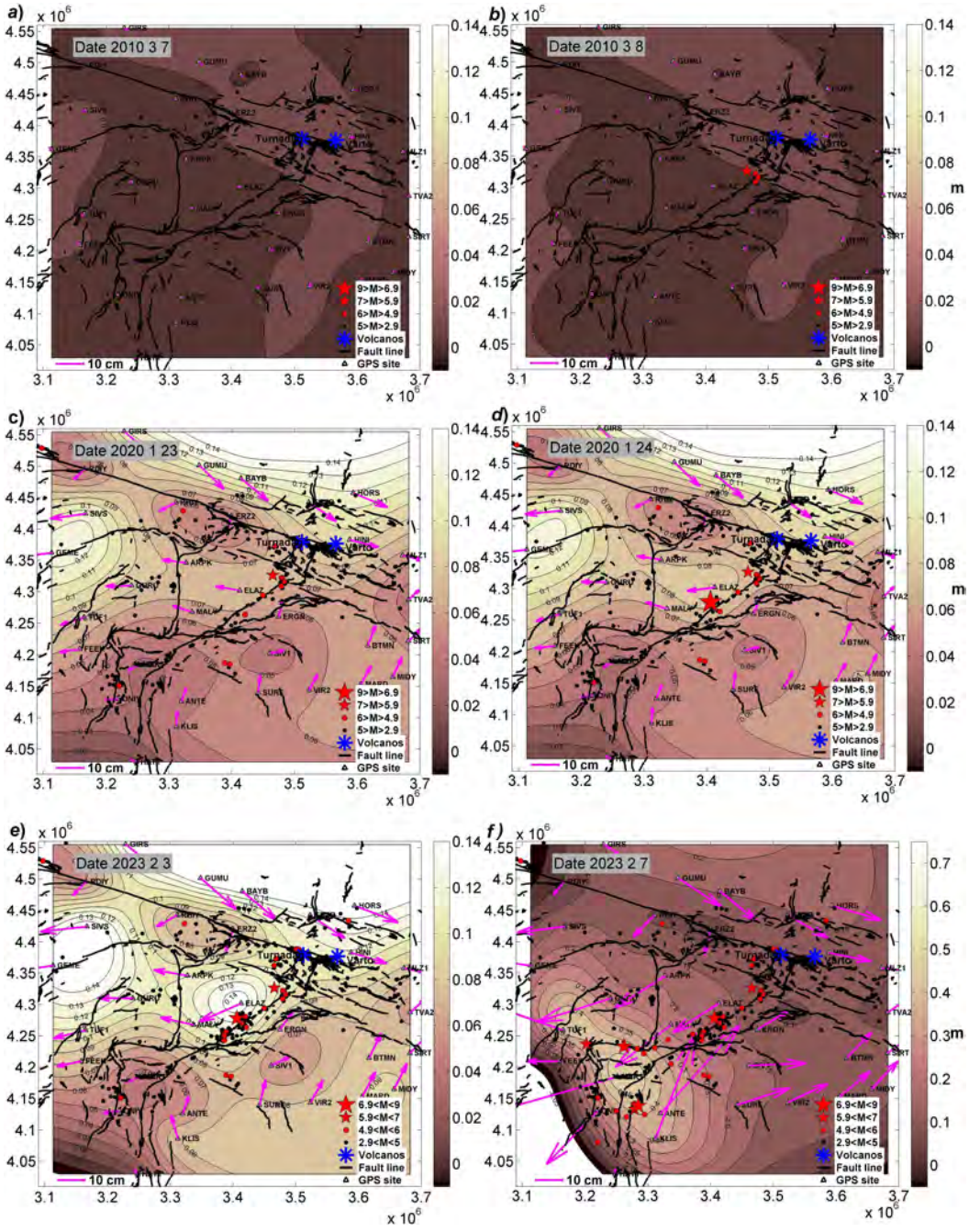


**Figure 4.** Evolution of the internal displacement deficit 2009–2023.

earthquakes in 2023, which occurred within this minimum. This result once again showed that the analysis of the deficit of internal displacements is very promising in solving the problem of predicting the location of strong earthquakes.

## 6. Discussion and Conclusion

In the present study, we attempt to show the spatial and temporal nature of periods of complete deformation through a synopsis of ongoing tectonism in the study area, to understand how horizontal vectors and deformation are consistent with the relative movements of the Anatolian and Arabian blocks. Spatial and temporal patterns of geodetic deformation evolution highlight a new perspective on KTJ. A new view is being formed on the KTJ as a source of stress propagation that determines the kinematics of the East Anatolian block. The concentration of subcrustal stresses occurs due to the collision of

the Arabian plate with the Eurasian plate in the VFZ. In this area, maximum compressive deformation is observed, which contributes to the formation of subcrustal lithospheric flows from the KTJ within the framework defined by the NAFZ and EAFZ. These currents in turn create an area of expansion at the southwestern end of the KTJ. Interestingly, this propagation of dilatation strain, framed by KTJ and Anatolian block deformation, obliquely points the Anatolian block to the SW rather than to the NW (or to the W), with strong support for strike-slip and fault deformation. Our main results are in good agreement with the orientations of maximum principal horizontal stresses published in the World Stress Map (WSM2016) and 3D deformation models published in previous studies [e.g., *Kutoglu et al.*, 2016]; the direction of maximum principal stress, oriented generally to the southwest, forms normal and strike-slip faults that extend prominently toward the southwestern end of the Anatolian block into the Maras Triple Junction (MTJ). Comparison of the calculated geodetic and seismic strains from WSM2016 with previously published results shows that the estimated tensile, compressive, and shear strain trajectories are kinematically correlated with MTJ and KTJ. This completes the southwest-directed oblique "transtensional" extrusion of the bilaterally locked Anatolian block, parallel/subparallel to the EAFZ and the Dead Sea Fault (DSF). This may be the reason why the left-lateral earthquake ruptures on February 6, 2023 ($M_w$ 7.7, 7.6) occurred in the area of MTJ.

Synoptic analysis of the evolution of total shear deformation allowed us to trace the flow of shear deformation from the KTJ, through the epicenters of large earthquakes to the southwest, up to the sites of the occurrence of a series of destructive earthquakes in Eastern Anatolia in February 2023. The maximum total shear strain occurred before the 2010 (Figure 3a,b) Elazig earthquake in the vicinity of its epicenter. From this area, shear deformation began to grow naturally along the NAFZ and EAFZ strike routes. It intensified in the area where the 2020 Elazig-Malatya earthquake occurred and continued southeast to the places of the 2023 East Anatolian earthquakes. An analysis of the evolution of the internal displacement deficit has shown the effectiveness of this characteristic for identifying the locations of strong earthquakes. A deficit of internal displacements is formed when it encounters an obstacle to movement in the area of increasing stress.

The conducted research suggests that the strongest events of 2009–2023 are connected by a unitary seismic deformation process. The most important action in this case is the SW movement of the Anatolian block as monolithic element. In the development of movements and deformations, a flow of increasing stresses is observed in the direction from KTJ to the SW to the area of the strongest seismic events on February 2023. It originates east of the KTJ where the Arabian Plate encounters an obstacle. We assume here the presence of a branch to the SW from the sublithospheric flow, pulling the Arabian plate mainly to the north.

Finally, our results conclude that the knowledge of the co- and pre-seismic crustal deformation patterns compared with the large recent earthquakes (2009 to 2023) in the Anatolia provides very important information on the location of the main faults, earthquakes and strain accumulation for seismic hazard assessment [e.g., *Kutoglu et al.*, 2016]. This motivates an agreement between the seismic and tectonic strains, which confirm that there are seismically active crustal deformations in Anatolia.

**Acknowledgments.** The work was carried out within the framework of the state assignment of the Geophysical Center of the Russian Academy of Sciences, approved by the Ministry of Science and Higher Education of the Russian Federation, and also within the working plans of Hacettepe University (Ankara) and Yuzuncu Yil University (Van) Geophysics Division, Turkey.

The authors would like to express their gratitude to the General Directorate of Mapping (from the Republic of Türkiye's Ministry of National Defence) for providing valuable daily GNSS observation data. This data, shared openly through their database, was instrumental in conducting the research presented in this article. The accessibility and quality of the data significantly contributed to the accuracy and reliability of our findings. We thank the distinguished reviewers for their careful reading of the manuscript and helpful recommendations for its improvement.

**References**

Angus, D. A., D. C. Wilson, E. Sandvol, and J. F. Ni (2006), Lithospheric structure of the Arabian and Eurasian collision zone in eastern Turkey from S-wave receiver functions, *Geophysical Journal International*, *166*(3), 1335–1346, https://doi.org/10.1111/j.1365-246X.2006.03070.x.

Bartol, J., and R. Govers (2014), A single cause for uplift of the Central and Eastern Anatolian plateau?, *Tectonophysics*, *637*, 116–136, https://doi.org/10.1016/j.tecto.2014.10.002.

Çetin, H., H. Güneyli, and L. Mayer (2003), Paleoseismology of the Palu-Lake Hazar segment of the East Anatolian Fault Zone, Turkey, *Tectonophysics*, *374*(3–4), 163–197, https://doi.org/10.1016/j.tecto.2003.08.003.

Dokukin, P., M. A. Guvenaltin, T. S. Irmak, V. Kaftan, and M. Toker (2023), Evolution of the crustal inner displacement deficit in a reference to Elazig earthquake series just before occurring the devastate Ekinozu-Nuradagi earthquakes (M7.5–7.8, 2023-02-06), https://doi.org/10.2205/ESDB-Ekinozu-Nurdagi-quakes.

Emre, O., T. Y. Duman, and H. Elmacı (2012), 1:250 000 Scale Active Fault Map Series of Turkey.

Gök, R., M. E. Pasyanos, and E. Zor (2007), Lithospheric structure of the continent-continent collision zone: eastern Turkey, *Geophysical Journal International*, *169*(3), 1079–1088, https://doi.org/10.1111/j.1365-246X.2006.03288.x.

Gvishiani, A. D., V. N. Tatarinov, V. I. Kaftan, A. I. Manevich, V. A. Minaev, S. A. Ustinov, and R. V. Shevchuk (2022), Geodynamic Model of the Northern Part of the Nizhnekansk Massif: Fault Tectonics, Deformations, and Insulation Properties of Rock Displacements, *Doklady Earth Sciences*, *507*(1), 909–915, https://doi.org/10.1134/S1028334X22600608.

Herring, T. A., M. A. Floyd, R. W. King, and S. C. McClusky (2018), *Global Kalman filter VLBI and GPS Analysis Program, GLOBK Reference Manual, Release 10.6. Department of Earth, Atmospheric and Planetary Sciences*, Massachusetts Institute of Technology, Cambridge, MA.

Irmak, T. S., M. Toker, E. Yavuz, E. Şentürk, and M. A. Güvenaltın (2021), New insight into the 24 January 2020, Mw 6.8 Elazığ earthquake (Turkey): An evidence for rupture-parallel pull-apart basin activation along the East Anatolian Fault Zone constrained by Geodetic and Seismological data, *Annals of Geophysics*, *64*(4), https://doi.org/10.4401/ag-8638.

Kaftan, V., and A. Melnikov (2019), *Migration of Earth Surface Deformation as a Large Earthquake Trigger*, pp. 71–78, Springer International Publishing, https://doi.org/10.1007/978-3-030-31970-0_8.

Kaftan, V., P. Dokukin, M. A. Guvenaltin, M. Toker, and T. S. Irmak (2023a), Fifteen-year evolution of the crustal dilatation in a reference to the recent East Anatolian earthquakes, https://doi.org/10.2205/ESDB-000877-d01.

Kaftan, V., P. Dokukin, M. A. Guvenaltin, M. Toker, and T. S. Irmak (2023b), Fifteen-year evolution of the crustal total shear strain in a reference to the recent East Anatolian earthquakes, https://doi.org/10.2205/ESDB-000877-d02.

Kaftan, V., P. Dokukin, M. A. Guvenaltin, M. Toker, and T. S. Irmak (2023c), Fifteen-year evolution of the crustal inner shear deficit in a reference to the recent East Anatolian earthquakes, https://doi.org/10.2205/ESDB-000877-d03.

Kaftan, V. I. (2021), An Analysis of Ground Movements and Deformations from 13-Year GPS Observations before and during the July 2019 Ridgecrest, USA Earthquakes, *Journal of Volcanology and Seismology*, *15*(2), 97–106, https://doi.org/10.1134/S0742046321010115.

Kaftan, V. I., and V. N. Tatarinov (2022), Registration of Slow Deformation Waves According to GNSS Observations, *Doklady Earth Sciences*, *505*(1), 489–495, https://doi.org/10.1134/S1028334X22070091.

Kaftan, V. I., V. N. Tatarinov, and R. V. Shevchuk (2022), Long-term changes in crustal movements and deformations before and during the 2016 Kumamoto earthquake sequence, *Geodynamics & Tectonophysics*, *13*(1), https://doi.org/10.5800/GT-2022-13-1-0570.

Karaoğlu, O., J. Browning, M. K. Salah, A. Elshaafi, and A. Gudmundsson (2018), Depths of magma chambers at three volcanic provinces in the Karlıova region of Eastern Turkey, *Bulletin of Volcanology*, *80*(9), https://doi.org/10.1007/s00445-018-1245-x.

KOERI, Boğaziçi University (2021), Kandilli Observatory and Earthquake Research Institute, Regional Earthquake-Tsunami Monitoring Center: Earthquake Catalogue, http://www.koeri.boun.edu.tr/sismo/zeqdb/, (date of access: 01/12/2021).

Konca, A. O., H. Karabulut, S. E. Güvercin, F. Eskiköy, S. Özarpacı, A. Özdemir, M. Floyd, S. Ergintav, and U. Doğan (2021), From Interseismic Deformation With Near-Repeating Earthquakes to Co-Seismic Rupture: A Unified View of the 2020 Mw6.8 Sivrice (Elazığ) Eastern Turkey Earthquake, *Journal of Geophysical Research: Solid Earth*, *126*(10), https://doi.org/10.1029/2021JB021830.

Kurt, A. İ., A. Cingöz, S. Özdemir, S. Peker, Ö. Özel, and M. Simav (2020), Türkiye Ulusal Temel GNSS Ağı (TUTGA) Güncel Koordinat ve Hızlarının GNSS Verilerinin Yeniden Değerlendirilmesi Kapsamında Hesaplanması, *Harita Dergisi*, *164*, 1–17.

Kutoglu, H. S., M. Toker, and C. Mekik (2016), The 3-D strain patterns in Turkey using geodetic velocity fields from the RTK-CORS (TR) network, *Journal of African Earth Sciences*, *115*, 246–270, https://doi.org/10.1016/j.jafrearsci.2015.12.002.

McClusky, S., S. Balassanian, A. Barka, C. Demir, S. Ergintav, I. Georgiev, O. Gurkan, M. Hamburger, K. Hurst, H. Kahle, K. Kastens, G. Kekelidze, R. King, V. Kotzev, O. Lenk, S. Mahmoud, A. Mishin, M. Nadariya, A. Ouzounis, D. Paradissis, Y. Peter, M. Prilepin, R. Reilinger, I. Sanli, H. Seeger, A. Tealeb, M. N. Toksöz, and G. Veis (2000), Global Positioning System constraints on plate kinematics and dynamics in the eastern Mediterranean and Caucasus, *Journal of Geophysical Research*, *105*(B3), 5695–5719, https://doi.org/10.1029/1996JB900351.

Reilinger, R., S. McClusky, P. Vernant, S. Lawrence, S. Ergintav, R. Cakmak, H. Ozener, F. Kadirov, I. Guliev, R. Stepanyan, M. Nadariya, G. Hahubia, S. Mahmoud, K. Sakr, A. ArRajehi, D. Paradissis, A. Al-Aydrus, M. Prilepin, T. Guseva, E. Evren, A. Dmitrotsa, S. V. Filikov, F. Gomez, R. Al-Ghazzi, and G. Karam (2006), GPS constraints on continental deformation in the Africa-Arabia-Eurasia continental collision zone and implications for the dynamics of plate interactions, *Journal of Geophysical Research: Solid Earth*, *111*(B5), https://doi.org/10.1029/2005JB004051.

Seyitoğlu, G., E. Tunçel, B. Kaypak, K. Esat, and E. Gökkaya (2022), The Anatolian Diagonal: a broad left lateral shear zone between the North Anatolian Fault Zone and the Aegean / Cyprus Arcs, *Türkiye Jeoloji Bülteni / Geological Bulletin of Turkey*, *65*(2), 93–116, https://doi.org/10.25288/tjb.1015537.

Taymaz, T., H. Eyidoğan, and J. Jackson (1991), Source parameters of large earthquakes in the East Anatolian Fault Zone (Turkey), *Geophysical Journal International*, *106*(3), 537–550, https://doi.org/10.1111/j.1365-246X.1991.tb06328.x.

Toker, M., and Ş. Şahin (2019), Crustal Poisson's ratio tomography and velocity modeling across tectono-magmatic lake regions of Eastern Anatolia (Turkey): New geophysical constraints for crustal tectonics, *Journal of Geodynamics*, *131*, 101,651, https://doi.org/10.1016/j.jog.2019.101651.

Toker, M., and Ş. Şahin (2022), Upper- to mid-crustal seismic attenuation structure above the mantle wedge in East Anatolia, Turkey: Imaging crustal scale segmentation and differentiation, *Physics of the Earth and Planetary Interiors*, *329–330*, 106,908, https://doi.org/10.1016/j.pepi.2022.106908.

Toker, M., E. Yavuz, M. Utkucu, and F. Uzunca (2023), Multiple segmentation and seismogenic evolution of the 6th February 2023 (*Mw* 7.8 and 7.7) consecutive earthquake ruptures and aftershock deformation in the Maras triple junction region of SE-Anatolia, Turkey, *Physics of the Earth and Planetary Interiors*, *345*, 107,114, https://doi.org/10.1016/j.pepi.2023.107114.

Wei, W., D. Zhao, F. Wei, X. Bai, and J. Xu (2019), Mantle Dynamics of the Eastern Mediterranean and Middle East: Constraints From P-Wave Anisotropic Tomography, *Geochemistry, Geophysics, Geosystems*, *20*(10), 4505–4530, https://doi.org/10.1029/2019GC008512.

Wu, J. C., H. W. Tang, Y. Q. Chen, and Y. X. Li (2006), The current strain distribution in the North China Basin of eastern China by least-squares collocation, *Journal of Geodynamics*, *41*(5), 462–470, https://doi.org/10.1016/j.jog.2006.01.003.

Yalvac, S. (2020), Determining the Effects of the 2020 Elazığ-Sivrice/Turkey (Mw 6.7) Earthquake from the Surrounding CORS-TR GNSS Stations by means of Relative GNSS Analysis, *Turkish Journal of Geosciences*, *1*(1), 15–21.

Russian Journal of Earth Sciences

# Study of the Impact of Climatic Changes in 1980–2021 on Railway Infrastructure in the Central and Western Russian Arctic Based on Advanced Electronic Atlas of Hydrometeorological Parameters (Version 2, 2023)

**A. D. Gvishiani[1,2], I. N. Rozenberg[3], A. A. Soloviev[1,2], R. I. Krasnoperov[1], O. O. Shevaldysheva[*,1,4], A. G. Kostianoy[1,5,6], S. A. Lebedev[1], I. A. Dubchak[3], N. V. Sazonov[7], I. M. Nikitina[1], S. A. Gvozdik[1], V. N. Sergeev[1], G. A. Gvozdik[1,4]**

[1]Geophysical Center of the Russian Academy of Sciences, Moscow, Russia
[2]Schmidt Institute of Physics of the Earth of the Russian Academy of Sciences, Moscow, Russia
[3]Russian University of Transport, Moscow, Russia
[4]Lomonosov Moscow State University, Moscow, Russia
[5]Shirshov Institute of Oceanology of the Russian Academy of Sciences, Moscow, Russia
[6]Witte Moscow University, Moscow, Russia
[7]Research and Design Institute of Informatization, Automation and Communications in Railway Transport, Moscow, Russia
* **Correspondence to:** Olga Shevaldysheva, o.shevaldysheva@gcras.ru

**Abstract:** Arctic zone of the Russian Federation (AZRF) is the region of intensive economic development. In this regard, it is critical to give an adequate assessment of natural factors that may have a negative impact on the growing technological infrastructure. Rapid climate change effects show a significant influence on this activity, including the railway network development. Hence, the decision-making community requires relevant information on climatic variations that can put at hazard the construction and operation of railway facilities. This paper presents the analysis of climatic changes within the region of Central and Western Russian Arctic in 1980–2021. It was performed using the new electronic Atlas of climatic variations in main hydrometeorological parameters, created for the Russian Railways in 2023. This geoinformatic product includes about 400 digital maps reflecting the variability of seven climatic parameters over more than four decades within the studied region. These parameters are air temperature, total precipitation, wind speed, soil temperature, soil moisture content, air humidity, and snow cover thickness. The analysis of climatic maps and their comparison between selected periods showed spatial and temporal heterogeneity of climatic variations in this region. This justifies the feasibility of further research using additional analytical instruments, such as Hovmöller diagrams, time series graphs, etc. The implementation of advanced geoinformatic products in the practice of the Russian Railways will facilitate sustainable development of its infrastructure in rapidly altering climatic conditions.

**Keywords:** Climate change, Russian Arctic, GIS, railway development, hydrometeorological parameters, electronic atlas.

**Citation:** Gvishiani, A. D., I. N. Rozenberg, A. A. Soloviev, R. I. Krasnoperov, O. O. Shevaldysheva, A. G. Kostianoy, S. A. Lebedev, I. A. Dubchak, N. V. Sazonov, I. M. Nikitina, S. A. Gvozdik, V. N. Sergeev, and G. A. Gvozdik (2023), Study of the Impact of Climatic Changes in 1980–2021 on Railway Infrastructure in the Central and Western Russian Arctic Based on Advanced Electronic Atlas of Hydrometeorological Parameters (Version 2, 2023), *Russian Journal of Earth Sciences*, 23, ES5006, EDN: ILWXRC, https://doi.org/10.2205/2023es000882

Research Article

Received: 18 October 2023
Accepted: 19 December 2023
Published: 30 December 2023

**Copyright:** © 2023. The Authors. This article is an open access article distributed under the terms and conditions of the Creative Commons Attribution (CC BY) license (https://creativecommons.org/licenses/by/4.0/).

## 1. Introduction

The Arctic Zone of the Russian Federation (AZRF) has taken incentives for development in recent years. As one of the richest regions in terms of valuable natural resources

[*Krivovichev*, 2019], it has received substantial support from the government to conduct economic activities within its territory. For instance, a reduced rate of mineral extraction tax (MET) has been established for new deposits of solid minerals, and there is no tax on the extraction of natural gas used for the production of liquefied gas or further petrochemical products, as well as other tax incentives [*Decree of the President of the Russian Federation*, 2014].

It is well known that the cost of transporting valuable minerals from remote deposits can significantly impact the overall cost of the final product. Therefore, exporting valuable minerals primarily by water transport becomes the only opportunity to make costly Arctic developments profitable [*Makarova et al.*, 2021].

Based on this, one of the most significant projects for the development of the region is the Northern Sea Route (NSR). This shipping route runs along the northern coasts of Russia in the Arctic Ocean, connecting European and Far Eastern ports. Estuaries of navigable Siberian rivers are also included into a unified transportation system. According to official statistical data, the cargo volume transported along the NSR in 2022 amounted to 34 million tons [*Department of Communications of the State Corporation "Rosatom"*, 2023]. It is planned to increase this volume to 150 million tons by 2030 and 220 million tons by 2035 [*Decree of the Government of the Russian Federation*, 2022]. The development of the NSR includes the construction of additional ice-class vessels, including icebreakers, and the expansion of port infrastructure in different regions of the AZRF.

The development of transportation infrastructure to increase cargo traffic along the NSR is connected to the delivery of goods to ports. The transportation infrastructure of AZRF encompasses all major modes of transportation: railways, roadways, waterways, and aviation. From an economic perspective, the combination of railway and water transport is often the most cost-effective option. For instance, when developing coal deposits and reaching full production capacity, it may be economically unfeasible to deliver the products to the port using railway transport only. The same applies to any other bulk cargo.

The only five out of the eight Arctic regions obtain railways. These are the Republic of Karelia, Murmansk and Arkhangelsk Oblasts, the Republic of Komi, and the Yamalo-Nenets Autonomous Okrug. Among private railways, it's well known the Norilsk Railway in Krasnoyarsk Krai, which runs from Dudinka to Talnakh, and a planned line from the Syradasai coal deposit to the Yenisei seaport. In the Republic of Sakha (Yakutia) and Khabarovsk Krai, the construction of the longest private railway, the Pacific Railway, is underway, connecting the Elginskoye coal deposit to the port of Elga on the Sea of Okhotsk. The total length of these railway tracks will exceed 500 kilometers.

The development of the state railway is planned for four Arctic regions: Arkhangelsk Oblast, Nenets Autonomous Okrug, Yamalo-Nenets Autonomous Okrug, and the Republic of Komi, as indicated in Table 1. This development primarily focuses on the western parts of the AZRF. This choice of the region for the present research is based on these development plans and priorities.

The area selected for the research in the limits of 55–80° N, 30–100° E is shown in Figure 1. This map provides an overview of the key ports and railway infrastructure in the western and central parts of the AZRF that are under the jurisdiction of the Russian Railways.

The AZRF is characterized by a range of characteristics that necessitate special approaches to its socio-economic development. Climate change, in particular, introduces risks to economic activities. Therefore, expansion of the railway infrastructure in the region requires understanding the trends in the regional climate change.

According to [*AMAP*, 2021], the average annual increase in surface air temperature in the Arctic has been 3.1 °C since 1971. Moreover, the reduction in climate severity is creating conditions conducive to more comfortable environments in the eastern part of the AZRF. Conversely, in the western part, such warming is accompanied by adverse consequences. For instance, the projected frequent transitions of air temperatures through 0 °C within the 21st century are expected to result in accelerated material aging and, ultimately, a reduction

**Table 1.** Fundamentals of the State Policy of the Russian Federation in the Arctic for the period up to 2035 [*Decree of the Government of the Russian Federation*, 2022]

| Subject of the Russian Federation | Railway mainline | Development plan |
|---|---|---|
| The Republic of Komi | Sosnogorsk–Indiga | Construction |
| Nenets Autonomous Okrug | Sosnogorsk–Indiga | The development of a construction project |
| | Konosha–Kotlas–Chum–Labytnangi | Reconstruction |
| | Mikun–Vendinga | Justification of the feasibility of building a section |
| | Vendinga–Karpogory | Site construction |
| Yamalo-Nenets Autonomous Okrug | Obskaya–Salekhard–Nadym–Pangody–Novy Urengoy–Korotchaevo | Construction and development of railway mainlines |
| | Obskaya–Bovanenkovo–Sabetta | Construction and development of railway mainlines |
| Arkhangelsk Oblast | Karpogory–Vendinga | Justification of the feasibility of building a railway section |
| | Mikun–Solikamsk | Justification of the feasibility of building a railway section |




**Figure 1.** Study area with a scheme of the main railways.

in their service life [*Kattsov*, 2022]. The increased period of warmth, together with changes in most climate parameters, is directly linked to the degradation of permafrost [*Kostianaia et al.*, 2021; *Serykh et al.*, 2022]. This, in turn, leads to changes in the landscape and the balance of water bodies in the region [*Vasiliev et al.*, 2020].

The changing climate conditions must be considered when operating existing railways and planning the new ones. This task becomes particularly crucial in the context of accelerated economic development in the region, where the burden on transportation infrastructure is expected to increase significantly over the next several decades. In 2022, *Gvishiani et al.* [2023a] have elaborated an "Electronic Atlas of Climatic Changes in the Western Russian Arctic in 1950–2021 as Geoinformatic Support of Railway Development" (Atlas-2022), and have analyzed the ongoing regional climate change based on a set of meteorological parameters derived from the MERRA-2 atmospheric reanalysis.

This article is dedicated to the investigation of interannual variability of key meteorological parameters in the western and central parts of the AZRF and its impact on railway infrastructure based on the second version of this Atlas. In Atlas-2023, the study area was expanded by 5 degrees to the South and to the North, and by 15 degrees to the East in comparison with the Atlas-2022. Thus, we investigated the western and central part of the Russian Arctic within the geographical boundaries 55–80° N, 30–100° E and time period from 1980 to 2022. To build the Atlas-2023 we used the same MERRA-2 atmospheric reanalysis and the same set of the main hydrometeorological parameters characterizing climate change in the region: air temperature, total precipitation, wind speed, soil temperature, soil moisture content, air humidity, and snow cover thickness. The choice of these meteorological parameters is determined by their influence on the infrastructure and reliable functioning of railways in the study area.

## 2. Data and Methods

### 2.1. Data

#### *2.1.1. MERRA-2 reanalysis*

The MERRA-2 reanalysis (Modern-Era Retrospective Analysis for Research and Applications, Second Edition) serves as an essential tool in climatology and meteorology, designed for the analysis and reconstruction of meteorological data within a historical context. This mission was initiated by the Global Modeling and Assimilation Office (GMAO), under the guidance of the National Aeronautics and Space Administration (NASA) [*Gelaro et al.*, 2017]. The primary objectives of MERRA-2 are to obtain and analyze historical meteorological and climatological data, including information on parameters such as temperature, pressure, humidity, wind, and various others, spanning several decades. These data are utilized for the analysis of climate changes, the development of climate models, and a deeper understanding of past climatic events. Additionally, MERRA-2 provides the capability to monitor climate changes based on long-term data, aiding scientists in gaining insights into climate trends and their implications.

The original MERRA project was created to synthesize the measurement results obtained from satellites into a unified climate catalog. Its primary goal was to analyze and describe the general hydrological cycle, encompassing processes from the upper atmospheric layers to the planet's surface. Starting in 1979, the MERRA project collected data and performed this task. However, by 2016, it was discontinued due to several shortcomings, such as errors in measurement systems, discrepancies in atmospheric and hydrological data, limited representation of the upper stratosphere, and challenges in integrating new data sources [*Gelaro et al.*, 2017]. The main objective of reprocessing and improving the MERRA project was to ensure continuous climate monitoring in near real-time mode, with data publication having only a small delay of a few weeks.

From a technical perspective, the MERRA-2 observation system, compared to the initial MERRA version, employed additional equipment to measure parameters such as atmospheric motion vectors (using the Advanced Very High Resolution Radiometer or AVHRR instrument), near-surface wind speed (using the Special Sensor Microwave Imager/Sounder or SSMIS), temperature profiles and ozone characteristics (utilizing instruments from the Earth Observing System and Aura MLS – Microwave Limb Sounder), among others [*McCarty et al.*, 2016]. Additionally, during the MERRA-2 reanalysis, the

sensors for measuring near-surface wind speeds and ozone content were enhanced and replaced with more modern models throughout the mission's development.

Some advantages of the MERRA-2 reanalysis over other missions and data sets include its extensive temporal coverage, providing continuous data from 1980 to the present day, allowing access to long-term time series, and high spatial resolution. It is important to emphasize the integrated methodology employed in MERRA-2, which involves the combination of data originating from diverse observational systems and atmospheric models. This combination serves to augment the precision and dependability of the data. Furthermore, MERRA-2 consistently refines its techniques related to methodology and signal processing, incorporating up-to-date data and innovative approaches to ensure the currency and trustworthiness of its outcomes.

In general, the compilation of MERRA-2 catalogs is based on a complex and multi-component process, involving the following fundamental principles: data collection, data assimilation, interpolation and extrapolation, numerical modeling, validation, and verification. Data collection involves acquisition of information from various channels, including observations from meteorological satellites, weather stations, buoys, probes, and other meteorological data sources. Subsequently, the data is fed into numerical atmospheric models to account for the non-uniformity and incompleteness of the initial data. Atmospheric models are utilized to create continuous temporal and spatial reconstructions of climate parameters. To construct a more comprehensive and consistent climate reconstruction, data is interpolated and extrapolated in time and space, thereby filling gaps in data and providing higher spatial and temporal resolution. Following this, the data is assimilated into various numerical atmospheric models, representing complex physical and chemical processes occurring in the atmosphere. These models enable the prediction of parameters that may be absent from observations. The results of assimilation and modeling are compared with real observations to evaluate the accuracy and quality of MERRA-2 data. This is an essential stage ensuring the reliability and completeness of the reconstructions. After completing all the stages, the data is compiled into catalogs, serving as a unified source of climate data accessible for scientific research and practical use.

Several scientific research have underscored the advantages of the reanalysis, particularly when compared to other climate data compilations, including the initial MERRA iteration. To illustrate, *Bosilovich et al.* [2016] exemplified the high-fidelity portrayal of atmospheric precipitation and temperature patterns across North America, utilizing data from MERRA-2. *Tilinina et al.* [2013] conducted an analysis demonstrating that MERRA excels in capturing the dynamics of atmospheric cyclones in the Atlantic-Eurasian sector of the Northern Hemisphere. *Bentamy et al.* [2017] showcased how MERRA aligns effectively with the statistical features of turbulent exchanges between the atmosphere and ocean over marine regions. The research by *Luo et al.* [2020] signified that MERRA-2 consistently replicates sea surface temperature, atmospheric temperature, and humidity values over the Atlantic Ocean. *Schubert et al.* [2022] presented research outcomes corroborating the high precision of MERRA-2 in representing extreme temperature anomalies in the Northern Hemisphere.

The MERRA-2 reanalysis data employed in this study were acquired on a standardized grid with spatial intervals of 0.5° latitude by 0.625° longitude. The considered climatic parameters include air temperature, total precipitation, wind speed, soil temperature, soil moisture content, air humidity, and snow cover thickness. In the case of air temperature, MERRA-2 leverages observations from meteorological satellites and weather stations, in combination with outputs from numerical models. Wind speed data within MERRA-2 is deduced from observations made by meteorological satellites and probes, as well as from numerical models describing atmospheric dynamics. Precipitation estimates are derived from satellite, buoy, and ground station datasets. In a general sense, all these parameters represent outcomes of measurements subjected to subsequent processing and numerical modeling.

In the MERRA-2 reanalysis, air temperature and humidity are measured using advanced instruments for vertical profiling these parameters. These instruments include the Cross-Track Infrared Sounder (CrIS) and the Advanced Technology Microwave Sounder (ATMS) [*Luo et al.*, 2020].

Total precipitation in the MERRA-2 reanalysis initially relies on precipitation data based on ground measurements from observatories and stations, which are later archived and parameterized into calculations based on satellite observations [*Chen et al.*, 2002; *Reichle et al.*, 2011].

Wind speed measurements using satellites involve decomposing wind speed into two orthogonal components: eastward and northward. The measurement methodology is largely analogous to the principles of a scatterometer, relying on the analysis of signals reflected from the sea surface [*Gelaro et al.*, 2017]. It is important to note that wind speed is significant not only as a climatic parameter but also as a factor for correcting other types of climatic data. Therefore, the MERRA-2 reanalysis utilizes data from both ground meteorological stations (e.g., University Corporation for Atmospheric Research – UCAR and National Centers for Environmental Prediction – NCEP) and various satellite systems [*Poli et al.*, 2013].

Regarding soil temperature measurements, specialized instruments and remote sensing methods are employed. These instruments emit signals, which are subsequently measured by sensors after interaction with the surface. In MERRA-2, soil temperature is remotely measured hourly, allowing tracking of short-term variations [*Ma et al.*, 2021].

For accurate soil moisture measurements, a radar and a radiometer are required, which are implemented in the SMAP (Soil Moisture Active Passive Observatory) system. It includes radiometric and radar instruments measuring surface soil parameters, enabling the assessment of soil moisture [*Reichle et al.*, 2011].

In MERRA-2, the reanalysis for air humidity employs normalized pseudo-relative humidity [*Holm*, 2003], which is calculated by normalizing it to the standard deviation of background error. MERRA-2 conducts a temporal series of total atmospheric water content and water transport from the ocean to the land.

When measuring the snow cover thickness, the reanalysis considers not only the moment of snowfall but also changes in the snow layer after compaction, accounting for possible melting. For this, a methodology estimating the thickness of already compacted snow is used, providing high-precision values.

### *2.1.2. GIS-instruments and data application*

The main geoinformatics instruments for the creation of the Atlas-2023 were Golden Software Surfer (version 17.1) [*Golden Software*, 2023] and ESRI ArcGIS (ArcMap) (version 10.8) [*ESRI ArcMAP*, 2023]. These software packages have a user-friendly interface and a wide range of functions for primary data processing, including interpolation capabilities. The resulting data were prepared for publication as a map service using a geoportal approach and exported as formatted maps.

The first step of Atlas-2023 creation was the preparation of initial data. For each parameter and each month within the considered period a catalogue was created. Then, calculations of mean-value data for certain periods were performed. The next stage was to create raster files with an interval similar to the one in the reanalysis (0.50° × 0.65°). Golden Software Surfer was selected as a tool for creating the grid (`.grd`) files.

To improve the quality of the climate parameter mapping, the raw data, which were presented on an irregular 0.50° × 0.65°-grid, were interpolated using a Kriging tool to achieve the resolution of 0.05°. The Kriging tool allows to preserve the data detail without adding artifacts when transforming point data of a regular grid, as well as smoothing transitions between values the interpolated data were converted into raster (`.flt`) format for future analysis. The process of this conversion was performed in the Surfer program. Although such a tool is also available in other software packages, Surfer was chosen because of its good interpolation quality and its ability to export data with minimal time loss.

The next stage of data processing involves the removal of data located outside the terrestrial boundaries. Such an operation was performed for the following climatic parameters: snow cover thickness, soil temperature, and soil moisture content. For this purpose, a software module was developed in Python 2.7 using Python ArcPy tools and Python.os library. The main processing tool is the Clip tool, which is the part of the ArcGIS raster data processing toolbox.

The module has a graphical interface and is integrated into the ArcMap package. The input parameters are as follows: the name of the catalogue with processed raster data (in `.tif` or `.flt` format), the name of a vector file with contour mask in the shapefile (`.shp`) format for data clipping, and the name of a catalogue for saving the results. The software module processes each raster file in the catalogue separately using the Python.os library. Each layer is cropped using the Clip tool along the contour mask in the specified area along the coastline. The obtained results are saved in the specified catalogue. The resulting raster data cover the area from 55° to 80° N and from 30° to 100° E.

The georeferencing of the data during the Atlas-2023 preparation was determined by the choice of the map projection. WGS-84 (World Geodetic System 1984) geographic coordinate system was used for the initial raster data. The final maps of the atlas were compiled using the equidistant conic projection (ESRI:102026) with the central meridian of 103°. This map projection was chosen because of the geographical peculiarities of the study area located in high latitudes. The most commonly used map projections, such as the Web Mercator projection (EPSG:3857), distort spatial information as latitude increases.

The next stage in the construction of the atlas was the creation of a color palette for the data groups, as well as the selection of a color scale to make their display more visual. A single color palette was used for one characteristic of each climatic parameter. At this stage, the raster file and its isolines represent a ready tool for comparative analysis of the obtained data both within and between data groups.

The last stage of the Atlas-2023 creation was the merging of the prepared data into finished maps and their incorporation into the atlas layout. A coordinate grid and general information including legend, color scale, and numerical and linear scales were added. For each dataset, a GIS project was created in the MXD (Map Exchange Document) format, which contains all the necessary cartographic material for quick access and editing. The resulting maps were exported as TIFF images to compile a single atlas document.

## 3. Results

The elements of the created Atlas-2023 are blocks of electronic maps reflecting seven climatic parameters: air temperature, total precipitation, wind speed, soil temperature, soil moisture content, air humidity, and snow cover thickness. The division into blocks was carried out according to climatic parameters, and time periods: characterization of changes in mean values on an annual scale, and analysis of parameters for each month separately. For each block of parameters for different time periods, the mean values for the selected period were calculated and mapped, as well as the values of parameter changes between periods 2010–2021 and 1980–1989, and the linear trend of the parameter change for the period 1980–2021.

Thus, 8 characteristics of interannual variability were calculated and plotted on maps for each parameter:

1. Mean values of the parameter for the period 1980–2021.
2. Mean values of the parameter for the year 2022.
3. Mean values of the parameter for the period 1980–1989.
4. Mean values of the parameter for the period 1990–1999.
5. Mean values of the parameter for the period 2000–2009.
6. Mean values of the parameter for the period 2010–2021.
7. Changes in the parameter between the periods 2010–2021 and 1980–1989 (difference in mean values between these periods).

8. Mean rate of change of monthly mean values of the parameter for the period 1980–2021.

Also, for each parameter, the characteristics for each month (from January to December) were calculated and plotted on maps:

1. Mean values of the parameter for the period 1980–2021 for each month.
2. Mean values of the parameter for each month of 2022.
3. Changes in the parameter between the periods 2010–2021 and 1980–1989 (the difference in mean values between these periods) for each month.
4. Mean rate of change in the monthly mean values of the parameter between 1980–2021 for each month.

Air temperature and air humidity in the Atlas-2023 are given at the height of 2 m above the surface, soil temperature and soil moisture content refer to the first 10 cm of the ground. Wind speed is given for the height of 10 m above the surface.

The new Atlas-2023 (Version 2, 2023) of climatic parameters has a number of distinctive features in comparison with the previous Atlas-2022 [*Gvishiani et al.*, 2023a,b]:

- In Atlas-2023, for all considered hydrometeorological parameters, the rates of change were calculated using absolute values of the parameter instead of anomalies of the parameter relative to seasonal variability as it was done for Atlas-2022;
- Soil temperature and humidity were given for the upper 10 cm of soil instead of the average value for the upper 10 m;
- Wind speed near the surface was given at the height of 10 m, instead of 50 m;
- The 42-year study period in Atlas-2023 is divided into 4 decades – from 1980 to 1989, from 1990 to 1999, from 2000 to 2009, and from 2010 to 2021. In Atlas-2022 it was divided into two 20-year periods;
- Calculation of interdecadal changes in hydrometeorological characteristics in Atlas-2023 is made between the last (2010–2021) and the first (1980–1989) decade to emphasize the significance of the changes. In Atlas-2022, these changes were fairly smoothed out, since the difference was calculated between two 20-year periods.

### 3.1. Air temperature

The air temperature near the surface is the most important climatic characteristic that significantly affects the operation of railways, especially in the Far North (Figure 2). Figure 3 presents a map of changes in the average monthly air temperature between the periods 2010–2021 and 1980–1989. In the central part of the study area there were no significant changes in air temperature over the past four decades, however, in the western, eastern and northern parts, the air temperature has increased from 0.5 to 1.5 °C, both in the northern areas (e.g., Igarka, Dudinka) and in the southern areas (e.g., Krasnoyarsk, St. Petersburg). Figure 3 clearly shows at which sections of the railway network the largest changes in air temperature have occurred. However, regional climate warming occurs significantly unevenly by space and by seasons. For instance, in January, along the conventional line Moscow–Syktyvkar–Pechora–Novy Urengoy, there were practically no temperature changes, while to the north-west of it, around St. Petersburg, the warming was up to 1.5 °C, and in the Barents Sea – up to 4 °C, and the south and east of this line, on the contrary, there is a decrease in temperature in some areas by 2.5 °C. In February, almost the entire study area warmed by 3.0 °C, with the exception of the Ob Bay, where a decrease in temperature by 1 °C was observed [*Geophysical Center of the RAS*, 2023]. Figure 4 shows the changes in monthly mean air temperature between the periods 2010–2021 and 1980–1989 (the difference in mean values between these periods) for March. In March, the warming to the northeast of the conventional line Naryan-Mar–Pechora–Khanty-Mansiysk–Tomsk was quite high – up to 7.5 °C in the Dudinka area, while in the southern part of the central region (Perm–Khanty-Mansiysk–Tyumen) the air temperature became lower by 1 °C.

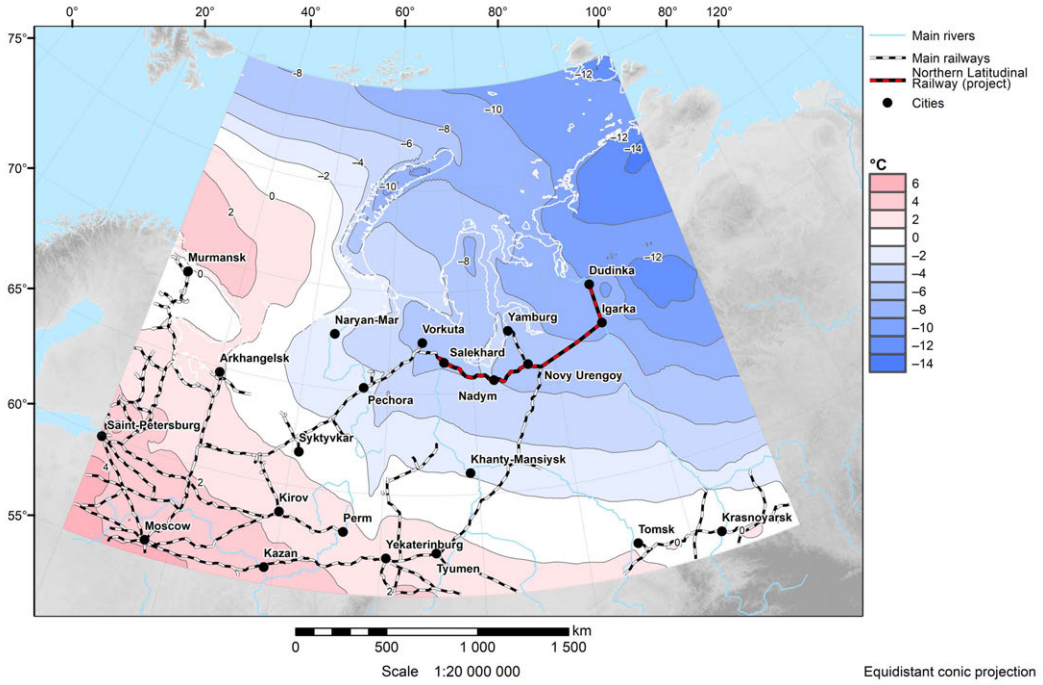


**Figure 2.** Mean annual monthly average air temperature for 1980–2021.

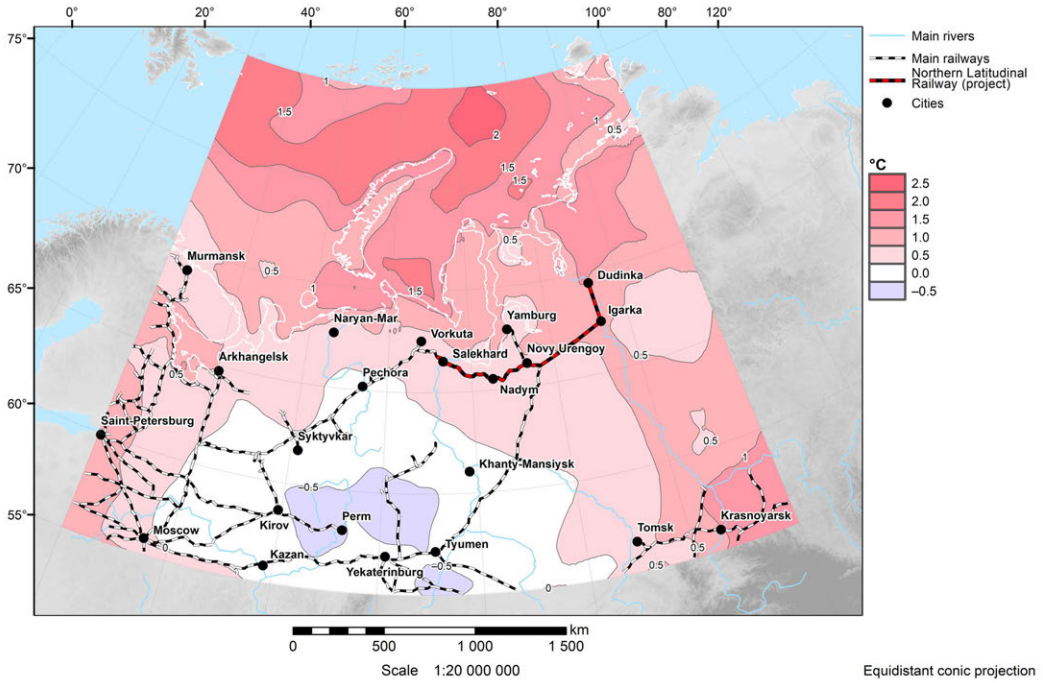


**Figure 3.** Changes in mean monthly average air temperature between the periods 2010–2021 and 1980–1989.

### 3.2. Soil temperature

Soil temperature is an important parameter for assessments of the reliability of railway operations, especially in areas with permafrost soils [*Kostianaia and Kostianoy*, 2023; *Kostianaia et al.*, 2021]. The permafrost soils contain ice, so when the soil temperature rises above 0 °C, the frozen soil thaws and its strength decreases sharply. Thawing of permafrost soils and a significant increase in average temperatures also leads to a change in the water balance of numerous rivers and lakes, to an intensification of snow-water flows, mudflow

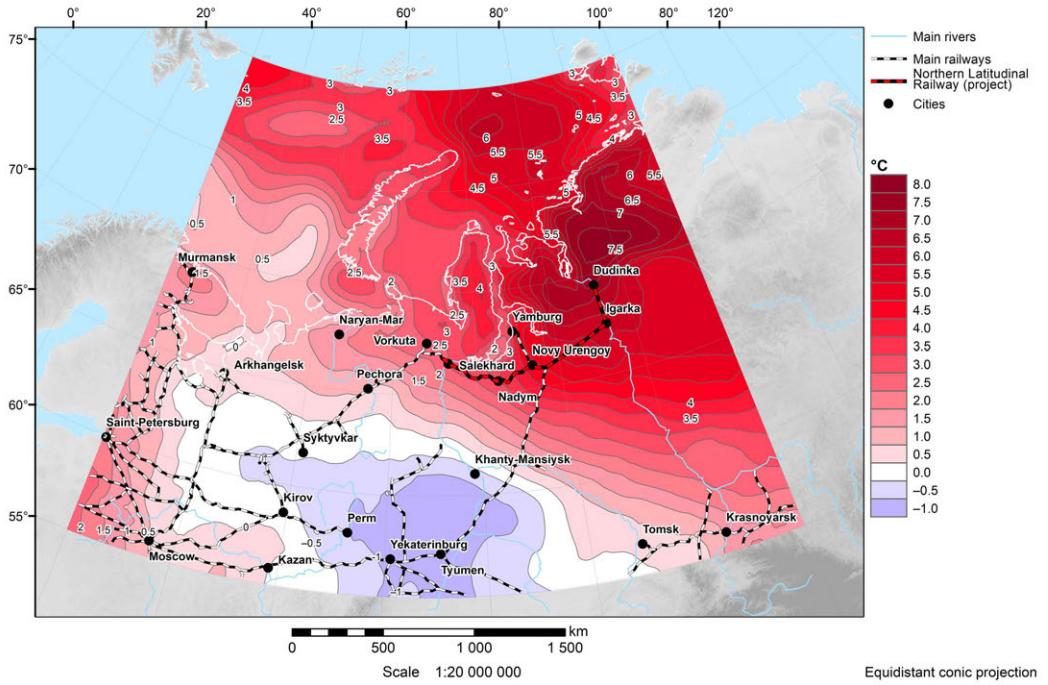


**Figure 4.** Changes in mean monthly average air temperature in March between the periods 2010–2021 and 1980–1989.

and landslides [*Romanenko and Shilovtseva*, 2016] and can have a negative impact on transport infrastructure [*Yakubovich and Yakubovich*, 2019]. This process can significantly affect the infrastructure and performance of the Russian Railways in the region under study. *Lebedev et al.* [2023] have showed for the North-West Arctic Zone of Russia that reanalysis describes well spatial and temporal variability of soil temperature which was proved by a comparison with *in situ* measurements made by bent-stem and extraction thermometers at 13 meteorological stations.

Figure 5 shows the average soil temperature field for 1980–2021. It shows that permafrost remained only in the northeastern part of the study area north of Vorkuta and Yamburg and north and east of Igarka. Figure 6 shows the changes in the average values of soil temperature between the periods 2010–2021 and 1980–1989. Soil temperature in the study area has increased over the four decades from 0.25 to 1 °C. The largest temperature increase (>0.75 °C) is observed in Karelia, Murmansk, Leningrad, and Moscow Oblasts, on the Pechora–Vorkuta–Salekhard railway section, between Novy Urengoy and Igarka, and in the Krasnoyarsk area. The greatest warming from 1 to 2 °C is registered in Taimyr, but there is no railway infrastructure there even in the plans for the development of northern regions.

### 3.3. Total precipitation

Large amounts of precipitation can lead to waterlogging or scouring of railway tracks, river overbanking, and destruction of railway tracks and even bridges, which require repair work. The highest amount of average monthly precipitation 60 mm/month is observed in the western part of the study region, from Moscow to Murmansk and from St. Petersburg to the Urals. In the eastern part of the region, this applies to the central part of the section from Tyumen to Novy Urengoy. Regarding the changes over the last four decades (Figure 7), precipitation has increased by about 10% north of Moscow, in Karelia, near Perm, from Novy Urengoy to Dudinka, near Khanty-Mansiysk, and has decreased significantly near Krasnoyarsk. There is still a significant spatial heterogeneity of these changes for each month separately. So, for example, in May, in the Arkhangelsk Region, precipitation

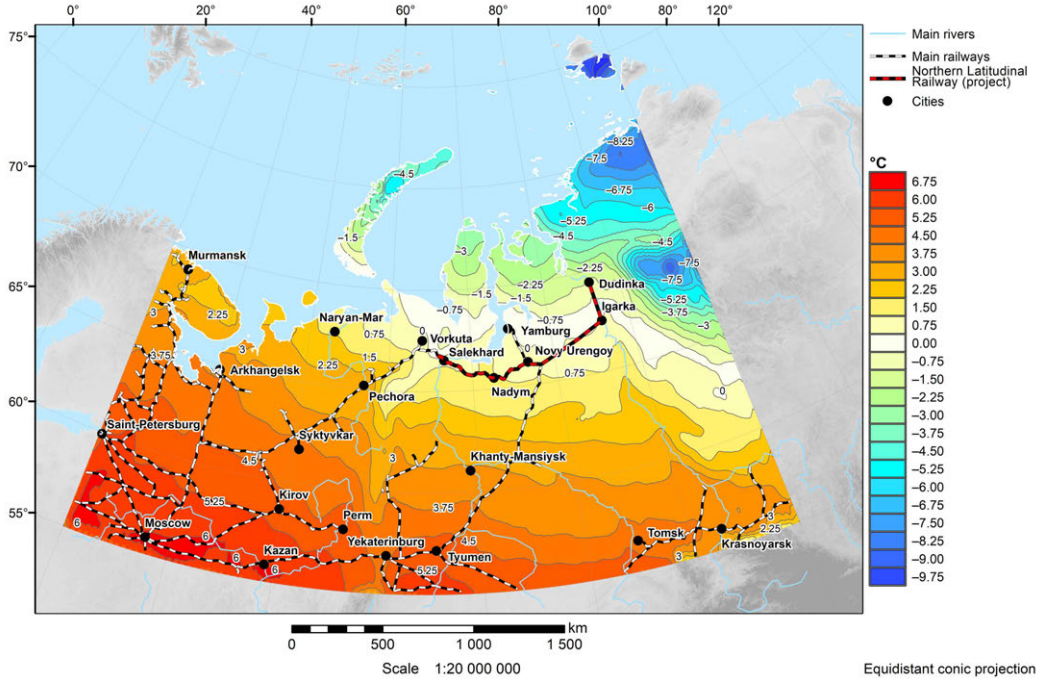


**Figure 5.** Mean annual monthly average soil temperature for 1980–2021.

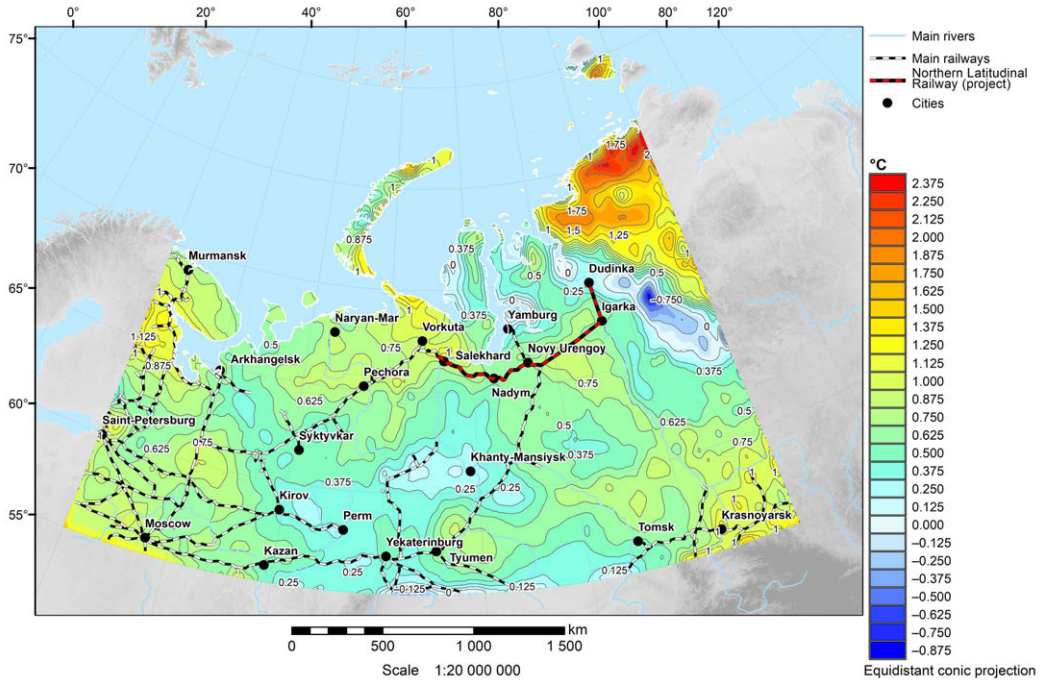


**Figure 6.** Changes in mean monthly average soil temperature between the periods 2010–2021 and 1980–1989.

decreased by 25 mm, in the Yekaterinburg region – by 35 mm, and from Novy Urengoy to Igarka, precipitation increased by 40 mm [*Geophysical Center of the RAS*, 2023].

### 3.4. Wind speed

High winds can cause loss of contact between the current collector and the contact wire, increasing the risk of derailment or train overturning [*Kostianaia et al.*, 2021]. Strong winds can also lead to accidents and disruption of the rail network due to trains colliding with fallen trees, branches, or debris on the tracks [*Baker et al.*, 2009]. The zone of strongest

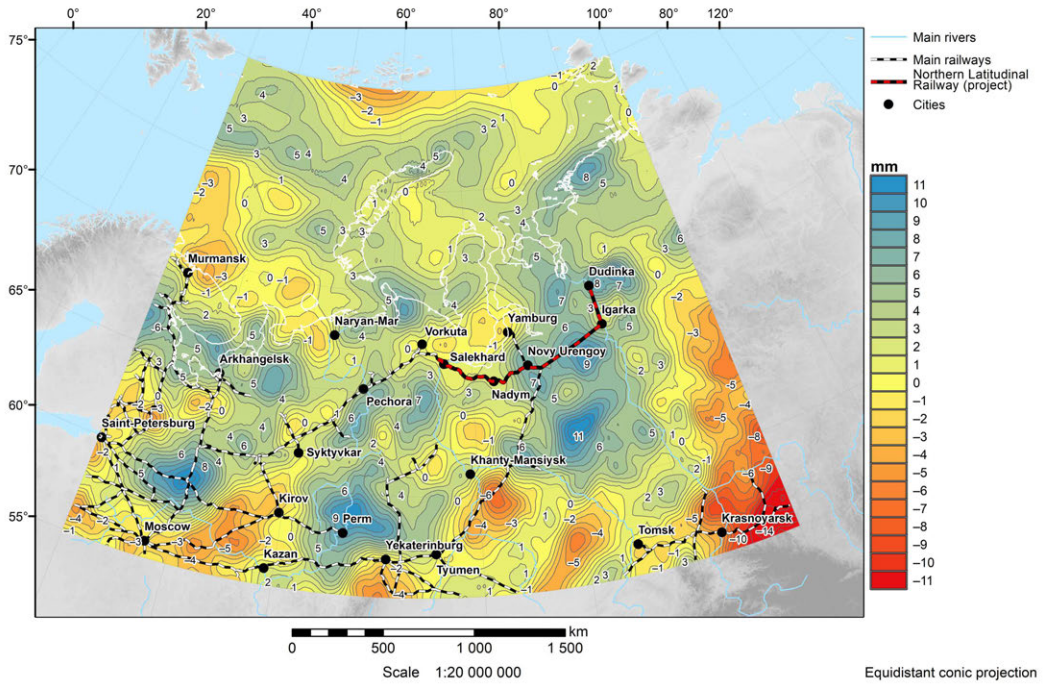


**Figure 7.** Changes in mean monthly average precipitation (mm) between the periods 2010–2021 and 1980–1989.

winds is located in the northern part of the study area and over the waters of the Barents and Kara Seas. This zone completely covers the area of construction of the Northern Latitudinal Railway. A similar zone of relatively strong winds runs along the southern edge of the study area along the conventional line Moscow–Kazan–Yekaterinburg–Tyumen–Tomsk–Krasnoyarsk. Between these zones lies a wide zone of relatively weak winds, where a fairly extensive railway network is located. As for the changes that have occurred over the last four decades (Figure 8), the wind speed has increased by about 10% over the water area of the Barents Sea, as well as on the sections of railways from Kazan to Krasnoyarsk along the southern edge of the study area. Over the rest of the territory the average wind speed remained practically unchanged.

However, there is a significant spatial heterogeneity in these changes for each month separately. For example, in March, wind speed has increased significantly throughout the eastern part of the study region, especially in its northern and southern parts. In the extreme western part of the region, and especially over the White Sea, wind speed, on the contrary, has decreased quite significantly [*Geophysical Center of the RAS*, 2023].

### 3.5. Soil moisture content

Soil moisture content is the percentage of water in the soil compared to the dry one. The general pattern of spatial distribution of soil moisture content is such that lower values are observed in the southern part of the study region and higher values are observed in the north. On some sections of the railway network, for example, south of Arkhangelsk, southwest of Syktyvkar, and between Pechora and Vorkuta, soil moisture exceeds 35%. As for the changes that have occurred over the last four decades (Figure 9), the pattern of changes is quite heterogeneous spatially. For example, in the southwestern part of the study region soil moisture has decreased by about 1–3% of soil moisture, in the area of the Yekaterinburg–Tyumen–Khanty-Mansiysk line by 1–2.5%, and in the area of Krasnoyarsk by 1–4%, which is about 10% of the average absolute value of soil moisture in these areas. In contrast, in the districts of Arkhangelsk, Perm, and Tomsk, soil moisture has increased by 1–4%.

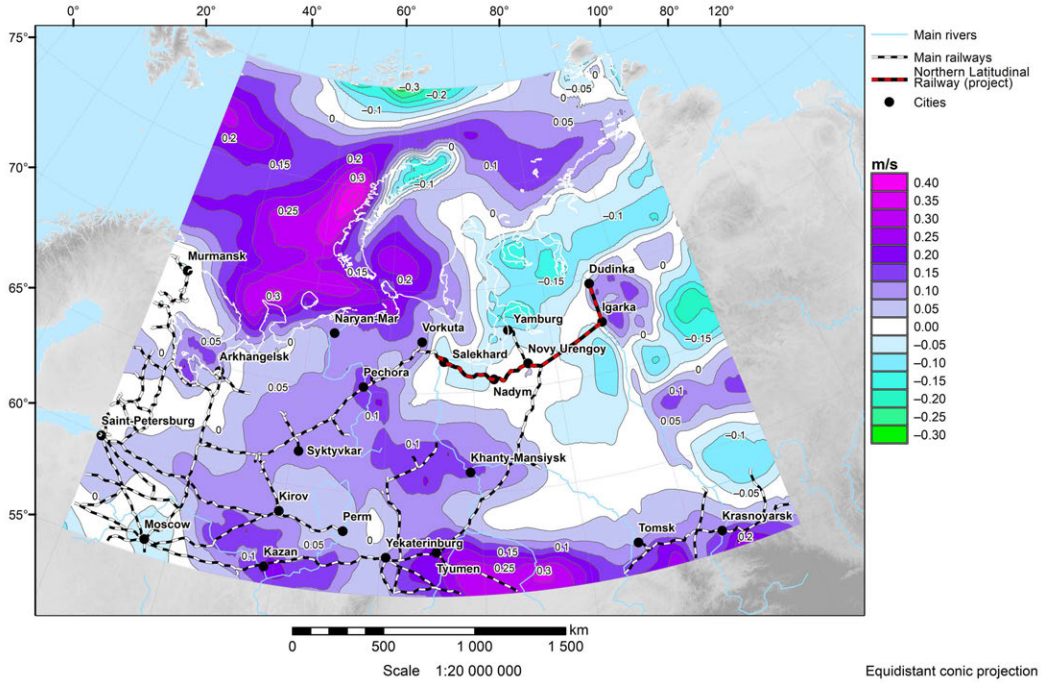


**Figure 8.** Changes in mean monthly average wind speed (m/s) between the periods 2010–2021 and 1980–1989.

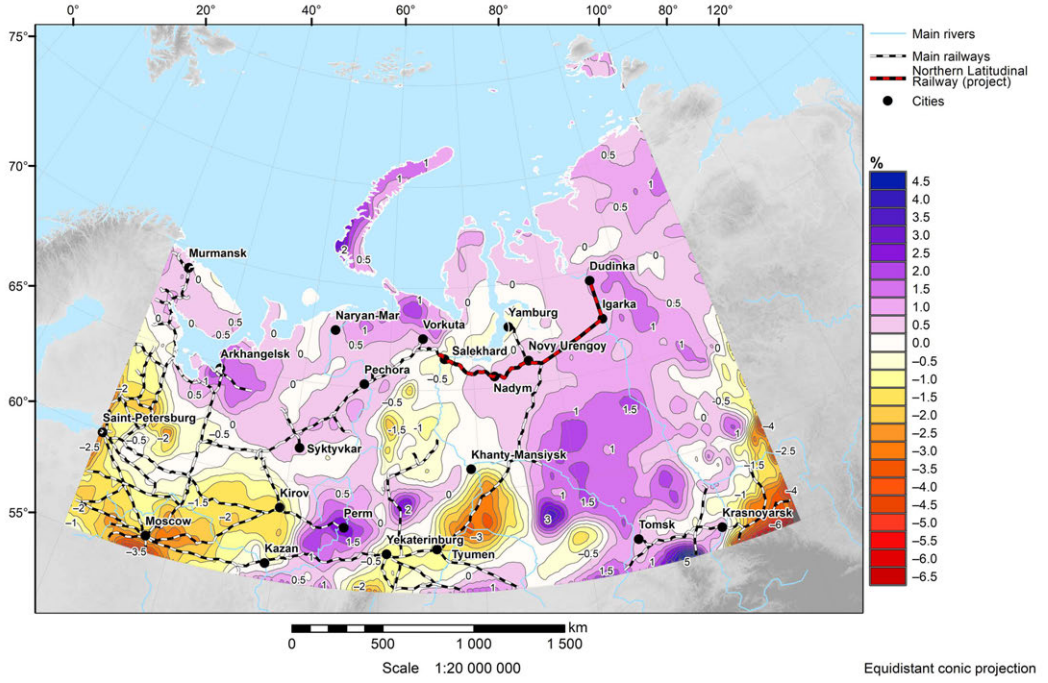


**Figure 9.** Changes in mean monthly average soil moisture content (%) between the periods 2010–2021 and 1980–1989.

There is significant spatial heterogeneity in these changes for each month separately. For example, in April, soil moisture increased significantly throughout almost the entire study area, with the greatest increase in humidity occurring in the Perm–Ekaterinburg–Tyumen region, where it increased by 7–14% of soil moisture [*Geophysical Center of the RAS*, 2023].

### 3.6. Air humidity

Air humidity characterizes the water vapor content in the atmosphere. The general picture of the spatial distribution of air humidity is such that it decreases from southwest to northeast, which is associated with a general decrease in air temperature in the same direction since absolute air humidity depends on its temperature.

Regarding the changes that have occurred over the last four decades (Figure 10), the pattern of changes is very heterogeneous spatially. For example, air humidity has increased by about 5% in the far western part of the study region, over the waters of the Barents and Kara Seas, as well as in the northeastern part of the region, which is explained by the air temperature increase by 1–2 °C in the same regions over the same period of time (Figure 3).

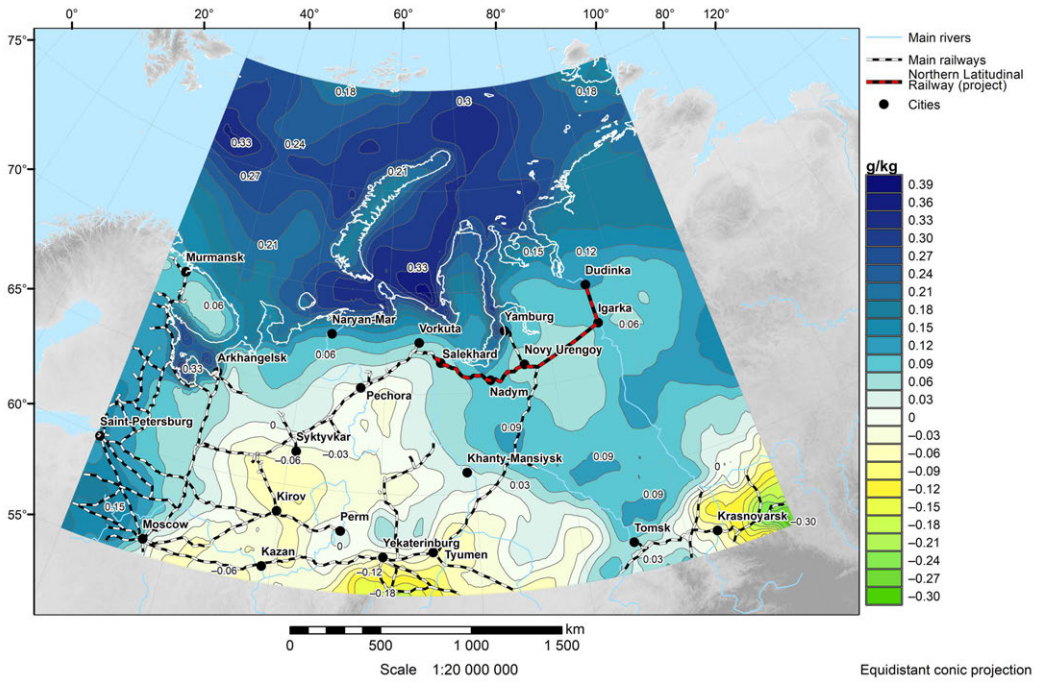


**Figure 10.** Changes in mean monthly average air humidity (g/kg) between the periods 2010–2021 and 1980–1989.

### 3.7. Snow cover thickness

The thickness of the snow cover is commonly referred to as the thickness of the layer of snow covering the surface of the ground. The general pattern of spatial distribution is determined mainly by the latitude of the location – the more northerly, the more snow. For example, in the area between Moscow and St. Petersburg, Yekaterinburg, and Tyumen, and near Krasnoyarsk, snow thickness is about 15 cm. In the northern regions snow thickness reaches 30 cm, and in the area of the Ural Mountains and east of Igarka–Dudinka it already exceeds 50 cm and in some places reaches 95 cm [*Geophysical Center of the RAS*, 2023].

As for the changes that have occurred over the last four decades (Figure 11), the pattern of changes is quite heterogeneous spatially. For example, in the far western and eastern parts of the study region, the snow thickness has decreased by 1–8 cm as a result of regional climate warming, while in the wide zone from Arkhangelsk to Perm and further to Kazan, as well as in the zone from Vorkuta to Yekaterinburg the snow cover thickness even has increased by 1–4 cm.

There is a significant spatial heterogeneity in these changes for each winter month separately. For example, in January, February, and March there was more snow throughout almost the entire study area, and in September and October, it became much less than four decades ago. This is an indirect sign of a shift in seasons, i.e. summer extends into autumn, and winter into spring [*Geophysical Center of the RAS*, 2023].

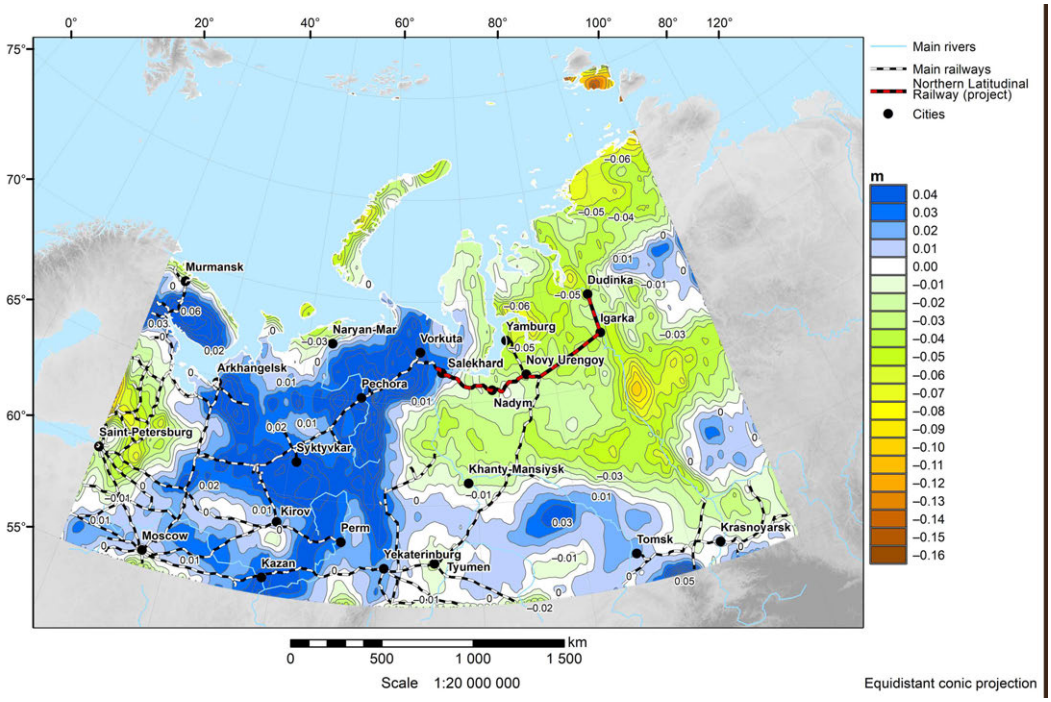


**Figure 11.** Changes in mean monthly average snow cover thickness (m) between the periods 2010–2021 and 1980–1989.

## 4. Discussion

This paper aimed to overview the content of the "Electronic Atlas of Climatic Changes of Hydrometeorological Parameters of the Western and Central Part of the Russian Arctic" (Atlas-2023). It is elaborated as a supporting tool for the Russian Railways development in this region, and to show the most interesting findings of the analysis of regional climate change, especially for railway operation. This is the second updated and upgraded version of the Atlas-2022, which was issued by the end of 2022 and transferred to the Russian Railways for practical use [*Gvishiani et al.*, 2023a]. In Atlas-2023, the study area was expanded by 5 degrees to the South and the North, and by 15 degrees to the East in comparison with Atlas-2022. Thus, we investigated the western and central part of the Russian Arctic within the geographical boundaries of 55–80° N, 30–100° E, and time period from 1980 to 2022.

To build this Atlas we used the same MERRA-2 atmospheric reanalysis and the same set of the main hydrometeorological parameters characterizing climate change in the region: air temperature, total precipitation, wind speed, soil temperature, soil moisture content, air humidity, and snow cover thickness. The choice of these meteorological parameters is determined by their influence on the infrastructure and reliable functioning of railways in the study area.

Air temperature at the earth's surface is the most important climatic characteristic. It significantly affects the functioning of railways, especially in the Far North. The ongoing warming of the regional climate leads to a thawing of permafrost soils, a change in the water balance of numerous rivers and lakes, and an intensification of such geomorphological processes as snow-water flows (a type of mudflow) and landslides. This may have a negative impact on the infrastructure of railways and roads, the oil and gas industry, and pipeline transport [*Kostianaia et al.*, 2021]. For example, previous study of changes in surface air temperature in the Murmansk and Arkhangelsk Oblasts and the Republic of Karelia showed *Serykh et al.* [2022], that in 1999–2020 there was a significant change in the regional climate. It was expressed in the warming of this region from +0.9 to +1.5 °C compared to previous years (1977–1998), in a sharp increase in air temperature growth (from +0.4 to +1.0 °C over 10 years), to a shift of the +2 °C isotherm by 550 km to the North up to the southern part

of the White Sea and the complete disappearance of average negative temperatures. An important conclusion follows from the study: objects on pile foundations with a depth of less than 6 m are at increased risk even with warming up to +2 °C. Therefore, engineering protection of these objects should be carried out at a pace that is faster than the warming of the regional climate [*Yakubovich and Yakubovich*, 2019].

Soil temperature is the second important parameter for assessing the reliability of railway operation, especially in areas with permafrost [*Kostianaia and Kostianoy*, 2023; *Kostianaia et al.*, 2021; *Lebedev et al.*, 2023]. The specificity of permafrost soils is that they contain ice. When the temperature rises above 0 °C, the frozen soil thaws, its strength decreases sharply, and other properties also change qualitatively, especially in silty-clayey soils. Under buildings, supports and railway tracks, unique "bowls" of thawing are formed. *Yakubovich and Yakubovich* [2019] showed that for the territory of the Kola Peninsula, characterized by high-temperature permafrost of rare island nature, construction objects foundation of which is formed by piles with a depth of 5 m or less are subject to very high risks of reducing their functionality, down to zero level. For example, with relatively small warming of up to +1 °C, piles 5 m deep, as a rule, still provide functionality $U = 0.65–0.85$ ($U = 1$ corresponds to the maximum level of functionality for the base, constant climate), which is considered as an average level of climate risk in relation to a transport infrastructure facility. Warming up to +2 °C often leads to a decrease in functionality to $U < 0.5$ (in the presence of low-humidity soils), and warming to +3 °C for construction objects in this group can be considered catastrophic; functionality is reduced to the level $U = 0–0.35$, which corresponds to an unacceptably high level of climate risks.

Large amounts of precipitation can lead to flooding or erosion of railway tracks, overflowing of rivers, and destruction of railway tracks and even bridges, which requires repair work [*Kostianaia et al.*, 2021].

Strong winds can cause the pantograph to lose contact with the trolley wire, increasing the risk of derailment or train overturning [*Kostianaia et al.*, 2021]. This has been the subject of research for high-speed trains in many countries, such as the X2000 in Sweden [*Andersson et al.*, 2004], the ICE in Germany [*Diedrichs et al.*, 2007], and the Class 390 Pendolino in the UK [*Baker et al.*, 2004]. For example, a study in Austria found that winds of more than 120 km/h could, under certain conditions, overturn a train or cause serious damage. Wind speeds greater than 130 km/h may cause the trolley wire to vibrate, which may increase the risk of serious problems with the pantograph. In addition, strong winds can also move parked freight cars and shift machinery and cargo inside freight cars [*Rachoy and Spazierer*, 2008]. High winds can also lead to accidents and disruptions to the rail network due to trains colliding with fallen trees, branches, or construction debris on the rails [*Baker et al.*, 2009]. Such high wind speeds are now more common in Europe. For example, on 18 January 2007, a windstorm swept through Europe, reaching a maximum wind speed of 216 km/h, in Germany – 148 km/h, and in Austria – 140 km/h. On 18 January 2018, windstorm "David" crossed Northern Europe with the strongest winds (up to 203 km/h recorded in Brocken, Germany). Deutsche Bahn canceled all intercity services and hired additional 150 foresters due to damage to railways caused by fallen trees. The total damage was estimated between 1 and 2.6 billion Euro. From 23 September to 4 October 2019, windstorm "Lorenzo" affected the UK, Ireland, and France with its strongest wind gust of 163 km/h and damage estimated at 284–330 million Euro. On 7–16 February 2020, windstorm "Ciara" affected the UK, Ireland, Isle of Man, Northern Europe, Western Europe, Central Europe, and Eastern Europe with its strongest wind gust of 219 km/h and damage ranging from 1.6 to 1.9 billion Euro. On 13–19 February 2020, windstorm "Dennis" affected the UK, Ireland, Iceland, Norway, Sweden, and the Netherlands with its strongest wind gust of 230 km/h. On 18–20 August 2020, windstorm "Ellen" hit the British Isles with its strongest wind gust of 143 km/h [*List of European windstorms*, 2023]. In autumn 2023, severe wind storms have continued to hit Europe [*2023–2024 European windstorm season*, 2023]:

- Storm "Agnes", 25–29 September 2023, UK, Ireland, 135 km/h (max wind gust);

- Storm "Babet", 16–22 October 2023, Western and Northern Europe, 185 km/h;
- Storm "Aline", 18–27 October 2023, Western Europe, 146 km/h;
- Storm "Bernard", 21–26 October 2023, Western Europe;
- Storm "Celine", 28 October – 3 November 2023, Western Europe, 90 km/h;
- Storm "Ciarán", 29 October – 4 November 2023, Western Europe, 207 km/h;
- Storm "Domingos", 3–5 November 2023, Western Europe.

Determining the degree of soil moisture is necessary for making competent design decisions on the location of railway infrastructure facilities, choosing the type of foundation, and other engineering decisions. The bearing capacity of the rock and its resistance to future loads directly depend on this parameter. Thus, with increasing humidity, friction between soil particles decreases and their displacement for dispersed rocks occurs. Clay soils transform into a fluid and also flexible plastic state, which leads to deformations. With regard to rocky soils, their bearing capacity is practically independent of humidity. At the same time, humidity also affects other significant characteristics of rocks: density, subsidence and compressibility, strength, swelling, and frost heaving. During design, it is extremely important to take into account these parameters for clayey, silty, fine sandy, and rocky soils. The competence of design decisions, budget, safety of construction, and operation of railway infrastructure directly depends on this.

It is well known that excess air humidity negatively affects the properties of various materials [*Vishnevsky and Chepurin*, 2010]. The vast majority of inorganic and organic materials, substances, and components have some degree of hygroscopicity, i.e. have the property of absorbing water vapor from the air. For all porous materials, there is a certain relationship between the amount of moisture they absorb (the so-called hygroscopic humidity) and the relative humidity of the surrounding air. The maximum hygroscopic humidity of materials corresponds to a maximum of 100% air humidity [*Vishnevsky and Chepurin*, 2010].

Regarding railway infrastructure, an increase in the hygroscopic humidity of materials will lead to an increase in weight and (or) volume (change in density); changes in electrical conductivity; changes in heat transfer; the occurrence of chemical reactions; changes in liquid viscosity; change in tensile strength; changes in the elasticity and plasticity of materials [*Vishnevsky and Chepurin*, 2010]. The influence of excessively humid air is dangerous not only for hygroscopic materials. Materials with negligible hygroscopicity are also susceptible to the effects of water vapor from humid air, which initially manifests itself in the surface layers. It is worth highlighting certain, frequently occurring negative consequences of excessive increases in air humidity, which may be directly related to the railway infrastructure [*Vishnevsky and Chepurin*, 2010]:

1. At high air humidity, the quality of resistance of electrical insulating materials deteriorates, including air itself as an electrical insulator. This leads to uncontrolled failures, which can lead to major accidents and disasters, primarily due to short circuits.
2. Relative humidity above 70% creates favorable conditions for the rapid growth of mold, the spores of which are present everywhere. At lower humidity values, mold growth stops completely.
3. Metals that are practically non-hygroscopic are susceptible to corrosion in air, the intensity of which also depends on air humidity. Low humidity guarantees low corrosion intensity. Iron has virtually no corrosion at relative humidity up to 40–45%. Minor corrosion of iron begins when the relative humidity increases from 40–45% to 60–70% (the so-called "critical" humidity value). Above this value, the corrosion rate of iron increases sharply (according to a logarithmic dependence), and rapid destruction of the metal occurs.
4. Another manifestation of high air humidity is observed when air saturated with moisture is cooled. The air then becomes supersaturated with moisture, and it begins to be released from it in the form of fog or dew. Two specific causes of condensation are most often encountered. Firstly, these are cold surfaces of equipment, the low temperature of which is due to technological processes. For example, all kinds of

pipelines, containers, etc. Secondly, condensation is associated with daily changes in air temperatures, which are most pronounced in continental climates and northern regions with low temperatures. Massive metal parts of structures and equipment cool down at night and, due to their significant heat capacity, remain supercooled in the morning and, partially, during the day. Atmospheric air relatively quickly increases its heat and moisture content in the morning hours. Due to this, its dew point under certain conditions exceeds the temperature of metal surfaces, resulting in condensation of excess moisture. The moisture condensed on external surfaces evaporates more or less quickly under the influence of wind, for example. Much more dangerous is the condensation of moisture on the internal surfaces of equipment in various hidden channels and cavities, since due to the high thermal conductivity of metals, the temperature on the internal surfaces differs little from the external ones. At the same time, in stagnant internal cavities and channels, condensed moisture evaporates little and gradually accumulates [*Vishnevsky and Chepurin*, 2010].

Heavy snowfalls, blizzards, snow drifts, and debris are among the types of natural disasters that significantly affect the performance and capacity of railways [*Pashchenko and Potapenko*, 2016]. Snow thickness is one of the parameters that is calculated in models and measured at weather stations, the influence of which on the functioning of railways is being studied in northern countries, for example, in Canada, Sweden and Russia [*Kostianaia and Kostianoy*, 2023].

When snow falls on a railway track, it creates resistance to the movement of trains, causes additional energy and fuel consumption, reduces travel speeds, delays trains, complicates the operational work of the snowed section [*Pashchenko and Potapenko*, 2016]. Snow drifts are usually the result of snowstorms and snow transfers. A snowdrift can form in a fairly short period of time. At the same time, the thickness of the snow cover can be measured in several meters, and it can be formed in 1–2 hours. In winter, the operating conditions of railways become significantly more complicated, especially in the northern regions of Russia, so much attention is paid to the timely and high-quality preparation of track facilities and other services for work in the winter. The concept of "snow fighting" implies a system of complex measures, including snow retention from the field sides of the railway and removal of snow from the railway. It should be borne in mind that snow removal is a much more expensive operation, so it is necessary to ensure maximum snow retention. The railway can be protected from snow drifts by protective forest plantations, permanent fences, portable shields, as well as natural forests, among them protective forest plantations are of great importance [*Pashchenko and Potapenko*, 2016].

## 5. Conclusions

A discussion of the above-mentioned meteorological parameters showed their vital importance for infrastructure and stable operability of the Russian Railways in the northern regions of Russia in the changing climate. The Atlas-2022 and Atlas-2023 have been transferred to the Russian Railways for practical use. This experience can be transferred to other sections of the Russian Railways in other regions of Russia, especially in Siberia where there are several plans of railway development related to an increase of trade with China, Central Asia, and other countries. These climatic atlases can be used for the analysis of the sustainable operability of automobile roads as well because the same set of meteorological parameters is important for the assessment of the quality of the roads and transportation of goods.

One of the most important conclusions from this research is that the climate warming as well as change of other meteorological parameters in the study area is very irregular within a year (by months), spatially, and even along each section of the railway. It is necessary to study thoroughly the climatic parameters along each railway section separately with the help of Hovmöller diagrams, as the performed analysis has shown significant spatial and temporal heterogeneity of the considered parameters variability during the past 40 years. This was done in the framework of the Russian Science Foundation Project No. 21-

77-30010 (2021–2024) "System analysis of geophysical process dynamics in the Russian Arctic and their impact on the development and operation of the railway infrastructure".

Future development of Atlas-2023 is related to: (1) the creation of maps and diagrams of spatial and temporal variability of extreme weather phenomena in the form of observed anomalies, occurrence frequency, and duration based on daily data instead of monthly averaged data; and (2) creation of forecast maps and diagrams of spatial and temporal variability of basic hydrometeorological parameters up to the end of 21st century for the existing and planned railway infrastructure.

We hope that the detailed analysis of the Atlas-2023 maps and Hovmöller diagrams prepared for the Russian Railways, along with the future generation of atlases will contribute to sustainable development and adaptation of the railway infrastructure to climate change in the northwestern and central part of the Russian Arctic.

**Acknowledgments.** The research was done in the framework of the Russian Science Foundation Project No. 21-77-30010 (2021–2024) "System analysis of geophysical process dynamics in the Russian Arctic and their impact on the development and operation of the railway infrastructure".

## References

2023–2024 European windstorm season (2023), Wikipedia. The Free Encyclopedia, https://en.wikipedia.org/wiki/2023-24_European_windstorm_season, (visited on 09.11.2023).

AMAP (2021), *Arctic Climate Change Update 2021: Key Trends and Impacts*, *Summary for Policy-Makers*, 16 pp., Arctic Monitoring and Assessment Programme (AMAP), Tromsø, Norway.

Andersson, E., J. Häggström, M. Sima, and S. Stichel (2004), Assessment of train-overturning risk due to strong cross-winds, *Proceedings of the Institution of Mechanical Engineers*, *Part F: Journal of Rail and Rapid Transit*, *218*(3), 213–223, https://doi.org/10.1243/0954409042389382.

Baker, C. J., J. Jones, F. Lopez-Calleja, and J. Munday (2004), Measurements of the cross wind forces on trains, *Journal of Wind Engineering and Industrial Aerodynamics*, *92*(7–8), 547–563, https://doi.org/10.1016/j.jweia.2004.03.002.

Baker, C. J., L. Chapman, A. Quinn, and K. Dobney (2009), Climate change and the railway industry: A review, *Proceedings of the Institution of Mechanical Engineers*, *Part C: Journal of Mechanical Engineering Science*, *224*(3), 519–528, https://doi.org/10.1243/09544062JMES1558.

Bentamy, A., J. F. Piollé, A. Grouazel, R. Danielson, S. Gulev, F. Paul, H. Azelmat, P. P. Mathieu, K. von Schuckmann, S. Sathyendranath, H. Evers-King, I. Esau, J. A. Johannessen, C. A. Clayson, R. T. Pinker, S. A. Grodsky, M. Bourassa, S. R. Smith, K. Haines, M. Valdivieso, C. J. Merchant, B. Chapron, A. Anderson, R. Hollmann, and S. A. Josey (2017), Review and assessment of latent and sensible heat flux accuracy over the global oceans, *Remote Sensing of Environment*, *201*, 196–218, https://doi.org/10.1016/j.rse.2017.08.016.

Bosilovich, M. G., R. Lucchesi, and M. Suarez (2016), MERRA-2: File Specification. GMAO Office Note No. 9 (Version 1.1), http://gmao.gsfc.nasa.gov/pubs/office_notes, Global Modeling and Assimilation Office.

Chen, M., P. Xie, J. E. Janowiak, and P. A. Arkin (2002), Global Land Precipitation: A 50-yr Monthly Analysis Based on Gauge Observations, *Journal of Hydrometeorology*, *3*(3), 249–266, https://doi.org/10.1175/1525-7541(2002)003<0249:GLPAYM>2.0.CO;2.

Decree of the Government of the Russian Federation (2022), "On approval of the Development Plan of the Northern Sea Route for the period up to 2035" of August 1, 2022, no. 2115-r (in Russian).

Decree of the President of the Russian Federation (2014), "On the land territories of the Arctic zone of the Russian Federation" of May 2, 2014 no. 296 (in Russian).

Department of Communications of the State Corporation "Rosatom" (2023), The volume of cargo transported along the Northern Sea Route in 2022 amounted to 34.117 million tons, https://rosatom.ru/journalist/news/obem-perevezennykh-gruzov-po-severnomu-morskomu-puti-v-2022-godu-sostavil-34-034-mln-tonn/ (in Russian), (visited on 11.08.2023).

Diedrichs, B., M. Sima, A. Orellano, and H. Tengstrand (2007), Crosswind stability of a high-speed train on a high embankment, *Proceedings of the Institution of Mechanical Engineers, Part F: Journal of Rail and Rapid Transit*, *221*(2), 205–225, https://doi.org/10.1243/0954409JRRT126.

ESRI ArcMAP (2023), ArcGIS Desktop. A complete suite for desktop GIS, https://www.esri.com/en-us/arcgis/products/arcgis-desktop/overview, (visited on 03.11.2022).

Gelaro, R., W. McCarty, M. J. Suárez, R. Todling, A. Molod, L. Takacs, C. A. Randles, A. Darmenov, M. G. Bosilovich, R. Reichle, K. Wargan, L. Coy, R. Cullather, C. Draper, S. Akella, V. Buchard, A. Conaty, A. M. da Silva, W. Gu, G.-K. Kim, R. Koster, R. Lucchesi, D. Merkova, J. E. Nielsen, G. Partyka, S. Pawson, W. Putman, M. Rienecker, S. D. Schubert, M. Sienkiewicz, and B. Zhao (2017), The Modern-Era Retrospective Analysis for Research and Applications, Version 2 (MERRA-2), *Journal of Climate*, *30*(14), 5419–5454, https://doi.org/10.1175/JCLI-D-16-0758.1.

Geophysical Center of the RAS (2023), Analysis of climate changes based on the atlas of main hydrometeorological parameters of the Central and Western part of the Russian Arctic for the period 1980–2021 and forecast for 2023–2064, *Tech. rep.* (in Russian).

Golden Software (2023), Surfer. Explore the Depths of Your Data, https://www.goldensoftware.com/products/surfer/, (visited on 01.11.2022).

Gvishiani, A. D., I. N. Rozenberg, A. A. Soloviev, A. G. Kostianoy, S. A. Gvozdik, I. V. Serykh, R. I. Krasnoperov, N. V. Sazonov, I. A. Dubchak, A. B. Popov, E. A. Kostianaia, and G. A. Gvozdik (2023a), Electronic Atlas of Climatic Changes in the Western Russian Arctic in 1950–2021 as Geoinformatic Support of Railway Development, *Applied Sciences*, *13*(9), 5278, https://doi.org/10.3390/app13095278.

Gvishiani, A. D., I. N. Rozenberg, A. A. Soloviev, A. G. Kostianoy, S. A. Gvozdik, I. V. Serykh, R. I. Krasnoperov, N. V. Sazonov, I. A. Dubchak, A. B. Popov, E. A. Kostianaia, and G. A. Gvozdik (2023b), *Atlas of climatic changes of the main hydrometeorological parameters of the western part of the Russian Arctic for the period 1950–2021*, Geophysical Center RAS, https://doi.org/10.2205/2023-atlas-cc.

Holm, E. V. (2003), Revision of the ECMWF humidity analysis: Construction of a Gaussian control variable, in *ECMWF/GEWEX Workshop on Humidity Analysis, 8–11 July 2002*, pp. 1–6, ECMWF.

Kattsov, V. M. (Ed.) (2022), *Roshydromet: Third assessment report on climate change and its consequences on the territory of the Russian Federation*, 124 pp., Naukoyemkie Technologii, St. Petersburg (in Russian), https://www.meteorf.gov.ru/upload/pdf_download/compressed.pdf.

Kostianaia, E. A., and A. G. Kostianoy (2023), Railway Transport Adaptation Strategies to Climate Change at High Latitudes: A Review of Experience from Canada, Sweden and China, *Transport and Telecommunication Journal*, *24*(2), 180–194, https://doi.org/10.2478/ttj-2023-0016.

Kostianaia, E. A., A. G. Kostianoy, M. A. Scheglov, A. I. Karelov, and A. S. Vasileisky (2021), Impact of Regional Climate Change on the Infrastructure and Operability of Railway Transport, *Transport and Telecommunication Journal*, *22*(2), 183–195, https://doi.org/10.2478/ttj-2021-0014.

Krivovichev, S. (2019), Editorial for Special Issue «Arctic Mineral Resources: Science and Technology», *Minerals*, *9*(3), 192, https://doi.org/10.3390/min9030192.

Lebedev, S., A. Kostianoy, and I. Tretiyak (2023), Temporal Variability of Soil Temperature in the North-West Arctic Zone of Russia. Part I: Interannual Linear Trends Based on Thermometer Measurements and Reanalysis Data, *Russian Journal of Earth Sciences*, *23*, https://doi.org/10.2205/2023ES02SI12.

List of European windstorms (2023), Wikipedia. The Free Encyclopedia, https://en.wikipedia.org/wiki/List_of_European_windstorms, (visited on 29.10.2023).

Luo, B., P. J. Minnett, M. Szczodrak, N. R. Nalli, and V. R. Morris (2020), Accuracy Assessment of MERRA-2 and ERA-Interim Sea Surface Temperature, Air Temperature, and Humidity Profiles over the Atlantic Ocean Using AEROSE Measurements, *Journal of Climate*, *33*(16), 6889–6909, https://doi.org/10.1175/JCLI-D-19-0955.1.

Ma, H., J. Zeng, X. Zhang, P. Fu, D. Zheng, J.-P. Wigneron, N. Chen, and D. Niyog (2021), Evaluation of six satellite- and model-based surface soil temperature datasets using global ground-based observations, *Remote Sensing of Environment*, *264*, 112,605, https://doi.org/10.1016/j.rse.2021.112605.

Makarova, I., L. Gubacheva, D. Makarov, and P. Buyvol (2021), Economic and environmental aspects of the development possibilities for the northern sea route, *Transportation Research Procedia*, *57*, 347–355, https://doi.org/10.1016/j.trpro.2021.09.060.

McCarty, W., L. Coy, R. Gelaro, A. Huang, D. Merkova, E. B. Smith, M. Sienkiewicz, and K. Wargan (2016), MERRA-2 Input Observations: Summary and Assessment. NASA Technical Report Series on Global Modeling and Data Assimilation, https://gmao.gsfc.nasa.gov/pubs/docs/McCarty885.pdf (visited on 06.11.2022).

Pashchenko, L. V., and V. I. Potapenko (2016), The struggle against snow bank at railway, in *Collection of scientific works of DonIZHT*, pp. 22–33, DonIZHT (in Russian).

Poli, P., H. Hersbach, D. Tan, D. P. Dee, J.-N. Thépaut, A. Simmons, C. Peubey, P. Laloyaux, T. Komori, P. Berrisford, R. Dragani, Y. Trémolet, E. Hólm, M. Bonavita, L. Isaksen, and M. Fisher (2013), The data assimilation system and initial performance evaluation of the ECMWF pilot reanalysis of the 20th-century assimilating surface observations only (ERA-20C). ERA Report Series No. 14, https://www.ecmwf.int/en/elibrary/76007-data-assimilation-system-and-initial-performance-evaluation-ecmwf-pilot.

Rachoy, C., and M. Spazierer (2008), Meteorological information and warning system for railway infrastructure decision support for natural hazards management, in *Proceedings of the World Congress on Rail Research*, International Railway Research Board (IRRB), Seoul, Korea.

Reichle, R. H., R. D. Koster, G. J. M. de Lannoy, B. A. Forman, Q. Liu, S. P. P. Mahanama, and A. Touré (2011), Assessment and Enhancement of MERRA Land Surface Hydrology Estimates, *Journal of Climate*, *24*(24), 6322–6338, https://doi.org/10.1175/JCLI-D-10-05033.1.

Romanenko, F. A., and O. A. Shilovtseva (2016), Geomorphological processes in the mountains of the Kola Peninsula and climate change, *Moscow University Bulletin. Series 5. Geography*, (6), 78–86 (in Russian), https://vestnik5.geogr.msu.ru/jour/article/view/261.

Schubert, S. D., Y. Chang, A. M. DeAngelis, R. D. Koster, Y.-K. Lim, and H. Wang (2022), Exceptional Warmth in the Northern Hemisphere during January–March of 2020: The Roles of Unforced and Forced Modes of Atmospheric Variability, *Journal of Climate*, *35*(8), 2565–2584, https://doi.org/10.1175/JCLI-D-21-0291.1.

Serykh, I. V., A. G. Kostianoy, S. A. Lebedev, and E. A. Kostianaia (2022), On the transition of temperature regime of the White Sea Region to a new phase state, *Fundamental and Applied Hydrophysics*, *15*(1), 98–111, https://doi.org/10.48612/fpg/k9x4-p8fz-5kz6.

Tilinina, N., S. K. Gulev, I. Rudeva, and P. Koltermann (2013), Comparing Cyclone Life Cycle Characteristics and Their Interannual Variability in Different Reanalyses, *Journal of Climate*, *26*(17), 6419–6438, https://doi.org/10.1175/JCLI-D-12-00777.1.

Vasiliev, A. A., D. S. Drozdov, A. G. Gravis, G. V. Malkova, K. E. Nyland, and D. A. Streletskiy (2020), Permafrost degradation in the Western Russian Arctic, *Environmental Research Letters*, *15*(4), 045,001, https://doi.org/10.1088/1748-9326/ab6f12.

Vishnevsky, E. P., and G. V. Chepurin (2010), The need for air drying and assessment of moisture surplus, *Plumbing. Heating. Conditioning. Energy Efficiency*, *4* (in Russian), https://www.c-o-k.ru/articles/neobhodimost-osusheniya-vozduha-i-ocenka-proficita-vlagi.

Yakubovich, A. N., and I. A. Yakubovich (2019), Forecasting climate change impact on the functionality of the transport infrastructure of the cryolith zone of Russia, *Intelligence. Innovations. Investment*, (1), 104–110, https://doi.org/10.25198/2077-7175-2019-1-104 (in Russian).

Russian Journal of Earth Sciences

# Mathematical Model of Freezing of Rocks Saturated With Salt Solution Taking Into Account the Influence of Osmosis

**M. M. Ramazanov**[*,1,2], **N. S. Bulgakova**[1,3], **L. I. Lobkovsky**[4,5]

[1] Institute for Geothermal Research and Renewable Energy (Branch of the Joint Institute for High Temperatures, Russian Academy of Sciences), Makhachkala, Russia
[2] Institute of Geospheres Dynamics of Russian Academy of Sciences, Moscow, Russia
[3] Dagestan State Institute of National Economy, Makhachkala, Russia
[4] Shirshov Institute of Oceanology, Russian Academy of Sciences, Moscow, Russia
[5] Moscow Institute of Physics and Technology (State University), Dolgoprudny, Moscow Oblast, Russia
* **Correspondence to:** M. M. Ramazanov, mukamay-ipg@mail.ru.

**Abstract:** The paper presents a mathematical model of rocks freezing saturated with salt solution under impact of osmotic force. Osmosis is related to the salt concentration gradient, which is characteristic for solutions, and it is a powerful mechanism for the movement of solutions in poorly permeable porous media. A mathematical criterion for the formation of closed "pockets" with brines (cryopags) in frozen rocks has been obtained. This criterion is shown to be significantly depends on the osmosis coefficient. The model includes three layers of a porous medium saturated, respectively, with ice, ice and solution, and salt solution only. A special case was studied when there is only a second layer with a movable boundary, on which a phase transition from the second layer to the third one occurs. The investigated layer is saturated with a salt solution and ice in thermodynamic equilibrium. Other layers are replaced by boundary conditions. An approximate analytical solution of the problem is found in a self-similar formulation. The nature of the influence of osmotic force on the freezing process of rocks saturated with solution is shown. The characteristic patterns associated with the considered process are revealed. One of the features of the osmosis influence is the fact that it can cause the movement (migration) of the solution in the direction of increasing pressure, i.e. in the direction opposite to the driving force caused by the pressure gradient.

**Keywords:** osmosis, freezing, porous medium, salt solution, filtration, phase transition.

**Citation:** Ramazanov, M. M., N. S. Bulgakova, L. I. Lobkovsky (2023), Mathematical Model of Freezing of Rocks Saturated With Salt Solution Taking Into Account the Influence of Osmosis, *Russian Journal of Earth Sciences*, 23, ES5007, EDN: BYCURY, https://doi.org/10.2205/2023es000857

## 1. Introduction

Understanding the regularities of freezing processes in rocks saturated with salt solution is important due to numerous practical applications. The problems of chemical contamination of the surface in cold regions due to the burial of various liquid radioactive waste in permafrost can be distinguished among them [*Chuvilin*, 1999]. In the cited work, based on the results of physical experiments, the behavior of ions of chemical elements in freezing and thawing soils and in ice is studied. The features characteristic for the interaction of frozen ground with salt solutions are described.

According to modern ideas, during the geological history permafrost in the coastal zone of the East Siberian Arctic shelf experienced alternation of freezing and thawing, as a result of which a large volume of hypersaline brines (called cryopags) were formed. At the same time, salty sea water and cryopags significantly contribute to the destruction and degradation of permafrost and, accordingly, the intensive release of methane as a result of the decomposition of metastable gas hydrates contained in frozen rocks in a self-preserved form [*Lobkovskii and Ramazanov*, 2018; *Shakhova et al.*, 2017]. Methane is a powerful greenhouse gas and affects global warming [*Yakushev*, 2009]. Therefore, studies of the

Research Article

Received: 20 March 2023
Accepted: 22 June 2023
Published: 30 December 2023

**Copyright:** © 2023. The Authors. This article is an open access article distributed under the terms and conditions of the Creative Commons Attribution (CC BY) license (https://creativecommons.org/licenses/by/4.0/).

regularities of cryopags formation during freezing of rocks saturated with a salt solution are very relevant. So, the developed mathematical model makes it possible to describe not only the freezing of porous media saturated with solution, but also to an equal extent the reverse process, i.e. the process of permafrost degradation taking into account the osmotic effect.

Modeling the processes of both freezing and thawing for rocks and soils saturated with salt solutions was carried out by some authors [*Tsypkin*, 2009]. The essential difference of our proposed model is that it takes into account osmosis associated with the salt concentration gradient, which is characteristic for salt solutions and is a powerful mechanism for the movement (migration) of solutions in poorly permeable porous media [*Ramazanov et al.*, 2019, 2022]. This, in particular, made it possible to find a criterion for the formation of cryopags, which significantly depends on the osmotic filtration coefficient.

It is generally believed that for the osmotic effect, it is necessary to have a semi-permeable membrane that passes water molecules and does not pass salt molecules. But this is an ideal case, in fact, this effect manifests itself locally in any sufficiently weakly permeable porous medium in the presence of a significant salt concentration gradient. This follows from thermodynamics, according to which the equilibrium of the solution requires the constancy of the chemical potential of both the dissolved component and the solvent [*Landau and Lifshitz*, 1976; *Ramazanov et al.*, 2019]. However, the degree of osmotic effect depends on the type of rock. In particular, it is well known that clays have semi-permeable and, consequently, osmotic properties [*Kemper*, 1961]. It follows from this that with a sufficient salt concentration gradient, the osmotic effect should be taken into account at permeabilities of the order of one mD or less, characteristic of clays. The need to take into account osmosis, in addition to the permeability coefficient, depends on specific conditions, in particular, on pressure gradients and salt concentration. In general, this question can be answered by comparing the estimates of osmotic force with the pressure gradient in the generalized Darcy's law given below.

## 2. Problem Formulation

There is a horizontal permeable layer saturated with a salt solution with a constant concentration and with a given temperature. At some point in time, at the upper boundary the temperature drops below the freezing point at a given local pressure and a given solution concentration. Then two freezing fronts of the solution will spread from top to bottom. The first front is the boundary between the upper completely frozen region of the formation and the region where both the solution and the ice are in thermodynamic equilibrium. The second boundary is the boundary between the indicated equilibrium partially frozen layer and the area saturated with liquid solution (Figure 1). It is required to formulate a mathematical model of the process under consideration and to investigate the laws of evolution of such a system taking into account the osmotic force.

## 3. Mathematical Model

We present sets of equations in each layer and boundary conditions at the interphase boundaries. Let's point the $z$ axis down and select the coordinate system as shown in Figure 1.

**Area I.** This layer contains only rocks and ice, so here we have only the equation of thermal conductivity

$$C_{mi}\frac{\partial T_i}{\partial t} = \lambda_{mi}\frac{\partial^2 T_i}{\partial z^2}, \quad C_{mi} = m\rho_i C_i + (1-m)C_s, \quad \lambda_{mi} = m\lambda_i + (1-m)\lambda_s.$$

Here $C_{mi}$ is the effective heat capacity of an unit volume of a porous medium saturated with ice; $T_i$ is the temperature; $\lambda_{mi}$ is the effective thermal conductivity of the saturated porous medium; $m$ is the porosity; $\rho_i$ is the density of ice; $C_i$, $C_s$ are the heat capacities of ice and rocks, respectively; $\lambda_i$, $\lambda_s$ are the thermal conductivities of ice and rocks.

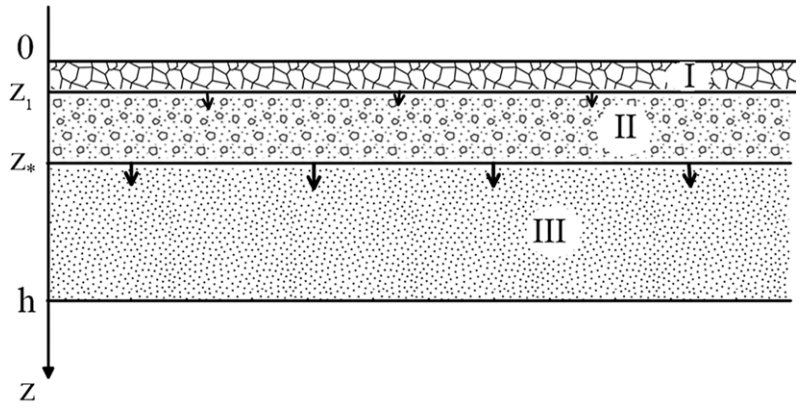


**Figure 1.** Diagram of the problem: I – frozen rocks containing ice; II – partially frozen layer saturated with ice and salt solution in thermodynamic equilibrium; III – unfrozen stratum saturated with salt solution; $z = z_1(t)$ is the movable boundary of the region I; $z = z_*(t)$ is the partial freezing front of the solution.

**Area II.** The system in this region is in a state of phase equilibrium, therefore, according to the equation of state, temperature is a function of pressure and concentration of salt. It is usually assumed that the temperature depends on the concentration linearly. In other words, the equation of state can be written as

$$T = T_w(p) - \psi_0 c. \tag{1}$$

Here $T_w(p)$ is the dependence of the freezing temperature on the pressure for pure water without impurities; $\psi_0$ is a constant characterizing the degree of decrease in the freezing temperature of water due to the presence of dissolved salt.

The dependency (1) can be written in another way:

$$p = P_w(T + \psi_0 c). \tag{2}$$

Here $p = P_w(T)$ is the known function that is the equation of state for a pure liquid, i.e. the inverse function with respect to $T_w(p)$. Next, we will use the form (2) for the equation of state.

The set of equations in the considered layer will be written as

$$\begin{aligned}
&\mathbf{v} = -\frac{k f_w(s)}{\eta}\left(\rho_w \frac{\partial \mu_1}{\partial c}\frac{\partial c}{\partial z} + \frac{dP}{dT}\left(\frac{\partial T}{\partial z} + \psi_0 \frac{\partial c}{\partial z}\right) - \rho_w g\right);\\
&\frac{\partial}{\partial t}\Big[m\big(s\rho_w + (1-s)\rho_i\big)\Big] + \frac{\partial}{\partial z}\big(\rho_w \mathbf{v}\big) = 0;\\
&\Big(ms + \Gamma\Big)\frac{\partial c}{\partial t} + \mathbf{v}\frac{\partial c}{\partial z} = m\frac{\partial}{\partial z}\left(sD\frac{\partial c}{\partial z}\right) - c_0\frac{m\rho_i}{\rho_w}\frac{\partial s}{\partial t}, \quad \Gamma(K,c) = \frac{\partial a(K,c)}{\partial c}, \quad \lim_{Kc\to\infty} a(K,c) = a_\infty;\\
&\bar{C}_m\frac{\partial T}{\partial t} + qm\rho_i\frac{\partial s}{\partial t} + \rho_w\bar{C}_w\mathbf{v}\frac{\partial T}{\partial z} = \frac{\partial}{\partial z}\left(\lambda_m\frac{\partial T}{\partial z}\right);\\
&\bar{C}_m = C_m - ms\beta_w T\frac{dP}{dT}, \quad \rho_w\bar{C}_w = \rho_w C_w - \beta_w T\frac{dP}{dT};\\
&C_m = m\Big[s\rho_w C_w + (1-s)\rho_i C_i\Big] + (1-m)C_s, \quad \lambda_m = m\Big[s\lambda_w + (1-s)\lambda_i\Big] + (1-m)\lambda_s,
\end{aligned} \tag{3}$$

where $k$ is the permeability; $s$ is the water saturation; $\rho$ is the density; $\mathbf{v}$ is the velocity field of the solution; $C$ is the heat capacity of the unit volume; $T$ is the temperature; $\lambda$ is the thermal conductivity; $m$ is the porosity; $\mu_1$ is the chemical potential of the solvent in the solution; $\eta$ is the viscosity of the solution; $D$ is the diffusion coefficient of salt in the solution; $q$ is the specific heat of melting of ice; $a$ is the concentration of salt in the solid

phase of a porous medium; $\beta_w$ is the coefficient of thermal expansion; indices: $i$ is ice, $w$ is water, $s$ is the skeleton of the rock.

Further, in this system we will assume $dP_w/dT$ as a constant value, and for simplicity we will consider the phase permeability of the solution to be linear, i.e. we will assume $f_w(s) = s$.

In (3) the steady-state adsorption of salt is taken into account. For example, in the case of the Langmuir isotherm, the adsorption equation has the form

$$a\Big(K, c\Big) = a_\infty \frac{Kc}{1 + Kc},$$

where $a_\infty$ is the value of the maximum adsorption; $c$ is the equilibrium concentration of the adsorbent in the solution; $K$ is the constant of the adsorption equilibrium.

Note that the first term in the Darcy's law in (3) being proportional to the concentration gradient is the osmotic force [*Ramazanov et al.*, 2019].

In the system (3), the first equation is the generalized Darcy's law, the second equation is the mass balance of water, the third and fourth ones are the equations of the balance of salt and energy. Later, we will assume that the inequality is satisfied:

$$\frac{\rho_w g}{\gamma dP/dT} \ll 1, \quad \gamma = \frac{T_0 - T^0}{h}. \tag{4}$$

The inequality (4) means that the temperature gradient on the saturation line caused by the hydrostatic pressure drop, which is estimated to be about one degree per hundred meters, is small compared to the temperature gradient under consideration.

In accordance with the condition (4), further, in the first equation of the system (3), we will neglect gravity.

**Area III.** In this area, the rocks are saturated only with a liquid solution. The set of equations in this unfrozen region can be obtained from (3) if we put the saturation of water constant and equal to one. However, in the problem considered here, it is advisable to introduce simplifications. In the area, the salt concentration will be considered weakly changing and therefore the osmotic effect is neglected. For simplicity, adsorption is also neglected, although, if necessary, these effects can be painlessly taken into account. As a result, we have

$$\begin{aligned}
&\mathbf{v} = -\frac{k}{\eta}\left(\frac{\partial p}{\partial z} - \rho_w g\right);\\
&\frac{\partial}{\partial t}(m\rho_w) + \frac{\partial}{\partial z}(\rho_w \mathbf{v}) = 0;\\
&m\frac{\partial c}{\partial t} + \mathbf{v}\frac{\partial c}{\partial z} = mD\frac{\partial^2 c}{\partial z^2};\\
&C_m\frac{\partial T}{\partial t} + \rho_w C_w \mathbf{v}\frac{\partial T}{\partial z} = \lambda_m \frac{\partial^2 T}{\partial z^2};\\
&C_m = m\rho_w C_w + (1-m)C_s, \quad \lambda_m = m\lambda_w + (1-m)\lambda_s.
\end{aligned}$$

**Boundary conditions.** Considering the lower layer to be infinite for simplicity, the boundary conditions characterizing the conservation of salt, energy and mass flows of water, we write

$$
\begin{aligned}
&z = 0: \quad T_i = T_i^0;\\
&z = z_1: \quad T_- = T_+ = T^0, \quad \lambda_{mi}\frac{\partial T_-}{\partial z} = \rho_i q m \frac{dz_1}{dt} + \lambda_m \frac{\partial T_+}{\partial z},\\
&\qquad s_1\left(D\frac{\partial c_+}{\partial z} + \frac{\rho_i}{\rho_w}c_+\frac{dz_1}{dt}\right) = 0, \quad \mathbf{v}_+ = s_1\left(1-\frac{\rho_i}{\rho_w}\right)m\frac{dz_1}{dt} = -\frac{ks_1}{\eta}\left(\rho_w\frac{\partial \mu_1}{\partial c}\frac{\partial c_+}{\partial z} + \frac{dP}{dT}\frac{\partial T_+}{\partial z}\right);\\
&z = z_*: \quad \rho_w\left(\mathbf{v}_- - ms_-\frac{dz_*}{dt}\right) - \rho_i m(1-s_-)\frac{dz_*}{dt} = \rho_w\left(\mathbf{v}_+ - m\frac{dz_*}{dt}\right),\\
&\qquad T_- = T_+ = T_*, \quad -\rho_i q m(1-s_-)\frac{dz_*}{dt} + \lambda\frac{\partial T_-}{\partial z} = \lambda_+\frac{\partial T_+}{\partial z},\\
&\qquad c_- = c_+ = c_*, \quad \left(\mathbf{v}_- - ms_-\frac{dz_*}{dt}\right)c_* - ms_- D\frac{\partial c_-}{\partial z} = \left(\mathbf{v}_+ - m\frac{dz_*}{dt}\right)c_* - mD\frac{\partial c_+}{\partial z},\\
&\qquad \mathbf{v}_+ = -\frac{k}{\mu}\frac{\partial p_+}{\partial z}, \quad p_- = p_+ = p_* = P(T_*);\\
&z \to \infty: \quad p \to p_0, \quad T \to T_0, \quad c \to c_0.
\end{aligned}
$$

Note that the water saturation at the boundaries of the phase transition can be discontinuous.

Later, the pressure will be counted from the hydrostatic pressure, and the temperature from $T^0$.

We can write the problem in the dimensionless form. To do this, we introduce scales:

$$
\begin{aligned}
&\Big[z\Big] = h, \quad \Big[v\Big] = -\frac{k}{\eta h}\frac{dP}{dT}\Big(T_0 - T^0\Big), \quad [t] = \frac{h}{[\mathbf{v}]}, \quad [T] = T_0 - T^0,\\
&[p] = -\frac{dP}{dT}(T_0 - T^0), \quad [c] = c_0.
\end{aligned}
$$

Keeping the notation, we have in dimensionless form

**in the Area I**

$$
\frac{\partial T}{\partial t} = \frac{1}{Pe_{T_i}}\frac{\partial^2 T}{\partial z^2}, \quad Pe_{T_i} = \frac{[\mathbf{v}]hC_{mi}}{\lambda_{mi}}, \tag{5}
$$

**in the Area II**

$$
\begin{aligned}
&\mathbf{v} = s\left[\Big(\gamma_f + \psi_0\Big)\frac{\partial c}{\partial z} + \frac{\partial T}{\partial z}\right];\\
&\frac{1}{N_s}\frac{\partial s}{\partial t} - \frac{1}{N_p}\left(\frac{\partial T}{\partial t} + \psi_0\frac{\partial c}{\partial t}\right) + \frac{\partial \mathbf{v}}{\partial z} = 0;\\
&\gamma_c\frac{\partial c}{\partial t} + \mathbf{v}\frac{\partial c}{\partial z} = \frac{s_0}{P_{e_c}}\frac{\partial^2 c}{\partial z^2} - \gamma_s\frac{\partial s}{\partial t};\\
&\gamma_T\frac{\partial T}{\partial t} + \gamma_q\frac{\partial s}{\partial t} + \mathbf{v}\frac{\partial T}{\partial z} = \frac{1}{P_{e_T}}\frac{\partial^2 T}{\partial z^2}.
\end{aligned} \tag{6}
$$

Here

$$\frac{1}{N_s}=m_0\Big(1-\frac{\rho_i}{\rho_w}\Big),\quad \frac{1}{N_p}=\left[\Big(s_0+(1-s_0)\frac{\rho_i}{\rho_w}\Big)\frac{\partial m}{\partial p}+\frac{m_0}{\rho_w}\Big(s_0\frac{\partial\rho_w}{\partial p}+(1-s_0)\frac{\partial\rho_i}{\partial p}\Big)\right]\Big(T_0-T^0\Big)\left|\frac{dP}{dT}\right|,$$

$$\gamma_f=\rho_w\left|\frac{\partial\mu_1}{\partial c}\right|c_0\left[\Big(T_0-T^0\Big)\left|\frac{dP}{dT}\right|\right]^{-1},\quad \gamma_c=m_0s_0+\Gamma,\quad \gamma_s=m_0\frac{\rho_i}{\rho_w},$$

$$\gamma_T=\frac{C_m+ms\beta_w\bar{T}\left|\frac{dP}{dT}\right|}{\rho_wC_w+\beta_w\bar{T}\left|\frac{dP}{dT}\right|},\quad \gamma_q=\frac{qm_0\rho_i}{\left[\rho_wC_w+\beta_w\bar{T}\left|\frac{dP}{dT}\right|\right]\Big(T_0-T^0\Big)},$$

$$P_{e_T}=\frac{[\mathbf{v}]h\left[\rho_wC_w+\beta_w\bar{T}\left|\frac{dP}{dT}\right|\right]}{\lambda_m},\quad P_{e_c}=\frac{[\mathbf{v}]h}{m_0D},\quad [\mathbf{v}]=\frac{k}{\eta h}\frac{dP}{dT}\Big|T_0-T^0\Big|.$$

**In the Area III**

$$\begin{aligned}
&\mathbf{v}=-\frac{\partial p}{\partial z};\\
&\frac{1}{N_{p_0}}\frac{\partial p}{\partial t}+\frac{\partial\mathbf{v}}{\partial z}=0,\quad \frac{1}{N_{p_0}}=\frac{1}{m_0}\left[\frac{\partial m}{\partial p}+\frac{m_0}{\rho_w}\frac{\partial\rho_w}{\partial p}\right]\Big(T_0-T^0\Big)\left|\frac{dP}{dT}\right|;\\
&\gamma_c\frac{\partial c}{\partial t}+\mathbf{v}\frac{\partial c}{\partial z}=\frac{1}{P_{e_c}}\frac{\partial^2c}{\partial z^2};\\
&\gamma_T\frac{\partial T}{\partial t}+\mathbf{v}\frac{\partial T}{\partial z}=\frac{1}{P_{e_T}}\frac{\partial^2T}{\partial z^2}.
\end{aligned}\tag{7}$$

**The Boundary Conditions are**

$$z=0:\quad T=T_i^0;$$

$$\begin{aligned}
z=z_1:\quad & T_-=T_+=T^0,\quad \frac{1}{Pe_{T_i}}\frac{\partial T_-}{\partial z}=\gamma_{qi}\frac{dz_1}{dt}+\frac{1}{Pe_{T_i}}\frac{\partial T_+}{\partial z},\\
& s_1\left(\frac{1}{Pe_{c_i}}\frac{\partial c_+}{\partial z}+\frac{\rho_i}{\rho_w}c_+\frac{dz_1}{dt}\right)=0,\quad \mathbf{v}_+=s_1\left(1-\frac{\rho_i}{\rho_w}\right)\frac{dz_1}{dt}=s_1\left[\Big(\gamma_f+\psi_0\Big)\frac{\partial c_+}{\partial z}+\frac{\partial T_+}{\partial z}\right];
\end{aligned}\tag{8}$$

$$\begin{aligned}
z=z_*:\quad & \rho_w\left(\mathbf{v}_--s_-\frac{dz_*}{\partial t}\right)-\rho_i(1-s_-)\frac{dz_*}{dt}=\rho_w\left(\mathbf{v}_+-\frac{dz_*}{\partial t}\right),\\
& T_-=T_+=T_*,\quad -\gamma_q(1-s_-)\frac{dz_*}{dt}+\frac{1}{Pe_T}\frac{\partial T_-}{\partial z}=\frac{1}{Pe_T}\frac{\partial T_+}{\partial z},\\
& c_-=c_+=c_*,\quad -\gamma_s(1-s_-)c_*\frac{dz_*}{dt}+\frac{s_-}{Pe_c}\frac{\partial c_-}{\partial z}=\frac{s_-}{Pe_c}\frac{\partial c_+}{\partial z},\\
& \mathbf{v}_+=-\frac{\partial p_+}{\partial z},\quad p_-=p_+=p_*=P(T_*);
\end{aligned}\tag{9}$$

$$z\to\infty:\quad p\to p_0,\quad T\to1,\quad c\to1.$$

## 4. Self-Similar Formulation and Solution of the Problem

We will look for a solution in a self-similar form introducing a new coordinate

$$\xi=\frac{z}{\sqrt{t}},\quad \mathbf{v}=\frac{\mathbf{v}(\xi)}{\sqrt{t}},\quad T=T(\xi),c=c(\xi),\quad p=p(\xi).\tag{10}$$

Then, we have **in the ice area**

$$-\frac{\xi}{2}\frac{dT_i}{d\xi}=\frac{1}{Pe_{T_i}}\frac{d^2T_i}{d\xi^2}.\tag{11}$$

The general solution to this problem can be written as

$$T = A_0 + A_1 erf\left(\frac{\sqrt{Pe_{T_i}}}{2}\xi\right). \tag{12}$$

**In the Partially Frozen Area**

$$\begin{gathered}
\mathbf{v} = s\left[\left(\gamma_f + \psi_0\right)\frac{dc}{d\xi} + \frac{dT}{d\xi}\right];\\
-\frac{\xi}{2N_s}\frac{ds}{d\xi} + \frac{\xi}{2N_p}\left(\frac{dT}{d\xi} + \psi_0\frac{dc}{d\xi}\right) + \frac{d\mathbf{v}}{d\xi} = 0;\\
-\left(\frac{\gamma_c\xi}{2} - \mathbf{v}\right)\frac{dc}{d\xi} = \frac{1}{Pe_c}\frac{d^2c}{d\xi^2} + \frac{\gamma_s\xi}{2}\frac{ds}{d\xi};\\
-\left(\frac{\gamma_T\xi}{2} - \mathbf{v}\right)\frac{dT}{d\xi} = \frac{1}{Pe_T}\frac{d^2T}{d\xi^2} + \frac{\gamma_q\xi}{2}\frac{ds}{d\xi}.
\end{gathered} \tag{13}$$

**In the Unfrozen Area – the Area III**

$$\begin{gathered}
\mathbf{v} = -\frac{dp}{d\xi} + \gamma_f\frac{dc}{d\xi}\\
-\frac{\xi}{2N_{p0}}\frac{dp}{d\xi} = \frac{d^2p}{d\xi^2} - \gamma_f\frac{d^2c}{d\xi^2}, \quad \frac{1}{N_{p0}} = \frac{1}{m_0}\left[\frac{dm}{dp} + \frac{m_0}{\rho_w}\frac{d\rho_w}{dp}\right]\left(T_0 - T^0\right)\left|\frac{dP}{dT}\right|\\
-\left(\frac{\gamma_c\xi}{2} - \mathbf{v}\right)\frac{dc}{d\xi} = \frac{1}{s_0Pe_c}\frac{d^2c}{d\xi^2}\\
-\left(\frac{\gamma_T\xi}{2} - \mathbf{v}\right)\frac{dT}{d\xi} = \frac{1}{Pe_T}\frac{d^2T}{d\xi^2}.
\end{gathered} \tag{14}$$

**Boundary Conditions in Self-Similar Coordinates**

$$\xi = 0: \quad T_i = \frac{-\delta T_i + \delta T}{\delta T}, \quad \delta T_i = T_0 - T_i^0, \quad \delta T = T_0 - T^0; \tag{15}$$

$$\begin{gathered}
\xi = \xi_1: \quad T_- = T_+ = 0, \quad \frac{1}{Pe_{T_i}}\frac{dT_-}{d\xi} = \frac{\gamma_{qi}}{2}\xi_1 + \frac{1}{Pe_T}\frac{dT_+}{d\xi},\\
s_1\left(\frac{1}{Pe_{c_i}}\frac{dc_+}{d\xi} + \frac{\rho_i}{\rho_w}\frac{\xi_1}{2}c_+\right) = 0, \quad \mathbf{v}_+ = s_1\left(1 - \frac{\rho_i}{\rho_w}\right)\frac{\xi_1}{2} = s_1\left(\frac{dc_+}{d\xi} + \gamma_f\frac{dT_+}{d\xi}\right),
\end{gathered}$$

$$\begin{gathered}
\xi = \xi_*: \quad \mathbf{v}_- - \frac{m_0}{2}s_*\xi_* - \frac{\rho_i m_0}{2\rho_w}(1 - s_*)\xi_* = \mathbf{v}_+ - \frac{m_0}{2}\xi_*,\\
T_- = T_+ = T_*, \quad -\gamma_q(1 - s_*)\frac{1}{2}\xi_* + \frac{1}{Pe_T}\frac{dT_-}{d\xi} = \frac{1}{Pe_T}\frac{dT_+}{d\xi},\\
c_- = c_+ = c_*, \quad -\gamma_s(1 - s_*)\frac{1}{2}\xi_* + \frac{1}{Pe_c}s_*\frac{dc_-}{d\xi} = \frac{1}{Pe_c}\frac{dc_+}{d\xi};
\end{gathered} \tag{16}$$

$$\xi \to \infty: \quad p \to p_0, \quad T \to 1, \quad c \to 1.$$

Here: $\delta T_i$, $\delta T$ are temperature drops at the top and bottom of the ice layer; $s_1$ is the water saturation at the boundary $\xi = \xi_1$ of the second (equilibrium) area with the ice layer.

Values $\delta T_i$ and $s_1$ are given. For solving the problem, it is necessary to find: moving boundaries of phase transitions $\xi_1$, $\xi_*$, the temperature in the ice layer; the temperature, salt concentration and water saturation in the equilibrium layer II and at its boundaries; the temperature and pressure in the unfrozen area III. In particular, it is necessary to find the temperature drop $\delta T$ at the boundary $\xi = \xi_1$. Note that the boundaries at the self-similar calculus simultaneously determine the speed of the corresponding fronts.

Equalities (5)–(9) and (10)–(16) at the self-similar statement, are a closed mathematical model of freezing of rocks saturated with salt solution, taking into account the osmotic driving force.

**Simplifications.** In the general case, the model is rather complicated, although it can be solved. For a more convex study of the influence of osmosis, we simplify the model. First of all, we obtain a condition under which the ice layer can be neglected. To do this, the first front must move much more slowly than the second, i.e.

$$\xi_1 \ll \xi_*. \tag{17}$$

We will consider the case when the filtration rate in a partially frozen layer (area II) is small, i.e.

$$\mathbf{v}_- \ll m_0 \xi_*.$$

To do this, either the water saturation, or the Peclet number for thermal diffusivity must be small (for example, due to low permeability), i.e.

$$s \ll 1 \text{ and/or } Pe_T \ll 1. \tag{18}$$

Then from the boundary conditions (15)–(16) we obtain the estimates

$$\begin{aligned}
&\xi_1^2 \sim \frac{\lambda_{mi}}{\rho_i q m_0}\left(T^0 - T_i^0\right);\\
&m_0\left(1 - \frac{\rho_i}{\rho_w}\right)(1 - s_*)\xi_* \sim \frac{k}{\eta}\frac{p_* - p_\infty}{l_p}, \qquad l_p \sim \sqrt{\frac{k}{\eta \beta_p}};\\
&T_* \sim T^0 + \frac{\xi_*}{l_T}\left(T_\infty - T^0\right);\\
&\frac{\rho_i q m_0 (1 - s_*)}{2\lambda}\xi_* \sim \frac{T_\infty - T_*}{l_T}, \qquad l_T \sim \sqrt{\frac{\lambda}{C_m}}.
\end{aligned} \tag{19}$$

Here $l_p, l_T$ are the effective thicknesses of the perturbed pressure and temperature areas, respectively, in the third layer in the self-similar representation. They are also equal to the propagation velocities of perturbations of the corresponding fields in the third layer.

Let's choose, for example, $T_i^0$, $p_\infty$, $T_\infty$ and other input parameters so that the characteristic pressure drops are of the order of 1 MPa, and the characteristic temperature drops are taken from the interval $\Delta T \sim (10^{-1} \div 10)$ °C.

Using the first two equations (19), we obtain an estimate for the permeability of dry rocks, in which the condition (17) is satisfied:

$$k \gg m_0\left(1 - \frac{\rho_i}{\rho_w}\right)^2 \frac{\lambda_{mi}}{\rho_i q}\frac{\eta}{\beta_p (p_* - p_\infty)^2}\left(T^0 - T_i^0\right) \sim 10^{-18}\left(10 \div 10^{-1}\right).$$

Thus, if the dry rock permeability is equal to or greater than $10^{-16}$, this approximation is acceptable.

Using (19) from the boundary conditions for the salt concentration in (16), we can estimate the concentration difference in the second and third layers.

Continuing the simplifications, we note that in the first consideration of the problem, without compromising the qualitative properties, in a satisfactory quantitative approximation, the third layer can also be ignored by setting fixed values of temperature and concentration at the phase transition boundary, since the temperature and salt concentration in this area change relatively weakly.

Thus, we will consider only the second partially frozen layer, where ice and solution are in thermodynamic equilibrium. The equations (13) are given for this layer. We will solve the problem in two stages. First, we find the zero approximation at a zero velocity

field, and then we find the correction associated with the motion of the solution. In the absence of motion, system (13) can be written as

$$
\begin{gathered}
-\frac{\xi}{2N_s}\frac{ds}{d\xi}+\frac{\xi}{2N_p}\left(\frac{dT}{d\xi}+\psi_0\frac{dc}{d\xi}\right)=0;\\
-\frac{\alpha_c\xi}{2}\frac{dc}{d\xi}=\frac{d^2c}{d\xi^2}-\frac{Pe_c\gamma_s\xi}{2}s_T\frac{dT}{d\xi},\quad \alpha_c=Pe_c(\gamma_c-\gamma_s s_c),\qquad s_c=-\frac{N_s}{N_p}\psi_0;\\
-\frac{\alpha_T\xi}{2}\frac{dT}{d\xi}=\frac{d^2T}{d\xi^2}-\frac{Pe_T\gamma_q\xi}{2}s_c\frac{dc}{d\xi},\quad \alpha_T=Pe_T\left(\gamma_T-\gamma_q s_T\right),\qquad s_T=-\frac{N_s}{N_p}.
\end{gathered}
\tag{20}
$$

We integrate the first equation in (20) and obtain

$$
s=s^0+\frac{N_s}{N_p}\left[T-\psi_0\left(c^0-c\right)\right]. \tag{21}
$$

The solution of the other equations will be sought in the form

$$
\begin{gathered}
c=c^0+C_1 erf\left(\frac{\sqrt{\tilde{\alpha_c}}}{2}\xi\right)+C_2 erf\left(\frac{\sqrt{\tilde{\alpha_T}}}{2}\xi\right);\\
T=C_3 erf\left(\frac{\sqrt{\tilde{\alpha_c}}}{2}\xi\right)+C_4 erf\left(\frac{\sqrt{\tilde{\alpha_T}}}{2}\xi\right).
\end{gathered}
\tag{22}
$$

Here the parameters $\tilde{\alpha_c}$, $\tilde{\alpha_T}$ need to be found, and $C_i$, $i=1$–$4$ are arbitrary constants.

Substituting (22) into (20), we obtain a linear homogeneous algebraic system of equations. The solvability condition for the system results in an identical quadratic equation for the parameters, solving which, we obtain

$$
\begin{gathered}
\tilde{\alpha_c}=\frac{\alpha_T+\alpha_c+\sqrt{(\alpha_c-\alpha_T)^2+4Pe_c\gamma_s s_T Pe_T\gamma_q s_c}}{2};\\
\tilde{\alpha_T}=\frac{\alpha_T+\alpha_c-\sqrt{(\alpha_c-\alpha_T)^2+4Pe_c\gamma_s s_T Pe_T\gamma_q s_c}}{2}.
\end{gathered}
\tag{23}
$$

After eliminating the dependent coefficients, the solution has the form

$$
\begin{gathered}
c=c^0+C_1 erf\left(\frac{\sqrt{\tilde{\alpha_c}}}{2}\xi\right)+\frac{Pe_c\gamma_s s_T}{\alpha_c-\tilde{\alpha_T}}C_3 erf\left(\frac{\sqrt{\tilde{\alpha_T}}}{2}\xi\right);\\
T=\frac{Pe_T\gamma_q s_c}{\alpha_T-\tilde{\alpha_c}}C_1 erf\left(\frac{\sqrt{\tilde{\alpha_c}}}{2}\xi\right)+C_3 erf\left(\frac{\sqrt{\tilde{\alpha_T}}}{2}\xi\right).
\end{gathered}
\tag{24}
$$

The remaining coefficients $C_1, C_3$ are determined from the boundary conditions

$$
\begin{gathered}
c_*=c^0+C_1 erf\left(\frac{\sqrt{\tilde{\alpha_c}}}{2}\xi_*\right)+\frac{Pe_c\gamma_s s_T}{\alpha_c-\tilde{\alpha_T}}C_3 erf\left(\frac{\sqrt{\tilde{\alpha_T}}}{2}\xi_*\right);\\
T_*=\frac{Pe_T\gamma_q s_c}{\alpha_T-\tilde{\alpha_c}}C_1 erf\left(\frac{\sqrt{\tilde{\alpha_c}}}{2}\xi_*\right)+C_3 erf\left(\frac{\sqrt{\tilde{\alpha_T}}}{2}\xi_*\right).
\end{gathered}
\tag{25}
$$

The salt concentration at the origin $c^0$ is determined from the condition that the velocity at this point is zero

$$
\left(\gamma_f+\psi_0\right)\left.\frac{dc}{d\xi}\right|_{\xi=0}+\left.\frac{dT}{d\xi}\right|_{\xi=0}=0.
$$

Substituting (24), we get

$$\left[\gamma_f+\psi_0+\frac{Pe_T\gamma_q s_c}{\alpha_T-\tilde{\alpha}_c}\right]\sqrt{\tilde{\alpha}_c}C_1+\left[\left(\gamma_f+\psi_0\right)\frac{Pe_c\gamma_s s_T}{\alpha_c-\tilde{\alpha}_T}+1\right]\sqrt{\tilde{\alpha}_T}C_3=0.$$

## 4. Mathematical Criterion for the Formation of Cryopags

In this section, we assume that the water saturation at the origin is zero. In the simplest case, for cryopag formation it is necessary that in addition to the origin of coordinates, the water saturation turned to zero at one more point $\xi_0$ ($0<\xi_0\le\xi_*$). The derivative of water saturation at this point must be negative, i.e. the conditions must be met:

$$\text{at } \xi=\xi_0\le\xi_*: \qquad s=0, \quad \frac{ds}{d\xi}<0. \tag{26}$$

We consider the complete equation for water saturation, which is obtained from system (13) after eliminating the second derivatives with respect to temperature and concentration

$$\begin{gathered}\left[\frac{1}{N_s}-\frac{2\left(\gamma_f+\psi_0\right)\frac{dc}{d\xi}+\frac{dT}{d\xi}}{\xi}+s\left(Pe_T\gamma_q+\left(\gamma_f+\psi_0\right)Pe_c\gamma_s\right)\right]\frac{ds}{d\xi}+\\ +s\left[Pe_T\left(\gamma_T-\frac{2\mathbf{v}}{\xi}\right)\frac{dT}{d\xi}+\left(\gamma_f+\psi_0\right)Pe_c\left(\gamma_c-\frac{2\mathbf{v}}{\xi}\right)\frac{dc}{d\xi}\right]=\frac{1}{N_p}\left(\frac{dT}{d\xi}+\psi_0\frac{dc}{d\xi}\right);\\ \mathbf{v}=s\left[\left(\gamma_f+\psi_0\right)\frac{dc}{d\xi}+\frac{dT}{d\xi}\right].\end{gathered} \tag{27}$$

We assume in this equation $s=0$, then we get

$$\left[\frac{1}{N_s}-\frac{2\left(\gamma_f+\psi_0\right)\frac{dc}{d\xi}+\frac{dT}{d\xi}}{\xi}\right]\frac{ds}{d\xi}=\frac{1}{N_p}\left(\frac{dT}{d\xi}+\psi_0\frac{dc}{d\xi}\right). \tag{28}$$

After expanding the solution in a Fourier series in powers of $\xi$, and taking into account the last two equations in (13), the conditions for cryopag appearance can be written as

$$\begin{gathered}\left.\frac{ds}{d\xi}\right|_{\xi=\xi_0}=\\ =\frac{N_s}{N_p}\frac{\left.\frac{\gamma_f}{\gamma_f+\psi_0}\frac{dT}{d\xi}\right|_{\xi=\xi_0}-\left[\frac{Pe_T}{2}\left(\gamma_T+\frac{\gamma_f}{\gamma_f+\psi_0}\frac{N_s}{N_p}\gamma_q\right)-\frac{Pe_c\psi_0}{2(\gamma_f+\psi_0)}\left(\gamma_c-\gamma_f\frac{N_s}{N_p}\gamma_s\right)\right]\left.\frac{\xi_0^2}{2}\frac{dT}{d\xi}\right|_{\xi=\xi_0}}{1+\left[\frac{Pe_T}{2}\left(\gamma_T+\frac{\gamma_f}{\gamma_f+\psi_0}\frac{N_s}{N_p}\gamma_q\right)-\frac{Pe_c}{2}\left(\gamma_c-\gamma_f\frac{N_s}{N_p}\gamma_s\right)\right]\xi_0\left.\frac{dT}{d\xi}\right|_{\xi=\xi_0}}<0\\ s(\xi_0)=0.\end{gathered} \tag{29}$$

Consider the case of low osmosis coefficients, when

$$\gamma_f\ll\psi_0. \tag{30}$$

Then from (26)–(27) we approximately obtain

$$Pe_T\gamma_T>Pe_c\gamma_c\left[1-\frac{\gamma_f}{\psi_0}\left(1-\frac{N_s\psi_0}{N_p\gamma_c}\gamma_s\right)-\frac{\gamma_f}{\psi_0}\frac{N_s}{N_p\gamma_T}\gamma_q\right], \quad \frac{\gamma_f}{\psi_0}\ll 1. \tag{31}$$

The value of $\xi_0$ is found from the second equation (29) or approximately from the equation

$$\frac{\gamma_f}{\psi_0} - \left[\frac{Pe_T}{2}\left(\gamma_T + \frac{\gamma_f}{\psi_0}\frac{N_s}{N_p}\gamma_q\right) - \frac{Pe_c}{2}\left(\gamma_c\left(1 - \frac{\gamma_f}{\psi_0}\right) - \gamma_f\frac{N_s}{N_p}\gamma_s\right)\right]\frac{{\xi_0}^2}{6} = 0;$$
$$\frac{Pe_T}{2}\left(\gamma_T + \frac{\gamma_f}{\psi_0}\frac{N_s}{N_p}\gamma_q\right) - \frac{Pe_c}{2}\left(\gamma_c\left(1 - \frac{\gamma_f}{\psi_0}\right) - \gamma_f\frac{N_s}{N_p}\gamma_s\right) > 0. \tag{32}$$

As a consequence, the cryopag requires the osmosis coefficient to be non-zero. In addition, from (29) it follows that with an increase in the osmosis coefficient, the $\xi_0$ increases and at some critical value $\gamma_{f_c}$, $\xi_0$ reaches the phase transition boundary $\xi_*$; with further growth of $\gamma_f$ the cryopag opens and the water saturation of the area under consideration at the phase boundary increases. Thus, on the one hand, small values of the osmosis coefficient are necessary for cryopag formation, and, on the other hand, if this coefficient exceeds the critical value, a closed cryopag is not formed.

The indicated critical value $\gamma_{f_c}$ is found from the condition $\xi_0 = \xi_*$ or

$$s(\xi_*) = 0. \tag{33}$$

Approximately $\gamma_{f_c}$ can be calculated assuming in (29) $\xi_0 = \xi_*$.

## 5. Results and Discussion

Thus, expressions (21)–(25) give the complete problem solving in the approximation of the absence of solution motion. Next we determine the approximate velocity field from the values of the temperature, concentration, and water saturation fields from the generalized Darcy law, taking into account osmosis (13)

$$\mathbf{v} = s\left[\left(\gamma_f + \psi_0\right)\frac{dc}{d\xi} + \frac{dT}{d\xi}\right]. \tag{34}$$

Finally, the corrected water saturation field is determined from the second equation (13) using (34). After integration, it can be written as

$$s = s^0 + \frac{N_s}{N_p}\left[T + \psi_0\left(c - c^0\right)\right] + \frac{\mathbf{v}}{\xi} + \int_0^\xi \frac{\mathbf{v}}{\xi^2}d\xi.$$

The resulting approximation is valid as long as the corrected water saturation approximation is close to the unperturbed one at zero velocity field. This is possible either when the Peclet number is small $Pe_T \ll 1$, or when the water saturation $s$ is sufficiently small.

In the problem of freezing of water-saturated rocks, two forces act: the force that pushes the solution into the unfrozen area, and the force that draws the solution in it. The pushing force is due to the fact that the equilibrium pressure increases with decreasing temperature, as well as the difference in the densities of water and ice, and the retracting force is due to the osmotic force. Depending on the values of the parameters, one or another force prevails.

Some of the obtained results are illustrated in Figures 2–4.

Figure 2 (a–c) shows the distributions of water saturation with depth in zero and first approximations (dotted line) for two different values of pore expansion coefficients $\beta_p$ (water capacity) (a, b) and two different values of the osmotic force coefficients $\gamma_f$ (a, c). Curves (1–2) correspond to two different moments of time; the dotted line shows the curves corrected with the filtration velocity field. Above the water saturation curves, the distributions of the respective filtration rates are shown.

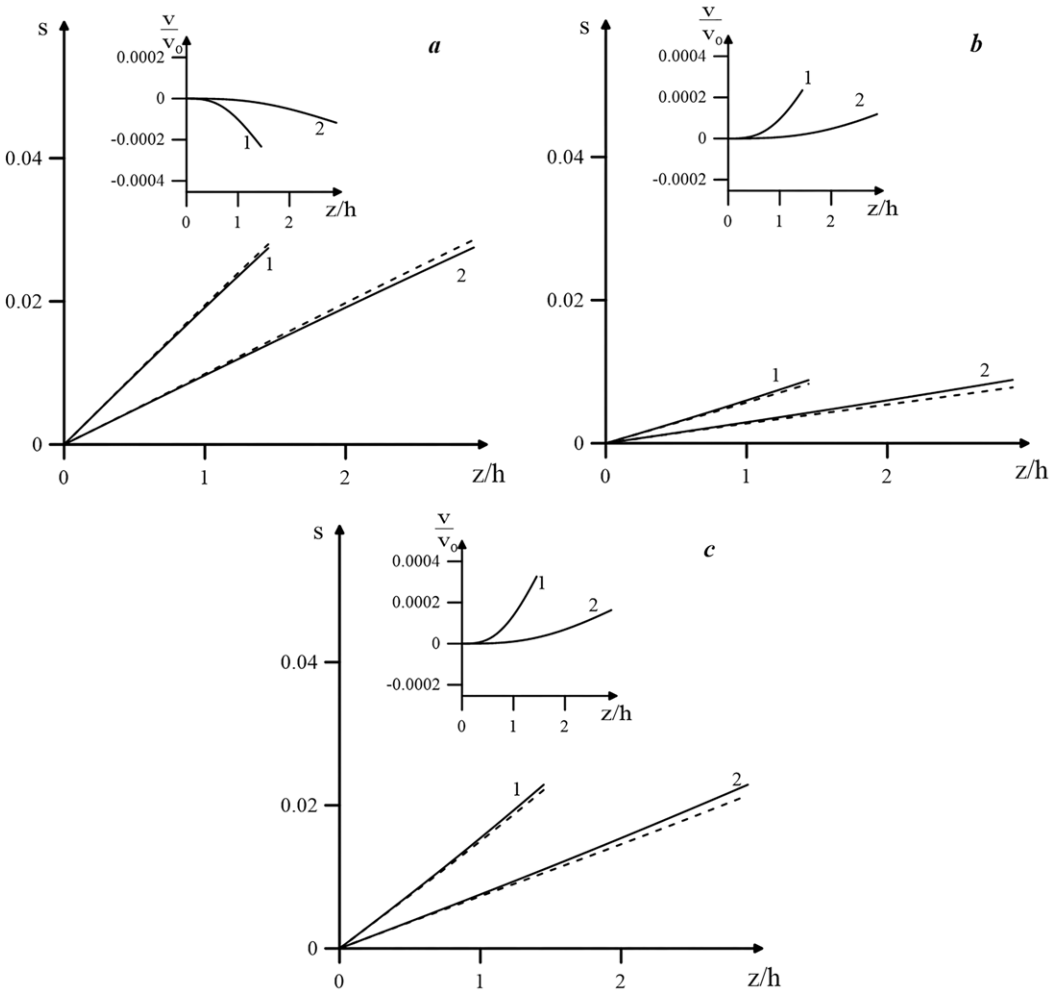


**Figure 2.** Water saturation distribution in the zero and first approximations (dashed line) for two points in time (the distributions of the filtration rate are shown above) for $P_{e_c} = 10$, $P_{e_T} = 10^{-2}$, $c_* = 2.8\%$, $T_0 = -1.88$ °C, $\psi_0 = 1.7$, $t = 1; 4$ (1–2), where $\left(\gamma_f, \frac{1}{N_p}\right) = (2, 0.01)$ a); $(2, 0.003)$ b); $(1, 0.01)$ c).

First of all, it follows from Figure 2 that, with time, the water saturation behind the phase transition front decreases monotonically due to freezing. In this case, the velocity field is negative, i.e. the solution is pulling into the partially frozen area from the thawed area by osmosis (Figure 2a). Accordingly, water saturation increased after correction for velocity (the dotted line is higher than the solid line). Comparing the solid and dotted lines, we see that the obtained solution has a very good accuracy with $Pe_T = 10^{-2}$.

If the water capacity $\beta_p$ is reduced with unchanged other parameters, the pushing force prevails (Figure 2b). In this case, the corrected water saturation decreased. In Figure 2c, in comparison with Figure 2a, the osmotic force coefficient is reduced. As can be seen from the comparison, a decrease in the osmotic force also resulted in predominance of the pushing force and so leads to decrease in water saturation.

These results are quite consistent with the results of physical experiments presented in [*Chuvilin*, 1999], where it is shown that clays under the considered freezing conditions draw the salt solution from the thawed area, but sands are pushed it out on the contrary. At the same time, as already noted, it is known that clays have semi-permeable and, consequently, osmotic properties [*Kemper*, 1961].

It should be emphasized that the patterns shown in Figure 2 associated with water saturation are valid, strictly speaking, only for the considered approximation of sufficiently low filtration rates. In the general case, an increase or decrease in water saturation depends not only on the inflow or outflow of the solution, but also on additional freezing of the

solution or melting of ice caused by a disturbance of the velocity field. As a result, at not too low speeds and certain values of the parameters, the dotted curve in Figure 2a can be below the solid line or cross it. This also applies to Figure 2b, c. As for the laws associated with osmosis and its influence on the direction of movement of the salt solution, in the case of "normal" osmosis it is also true for not low filtration rates.

Figure 3a–d shows the distributions of salt concentration in solution, temperature, pressure and filtration velocity fields for two different values of pore expansion coefficients $\beta_p$ (water capacity) and two different values of osmotic force coefficients. We take curves 1 as the base curves for comparison. Figure 3a (curve 2) showed that a decrease in the water capacity resulted in a decrease in the salt concentration.

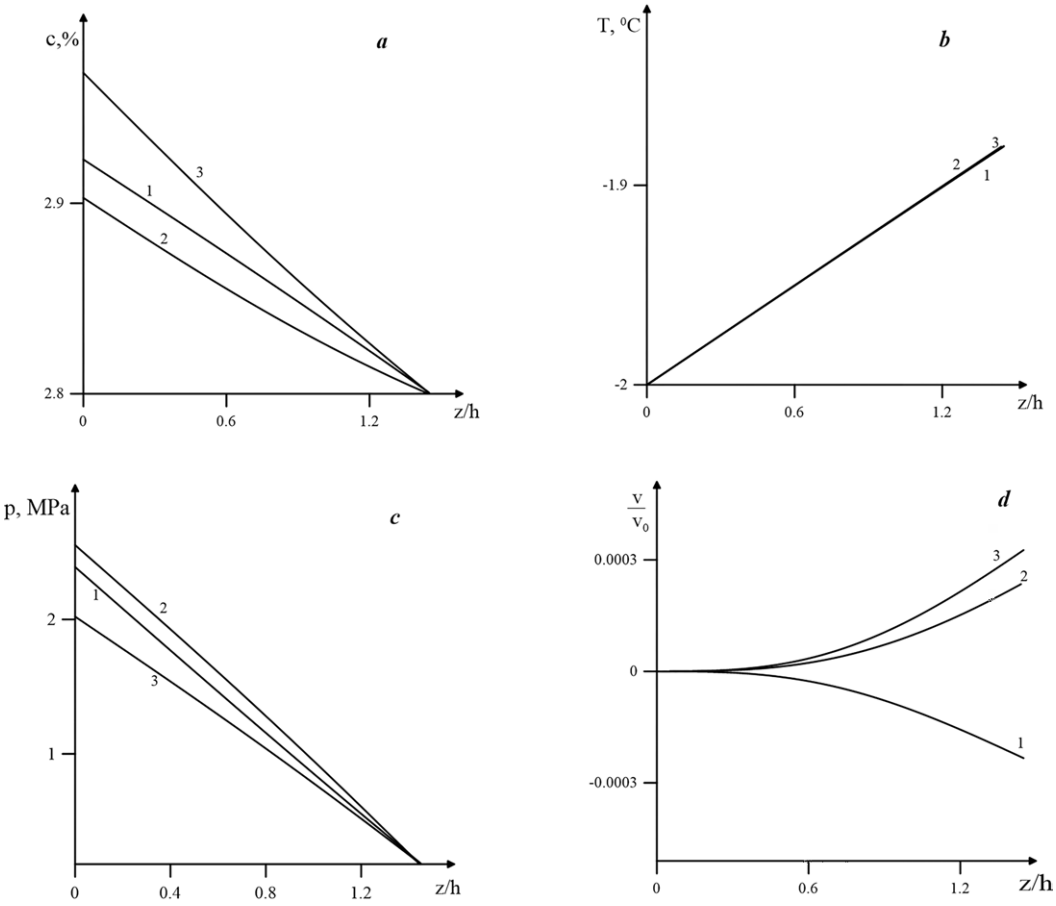


**Figure 3.** Distribution of salt concentration (a); temperature (b), pressure (c) and filtration rate (d) at $Pe_c = 10$, $Pe_T = 10^{-2}$, $c_* = 2.8\%$, $T_0 = -2$ °C, $\psi_0 = 1.7$, where: $\left(\gamma_f, \beta_p = \frac{1}{N_p}\right) = (2, 0.01)$ 1); $(2, 0.003)$ 2); $(1, 0.01)$ 3).

The curve 3 in Figure 3a shows that a decrease in the osmotic force coefficient leads to an increase in solution concentration. To explain these properties, first of all, we note that, as follows from Figure 3b, the temperature distributions for the three considered cases almost coincide. Such a low sensitivity of temperature to the considered changes in parameters is due to the fact that, in contrast to the concentration, the temperature is fixed at both boundaries and the curves are almost linear at the considered small Peclet numbers. The concentration at the origin is not specified, but it is found from the solution of the problem of freezing.

At a constant temperature, it follows from the condition of thermodynamic equilibrium (1)–(2) that with increasing pressure, the concentration of the solution decreases and vice versa. At the same time, a decrease in water capacity (compressibility of the skeleton) leads to an increase in pressure, and a decrease in the osmosis coefficient results in a decrease in pressure (see Figure 3c), which explains the patterns in Figure 3a–c.

Finally, from Figure 3c (curve 1), we can see that for these parameters the salt solution is drawn into the considered area. The curves 2 and 3 showed that both a decrease in water capacity and a decrease in osmotic force resulted in a predominance of the pushing force.

Thus, under certain conditions of freezing of rocks saturated with salt solution, cryopags (closed "pockets with brine") can form in the permafrost. The mathematical criterion for the formation of a cryopag in the framework of this problem is given by formulas (26)–(33). However, the authors do not deny the possibility of other mechanisms of cryopag formation.

Some of the properties associated with cryopags are illustrated in Figure 4a, b. As calculations show, cryopags under the given conditions are formed in the presence of an osmosis coefficient $\gamma_f$, but it should be sufficiently small. Figure 4a shows that with an increase in the osmosis coefficient, the cryopag grows and expands (curve 2). With further increase in $\gamma_f$, the cryopag opens (curve 3). Figure 4b shows the evolution of the cryopag over time. The top corner shows the velocity field. We can see that the cryopag expands as the freezing front advances. In addition, we note that the solution inside the cryopag is practically immobile.

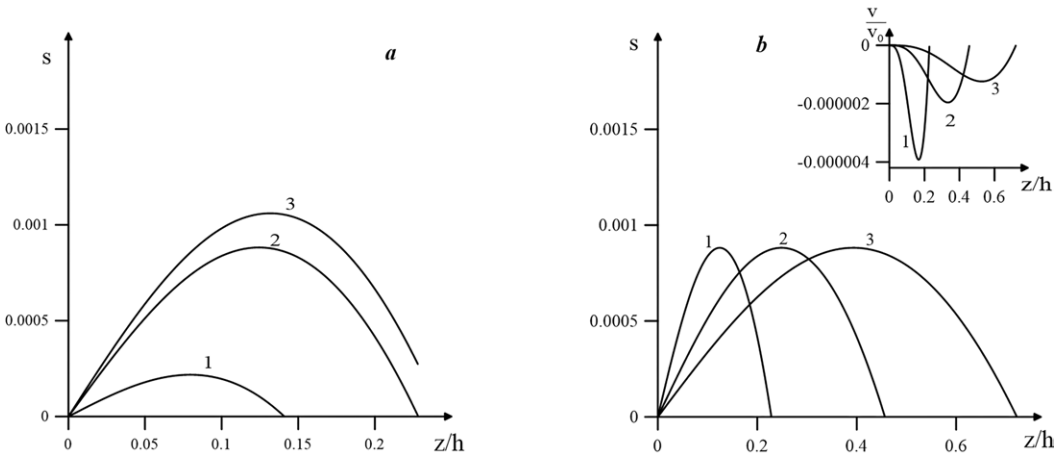


**Figure 4.** a) Distribution of water saturation with depth for different values of the osmosis coefficient: $\gamma_f/\gamma_{f_0} = 0, 3; 0.79; 0.9$ (1–3); b) Distribution of water saturation with depth for $\gamma_f/\gamma_{f_0} = 0.79$ for different time values: $t = 1; 4; 10$ (1–3); General values of parameters: $Pe_c = 10, Pe_T = 1.55$, $\frac{1}{N_p} = 0.1$, $\psi_0 = 1.7$, $c_* = 2.8\%$, $T_0 = -2$ °C, $T_* = -1.88$ °C.

## 6. Conclusion

A mathematical model of freezing for rocks saturated with salt solution is proposed. An approximate analytical solution of the problem in a self-similar formulation has been obtained, and the properties of the solution have been studied. A mathematical criterion for the formation of closed "pockets" with brines (cryopags) in frozen rocks is derived. The regularities of the osmosis effect on the process of freezing of rocks are shown, as well as the criterion for the formation of cryopags.

At high values of the osmotic coefficient, the solution is shown to be drawn into the freezing zone from the thawing zone, and at low values, on the contrary, it is pushed out. The pushing force is due to the fact that the equilibrium pressure increases with decreasing temperature, as well as to the difference in the densities of water and ice. This is quite consistent with the results of physical experiments on freezing clay and sand, where clay, in which osmotic properties are strongly pronounced, retract the salt solution, but sands, on the contrary, push it out [*Chuvilin*, 1999].

The proposed mathematical model makes it possible to describe not only the freezing of saturated porous media, but also the reverse process of permafrost degradation, taking into account the osmotic effect.

Note that when the phase boundary approaches the lower boundary of the reservoir, the self-similar approximation will be violated, but this does not apply to the resulting model itself. On a finite time, interval, the solution will be essentially non-stationary and, in the limit, will pass into a stationary solution.

**Acknowledgments.** This research, in general, was funded by the Russian Science Foundation, grant No. 22-67-00025.

**References**

Chuvilin, E. M. (1999), Migration of ions of chemical elements in freezing and frozen soils, *Polar Record*, *35*(192), 59–66, https://doi.org/10.1017/s0032247400026346.

Kemper, W. D. (1961), Movement of Water as Effected by Free Energy and Pressure Gradients: II. Experimental Analysis of Porous Systems in Which Free Energy and Pressure Gradients Act in Opposite Directions, *Soil Science Society of America Journal*, *25*(4), 260–265, https://doi.org/10.2136/sssaj1961.03615995002500040010x.

Landau, L. D., and E. M. Lifshitz (1976), *Theoretical Physics: Volume 5*, Nauka, Moscow (in Russian).

Lobkovskii, L. I., and M. M. Ramazanov (2018), Front Regime of Heat and Mass Transfer in a Gas Hydrate Reservoir under the Negative Temperature Conditions, *Fluid Dynamics*, *53*(4), 517–530, https://doi.org/10.1134/s0015462818040092.

Ramazanov, M. M., A. V. Karakin, and L. I. Lobkovskiy (2019), Mathematical Model for the Motion of Solutions Taking into Account the Osmotic Effect, *Doklady Earth Sciences*, *489*(1), 1306–1309, https://doi.org/10.1134/s1028334x19110060.

Ramazanov, M. M., N. S. Bulgakova, and L. I. Lobkovskiy (2022), Osmotic Convection, *Doklady Physics*, *67*(5), 153–158, https://doi.org/10.1134/s1028335822040061.

Shakhova, N., I. Semiletov, O. Gustafsson, V. Sergienko, L. Lobkovsky, O. Dudarev, V. Tumskoy, M. Grigoriev, A. Mazurov, A. Salyuk, R. Ananiev, A. Koshurnikov, D. Kosmach, A. Charkin, N. Dmitrevsky, V. Karnaukh, A. Gunar, A. Meluzov, and D. Chernykh (2017), Current rates and mechanisms of subsea permafrost degradation in the East Siberian Arctic Shelf, *Nature Communications*, *8*(1), https://doi.org/10.1038/ncomms15872.

Tsypkin, G. G. (2009), *Flows with phase transitions in porous media*, Fizmatlit, Moscow (in Russian).

Yakushev, V. S. (2009), *Natural gas and gas hydrates in permafrost*, VNIIGAZ, Moscow (in Russian).

Russian Journal of Earth Sciences

# Анализ локальной сейсмичности западной части полуострова Таймыр по данным сейсмической станции «Колба»

**Я. В. Конечная*[,1,2] и Г. Н. Антоновская[1]**

[1]Федеральный исследовательский центр комплексного изучения Арктики им. академика Н. П. Лаверова УрО РАН, Архангельск, Россия
[2]Единая геофизическая служба Российской академии наук, Обнинск, Россия
* **Контакт:** Я. В. Конечная, yanakon@mail.ru

В последние годы в западной части полуострова Таймыр ведется активная разработка угольных месторождений и проводятся работы, связанные с созданием соответствующей инфраструктуры (порты, дороги и т.д.). Установленная в октябре 2020 года сейсмическая станция «Колба», входящая в состав уникальной научной установки «Архангельская сейсмическая сеть», регулярно регистрирует локальные сейсмические события, естественная природа которых ставится под сомнение. За период с октября 2020 г. по февраль 2023 г. на расстояниях до 200 км от станции зарегистрировано 150 сейсмических событий. Для очистки сейсмического каталога от событий техногенной природы мы использовали следующие критерии: локация событий по данным сейсмической станции «Колба», анализ волновых форм и спектрально-временных (СВАН) диаграмм, расчет соотношения амплитуд объемных волн $S/P$, анализ суточного распределения событий и их магнитудный диапазон. Сложность заключается в отсутствии регионального годографа для данного района, что сказывается на точности локации сейсмических событий. Использованный набор критериев позволил провести очистку сейсмического каталога и отнести все 150 событий к техногенной сейсмичности. Наиболее эффективными критериями являются анализ сонограмм событий и соотношение $S/P$. В отдельных случаях по виду волновых форм также можно определить принадлежность события к определенному промышленному объекту (в частности, к порту Бухта Север).

**Ключевые слова:** Полуостров Таймыр, землетрясение, техногенное событие, критерии определения природы событий

**Цитирование:** Конечная, Я. В. и Антоновская Г. Н. Анализ локальной сейсмичности западной части полуострова Таймыр по данным сейсмической станции «Колба» // Russian Journal of Earth Sciences. — 2023. — Т. 23. — ES5008. — DOI: 10.2205/2023es000858 — EDN: JLBHNY

## Введение

В связи с расширением деятельности по разведке и добыче ресурсов на арктическом континентальном шельфе необходимым условием освоения территорий является минимизация воздействия процессов естественного и искусственного происхождения на инженерно-технические объекты. Возведение хранилищ углеводородного сырья, прокладка трубопроводов и пр. требует более тщательной оценки сейсмической опасности района их размещения.

Северный морской путь (СМП) является важнейшей частью инфраструктуры экономического комплекса Крайнего Севера и связующим звеном между российским Дальним Востоком и западными районами страны. На сегодняшний день трасса СМП крайне неравномерно охвачена инструментальными сейсмическими наблюдениями по причине суровых климатических и неблагоприятных географических условий, финансовой дороговизны проведения экспедиционных работ. Начиная с 2011 г., благодаря

https://elibrary.ru/jlbhny

Получено: 31 мая 2023 г.
Принято: 22 июня 2023 г.
Опубликовано: 30 декабря 2023 г.

© 2023. Коллектив авторов.

усилиям сотрудников Федерального исследовательского центра комплексного изучения Арктики им. академика Н. П. Лаверова Уральского отделения РАН (ФИЦКИА УрО РАН), стали развиваться инструментальные сейсмические наблюдения на побережье Карского моря и арктических российских архипелагах Земля Франца-Иосифа, Северная Земля и Новая Земля [*Антоновская и др.*, 2022a]. Кольским филиалом Федерального исследовательского центра «Единая геофизическая служба РАН» (ФИЦ ЕГС РАН) установлены новые станции на севере Кольского полуострова и на полуострове Ямал. Якутским филиалом ФИЦ ЕГС РАН установлены новые станции на севере Якутии [*ФИЦ ЕГС РАН*, 1993].

Стационарная широкополосная сейсмическая станция «Колба», вошедшая в состав Архангельской сейсмической сети ФИЦКИА УрО РАН, была открыта 11 октября 2020 г. Станция установлена в районе пгт. Диксон Таймырского Долгано-Ненецкого района Красноярского края на территории геофизической станции «Колба» им. В. В. Ходова Северного управления по гидрометеорологии и мониторингу окружающей среды (см. рис. 1). Международный и региональный код станции – KOLBA, ее координаты: $\varphi$ =73,529°N, $\lambda$ =80,701°E, $h$ = 11 м.

Первые результаты работы станции «Колба» подробно проанализированы в работе [*Антоновская и др.*, 2022b], в которой были представлены результаты оценки уровня микросейсмического фона и возможности сейсмической станции при проведении регионального мониторинга. В работе [*Антоновская и др.*, 2022b] упоминались локальные сейсмические события, природа которых ассоциировалась либо с техногенной деятельностью в районе порта Бухта Север, либо с динамикой разломных зон рассматриваемого района. Однако, более подробного анализа проявления локальной сейсмичности рассмотрено не было, что послужило основанием для данной работы. Очистка сейсмических каталогов от техногенных событий всегда была актуальной задачей, особенно после установки новой станции в малоизученном районе. Цель проведенных исследований – на основании подобранных критериев дать обоснованный ответ о природе зарегистрированных локальных событий: землетрясения или техногенные события.

По данным открытых источников [*Корабел.ру*, 2021; *Роснефть*, 2021; *Свинцова*, 2022] в западной части Таймырского полуострова в последние 3–5 лет отмечаются активные работы по освоению угольных месторождений и возведению необходимой инфраструктуры (строительство морских портов, терминалов, железных и автомобильных дорог). Основные месторождения и промышленные объекты показаны на рис. 1.

В западной части Таймырского полуострова расположены сразу несколько крупных промышленных объектов. Наиболее известным является Норильский промышленный район (или Норильский рудный район), в котором находятся 8 рудников и шахт, 2 обогатительные фабрики и 3 металлургических завода [*Энциклопедия Красноярского края*, 2015]. На протяжении всего периода работы сейсмическая станция «Колба» фиксирует техногенные события, связанные с деятельностью Норильского рудного района. Мониторинг локальной сейсмичности этого промышленного района обеспечивает станция «Норильск» (NRIK). Сейсмической станцией «Колба» регистрируются лишь наиболее сильные события. Они были рассмотрены в [*Антоновская и др.*, 2022b] и относятся к региональным техногенным сейсмическим событиям.

В 2020 г. начато строительство обогатительного комбината на одном из крупнейших в мире Сырадасайском угольном месторождении (рис. 1) [*Недра-Эксперт*, 2018c; *Свинцова*, 2022] и строительство морского порта Енисей [*Дела.ru*, 2023; *Корабел.ру*, 2021], который будет грузовым терминалом месторождения. В 2021 г. начата реализация проекта по строительству нефтеналивного терминала порт Бухта Север [*Роснефть*, 2021; 2023], расположенного в 42 км от сейсмической станции «Колба». Продолжается обустройство магистрального нефтепровода общей протяжённостью более 400 км. Лемберовская площадь (рис. 1), в состав которой входят Нижнелемберовское и Малолемберовское месторождения угля, также открыта относительно недавно – в 2018 году [*Neftegaz.ru*, 2020; *Недра-Эксперт*, 2018a,b]. Добываемый уголь будет поставляться на экспорт по Севморпути через порт Диксон.

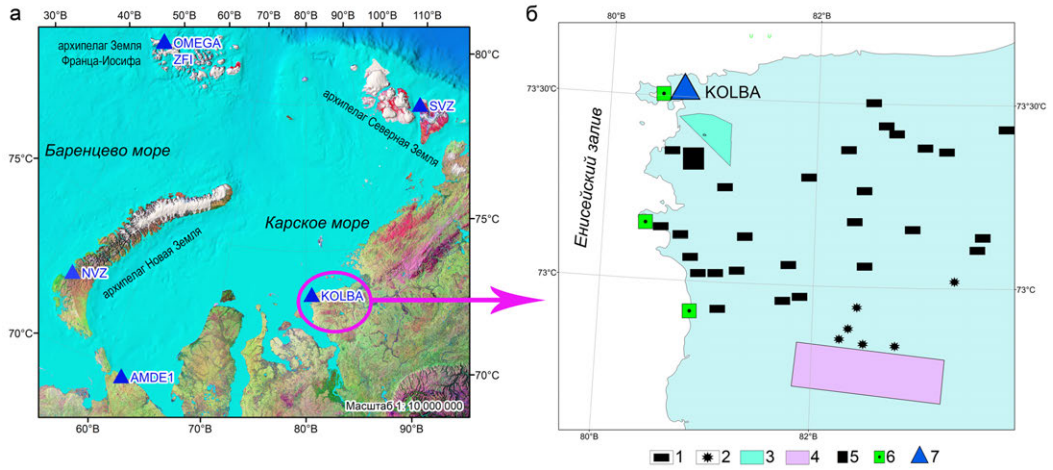


**Рис. 1.** Физико-географическая карта с расположением сейсмических станций Архангельской сейсмической сети ФГБУН ФИЦКИА УрО РАН (а) и действующие промышленные объекты в западной части полуострова Таймыр с указанием ряда полезных ископаемых (б). Некоторые полезные ископаемые: 1 – каменный уголь, 2 – драгоценные и поделочные камни. Угольные месторождения: 3 – Малолемберовское, 4 – Сыродасайское, 5 – Нижнелемберовское. 6 – порты, сверху вниз: Диксон, Бухта Север, Енисей. 7 – сейсмическая станция «Колба».

## Данные и методы

Сейсмическая станция «Колба» оснащена высокочувствительной аппаратурой фирмы Nanometrics (Канада) – широкополосным сейсмометром TC-120s и регистратором Centaur. Данные поступают на сервер лаборатории сейсмологии ФГБУН ФИЦКИА УрО РАН по протоколу SeedLink через сеть Интернет. Исходные данные представляют собой непрерывную сейсмическую запись в частотном диапазоне от 0,033 до 25 Гц с частотой опроса 50 отсч/с.

Обработка сейсмических данных проводится в программном комплексе WSG (Windows Seismic Grapher) совместной разработки Единой геофизической службы РАН и НПП «Геотех» [*Акимов и Красилов*, 2020]. Первичный просмотр предполагает анализ исходной записи на предмет выявления телесейсмических, региональных и локальных сейсмических событий с занесением информации в станционный бюллетень. В ходе регионального мониторинга данные сейсмической станции «Колба» подключаются к сводной обработке региональных землетрясений по данным Архангельской сейсмической сети (АСС) с привлечением исходных записей сейсмических станций международных и региональных сейсмологических агентств.

События, зарегистрированные только сейсмической станцией «Колба» и невыявленные на записях других станций, обрабатываются в программе EventLocator [*Асминг*, 2011]. Эпицентр определяется по вычисленному эпицентральному расстоянию и обратному азимуту. Это, безусловно, менее надежный метод локации, но он позволяет получить в первом приближении представление о распределении эпицентров событий.

Ввиду отсутствия регионального скоростного годографа для полуострова Таймыр при обработке в программе EventLocator используется скоростная модель BARENTS для определения координат землетрясений и времени в очаге (разработка Кольского филиала ФИЦ ЕГС РАН [*Kremenetskaya et al.*, 2001]). Для определения значений локальной магнитуды ML используется уточненная шкала для западной части Евразийской Арктики [*Морозов и др.*, 2020].

Основой для анализа служит скомпилированный каталог сейсмических событий, зарегистрированных сейсмической станцией «Колба» в период с октября 2020 г. по февраль 2023 г. на расстояниях до 200 км от станции, включающий 150 сейсмических событий.

В условиях отсутствия каких-либо опорных данных (образцы волновых форм, достоверная информация о месте, времени и способах проведения промышленных взрывов, отсутствие событий на записях других сейсмических станций) по техногенной сейсмичности в западной части полуострова Таймыр критерии определения природы событий сводятся к рассмотрению следующих косвенных признаков:

- Локация события вблизи промышленного объекта. В обычных случаях точность локации сейсмического события является решающим фактором определения его природы: если событие произошло в районе действующего добывающего предприятия, то велика вероятность, что это взрыв. События, произошедшие вне промышленных объектов, требуют более тщательного анализа, поскольку во многих случаях, на основании только сейсмических записей, невозможно определить, является ли данное событие взрывом или землетрясением. Однако, именно в случае регистрации событий сейсмической станцией «Колба» в западной части полуострова Таймыр и возникла ситуация, когда локация не является ключевым критерием в силу обработки данных по одной станции.
- Анализ СВАН-диаграмм и волновых форм сейсмических событий. Одним из более или менее стабильных критериев идентификации техногенных событий является спектральный анализ сейсмической записи. В работе представлены СВАН-диаграммы (или сонограммы), построенные в программе Geopsy. Известно [*Асминг и др.*, 2010], что сонограммы карьерных взрывов имеют характерные «полосы» в области высоких частот. Наличие в сейсмическом сигнале на протяжении всей записи события одной и той же частоты свидетельствует о техногенной природе данного события, чего никогда не наблюдается для землетрясений. Анализ волновых форм является субъективным критерием, связанным с опытом интерпретатора. Однако, со временем интерпретатор может сформировать представление о типичной записи техногенного события, связанного с конкретным промышленным районом.
- Анализ соотношения $S/P$. Отношение амплитуд объемных $P$ и $S$ волн является распространенным критерием идентификации техногенных событий. Согласно работе [*Асминг и др.*, 2010] отношения $S/P$ для землетрясений должны весьма отличаться от отношения амплитуд объемных волн в большую сторону по сравнению с техногенными событиями. Иными словами, для землетрясений характерны высокие значения соотношения $S/P$ (больше 3–4). Однако, могут быть исключения. Некоторые региональные и локальные землетрясения могут иметь амплитуды $P$ превышающие $S$ (малое значение $S/P$). Это объясняется геологическими особенностями трассы прохождения сейсмических волн.
- Анализ суточного распределения сейсмических событий. Может служить важным дополнением к остальным критериям, поскольку распределение событий в рабочие часы указывает на их техногенную природу.
- Анализ магнитудного диапазона зарегистрированных событий. Если магнитуды всех событий имеют низкие значения (например, $ML$ <3,0), то вероятна их техногенная природа. Технология взрывных работ всегда ограничена некой максимальной массой взрывчатого вещества, и взрывы не могут быть сколько угодно сильными [*Федеральная служба по экологическому, технологическому и атомному надзору*, 2020].

Несмотря на то, что по отдельности каждый признак не является прямым доказательством техногенной природы событий, их совокупность можно принять в качестве решения об исключении события из сейсмического каталога или пометки его как события техногенной природы.

**Результаты исследования и их обсуждение**

Все локальные сейсмические события, содержащиеся в скомпилированном каталоге, зарегистрированы только сейсмической станцией «Колба». Распределение эпицентров событий показано на рис. 2. Эпицентральные расстояния составляют от 42 до 165 км. Ошибка в локации событий, связанная с неточностью определения обратного азимута

(±10°), оценивается в 7–8,5 км для порта Бухта Север и 12–29 км для всех остальных событий. Следует заметить, что эта погрешность варьируется вдоль направления долготы. Значения локальных магнитуд $ML$ находятся в диапазоне от 0,4 до 2,4.

Выделено несколько групп событий (рис. 2), связанных с локацией вблизи промышленных объектов: порт Бухта Север, порт Енисей, Сырадасайское месторождение, южнее Сырадасайского месторождения, севернее Сырадасайского месторождения. В районе Нижнелемберовского угольного месторождения и порта Диксон событий не зарегистрировано.

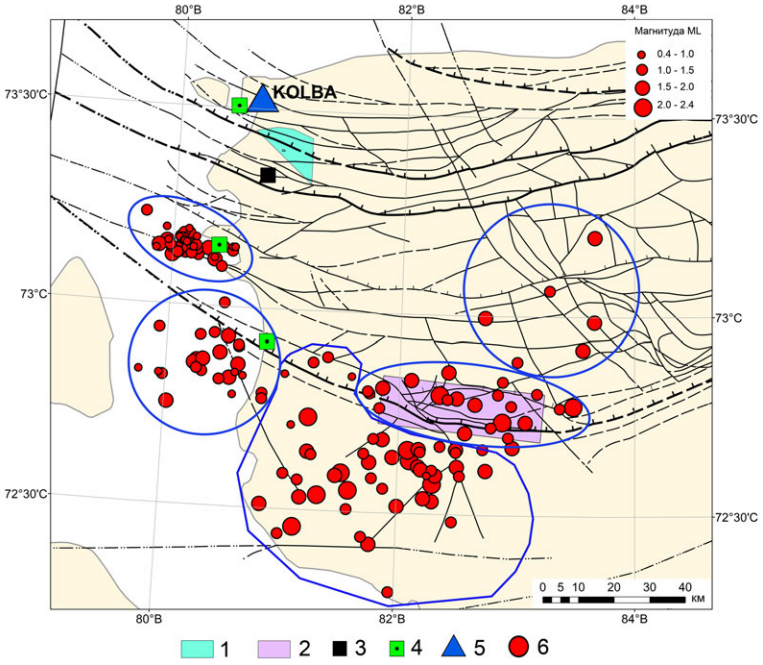


**Рис. 2.** Карта распределения эпицентров локальных сейсмических событий по данным сейсмической станции «Колба» за период с октября 2020 г. по февраль 2023 г. Угольные месторождения: 1 – Малолемберовское, 2 – Сыродасайское, 3 – Нижнелемберовское. 4 – порты, сверху вниз: Диксон, Бухта Север, Енисей. 5 – сейсмическая станция «Колба». 6 – локальные события. Синими линиями выделены группы событий. Черными линиями показаны разрывные нарушения различного типа.

Очевидно, что локация событий, как критерий распознавания техногенных событий, в данном случае оправдывает себя лишь частично. Более приемлемая локация, с учетом оценки погрешности, получена лишь для порта Бухта Север. Как было сказано ранее, это связано с определением параметров эпицентров по данным одной сейсмической станции «Колба». Кроме того, отсутствие регионального годографа также сказывается на точности локации сейсмических событий.

Диаграммы суточного распределения сейсмических событий в районе порта Бухта Север и связке порт Енисей – Сырадасайское месторождение показаны на рис. 3.

Как видно из рис. 3, практически все локальные сейсмические события зарегистрированы в дневное время с пиковыми значениями в 13–14 часов и в 19–20 часов. Причем время происхождения многих событий укладывается в интервал несколько минут, например, с 18:47 до 18:57 зафиксировано 11 событий. Подобное распределение указывает на проведение работ в районе промышленных объектов, а, следовательно, и на техногенную природу анализируемых событий.

Для всех событий было определено соотношение $S/P$, которое является одним из критериев распознавания техногенных событий. Количество событий и среднее $S/P$ в зависимости от района приведено в табл. 1. Очевидно, что события вне зависимости от района имеют низкие значения $S/P$ (меньше 3,0). Отсутствие в выборке событий с высокими значениями $S/P$ вероятнее всего свидетельствует об отсутствии в ней землетрясений.

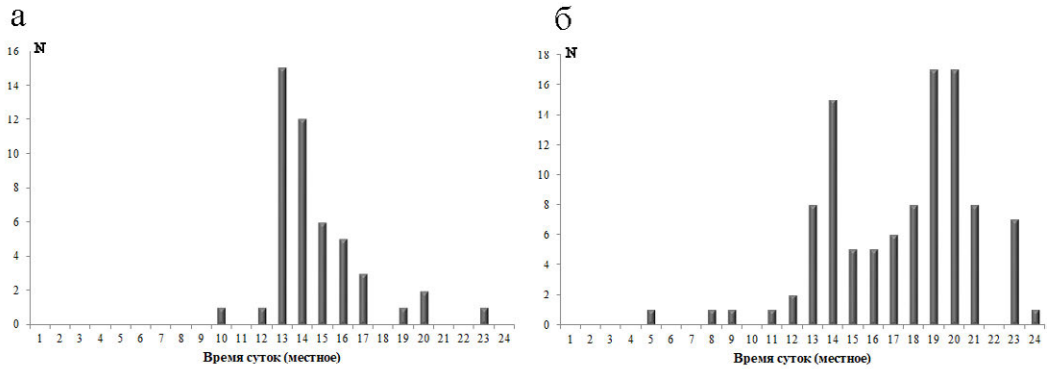


**Рис. 3.** Суточное распределение (по местному времени) локальных сейсмических событий, зарегистрированных сейсмической станцией «Колба»: а) – в районе порта Бухта Север; б) – в районе порта Енисей и Сырадасайского месторождения.

В районе порта Бухта Север, где летом 2021 г. начаты строительные работы, выделено 46 сейсмических событий за период с октября 2020 г. по февраль 2023 г. (рис. 4а) с магнитудами $ML$ от 0,7 до 1,8. Волновая картина подобных событий имеет характерный для взрывов вид. Из-за малых эпицентральных расстояний объемная $S$-волна и поверхностные волны не успевают сформироваться и приходят на станцию практически одновременно. Фазы объемных волн выделяются не только на фильтрованной записи, но и на исходном сигнале. Отмечается наличие акустического сигнала на записях более сильных событий. Стоит отметить, что волновые формы событий из района порта Бухта Север аналогичны взрывам из карьера Покровское (Архангельская область) на записях станции «Андозеро».

Остальные события, относящиеся к связке порт Енисей – Сырадасайское месторождение имеют более классический вид записей (рис. 4б) и похожи друг на друга. Из-за эпицентральных расстояний, превышающих 100 км, выделение фаз практически во всех случаях происходит с помощью высокочастотных фильтров, а объемные и поверхностные волны уже успевают сформироваться. Акустические сигналы отсутствуют.

Более информативным инструментом для идентификации техногенных событий является анализ СВАН-диаграмм (или сонограмм). Для всех групп событий, зарегистрированных сейсмической станцией «Колба», были получены СВАН-диаграммы по районам регистрации: порт Бухта Север, порт Енисей, южнее и севернее Сырадасайского месторождения и район самого месторождения (рис. 5). Очевидно, что все они содержат «полосы» в области высоких частот. Многие события, особенно лоцированные в Енисейском заливе, имеют 2–3 «полосы», что свидетельствует о характере работ, связанных с подводными взрывами. Максимумы амплитуд в выделенных «полосах» составляют, как правило, 9,5 Гц, 11,5 Гц, 13,5 Гц, 16,5 Гц и 19,5 Гц.

**Таблица 1.** Количество и средние значения $S/P$ для разных районов

| Район | N, шт. | Среднее $S/P$ | Среднеквадратичное отклонение $S/P$ |
|---|---|---|---|
| порт Бухта Север | 46 | 1,39 | 0,61 |
| порт Енисей | 24 | 2,36 | 0,41 |
| южнее Сырадасайского месторождения | 53 | 1,96 | 0,48 |
| севернее Сырадасайского месторождения | 6 | 1,90 | 0,41 |
| Сарыдагайское месторождение | 20 | 2,09 | 0,62 |

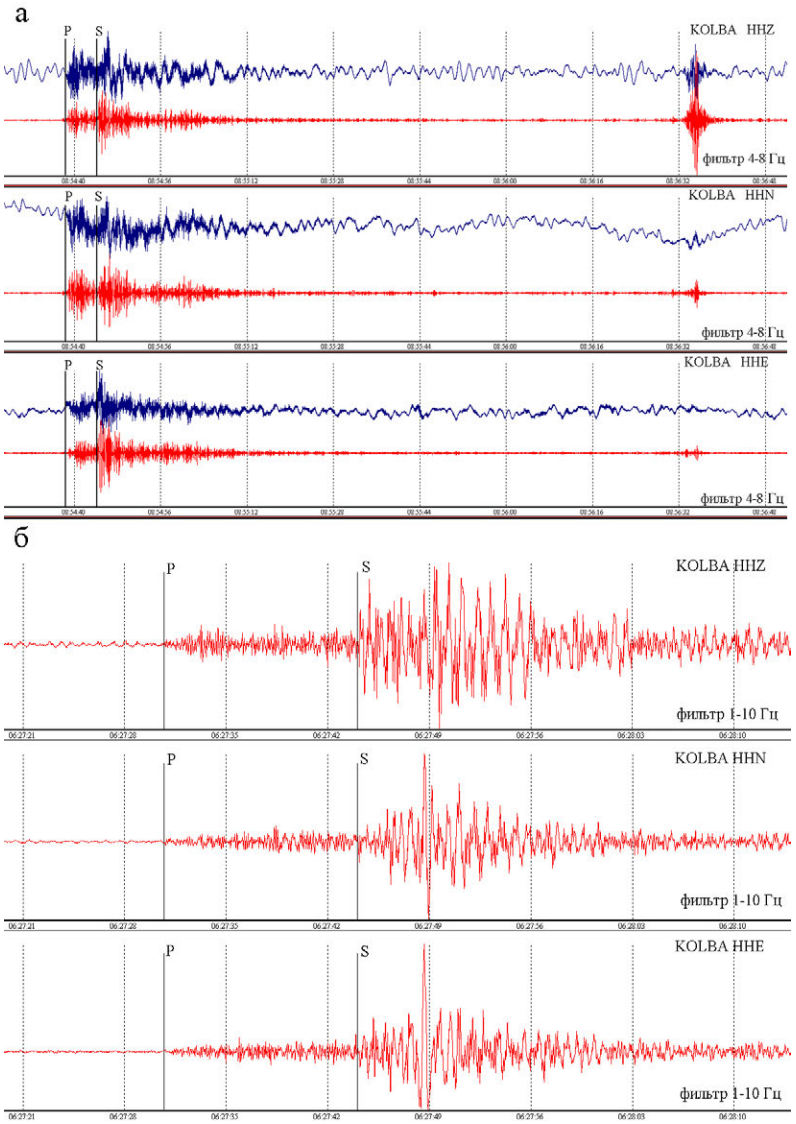


**Рис. 4.** Волновые формы локальных сейсмических событий, зарегистрированных сейсмической станцией «Колба»: а) – в районе объекта порт Бухта Север 09.10.2022 г.; б) – южнее Сырадасайского месторождения 02.12.2022 г.

На СВАН-диаграммах в районе порта Бухта Север выделяется акустический сигнал, но нет поверхностной волны. В других районах, напротив, – на низких частотах выделяется поверхностная волна (до 2 Гц), а акустический сигнал отсутствует.

**Заключение**

Сформулированные критерии идентификации техногенных событий на сейсмических записях позволили определить природу зарегистрированных сейсмической станцией «Колба» событий. Даже несмотря на отсутствие данных других сейсмических станций и большой разброс в локации событий относительно промышленных объектов, нам удалось сделать вывод об их техногенной природе и исключить их из сейсмического каталога. Из 150 зарегистрированных событий не выявлено ни одного землетрясения.

Наиболее значимыми критериями для определения природы событий мы выделяем СВАН-диаграммы, соотношения $S/P$ и суточное распределение событий. Для порта Бухта Север волновая форма также указывает на техногенную природу и может быть использована в качестве дальнейшего идентификатора природы событий. Локация и значения магнитуд всех событий являются косвенными признаками.

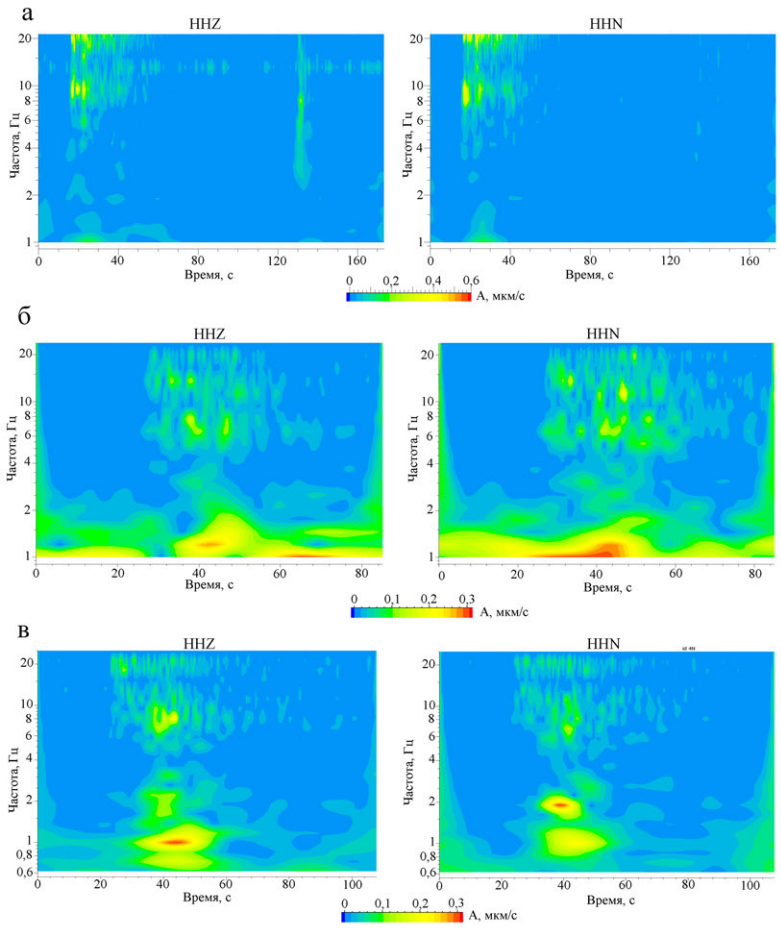


**Рис. 5.** СВАН-диаграммы локальных сейсмических событий, зарегистрированных сейсмической станцией «Колба» для вертикального ($Z$) и горизонтального ($N$) каналов: а) – порт Бухта Север 09.10.2022 г.; б) – порт Енисей 15.10.2021 г.; в – южнее Сырадасайского месторождения 18.12.2022 г.

В дальнейшем, в ходе просмотра записей и рутинной обработки событий полуострова Таймыр, следует придерживаться следующего алгоритма. Во-первых, по типу волновой формы определить события, относящиеся к порту Бухта Север. Во-вторых, оценить время в очаге. Этого будет достаточно для занесения события в группу с техногенной природой. Для других событий следует провести более углубленную интерпретацию с расчетом отношения $S/P$ и построением сонограмм.

**Благодарности.** Работа выполнена в рамках темы государственного задания Федерального исследовательского центра комплексного изучения Арктики имени академика Н. П. Лавёрова Уральского отделения Российской академии наук, № гос. регистрации 122011300389-8.

**Список литературы**

Neftegaz.ru. Нижнелемберовское каменноугольное месторождение. — 2020. — URL: https://neftegaz.ru/tech-library/mestorozhdeniya/555891-nizhnelemberovskoe-kamennougolnoe-mestorozhdenie/ (дата обр. 23.05.2023).

Акимов А. П., Красилов С. А. Программный комплекс WSG «Система обработки сейсмических данных»: Свидетельство о государственной регистрации программы для ЭВМ № 2020664678 от 16.11.2020. — 2020. — URL: http://www.gsras.ru/new/soft/WSG/.

Антоновская Г. Н., Конечная Я. В., Ваганова Н. В. *и др.* Вклад уникальной научной установки «Архангельская сейсмическая сеть» в изучение сейсмичности Российской Арктики // Геодинамика и тектонофизика. — 2022а. — Т. 13, № 2. — DOI: 10.5800/GT-2022-13-2-0587.

Антоновская Г. Н., Морозова Е. Р., Конечная Я. В. *и др.* Оценка регистрационных возможностей сейсмической станции «Колба» для мониторинга западного сектора Российской Арктики // Сейсмические приборы. — 2022b. — Т. 58, № 4. — DOI: 10.21455/si2022.4-8.

Асминг В. Э. Программный комплекс EL (ELRESS). Свидетельство о государственной регистрации программы для ЭВМ № 2011619620 от 20.10.2011. — 2011. — URL: http://www.krsc.ru/?q=ru/EL (дата обр. 23.05.2023).

Асминг В. Э., Кременецкая О. Е., Виноградов Ю. А. *и др.* Использование критериев идентификации взрывов и землетрясений для уточнения оценки сейсмической опасности региона // Вестник МГТУ. — 2010. — Т. 3, № 4/2. — С. 998—1007.

Дела.ru. На Таймыре строят глубоководный порт для нового угольного терминала. — 2023. — URL: https://dela.ru/news/279567/ (дата обр. 23.05.2023).

Корабел.ру. В строящийся порт «Енисей» смогут заходить крупные суда. — 2021. — URL: https://www.korabel.ru/news/comments/na_taymyre_aktivno_idet_stroitelstvo_morskogo_porta_enisey.html (дата обр. 23.05.2023).

Морозов А. Н., Ваганова Н. В., Асминг В. Э. *и др.* Шкала ML для западной части Евразийской Арктики // Российский сейсмологический журнал. — 2020. — Т. 2, № 4. — С. 63—68. — DOI: 10.35540/2686-7907.2020.4.06.

Недра-Эксперт. Лемберовская площадь. — 2018a. — URL: https://www.nedraexpert.ru/subsurface/77251/1 (дата обр. 23.05.2023).

Недра-Эксперт. Месторождение Малолемберовское. — 2018b. — URL: https://www.nedraexpert.ru/subsurface/1200037878/1 (дата обр. 23.05.2023).

Недра-Эксперт. Сырадасайское месторождение. — 2018c. — URL: https://www.nedraexpert.ru/subsurface/1200006811/1 (дата обр. 23.05.2023).

Роснефть. «Роснефть» приступила к реализации проекта по строительству нефтеналивного терминала порт «Бухта Север». — 2021. — URL: https://www.rosneft.ru/press/releases/item/206295/ (дата обр. 23.05.2023).

Роснефть. Результаты ПАО «НК «РОСНЕФТЬ» за 12 мес. 2022 г. по МСФО. — 2023. — URL: https://www.rosneft.ru/press/releases/item/214041 (дата обр. 23.05.2023).

Свинцова Е. На Сырадасайском месторождении на Таймыре отгрузили первую партию угля. — 2022. — URL: https://neftegaz.ru/news/coal/753225-na-syradasayskom-mestorozhdenii-na-taymyre-otgruzili-pervuyu-partiyu-uglya/ (дата обр. 23.05.2023).

Федеральная служба по экологическому, технологическому и атомному надзору. Приказ №494 от 3 декабря 2020 Об утверждении Федеральных норм и правил в области промышленной безопасности «Правила безопасности при производстве, хранении и применении взрывчатых материалов промышленного назначения». — 2020. — URL: http://pravo.gov.ru/proxy/ips/?docbody=&link_id=0&nd=602020534 (дата обр. 16.06.2023).

ФИЦ ЕГС РАН. Сеть сейсмических станций. — 1993. — URL: http://www.ceme.gsras.ru/new/struct/ (дата обр. 23.05.2023).

Энциклопедия Красноярского края. Норильский рудный район. — 2015. — URL: http://my.krskstate.ru/docs/minerals/norilskiy-rudnyy-rayon/ (дата обр. 23.05.2023).

Kremenetskaya E., Asming V., Ringdal F. Seismic Location Calibration of the European Arctic // Pure and Applied Geophysics. — 2001. — Vol. 158, no. 1. — P. 117–128. — DOI: 10.1007/pl00001151.

Russian Journal of Earth Sciences

# Local Seismicity Analysis of the Western Part of the Taimyr Peninsula According to the Data of the Single Seismic Station "KOLBA"

**Ya. V. Konechnaya**[**,1,2], **and G. N. Antonovskaya**[1,]

[1]N. Laverov Federal Center for Integrated Arctic Research of the Ural Branch of the Russian Academy of Sciences, Arkhangelsk, Russia
[2]Geophysical Survey of the Russian Academy of Sciences, Obninsk, Russia

**Correspondence to: Ya. V. Konechnaya, yanakon@mail.ru

In recent years, active development of coal deposits and works related to the creation of appropriate infrastructure (ports, roads, etc.) have been carried out in the western part of the Taimyr peninsula. The main objects are the port Buhta Sever (oil loading terminal), the Syradasay coal deposit and the port Yenisei. Work is also underway in the Lembersk coal mine and the associated port Dixon.

The single seismic station "KOLBA" of the Arkhangelsk seismic network installed in October 2020 near Dixson regularly registers local seismic events, the natural nature of which is questioned. From October 2020 to February 2023, 150 seismic events with a magnitude range of ML from 0.4 to 2.4 were registered at distances up to 200 km from the seismic station. The purpose of our research is to give a reasonable answer on the basis of selected criteria about the nature of registered local events: earthquakes or man-made events. Cleaning seismic catalogs from man-made events has always been an urgent task, especially after the installation of each new seismic station in a little-studied area of the Arctic.

The difficulty in determining the event nature lies in the absence of a regional hodograph and any reference data such as samples of waveforms, reliable information about the place, time and methods of industrial explosions, the absence of these events on the records of other seismic stations. In this regard, we have defined a set of criteria for determining the nature of events, which are reduced to the consideration of indirect signs. These are the location of an event near an industrial facility, the analysis of spectral-time diagrams and waveforms of seismic events, the analysis of the amplitudes ratio of volume and $S/P$ waves, the daily distribution of seismic events and the magnitude range of recorded events. Despite the fact that individually each criteria is not a direct proof of the man-made events nature, their totality can be taken as a decision to exclude the event from the seismic catalog.

In the process of determining the epicenters of events, we identified several groups related to various industrial facilities. The daily distribution diagram shows that local seismic events were recorded in the daytime with peak values at 13–14 hours and at 19–20 hours, which indicates the technogenic nature of events. The $S/P$ ratio is $< 3.0$ for all events, which most likely also indicates a technogenic nature, as with the presence of "bands" in the high frequency range on the spectral-time diagrams. The developed set of criteria for the identification of technogenic events allowed us to clean up the seismic catalog and attribute all 150 events to the manifestation of technogenic seismicity. The most effective criteria are the analysis of spectral-time diagrams, the $S/P$ ratio and the daily distribution of events. In some cases, by the waveform types, it is also possible to determine whether an event belongs to a certain industrial facility (in particular, to the port of Buhta Sever).

Received: 31 May 2023
Accepted: 22 June 2023
Published: 30 December 2023

© 2023. The Authors.

**Keywords:** Taimyr Peninsula, earthquake, technogenic event, criteria for determining the events nature

**Citation:** Konechnaya, Ya. V., and G. N. Antonovskaya (2023), Local Seismicity Analysis of the Western Part of the Taimyr Peninsula According to the Data of the Single Seismic Station "KOLBA", *Russian Journal of Earth Sciences*, 23, ES5008, https://doi.org/10.2205/2023ES000858 EDN: JLBHNY

## References

Akimov A. P., Krasilov S. A. Software complex WSG "Seismic data processing system": Certificate of state registration of the computer program No. 2020664678 dated 16.11.2020. — 2020. — URL: http://www.gsras.ru/new/soft/WSG/.

Antonovskaya G. N., Konechnaya Y. V., Vaganova N. V., *et al.* Contribution of the unique scientific facilities "Arkhangelsk seismic network" to the Russian Arctic seismicity study // Geodynamics & Tectonophysics. — 2022a. — Vol. 13, no. 2. — DOI: 10.5800/GT-2022-13-2-0587.

Antonovskaya G. N., Morozova E. R., Konechnaya Y. V., *et al.* Evaluation of the registration capabilities of the Kolba seismic station for monitoring the western sector of the Russian Arctic // Seismic Instruments. — 2022b. — Vol. 58, no. 4. — DOI: 10.21455/si2022.4-8.

Asming V. E. EL software package (ELRESS). Certificate of state registration of a computer program No. 2011619620 dated 10/20/2011. — 2011. — URL: http://www.krsc.ru/?q=ru/EL ; (date of access 23.05.2023).

Asming V. E., Kremenetskaya O. E., Vinogradov Y. A., *et al.* Using the criteria for identifying explosions and earthquakes to refine the assessment of the seismic hazard of the region // Bulletin of MSTU. — 2010. — Vol. 3, no. 4/2. — P. 998–1007.

Dela.ru. A deep-water port for a new coal terminal is being built in Taimyr. — 2023. — URL: https://dela.ru/news/279567/ ; (date of access 23.05.2023).

Encyclopedia of the Krasnoyarsk Territory. Norilsk ore district. — 2015. — URL: http://my.krskstate.ru/docs/minerals/norilskiy-rudnyy-rayon/ ; (date of access 23.05.2023).

Federal Service for Environmental, Technological and Nuclear Supervision. Order No. 494 of December 3, 2020 On approval of Federal norms and rules in the field of industrial safety "Safety rules for the production, storage and use of explosive materials for industrial use". — 2020. — URL: http://pravo.gov.ru/proxy/ips/?docbody=&link_id=0&nd=602020534 ; (date of access 16.06.2023).

Geophysical Survey of Russia Academy of Sciences. Network of seismic stations. — 1993. — URL: http://www.ceme.gsras.ru/new/struct/ ; (date of access 23.05.2023).

Korabel.ru. Large ships will be able to enter the Yenisei port under construction. — 2021. — URL: https://www.korabel.ru/news/comments/na_taymyre_aktivno_idet_stroitelstvo_morskogo_porta_enisey.html ; (date of access 05/23/2023).

Kremenetskaya E., Asming V., Ringdal F. Seismic Location Calibration of the European Arctic // Pure and Applied Geophysics. — 2001. — Vol. 158, no. 1. — P. 117–128. — DOI: 10.1007/pl00001151.

Morozov A. N., Vaganova N. V., Asming V. E., *et al.* The ML scale in western Eurasian Arctic // Russian Journal of Seismology. — 2020. — Vol. 2, no. 4. — P. 63–68. — DOI: 10.35540/2686-7907.2020.4.06.

Nedra-Expert. Lemberovskaya Square. — 2018a. — URL: https://www.nedraexpert.ru/subsurface/77251/1 ; (date of access 23.05.2023).

Nedra-Expert. Malolemberovskoye field. — 2018b. — URL: https://www.nedraexpert.ru/subsurface/1200037878/1 ; (date of access 23.05.2023).

Nedra-Expert. Syradasayskoye field. — 2018c. — URL: https://www.nedraexpert.ru/subsurface/1200006811/1 ; (date of access 23.05.2023).

Neftegaz.ru. Nizhnelemberovskoe coal field. — 2020. — URL: https://neftegaz.ru/tech-library/mestorozhdeniya/555891-nizhnelemberovskoe-kamennougolnoe-mestorozhdenie/ ; (date of access 23.05.2023).

Rosneft. Rosneft has begun implementing a project to build an oil terminal at the Bukhta Sever port. — 2021. — URL: https://www.rosneft.ru/press/releases/item/206295/ ; (date of access 23.05.2023).

Rosneft. Performance results of PJSC "OC ROSNEFT" for 12 months. 2022 according to International Financial Reporting Standards. — 2023. — URL: https://www.rosneft.ru/press/releases/item/214041 ; (date of access 23.05.2023).

Svintsova E. The first batch of coal was shipped at the Syradasai field in Taimyr. — 2022. — URL: https://neftegaz.ru/news/coal/753225-na-syradasayskom-mestorozhdenii-na-taymyre-otgruzili-pervuyu-partiyu-uglya/ ; (date of access 23.05.2023).

Russian Journal of Earth Sciences

# Формы переноса РЗЭ фторидно-карбонатно-хлоридными охлаждающимися гидротермальными флюидами в присутствии барита и целестина (термодинамическое моделирование)

**Г. П. Широносова*,[1], и И. Р. Прокопьев[1,2]**

[1]Институт геологии и минералогии им. В. С. Соболева СО РАН, Новосибирск, Россия
[2]Новосибирский государственный университет, Новосибирск, Россия
* **Контакт:** Галина Петровна Широносова, shiron@igm.nsc.ru

Термодинамическое исследование проведено с целью определения для всего ряда лантаноидов форм переноса при изменяющихся параметрах гидротермального флюида умеренной концентрации хлоридной, карбонатной и фторидной составляющих. Моделировался процесс, в ходе которого гидротермальный раствор, охлаждающийся от 500 до 100 °С, воздействовал на барит и целестин, которые использованы в качестве источника сульфатной серы, монацит – в качестве источника редкоземельных элементов (РЗЭ) и фосфора, и кальцит – в качестве источника кальция. Установлено, что в слабокислых условиях (pH около 4,1) равновесная минеральная ассоциация представлена редкоземельным флюоритом, монацитом, редкоземельным фторапатитом и Sr-содержащим баритом. В высокотемпературной области для легких и средних РЗЭ ведущим является первый хлорокомплекс $LnCl^{+2}$. Для тяжелых РЗЭ на первое место выходит второй фторокомплекс $LnF_2^+$, у тербия и диспрозия выявлено резкое преобладание сульфатного комплекса. Особая картина наблюдается при 100 °С: лидирующую позицию занимает акватированный катион $Ln^{+3}$ и для легких, и для тяжелых РЗЭ в силу ослабления комплексообразования. В случае слабощелочного флюида (pH около 7,1) равновесная минеральная ассоциация представлена кальцитом, монацитом, РЗЭ-флюоритом, РЗЭ-фторапатитом, Sr-содержащим баритом и стронцианитом. Появление последнего в природных ассоциациях может служить указанием на повышенную щелочность среды рудообразования. В равновесном слабощелочном флюиде вплоть до 200 °С для всех РЗЭ превалирующими оказываются гидроксокомплексы при соотношении $Ln(OH)_3^0 > Ln(OH)_2^+$. За ними следуют для легких РЗЭ при 500–400 °С первый хлорокомплекс, для средних и тяжелых – второй фторокомплекс. При 100 °С концентрация гидроксокомплексов резко уменьшается, и на первое место выходят фторо- и карбонатный комплексы. В целом наблюдается повышенная устойчивость первого хлорокомплекса в высокотемпературной области, а с понижением температуры усиливается роль фторокомплексов РЗЭ. Два варианта расчетов по кислотности-щелочности предположительно соответствуют моделированию воздействия двух типов флюидов: грейзенезирующего-слабокислого и карбонатитообразующего-слабощелочного.

**Ключевые слова:** лантаноиды, формы переноса, гидротермальные флюиды, монацит, редкоземельный флюорит, фторапатит, барит, целестин, стронцианит

https://elibrary.ru/igmqvp

Получено: 11 января 2023 г.
Принято: 3 июля 2023 г.
Опубликовано: 30 декабря 2023 г.

**Цитирование:** Широносова, Г. П., и И. Р. Прокопьев Формы переноса РЗЭ фторидно-карбонатно-хлоридными охлаждающимися гидротермальными флюидами в присутствии барита и целестина (термодинамическое моделирование) // Russian Journal of Earth Sciences. — 2023. — Т. 23. — ES5009. — DOI: 10.2205/2023es000859 — EDN: IGMQVP

© 2023. Коллектив авторов.

## 1. Введение и постановка проблемы

Значение редкоземельных элементов (РЗЭ) в мировой экономике возросло за последние десятилетия из-за их разнообразного использования в высокотехнологичных и экологически чистых отраслях [*Hatch*, 2012]. Термодинамические расчеты равновесия флюид–минерал значительно расширяют наши возможности по проверке гипотез относительно массопереноса в геологических системах. Важную роль в переносе и осаждении РЗЭ играют гидротермальные флюиды. Как правило, на ранних высокотемпературных стадиях рудообразования они характеризуются очень высокими концентрациями компонентов вплоть до рассолов, но на поздних стадиях с понижением $T$-$P$ параметров флюиды становятся менее концентрированными [*Nikolenko et al.*, 2018; *Prokopyev et al.*, 2023; *Yu et al.*, 2019]. В работе [*Li et al.*, 2019] по результатам исследований флюидных включений приводятся концентрации богатого фтором и хлором флюида от 1,4 до 12 мас.% NaCl-экв. При изучении флюидных включений в постмагматическом гидротермальном барите авторы работы [*Shu and Liu*, 2019] обнаружили около 0,2$m$ фторида и до 0,02$m$ сульфатной серы (здесь и далее $m$ – моль/кг $H_2O$). Авторы публикации [*Xing et al.*, 2019] исследовали потенциал гранитных пород как источника F и металлов (Fe, РЗЭ и U), используя термодинамическое моделирование. После моделирования воздействия гидротермального раствора на 1 кг гранита ими установлено, что возможное выделение фтора при этом должно составлять 0,002–0,004$m$ (пересчет с рис. 7 в работе [*Xing et al.*, 2019]). Зачастую на ранних стадиях гидротермального РЗЭ рудообразования отмечается наличие апатита, монацита, ксенотима и флюорита, а на поздних стадиях барита [*Mitchell and Smith*, 2017], барита с целестином и монацитом [*Shu and Liu*, 2019], барита, стронцианита, целестина в ассоциации с монацитом и кальцитом при пониженных концентрациях флюида гидрокарбонатно-хлоридного состава при 150–250 °C [*Prokopyev et al.*, 2016; 2023; 2020].

Распределению РЗЭ во флюидах в гидротермальных условиях посвящен целый ряд как экспериментальных работ, так и публикаций по термодинамическому моделированию. Наиболее значимы работы Мигдисова с соавторами [*Migdisov and Williams-Jones*, 2014; *Migdisov et al.*, 2009; 2016], в которых приводятся как экспериментально определенные константы устойчивости отдельных хлоро-, фторо- и сульфатных комплексов, так и проводится анализ распределении ряда лантаноидов при повышенных температурах. Работа [*Gysi et al.*, 2015] посвящена моделированию комплексообразования Ce, Y и Zr в зависимости от pH при 150 и 400 °C в присутствии карбонат-содержащей породы и флюида с концентрацией 0,2$m$ $H_3PO_4$, 0,4$m$ HF и 0,4$m$ HCl. Авторы [*Perry and Gysi*, 2018] приводят результаты численного моделирования комплексообразования в гидротермальных флюидах при температурах ~ 100–400 °C и давлениях до 1 кбар. Ими показано распределение по формам церия, неодима и эрбия в интервале 0,5 и 20 вес.% NaCl в зависимости от температуры, а также в системах с $CO_2$–NaCl в зависимости от pH. В отличие от наших расчетов, в их моделях не учитывалось наличие F, P и S. В нашей предыдущей работе [*Широносова и Прокопьев*, 2019] рассмотрено распределение по формам всех 14 лантаноидов + Y в высококонцентрированном охлаждающемся хлоридно-сульфатно-карбонатном флюиде с подчиненными концентрациями в нем фторида и сульфидной серы.

## 2. Методика

В настоящей работе термодинамическое исследование проведено с целью определения для всего ряда лантаноидов форм переноса и соотношения их при изменяющихся параметрах гидротермального флюида умеренной концентрации хлоридной, карбонатной и фторидной составляющих. $T$-$P$ параметры одновременного понижения температуры и давления флюида выбраны произвольно, исходя из общей логики процесса. Мы приняли за основу исходный состав раствора 1$m$ NaCl + 0,5$m$ $H_2CO_3$ + 0,1$m$ HF + 1 кг $H_2O$ (что соответствует примерно 8,5 % NaCl-экв.) в присутствии барита и целестина в качестве источника сульфатной серы. Для получения определенного pH дополнительно в нужных количествах вводились HCl и KOH. Источником РЗЭ в составе системы

являлся монацит, вводимый в избыточном количестве (около $5\times10^{-3}$ моль), содержащий РЗЭ в соотношении (моли соответствующих фосфатов): La – $1{,}3\times10^{-3}$; Ce – $2{,}4\times10^{-3}$; Pr – $2{,}7\times10^{-4}$; Nd – $8{,}3\times10^{-4}$; Sm – $1{,}17\times10^{-4}$; Eu – $4{,}7\times10^{-6}$; Gd – $9\times10^{-5}$; Tb – $9{,}17\times10^{-6}$; Dy – $3{,}8\times10^{-5}$; Ho – $5{,}2\times10^{-8}$; Er – $9{,}5\times10^{-6}$; Yb – $2{,}7\times10^{-6}$; Lu – $2\times10^{-7}$. В качестве источника кальция использовался кальцит, как правило в количестве 0,1 моль. Количество барита и целестина было принято $10^{-3}$ и $10^{-4}$ моль соответственно. Такие значения были специально подобраны с помощью пробных вариантов расчетов с тем, чтобы эти минералы появлялись в равновесных расчетных ассоциациях при пониженных *T-P* параметрах системы согласно природным данным [*Shu and Liu*, 2019]. В качестве возможных твердых фаз в равновесной минеральной ассоциации помимо исходных предусмотрена возможность образования идеальных твердых растворов монацита ($LnPO_4$, где Ln–La, Ce, Pr, Nd, Sm, Eu, Gd); РЗЭ-содержащего флюорита ($CaF_2$–(Ln, Y)$F_3$) и РЗЭ-содержащего фторапатита ($Ca_5(PO_4)_3F$–(Ln, Y)$_3(PO_4)_3$), где Ln весь ряд от La до Lu, ксенотима (Y, Ln)$PO_4$, где Ln–Tb, Dy, Er, Yb, Lu и Sr-содержащего барита (Ba, Sr)$SO_4$, а также стронцианита $SrCO_3$. Стронцианит и витерит ($BaCO_3$) образуют полный ряд твёрдых растворов, но этот твердый раствор опущен для упрощения расчетов из-за перегруженности системы уже учтенными пятью идеальными твердыми растворами: монацит, ксенотим, РЗЭ-содержащие фторапатит и флюорит, стронций содержащий барит.

Термодинамические расчеты проведены с использованием программного комплекса HCh [*Shvarov*, 2008; *Shvarov and Bastrakov*, 1999] в сочетании с термодинамической базой данных UNITHERM, дополненной новыми данными по РЗЭ фосфатам и хлоридным, фторидным и сульфатным комплексам лантаноидов во флюиде согласно последним экспериментальным данным [*Gysi et al.*, 2016; 2015; *Migdisov et al.*, 2016]. Данные для кальцита, флюорита и фторапатита заимствованы из [*Robie and Hemingway*, 1995]. Для водных гидроксокомплексов, бикарбонатных, карбонатных и фосфатных комплексов РЗЭ данные взяты из работы [*Haas et al.*, 1995]. В исследовании [*Степанчикова и др.*, 2014] при обработке спектральных данных обнаружено, что в интервале значений pH от 8 до 11 в изучаемых растворах присутствуют, кроме моногидроксокомплексов лантаноидов $Ln(OH)^{2+}$, комплексные формы со стехиометрией $Ln(OH)_2^+$ и $Ln(OH)_3^0$, четвертый гидроксокомплекс не обнаружен, поэтому в настоящей работе мы исключили его из числа возможных РЗЭ форм в гидротермальных условиях. Термодинамические данные для базовых ионов и комплексов макросистемы заимствованы из базы данных SUPCRT [*Johnson et al.*, 1992; *Shock et al.*, 1997; *Sverjensky et al.*, 1997], а для HCl взяты из публикации [*Tagirov et al.*, 1997]. В используемой программе коэффициенты активности частиц раствора рассчитываются по расширенному уравнению Дебая – Хюккеля, при этом предусмотрена возможность использования дополнительного параметра *b* для NaCl как базового электролита. Расчеты проведены для слабокислых и слабощелочных условий, предположительно соответствующих моделированию двух типов флюидов: грейзенезирующего-слабокислого и карбонатитообразующего-слабощелочного.

## 3. Результаты исследований

### *3.1. Расчеты равновесий в слабокислых условиях*

При воздействии на ассоциацию монацита с кальцитом в присутствии $BaSO_4$ и $SrSO_4$ слабокислого (pH = 4,1) охлаждающегося фторидно-карбонатно-хлоридного флюида во всем температурном интервале в равновесной минеральной ассоциации преобладающим оказывается редкоземельный флюорит (РЗЭ-флюорит).

Вторым по значимости является остаточный монацит (который был взят в избытке), затем редкоземельный фторапатит (РЗЭ-фторапатит). В интервале 300–100 °C появляется барит, содержащий незначительное количество Sr. Соотношение количеств этих равновесных фаз показано на рис. 1. Хорошо видно, что количество новообразованного РЗЭ-флюорита, показанное на левой оси ординат, резко возрастает с понижением *T-P* параметров флюида, тогда как количество новообразованного РЗЭ фторапатита (показан на правой оси ординат) постепенно снижается при охлаждении флюида. Коли-

чество стронциобарита (также правая ось ординат) возрастает от $4{,}1\times10^{-4}$ до $7{,}6\times10^{-4}$ моль, при этом мольная доля $SrSO_4$ в барите уменьшается от 0,012 до 0,0018 при снижении температуры от 300 до 100 °C. Исходный кальцит оказывается полностью израсходованным на образование редкоземельных флюорита и фторапатита.

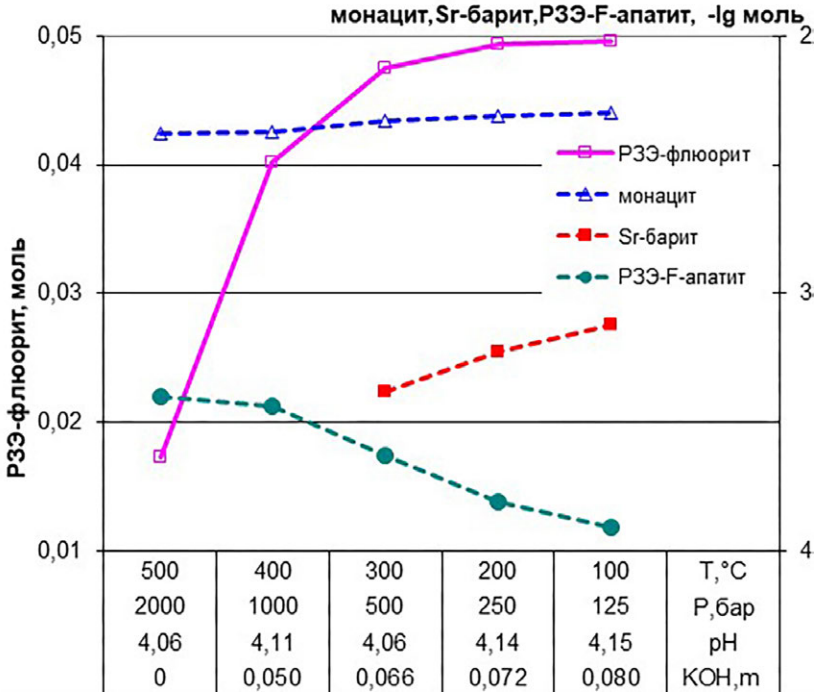


**Рис. 1.** Соотношение количеств равновесных твердых фаз в зависимости от *T*-*P*- параметров системы при моделировании воздействия на ассоциацию монацит + кальцит + барит + целестин слабокислого фторидно-карбонатно-хлоридного охлаждающегося флюида. Исходный состав системы: $0{,}1m$ $CaCO_3$+$5\times10^{-3}m$ монацит + $10^{-3}m$ $BaSO_4$+ $10^{-4}m$ $SrSO_4$ + $1m$ NaCl + $0{,}5m$ $H_2CO_3$ + $0{,}1m$ HF + $0{,}17m$ HCl + $m$ KOH + 1 кг $H_2O$ (концентрацию KOH см. в подписи к оси абсцисс). РЗЭ-флюорит – РЗЭ-содержащий флюорит; РЗЭ-F-апатит – РЗЭ-содержащий фторапатит; Sr-барит – Sr-содержащий барит.

На рис. 2 приведено распределение по формам La, Ce и Pr – представителей легких РЗЭ (ЛРЗЭ) в слабокислом фторидно-карбонатно-хлоридном охлаждающемся флюиде, состав которого детально отображен на рис. 1 и в подрисуночной подписи к нему. Для всех трех лантаноидов отмечается преобладание первого хлорокомплекса $LnCl^{+2}$ только при повышенных температурах, причем оно заметнее для церия и празеодима, тогда как у лантана уже при 300 °C и ниже наблюдается сближение концентраций второго хлорокомплекса и первого фторокомплекса. В области повышенных температур второе место по концентрации принадлежит первому фторокомплексу $LnF^{+2}$, концентрация которого начиная с 300 °C и ниже сравнивается с таковой хлорокомплексов, несмотря на возрастающее количество новообразованного РЗЭ-флюорита в этой области и на порядок превышающую исходную концентрацию хлорид-иона над фторидом. На третьем месте здесь оказывается второй хлорокомплекс ЛРЗЭ $LnCl_2^+$. Четвертую позицию у лантана и церия при 500–400 °C занимает второй фторокомплекс $LnF_2^+$. При понижении температуры в интервале 400–200 °C к нему присоединяется первый гидроксокомплекс $LnOH^{+2}$. При 100 °C на первое место по концентрации выходит форма $Ln^{+3}$.

Распределение по формам Nd, Sm и Gd в равновесном слабокислом флюиде представлено на рис. 3. Для них также первую позицию при повышенных температурах занимает первый хлорокомплекс, концентрация которого у неодима и самария с понижением температуры уменьшается примерно на 2,5 порядка, как и общая их концентрация, тогда как у гадолиния она держится на одном уровне во всем температурном интервале

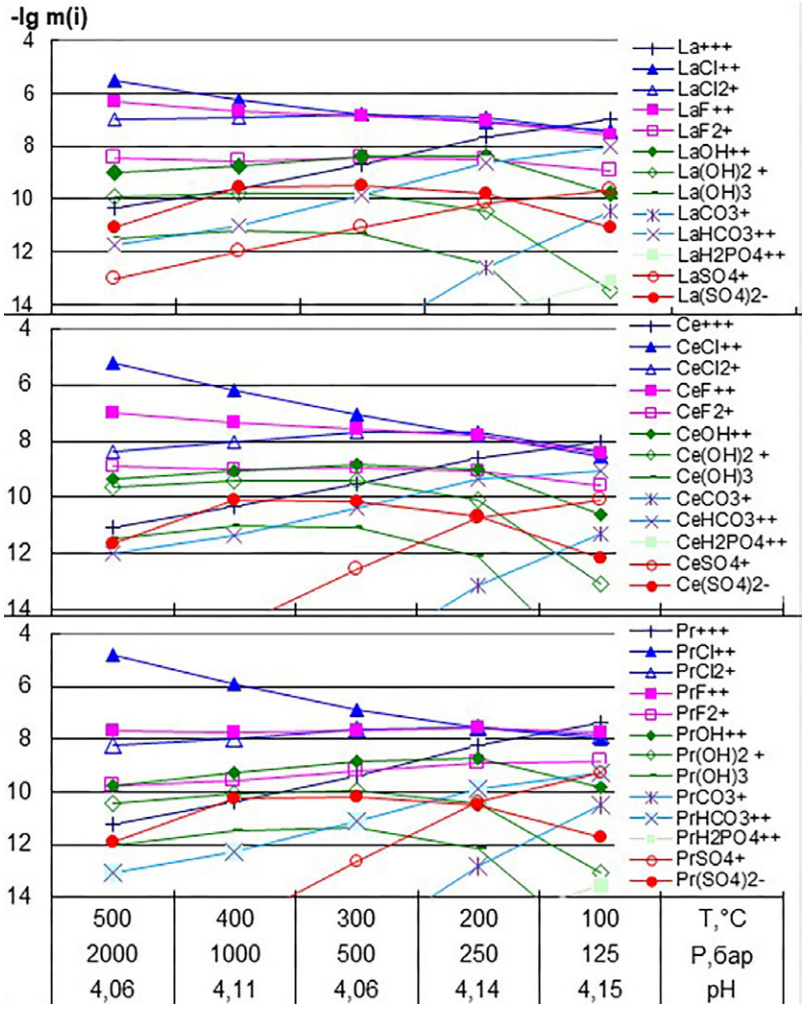


**Рис. 2.** Распределение по формам представителей легких РЗЭ (ЛРЗЭ) в слабокислом фторидно-карбонатно-хлоридном охлаждающемся флюиде (см. рис. 1). Здесь и далее $m(i)$ – концентрация в моляльности (моль/кг $H_2O$) каждой частицы, показанной в легенде.

и вплоть до температуры 200 °C концентрация первого хлорокомплекса оказывается соизмеримой с концентрациями вторых хлоро- и фторокомплексов.

У неодима и самария при 500–400 °C вторую позицию занимают их первые фторокомплексы, но у самария появляется дисульфатный комплекс $Sm(SO_4)_2^-$. У неодима при этих температурах дисульфатный комплекс занимает четвертое место по значимости после второго хлорокомплекса. С понижением температуры концентрация дисульфатного комплекса обоих лантаноидов резко падает и в балансе общей концентрации этих элементов уже не имеет значения. В интервале 200–100 °C возрастает роль первого фторокомплекса, а концентрация второго хлорокомплекса в этом интервале уменьшается от неодима к самарию и гадолинию, но при 100 °C на первое место у всех трех лантаноидов выходит форма $Ln^{+3}$.

Формы переноса тербия, диспрозия и эрбия – представителей тяжелых лантаноидов (ТРЗЭ) отображает рис. 4, и здесь картина резко меняется. У Tb до 200 °C, а у Dy до 300 °C главными комплексами оказываются $LnSO_4^+$, концентрации которых резко превышают (у тербия при 500–400 °C на целых 4 порядка) концентрации прочих форм в равновесном слабокислом флюиде. У тербия затем идут первый фторокомплекс, первый и второй хлорокомплексы, но вплоть до 200 °C на уровне $10^{-12}m$ и только при 100 °C на первое место выходит частица $Tb^{+3}$, за нею следуют по порядку первые фторо- и хлорокомплексы, и затем вторые фторо- и хлорокомплексы. У диспрозия в интервале 500–300 °C на второе место (но уже значимое – около $10^{-9,5}m$) также выходит

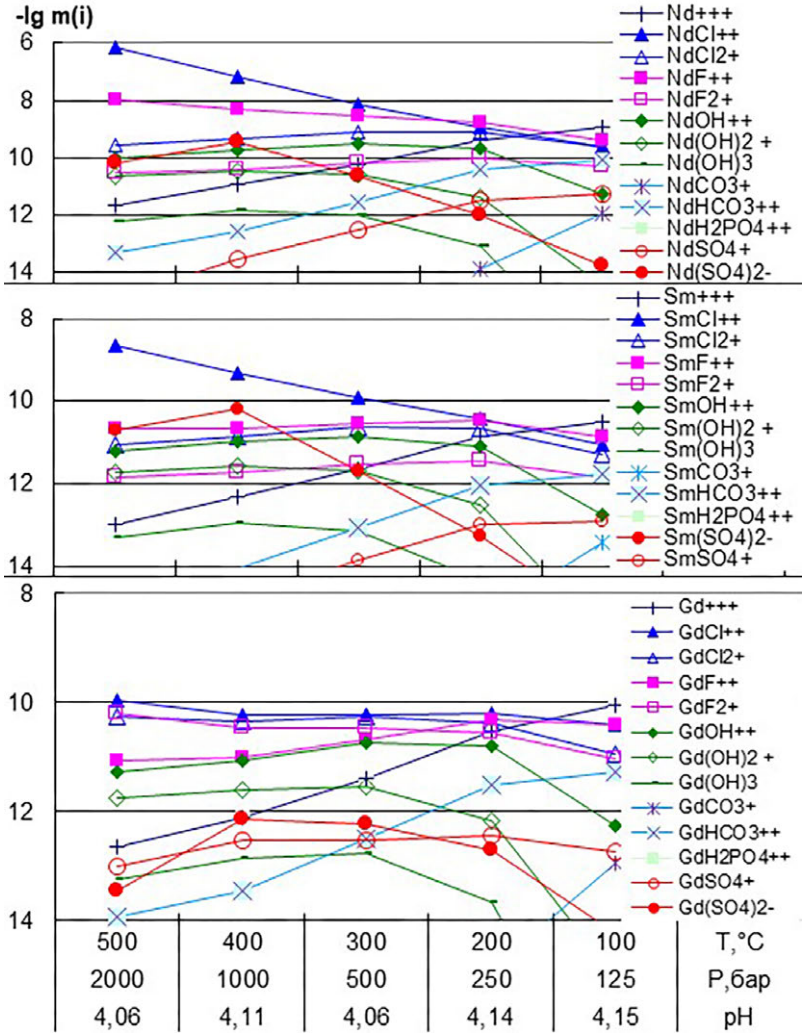


**Рис. 3.** Распределение по формам Nd, Sm и Gd в слабокислом фторидно-карбонатно-хлоридном охлаждающемся флюиде (см. рис. 1).

фторокомплекс, и на порядок ниже идут вместе первый и второй хлорокомплексы. При 200 градусах второй фторокомплекс выходит на первое место, и далее за ним близко следуют первые хлоро-, фторокомплексы и второй хлорокомплекс, с концентрацией которого сравнивается концентрация $Dy^{+3}$. При 100 °C порядок следования форм у диспрозия такой же как у тербия. У эрбия картина распределения его по формам в слабокислом флюиде отличается от тербия и диспрозия тем, что с понижением температуры общая концентрация его во флюиде возрастает, и на первом месте оказывается второй фторокомплекс от 500 вплоть до 200 °C. В этом же интервале последовательно идут первый и второй хлорокомплексы, при этом последний при 200 °C уступает место второму фторокомплексу и частице $Er^{+3}$. При 100 °C порядок следования форм у эрбия такой же как у тербия и диспрозия.

В целом можно видеть, что с повышением атомного номера лантаноида ведущая форма – первый хлорокомплекс для ЛРЗЭ – постепенно уступает место второму фторокомплексу $LnF_2^+$, но при 100 °C у всех лантаноидов на первое место выходит форма $Ln^{+3}$, затем идут первые фторо- и хлорокомплексы, и далее вторые фторо- и хлорокомплексы. Несмотря на низкую концентрацию сульфат-иона во флюиде, для тербия и диспрозия на первое место выходит моносульфатный комплекс. Из рисунков 2–4 можно видеть, что остальные из принятых в качестве возможных форм переноса (карбонатные, фосфатные и гидрокарбонатные комплексы) не играют существенной роли в транспорте РЗЭ слабокислым флюидом.

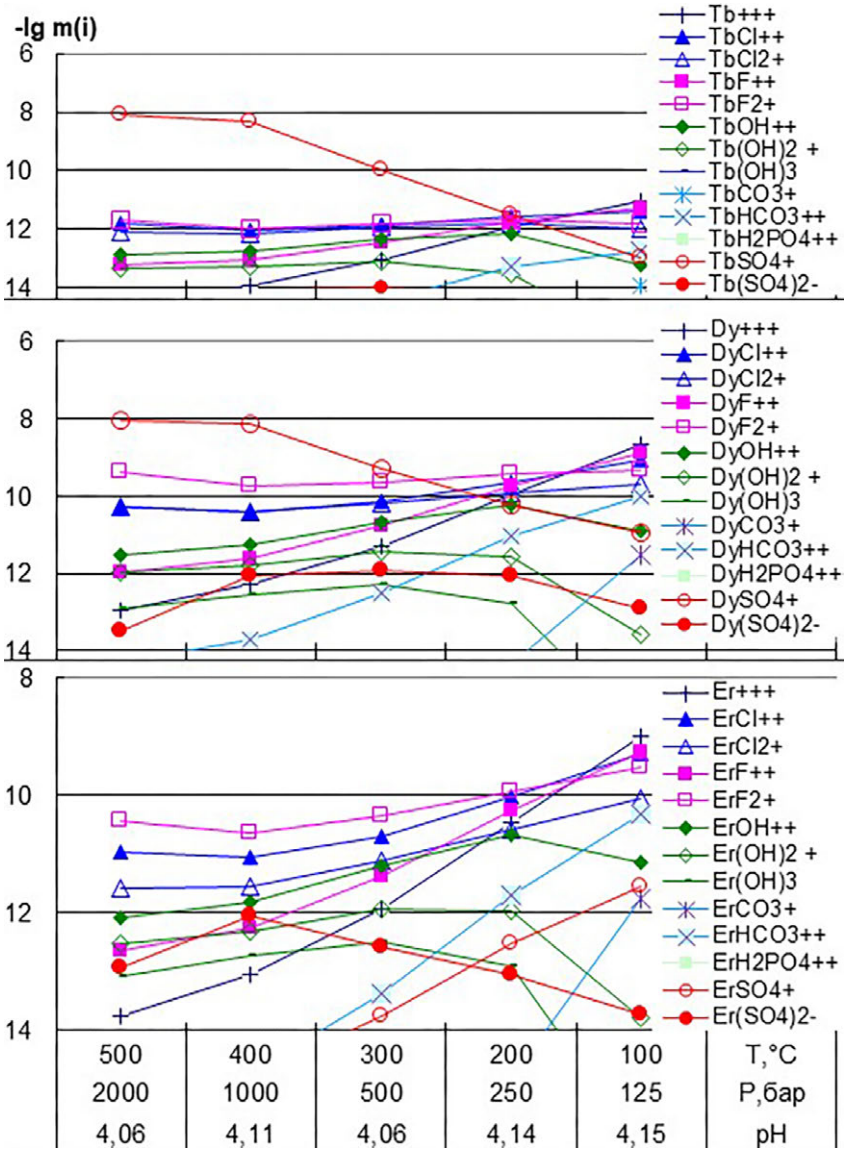


**Рис. 4.** Распределение по формам представителей тяжелых РЗЭ (ТРЗЭ) в слабокислом фторидно-карбонатно-хлоридном охлаждающемся флюиде (см. рис. 1).

### *3.2. Расчеты равновесий в слабощелочных условиях*

Соотношение количеств равновесных твердых фаз при воздействии на исследуемую ассоциацию слабощелочного (pH = 7,1) фторидно-карбонатно-хлоридного охлаждающегося флюида приведено на рис. 5. На левой оси ординат показано количество молей оставшегося неизрасходованным кальцита и новообразованного за счет него флюорита (сплошные линии). Их кривые оказываются зеркальным отображением друг друга; так при 300 и 200 °C получены несколько более высокие значения pH, что способствует сохранению исходного кальцита и одновременному уменьшению количества равновесного флюорита.

Правая ось ординат рис. 5 отражает количества неизрасходованного монацита и новообразованных РЗЭ-содержащего фторапатита, стронцианита ($SrCO_3$) и Sr-содержащего барита (штриховые линии). Хорошо видно, что при понижении температуры количество монацита несколько возрастает, тогда как концентрация фторапатита заметно уменьшается. Несмотря на низкое содержание в исходном составе системы, стронций при 200 и 100 °C выделяется в виде самостоятельной фазы – стронцианита, а при 100 °C еще и входит в состав Sr-содержащего барита. Таким образом, наличие

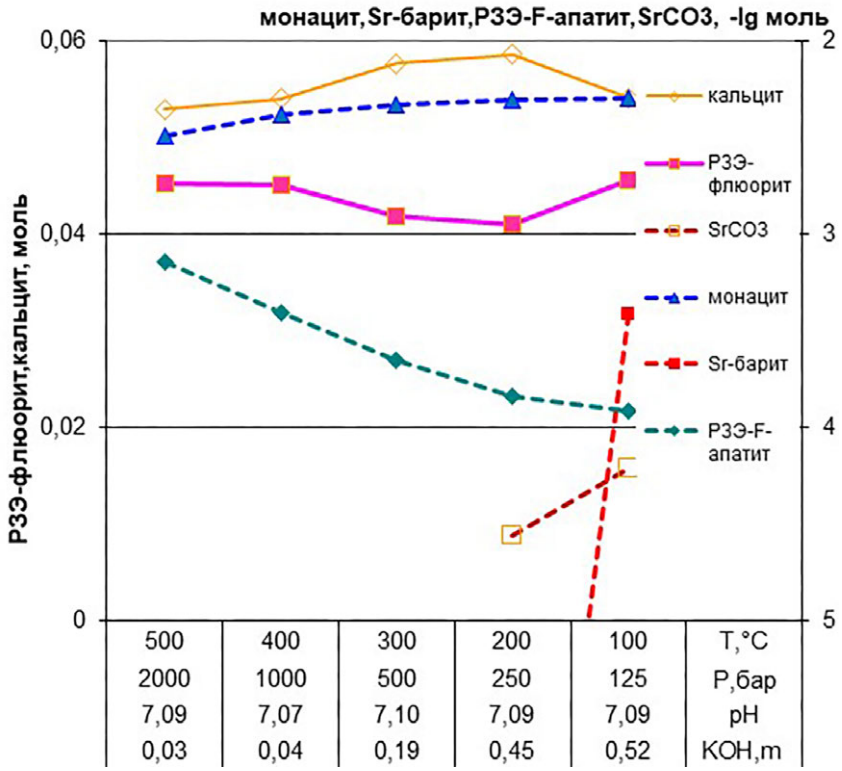


**Рис. 5.** Соотношение количеств равновесных твердых фаз в зависимости от *T*-*P*-X параметров системы при моделировании воздействия на ассоциацию монацит + кальцит + барит + целестин слабощелочного фторидно-карбонатно-хлоридного охлаждающегося флюида. Исходный состав системы: 0,1*m* $CaCO_3$ + $5\times10^{-3}m$ монацит + $10^{-3}m$ $BaSO_4$+ $10^{-4}m$ $SrSO_4$ + 1*m* NaCl + 0,5*m* $H_2CO_3$ + 0,1*m* HF + *m* KOH + 1 кг $H_2O$ (концентрацию KOH см. в подписи к оси абсцисс). РЗЭ-флюорит – РЗЭ-содержащий флюорит; РЗЭ-F-апатит – РЗЭ-содержащий фторапатит; Sr-барит – Sr-содержащий барит.

в природной минеральной ассоциации стронцианита можно расценивать как показатель повышенной щелочности рудообразующего флюида.

Формы нахождения лантаноидов в рассматриваемом варианте слабощелочного флюида отражены на рис. 6 избирательно: в качестве представителя ЛРЗЭ приведен празеодим, средних – гадолиний и ТРЗЭ – эрбий. Это обусловлено тем, что преобладающими формами для всех РЗЭ в слабощелочном варианте являются гидроксокомплексы $Ln(OH)^0_3 > Ln(OH)^+_2$. $Ln(OH)^{+2}$ занимает как правило четвертую позицию, а третьими по концентрации при высоких температурах оказываются для ЛРЗЭ первые хлоро- и фторокомплексы.

Начиная с 200 °C у празеодима происходит инверсия стехиометрии фторокомплексов: $PrF^+_2 > PrF^{+2}$, при этом концентрация хлорокомплекса резко понижается, и уже не вносит значимой доли в транспорт празеодима. К 100 °C концентрация его гидроксокомплексов также значительно понижается, и на первое место выходят фторокомплексы в соотношении: $PrF^+_2 > PrF^{+2}$. Между ними промежуточное место занимает карбонатный комплекс $PrCO^+_3$, концентрация которого резко возросла именно при 100 °C. Для средних (Gd) и тяжелых РЗЭ (Er) вплоть до 200 °C третью позицию после гидроксокомплексов занимает второй фторокомплекс $LnF^+_2$, который оказывается лидирующим при 100 °C, как и для празеодима. Следует заметить, что при 100 °C соотношение форм переноса для гадолиния аналогично таковому для празеодима, тогда как у эрбия между вторым и первым фторокомплексами оказываются с равными концентрациями карбонатный комплекс $ErCO^+_3$ и нейтральный гидроксокомплекс $Er(OH)^0_3$.

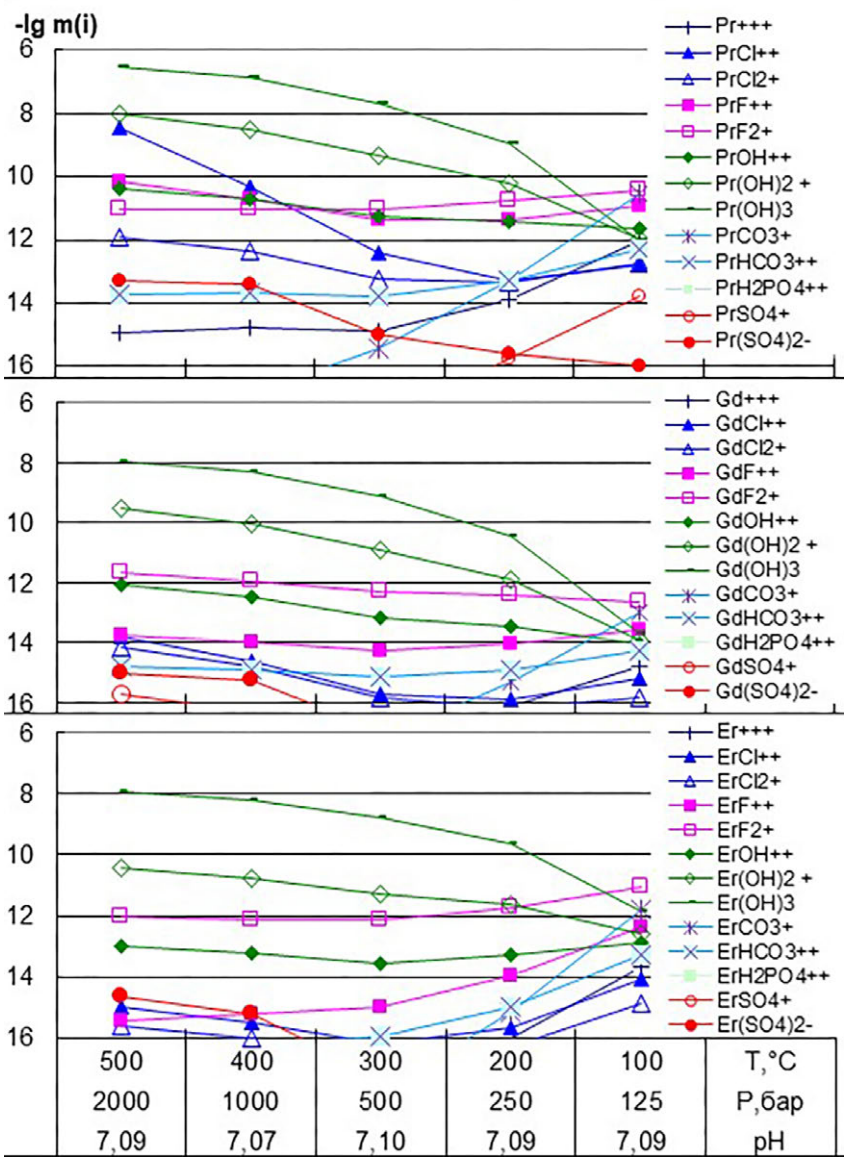


**Рис. 6.** Распределение по формам Pr, Gd и Er представителей легких, средних и тяжелых РЗЭ в слабощелочном фторидно-карбонатно-хлоридном охлаждающемся флюиде: 0,1$m$ $CaCO_3$+5×10$^{-3}$$m$ монацит+10$^{-3}$$m$ $BaSO_4$+ 10$^{-4}$$m$ $SrSO_4$ + 1$m$ NaCl + 0,5$m$ $H_2CO_3$ + 0,1$m$ HF + $m$ KOH + 1 кг $H_2O$ (концентрацию KOH см. в подписи к оси абсцисс рис. 5).

## 4. Обсуждение результатов

Обобщая вышесказанное, обратим внимание на то, что два варианта расчетов по кислотности-щелочности системы предположительно соответствуют моделированию воздействия двух типов флюидов: грейзенезирующего-слабокислого и карбонатитообразующего-слабощелочного. При этом нахождение в природных минеральных ассоциациях карбонатитовых месторождений РЗЭ стронцианита и кальцита [*Prokopyev et al.*, 2016; 2020] можно воспринимать как указание на повышенную щелочность рудообразующей среды.

Авторы исследования [*Tillberg et al.*, 2019], посвященного изучению фракционирования РЗЭ в грейзенах и связанной с ними жильной минерализации, приходят к выводу, что богатые хлором грейзеновые и жильные флюиды с температурой до 430 °C способствовали транспорту РЗЭ в виде хлоридных комплексов более устойчивых к ЛРЗЭ, чем к ТРЗЭ. Они также предполагают, что гидроксид не был значительным транспортным агентом на ранних стадиях грейзена, поскольку флюиды скорее всего имели низкий pH.

Это согласуется с результатами наших расчетов в слабокислых условиях: в области повышенных температур отчетливо прослеживается преобладание хлорокомплекса для легких РЗЭ и его подчиненная значимость для тяжелых лантаноидов (см. рис. 2 и 4).

Сопоставление результатов, представленных на рис. 2–4 показывает, что в слабокислых условиях рудообразования возможно фракционирование лантаноидов с преимущественным выносом легких и осаждением тяжелых РЗЭ во всем охваченном расчетами интервале температур. Так для легких РЗЭ при 500 °C ведущий хлорокомплекс обеспечивает концентрацию порядка $10^{-5}m$, а при 100 °C общая концентрация РЗЭ составляет около $10^{-8}m$ (рис. 2). Для представителей тяжелых лантаноидов Tb и Dy даже при 500–400 °C максимальная их концентрация составляет величину на 3 порядка ниже ($10^{-8}m$), а для Er во всем температурном интервале колеблется на уровне $10^{-10}$–$10^{-9}m$ (рис. 4).

В работе Лиу с соавторами [*Liu et al.*, 2018] приводится интересный материал по изучению флюидных включений в минералах карбонатитового F-РЗЭ месторождения Маониупинг (Maoniuping, Китай). Ими обнаружены кристалло-флюидные включения с сульфатсодержащими фазами, гомогенизация которых происходит при температуре 300–400 °C, при этом захват таких включений происходил при понижении температуры минералообразующей гидротермальной системы, вызывая одновременное понижение концентрации флюидов. Отмечается, что во включениях в низкотемпературном флюорите (110–230 °C) обнаруживается довольно низкая соленость порядка 0,9–1,4 мас.% NaCl-экв. К аналогичному выводу приходят авторы работы [*Zheng et al.*, 2021], предполагающие, что рудные флюиды эволюционировали от гидротермальной стадии I (фенитизация при высоких температурах ~480 °C), где они представляли собой высококонцентрированную высокотемпературную кислую флюидную систему (pH < 3,5), до гидротермальной стадии II (кристаллизация кальцита, кварца, барита и флюорита при температурах 300–350 °C) и солености ~20 мас.% NaCl-экв., а затем происходил переход на стадию кристаллизации РЗЭ минералов при температурах ~200 °C и низкой солености ~ 9 мас.% NaCl-экв. Результаты наших расчетов показывают, что устойчивость кальцита может свидетельствовать о повышенной щелочности флюидов, поэтому можно предположить, что на гидротермальной стадии II произошло повышение щелочности среды рудообразования. Распределение РЗЭ по формам в высококонцентрированном охлаждающемся хлоридно-сульфатно-карбонатном флюиде рассмотрено в нашей предыдущей работе [*Широносова и Прокопьев*, 2019].

В настоящей работе, посвященной распределению РЗЭ по формам в растворах умеренной концентрации, установлено, что в случае слабощелочного фторидно-карбонатно-хлоридного охлаждающегося флюида при температурах до 200 °C решающее значение имеют гидроксокомплексы. При этом в интервале температур 500–200 °C наблюдается превышение концентраций легких РЗЭ над тяжелыми на два порядка, что может свидетельствовать о преимущественном выносе легких РЗЭ по сравнению с тяжелыми при повышенных $T$-$P$ параметрах рудообразования. На рис. 7 приведено сравнение суммарных концентраций РЗЭ в прореагировавших с твердофазовой ассоциацией равновесных слабокислых и слабощелочных флюидах. Хорошо видно, что слабокислые условия как в высокотемпературной, так и в области пониженных температур, более способствуют переходу РЗЭ во флюид по сравнению со слабощелочными флюидами, и только в среднетемпературных условиях рудоносность флюидов уравнивается.

В случае слабощелочного варианта можно предположить, что одним из недостатков моделирования является неучет вхождения лантаноидов в состав равновесного кальцита. Сравнение полученных результатов с экспериментальными данными показывает, что сделанное допущение не должно повлиять на конечный результат. Так, исследователи [*Perry and Gysi*, 2020] провели эксперименты по вхождению всего ряда лантаноидов в кальцит при 200 °C. По их данным наиболее совместимым с кальцитом оказывается лантан, и при 200 °C (согласно рис. 2 и 4 их статьи) его мольная доля в кальците составляет $3{\times}10^{-5}$. В нашем расчете количество кальцита при 200 °C (рис. 5) составляет $5{,}86{\times}10^{-2}$ моль, и в таком случае количество La в $CaCO_3$ должно составлять

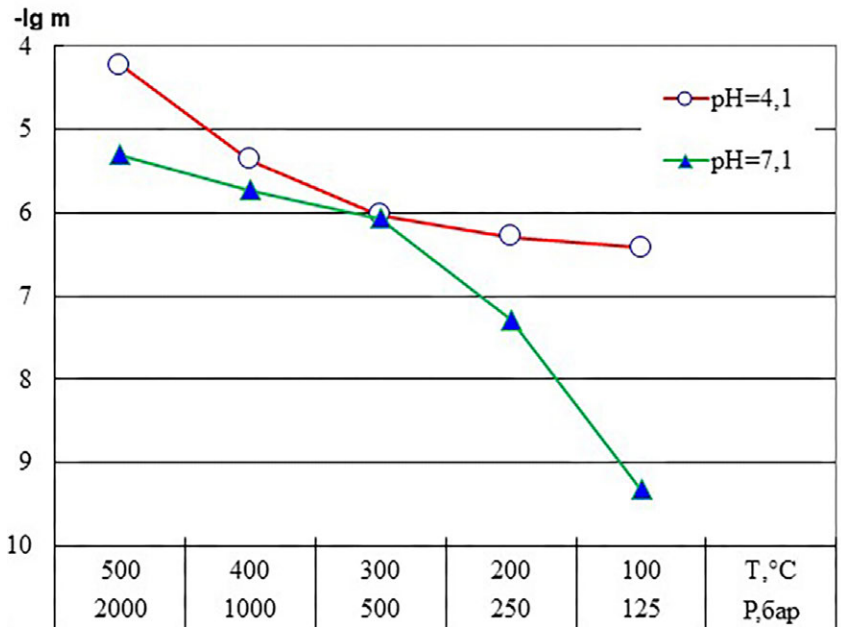


**Рис. 7.** Суммарная концентрация РЗЭ в равновесных слабокислом (pH = 4,1) и слабощелочном (pH = 7,1) флюидах в зависимости от $T$-$P$ параметров системы.

порядка $1{,}8\times10^{-6}$ моль. В наших расчетах при 200 °C pH = 7,09 общее содержание лантана составляет около $10^{-9}m$, при этом он осаждается преимущественно с монацитом ($1{,}24\times10^{-3}$ моль), меньше с РЗЭ-флюоритом ($8{,}2\times10^{-5}$ моль) и в пренебрежимо малом количестве с РЗЭ-фторапатитом ($2\times10^{-7}$ моль). Таким образом, на примере наиболее совместимого с кальцитом лантана, неучет соосаждения лантаноидов с кальцитом в нашем случае не должен сказаться на конечном результате расчетов.

Следует также оговориться, что резко превалирующая концентрация гидроксокомплексов в слабощелочном флюиде может оказаться завышенной, т.к. исходные термодинамические данные для них получены экстраполяцией от комнатных температур [*Haas et al.*, 1995]. Это вызывает необходимость дальнейших экспериментальных исследований устойчивости этих комплексов РЗЭ при повышенных температурах. В целом, полученные результаты показывают скорее основные тенденции изменения количеств равновесных твердых фаз в зависимости от $T$-$P$-$X$ параметров системы, т.к. точность расчетов ограничена использованием модели идеальных твердых растворов, которая в данном случае даёт первое приближение из-за отсутствия структурного соответствия между соответствующими конечными членами.

## 5. Заключение

С помощью проведенных термодинамических расчетов показано, что слабокислые условия как в высокотемпературной, так и в области пониженных температур, более способствуют накоплению РЗЭ во флюиде по сравнению со слабощелочными флюидами. В слабокислых условиях равновесная минеральная ассоциация представлена редкоземельным флюоритом, монацитом, редкоземельным фторапатитом и Sr-содержащим баритом. Установлено, что в слабокислом фторидно-карбонатно-хлоридном охлаждающемся флюиде наблюдается большая устойчивость хлоридных комплексов ЛРЗЭ, чем ТРЗЭ. Отметим, что в слабокислом варианте флюида даже при 100 °C карбонатный и гидрокарбонатный комплексы не вносят существенного вклада в общую концентрацию лантаноидов в растворе.

В случае слабощелочного варианта условий системы равновесная минеральная ассоциация представлена монацитом, РЗЭ-флюоритом, РЗЭ-фторапатитом, кальцитом, Sr-содержащим баритом и стронцианитом. Появление кальцита и стронцианита в природных ассоциациях может служить указанием на повышенную щелочность среды

рудообразования. В равновесном слабощелочном флюиде вплоть до 200 °C для всех РЗЭ превалирующими оказываются гидроксокомплексы при соотношении $Ln(OH)_3^0 > Ln(OH)_2^+$. К 100 °C концентрация гидроксокомплексов значительно понижается, и на первое место выходят фторокомплексы в соотношении: $LnF_2^+ > LnF^{+2}$. Фосфатные комплексы в исследованных условиях во всем температурном интервале не вносят вклада в транспорт РЗЭ, также как гидрокарбонатный и карбонатный комплексы при повышенных температурах, но исходные термодинамические данные для них получены экстраполяцией от комнатных температур [*Haas et al.*, 1995].

**Благодарности.** Авторы благодарны рецензентам за ценные замечания, что позволило улучшить качество работы. Работа выполнена в рамках государственного задания ИГМ СО РАН (122041400241-5). Численные эксперименты в щелочных системах проведены за счет средств гранта РНФ 22-17-00078.

**Список литературы**

Степанчикова С. А., Битейкина Р. П., Широносова Г. П. *и др.* Экспериментальное изучение поведения гидроксидных комплексов в близнейтральных и щелочных растворах редкоземельных элементов и иттрия при 25 °C // Геология и геофизика. — 2014. — Т. 55, № 8. — С. 1188—1193.

Широносова Г. П., Прокопьев И. Р. Термодинамическое моделирование распределения РЗЭ+Y по формам в охлаждающихся богатых сульфатной серой флюидах // Известия Томского политехнического университета. Инжиниринг георесурсов. — 2019. — Т. 330, № 11. — С. 7—18. — DOI: 10.18799/24131830/2019/11/2343.

Gysi A. P., Harlov D., Filho D. C., *et al.* Experimental determination of the high temperature heat capacity of a natural xenotime-(Y) solid solution and synthetic DyPO4 and ErPO4 endmembers // Thermochimica Acta. — 2016. — Vol. 627–629. — P. 61–67. — DOI: 10.1016/j.tca.2016.01.016.

Gysi A. P., Williams-Jones A. E., Harlov D. The solubility of xenotime-(Y) and other HREE phosphates ($DyPO_4$, $ErPO_4$ and $YbPO_4$) in aqueous solutions from 100 to 250 °C and $p_{sat}$ // Chemical Geology. — 2015. — Vol. 401. — P. 83–95. — DOI: 10.1016/j.chemgeo.2015.02.023.

Haas J. R., Shock E. L., Sassani D. C. Rare earth elements in hydrothermal systems: Estimates of standard partial molal thermodynamic properties of aqueous complexes of the rare earth elements at high pressures and temperatures // Geochimica et Cosmochimica Acta. — 1995. — Vol. 59, no. 21. — P. 4329–4350. — DOI: 10.1016/0016-7037(95)00314-P.

Hatch G. P. Dynamics in the Global Market for Rare Earths // Elements. — 2012. — Vol. 8, no. 5. — P. 341–346. — DOI: 10.2113/gselements.8.5.341.

Johnson J. W., Oelkers E. H., Helgeson H. C. SUPCRT92: a software package for calculating the standard molal thermodynamic properties of minerals, gases, aqueous species, and reactions from 1 to 5000 bar and 0 to 1000 °C // Computers & Geosciences. — 1992. — Vol. 18, no. 7. — P. 899–947. — DOI: 10.1016/0098-3004(92)90029-q.

Li J., Liu C., Liu X., *et al.* Tantalum and niobium mineralization from F- and Cl-rich fluid in the lepidolite-rich pegmatite from the Renli deposit in northern Hunan, China: Constraints of fluid inclusions and lepidolite crystallization experiments // Ore Geology Reviews. — 2019. — Vol. 115. — P. 103187. — DOI: 10.1016/j.oregeorev.2019.103187.

Liu Y., Chakhmouradian A. R., Hou Z., *et al.* Development of REE mineralization in the giant Maoniuping deposit (Sichuan, China): insights from mineralogy, fluid inclusions, and trace-element geochemistry // Mineralium Deposita. — 2018. — Vol. 54, no. 5. — P. 701–718. — DOI: 10.1007/s00126-018-0836-y.

Migdisov A. A., Williams-Jones A. E. Hydrothermal transport and deposition of the rare earth elements by fluorine-bearing aqueous liquids // Mineralium Deposita. — 2014. — Vol. 49, no. 8. — P. 987–997. — DOI: 10.1007/s00126-014-0554-z.

Migdisov A. A., Williams-Jones A. E., Wagner T. An experimental study of the solubility and speciation of the Rare Earth Elements (III) in fluoride- and chloride-bearing aqueous solutions at temperatures up to 300 °C // Geochimica et Cosmochimica Acta. — 2009. — Vol. 73, no. 23. — P. 7087–7109. — DOI: 10.1016/j.gca.2009.08.023.

Migdisov A. A., Williams-Jones A., Brugger J., *et al.* Hydrothermal transport, deposition, and fractionation of the REE: Experimental data and thermodynamic calculations // Chemical Geology. — 2016. — Vol. 439. — P. 13–42. — DOI: 10.1016/j.chemgeo.2016.06.005.

Mitchell R. H., Smith D. L. Geology and mineralogy of the Ashram Zone carbonatite, Eldor Complex, Quebec // Ore Geology Reviews. — 2017. — Vol. 86. — P. 784–806. — DOI: 10.1016/j.oregeorev.2017.04.004.

Nikolenko A. M., Redina A. A., Doroshkevich A. G., *et al.* The origin of magnetite-apatite rocks of Mushgai-Khudag Complex, South Mongolia: mineral chemistry and studies of melt and fluid inclusions // Lithos. — 2018. — Vol. 320/321. — P. 567–582. — DOI: 10.1016/j.lithos.2018.08.030.

Perry E., Gysi A. P. Hydrothermal calcite-fluid REE partitioning experiments at 200 °C and saturated water vapor pressure // Geochimica et Cosmochimica Acta. — 2020. — Vol. 286. — P. 177–197. — DOI: 10.1016/j.gca.2020.07.018.

Perry E. P., Gysi A. P. Rare Earth Elements in Mineral Deposits: Speciation in Hydrothermal Fluids and Partitioning in Calcite // Geofluids. — 2018. — Vol. 2018. — P. 1–19. — DOI: 10.1155/2018/5382480.

Prokopyev I., Borisenko A., Borovikov A., *et al.* Origin of REE-rich ferrocarbonatites in southern Siberia (Russia): implications based on melt and fluid inclusions // Mineralogy and Petrology. — 2016. — Vol. 110, no. 6. — P. 845–859. — DOI: 10.1007/s00710-016-0449-z.

Prokopyev I., Doroshkevich A., Redina A. Brine-Melts and Fluids of the Fe-F-P-(Ba)-(Sr)-REE Central Asian Carbonatite Province (Southern Siberia and Mongolia): The Petrogenetic Aspects // Minerals. — 2023. — Vol. 13, no. 4. — P. 573. — DOI: 10.3390/min13040573.

Prokopyev I., Kozlov E., Fomina E., *et al.* Mineralogy and Fluid Regime of Formation of the REE-Late-Stage Hydrothermal Mineralization of Petyayan-Vara Carbonatites (Vuoriyarvi, Kola Region, NW Russia) // Minerals. — 2020. — Vol. 10, no. 5. — P. 405. — DOI: 10.3390/min10050405.

Robie R. A., Hemingway B. S. Thermodynamic properties of minerals and related substances at 298.15 K and 1 bar ($10^5$ pascals) pressure and at higher temperatures : tech. rep. — 1995. — DOI: 10.3133/b2131.

Shock E. L., Sassani D. C., Willis M., *et al.* Inorganic species in geologic fluids: Correlations among standard molal thermodynamic properties of aqueous ions and hydroxide complexes // Geochimica et Cosmochimica Acta. — 1997. — Vol. 61, no. 5. — P. 907–950. — DOI: 10.1016/S0016-7037(96)00339-0.

Shu X., Liu Y. Fluid inclusion constraints on the hydrothermal evolution of the Dalucao Carbonatite-related REE deposit, Sichuan Province, China // Ore Geology Reviews. — 2019. — Vol. 107. — P. 41–57. — DOI: 10.1016/j.oregeorev.2019.02.014.

Shvarov Y. V. HCh: New potentialities for the thermodynamic simulation of geochemical systems offered by windows // Geochemistry International. — 2008. — Т. 46, № 8. — С. 834—839. — DOI: 10.1134/S0016702908080089. — URL: https://doi.org/10.1134/S0016702908080089.

Shvarov Y. V., Bastrakov E. N. HCh: a Software Package for Geochemical Equilibrium Modeling: User's Guide. — Australian Geological Survey Organisation, 1999.

Sverjensky D. A., Shock E. L., Helgeson H. C. Prediction of the thermodynamic properties of aqueous metal complexes to 1000 °C and 5 kb // Geochimica et Cosmochimica Acta. — 1997. — Vol. 61, no. 7. — P. 1359–1412. — DOI: 10.1016/s0016-7037(97)00009-4.

Tagirov B. R., Zotov A. V., Akinfiev N. N. Experimental study of dissociation of HCl from 350 to 500 °C and from 500 to 2500 bars: Thermodynamic properties of HCl°(aq) // Geochimica et Cosmochimica Acta. — 1997. — Vol. 61, no. 20. — P. 4267–4280. — DOI: 10.1016/s0016-7037(97)00274-3.

Tillberg M., Maskenskaya O. M., Drake H., *et al.* Fractionation of Rare Earth Elements in Greisen and Hydrothermal Veins Related to A-Type Magmatism // Geofluids. — 2019. — Vol. 2019. — P. 1–20. — DOI: 10.1155/2019/4523214.

Xing Y., Etschmann B., Liu W., *et al.* The role of fluorine in hydrothermal mobilization and transportation of Fe, U and REE and the formation of IOCG deposits // Chemical Geology. — 2019. — Vol. 504. — P. 158–176. — DOI: 10.1016/j.chemgeo.2018.11.008.

Yu G.-Y., Li S.-D., Wang Y.-C., *et al.* Fluid Evolution and Ore Genesis of the Qibaoshan Polymetallic Ore Field, Shandong Province, China: Constraints from Fluid Inclusions and H-O-S Isotopic Compositions // Minerals. — 2019. — Vol. 9, no. 7. — P. 394. — DOI: 10.3390/min9070394.

Zheng X., Liu Y., Zhang L. The role of sulfate-, alkali-, and halogen-rich fluids in mobilization and mineralization of rare earth elements: Insights from bulk fluid compositions in the Mianning-Dechang carbonatite-related REE belt, southwestern China // Lithos. — 2021. — Vol. 386/387. — P. 106008. — DOI: 10.1016/j.lithos.2021.106008.

Russian Journal of Earth Sciences

# REE Speciation in Fluoride-Carbonate-Chloride Cooling Hydrothermal Fluids in the Presence of Barite and Celestine (Thermodynamic Modeling)

**Galina Shironosova** **,[1], **Ilya Prokopyev** [1,2]

[1]Sobolev Institute of Geology and Mineralogy SB RAS, Novosibirsk, Russia
[2]Novosibirsk State University, Novosibirsk, Russia
****Correspondence to:** Galina P. Shironosova, shiron@igm.nsc.ru

A thermodynamic study was carried out in order to determine the forms of transport for the entire series of lanthanides and their ratio with changing parameters of a hydrothermal fluid of moderate concentrations of chloride, carbonate and fluoride components. Hydrothermal solution, cooling from 500 to 100 °C, affected barite and celestine, which are used as a source of sulfate sulfur, monazite as a source of rare earth elements (REE) and phosphorus, and calcite as a source of calcium. It has been established that, under weakly acidic (pH about 4.1) conditions, the equilibrium mineral association is represented by rare earth fluorite, monazite, rare earth fluorapatite, and strontiobarite. In the high-temperature region for light and medium REE, the leading is the first chlorocomplex $LnCl^{+2}$. For heavy REE, the second fluorine complex $LnF_2^+$ takes the first place, except for terbium and dysprosium, for which a sharp predominance of the sulfate complex is revealed. A special picture is observed at 100 °C: the leading position is occupied by $Ln^{+3}$ for both light and heavy REE. In the case of a near neutral weakly alkaline fluid (pH about 7.1), the equilibrium mineral association is represented by calcite, monazite, REE-fluorite, REE-fluorapatite, strontiobarite, and strontianite. The appearance of the latter in natural associations may serve as an indication of the increased alkalinity of the ore-forming environment. In an equilibrium weakly alkaline fluid up to 200 °C, hydroxocomplexes are prevalent for all REEs with the ratio $Ln(OH)_3^0 > Ln(OH)_2^+$. The first chloro complex for light REE at 500–400 °C, and the second fluoro complex for medium and heavy REEs follow them. At 100 °C, the concentration of hydroxocomplexes sharply decreases, and fluorine and carbonate complexes come to the fore. In general, there is an increased stability of the first chlorocomplex in the high-temperature region, and with decreasing temperature, the role of REE fluorocomplexes increases. Two variants of acidity-alkalinity calculations presumably correspond to modeling of two types of fluids: greisenizing – weakly acidic and carbonatite-forming – weakly alkaline.

**Keywords:** lanthanides, transport forms, hydrothermal fluids, monazite, rare earth fluorite, rare earth fluorapatite, barite, celestine, strontianite

Recieved: 11 January 2022
Accepted: 3 July 2023
Published: 30 December 2023

**Citation:** Shironosova, Galina, and Prokopyev, Ilya (2023), REE Speciation in Fluoride-Carbonate-Chloride Cooling Hydrothermal Fluids in the Presence of Barite and Celestine (Thermodynamic Modeling), *Russian Journal of Earth Sciences*, 23, ES5009, https://doi.org/10.2205/2023ES000859 EDN: IGMQVP

© 2023. The Authors.

**References**

Gysi A. P., Harlov D., Filho D. C., *et al.* Experimental determination of the high temperature heat capacity of a natural xenotime-(Y) solid solution and synthetic DyPO4 and ErPO4 endmembers // Thermochimica Acta. — 2016. — Vol. 627–629. — P. 61–67. — DOI: 10.1016/j.tca.2016.01.016.

Gysi A. P., Williams-Jones A. E., Harlov D. The solubility of xenotime-(Y) and other HREE phosphates (DyPO4, ErPO4 and YbPO4) in aqueous solutions from 100 to 250°C and $p_{sat}$ // Chemical Geology. — 2015. — Vol. 401. — P. 83–95. — DOI: 10.1016/j.chemgeo.2015.02.023.

Haas J. R., Shock E. L., Sassani D. C. Rare earth elements in hydrothermal systems: Estimates of standard partial molal thermodynamic properties of aqueous complexes of the rare earth elements at high pressures and temperatures // Geochimica et Cosmochimica Acta. — 1995. — Vol. 59, no. 21. — P. 4329–4350. — DOI: 10.1016/0016-7037(95)00314-P.

Hatch G. P. Dynamics in the Global Market for Rare Earths // Elements. — 2012. — Vol. 8, no. 5. — P. 341–346. — DOI: 10.2113/gselements.8.5.341.

Johnson J. W., Oelkers E. H., Helgeson H. C. SUPCRT92: a software package for calculating the standard molal thermodynamic properties of minerals, gases, aqueous species, and reactions from 1 to 5000 bar and 0 to 1000 °C // Computers & Geosciences. — 1992. — Vol. 18, no. 7. — P. 899–947. — DOI: 10.1016/0098-3004(92)90029-q.

Li J., Liu C., Liu X., *et al.* Tantalum and niobium mineralization from F- and Cl-rich fluid in the lepidolite-rich pegmatite from the Renli deposit in northern Hunan, China: Constraints of fluid inclusions and lepidolite crystallization experiments // Ore Geology Reviews. — 2019. — Vol. 115. — P. 103187. — DOI: 10.1016/j.oregeorev.2019.103187.

Liu Y., Chakhmouradian A. R., Hou Z., *et al.* Development of REE mineralization in the giant Maoniuping deposit (Sichuan, China): insights from mineralogy, fluid inclusions, and trace-element geochemistry // Mineralium Deposita. — 2018. — Vol. 54, no. 5. — P. 701–718. — DOI: 10.1007/s00126-018-0836-y.

Migdisov A., Williams-Jones A., Brugger J., *et al.* Hydrothermal transport, deposition, and fractionation of the REE: Experimental data and thermodynamic calculations // Chemical Geology. — 2016. — Vol. 439. — P. 13–42. — DOI: 10.1016/j.chemgeo.2016.06.005.

Migdisov A. A., Williams-Jones A. E. Hydrothermal transport and deposition of the rare earth elements by fluorine-bearing aqueous liquids // Mineralium Deposita. — 2014. — Vol. 49, no. 8. — P. 987–997. — DOI: 10.1007/s00126-014-0554-z.

Migdisov A. A., Williams-Jones A. E., Wagner T. An experimental study of the solubility and speciation of the Rare Earth Elements (III) in fluoride- and chloride-bearing aqueous solutions at temperatures up to 300 °C // Geochimica et Cosmochimica Acta. — 2009. — Vol. 73, no. 23. — P. 7087–7109. — DOI: 10.1016/j.gca.2009.08.023.

Mitchell R. H., Smith D. L. Geology and mineralogy of the Ashram Zone carbonatite, Eldor Complex, Quebec // Ore Geology Reviews. — 2017. — Vol. 86. — P. 784–806. — DOI: 10.1016/j.oregeorev.2017.04.004.

Nikolenko A. M., Redina A. A., Doroshkevich A. G., *et al.* The origin of magnetite-apatite rocks of Mushgai-Khudag Complex, South Mongolia: mineral chemistry and studies of melt and fluid inclusions // Lithos. — 2018. — Vol. 320/321. — P. 567–582. — DOI: 10.1016/j.lithos.2018.08.030.

Perry E., Gysi A. P. Hydrothermal calcite-fluid REE partitioning experiments at 200 °C and saturated water vapor pressure // Geochimica et Cosmochimica Acta. — 2020. — Vol. 286. — P. 177–197. — DOI: 10.1016/j.gca.2020.07.018.

Perry E. P., Gysi A. P. Rare Earth Elements in Mineral Deposits: Speciation in Hydrothermal Fluids and Partitioning in Calcite // Geofluids. — 2018. — Vol. 2018. — P. 1–19. — DOI: 10.1155/2018/5382480.

Prokopyev I., Doroshkevich A., Redina A. Brine-Melts and Fluids of the Fe-F-P-(Ba)-(Sr)-REE Central Asian Carbonatite Province (Southern Siberia and Mongolia): The Petrogenetic Aspects // Minerals. — 2023. — Vol. 13, no. 4. — P. 573. — DOI: 10.3390/min13040573.

Prokopyev I., Kozlov E., Fomina E., *et al.* Mineralogy and Fluid Regime of Formation of the REE-Late-Stage Hydrothermal Mineralization of Petyayan-Vara Carbonatites (Vuoriyarvi, Kola Region, NW Russia) // Minerals. — 2020. — Vol. 10, no. 5. — P. 405. — DOI: 10.3390/min10050405.

Prokopyev I. R., Borisenko A. S., Borovikov A. A., *et al.* Origin of REE-rich ferrocarbonatites in southern Siberia (Russia): implications based on melt and fluid inclusions // Mineralogy and Petrology. — 2016. — Vol. 110, no. 6. — P. 845–859. — DOI: 10.1007/s00710-016-0449-z.

Robie R. A., Hemingway B. S. Thermodynamic properties of minerals and related substances at 298.15 K and 1 bar ($10^5$ pascals) pressure and at higher temperatures : tech. rep. — 1995. — DOI: 10.3133/b2131.

Shironosova G. P., Prokopyev I. R. Thermodynamic modeling of REE + Y speciation in cooling sulfate-rich fluids // Bulletin of the Tomsk Polytechnic University. Geo Assets Engineering. — 2019. — Vol. 330, no. 11. — P. 7–18. — DOI: 10.18799/24131830/2019/11/2343.

Shock E. L., Sassani D. C., Willis M., *et al.* Inorganic species in geologic fluids: Correlations among standard molal thermodynamic properties of aqueous ions and hydroxide complexes // Geochimica et Cosmochimica Acta. — 1997. — Vol. 61, no. 5. — P. 907–950. — DOI: 10.1016/S0016-7037(96)00339-0.

Shu X., Liu Y. Fluid inclusion constraints on the hydrothermal evolution of the Dalucao Carbonatite-related REE deposit, Sichuan Province, China // Ore Geology Reviews. — 2019. — Vol. 107. — P. 41–57. — DOI: 10.1016/j.oregeorev.2019.02.014.

Shvarov Y. V. HCh: New potentialities for the thermodynamic simulation of geochemical systems offered by windows // Geochemistry International. — 2008. — Vol. 46, no. 8. — P. 834–839. — DOI: 10.1134/s0016702908080089.

Shvarov Y. V., Bastrakov E. HCh: a Software Package for Geochemical Equilibrium Modeling: User's Guide. — Australian Geological Survey Organisation, 1999.

Stepanchikova S. A., Biteikina R. P., Shironosova G. P., *et al.* An experimental study of hydroxo complex formation in basic and near-neutral solutions of rare-earth elements and yttrium at 25 °C // Russian Geology and Geophysics. — 2014. — Vol. 55, no. 8. — P. 1188–1193.

Sverjensky D. A., Shock E. L., Helgeson H. C. Prediction of the thermodynamic properties of aqueous metal complexes to 1000 °C and 5 kb // Geochimica et Cosmochimica Acta. — 1997. — Vol. 61, no. 7. — P. 1359–1412. — DOI: 10.1016/s0016-7037(97)00009-4.

Tagirov B. R., Zotov A. V., Akinfiev N. N. Experimental study of dissociation of HCl from 350 to 500°C and from 500 to 2500 bars: Thermodynamic properties of HCl°(aq) // Geochimica et Cosmochimica Acta. — 1997. — Vol. 61, no. 20. — P. 4267–4280. — DOI: 10.1016/s0016-7037(97)00274-3.

Tillberg M., Maskenskaya O. M., Drake H., *et al.* Fractionation of Rare Earth Elements in Greisen and Hydrothermal Veins Related to A-Type Magmatism // Geofluids. — 2019. — Vol. 2019. — P. 1–20. — DOI: 10.1155/2019/4523214.

Xing Y., Etschmann B., Liu W., *et al.* The role of fluorine in hydrothermal mobilization and transportation of Fe, U and REE and the formation of IOCG deposits // Chemical Geology. — 2019. — Vol. 504. — P. 158–176. — DOI: 10.1016/j.chemgeo.2018.11.008.

Yu G.-Y., Li S.-D., Wang Y.-C., *et al.* Fluid Evolution and Ore Genesis of the Qibaoshan Polymetallic Ore Field, Shandong Province, China: Constraints from Fluid Inclusions and H-O-S Isotopic Compositions // Minerals. — 2019. — Vol. 9, no. 7. — P. 394. — DOI: 10.3390/min9070394.

Zheng X., Liu Y., Zhang L. The role of sulfate-, alkali-, and halogen-rich fluids in mobilization and mineralization of rare earth elements: Insights from bulk fluid compositions in the Mianning-Dechang carbonatite-related REE belt, southwestern China // Lithos. — 2021. — Vol. 386/387. — P. 106008. — DOI: 10.1016/j.lithos.2021.106008.

Russian Journal of Earth Sciences

# New Data on the Mineral and Geochemical Composition of Bottom Sediments in the Tanatar Soda Lakes (Kulunda Plain, Russia)

**Ekaterina Ovdina[*,1], Vera Strakhovenko[1], Georgy Malov[1], Victor Malov[1], Emilia Solotchina[1]**

[1] V. S. Sobolev Institute of Geology and Mineralogy Siberian Branch of the Russian Academy of Sciences (IGM SB RAS), Novosibirsk, Russia

* **Correspondence to:** Ekaterina Ovdina, ovdina@igm.nsc.ru.

**Abstract:** The lakes of the Kulunda plain have long attracted the attention of researchers. A detailed geochemical testing of a chain of four small soda lakes of the Tanatar group allowed answering a number of questions. We used a complex of modern methods of mineralogy and geochemistry to update and add new data on the main phases of bottom sediments. The studied lakes have a pH ≥ 8 and a TDS of 2.1–41.5 g/L and a soda water composition. It has been established that over the past ~ 100 years there has been no change in the mineral composition of bottom sediments. The main phases of the bottom sediments consist of intermediate and high–Mg calcite and Ca-excess dolomite. Magnesite is presented only as a small impurity. The formation and accumulation of these minerals occur throughout the core of bottom sediments. According to received data, a change in the hydrological regime of the catchment area was established. The feeding regime of the lakes has been changed because of the drying up of the Rublevaya River.

**Keywords:** small soda lakes, bottom sediments, high-magnesium carbonates, Ca-excess dolomite, Tanatar lakes, Kulunda plain

**Citation:** Ovdina, E., V. Strakhovenko, G. Malov, V. Malov, and E. Solotchina (2023), New Data on the Mineral and Geochemical Composition of Bottom Sediments in the Tanatar Soda Lakes (Kulunda Plain, Russia), *Russian Journal of Earth Sciences*, 23, ES5010, EDN: AQPSSL, https://doi.org/10.2205/2023es000864

## Introduction

Historically, researchers have focused on bigger water bodies like oceans, seas and large lakes. Data of the ILEC World Lake Database [*International Lake Environment Committee Foundation (ILEC)*, 1999] shows that researchers around the world are still most interested in large lakes. The study of small inland lakes is getting more relevant according to the works from various fields of science [*Bartosiewicz et al.*, 2015; *Borzenko*, 2020; *Galbarczyk-Gąsiorowska et al.*, 2009; *Strakhovenko et al.*, 2014; *Zheng*, 2014].

Small lakes are open systems where is a clear relationship between sedimentation process and physical, chemical, geographical, and climatic conditions. Each component of the lake (water, sediments, soils, soil-forming substrate and biota) is connected to each other and is a subject to anthropogenic impact. The geochemical and mineral compositions of bottom sediments reflect the lake environment and the interplay of various factors inside and outside the reservoir. It makes lakes informative and important objects of research [*Hammer*, 1986; *Solotchina et al.*, 2019; *Stankevica et al.*, 2020; *Strakhovenko et al.*, 2014].

In the south of Western Siberia, the lake area percentage averages ~ 2% [*Izmailova and Korneenkova*, 2020]. Lakes are mainly small according to the classification by [*Ivanov*, 1948], shallow (up to 3–5 m deep) and drainless [*Savchenko*, 1997].

The water composition of the small lakes in the south of Western Siberia varies from bicarbonate magnesium-calcium freshwater (in the north, taiga zone) to sodium chloride brines (in the south, the steppe zone and the ribbon forest subzone). The meridional (from north to south) change in the ionic composition and total dissolved solids (TDS) of

Research Article

Received: 24 January 2023
Accepted: 20 July 2023
Published: 30 December 2023

**Copyright:** © 2023. The Authors. This article is an open access article distributed under the terms and conditions of the Creative Commons Attribution (CC BY) license (https://creativecommons.org/licenses/by/4.0/).

water is complicated by the presence of numerous small lakes with a bicarbonate-sodium (soda) water composition and an increased pH (> 8) [*Kolpakova et al.*, 2016; *Savchenko*, 1997; *Strakhov*, 1951; *Strakhovenko et al.*, 2019]. The influence of climatic and landscape conditions leads to a complex factors affecting on soda lakes water. It determines a wide range of the TDS in lake waters [*Kurnakov*, 1935; *Sorokin et al.*, 2015]. The Kulunda lakes take place in a cryoarid climate and are the only example of ultrahaline soda lakes in Russia [*Sapozhnikov et al.*, 2016].

For over 100 years, researchers in various fields of science have been interested in the group of Tanatar soda lakes, especially, Rublevo–Demkino–Tanatar-4–Tanatar-6. The 1930s can be considered as a certain frontier, when large-scale soil science, geomorphological, limnological, and biological and other studies began in 1931–1933 by the Kulunda expedition of the USSR Academy of Sciences for soda deposit exploration [*Kurnakov*, 1935]. The obtained results formed the work basis of many researchers, and many of the results are still relevant.

Further, it is worth noting the work of [*Nikol'skaya*, 1961]. In 1949–1954, she studied in detail the hydrochemistry of rivers and lakes of the Kulunda steppe, considered the issues of the salt formation in lakes and its relationship with the water composition and soil-forming processes [*Nikol'skaya*, 1961]. Her work presents data on the composition and physical and chemical parameters of water for more than 100 lakes, including the group of Tanatar soda lakes. In the bottom sediments of soda lakes, along with trona, mirabilite, halite, etc., calcium and magnesium carbonates were noted.

In the 1940–50s, the first data on the model system of soda lakes Rublevo–Demkino–Tanatar-4–Tanatar-6 of the Tanatar group were obtained by [*Strakhov*, 1951]. This lakes system considered as "natural laboratory" in which metamorphism of water of the same composition occurred under natural conditions. At that time, it gave new ideas about soda continental reservoirs and the processes occurring in them.

The first data on carbonate paragenesis in the sediments of soda lakes of the Tanatar group were obtained [*Strakhov*, 1951]. The study was both from an experimental point of view (experiments on the deposition of carbonate minerals from solutions corresponding to the waters of the studied lakes) and from the empirical (studies of sediments and lake water samples). The carbonate paragenesis in the sediments of soda lakes consisted of authigenic calcite, dolomite, and brucite (?). Along with carbonate minerals, Mg-silicates of the sepiolite-kerolite type were determined in the main phase of the bottom sediments. The obtained amount of magnesium silicates ranged from 3–4 to 22–24% of the total sediment [*Strakhov*, 1951].

Modern works on the Kulunda soda lakes are related to biodiversity and the functioning of microbial communities of aquatic and terrestrial systems and hydrology. Despite the extreme conditions in soda lakes, their inhabitants are characterized by high productivity and biological diversity [*Kompantseva et al.*, 2009; *Samylina et al.*, 2014; *Sapozhnikov et al.*, 2016; *Sorokin et al.*, 2015; *Zavarzin and Zhilina*, 2000]. However, the geochemistry and mineralogy of the sedimentary process is considered in a number of works, including the authors of this study [*Gas'kova et al.*, 2017; *Lebedeva (Verba) et al.*, 2008; *Ovdina et al.*, 2020].

The authigenic carbonates and, accordingly, carbonate sediments in water bodies are an important source of information for the paleoclimate reconstruction and have been a topic of discussion for many years [*Chagas et al.*, 2016; *Deelman*, 2011; *Fussmann et al.*, 2020; *Kelts and Hsü*, 1978; *Last et al.*, 2012; *Solotchin et al.*, 2017; *Strakhovenko et al.*, 2015]. The beginning of an integrated approach to the minerals study as an object of interaction between different (litho-, hydro-, bio-, etc.) geospheres was laid back in the first half of the 20th century in the works of [*Vernadsky*, 1927]. In the modern scientific world, the direct connection of the minerals formation with the physical, chemical and climatic conditions of the environment has already been irrefutably proved. In this regard, the mineral and, accordingly, the geochemical composition of the lacustrine bottom sediments can be used as a reliable highlighter of natural environment changes.

The work aims to identify the features of the mineral and geochemical composition of bottom sediments in the model lakes of the Tanatar system (Demkino–Rublevo–Tanatar-4–Tanatar-6) and to assess the environmental changes over the past ~ 100 years.

## Material and Methods

*Subject and Objects of Research*

The object of the study is a system of four small lakes (area ≤10 km$^2$, depth ≤5 m): Tanatar-6, Tanatar-4, Demkino and Rublevo (Figure 1). The study area (southwest of the Kulunda plain) belongs to the subboreal continental group and is an accumulative lowland plain. This is a regional scale alluvial fan. Its topography consist of parallel-elongated hill ranges and valleys between them. Sandy deposits constitute hills and valley bottoms. Because of it, there are ribbon forests grow on bands of sandy soil. There is a local redistribution of moisture and easily soluble salts. They flow from hill ranges into the space between them, where lakes are located due to the landscape features (parallel-elongated hill ranges 40–60 m high, 0.2 to 2 km wide and depressions of the northeastern extension).

The bottom sediments of the studied small lakes are organic-mineral bottom sediments (sapropel). The texture of sediment is massive, finely lumpy, and nutty-lumpy. Sometimes there are remnants of macrophytes and algae. The color of bottom sediments can be different: bluish-green, olive, tobacco-green, brown, and black. Bottom sediments have a strong smell of hydrogen sulfide. High density is a characteristic of the lower horizons. The moisture content (from top to bottom) varies from 98 to 70%. In all the studied lakes at the water–bottom sediment boundary, a dense suspension is formed, similar to fluffy layer [*Lein et al.*, 2011], gradually turning into liquid sapropel; the humidity of which is 98–99% [*Strakhovenko et al.*, 2014].




**Figure 1.** The layout of the studied Tanatar soda lake system: 1 – Tanatar-6; 2 – Tanatar-4; 3 – Demkino; 4 – Rublevo based on Yandex Maps. Yellow circles – sampling points of bottom sediments and water; pink star – the Mikhailovsky Chemical Reagents Plant.

We classified the sapropels in types by [*Korde*, 1969] and in classes and species (Table 1) according to [*Strakhovenko et al.*, 2014] based on mineral, geochemical and biological data.

The Lake Tanatar-4 sapropel is a planktonic species by the sort of dominant primary production that adds organic matter. Sapropel of Lakes Rublevo and Demkino is a planktonic-macrophytic species. In all the aforementioned lakes, sapropel belongs to the calcium class according to the Si/Ca ratio and to the mineral-organic type according to ash content. Sapropel of Lake Tanatar-6 also is a planktonic species, but it belongs to the

silicon class (Si>Ca). Ash content in Lake Tanatar-6 sapropel is quite high, and it belongs to the mineralized type.

**Table 1.** Classification of the studied small soda lakes sapropel by types, classes and species

| Type | Ash content (%) | Class | Species | Lake |
|---|---|---|---|---|
| mineral-organic | 50–70 | calcium | planktonic, planktonic-macrophytic | Tanatar-4, Rublevo, Demkino |
| mineralized | 70–85 | silicon | planktonic | Tanatar-6 |

*Methods*

Fieldwork was conducted in 2015 and 2019. Bottom sediment sampling (51 sample) (Table 2) was carried out in the center of the lake from the rubber boat using a cylindrical sampler (diameter 82 mm, length 120 cm) with a vacuum seal (Taifun Research and Production Association, Russia). Using a cylindrical sampler allowed us to collect stratigraphic sediment cores and keep the water-bottom sediment boundary undisturbed. The core of bottom sediments was tested in layers that were 5 cm thick to a depth up to 75 cm.

**Table 2.** Number of bottom sediment and water samples, core (cm) and water (m) depth

| Lake | Bottom sediments samples | Core depth, cm | Water samples | Water depth, m |
|---|---|---|---|---|
| Tanatar-6 | 11 | 55 | 4 | 0.8 |
| Tanatar-4 | 12 | 60 | 4 | 1.7 |
| Rublevo | 15 | 75 | 4 | 1.5 |
| Demkino | 13 | 65 | 4 | 1.5 |
| Spring-1 (near Tanatar) | – | – | 3 | – |
| Spring-2 (near Rublevo) | – | – | 3 | – |

The water samples (22) (Table 2) were taken in the center of the lake. We used plastic bottles of 1 and 0.5 L for determining the major and trace element composition, and 0.33 L glass bottles for determining the content of mercury. Physical and chemical variables of water were recorded *in situ* (pH, TDS) using an ANION-7000 portable liquid analyzer (Biomer, Novosibirsk, Russia).

Analytical studies of the lake components were conducted in the Analytical Center for multi-elemental and isotope research SB RAS, Novosibirsk. Major and trace elements were determined via atomic absorption using a Solaar M6 instrument equipped with a Zeeman and deuterium background corrector (Thermo Electron, Waltham, MA, USA). The major element composition was determined by X-ray fluorescence analysis (ARL-9900-XP, Applied Research Laboratories, Austin, TX, USA). The sample morphology, phase and elemental composition were determined using a scanning electron microscopy (SEM) (Mira 3 Tescan, Tescan, Brno-Kohoutovice, Czech Republic). The INCA Energy 300 program (Labspec 5) was used for quantitative chemical analysis with reference standards.

X-ray diffractometry (XRD) was used to determine sample mineral composition (ARLX'TRA, Thermo Fisher Scientific (Ecublens) SARL, Waltham, MA, USA) (emission CuK$\alpha$). For phase analysis, the samples were scanned in a range from 2° to 65° (2$\Theta$) with a step of 0.05°; the scanning time at the point was 3 s. For studying the XRD profiles of the sediment carbonate component, scanning was carried out in the range from 28° to 32° (2$\Theta$) with the same step, but a longer scanning time (15 s). The differential diagnostics of low-temperature calcite–dolomite carbonates presented certain difficulties due to their high dispersion (crystallite sizes < 10 μm). XRD analysis was performed using the most

intense reflections of hkl = 104 in the area of angles 28–32° 2Θ CuKα for trigonal carbonates. The values of the $d_{104}$ interplane distances ranged from 3.036 Å Å (calcite) to 2.887 Å (stoichiometric dolomite) and are as a magnesium measure of the carbonate minerals.

Magnesium-calcites were divided into three groups according to the $d_{104}$ value: *low-magnesium calcites* with a $MgCO_3$ content in the structure of < 4–5 mol. % (3.036 Å > $d_{104}$ > 3.020 Å); *intermediate-magnesium calcites* with 5–18 mol. % $MgCO_3$ in the structure (3.02 Å > $d_{104}$ > 2.98 Å), and *high-magnesium calcites* with 30–43 mol. % $MgCO_3$ (2.94 Å > $d_{104}$> 2.91 Å). *Ca-excess dolomites*, in the structure of which the excess of $CaCO_3$ can reach 7 mol. % in relation to stoichiometric dolomite, are characterized by the values of $d_{104}$ from 2.910 to 2.887 Å [*Ovdina et al.*, 2020; *Solotchina and Solotchin*, 2014].

Decomposition of the extended diffraction maxima, which had a complex configuration and represented a superposition of several peaks of carbonate phases with different Mg contents in the structure, into individual peaks using the Pearson VII function allowed us to establish the position and integral intensity of each peak and obtain quantitative ratios of carbonates [*Ovdina et al.*, 2020; *Solotchina and Solotchin*, 2014]. The convergence of the experimental and simulated profiles is estimated as the standard deviation of the intensity at the calculated point of the model profile. The applicability of the model is described by the following expression: $R = \sum_{i=1}^{N}(I_{calc}(2\Theta_i) - I_{obs}(2\Theta_i))^2$, where $N$ is the number of the point at which the model is calculated, $I_{calc}$ is the calculated intensity and $I_{obs}$ is the observed (experimental) one at the point

The calculation of the water chemical composition was carried out using the formula by [*Kurlov*, 1928], which is used to express the chemical composition of water. Anions and cations with a content of more than 10 mg-eq% are introduced into the formula. The name of the chemical type of water involves anions and cations with a content of 25 mg-eq% (for mineral waters from 20 mg-eq%). The name of the water composition is given in increasing order of the anions and cations content.

## Results and Discussion

### *Composition, Physical and Chemical Features of Lakes Water*

According to physical and chemical features in the considered chain of lakes, the waters are soda, alkaline, and have a wide range of TDS (g/L). From Lake Rublevo to Lake Tanatar-6, there is an increase in pH and TDS (Table 3). The water samples taken in 2015 and 2019 did not differ.

The composition of modern lake waters varies from $HCO_3$–Mg–Na (Lakes Rublevo and Demkino) through $HCO_3$–Na (Tanatar-4) to $HCO_3$–Cl–Na (Tanatar-6) (Table 3). From Lake Rublevo to Lake Tanatar-6, in the anionic composition $HCO_3^-$ is partially replaced by $Cl^-$, and in the cationic composition $Na^+$ begins to prevail, while $Ca^{2+}$ and $Mg^{2+}$ ions significantly reduced. As the value of TDS increases, the value of $Ca/Mg_{water}$ in the water decreases.

The data obtained by [*Nikol'skaya*, 1961] after water sampling in 1949 and calculated by us according to the Kurlov formula [*Kurlov*, 1928] are shown in (Table 3). Comparison of these data with the authors' data for 2015 shows that the value of TDS in all lakes has increased 2–4 times over 66 years. The content of $SO_4^{2-}$ and $Cl^-$ ions has decreased to varying degrees, as well as $Ca/Mg_{water}$. For Lake Tanatar-6, the significant decrease in Ca/Mg in water was noted from 3.6 to 0.1 when the composition of lake water almost unchanged.

We also studied the water of two springs (self-discharge), Spring-1 (near Tanatar) and Spring-2 (near Rublevo) located near the lakes Tanatar-6 and Rublevo (Table 3). There are differences in composition and physical and chemical parameters of the springs' water compared to lakes' water. The springs' water characterizes the composition of groundwater feeding lakes. Water of the Spring-1 (Tanatar) is $HCO_3$–Ca–Na, fresh, pH 7.8. Water of the Spring-2 (Rublevo) is $HCO_3$–Na–Ca, fresh, pH 7.5.

**Table 3.** Water composition, physical and chemical parameters of small soda lakes of the Tanatar system (and springs near Lakes Tanatar-6 and Rublevo) by authors' data (for 2015) and [*Nikol'skaya*, 1961] (for 1949)

| Lake | pH | TDS, g/L | Water composition | $Ca/Mg_{water}$ | TDS, g/L | Water composition | $Ca/Mg_{water}$ |
|---|---|---|---|---|---|---|---|
| | | | Author's data (2015) | | | [*Nikol'skaya*, 1961] (1949) | |
| Tanatar-6 | 9.8 | 41.5 | Cl 56 $HCO_3$ 32 [$SO_4$ 12] Na 100 | 0.1 | 9.2 | Cl 57 $HCO_3$ 31 [$SO_4$ 12] Na 93 [Ca 5] | 3.6 |
| Tanatar-4 | 9.5 | 9.0 | $HCO_3$ 82 [Cl 15] Na 93 [Mg 6] | 0.1 | 4.4 | $HCO_3$ 54 Cl 39 [$SO_4$ 7] Na 93 [Mg 6] | 0.4 |
| Demkino | 9.0 | 2.1 | $HCO_3$ 89 [Cl 9] Na 66 Mg 30 | 0.2 | 1.5 | $HCO_3$ 84 [Cl 13] Na 61 Mg 26 [Ca 13] | 0.8 |
| Rublevo | 9.1 | 2.6 | $HCO_3$ 94 [Cl 5] Na 67 Mg 29 | 0.2 | 1.2 | $HCO_3$ 81 [Cl 15] Na 62 Mg 26 [Ca 12] | 0.8 |
| Bych'e | – | – | – | – | 4.0 | $SO_4$ 51 $HCO_3$ 34 [Cl 15] Na 84 [Mg 15] | 0.2 |
| Zolotoe | – | – | – | – | 2.2 | $HCO_3$ 92 Na 75 [Mg 22] | 0.2 |
| Spring-1 (near Tanatar) | 7.8 | 0.4 | $HCO_3$ 82 [$SO_4$ 11 Cl 7] Na 64 Ca 33 | 16.7 | – | – | – |
| Spring-2 (near Rublevo) | 7.5 | 0.5 | $HCO_3$ 97 Ca 56 Na 40 | 3.2 | – | – | – |

Note: pH – *in situ* measurements during fieldwork, TDS (g/L) – calculation according to the Kurlov formula [*Kurlov*, 1928]

*Geochemistry and Mineralogy of Bottom Sediments*

The average elements concentrations in the lacustrine sediments were compared to the elements' concentrations in the upper continental crust, according to [*Wedepohl*, 1995]. A comparison showed increased concentrations of Ca, Mg (major elements) and Sr (trace elements) in all studied lakes (Figure 2). The cause is accumulation of authigenic carbonates in the bottom sediments. Depletion of other trace elements is due to the dilution effect of sediments by carbonates and organic matter. This has also been shown to be the case for the south of Western Siberia [*Ovdina et al.*, 2020].

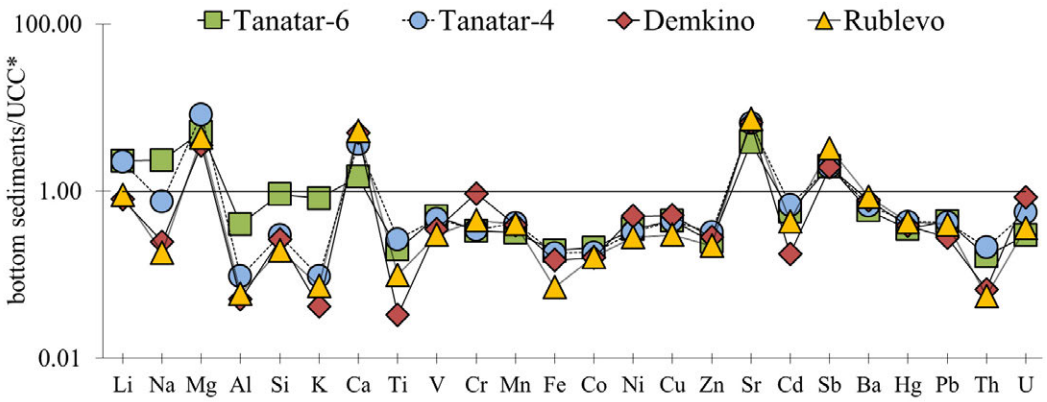


**Figure 2.** The multi-element spectrum of the studied elements (averaged values) in the bottom sediments of the Tanatar soda lake system normalized to the elements' concentrations in the upper continental crust according to [*Wedepohl*, 1995].

A high content of Sb relative to the upper continental crust was found in the sediments of the studied lakes (Figure 2). According to the configuration graphs of the Sb, Pb, Cd, Hg and ash content (%) distribution (Figure 3), a separate distribution of Sb is traced along the

core. The ash content in the bottom sediments increases as the depth increases (Figure 3). Both natural and anthropogenic factors can be associated with this aspect. Sb can enter the bottom sediments of lakes with eolian material: sandstorms are characteristic of the territory [*Gavshin et al.*, 1999], which can transport eolian material over long distances, and more than 10 polymetallic ore deposits of Ore Altai are located within a radius of ~100 km. A possible anthropogenic source may be the Mikhailovsky Chemical Reagents Plant, which is located in 6 km from the studied lakes in vil. Malinovoe ozero and the highway of regional significance 01K–21 (Rubtsovsk–Uglovskoye–Mikhailovskoye) of the Altai Territory (Figure 1).

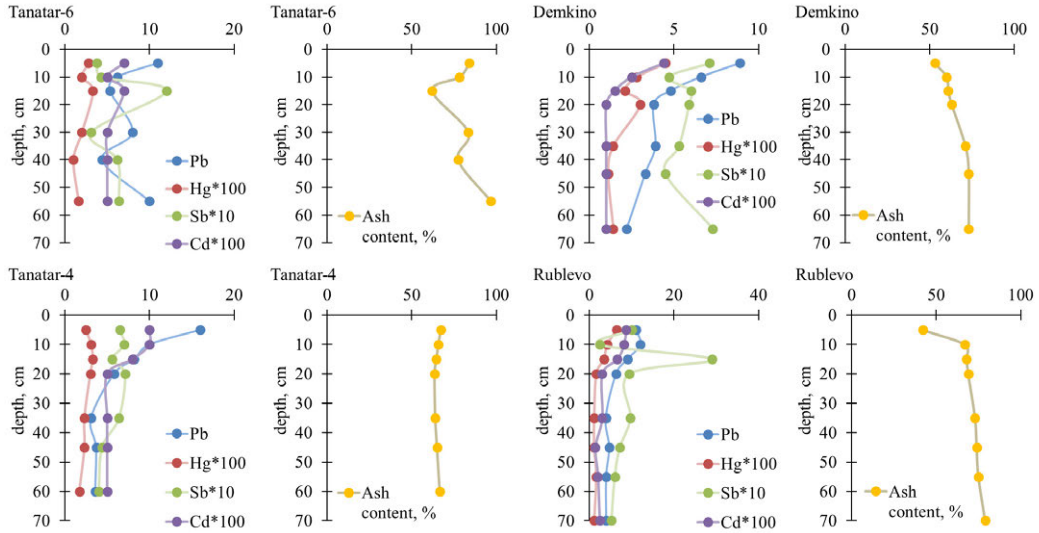


**Figure 3.** Configuration charts of vertical distribution of Sb, Pb, Cd, Hg and ash content (%) in the bottom sediments of the studied lakes.

The terrigenous component is represented as sharp-angled clastic forms and well-rounded grains of eolian origin (Figure 4) [*Gavshin et al.*, 1999; *Strakhovenko et al.*, 2014].

It is found that the Ca/Mg ratio decreases in the upper horizon (0–20) of the sediments in all the studied lakes (Figure 5) due to a decrease in the content of Mg, while Ca is ± constant.

A decrease in Mg content up the core is noted at a depth of 15–20 cm. The sedimentation rate for small lakes in southern Siberia is 0.35 cm per year, according to [*Strakhovenko et al.*, 2010]. Comparison of the Ca/Mg distribution and the sedimentation rate shown that the moment of change in the Mg accumulation is around 1950–1960. We considered possible changes in the feeding of lakes to explain the behavior of magnesium. One of

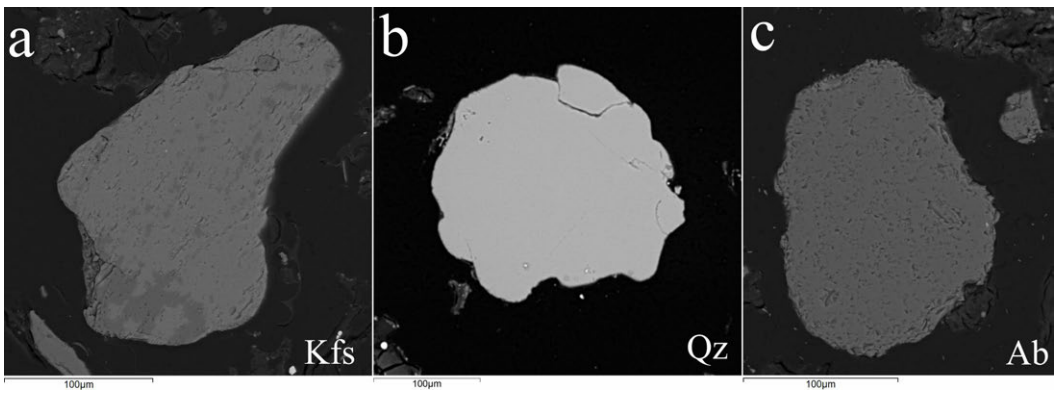


**Figure 4.** Photos of terrigenous component of bottom sediments. a – potassium feldspar (Kfs), b – quartz (Qz), c – albite (Ab) (SEM MIRA 3 TESCAN, BSE).

the sources in the number of works [*Kurnakov*, 1935; *Nikol'skaya*, 1961; *Strakhov*, 1951] was noted the Rublevaya River. Its source was near Lakes Bychye and Zolotoe (to the northeast of the Tanatar lakes), and the mouth on the southeast shore of Lake Demkino. The river was temporary and flowed only in spring. Presumably, the river water inherited the composition of Lakes Bychye and Zolotoe waters and could be an additional source of Mg. This is confirmed by the Ca/Mg ratio in the waters of Lakes Bychye and Zolotoe, which was 0.2 (Table 3). Now, the Rublevaya River has not been established either in fact or according to satellite images.

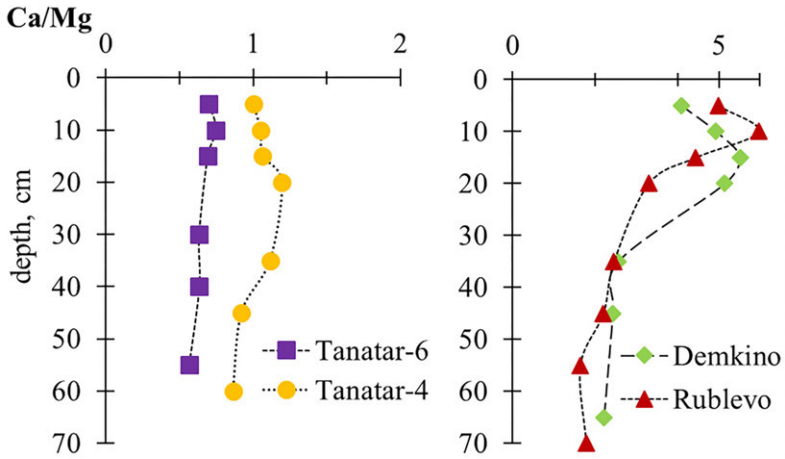


**Figure 5.** Vertical distribution of Ca/Mg in the sediments of the studied lakes.

According to [*Kharlamova*, 2019], the trends of annual precipitation and moisture coefficients are negative for almost the entire territory of the forest-steppe and steppe regions of Kulunda in the Altai Territory during the almost 50-year period of 1966–2012. It could lead to the drying up of the river and the disappearance of an additional and significant source of Mg in the lakes of the Tanatar group because the composition of groundwater (spring waters) does not contain Mg (Table 3).

The modern authigenic component of the water-bottom sediment boundary in the considered lakes mainly consists of high–Mg–Cal – Ca–Dol carbonates series, quartz, feldspar, calcite, and dolomite. Disordered smectite, aragonite, magnesite, chlorite, siderite, mica are impurities (Table 4, Figure 6). In all studied lakes, carbonates of the high–Mg–Cal – Ca–Dol series are formed and preserved throughout the core of bottom sediments (Table 4).

According to [*Strakhov*, 1951], a significant proportion of magnesian silicates of the sepiolite ($Mg_4(Si_6O_{15})(OH)_2{\cdot}6H_2O$) – kerolite ($(Mg,Ni)_3Si_4O_{10}(OH)_2{\cdot}nH_2O$ ($n \sim 1$) type was found in the bottom sediments of Lakes Tanatar-4 and Rublevo (Table 4). However, the authors of this study did not establish them either by XRD (Figure 6) or by SEM (Figure 7, 8). In addition, according to the geochemical composition of bottom sediments, there is no accumulation of Ni (Figure 2), which could be assumed during the formation of kerolite. The Ni content is lower or corresponds to the background values (10 mg/kg) in the bottom sediments of this area. There are no outcrops of ultrabasic rocks on the studied territory, and the parent rocks are Upper Pleistocene pebble gravel beds, sands, silts, siltstones, clays.

In order to specify the composition of modern bottom sediments, we used additional studies by XRD and SEM methods. Modeling of experimental XRD profiles of carbonates in the range of $d_{104}$ peaks was included in a more detailed study on Lakes Tanatar-4 and Rublevo (Figure 6).

The total modeled profiles (solid line) are in agreement with the experimental ones (dotted line). The diffraction peaks of individual phases are described by Pearson VII function. The modeling approach ensures a reliable differential identification of the entire

set of present carbonate minerals and determination of their quantitative ratios. The total content of carbonates in the sample is taken equal to 100%.

Modeling of experimental XRD profiles of carbonates reflected the results of X-ray diffractometry (XRD), clarified the percentage of high-magnesian carbonates and Ca-excess dolomite, and confirmed the absence of magnesium silicates in the main phase of modern bottom sediments of the studied lakes.

At high TDS (> 9 g/L) and pH (> 9.5), Ca-excess dolomite prevails in the main phase of bottom sediments in lakes Tanatar-6 and Tanatar-4 (Table 4). This is again confirmed by the data obtained using SEM (Figure 6a, 7). The CaO/MgO ratio in bottom sediments is 0.7 and 0.9, respectively.

In Demkino and Rublevo lakes, the TDS and pH in water are similar (TDS = 2.1–2.6 g/L, pH ≈ 9.0) (Table 4). High–Mg calcite, intermediate-Mg calcite and Ca-excess dolomite dominate in the main phase of bottom sediments (Figure 6b, 8). The CaO/MgO ratio in the bottom sediments is 3.8 and 5.9, respectively.

It should be noted that Mg-silicates were determined not in fact, but by calculations based on the definitions of macro- and microscopic methods of micaceous sericite-like mineral in bottom sediments and the establishment of a hydromica type peak by thermography [*Strakhov*, 1951]. The results showed that a lot of MgO, $SiO_2$ and $Al_2O_3$ remained after calculating the dolomite and calcite content (using CaO, MgO and $CO_2$). So further calculation was done for silicates or aluminosilicates. Even after recalculation, in most cases there was either an excess of MgO, or it was not enough to saturate the entire $SiO_2$. In this case, it was assumed that there was excess magnesium hydroxide in the form of brucite (?).

According to [*Strakhov*, 1951], bottom sediments of the Tanatar lake group contain only calcite and dolomite within carbonates. However, when describing experimental data on the salts' deposition from solutions corresponding in composition to the lakes waters, there was a "certain admixture" of $MgCO_3$ in calcite.

Our modern data show that carbonates in the main phase of the bottom sediment are intermediate-Mg calcite (from 5–18 mol.% $MgCO_3$ in the structure), high–Mg calcite (with 30–43 mol.% $MgCO_3$) and Ca-dolomite (excess $CaCO_3$ up to 7 mol.% relative to stoichiometric dolomite). This aspect explains the excess of MgO in the calculations of the bottom sediments mineral composition by [*Strakhov*, 1951]. As well as the presence of

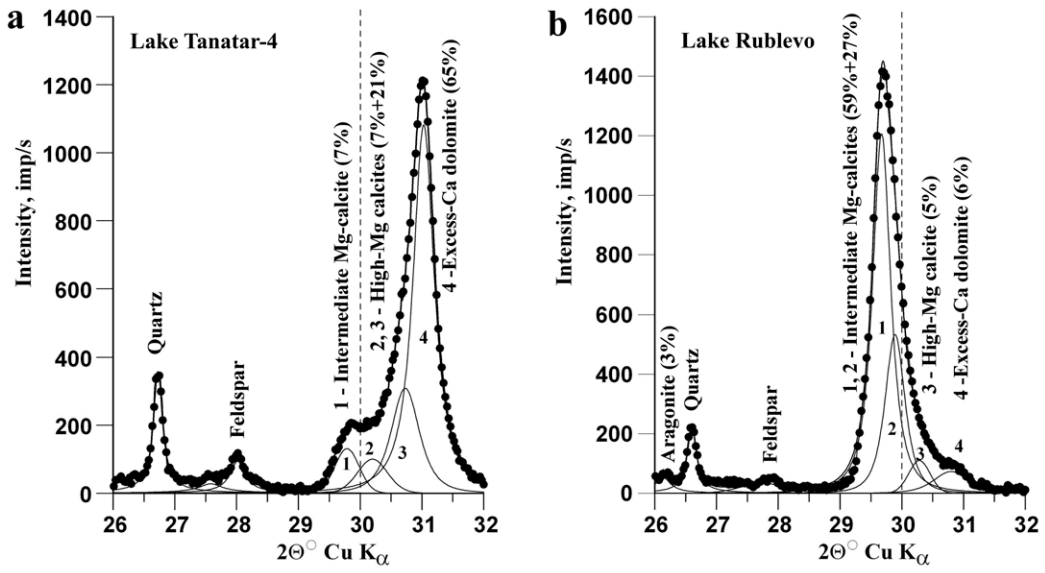


**Figure 6.** Results of experimental XRD profiles modeling of carbonates in the range of $d_{104}$ peaks: (a) – Lake Tanatar-4, (b) – Lake Rublevo.

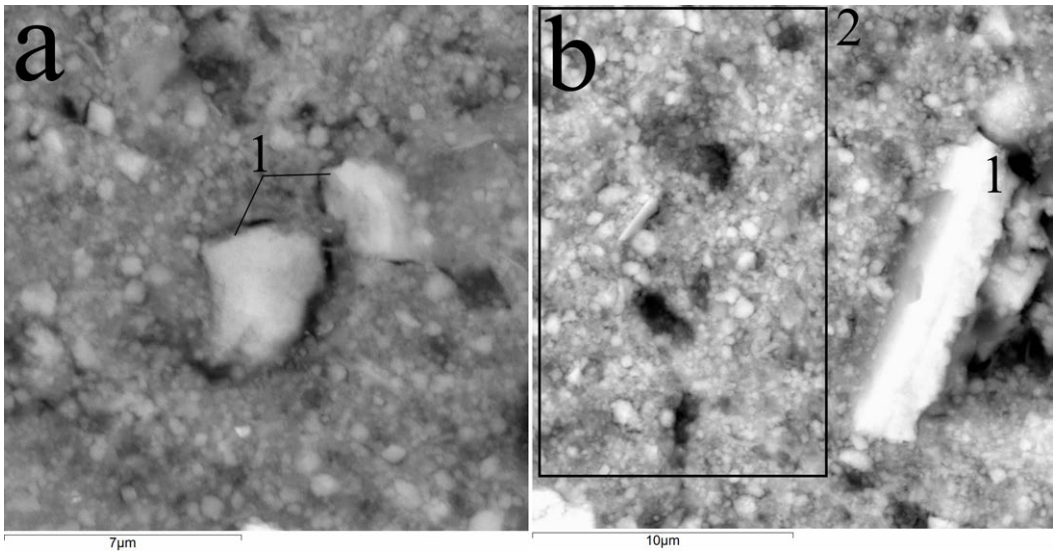


**Figure 7.** Photos of high–Mg carbonates in bottom sediments of Lake Tanatar-4, depth 0–5 cm: (a) – Ca-dolomite grains in small-lumpy bulk (mixture) having the composition of high–Mg calcite, Ca-excess dolomite, trona; (b) 1 – plagioclase, 2 – small-lumpy bulk (mixture) having the composition of high–Mg calcite, Ca-excess dolomite, trona (SEM MIRA 3 TESCAN, BSE).

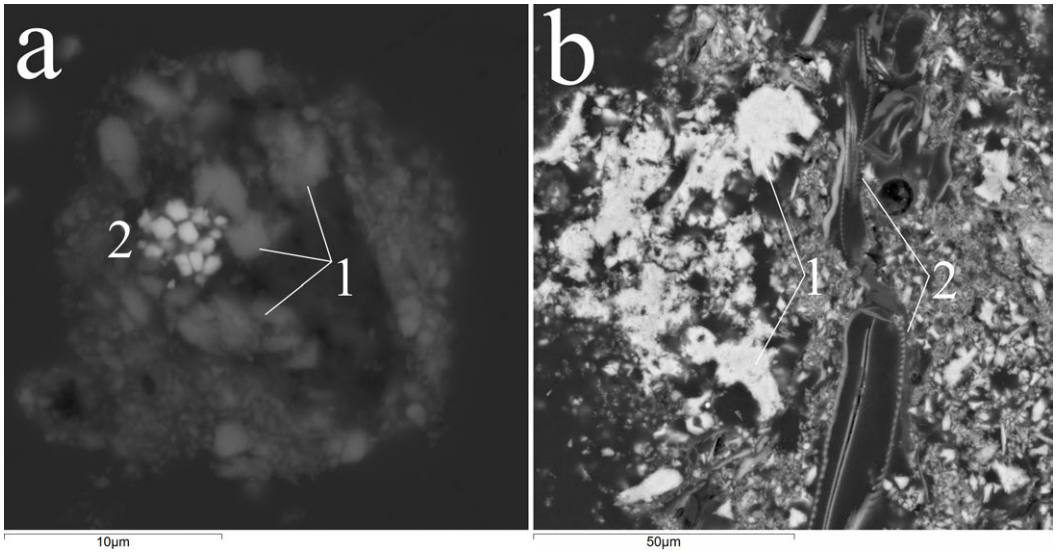


**Figure 8.** Photos of high–Mg carbonates in bottom sediments of Lake Rublevo, depth 0–5 cm, (a) 1 – high–Mg calcite; 2 – cluster of pyrite crystals; (b) 1 – high–Mg calcite, 2 – shells of diatoms ($SiO_{2bio}$) (SEM MIRA 3 TESCAN, BSE).

magnesite in the form of a small impurity (Table 4) in the bottom sediments of the studied lakes can introduce MgO.

The content of $SiO_2$ and $Al_2O_3$ in the bottom sediments of small lakes in the south of Western Siberia corresponds to the composition of the terrigenous component (mainly quartz, feldspar and mica). Additionally, the $SiO_2$ content is controlled by the presence of a significant amount of biogenic $SiO_2$ in sapropel deposits. Biogenic $SiO_2$ ($SiO_2nH_2O$) is usually composed of diatom shells (Figure 8b, 9) and macrophyte remains. This explains the excess of $SiO_2$ obtained during the calculations by the [*Strakhov*, 1951].

**Table 4.** X-ray diffractometry (XRD) results of small soda lakes bottom sediments (Tanatar system) by authors' data and data of optical, wet chemical methods, X-ray and part of thermal research by [*Strakhov*, 1951]

| Lake | TDS, g/L | $CaO/MgO_{bs}$ | Mineral composition | Salinity, % | $CaO/MgO_{bs}$ | Mineral composition |
|---|---|---|---|---|---|---|
| | | Authors' data | | [*Strakhov*, 1951] | | |
| Tanatar-6 | 41.5 | 0.7 | **0–5 cm** Main phase Qz, Pl, ***Ca-Dol***, ***Dol***, ***Cal***, Hal, impurity Kfs, trona, disordered smectite; small impurity mica, chlorite, siderite | – | – | – |
| | | | **50–55 cm** Main phase Qz, Pl, impurity Kfs, ***Dol***, Hal, small impurity disordered smectite, trona, ***Cal***, mica, chlorite, kaolinite, siderite | | – | – |
| Tanatar-4 | 9.0 | 0.9 | **0–5 cm** Main phase ***Ca-Dol***, impurity ***high–Mg–Cal,*** disordered smectite, Qz; small impurity Pl, goethite, traces chlorite, siderite, mica | 1 | 0.94 | Main phase ***Dol, Mg-silicates***; impurity Cal |
| | | | **55–60 cm** Main phase ***Ca-Dol***, impurity ***high–Mg–Cal***, disordered smectite, small impurity Qz, Pl, traces siderite, goethite, chlorite | | – | – |
| Demkino | 2.1 | 3.8 | **0–5 cm** Main phase ***high–Mg–Cal***, small impurity Qz, traces Pl, Kfs, aragonite, disordered smectite (?), a lot of X-ray amorphous component | – | – | – |
| | | | **60–65 cm** Main phase ***high–Mg–Cal – Ca-Dol carbonates series***, impurity smectite, small impurity Qz, traces Pl | | – | – |
| Rublevo | 2.6 | 5.9 | **0–5 cm** Main phase ***intermediate-Mg-Cal, Ca-Dol***, small impurity Qz, magnesite? a lot of X-ray amorphous component | 0.3 | 1.72 | Main phase ***Cal;*** impurity **Dol**, Mg-silicates |
| | | | **75–82 cm** Main phase ***high–Mg–Cal – Ca–Dol carbonates series;*** impurity smectite, Qz; traces **Pl,** Kfs | | – | – |

Note: High–Mg–Cal – high-magnesium calcite; Ca–Dol – Ca–excess dolomite; Dol – dolomite; Cal – calcite; Qz – quartz; Kfs – potassium feldspar; Pl – plagioclase; Hal – halite. Almost all minerals have a low degree of crystallinity.

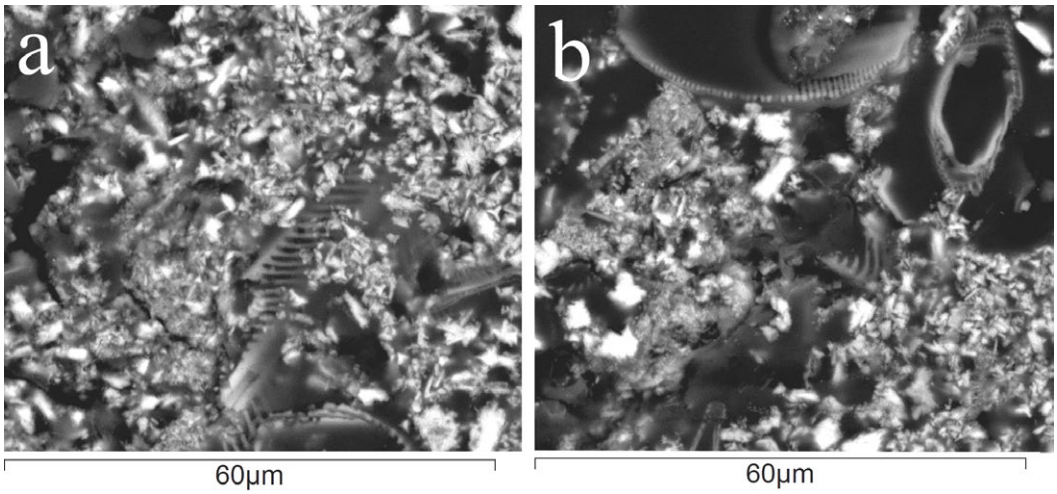


**Figure 9.** Photos of diatom shells in small-lumpy bulk having the composition of high–Mg calcite (SEM MIRA 3 TESCAN, BSE).

## Conclusion

The results obtained on the geochemical and mineral composition of bottom sediments in the model lakes of the Tanatar group (Demkino-Rublevo-Tanatar-4-Tanatar-6) allowed us to draw a number of conclusions:

1. Over the past 100 years, a change in the hydrological regime of lake feeding has been revealed in the catchment area (drying up of the Rublevaya River feeding the lakes under study). It has changed the nature of Mg accumulation in the upper horizons of bottom sediments. In addition, there has been a $TDS_{water}$ increase in lakes by 2 to 4 times;
2. Throughout the core depth, the mineral composition of the authigenic component does not change and is represented by carbonates of the Cal–Dol series (high–Mg Cal, Ca–excess Dol). It has been established that Mg-containing minerals are represented by carbonates, while Mg-silicates of the sepiolite-kerolite type in the bottom sediment have not been established;
3. The results obtained can be further used for detailed complex paleoreconstructions of the climate.

**Acknowledgments.** Work is done on state assignment of IGM SB RAS (No. 122041400193-7) with funding from the Ministry of Science and Higher Education of the Russian Federation. The authors are grateful to the anonymous Reviewers for the insightful comments and valuable improvements to our paper.

## References

Bartosiewicz, M., I. Laurion, and S. MacIntyre (2015), Greenhouse gas emission and storage in a small shallow lake, *Hydrobiologia*, *757*(1), 101–115, https://doi.org/10.1007/s10750-015-2240-2.

Borzenko, S. V. (2020), Principal Parameters Controlling Water Composition in Saline and Brackish Lakes in Eastern Transbaikalia, *Geochemistry International*, *58*(12), 1356–1373, https://doi.org/10.1134/s0016702920090037.

Chagas, A. A. P., G. E. Webb, R. V. Burne, and G. Southam (2016), Modern lacustrine microbialites: Towards a synthesis of aqueous and carbonate geochemistry and mineralogy, *Earth-Science Reviews*, *162*, 338–363, https://doi.org/10.1016/j.earscirev.2016.09.012.

Deelman, J. C. (2011), *Low-temperature formation of dolomite and magnesite*, Compact Disc Publications, Geology Series, Eindhoven, Netherlands.

Fussmann, D., A. J. E. von Hoyningen-Huene, A. Reimer, D. Schneider, H. Babková, R. Peticzka, A. Maier, G. Arp, R. Daniel, and P. Meister (2020), Authigenic formation of Ca-Mg carbonates in the shallow alkaline Lake Neusiedl, Austria, *Biogeosciences*, *17*(7), 2085–2106, https://doi.org/10.5194/bg-17-2085-2020.

Galbarczyk-Gąsiorowska, L., M. Gąsiorowski, and K. Szeroczyńska (2009), Reconstruction of human influence during the last two centuries on two small oxbow lakes near Warsaw (Poland), *Hydrobiologia*, *631*(1), 173–183, https://doi.org/10.1007/s10750-009-9809-6.

Gas'kova, O. L., V. D. Strakhovenko, and E. A. Ovdina (2017), Composition of brines and mineral zoning of the bottom sediments of soda lakes in the Kulunda steppe (West Siberia), *Russian Geology and Geophysics*, *58*(10), 1199–1210, https://doi.org/10.1016/j.rgg.2016.09.034.

Gavshin, V. M., B. L. Scherbov, M. S. Melgunov, V. D. Strakhovenko, V. A. Bobrov, and V. M. Tsibulchik (1999), 137Cs and 210Pb in lake sediments of the Steppe Altai as indicators of the dynamics of the anthropogenic changes in the geochemical background during the XX century, *Russian Geology and Geophysics*, pp. 1331–1341.

Hammer, U. T. (1986), *Saline lake ecosystems of the world*, Springer Dordrecht.

International Lake Environment Committee Foundation (ILEC) (1999), World Lake Database, https://wldb.ilec.or.jp/.

Ivanov, P. V. (1948), Classification of lakes of the world by size and by their average depth, *Bulletin of LSU*, *20*, 29–36 (in Russian).

Izmailova, A. V., and N. Y. Korneenkova (2020), Lake Area Percentage in Russian Federation Territory and Its Governing Factors, *Water Resources*, *47*(1), 13–21, https://doi.org/10.1134/s009780782001008x.

Kelts, K., and K. J. Hsü (1978), Freshwater Carbonate Sedimentation, in *Lakes*, pp. 295–323, Springer New York, https://doi.org/10.1007/978-1-4757-1152-3_9.

Kharlamova, N. F. (2019), Climatic Variability of the Kulunda Steppe, in *KULUNDA: Climate Smart Agriculture*, pp. 19–32, Springer International Publishing, https://doi.org/10.1007/978-3-030-15927-6_3.

Kolpakova, M. N., S. L. Shvartsev, S. V. Borzenko, V. P. Isupov, and S. S. Shatskaya (2016), Geochemical features of Kulunda plain lakes (Altay region, Russia), *IOP Conference Series: Earth and Environmental Science*, *33*, 012,007, https://doi.org/10.1088/1755-1315/33/1/012007.

Kompantseva, E. I., A. V. Komova, I. I. Rusanov, N. V. Pimenov, and D. Y. Sorokin (2009), Primary production of organic matter and phototrophic communities in the soda lakes of the Kulunda steppe (Altai krai), *Microbiology*, *78*(5), 643–649, https://doi.org/10.1134/S002626170905018X.

Korde, N. V. (1969), *Biostratigraphy and typology of Russian sapropels*, Publishing House of the USSR Academy of Sciences, Moscow (in Russian).

Kurlov, M. G. (1928), *Classification of Siberian healing mineral waters*, Publishing House of the Physiotherapy Institute in Tomsk, Tomsk (in Russian).

Kurnakov, N. S. (Ed.) (1935), *Kulunda Expedition of the USSR Academy of Sciences 1931-1933. Part 3: Study of the soil-geomorphological cycle*, Publishing House of the USSR Academy of Sciences (in Russian).

Last, F. M., W. M. Last, and N. M. Halden (2012), Modern and late Holocene dolomite formation: Manito Lake, Saskatchewan, Canada, *Sedimentary Geology*, *281*, 222–237, https://doi.org/10.1016/j.sedgeo.2012.09.012.

Lebedeva (Verba), M. P., O. V. Lopukhina, and N. V. Kalinina (2008), Specificity of the chemical and mineralogical composition of salts in solonchak playas and lakes of the Kulunda steppe, *Eurasian Soil Science*, *41*(4), 416–428, https://doi.org/10.1134/s106422930804008x.

Lein, A. Y., N. A. Belyaev, M. D. Kravchishina, A. S. Savvichev, M. V. Ivanov, and A. P. Lisitsyn (2011), Isotopic markers of organic matter transformation at the water-sediment geochemical boundary, *Doklady Earth Sciences*, *436*(1), 83–87, https://doi.org/10.1134/s1028334x11010156.

Nikol'skaya, Y. P. (1961), *Processes of salt formation in lakes and waters of the Kulunda steppe*, Publishing House of the Siberian Branch of the USSR Academy of Sciences, Novosibirsk (in Russian).

Ovdina, E., V. Strakhovenko, and E. Solotchina (2020), Authigenic Carbonates in the Water-Biota-Bottom Sediments' System of Small Lakes (South of Western Siberia), *Minerals*, *10*(6), 552, https://doi.org/10.3390/min10060552.

Samylina, O. S., F. V. Sapozhnikov, O. Y. Gainanova, A. V. Ryabova, M. A. Nikitin, and D. Y. Sorokin (2014), Algobacterial communities of the Kulunda steppe (Altai Region, Russia) Soda Lakes, *Microbiology*, *83*(6), 849–860, https://doi.org/10.1134/S0026261714060162.

Sapozhnikov, P. V., O. Y. Kalinina, M. A. Nikitin, and O. S. Samylina (2016), Cenoses of phototrophic algae of ultrasaline lakes in the Kulunda steppe (Altai krai, Russian Federation), *Oceanology*, *56*(1), 95–106, https://doi.org/10.1134/S0001437016010173.

Savchenko, N. V. (1997), *Lakes of the Southern Plains of Western Siberia*, Publishing House of the Siberian Branch of the Russian Academy of Sciences, Novosibirsk (in Russian).

Solotchin, P. A., E. V. Sklyarov, E. P. Solotchina, and Y. N. Markova (2017), Carbonate sedimentation in shallow saline lakes of Western Transbaikalia: The response to Holocene climate changes, *Doklady Earth Sciences*, *473*(2), 461–466, https://doi.org/10.1134/S1028334X17040213.

Solotchina, E. P., and P. A. Solotchin (2014), Composition and structure of low-temperature natural carbonates of the calcite-dolomite series, *Journal of Structural Chemistry*, *55*(4), 779–785, https://doi.org/10.1134/S0022476614040295.

Solotchina, E. P., M. I. Kuzmin, P. A. Solotchin, A. E. Maltsev, G. A. Leonova, and I. V. Danilenko (2019), Authigenic Carbonates from Holocene Sediments of Lake Itkul (South of West Siberia) as Indicators of Climate Changes, *Doklady Earth Sciences*, *487*(1), 745–750, https://doi.org/10.1134/S1028334X19070079.

Sorokin, D. Y., B. Abbas, M. Geleijnse, N. V. Pimenov, M. V. Sukhacheva, and M. C. M. van Loosdrecht (2015), Methanogenesis at extremely haloalkaline conditions in the soda lakes of Kulunda Steppe (Altai, Russia), *FEMS Microbiology Ecology*, *91*(4), https://doi.org/10.1093/femsec/fiv016.

Stankevica, K., Z. Vincevica-Gaile, M. Klavins, L. Kalnina, N. Stivrins, I. Grudzinska, and E. Kaup (2020), Accumulation of metals and changes in composition of freshwater lake organic sediments during the Holocene, *Chemical Geology*, *539*, 119,502, https://doi.org/10.1016/j.chemgeo.2020.119502.

Strakhov, N. M. (1951), *Calcareous-dolomite facies of modern and ancient reservoirs*, Publishing House of the USSR Academy of Sciences, Moscow (in Russian).

Strakhovenko, V. D., B. L. Shcherbov, I. N. Malikova, and Y. S. Vosel' (2010), The regularities of distribution of radionuclides and rare-earth elements in bottom sediments of Siberian lakes, *Russian Geology and Geophysics*, *51*(11), 1167–1178, https://doi.org/10.1016/j.rgg.2010.10.002.

Strakhovenko, V. D., O. P. Taran, and N. I. Ermolaeva (2014), Geochemical characteristics of the sapropel sediments of small lakes in the Ob'-Irtysh interfluve, *Russian Geology and Geophysics*, *55*(10), 1160–1169, https://doi.org/10.1016/j.rgg.2014.09.002.

Strakhovenko, V. D., E. P. Solotchina, Y. S. Vosel', and P. A. Solotchin (2015), Geochemical factors for endogenic mineral formation in the bottom sediments of the Tazheran lakes (Baikal area), *Russian Geology and Geophysics*, *56*(10), 1437–1450, https://doi.org/10.1016/j.rgg.2015.09.006.

Strakhovenko, V. D., E. A. Ovdina, G. I. Malov, N. I. Yermolaeva, E. Y. Zarubina, O. P. Taran, and V. V. Boltenkov (2019), Genesis of Organomineral Deposits in Lakes of the Central Part of the Baraba Lowland (South of West Siberia), *Russian Geology and Geophysics*, *60*(9), 978–989, https://doi.org/10.15372/rgg2019093.

Vernadsky, V. I. (1927), *History of minerals of the Earth's crust*, Scientific chemical and technical publishing house, Leningrad (in Russian).

Wedepohl, K. H. (1995), The composition of the continental crust, *Geochimica et Cosmochimica Acta*, *59*(7), 1217–1232, https://doi.org/10.1016/0016-7037(95)00038-2.

Zavarzin, G. A., and T. N. Zhilina (2000), Soda lakes as a natural model of the ancient biosphere, *Priroda*, *2*, 44–55 (in Russian).

Zheng, M. (2014), *Saline lakes and salt basin deposits in China*, Science Press, Beijing.

Russian Journal of Earth Sciences

# Possible Nutrient Load Reduction on the Large River Catchment Due to the Best Available Techniques Introduction in Agricultural Production

**Aleksandr Briukhanov[1], Sergey Kondratyev[2], Marina Shamkova[2], Eduard Vasilev[1], Natalia Oblomkova[*,1]**

[1] Federal Scientific Agroengineering Center VIM, Saint Petersburg, Tyarlevo set., Russia
[2] Institute of Limnology of the Russian Academy of Sciences, St. Petersburg Federal Research Center RAS, Saint Petersburg, Russia Federation
* **Correspondence to:** Natalia Oblomkova, oblomkovans@gmail.com.

**Abstract:** The study aimed to assess the possible reduction of the nutrient load and nitrogen and phosphorus losses from the Russian part of the Irtysh River catchment, one of our country's largest transboundary rivers, by implementing the best available techniques (BAT) in agricultural production. The Institute of Limnology Load Model (ILLM) mathematical model of nutrient load on the river watershed was used to solve the problem. Information on the primary sources of the nutrient load was collected for the entire Russian part of the Irtysh River catchment and tributaries catchments: Om, Ishim, Tobol, and Konda rivers. Agricultural activity of more than 800 enterprises concentrated mainly in the southern part of the Russian basin was analyzed. The calculations show that the most significant reduction of agricultural nutrient load due to BAT implementation is achieved in the Russian part of the catchment area of the Tobol River (31% for nitrogen and 25% for phosphorus from the total load on the catchment). The nutrient load can be reduced by 23% of nitrogen and 18% of phosphorus due to BAT implementation from the entire catchment of the Irtysh River (Russian part), which will lead to a corresponding reduction in a nutrient run-off by 13% of nitrogen and 4% of phosphorus. Therefore, a significant decrease in nutrient transport by river flow cannot be expected. However, it is essential to confirm the possibility of nutrient load reduction through the implementation of BAT, aiming at the transition to modern production technologies by minimizing the impact on the environment and maintaining the economic efficiency of agricultural production.

**Keywords:** nutrient load, modeling, river basin, best available techniques

**Citation:** Briukhanov, Aleksandr, Sergey Kondratyev, Marina Shamkova, Eduard Vasilev, Natalia Oblomkova (2023), Possible Nutrient Load Reduction on the Large River Catchment Due to the Best Available Techniques Introduction in Agricultural Production, *Russian Journal of Earth Sciences*, 23, ES5011, EDN: SIQKDD, https://doi.org/10.2205/2023es000865

## 1. Introduction

The input of different substances from anthropogenic sources causes pollution and anthropogenic eutrophication of the water bodies. Agricultural activity is a significant source of diffuse (dispersed anthropogenic) pressure on watersheds and their primary hydrographic network [*HELCOM*, 2022] and is recognized as the main source of diffuse input of nutrients into water bodies [*HELCOM*, 2018; *Sandström et al.*, 2020].

According to the results of recent studies, nitrogen losses vary widely, ranging from 6.6 to 100 kg ha$^{-1}$. In most cases, the transport to water bodies falls within the range of 20 to 45 kg ha$^{-1}$ [*Chen and Bechmann*, 2019; *Jansson et al.*, 2019b; *Kaur et al.*, 2017]. The specific phosphorus input, as determined by research in the Baltic region countries, varies between 0.15 and 1 kg ha$^{-1}$ [*Jacobsson*, 2012].

Several studies indicate the primary importance of improving manure management to reduce nutrient surplus and the associated risks of water body eutrophication [*Buckwell and Nadeu*, 2016; *Oenema et al.*, 2007; *Tybirk et al.*, 2013].

One main direction for improving intensive agricultural production's environmental safety is introducing the best available techniques (BAT). These include [*GOST R*

Research Article

Received: 21 September 2023
Accepted: 10 November 2023
Published: 30 December 2023

**Copyright:** © 2023. The Authors. This article is an open access article distributed under the terms and conditions of the Creative Commons Attribution (CC BY) license (https://creativecommons.org/licenses/by/4.0/).

*56828.15-2016*, 2019] technological processes, methods, and procedures for organizing the production, performance of work, or provision of services, including environmental and energy management systems, as well as design, construction, and operation of structures and equipment, which ensure reduction and (or) prevention of environmental pollution and waste production, compared to the current level. Using BAT is the most effective way to ensure environmental quality standards and standards of permissible environmental impact, considering economic and technical feasibility. BAT related to nutrient load reduction in agriculture includes technologies for processing and storing manure from livestock farms and poultry farms, as well as organic and mineral fertilizers application techniques in accordance with agrotechnical requirements.

Previous studies have shown that the introduction of best available techniques in manure management can lead to a reduction in diffuse nitrogen losses by 16.8% in the Leningrad region and 14.7% in the Kaliningrad region. Similarly, for phosphorus, the reduction can reach 9.1% and 8.4% respectively in these regions.

Similar studies conducted for the Baltic Sea region have shown that the maximum reduction of nitrogen loss resulting from improvement of manure management system can reach 10% of the current impact level [*Jansson et al.*, 2019b]. Reduction in production capacity and the share of cultivated agricultural land in EU countries, in the absence of financial incentives, can lead to a reduction in nutrient load ranging from 0.5% to 4%, depending on the basin [*Jansson et al.*, 2019a].

The study aimed to assess the possible reduction of the nutrient load and nitrogen and phosphorus losses from the Russian part of the Irtysh River catchment, one of our country's largest transboundary rivers, by implementing the best available techniques in agricultural production.

## 2. Study Area

The main object of study is the Russian part of the Irtysh River basin [*Nizhne-Ob Basin Water Administration*, 2014], one of the most important transboundary rivers of the Russian Federation with a complex water management situation. It flows through the territory of China and Kazakhstan in its upper and middle reaches. The Irtysh basin is impacted by the extraction and processing of natural resources, metallurgical, chemical-metallurgical, and chemical production, engineering, as well as the presence of energy facilities, major cities, transportation infrastructure, and agricultural production, which are sources of local and diffuse water pollution. The situation is further aggravated by the irreversible water intake from the Kar-Irtysh River within Chinese territory and the regulated flow within the borders of Kazakhstan. As a result, regions within the territory of Russia are experiencing a deficit of water resources against the backdrop deteriorating water quality. Until now, nutrient and pollution loads assessments haven't been carried out. These circumstances hinder the development of ecologically justified management decisions aimed at improving the environmental conditions in the considered basin.

Within Russian Federation, Irtysh River catchment includes territories of the Omsk, Chelyabinsk, Kurgan, Sverdlovsk, Novosibirsk, Tyumen regions, and the Khanty-Mansi Autonomous Okrug. The minor part of the catchment belongs to Perm region, the Orenburg region, and the Republic of Bashkortostan. Most of the basin is in the steppe and forest-steppe area, with only a relatively small lower part of the basin lying in the forest area. From the state border to Omsk, the Irtysh River does not have large tributaries. Within this stretch, the riverbed is winding and unstable, with multiple channels. The width of the valley varies from 5 to 19 km, narrowing to 2 km near Omsk, and the floodplain has numerous old riverbeds and lakes. From Omsk to Tobolsk, the Irtysh receives major tributaries such as the Om and Ishim rivers resulting in the widening of the valley to 6–8 km and the formation of large river deltas. Below the confluence with the Tobol River, the Irtysh flows north through the most marshy part of the West Siberian Plain. The width of the valley expands to 10–20 km. Near the mouth, the riverbed widens to 1.2 km, becomes multi-channeled, and contains islands. The water supply is mixed, including snowmelt, rainfall, and ground-

water. The average annual water discharge at Ust-Kamenogorsk is 590 $m^3 s^{-1}$. Chemical composition studies of the Irtysh River water at the Khanty-Mansiysk site [*Pozdnyakov et al.*, 2022] from 1987 to 2020 revealed significant fluctuations in the nitrogen and phosphorus content over the long-term series, occasionally exceeding regulatory values. No consistent directional changes in these series were observed. The concentrations of inorganic forms of nutrients varied within the following ranges: $N-NH_4^+$ – 0.089–1.53 mg $L^{-1}$, $N-NO_2^-$ – 0.003–0.044 mg $L^{-1}$, $N-NO_3^-$ – 0.017–0.395 mg $L^{-1}$, and phosphorus as phosphates – 0.019–0.146 mg $L^{-1}$. Most of the territory is occupied by sod-podzolic, chernozem, and peat soils. The proportion of solonchaks, located in the steppe zone, is high, accounting for about 14% of the total basin area. Heavy soils (clayey and loamy) dominate 90% of the watershed area [*Pozdnyakov et al.*, 2022].

The Russian part of the Irtysh catchment has been divided into seven hydrographic units (sub-basins) as shown in Figure 1, namely: 14.01.01 – the Irtysh River at Ust-Ishim (Russian part of the basin); 14.01.02 – Om River; 14.01.03 – Ishim River (Russian part); 14.01.04 – the Irtysh River from Ishim to Tobol; 14.01.05 – Tobol River (Russian part); 14.01.06 – Konda River; 14.01.07 – the Irtysh River from Tobol to the Ob (Figure 1).

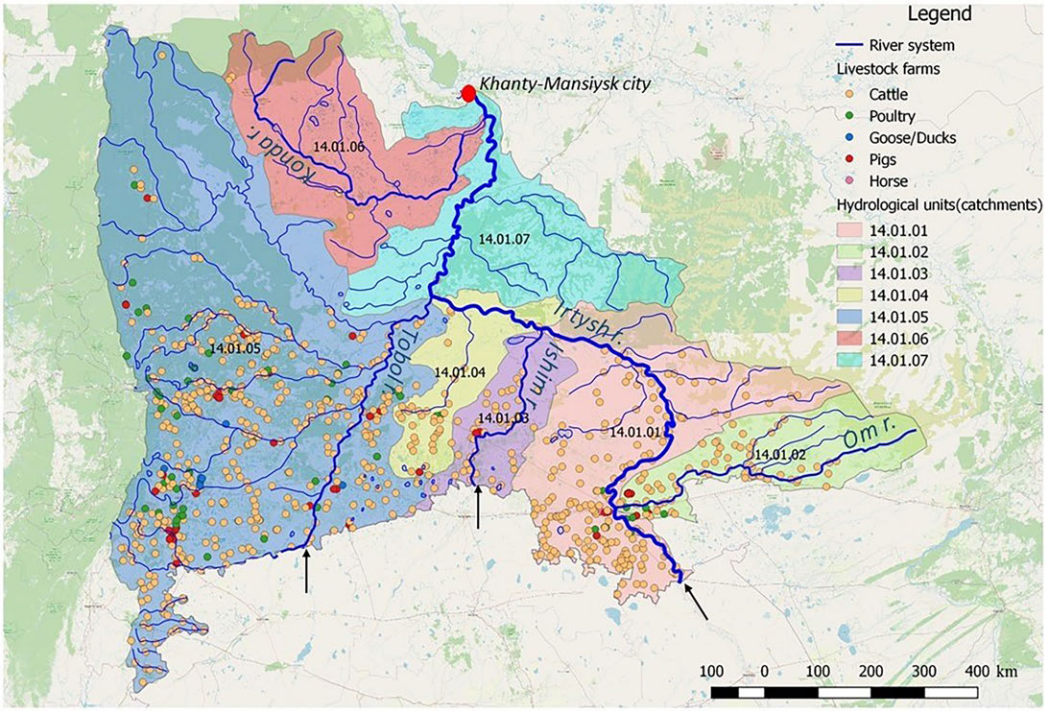


**Figure 1.** A scheme of the Russian part of the Irtysh River used to determine nutrient and pollution loads on the river system per hydrographic units: 14.01.01 – the Irtysh River at Ust-Ishim (Russian part of the basin); 14.01.02 – Om River; 14.01.03 – Ishim River (Russian part); 14.01.04 – the Irtysh River from Ishim to Tobol; 14.01.05 – Tobol River (Russian part); 14.01.06 – Konda River; 14.01.07 – the Irtysh River from Tobol to the Ob.

## 3. Material and Methods

In the first stage, the exact location of more than 800 agricultural enterprises, concentrated mainly in the southern part of the Russian part of the basin, has been determined (Figure 1). Input data regarding the use of nutrients within the studied area have been collected and analyzed. As defined during research, there are mega-large cattle farms with a population of over 8000 heads and mega-large pig farms. There are 744 cattle farms with overall population more than 970,000 heads. Additionally, there are 65 poultry farms, with a total poultry population exceeding 66 million heads. The remaining facilities are

dedicated to pig farming, with population of over 3 million heads. The largest enterprises are located in the Sverdlovsk, Tyumen, and Chelyabinsk regions.

Most farms lack waterproof storage for manure and organic fertilizers. Finally, areas with high pig and poultry density per agricultural area have been identified.

Data on the amount of manure produced in the Irtysh River basin are presented on Figure 2.

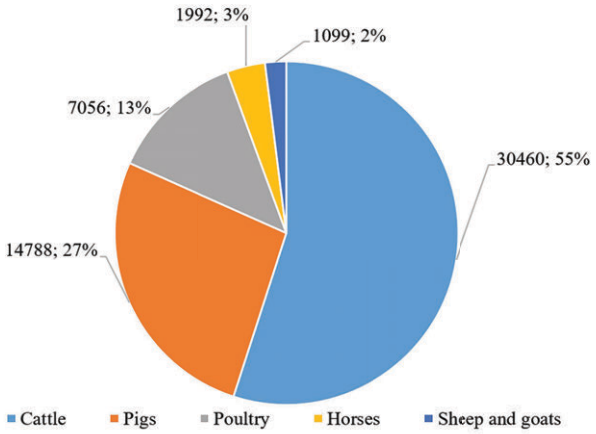


**Figure 2.** Amount of manure produced in the Irtysh River basin by animal category in 2021, thousand tons.

As indicated in Figure 2, over 55% of the total manure produced by large cattle farms. Analysis of satellite imagery has shown that more than 90% of the cattle farms lack impermeable manure storage facilities, which can lead to increased soil and water pollution.

An analysis of agricultural activities within the sub-basins of the Irtysh River has revealed uneven distribution of agricultural facilities, predominantly located in the southern parts of the sub-basins.

Nutrient losses and transport have been quantified using the Institute of Limnology Load Model (ILLM), accomplished by Methodology developed in the Institute for Engineering and Environmental Problems in Agricultural Production (IEEP) – branch of FSAC VIM [*Briukhanov et al.*, 2016, 2018; *Kondratyev and Shmakova*, 2019; *Pozdnyakov et al.*, 2020, 2022].

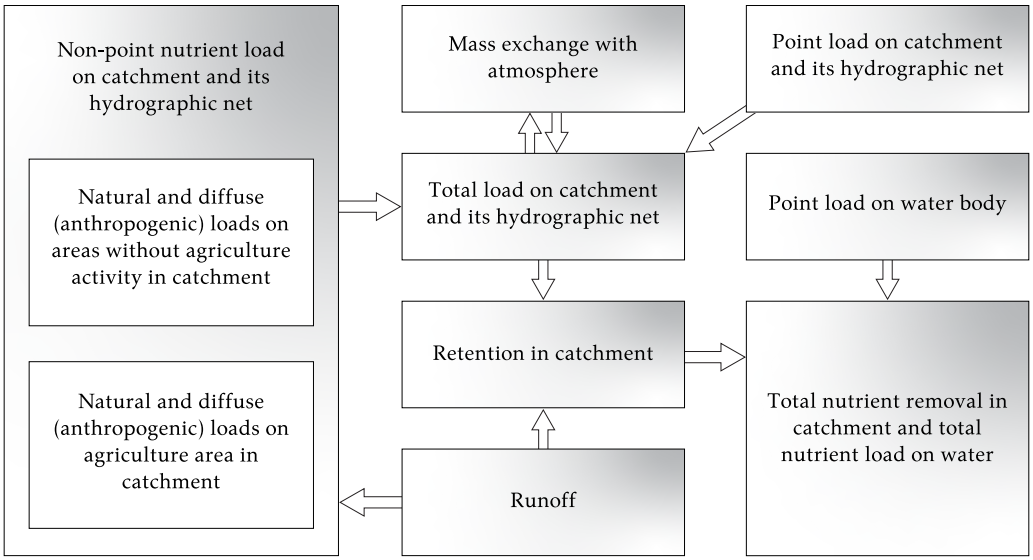


**Figure 3.** Algorithm for quantifying overall nutrient load by the ILLM model.

The ILLM model has been included in the list of models and methods used by the Contracting Parties of HELCOM to quantify nutrient loads from the Baltic Sea catchment area [*Svendsen*, 2019].

The main components of the external nutrient load on a water body ($L$) are (Figure 3): losses from unmanaged lands considered as natural background load ($L_e$), nutrient losses originating from agricultural activities ($L_{\text{agr}}$), point sources discharging to the surface waters on the catchment ($L_{P1}$) and directly to the receiving water body (e.g. lake, sea) ($L_{P2}$), as well as mass exchange with the atmosphere ($L_a$) [*Kondratyev*, 2007; *Kondratyev and Shmakova*, 2019]:

$$L = \left(L_e + L_{\text{agr}} + L_{P1} + L_a\right)(1 - k_r) + L_{P2}, \quad (1)$$

where $k_r$ is the dimensionless coefficient defining the nutrient retention by the catchment and hydrographic network. All other components of equation (1) have a [t year$^{-1}$] dimension.

Methods for setting input values and the ILLM model parameters are described in detail in [*Kondratyev and Shmakova*, 2019]. The types of underlying watershed surfaces were classified for information support of the model. The instrument was the United Nations Land Cover Classification System (LCCS) based on images from the PROBA-V (PROBA-Vegetation) and Sentinel-2 satellites. Surface types were combined to obtain five classes, which are necessary for calculating the load on a water body: 1 – floodplains, meadows, forest-steppe; 2 – agricultural areas; 3 – urban areas and other anthropogenic landscapes; 4 – forest, swamp; 5 – permanent water bodies. The emission characteristics of total nitrogen and total phosphorus loss with the runoff from each type of underlying surface were estimated based on the analysis of literature data [*Lobchenko et al.*, 2016; *Vtorova et al.*, 2000; *Yakutina*, 2014].

The average annual runoff for years of 5%, 50%, and 95% duration flow is calculated according to the method described in Code SP 33-101-2003 for cases then hydrometric observations data are available [*SP 33-101-2003*, 2004]. Information collected from statistical reporting forms of the State Water Register online database for the period 2009–2020 (form 2.11-gvr) was used to obtain values of point source discharges to receiving river system on the studied catchment. Average annual precipitation of total phosphorus from the atmospheric was determined based on known geostatic dependencies [*Kondratyev and Shmakova*, 2019].

As a rule, a significant part of pollutants entering the catchment area from various sources does not reach the mouth of large rivers due to retention in the hydrographic network. The following equation has been used to estimate nutrient retention in the river system [*Behrendt and Dannowski*, 2005; *Kondratyev and Shmakova*, 2019]:

$$k_r = k^*\left(1 - \frac{1}{1 + aq^b}\right), \tag{2}$$

where $k^*$ is a calibration parameter that considers the local features of nutrient retention, $a$ and $b$ are dimensionless empirical parameters. Specific run-off $q$ can be determined by runoff $y$ (mm year$^{-1}$) by following relation $q = 0.03171y$.

Methodology for calculating the diffuse load of nitrogen and phosphorus originating from agricultural activities on the catchments and the potential for its reduction due to BAT introduction in agriculture, developed by the Institute for Engineering and Environmental Problems in Agricultural Production (IEEP) – branch of FSAC VIM, was used to calculate nitrogen and phosphorous losses from agriculture-related sources ($L_{\text{agr}}$ in equation (1)). According to this methodology, the diffuse load of nitrogen (N) and phosphorus (P) from farming in the Russian part of the Irtysh River are calculated by the following equation :

$$L_{\text{agr}} = 10^{-3}\sum_{i=1}^{n_1} A_i(M_{\text{soil}\,i}K_1 + (\alpha_1 M_{\text{min}\,i} + \alpha_2 M_{\text{org}\,i})K_6)K_2K_3K_4K_5, \tag{3}$$

where, $L_{agr}$ is the load generated in the farm fields and entered the nearest watercourse (t year$^{-1}$);
$M_{soil\,i}$ is the nutrient content in the field topsoil of the $i$-th farm (kg ha$^{-1}$);
$M_{min\,i}$ and $M_{org\,i}$ are the doses of mineral and organic fertilizers applied to the fields of the $i$-th farm (kg ha$^{-1}$);
$A_i$ is the agricultural land area of the $i$-th farm (ha);
$\alpha_1$ and $\alpha_2$ are the coefficients of nutrients entering the runoff, taking into account the uptake of mineral (1) and organic (2) fertilizers by crops;
$K_1$ is the coefficient characterizing the nutrients loss from the topsoil;
$K_2$ is the coefficient of the distance between the agricultural land and the hydrographic network;

$K_3$ is the coefficient indicating the type of soil by origin;
$K_4$ is the coefficient representing soil texture;
$K_5$ is the coefficient that takes into account the farm type and the farmland structure;
$K_6$ is the coefficient describing the compliance of organic and mineral fertilizer application technology with relevant BATs.
All coefficients are dimensionless.

The Methodology involves collecting of detailed information on agricultural activities and natural conditions on the territory under study and does not require special field measurements. After primary analysis and processing using GIS technologies, official open-source statistical data are used as input data in the information Methodology.

The factor of applying BAT for the utilization of manure takes into account the influence of the machinery technologies used and compliance with regulations regarding runoff of nitrogen and phosphorus contained in organic fertilizers. The following BATs were considered in assessing the impact of this factor:

- Application of organic and mineral fertilizers using intelligent machines equipped with special working tools, a process monitoring system with automatic adjustment of parameters and operating modes;
- Incorporation of organic fertilizers into the soil using soil tillage machines that ensure thorough mixing with the soil;
- Creation of buffer strips on cultivated fields near water bodies;
- Implementation of technological regulations and establishing application rates for manure based on nitrogen and phosphorus content in organic fertilizers, considering soil characteristics (e.g., nutrient content), seasonal requirements of cultivated crops, and weather or field conditions that may lead to runoff occurrence.

A complete list of agro-engineering and organizational requirements for complying with BATs is included in the Russian reference documents "NDT-ITS NDT-41" and "NDT-ITS NDT-42" for intensive pig and poultry farming, approved by the orders of Rosstandart No. 2819 dated 13.12.17 and No. 2667 dated 29.11.17.

The Methodology has the following assumptions and restrictions: a) quantification is performed for average water runoff conditions; b) statistical data about fertilizer application, collected based on the municipal district level, are used for different parts of the district based on the assumption about the similarity of agricultural activities; c) possible natural variability of the coefficients within the considered homogeneous areas has not been taken into account, although the weighted average value of the field's distance from the primary hydrographic network is considered; d) the nutrient load reduction potential due to BAT introduction is assumed to be the same for all categories of livestock farms; e) it was assumed that all farms comply with the basic requirements of the legislation regarding the storage, processing, and application of manure, although in actual conditions significant violations of environmental requirements are often observed during manure management, leading to pollution of water bodies. In such cases, the environmental effect of the BAT introduction can be significantly higher.

## 4. Results

Diffuse load of N and P originating from farming activities on water bodies in the Russian part of Irtysh River in 2021 was calculated using the algorithm of the Methodology (equation 3) and input data collected from state databases and processed in GIS.

Based on calculations, the annual nitrogen and phosphorus load on water bodies for the year 2021 has been determined, along with specific losses per hectare of agricultural land. The highest nutrient losses is observed from agricultural lands in the Tobol River basin (16 kg $ha^{-1}$ of nitrogen and 0.81 kg $ha^{-1}$ of phosphorus), while the lowest values are found in the lower part of the Irtysh River basin before its confluence with the Ob River (6.2 kg $ha^{-1}$ of nitrogen and 0.28 kg $ha^{-1}$ of phosphorus).

Quantification of the nutrient run-off with the Irtysh River near Khanty-Mansiysk averaged for 2009–2020 is presented in Table 1. The main components of the load from

the Russian part of the Irtysh River's catchment are calculated by the ILLM model. ILLM model calibration was carried out according to the observational data in the cross-section in the city of Khanty-Mansiysk, located at Irtysh River mouth for a 50% duration flow conditions.

**Table 1.** Nutrient input (t year$^{-1}$) in the city of Khanty-Mansiysk cross-section for average flow (82.9 mm year$^{-1}$)

| Parameter | $N_{tot}$ | $P_{tot}$ |
|---|---|---|
| External input (transboundary) | 26,770 | 1162 |
| Point sources | 27.4 | 7681 |
| Agriculture | 113,926 | 5630 |
| Deposition from atmosphere | 0 | 3285 |
| Loss from different types of areas (except agricultural) | 59,871 | 9778 |
| The total load on the river system | 200,594 | 27,537 |
| Retention by the river system | 76,798 | 16,792 |
| **Modeled input from the catchment** | **123,795** | **10,744** |
| **Nutrient input in the river mouth based on Roshydromet data** | **124,034** | **10,888** |
| Diffuse sources input | 69,388 | 3097 |
| Input from natural background sources | 37,869 | 2914 |
| Point sources input | 16.9 | 2997 |
| Transboundary input | 16,520 | 453 |
| Input from atmosphere | 0 | 1282 |
| Retention coefficient, dimensionless | 0.382 | 0.609 |

As shown in Table 1, ILLM model calculation results ("modeled input from the catchment") differ by no more than 2% from the values calculated based on the direct measurements on the Roshydromet observation network in the Irtysh River ("nutrient input in the river mouth based on Roshydromet data). According to modeling results, nutrient input for average flow can be estimated at 123,795 t N year$^{-1}$ and 10,744 t P year$^{-1}$. The most significant part belongs to diffuse sources (69,388 t N year$^{-1}$ and 3097 t P year$^{-1}$) due to the considerable impact of agriculture. Transboundary load at the mouth can amount 16,520 t N year$^{-1}$ and 453 t P year$^{-1}$.

Table 2 presents an assessment of the various sources' contribution (%) to nutrient transport with Irtysh River in the Ust-Ishim (14.01.01) cross-section, as well as tributaries of the Om River (14.01.02), Ishim (14.01.05), Tobol (14.01.05) and Konda (14.01.06). The results are shown as a percentage of the total load at the mouth cross-section. The calculations were performed for an average water flow of 65.6 mm year$^{-1}$ for the catchment area of the Irtysh River at the mouth, 36.7 mm year$^{-1}$ for cross-section in Ust-Ishim, 22.1 mm year$^{-1}$ for the Om River, 78.1 for Ishim River, and 170.5 for the Tobol River. Dominant values are highlighted in grey.

It can be concluded that the diffuse nutrient load prevails both in the entire Russian part of the Irtysh River's catchment area (56.0% nitrogen and 28.8% phosphorus of the total load from the catchment), and the Irtysh River in Ust-Ishim (57.5% nitrogen and 46.6% phosphorus), as well as Om River (84.8% nitrogen and 64.1% phosphorus), Ishim River (66.4% nitrogen) and Tobol River (65.1% nitrogen and 44.7% phosphorus).

Intensive agriculture production can be the reason for the dominance of the diffuse sources in southern parts of the catchment with high livestock density values. The minimum agricultural activity caused the predominance of the natural (background) load on the northernmost watercourse of the Konda River (95.7% nitrogen and 64.3% phosphorus of the total input from the catchment). The Russian part of the catchment of the Ishim River has the biggest share of the point phosphorus load (64.3%).

**Table 2.** Contribution of nutrient load components (%) to the total nutrient transport in the outlets from the studied catchments (hydrological units)

| Hydrological unit | Transboundary load | Point sources | Natural background sources | Diffuse antropogenic sources |
|---|---|---|---|---|
| **Total nitrogen** | | | | |
| 14.01.01 | 32.8 | 0.0* | 9.7 | 57.5 |
| 14.01.02 | 0.0 | 0.0 | 15.2 | 84.8 |
| 14.01.03 | 23.2 | 0.0 | 10.4 | 66.4 |
| 14.01.05 | 5.3 | 0.0 | 29.6 | 65.1 |
| 14.01.06 | 0.0 | 0.0 | 95.7 | 4.3 |
| **Total phosphorous** | | | | |
| 14.01.01 | 19.1 | 8.8 | 16.4 | 46.6 |
| 14.01.02 | 0.0 | 0.7 | 17.8 | 64.1 |
| 14.01.03 | 8.0 | 58.1 | 5.5 | 19.4 |
| 14.01.05 | 1.2 | 21.0 | 20.9 | 44.7 |
| 14.01.06 | 0.0 | 0.7 | 64.3 | 20.8 |

* point sources input is less than 0.1%.

The significant impact of transboundary input can be found in the Ust-Ishim cross-section on the Irtysh River – 32.8% for nitrogen and 19.1% for phosphorus from the total input and at the outlet of the Ishim River – 23.2% for nitrogen, 8.0% for phosphorus. In general, the share of transboundary load in the Irtysh River nutrient transport at the outlet in the city Khanty-Mansiysk can amount 13.4% for nitrogen and 4.2% for phosphorus of total input from all sources for average water flow.

Quantification results of the current (for 2021) and potential (due to BAT introduction) nutrient loss to the river system from agriculture on the studied catchments within Russian borders, can be found in the Table 3.

**Table 3.** Actual (for 2021) and potential (due to BAT introduction) nutrient loss to the river system from agriculture on the studied catchments within Russian borders

| Hydrological unit | N, t year$^{-1}$ (2021) | N, t year$^{-1}$ (BAT) | P, t year$^{-1}$ (2021) | P, t year$^{-1}$ (BAT) | ΔN, % | ΔP, % |
|---|---|---|---|---|---|---|
| 14.01.01 | 37,673 | 31,941 | 1689 | 1520 | 15 | 10 |
| 14.01.02 | 12,097 | 10,688 | 701 | 652 | 12 | 7 |
| 14.01.03 | 4158 | 3195 | 209 | 174 | 23 | 17 |
| 14.01.05 | 56,296 | 38,794 | 2833 | 2124 | 31 | 25 |
| 14.01.06 | 37 | 26 | 2 | 2 | 30 | 0 |
| 14.01 – Russian part of the Irtysh River catchment | 11,3925 | 87,449 | 5630 | 4636 | 23 | 18 |

* ΔN, %, ΔP, % – with regard to load reduction.

The greatest reduction of the agricultural nutrient load in the study areas due to BAT introduction can be achieved in the Russian part of the Tobol River catchment area (31% nitrogen and 25% phosphorus of the total agricultural load). The apparent reason for this is the maximum concentration of agricultural production within this unit. In general, BAT introduction on the whole Russian part of the Irtysh River catchment area can decrease nutrient loss by 23% for nitrogen and 18% for phosphorus.

Quantification of the nutrient input from all sources for the lowest cross-section and potential reduction due to BAT introduction presented in Table 4.

**Table 4.** Actual (for 2021) and potential (due to BAT introduction) nutrient input with Irtysh River and its tributaries on the Russian part of the catchment

| Hydrological unit | N, t year$^{-1}$ (2021) | N, t year$^{-1}$ (BAT) | P, t year$^{-1}$ (2021) | P, t year$^{-1}$ (BAT) | ΔN, % | ΔP, % |
|---|---|---|---|---|---|---|
| 14.01.01 | 38,782 | 35,371 | 1541 | 1401 | 9 | 9 |
| 14.01.02 | 7819 | 7041 | 406 | 391 | 10 | 4 |
| 14.01.03 | 3287 | 2779 | 492 | 412 | 15 | 16 |
| 14.01.05 | 49,299 | 38,929 | 5372 | 5126 | 21 | 5 |
| 14.01.06 | 10,008 | 10,000 | 1490 | 1490 | 0 | 0 |
| 14.01 – Russian part of the Irtysh River catchment | 123,795 | 107,455 | 10,744 | 10,356 | 13 | 4 |

* ΔN, %, ΔP, % – with regard to load reduction.

Calculation results are significantly impacted by the agriculture load and other sources' input, as well as runoff volume, which determines the migration of nutrients to the river system (see equation (2)). The combination of these factors leads to the fact that the BAT introduction has the maximum impact on nitrogen load reduction in the Tobol River catchment area (21% of total nitrogen input) and phosphorus load reduction in the Russian part of the Ishim River catchment (16%). In general, BAT introduction on the whole Russian part of the Irtysh River catchment area can decrease total nutrient input by 13% for nitrogen and 4% for phosphorus.

An example of the possible BAT introduction effect is illustrated in Figure 4.

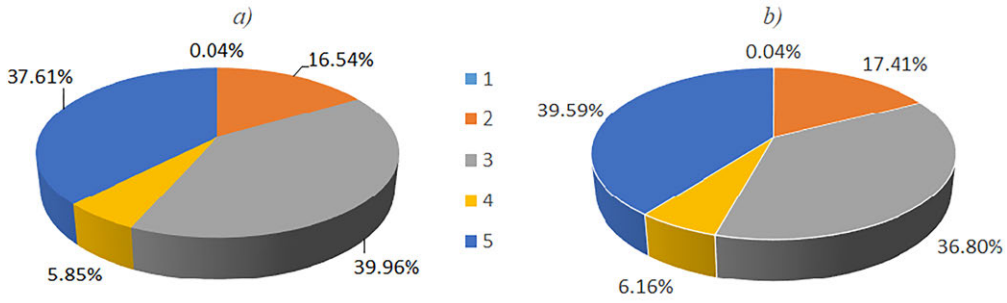


**Figure 4.** Source-apportionment of the Irtysh River total phosphorous ($P_{tot}$) input (outlet in the city of Khanty-Mansiysk) for average flow conditions for the current situation (a) and in case of BAT introduction (b): 1 – point sources input; 2 – atmospheric deposition; 3 – diffuse sources input; 4 – transboundary input; 5 – natural background load.

After the introduction of the best available techniques (BAT), decrease in agricultural phosphorus load on the water basin and its hydrographic network can achieve up to 18% annually for average flow conditions (Table 3). Diffuse sources have the highest influence on phosphorus input, accounting for 39.96% of the total phosphorus export value with the Irtysh River (Figure 4a). However, after introduction of the best available techniques, the contribution of diffuse pollution is reduced to 36.8%. At the same time, the natural component begins to dominate (Figure 4b). The overall reduction in phosphorus export with the Irtysh River due to introduction of the BAT is estimated to be approximately 4%.

## 5. Conclusions

Usually, the main recommendation regarding improving the ecological state of water bodies concerns lowering nutrient application rates during fertilization to reduce the risk of

anthropogenic eutrophication. However, it is evident that in a situation of negative nutrient surplus, typical for agricultural lands in the Russian part of the Irtysh River's catchment area, lower fertilizers application rates lead to a decrease in agricultural production. At the same time, the main aim for farmers is to increase production volumes by seeking resources to raise fertilizer application rates. In such a situation, the BAT introduction is the only real mechanism for combining reducing the negative impact on the environment and increasing agricultural production with minimizing labor and energy costs. Mathematical modeling methods are a fundamental tool for quantifying the environmental impact of different components of agricultural production and defining the most convenient combination of measures to achieve environmental goals.

Modeling allows the identification of areas with the maximum risk of nutrient transport to the water bodies and planning measures to minimize it. The measures include not only BAT introduction, but also a number of technological and landscape solutions, for example, the creation of natural biofilters and special amelioration facilities, the use of special equipment for fertilizer application, etc.

It can be noted that the estimated nutrient load reduction from agriculture is hardly enough for the dramatic decrease of the Irtysh River nutrient input to the Ob River.

BAT introduction has the maximum impact on nitrogen load reduction in the Tobol River catchment area (21% of total nitrogen input) and phosphorus load reduction in the Russian part of the Ishim River catchment (16%). In general, BAT introduction on the whole Russian part of the Irtysh River catchment area can decrease total nutrient input by 13% for nitrogen and 4% for phosphorus.

According to the calculations, currently, diffuse (anthropogenic) pollution has the highest influence on phosphorus export with the Irtysh River at the Khanty-Mansiysk cross-section, accounting for 39.96% of the total export value. After the introduction of the BAT, there should be a reduction of 18% of agricultural phosphorus losses to water. The overall reduction in phosphorus export with the Irtysh River due to introduction of the BAT is estimated to be approximately 4%. The phosphorus load source apportionment will significantly change, with the contribution of diffuse pollution decreasing to 36.8%, and an increase shares of atmospheric load and transboundary transport, while the natural component begins to dominate.

However, the result confirms the possibility of decreasing Irtysh River nutrient transport due to BAT's introduction in agriculture to minimize labor and energy costs, which is an extremely important conclusion. At the same time, it is important that decision-makers have reliable estimates of the possible effects and perspectives of different environmental measures.

**Acknowledgments.** The funds of the State Procurement theme FMNG-2019-0001 were used for this study implementation.

## References

Behrendt, H., and R. Dannowski (Eds.) (2005), *Nutrients and Heavy Metals in the Odra River System*, Schweizerbart Science Publishers, Stuttgart, Germany.

Briukhanov, A. Y., S. A. Kondratyev, N. S. Oblomkova, A. S. Ogluzdin, and I. A. Subbotin (2016), Calculation method of agricultural nutrient load on water bodies, *Technologies, machines and equipment for mechanised crop and livestock production*, pp. 175–186 (in Russian).

Briukhanov, A. Y., R. A. Uvarov, and I. A. Subbotin (2018), The Practice of best available technologies of poultry manure utilization in Leningrad region, *Poultry and Chicken Products*, *20*(3), 26–28, https://doi.org/10.30975/2073-4999-2018-20-3-26-28 (in Russian).

Buckwell, A., and E. Nadeu (2016), *Nutrient Recovery and Reuse (NRR) in European agriculture. A review of the issues,opportunities, and actions*, RISE Foundation, Brussels.

Chen, X., and M. Bechmann (2019), Nitrogen losses from two contrasting agricultural catchments in Norway, *Royal Society Open Science*, *6*(12), 190,490, https://doi.org/10.1098/rsos.190490.

GOST R 56828.15-2016 (2019), *National standard of the Russian Federation. Best Available Techniques. Terms and Definitions*, 50 pp., Standartinform, Moscow (in Russian).

HELCOM (2018), *Sources and pathways of nutrients to the Baltic Sea*, 153, Baltic Sea Environment Proceedings.

HELCOM (2022), Guidelines for the annual and periodical compilation and reporting of waterborne pollution inputs to the Baltic Sea (PLC-Water), https://doi.org/10.25607/OBP-1927.

Jacobsson, C. (Ed.) (2012), *Ecosystem Health and Sustainable Agriculture. Sustainable Agriculture*, 1, The Baltic University Programme, Uppsala University.

Jansson, T., H. E. Andersen, B. G. Gustafsson, B. Hasler, L. Höglind, and H. Choi (2019a), Baltic Sea eutrophication status is not improved by the first pillar of the European Union Common Agricultural Policy, *Regional Environmental Change*, *19*(8), 2465–2476, https://doi.org/10.1007/s10113-019-01559-8.

Jansson, T., H. E. Andersen, B. Hasler, L. Höglind, and B. G. Gustafsson (2019b), Can investments in manure technology reduce nutrient leakage to the Baltic Sea?, *Ambio*, *48*(11), 1264–1277, https://doi.org/10.1007/s13280-019-01251-5.

Kaur, K., A. Vassiljev, I. Annus, and P. Stålnacke (2017), Source apportionment of nitrogen in Estonian rivers, *Journal of Water Supply: Research and Technology - Aqua*, https://doi.org/10.2166/aqua.2017.036.

Kondratyev, S. A. (2007), *Formation of external load on water bodies: modeling problems*, Nauka, St. Petersburg (in Russian).

Kondratyev, S. A., and M. V. Shmakova (2019), *Mathematical modeling of mass transfer in the system: catchment - watercourse - water body*, Nestor-History, St. Petersburg (in Russian).

Lobchenko, Y. Y., N. Y. Lavrenko, I. P. Nichiporova, and A. V. Goncharov (2016), Dynamics of Organic and Biogenic Matter Content in the Ob River Basin Pyshma and Kunara Rivers, *Water sector of Russia: problems, technologies, management*, (2), 4–15, https://doi.org/10.35567/1999-4508-2016-2-1 (in Russian).

Nizhne-Ob Basin Water Administration (2014), *Scheme for the integrated use and protection of water bodies in the Irtysh River basin. Book 1. General characteristics of the river basin*, 303 pp. (in Russian).

Oenema, O., D. Oudendag, and G. L. Velthof (2007), Nutrient losses from manure management in the European Union, *Livestock Science*, *112*(3), 261–272, https://doi.org/10.1016/j.livsci.2007.09.007.

Pozdnyakov, S. R., A. Y. Bryukhanov, S. A. Kondratiev, N. V. Ignatieva, M. V. Shmakova, E. A. Minakova, A. M. Rasulova, N. S. Oblomkova, E. V. Vasiliev, and A. V. Terekhov (2020), Prospects of nutrients input reduction from river watersheds due to introduction of the best available technologies (BAT) for agricultural production (based on modeling results), *Water Resources*, *47*(5), 588–602, https://doi.org/10.31857/S0321059620050168 (in Russian).

Pozdnyakov, S. R., S. A. Kondratiev, E. A. Minakova, A. Y. Bryukhanov, and N. V. Ignatieva (2022), Results of assessing the dynamics and main trends in the content of chemical substances and the variability of the state of water bodies in the basin of the river irtysh in order to identify the pollution types, *resreport*, Barnaul (in Russian).

Sandström, S., M. N. Futter, K. Kyllmar, K. Bishop, D. W. O'Connell, and F. Djodjic (2020), Particulate phosphorus and suspended solids losses from small agricultural catchments: Links to stream and catchment characteristics, *Science of The Total Environment*, *711*, 134,616, https://doi.org/10.1016/j.scitotenv.2019.134616.

SP 33-101-2003 (2004), *The system of regulatory documents in construction. Code of rules for design and construction. Determination of Basic Design Hydrological Characteristics*, 73 pp., Gosstroy Rossii, Moscow (in Russian).

Svendsen, L. M. (Ed.) (2019), *Applied methodology for the PLC-6 assessment*, Baltic Marine Environment Protection Commission.

Tybirk, K., S. Luostarinen, L. Hamelin, L. Rodhe, S. Haneklaus, H. D. Poulsen, and A. L. S. Jensen (2013), *Sustainable Manure Management in the Baltic Sea Region*, Baltic Manure Business Opportunities.

Vtorova, A. I., M. V. Panina, and I. N. Likhodumova (2000), On the issue of monitoring the hydrological and hydrochemical regime of transboundary waters in the upper reaches of the Tobol river basin, in *Proceedings of the conference IVEP SB RAS*, pp. 27–34, IVEP SB RAS, Barnaul, Russia (in Russian).

Yakutina, O. P. (2014), Content of phosphorus in the surface runoff during snowmelt in the south of Western Siberia, *Problems of Agrochemistry and Ecology*, (1), 55–57 (in Russian).

Russian Journal of Earth Sciences

# Integrating Passive and Active Remote Sensing Data with Spatial Filters for Urban Growth Analysis in Urmia, Iran

**Vahid Isazade[1], Esmail Isazade[2], Abdul Baser Qasimi[*,3], and Ahmed Serwa[4]**

[1] Department of department of geographical science, Kharazmi University, Tehran, Iran
[2] Department of Urban planning, Tarbiat Modares University, Tehran, Iran
[3] Department of geography, Faculty of Education, Samangan university, Samangan, Afghanistan
[4] Faculty of Engineering in El-Mataria, Helwan University, Cairo, Egypt
* **Correspondence to:** Abdul Baser Qasimi, qasimi.abdul.a@gmail.com.

**Abstract:** Active remote sensing and related technologies are one of the new tools recently used to monitor complications and urban growth. This research aims to investigate the effect of spatial filters on urban complications. The aim of this paper is to compare Lee, Frost and Average spatial filters with Landsat 8 satellite images and radar images with HH/HV polarization to investigate and identify urban features in the west of Urmia City. The results showed that Filterelli with the kernel $3 \times 3$ had reduced the spike noise in Alus Palsard satellite radar images in identifying the growth of urban tolls. Also, the results of K-means classification, the Lee filter with kernel size $3 \times 3$ more accurately identifies the urban features of the west of Urmia City. The kappa coefficient was 0.96%, and the overall accuracy of this filter was 97.36%. Therefore, Lee's spatial filter has successfully identified the urban features of west Urmia with high accuracy. This system can be implemented in any other field due to its generality and reliability. This system may be a step towards remote sensing automation.

**Keywords:** Urban growth, Active remote sensing, Passive remote sensing, Lee filter, Urmia.

**Citation:** Isazade, V., E. Isazade, A. B. Qasimi, and A. Serwa (2023), Integrating Passive and Active Remote Sensing Data with Spatial Filters for Urban Growth Analysis in Urmia, Iran, *Russian Journal of Earth Sciences*, 23, ES5012, EDN: TSPARR, https://doi.org/10.2205/2023es000861

## 1. Introduction

Fusing different remote sensing data types (active and passive) can improve the performance of any spatial system [*Serwa and Saleh*, 2021]. The world is developing fast the motion Toward urbanization is built mainly through updating the texture maps [*Seto et al.*, 2012; *Sun et al.*, 2007]. Land use/cover maps are suitable for planning, environmental administration, disaster management, and public education on global development status [*Qasimi et al.*, 2022]. The impacts of the growth of urbanization on the environment consist of triggering possibly destructive feedback such as a massive change in climate, water pollution, and destruction of nature by developing settlement areas [*Ghanbari et al.*, 2022; *Mohan and Kandya*, 2015; *Zia et al.*, 2015]. Urbanization accelerates significantly, and the number of sizable metropolises continues to grow [*Hu et al.*, 2016]. For multiple years remote sensing of the satellite has been used for continuous mapping and observing various earth countenance consisting of urban objects [*Isazade et al.*, 2022; *Yang et al.*, 2016]. Methods and techniques are desired over manual view methods because of additional effectiveness and accuracy, like time and spatial coverage [*Isazade et al.*, 2022; *NISAR*, 2018; *Podest*, 2018]. Some international spaces agencies, including India and the European place agency the National Aeronautics and place command [*Attarchi et al.*, 2020; *Podest*, 2018], have successfully developed and designed several optical satellites to observe and measure the features of the earth's surface, such as Landsat and IRS series [*Kraus*, 2003; *Li et al.*, 2020; *NISAR*, 2018], Sentinel 2 along with artificial crevice radar (SAR) satellites so as RISAT-1, Sentinel 1-6, MODIS Aqua, Terra. In the last few years, optical remote sensing observations are getting outmoded, as expected by their ineffectiveness in piercing past the dense cloudy cover [*Kraus*, 2003; *Li et al.*, 2020].

Research Article

Received: 15 May 2023
Accepted: 7 July 2023
Published: 30 December 2023

**Copyright:** © 2023. The Authors. This article is an open access article distributed under the terms and conditions of the Creative Commons Attribution (CC BY) license (https://creativecommons.org/licenses/by/4.0/).

Nowadays, optical satellites are generally utilized for some schematization and monitoring operations. Though in some positions, it is essential for remote sensing to survey and observe the status of the earth's surface condition in the period of cloud cover and terrible climate conditions [*Isazade et al.*, 2021]. Multispectral satellite images are more general than optical ones due to the variety of spectral resolutions and bands [*Serwa and Elbialy*, 2021]. Using active sensing data perfectly performs to obtain spatial data [*Serwa and Saleh*, 2021]. Monitoring surface situations using radar equipment has a different view and provides several states for feature recognition [*Alves et al.*, 2020; *Leiva-Murillo et al.*, 2013]. However, acquiring any radar images comes up with multi-dimensional issues containing quality of the information, cost of acquisition, preprocessing of the data or methods of correction, and enhanced distortion. This data collection becomes offender the efficacy cited by some caused mistakes that need information processing [*Betbeder et al.*, 2015]. A prominent section of the processing functions underscores the drop of extended contortion or noise from the accepted SAR images. In this issue, the European charge holds attended to institute the Program of Copernicus, which designed a novel model mutation toward the accessibility and availability of information to hand over different earth-seeing services by the support of satellites and in site information down six present Copernicus services [*Kaushik and Kumar*, 2020]. Lines and edges are commonly easy visages to be isolated from a satellite image so that they can be operated for subsequent studies in the domains of image processing, computer perspective, remote sensing, and photogrammetry [*Rasche*, 2018; *Seo*, 2018, 2019a,b]. *Zakeri et al.* [2017] utilized S1 and ALOS- 2 PALSAR-2 images for land cover classification in Tehran. Utilizing the backscattering worth on S1 images for the support vector machine classification of land cover by five categories, Kappa stood at 0.30 and the OA 45.70%. Additionally, elements that had surfaces were selected through the PCA and plugged with the backscattering polarized satellite imagery.

*Osgouei et al.* [2019] used enhanced image classification to map the land cover for Istanbul, acquired from sentinel 2A data, employing SVM. The normalized deference tillage index was utilized to determine built-up elements as the domain of a three-band synthesized image, comprising the vermilion-edging-based normalized dissimilarity vegetation index and the corrected, normalized distinction water index. *Camargo et al.* [2019] and *Lapini et al.* [2020] employed SAR imagery for Brazil's equatorial savannah land cover classes and the Mediterranean region's forest classes.

Previous studies also offered MLP, RBF and Support vector machine (SVM) as the exact arranger. Also, the decision tree exhibited a refined version for observing specific land cover categories (e.g., vegetation). Deep learning classifiers are proven perfect [*Serwa*, 2020]. *Li et al.* [2020], *Mun et al.* [2019], and *Routray et al.* [2020] focused instead on filtering out the performance and worth keeping of an image. Speckle noise can bring down the modality of the image. Due to this reasoning, the assessment has carried a position among untroubled and filtered imagery. The spot degradation is accomplished at the damage by protection data.

Established at this, an equivalent extent has been given to estimating the speckle filtering and filtering efficiency and retinue in detail. *Wei and Blaschke* [2018] created a collation between supervised classification, object-based, and pixel-based unsupervised category, and the object-based process is recommended for the category of increased-solution images. *Abdollahi et al.* [2017] illustrated the road extraction, acquired by SVM, level set method and Otsu's algorithm with Comprehensiveness and feasible Correctness. However, it is limited to images with only a spatial resolution of 0.21 m. *Dai et al.* [2020] defined path exploitation acquired utilizing Preprocessing, smoothing, segmentation, and eventually and eventually flexible path factor acquiring per a specific histogram MLSOH is intended to extract the road and its orientation by Correctness of 99.54%, with a Totality 97.73%. However, it is not reasonable for the extensive shadow area, and the image is regularly essential to be enhanced. *Shi et al.* [2019] extracted constructions using artefact features well-found in building measures, figures, tissue, paint, shade, and roof textile. In common, the broadly utilized methodology for remote sensing feature detection is

classification-based. Building extraction is done by separating its elements and applying classification techniques like Support vector machine or RF.

*Isazade et al.* [2021], spectral indices and constructed and non-constructed urban features and their comparison with surface temperature using Landsat satellite images for the city of Tehran were evaluated. Their results showed that VbSWIR_BI and IBI indices have the highest accuracy compared to other indices. With the increase in construction, the temperature has risen in the central and northern parts of the Tehran metropolitan. *Ghorbanian et al.* [2020] demonstrated the acceptable granular noise decrease to dissolve the difficulty relevant to the SAR data used for the broad application areas. A comparative analysis of filters is highlighted to figure out the performance of the filters and the ability to extract edges, lines, and points. *Dass and Yadav* [2020] Examined Radarset-2 images for the speckle containment with the Lee, Lee-sigma, Frost and Gamma-map. In common, the median & mean filters are also contained *Alves et al.* [2020], *Liu et al.* [2019], all filters are evaluated and show that some filters perform well in reducing the effect of granular noise and conserving the details of the edge.

The study aims to compare different filters' performance on AlosPalsar satellite bands for noise reduction and feature extraction in urban environments, focusing on the northwest region of Urmia City, Iran. Specifically, the Lee, Gamma-Map, Frost, and Average filters will be compared using $K$-means classification to identify the filter that provides the closest results to surface phenomena. Additionally, the study seeks to investigate the impact of the HV band's polarization properties and sensitivity on urban feature evaluation and resolution. Moreover, the research aims to determine the suitability of the SSI index for estimating noise-free gray levels. Overall, the study aims to contribute to improving remote sensing automation and monitoring of earth changes in sensitive areas such as natural resources, the environment, and agriculture.

The innovation of this paper lies in its application and evaluation of different spatial filters, specifically Lee, Frost, and Average filters, for monitoring urban complications using active remote sensing technologies. The paper focuses on comparing the effectiveness of these filters in identifying and characterizing urban features in the west of Urmia City using Landsat 8 satellite images and radar images with HH/HV polarization.

## 2. Study Area

Urmia locates in the central part of the province of West Azerbaijan, covering an area of about 5227 km$^2$ (Figure 1). It is the most populous city in the province, with a relative share of 31.28%. The study area shares borders with Turkey in the west, Lake Urmia in the east, the cities of Naqadeh, Mahabad, and Oshnavieh in the south, and Salmas in the north. According to the 2016 census, it has 736,224 inhabitants [*Fazel et al.*, 2017]. According to environmental considerations, the Urmia Basin's cities are vital in agricultural and industrial activities. There are 43 urban centers and 520 villages with about 7.3 million canteens, 9 to 10% of the total population. [*Fazel et al.*, 2017; *Nouri et al.*, 2017; *Shokati and Feizizadeh*, 2018].

## 3. Data and Methodology

### 3.1. Data

AlosPalsar radar images ( HH and HV) sensors for the research area are used with a rare angle of 34.3 degrees. The second data used in this study is Landsat 8 bands (Blue, Near infrared, and Mid-infrared bands) for 2020 west Urmia City. Specifications of AlosPalsar Landsat 8 images are presented in Tables 1 and 2.

### 3.2. Geometric Correction and Calibration

In order to apply the geometric corrections for the radar images of the west Urmia City, the Snap 5.3 software was used. Then its pixel size was changed to 30 meters and the color image (HH-HV-HH/HV) RGB After generating the comment, the polarimetric images (HV) and (HH) are subject to geometric correction.The results showed that spectral

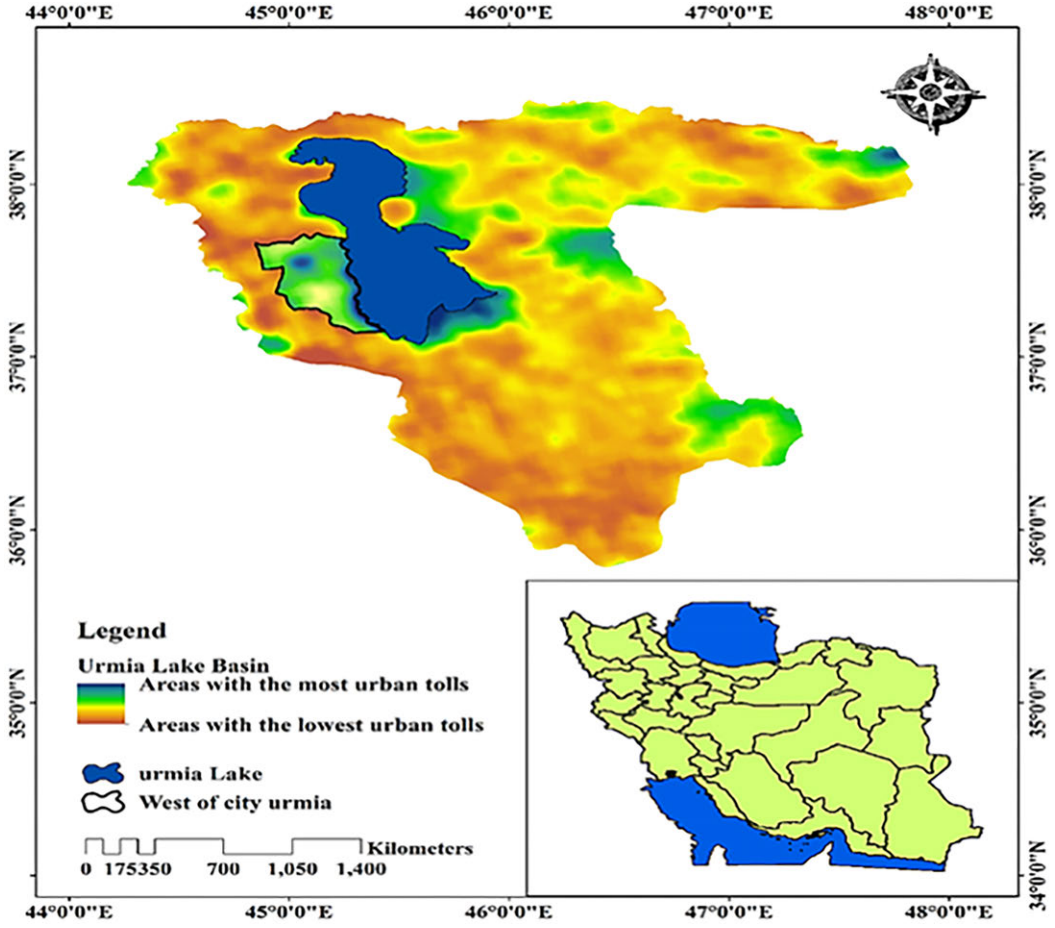


**Figure 1.** Study area west Urmia City.

**Table 1.** Profile of AlosPalsar radar images (https://www.eorc.jaxa.jp/ALOS/en/alos/sensor/palsar_e.htm)

| Mode | Fine | | ScanSAR | Polarimetric (Experimental mode) |
|---|---|---|---|---|
| Center Frequency | 1270 MHz (L-band) | | | |
| Chirp Bandwidth | 28 MHz | 14 MHz | 14 MHz, 28 MHz | 14 MHz |
| Polarization | HH or VV | HH+HV or VV+VH | HH or VV | HH+HV+VH+VV |
| Incident angle | 8 to 60° | 8 to 60° | 18 to 43° | 8 to 30° |
| Range Resolution | 7 to 44 m | 14 to 88 m | 100 m (multi look) | 24 to 89 m |
| Observation Swath | 40 to 70 km | 40 to 70 km | 250 to 350 km | 20 to 65 km |
| Bit Length | 5 bits | 5 bits | 5 bits | 3 or 5 bits |
| Data rate | 240 Mbps | 240 Mbps | 120 Mbps, 240 Mbps | 240 Mbps |
| NE sigma zero | < −23 dB (Swath Width 70 km)<br>< −25 dB (Swath Width 60 km) | | < −25 dB | < −29 dB |
| S/A | > 16 dB (Swath Width 70 km)<br>> 21 dB (Swath Width 60 km) | | > 21 dB | > 19 dB |
| Radiometric accuracy | scene: 1 dB / orbit: 1.5 dB | | | |

noise was observed in both produced images. The replay values of the HH/HV sensor polarizations are presented in Table 3. Methodology for identifying urban landscapes using radar and land images (Figure 2).

**Table 2.** Landsat satellite bands 8 OLI sensors (http://mehdigis.blogfa.com/post/266)

| Spectral Bands | Wavelength in μm | Resolution in m |
|---|---|---|
| Coastal / Aerosol | 0.433–0.453 | 30 |
| Blue | 0.450–0.515 | 30 |
| Green | 0.525–0.600 | 30 |
| Red | 0.630–0.680 | 30 |
| Near Infrared | 0.845–0.885 | 30 |
| Short Wavelength Infrared | 1.560–1.660 | 30 |
| Short Wavelength Infrared | 2.100–2.300 | 30 |
| Panchromatic | 0.500–0.680 | 15 |
| Cirrus | 1.360–1.390 | 30 |

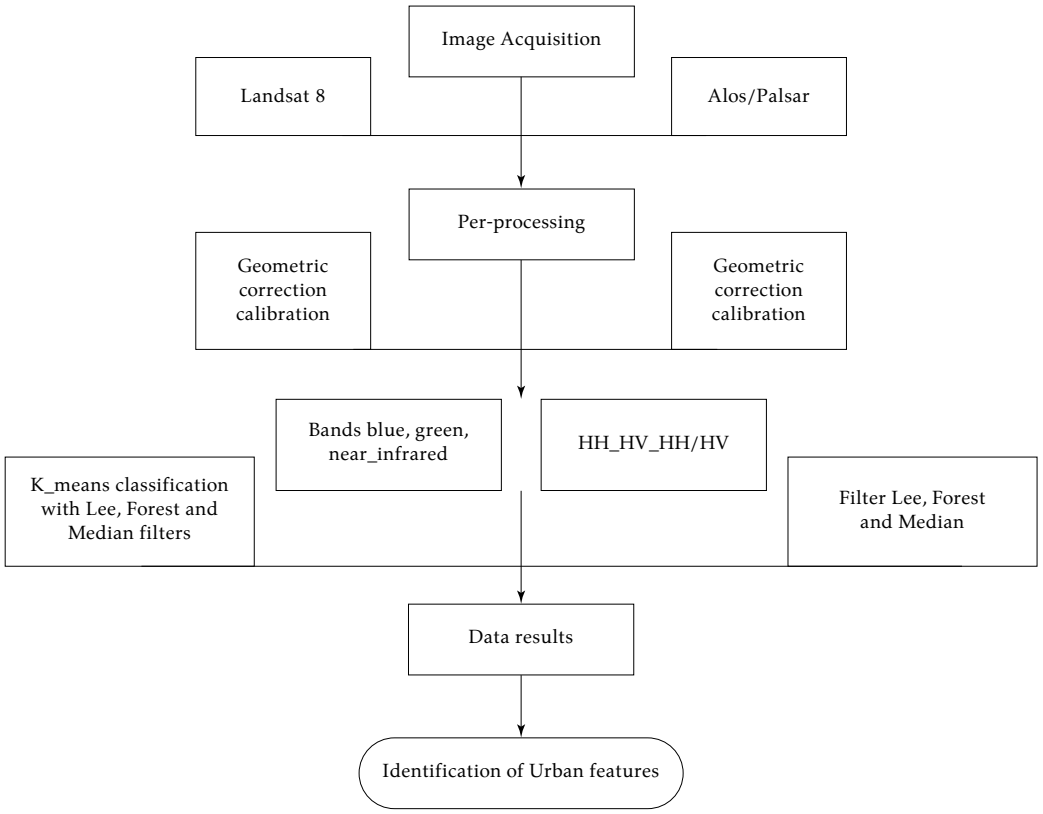


**Figure 2.** Workflow of the methodology.

**Table 3.** Sensor polarization replay values

| Polarized | Min | Max | Mean | StdDev |
|---|---|---|---|---|
| HH | 0.0005 | 22.5697 | 0.0987 | 0.4116 |
| HV | 0.0002 | 21.2345 | 0.0325 | 0.0721 |

## 4. Results and Discussion

In order to improve the range of radar images and to distribute them in a better range, they were converted to decibels after calibration. The results showed that by applying this algorithm on each band, the output images of west Urmia City, had better brightness, and the phenomena that were not clear became somewhat more transparent. Calibrated imagery by the HH and HV bands is displayed in Figures 3 and 4.

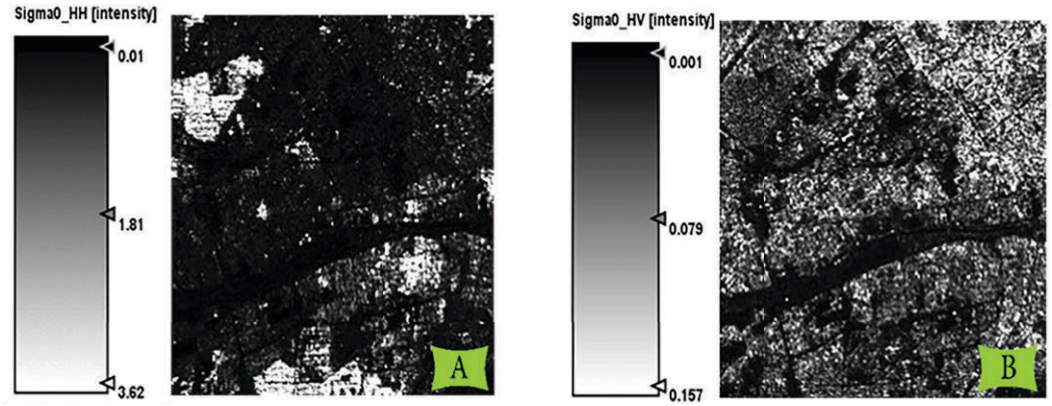


**Figure 3.** (a), HH and (b), for the HV band (calibrated) west of Urmia City.

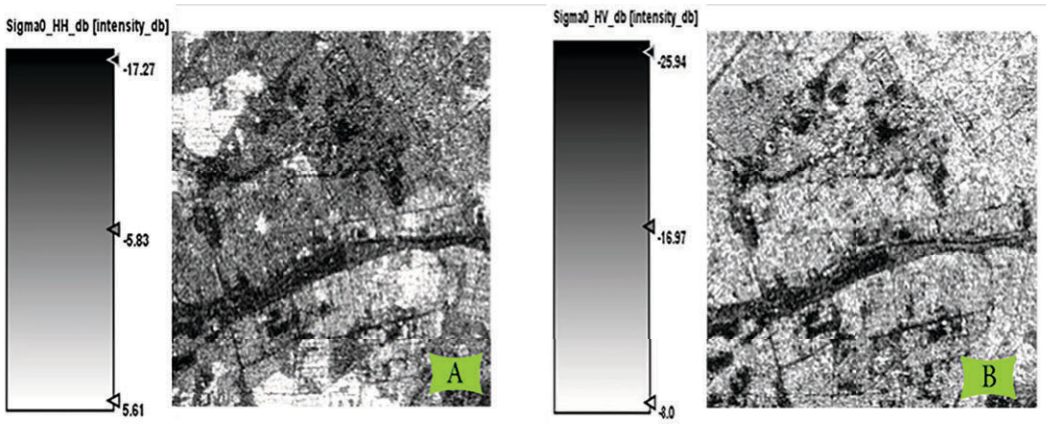


**Figure 4.** (a), calibrated HH band and, Sigma_0 (b), calibrated HV band Sigma 0 and db west of Urmia City.

Figure 3, shows A of the HH band, with intensities ranging from (0.01 to 3.62%), and Figure B of the HV band, which has intensities ranging from (0.001 to 0.157%), which are brighter than the HH band. The donor is that image B of the HV band evaluates and identifies urban landscapes with greater accuracy.

While Figure 4a shows the calibrated HH band Sigma 0 converted to decibels, its values range from – (17.27% to 5.61%), and Figure 4b shows the calibrated HH band Sigma 0 converted to decibels. Bell is converted, and its values are between (−25.94% and −8.0%).

Therefore, it is assumed that after converting to Sigma0 and converting it to decibels, its intensity values are distributed and stretched in such a manner that it causes better and more precise detection of urban west of Urmia City features in the image. Additionally, it makes it possible to detect urban features. It Improves the image using the relevant histograms shown in Figure 5, where the distribution and elongation of the values can be observed.

### 4.1. Average Filter

The Average filter is a regular averaging, which changes the central pixel's value with the average of the surrounding pixel's values. This filter has an excellent ability to smooth out noise. However, treating the moderation action the same will result in a reduction in resolution around sharp edges. Kernel windows with sizes of $3 \times 3$ or $5 \times 5$ are typically used to reduce this problem [*Shanthi and Valarmathi*, 2013].

Figure 6, presents the application of the average filter on the HH band with the kernel size $3 \times 3 \times 5 \times 9 \times 9$. Larger sizes are mixed, reducing the accuracy of the segregation of urban toll assessments. In addition to reducing spectral noise, selecting a $3 \times 3$ kernel size

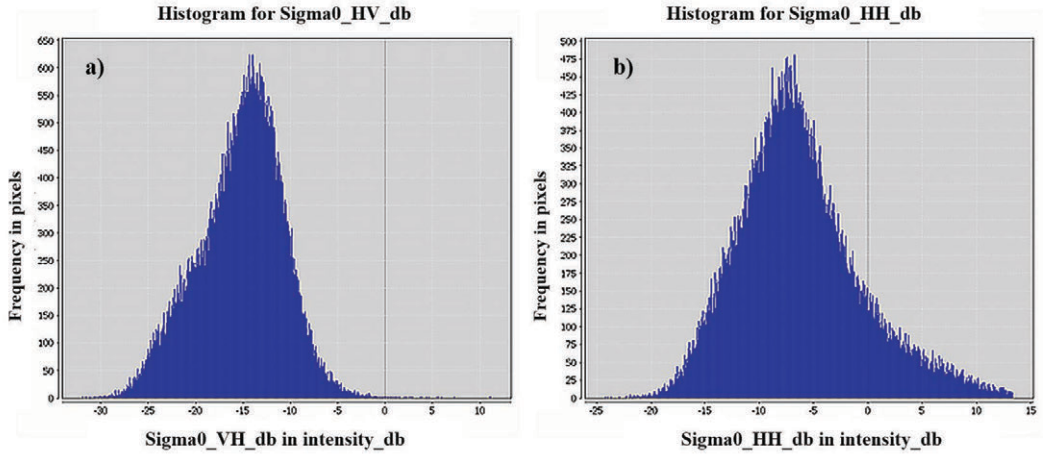


**Figure 5.** (a) sigma 0 calibrated HH band histogram converted to decibels, (b) and Sigma 0 calibrated HV band histogram converted to decibels.

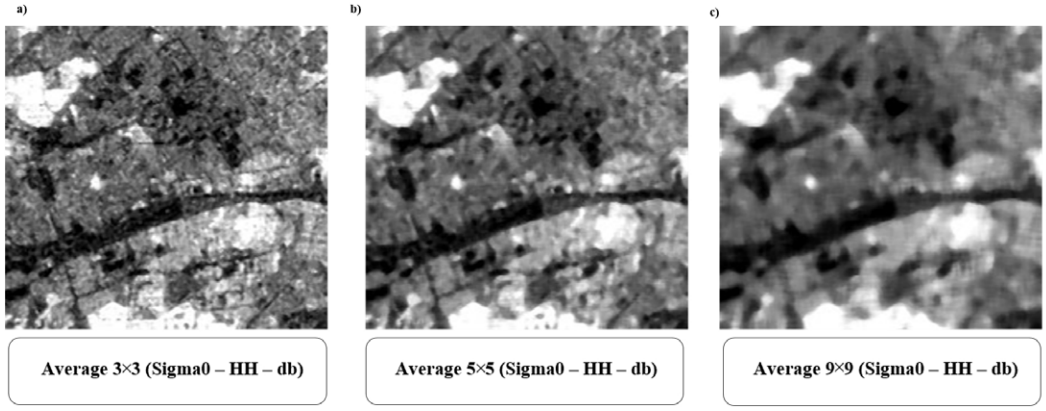


**Figure 6.** Average filter with kernel size (a) $3 \times 3$, (b) $5 \times 5$, (c) $9 \times 9$, applied on HH band (Sigma 0 – db) west of Urmia City.

also displays the existing urban west of Urmia city features in the image in smaller pixel sizes. It makes the resolution of the features more accurate.

Figure 7, which, with expanding the kernel size of histogram values, has increased from (0 to 12.5%), which causes the smoothing of urban west of Urmia city features in the image Figure 8.

In previous studies, Urban features show themselves more accurately with minor changes in the values within the specified location. *Alenin and Tyo* [2014] examined a different despeckling algorithm for (SAR) data based on the shrinkage of the wavelet and non-local concepts. *LaCasse et al.* [2011] conducted research that combined two methods for constructing images based on mathematical structure. They proved that the demosaicking method corresponds with the channel filtering technique. However, when utilizing the implied filters in that technique, the constructed image with available objects in a higher part of frequencies resulted in a higher-quality image.

### 4.2. Lee Filter

Jong-Sen-Lee established the Lee filter in 1982; the base concepts of these filters are Gaussian dispersion. In general, the statistical distribution of the image is the output of these filters. We acquire some statistical information such as median, Mean and Standard Deviation. This information provides the knowledge to assess the performance of speckle noise. The kernel size is also essential in speckle noise reduction and varies from $5 \times 5$ to $17 \times 17$ in some software such as snap. The size of kernels is odd numbers [*Lee*, 1986].

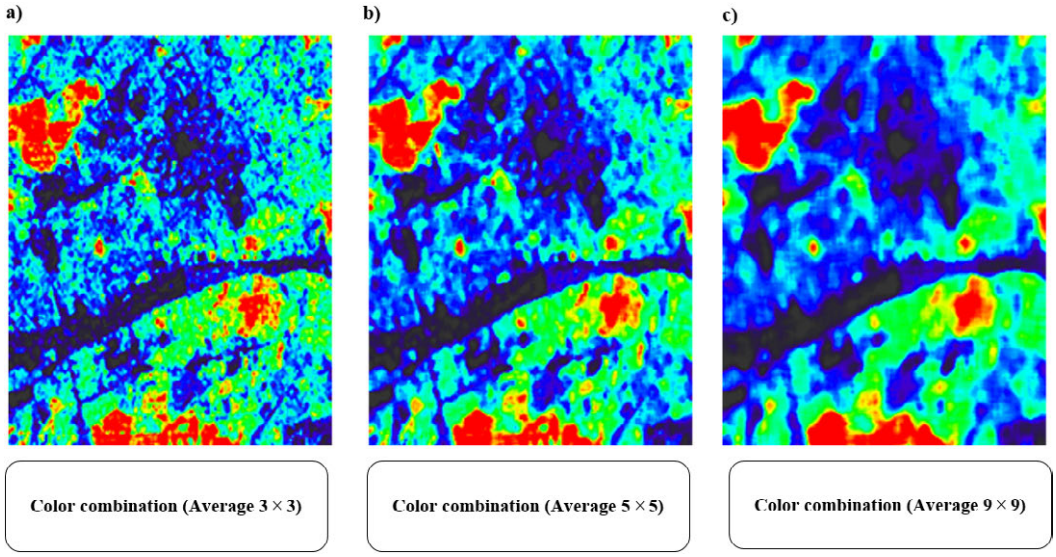


**Figure 7.** Color combination of average filter with kernel size (a) 3 × 3, (b) 5 × 5, (c) 9 × 9, applied on HH band (Sigma 0 – db) west of Urmia City.

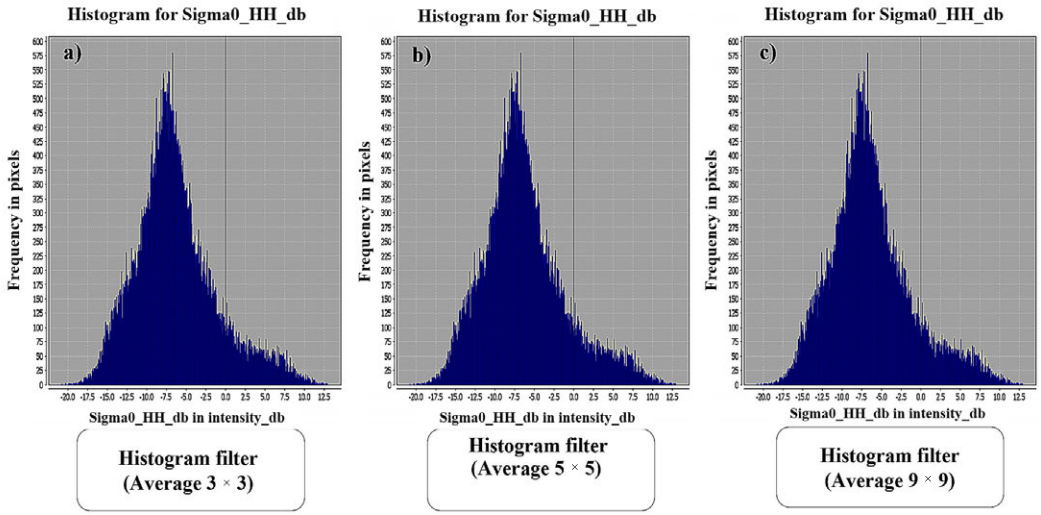


**Figure 8.** Mean histogram filter with kernel size (a) 3 × 3, (b) 5 × 5, (c) 9 × 9, applied on HH band (Sigma 0 – db).

Figure 9, presents the application of the Lee filter on the HH band with a kernel size 3 × 3 × 5 × 9 × 9.

The image in the pixel is mixed in larger sizes, which reduces the resolution of the features with low density.

However, almost all three selected kernel sizes can accurately distinguish high-density urban west of Urmia City features. In the image, it should be displayed in smaller pixel sizes, and the resolution of the effects should be made with better accuracy. In Figure 10, the color combination of the Lee filter applied on the HH band with the kernel size 3 × 3, 5 × 5, 9 × 9 confirms this result. However, the results obtained from Lee filter histograms on the HH band with kernel size 3 × 3, 5 × 5, 9 × 9 show Figure 11 that with increasing kernel size, the histogram values from 0 to 12.5, also decrease to some extent. Finds that make the image Smooth.

Therefore, it could be mentioned that the more changes in the values in the mentioned range, the better the effects. In addition to the mentioned range of kernel size values 3 × 3 and 5 × 5, other values are available that have unique functions in differentiating the effects. However, these values range between from −17.5 to 10. The kernel size histogram 9 × 9 has

values ranging from −15.0 to 10. Expanding the kernel size results in a smoother image but reduces the accuracy of detecting complications with low density.

*Lee et al.* [2015] used the boxcar and sigma filters as initial filters. Nevertheless, extending the intended approach to most available filtering methods is uncomplicated. Moreover, the spatial filters vary commonly in the way of determining the adjacent uniform pixels [*Lee et al.*, 1999], the scattering model-based method [*Lee et al.*, 2006], the sigma range [*Lee et al.*, 2015], the scattering mechanism, and the intensity information [*Wang et al.*, 2016], homogeneity measurement [*Lang et al.*, 2015], NL [*Chen et al.*, 2011; *Lang et al.*, 2014], region growing [*Vasile et al.*, 2006].

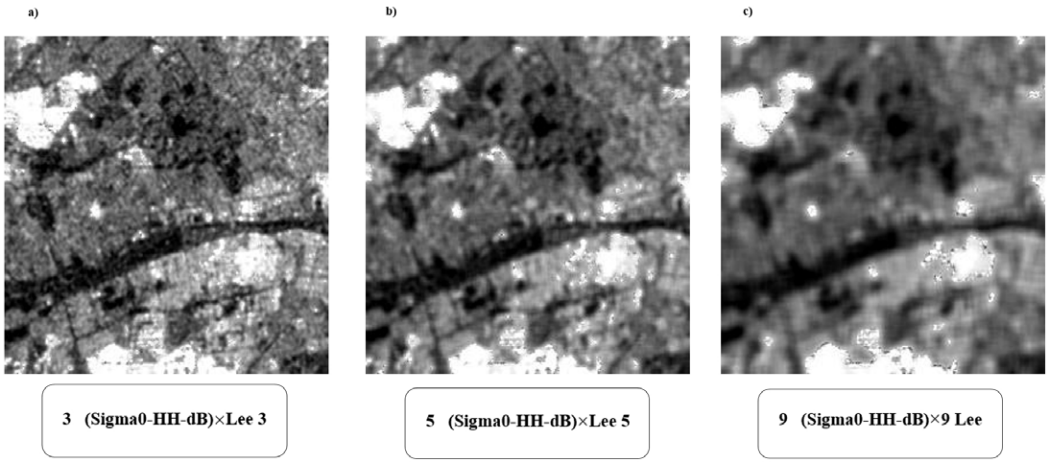


**Figure 9.** Lee filter with kernel size (a) 3 × 3, (b) 5 × 5, (c) 9 × 9, applied on the HH band (Sigma 0 – db) west of Urmia City.

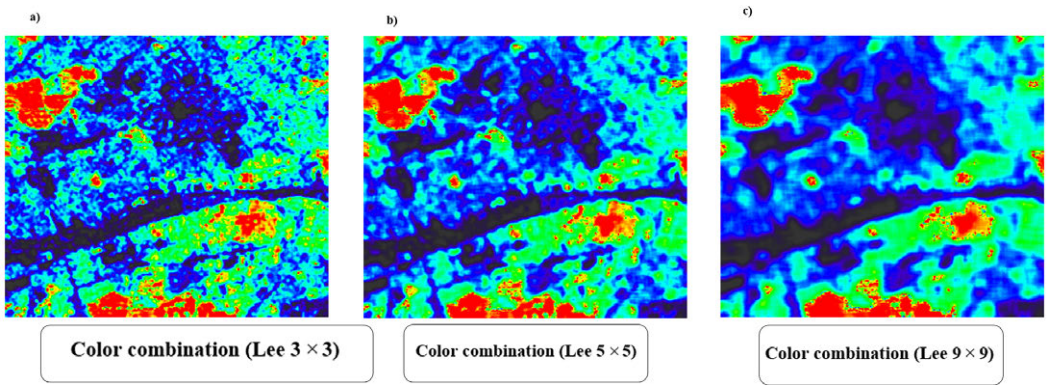


**Figure 10.** Combined Lee color filter with kernel size (a) 3 × 3, (b) 5 × 5, (c) 9 × 9, applied on HH band (Sigma 0 – db) west of Urmia City.

### 4.3. Frost Filter

The Frost filter is a widely used filter with variable parameters. It uses a weighted average on kernel pixels to soften images. The weight assigned to each pixel is a function of the kernel adjustment coefficient, mean, variance, and center pixel distance from the mean in the kernel gray [*Frost et al.*, 1982].

Figure 12, indicates the application of the Frost filter on the HH band with a kernel size 3 × 3 × 5 × 9 × 9; this increases the separation accuracy of high-density features. Nevertheless, almost all three selected kernel sizes can accurately distinguish high-density features. However, it is impossible to separate low-density tolls, and it causes urban tolls to be mixed. In addition to reducing separation accuracy, it also causes classification errors. In this filter, as in the previous filter, selecting a 3 × 3 kernel size causes the effects in the image to be displayed in smaller pixel sizes and the resolution of the effects to be done more accurately,

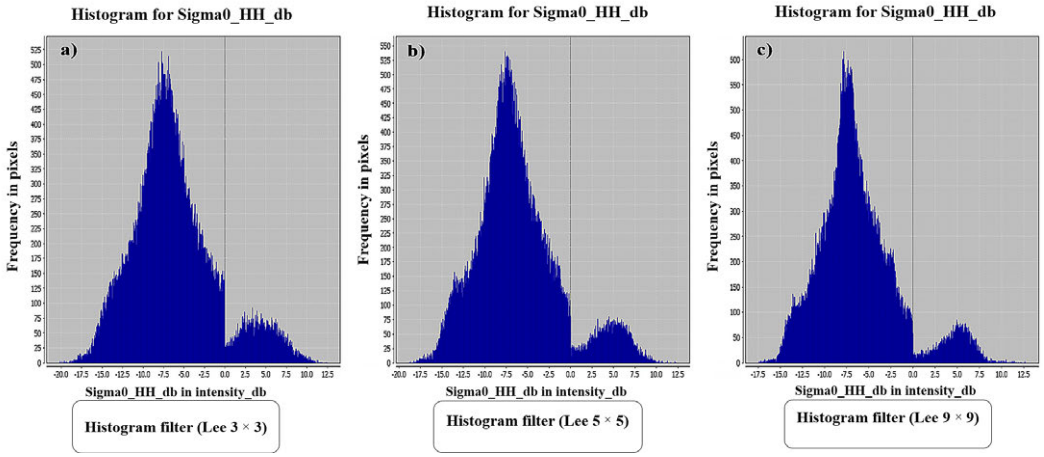


**Figure 11.** Lee filter histogram with kernel size (a) 3 × 3, (b) 5 × 5, (c) 9 × 9, applied on HH band (Sigma0 – db).

in addition to reducing spectral noise. In Figure 13, the color combination of the Frost filter applied on the HH band with the kernel size 3 × 3, 5 × 5, 9 × 9 confirms this result.

However, the results obtained from the Frost filter histograms on the HH band with The kernel size 3×3, 5×5, 9×9 show Figure 14 with increasing the kernel size, the histogram values decrease from 0 to 12.), to some extent, which makes the image smoother. Therefore, it can be concluded that more changes in the values in the mentioned range show better effects on extracting urban west of Urmia City features. Also, kernel size values 3 × 3 and 5 × 5, other than the mentioned range, differ, with values between 17.5.

They have ten and have their unique functions in differentiating different effects. According to the kernel size histogram 9×9, the values of which range from −15.0 to 10, the distribution of values of the histogram in this image becomes more compact. However, this indicates a more compact distribution of values in the histogram. It is worth mentioning that expanding the kernel size makes the image smoother and reduces the accuracy of detecting features with low density, making the distribution of intensity values more compact.

In previous studies, Improved AGGD-based noise reduction is presented to enhance the quality of the reconstructed image. Moreover, for quality enhancement, the cost of implementation is lower than the alternative methods (improved AGGD [*Golilarz et al.*, 2019], HHO [*Golilarz et al.*, 2019], and Bayes [*Chang et al.*, 2000].

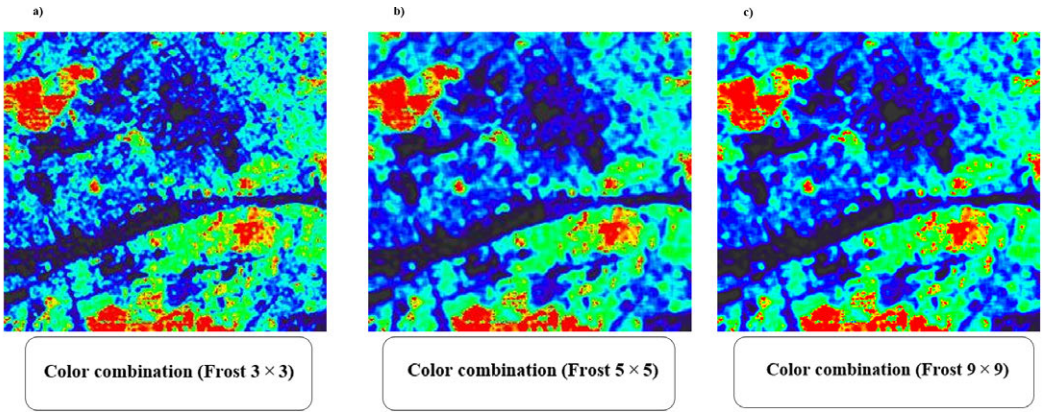


**Figure 12.** Frost filter with kernel size (a) 3 × 3, (b) 5 × 5, (c) 9 × 9, applied on HH band (Sigma 0 – db) west of Urmia City.

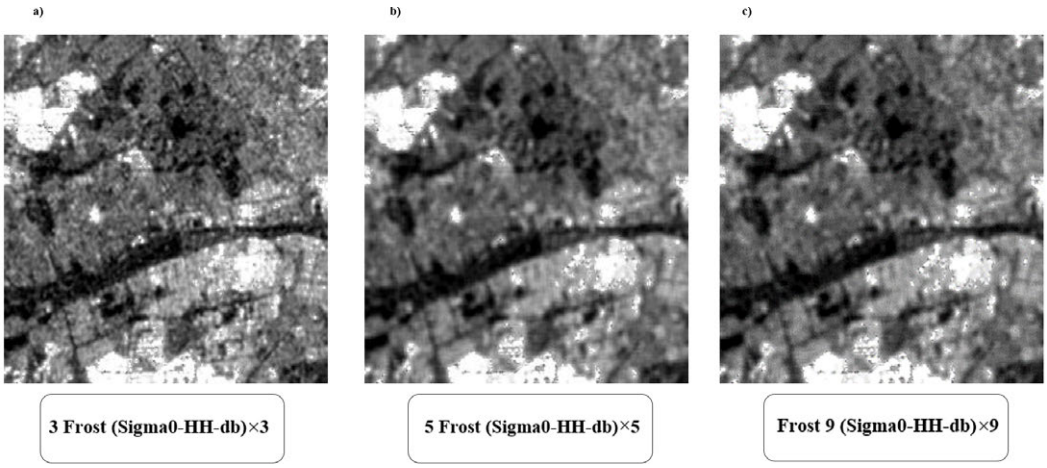


**Figure 13.** (a) frost filter with kernel size $3 \times 3$, (b) $5 \times 5$, (c) $9 \times 9$ applied on HH band (Sigma 0 – db) west of Urmia City.

### 4.4. Quantitative SSI Parameter

The quantitative SSI parameter in radar images is used to evaluate the filtering performance. The SSI parameter is a standard for quantifying and evaluating the performance of radar filters in which the average values of playback and standard deviation of images before and after application are used. Values less than one of these criteria indicate that the filter performed better. The SSI quantitative parameter was used to evaluate the performance of LEE, Average, and Frost filters, the results of which are presented in Table 4.

**Table 4.** SSI index values in different filter dimensions Average, Lee, Forst

| SSI Parameter | Filters |
|---|---|
| 0.563 | Lee $3 \times 3$ |
| 0.675 | Lee $5 \times 5$ |
| 0.896 | Lee $7 \times 7$ |
| 0.590 | Frost $3 \times 3$ |
| 0.601 | Frost $5 \times 5$ |
| 0.789 | Frost $9 \times 9$ |
| 0.683 | Average $3 \times 3$ |
| 0.630 | Average $5 \times 5$ |
| 0.785 | Average $9 \times 9$ |

### 4.5. Classification of Images by K-Means Method

According to Figure 14, four classes were extracted from the classification of $K$-means on Frost, Lee and Average filters. Comparing filters with the classification results on Landsat 8 images showed that the closest result is accurate. Above is the Lee filter with a $3 \times 3$ size kernel. The total accuracy obtained is (97.36%), and the kappa coefficient is (0.96%). Between a classified land cover map and a reference or actual land map, the producer error is related to the percentage of pixels related to the classes but classified as other classes. On the other hand, user error is an error that is calculated based on user accuracy and is equivalent to the percentage of pixels that do not belong to the class in question but are considered in that classification.

## 5. Conclusion

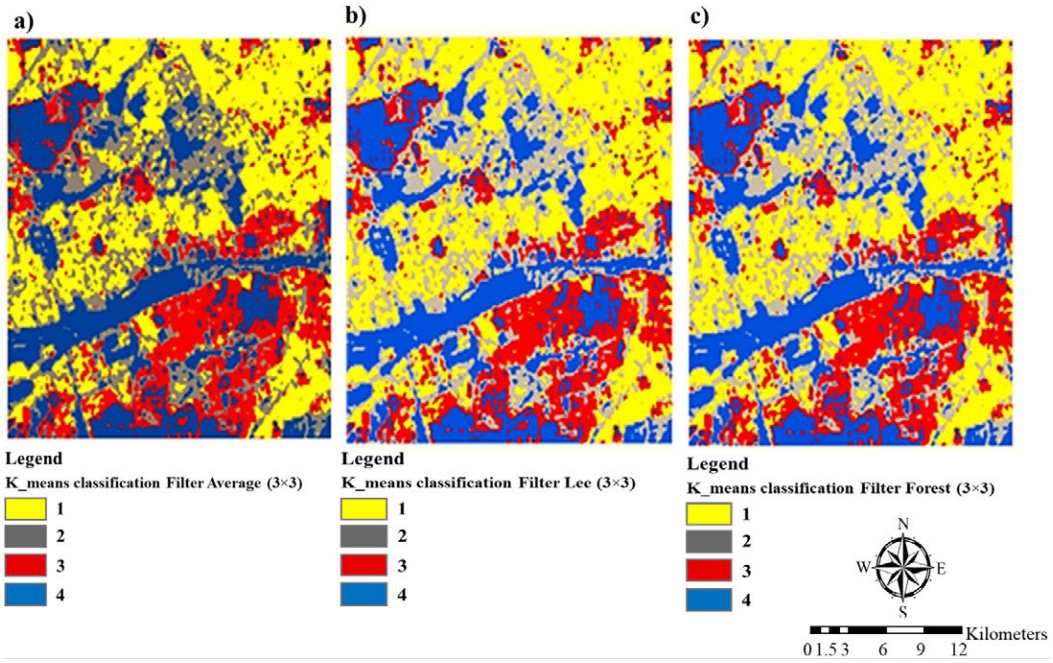


**Figure 14.** Classification of (a) *K*-means Average filter, (b) Lee filter, (c) Frost filter west of Urmia City.

Nowadays, images with the appropriate spatial and spectral resolution are often used to monitor the earth for various purposes, such as detecting changes, classifying land cover, and diagnosing complications. These techniques are especially important when data is used in sensitive areas such as the environment, natural resources, and agriculture. Based on the outputs obtained in this study, it has been shown that the HV band has better evaluation and resolution in an urban environment with artificial features such as buildings and different metal structures due to its polarization properties and sensitivity to the phenomenon in the city. In this study, different filters were applied on the images of both AlosPalsar satellite bands to estimate the degree of noise-free gray in the northwest of Urmia City according to the averages through the SSI index. The results include filters that can help reduce spike noise in AlosPalsar satellite radar images, such as the Lee filter with $3 \times 3$ kernel size.

Additionally, it is essential to note that the output from the filters may vary depending on the bands of the AlosPalsar satellite. However, after conducting *K*-means classification on Lee, Gamma-Map, Frost, and Average filters, the Lee filter with a $3 \times 3$ kernel size has been identified to provide the closest results to surface phenomena. Specifically, it produced a kappa coefficient of 0.96% and an accuracy of 97.36% in the northwest area of Urmia. Future research could include exploring the impact of different filter parameters on noise reduction and feature extraction accuracy in urban environments and comparing the results of different satellite systems in monitoring earth changes in sensitive areas.

**Acknowledgments.** We, the authors, thank the respected reviewers for reviewing this article. The research does not receive any funding. Data will be available based on request.

## References

Abdollahi, A., H. R. R. Bakhtiari, and M. P. Nejad (2017), Investigation of SVM and Level Set Interactive Methods for Road Extraction from Google Earth Images, *Journal of the Indian Society of Remote Sensing*, *46*(3), 423–430, https://doi.org/10.1007/s12524-017-0702-x.

Alenin, A. S., and J. S. Tyo (2014), Generalized channeled polarimetry, *Journal of the Optical Society of America A*, *31*(5), 1013, https://doi.org/10.1364/josaa.31.001013.

Alves, W. A. L., C. F. Gobber, D. J. Silva, A. Morimitsu, R. F. Hashimoto, and B. Marcotegui (2020), Image segmentation based on ultimate levelings: From attribute filters to machine learning strategies, *Pattern Recognition Letters*, *133*, 264–271, https://doi.org/10.1016/j.patrec.2020.03.013.

Attarchi, S., M. Poorrahimi, and V. Isazade (2020), Comparison of spectral indices and object-based classification for built-up area extraction in different urban areas, *Geographical Urban Planning Research (GUPR)*, *8*(1), 23–43, https://doi.org/10.22059/jurbangeo.2020.299492.1249.

Betbeder, J., S. Rapinel, S. Corgne, E. Pottier, and L. Hubert-Moy (2015), TerraSAR-X dual-pol time-series for mapping of wetland vegetation, *ISPRS Journal of Photogrammetry and Remote Sensing*, *107*, 90–98, https://doi.org/10.1016/j.isprsjprs.2015.05.001.

Camargo, F. F., E. E. Sano, C. M. Almeida, J. C. Mura, and T. Almeida (2019), A Comparative Assessment of Machine-Learning Techniques for Land Use and Land Cover Classification of the Brazilian Tropical Savanna Using ALOS-2/PALSAR-2 Polarimetric Images, *Remote Sensing*, *11*(13), 1600, https://doi.org/10.3390/rs11131600.

Chang, S. G., B. Yu, and M. Vetterli (2000), Adaptive wavelet thresholding for image denoising and compression, *IEEE Transactions on Image Processing*, *9*(9), 1532–1546, https://doi.org/10.1109/83.862633.

Chen, J., Y. Chen, W. An, Y. Cui, and J. Yang (2011), Nonlocal Filtering for Polarimetric SAR Data: A Pretest Approach, *IEEE Transactions on Geoscience and Remote Sensing*, *49*(5), 1744–1754, https://doi.org/10.1109/tgrs.2010.2087763.

Dai, J., T. Zhu, Y. Wang, R. Ma, and X. Fang (2020), Road Extraction From High-Resolution Satellite Images Based on Multiple Descriptors, *IEEE Journal of Selected Topics in Applied Earth Observations and Remote Sensing*, *13*, 227–240, https://doi.org/10.1109/jstars.2019.2955277.

Dass, R., and N. Yadav (2020), Image Quality Assessment Parameters for Despeckling Filters, *Procedia Computer Science*, *167*, 2382–2392, https://doi.org/10.1016/j.procs.2020.03.291.

Fazel, N., R. Berndtsson, C. B. Uvo, K. Madani, and B. Kløve (2017), Regionalization of precipitation characteristics in Iran's Lake Urmia basin, *Theoretical and Applied Climatology*, *132*(1-2), 363–373, https://doi.org/10.1007/s00704-017-2090-0.

Frost, V. S., J. A. Stiles, K. S. Shanmugan, and J. C. Holtzman (1982), A Model for Radar Images and Its Application to Adaptive Digital Filtering of Multiplicative Noise, *IEEE Transactions on Pattern Analysis and Machine Intelligence*, *PAMI-4*(2), 157–166, https://doi.org/10.1109/tpami.1982.4767223.

Ghanbari, A., V. Isazade, and Z. Alibeigy (2022), Analysis of Spatial Justice in Dealing with Urban Facilities Using Quantitative, Spatial and Moran Correlation Models (Study Area: Isfahan), *Journal Research and Urban Planning*, *13*(50), 240–254.

Ghorbanian, A., M. Kakooei, M. Amani, S. Mahdavi, A. Mohammadzadeh, and M. Hasanlou (2020), Improved land cover map of Iran using Sentinel imagery within Google Earth Engine and a novel automatic workflow for land cover classification using migrated training samples, *ISPRS Journal of Photogrammetry and Remote Sensing*, *167*, 276–288, https://doi.org/10.1016/j.isprsjprs.2020.07.013.

Golilarz, N. A., H. Gao, and H. Demirel (2019), Satellite Image De-Noising With Harris Hawks Meta Heuristic Optimization Algorithm and Improved Adaptive Generalized Gaussian Distribution Threshold Function, *IEEE Access*, *7*, 57,459–57,468, https://doi.org/10.1109/access.2019.2914101.

Hu, T., J. Yang, X. Li, and P. Gong (2016), Mapping Urban Land Use by Using Landsat Images and Open Social Data, *Remote Sensing*, *8*(2), 151, https://doi.org/10.3390/rs8020151.

Isazade, V., A. Ghanbari, and K. Valizadeh (2021), Evaluation of spectral indices and extraction of constructed and non-constructed urban features and its comparison with ground surface temperature using Landsat 7 and 8 satellite images (Study area, Tehran), *Journal of Spatial Planning*, *11*(4), 23–39, https://doi.org/10.30488/GPS.2021.243118.3283.

Isazade, V., A. B. Qasimi, and E. Isazade (2022), Environmental dust effect phenomenon on the sustainability of urban areas using remote sensing data in GEE, *Safety in Extreme Environments*, *5*(1), 59–67, https://doi.org/10.1007/s42797-022-00067-z.

Kaushik, K., and D. Kumar (2020), Forest Disturbance Mapping with Microwave Remote Sensing, *Journal of Landscape Ecology*, *13*(2), 95–128, https://doi.org/10.2478/jlecol-2020-0012.

Kraus, K. (2003), Photogrammetry, Remote Sensing and Spatial Information Sciences for heritage documentation, in *Proceedings of the XIXth International Symposium, CIPA 2003: new perspectives to save cultural heritage*, pp. 17–24, CIPA 2003 Organising Committee, Antalya (Turkey).

LaCasse, C. F., R. A. Chipman, and J. S. Tyo (2011), Band limited data reconstruction in modulated polarimeters, *Optics Express*, *19*(16), 14,976, https://doi.org/10.1364/oe.19.014976.

Lang, F., J. Yang, D. Li, L. Shi, and J. Wei (2014), Mean-Shift-Based Speckle Filtering of Polarimetric SAR Data, *IEEE Transactions on Geoscience and Remote Sensing*, *52*(7), 4440–4454, https://doi.org/10.1109/tgrs.2013.2282036.

Lang, F., J. Yang, and D. Li (2015), Adaptive-Window Polarimetric SAR Image Speckle Filtering Based on a Homogeneity Measurement, *IEEE Transactions on Geoscience and Remote Sensing*, *53*(10), 5435–5446, https://doi.org/10.1109/tgrs.2015.2422737.

Lapini, A., S. Pettinato, E. Santi, S. Paloscia, G. Fontanelli, and A. Garzelli (2020), Comparison of Machine Learning Methods Applied to SAR Images for Forest Classification in Mediterranean Areas, *Remote Sensing*, *12*(3), 369, https://doi.org/10.3390/rs12030369.

Lee, J.-S. (1986), Speckle Suppression And Analysis For Synthetic Aperture Radar Images, *Optical Engineering*, *25*(5), 255,636, https://doi.org/10.1117/12.7973877.

Lee, J.-S., M. R. Grunes, and G. de Grandi (1999), Polarimetric SAR speckle filtering and its implication for classification, *IEEE Transactions on Geoscience and Remote Sensing*, *37*(5), 2363–2373, https://doi.org/10.1109/36.789635.

Lee, J.-S., M. R. Grunes, D. L. Schuler, E. Pottier, and L. Ferro-Famil (2006), Scattering-model-based speckle filtering of polarimetric SAR data, *IEEE Transactions on Geoscience and Remote Sensing*, *44*(1), 176–187, https://doi.org/10.1109/tgrs.2005.859338.

Lee, J.-S., T. L. Ainsworth, Y. Wang, and K.-S. Chen (2015), Polarimetric SAR Speckle Filtering and the Extended Sigma Filter, *IEEE Transactions on Geoscience and Remote Sensing*, *53*(3), 1150–1160, https://doi.org/10.1109/tgrs.2014.2335114.

Leiva-Murillo, J. M., L. Gomez-Chova, and G. Camps-Valls (2013), Multitask Remote Sensing Data Classification, *IEEE Transactions on Geoscience and Remote Sensing*, *51*(1), 151–161, https://doi.org/10.1109/TGRS.2012.2200043.

Li, Y., S. Wang, Q. Zhao, and G. Wang (2020), A new SAR image filter for preserving speckle statistical distribution, *Signal Processing*, *176*, 107,706, https://doi.org/10.1016/j.sigpro.2020.107706.

Liu, N., Z. Cao, Z. Cui, Y. Pi, and S. Dang (2019), Multi-Scale Proposal Generation for Ship Detection in SAR Images, *Remote Sensing*, *11*(5), 526, https://doi.org/10.3390/rs11050526.

Mohan, M., and A. Kandya (2015), Impact of urbanization and land-use/land-cover change on diurnal temperature range: A case study of tropical urban airshed of India using remote sensing data, *Science of The Total Environment*, *506-507*, 453–465, https://doi.org/10.1016/j.scitotenv.2014.11.006.

Mun, J., Y. Jang, Y. Nam, and J. Kim (2019), Edge-enhancing bi-histogram equalisation using guided image filter, *Journal of Visual Communication and Image Representation*, *58*, 688–700, https://doi.org/10.1016/j.jvcir.2018.12.037.

NISAR (2018), *NASA-ISRO SAR (NISAR) Mission Science Users' Handbook*, NASA Jet Propulsion Laboratory.

Nouri, H., R. J. Mason, and N. Moradi (2017), Land suitability evaluation for changing spatial organization in Urmia County towards conservation of Urmia Lake, *Applied Geography*, *81*, 1–12, https://doi.org/10.1016/j.apgeog.2017.02.006.

Osgouei, P. E., S. Kaya, E. Sertel, and U. Alganci (2019), Separating Built-Up Areas from Bare Land in Mediterranean Cities Using Sentinel-2A Imagery, *Remote Sensing*, *11*(3), 345, https://doi.org/10.3390/rs11030345.

Podest, E. (2018), *SAR for Mapping Land Cover*, National Aeronautics and Space Administration.

Qasimi, A. B., V. Isazade, G. Kaplan, and Z. Nadry (2022), Spatiotemporal and multi-sensor analysis of surface temperature, NDVI, and precipitation using google earth engine cloud computing platform, *Russian Journal of Earth Sciences*, *22*(6), 1–12, https://doi.org/10.2205/2022ES000812.

Rasche, C. (2018), Rapid contour detection for image classification, *IET Image Processing*, *12*(4), 532–538, https://doi.org/10.1049/iet-ipr.2017.1066.

Routray, S., P. P. Malla, S. K. Sharma, S. K. Panda, and G. Palai (2020), A new image denoising framework using bilateral filtering based non-subsampled shearlet transform, *Optik*, *216*, 164,903, https://doi.org/10.1016/j.ijleo.2020.164903.

Seo, S. (2018), Subpixel Edge Localization Based on Adaptive Weighting of Gradients, *IEEE Transactions on Image Processing*, *27*(11), 5501–5513, https://doi.org/10.1109/tip.2018.2860241.

Seo, S. (2019a), Subpixel Line Localization With Normalized Sums of Gradients and Location Linking With Straightness and Omni-Directionality, *IEEE Access*, *7*, 155–167, https://doi.org/10.1109/access.2019.2959320.

Seo, S. (2019b), Line-Detection Based on the Sum of Gradient Angle Differences, *Applied Sciences*, *10*(1), 254, https://doi.org/10.3390/app10010254.

Serwa, A. (2020), Studying the Potentiality of Using Digital Gaussian Pyramids in Multi-spectral Satellites Images Classification, *Journal of the Indian Society of Remote Sensing*, *48*(12), 1651–1660, https://doi.org/10.1007/s12524-020-01173-w.

Serwa, A., and S. Elbialy (2021), Enhancement of classification accuracy of multi-spectral satellites' images using Laplacian pyramids, *The Egyptian Journal of Remote Sensing and Space Science*, *24*(2), 283–291, https://doi.org/10.1016/j.ejrs.2020.12.006.

Serwa, A., and M. Saleh (2021), New semi-automatic 3D registration method for terrestrial laser scanning data of bridge structures based on artificial neural networks, *The Egyptian Journal of Remote Sensing and Space Science*, *24*(3, Part 2), 787–798, https://doi.org/10.1016/j.ejrs.2021.06.003.

Seto, K. C., B. Güneralp, and L. R. Hutyra (2012), Global forecasts of urban expansion to 2030 and direct impacts on biodiversity and carbon pools, *Proceedings of the National Academy of Sciences*, *109*(40), 16,083–16,088, https://doi.org/10.1073/pnas.1211658109.

Shanthi, I., and M. L. Valarmathi (2013), SAR image despeckling using possibilistic fuzzy C-means clustering and edge detection in bandelet domain, *Neural Computing and Applications*, *23*(S1), 279–291, https://doi.org/10.1007/s00521-013-1394-y.

Shi, Y., Q. Li, and X. X. Zhu (2019), Building Footprint Generation Using Improved Generative Adversarial Networks, *IEEE Geoscience and Remote Sensing Letters*, *16*(4), 603–607, https://doi.org/10.1109/LGRS.2018.2878486.

Shokati, B., and B. Feizizadeh (2018), Sensitivity and uncertainty analysis of agro-ecological modeling for saffron plant cultivation using GIS spatial decision-making methods, *Journal of Environmental Planning and Management*, *62*(3), 517–533, https://doi.org/10.1080/09640568.2018.1427561.

Sun, H., W. Forsythe, and N. Waters (2007), Modeling Urban Land Use Change and Urban Sprawl: Calgary, Alberta, Canada, *Networks and Spatial Economics*, *7*(4), 353–376, https://doi.org/10.1007/s11067-007-9030-y.

Vasile, G., E. Trouve, J.-S. Lee, and V. Buzuloiu (2006), Intensity-driven adaptive-neighborhood technique for polarimetric and interferometric SAR parameters estimation, *IEEE Transactions on Geoscience and Remote Sensing*, *44*(6), 1609–1621, https://doi.org/10.1109/tgrs.2005.864142.

Wang, Y., J. Yang, and J. Li (2016), Similarity-intensity joint PolSAR speckle filtering, in *2016 CIE International Conference on Radar (RADAR)*, pp. 1–5, https://doi.org/10.1109/RADAR.2016.8059213.

Wei, C., and T. Blaschke (2018), Pixel-Wise vs. Object-Based Impervious Surface Analysis from Remote Sensing: Correlations with Land Surface Temperature and Population Density, *Urban Science*, *2*(1), https://doi.org/10.3390/urbansci2010002.

Yang, C. H., B. K. Kenduiywo, and U. Soergel (2016), Change detection based on persistent scatterer interferometry – a new method of monitoring building changes, *ISPRS Annals of the Photogrammetry, Remote Sensing and Spatial Information Sciences*, *III-7*, 243–250, https://doi.org/10.5194/isprs-annals-III-7-243-2016.

Zakeri, H., F. Yamazaki, and W. Liu (2017), Texture Analysis and Land Cover Classification of Tehran Using Polarimetric Synthetic Aperture Radar Imagery, *Applied Sciences*, *7*(5), 452, https://doi.org/10.3390/app7050452.

Zia, S., S. A. Shirazi, M. N. Bhalli, and S. Kausar (2015), The Impact Of Urbanization On Mean Annual Temperature Of Lahore Metropolitan Area, Pakistan, *Pakistan Journal of Science*, *67*(3).

Russian Journal of Earth Sciences

Special Issue: "Fundamental and Applied Aspects of Geology, Geophysics and Geoecology"

# Review of Models for Estimating and Predicting the Amount of Energy Produced by Solar Energy Systems

**Vladimir S. Simankov[1], Pavel Yu. Buchatskiy*[,2], Stefan V. Onishchenko[2], Semen V. Teploukhov[2]**

[1] Kuban State Technological University, Krasnodar, Russia
[2] Adyghe State University, Maykop, Russia
* **Correspondence to:** Pavel Yu. Buchatskiy, butch_p99@mail.ru

**Abstract:** Energy production based on renewable sources is a fundamental aspect of society's sustainable development. The involvement of renewable energy sources in the implementation of modern energy systems can significantly reduce the amount of harmful emissions into the atmosphere and provide greater flexibility of energy infrastructure. The first step in determining the feasibility of involving a particular energy source in the overall energy system of the region is a preliminary assessment of the energy potential to determine the possible percentage of substitution of traditional energy. To solve this problem, it is necessary to use the models of energy supply, which are currently presented in a wide variety. In this regard, this paper proposes to consider various models for estimating the solar energy potential, which can be divided into empirical models and models based on the application of modern intelligent data analysis technologies. Such models are based on many different climatic and geographical indicators, such as: longitude of sunshine, ambient temperature, serial number of the day of the current year, amount of precipitation, average and maximum values of wind speed and so on. The paper analyzed the existing models for estimating the amount of energy, which can be used in the system designed to determine the most optimal configuration of the energy system based on the use of various conversion technologies most relevant to the case under study, and also serve as the basis for creating digital twins designed to model and optimize the operation of the projected energy complex.

**Keywords:** potential assessment models, smart models, renewable energy, solar energy.

**Citation:** Simankov V. S., Buchatskiy P. Yu., Onishchenko S. V., Teploukhov S. V. (2023), Review of Models for Estimating and Predicting the Amount of Energy Produced by Solar Energy Systems, *Russian Journal of Earth Sciences*, Vol. 23, ES0201, https://doi.org/10.2205/2023ES02SI01

## 1. Introduction

Currently, the energy sector has a great impact on the state economy, national security, which is critical for successful socio-economic development. The development of the energy complex plays a fundamental role in the world economic system and played a key role in the previous three technological revolutions. In accordance with the objectives of the policy of general decarbonization [*Iktisanov and Shkrudnev*, 2021], energy transformation is taking place, resulting in a significant increase in the share of clean energy capacity in the world, such as photovoltaic and wind energy [*IRENA, IEA and REN21*, 2018; *Liu et al.*, 2021].

Against the backdrop of the Covid-19 pandemic that has occurred, renewable energy worldwide has acquired record power generation capacity in 2020–2021 and is the only source with a net increase in total power generation capacity [*REN21*, 2020; *REN21*, 2021]. It is widely known that renewable energy sources have various advantages over carbon resources, such as: lower energy costs compared with traditional energy sources, no harmful emissions, contributing to the improvement of the overall world pollution and stimulating economic growth [*EPA*, 2018].

Research Article

Received: 20 October 2023
Accepted: 27 November 2023
Published: 15 December 2023

**Copyright:** © 2023. The Authors. This article is an open access article distributed under the terms and conditions of the Creative Commons Attribution (CC BY) license (https://creativecommons.org/licenses/by/4.0/).

The situation is somewhat different in the Russian Federation. At present the percentage of energy production on the basis of alternative sources is about 0.69–0.75% [*Russia Renewable Energy Development Association (RREDA)*, 2022], which does not compare with European countries, where energy production on the basis of "green" energy reaches values of 25–30% (and up to 60% in some cases, for example, in Denmark) [*IEA*, 2023] of total energy production.

Despite such a small percentage of power generation on the basis of alternative sources, there is a constant growth of RES energy generation and commissioning of new power plants. Contributes to this overall concept of energy transformation and the adopted energy strategy for the period up to 2030 [*Energy strategy of the Russian Federation for the period until 2035*, 2020], which involves the process of optimizing the entire structure of the fuel and energy balance of the state, including by increasing the share of non-fuel energy to 13–14% of total energy production.

The implementation of such a strategy of energy transformation requires a comprehensive approach, consisting of many stages, the initial of which is the stage of assessing the involvement of a particular type of resource [*Simankov*, 2002] or a set of several resources to determine the economic efficiency of such an implementation [*Simankov and Buchatskiy*, 2021].

In this regard, the paper proposes an analysis of existing approaches to modeling and estimating the amount of solar energy, which is one of the most common renewable energy sources.

## 2. Materials and Methods

In general, models for estimating solar energy can be divided into the following groups [*Vaskov and Narynbaev*, 2020]:

1. mathematical models (linear and nonlinear empirical models);
2. models based on artificial intelligence methods and data mining.

Let us first consider the existing mathematical models for estimating and modeling the amount of solar energy inflow. These models are usually based on the following group of parameters [*Besharat et al.*, 2013]:

1. geographic, such as latitude and longitude, altitude above sea level, and albedo of the terrain;
2. geometric, taking into account the position of the converting elements in space;
3. physical parameters, allowing to take into account such factors as dusting and dispersion of air molecules;
4. meteorological parameters such as temperature, precipitation, humidity, cloudiness, etc.

### 2.1. Mathematical models to estimate the theoretical solar energy potential

According to the study [*Demain et al.*, 2013], all models can be divided into two groups:

1. isotropic models, which are rather simple models assuming uniform distribution of scattered radiation over the sky dome;
2. anisotropic models, which allow taking into account the scattering coefficients of solar radiation.

Thus, the incoming global solar radiation on the inclined surface, $G_\beta$, can be divided into three components:

1. the direct component of irradiation of the inclined surface – $B_\beta$;
2. scattered component – $D_\beta$;
3. the reflected component, which quantifies the radiation reflected from the ground to the inclined surface $R_\beta$:

$$G_\beta = B_\beta + D_\beta + R_\beta \quad (1)$$

Further studies showed that the diffuse component (scattered) consists of the following three components: $D_{\beta,\,\mathrm{iso}}$ – isotropic diffuse component; $D_{\beta,\,\mathrm{cs}}$ – circumsolar diffuse component; $D_{\beta,\,\mathrm{hb}}$ – horizon brightening component, so that the total solar radiation arriving at the surface is expressed as:

$$G_\beta = B_\beta + (D_{\beta,\,\mathrm{iso}} + D_{\beta,\,\mathrm{cs}} + D_{\beta,\,\mathrm{hb}}) + R_\beta \quad (2)$$

The calculation of the direct component $B_\beta$ is purely geometric and is performed using certain expressions, so many models focus on the calculation of the diffuse component $D_\beta$, and in particular on the diffuse transfer coefficient $R_d$, which is the ratio of diffuse radiation on an inclined surface to radiation on a horizontal surface.

An isotropic model, called the Lew-Jordan model, was one of the first to be proposed [*Liu and Jordan*, 1962]:

$$R_d = \frac{1+\cos\beta}{2} \quad (3)$$

Later, various improvements to this model presented in [*Badescu*, 2002; *Hamilton and Jackson*, 1985; *Koronakis*, 1986] were considered, resulting in the following expression:

$$R_d = \frac{1}{4}(3+\cos(2\beta)\,) \quad (4)$$

There are a number of papers investigating and proposing anisotropic models to account for each component of diffuse radiation [*Bugler*, 1977; *Klucher*, 1979; *Ma and Iqbal*, 1983; *Muneer and Kambezidis*, 1997; *Perez et al.*, 1987; *Willmott*, 1982], but the authors of the study [*Demain et al.*, 2013] evaluated and examined these models, resulting in the selection of three most appropriate models.

The first of the selected models [*Bugler*, 1977] gives the best results for clear skies with the fewest clouds, according to which the diffuse transfer coefficient can be calculated as:

$$R_d = \frac{1}{2}(1+\cos\beta) + 0.05\frac{B_\beta}{D}\left(\cos\theta_i - \frac{1}{\cos\theta_z}\left(\frac{1+\cos\beta}{2}\right)\right) \quad (5)$$

Here we added the consideration of the angular height of the sun above the horizon, which increased the accuracy of the calculations. The author suggested using the anisotropic reduction factor, which made it possible to take into account the presence of partial shading.

The second of the models [*Willmott*, 1982] chosen by the authors shows the best results in partially shaded skies, with variable cloud cover (but not constant):

$$R_d = \frac{B_{Nb}}{S_o} + C_\beta\left(1 - \frac{B_N}{S_o}\right), \quad (6)$$

where $C_\beta = 1.011 - 0.20293\beta - 0.080823\beta^2$, $\beta$ is expressed in radians. So is the solar constant (i.e., 1367 $\mathrm{Wm^{-2}}$).

The latter model [*Perez et al.*, 1987] is the most suitable for use in cloudy weather conditions. The author in his model proposed the input of specialized coefficients, which were obtained empirically:

$$R_d = F_1\frac{a}{b} + (1-F_1)\frac{1+\cos\beta}{2} + F_2\sin\beta, \quad (7)$$

where $F_1$ and $F_2$ are the sky brightness ratios for the near-solar region and the region above the horizon line, respectively.

There are a number of clear-sky models based on the atmospheric turbidity coefficient, which were discussed in [*Moldovan et al.*, 2020]. The use of such models makes it possible to estimate the amount of incoming solar radiation in the absence of cloudiness, but in the

presence of some turbidity due to the presence of water vapor in the atmosphere or other aerosol compounds [*Rigollier et al.*, 2002].

To determine the amount of solar radiation arriving at the Earth's surface [*Bird and Hulstrom*, 1981], we can consider the model presented by the authors in [*Achituev and Enebish*, 2015]. The total solar radiation for the plane outside the Earth's atmosphere can be determined as follows:

$$H_0' = \left(\frac{t_s G_0}{\pi}\right)\left[\cos\varphi\cos\delta\sin\omega_s + \frac{2\pi\omega_s}{360}\sin\varphi\sin\delta\right], \tag{8}$$

where $G_0$ – solar constant, equal to 1340 W/m$^2$, $\varphi$ – geographical latitude of area, $\delta = \frac{23.45}{180}\pi\sin\left[\frac{284+n}{365}2\pi\right]$ – declination, $n$ – number of day in year, $t_s = 480\arccos(-\tan\varphi\tan\delta$ – day duration, $\omega_s = \arccos(-\tan\varphi\tan\delta)$ – hour angle at sunset.

When taking into account the ellipticity of the orbit, the expression for calculating the real value of the extra-atmospheric daily solar radiation is converted into the following relation:

$$H_0\left[1 + ecos\left(\frac{360n}{365}\right)\right]H_0', \tag{9}$$

where $e = 0.333$ is the eccentricity of the orbit, $n$ is the number of days in the year.

To determine the amount of radiation dissipated in the atmosphere, the clarity index $K_T$, equal to the ratio of the total daily radiation arriving at the Earth's surface to the total daily solar radiation arriving at the site outside the atmosphere, is used.

Using this index, the fraction of diffuse solar radiation can be calculated:

$$\frac{H_D}{H} = 1.39 - 4.03K_T + 5.53K_T^2 - 3.11K_T^3. \tag{10}$$

Thus, the total solar radiation arriving at the surface at angle $\beta$ can be defined as:

$$H_\beta = H\left[\left(1 - \frac{H_D}{H}\right)R + \frac{H_D}{H}\frac{1-\cos\beta}{2} + \rho\frac{1-\cos\beta}{2}\right], \tag{11}$$

where $\rho$ is the albedo of the terrain;

$$R = \frac{\cos(\varphi-\beta)\cos\delta sin\omega_s + \frac{\pi}{180}\omega_s\sin(\varphi-\beta)\sin\delta}{\cos\varphi\cos\delta\ sin\omega_s + \frac{\pi}{180}\omega_s\sin\varphi\ \sin\delta} \tag{12}$$

For this model, the necessary input data are the following parameters: geographic latitude of the area, data on total and reflected solar radiation, and the angle of inclination of the panel surface. The result is the value of solar radiation coming to the surface. This model has high accuracy (calculation error does not exceed 4%).

The authors in [*Simankov et al.*, 2000] considered different models to estimate the amount of solar insolation, allowing simulation in clear sky and cloudy conditions. In addition, two models for estimating cloud formation were considered:

- A model of the evolution of layered cloud cover;
- A statistical model of cloud cover.

In [*Simankov and Buchatskiy*, 2019], the authors presented a set of basic mathematical models for assessing renewable energy sources, among which there are models for estimating the energy potential of solar energy (a cloudless sky model and a cloudless sky model) and a model that allows forecasting the performance of a photovoltaic plant (Table 1).

The following study [*An et al.*, 2020] presents another model to estimate the total solar radiation arriving at the horizontal surface during the day. The proposed method is based on the use of a new algorithm for estimating illuminance with a 10-minute time step. The proposed algorithm used for illuminance estimation assumes that the solar radiation varies linearly over a 1-hour period, and the slope is estimated based on the values of

**Table 1**. Complex of mathematical models for RES evaluation.

| Model name | | Model type |
|---|---|---|
| Model of solar radiation input | model with a cloudless sky | $Q_{\text{day}}^{\text{possibility}} = \text{SA}\int_{t_{\text{sun}}^{\text{sunrise}}}^{t_{\text{sun}}^{\text{sunset}}}\left[\left(-B\cdot\omega - C\cdot r - D\frac{1}{\sin(\text{Al}(t))+}\right)\cdot\sin(\text{Al}(t))\right]dt$ |
| | cloud cover model | $Q^{\text{day}} = Q_{\text{relative}}\cdot Q_{\text{possibility}}^{\text{day}}$, $f(Q_{\text{relative}}) = \frac{1}{B(a,b)}Q_{\text{relative}}^{(\text{a-1})}\cdot(1-Q_{\text{relative}})^{(b-1)}$, $B(a,b) = \int_0^1\left[Q_{\text{relative}}^{(}a-b)\cdot(1-Q_{\text{relative}})^{(b-1)}\right]d(Q_{\text{relative}})$ |
| Wind flow energy inflow | | $E = \frac{1}{2}q\bar{v}_w^3$, $p(v_w) = \frac{k_1}{A_1}\left(\frac{v_\beta}{A_1}\right)^{k_1-1}\exp\left[-\left(\frac{v_w}{A_1}\right)^{k_1}\right]$ |
| Model of a photovoltaic system | | $I_H = I_\varnothing - I_0\left(\exp\frac{qU_H}{\text{AKT}-1}\right)$ |
| Model wind turbine | | $P_w = \frac{p_w^{\max}}{\varphi_{\text{nominal}}-\varphi_{\text{on}}}\left\{G_k(\varphi_{\text{nominal}}) - G_k(\varphi_{\text{on}}) - \exp\left(-\left(\frac{v_\beta}{A_1}\right)^{K_1}\right)\right\}$ |
| Model energy storage (chemical current sources) | | $U_{RB} = E(Q;I_{\text{EXT}}) - 1\cdot R_{\text{EXT}}(Q;I_{RB})$, $E(Q;I_{RB}) = E_0 + \frac{\Psi_0}{Q\Psi}(Q\Psi - I_{RB}\cdot t) + \varphi_0\exp\left(-\frac{3I_{RB}\cdot t}{Q_\varphi}\right)$, $R_{\text{EXT}}(Q;I_{RB}) = A_2\cdot\left(\frac{Q\Psi - IAB\cdot t}{Q\Psi}\right)^2 + B_2\left(\frac{\alpha}{I_{RB}^\beta}-1\right)$ |

solar insolation during the last hour, the current hour, and the next hour. The approach proposed by the authors, consists of the following steps:

1. Calculation of the time of sunrise, solar noon and sunset;
2. Calculation of instantaneous solar irradiance in the middle of each hour using the following formula:

$$SG_{\text{mid},i} = \text{SI}_i/(t_{\text{end},i} - t_{\text{start},i}). \tag{13}$$

where $i$ is the current hour, $t_{\text{end}}$ and $t_{\text{start}}$ are the start and end times of each hour, $G_{\text{mid}}$ is the instantaneous solar radiation at the midpoint in W/m$^2$, SI is the hourly solar insolation in W h/m$^2$.

3. For normal hours between sunrise and sunset, the slope of the solar radiation arrival over a period of one hour is calculated based on the following expression:

$$\text{SLOPE}_i = \begin{cases} \min\left(\frac{SG_{\text{mid},i} - SG_{\text{mid},i-1}}{t_{\text{mid},i} - t_{\text{mid},i-1}}, \frac{SG_{\text{mid},i+1} - SG_{\text{mid},i}}{t_{\text{mid},i+1} - t_{\text{mid},i}}\right) SG_{\text{mid},i-1} \le SG_{\text{mid},i} \le SG_{\text{mid},i+1} \\ \max\left(\frac{SG_{\text{mid},i} - SG_{\text{mid},i-1}}{t_{\text{mid},i} - t_{\text{mid},i-1}}, \frac{SG_{\text{mid},i+1} - SG_{\text{mid},i}}{t_{\text{mid},i} + 1 - t_{\text{mid},i}}\right) SG_{\text{mid},i-1} > SG_{\text{mid},i} > SG_{\text{mid},i+1} \\ -1\times\min\left(\left|\frac{SG_{\text{mid},i} - SG_{\text{mid},i-1}}{t_{\text{mid},i} - t_{\text{mid},i-1}}\right|, \left|\frac{SG_{\text{mid},i+1} - SG_{\text{mid},i}}{t_{\text{mid},i+1} - t_{\text{mid},i}}\right|, \left|\frac{2SG_{\text{mid},i}}{t_{end,i} - t_{\text{start},i}}\right|\right) \text{else, when } t_{\text{mid},i} \le t_{\text{solarnoon}} \\ \min\left(\left|\frac{SG_{\text{mid},i} - SG_{\text{mid},i-1}}{t_{\text{mid},i} - t_{\text{mid},i-1}}\right|, \left|\frac{SG_{\text{mid},i+1} - SG_{\text{mid},i}}{t_{\text{mid},i+1} - t_{\text{mid},i}}\right|, \left|\frac{2SG_{\text{mid},i}}{t_{end,i} - t_{start,i}}\right|\right) \text{else, when } t_{\text{mid},i} > t_{\text{solarnoon}} \end{cases}$$

where $i-1, i, i+1$ are the preceding current and next hours, respectively; $t_{\text{mid},i}$ is the middle of each hour; $t_{\text{solarnoon}}$ is the time of solar noon; $\text{SLOPE}_i$ is the slope of incoming solar radiation during the hour.

4. In addition, we calculate the solar insolation for the first and last hours of radiation.

Thus, the method proposed by the authors allows us to obtain more accurate values of the incoming solar radiation, compared with the approaches described in [*Zhu et al.*, 2012], since greater accuracy is achieved by using different time intervals and values in the middle of the current hour.

There are a number of mathematical models such as the Justus method [*Justus et al.*, 1978], Leesen method [*Lysen*, 1982], maximum likelihood method [*Stevens and Smulders*, 1979], energy density method [*George*, 2014], Rayleigh distribution [*Tonsie Djiela et al.*, 2020], Mabchur empirical method [*Zohbi et al.*, 2014], energy pattern method [*Akdağ and Dinler*, 2009], energy distribution factor method [*Akdağ and Güler*, 2015] used to determine solar radiation potential based on the Weibull probability distribution, reviewed and analyzed in [*Koholé et al.*, 2023]. According to the conclusion of the authors, based on a statistical study of each of these methods, it was found that each of the considered approaches provides acceptable accuracy results for predicting the amount of solar radiation. The authors used the following approach, depicted in Figure 1, to test the adequacy of each of the models under study.

There are a number of models to estimate the solar radiation based on various astronomical parameters, which are considered below, before proceeding to consider these models [*Mghouchi et al.*, 2016]:

Distance to the Sun, which can vary since the orbit is elliptical:

$$C_t = 1 + 0.034\cos(j-2), \tag{14}$$

where $j$ is the number of the day of the year.

Solar deviation [*Cooper*, 1969]:

$$\delta = 23.45\sin(0.986(j+284)). \tag{15}$$

Clock Angle:

$$\omega = 15(12 - T_{sv}), \tag{16}$$

where $T_{\text{sv}}$ is the True Solar Time at a certain point, which can be calculated as:

$$T_{sv} = T_l - DT_l + (D_{\text{hg}} + E/60)/60, \tag{17}$$

where $T_l$ is local time, $DT_l$ is the difference between local and standard time, $D_{\text{hg}}$ is the time difference (4 minutes ahead by one degree), $E$ is the time equation:

$$E = 450.8\sin(2\pi j/365 - 0.026903) + 595.4\sin(4\pi j/365 + 0.352835). \tag{18}$$

The height of the Sun:

$$h = \sin^{-1}(\sin(\varphi)\sin(\delta) + \cos(\varphi)\cos(\delta)\cos(\omega)), \tag{19}$$

where $\varphi$ is the geographic latitude.

Azimuth of the Sun:

$$\psi = sin^{-1}(\cos(\delta)\sin(\omega)/\cos(h). \tag{20}$$

Duration of the day:

$$S_j = 24(1 - \cos^{-1}(\tan(\delta)\tan(\lambda))/\pi, \tag{21}$$

where $\lambda$ is the geographical longitude.

Duration of the Sun's aurora:

$$S_e = \frac{2}{15} cos^{-1}\ (-\tan(\varphi)\tan(\delta)). \tag{22}$$

Using these characteristics, we can calculate the parameters forming the global solar radiation $G$, consisting of the direct $I$ and diffuse $D$.

Thus, using Guard's model [*Saïghi*, 2002], we can calculate all these parameters:

$$I = I_0 C_t A_1 \left(-\frac{A_2}{\sin(h)}\right)\sin(h). \tag{23}$$

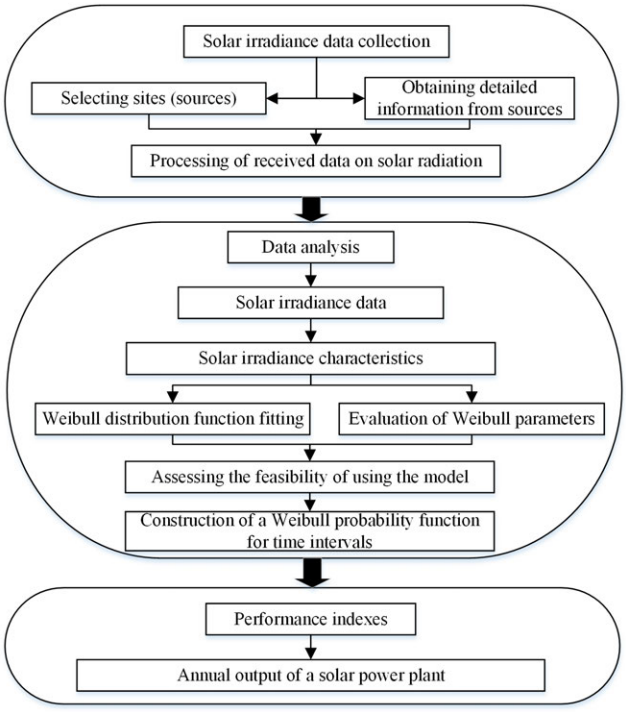


**Figure 1.** Research methodology for models to estimate solar irradiance based on the Weibull distribution [*Koholé et al.*, 2023].

$$D = I_0 C_t \left[0.271 - 0.2939 A_1 \exp\left(-\frac{A_2}{\sin(h)}\right)\right] \sin(h). \tag{24}$$

$$G = 0.271 I_0 C_t A_1 \sin(h) + 0.706 I_0 C_t A_1 \sin(h) \exp\left(-\frac{A_2}{\sin(h)}\right), \tag{25}$$

where $I_0$ is the solar constant equal to 1367 W/m$^2$, $A_1$ and $A_2$ are the atmospheric turbidity coefficients presented below (Table 2).

**Table 2.** Turbidity coefficients depending on climatic conditions.

| Climatic conditions | Sky very clean | Normal conditions | Sky very polluted |
|---|---|---|---|
| $A_1$ | 0.87 | 0.88 | 0.91 |
| $A_2$ | 0.17 | 0.26 | 0.43 |

Another model that is based on the same data is described in [*Perrin de Brichambaut*, 1975]:

$$D = 125C(\sin(h))^{0.4}. \tag{26}$$

$$I = R\exp\left(\frac{-A}{B\sin(h+1)}\right) \tag{27}$$

$$G = I + D, \tag{28}$$

where $R$ is off-ground radiation, $A$, $B$, and $C$ are the dimensionless coefficients shown below (Table 3).

Using similar data, Capderou models [*Capderou*, 1985] and the Byrd and Halmstron model [*Bird and Hulstrom*, 1981] are also constructed.

**Table 3**. Values of $R, A, B$ and $C$.

| Atmospheric conditions | R | A | B | C |
|---|---|---|---|---|
| Clear skies | 1210 | 1.67 | 3.9 | 0.67 |
| Normal conditions | 1230 | 1.61 | 3.1 | 0.47 |
| Industrial zones | 1260 | 2.23 | 4 | 0.45 |

Since each of the models must be tested for accuracy, there are different approaches to estimation [*Li et al.*, 2011; *Mghouchi et al.*, 2016]. Let us consider the approach presented in [*Li et al.*, 2011].

Model performance is evaluated using the following statistical error tests: mean absolute percentage error (MAPE), mean bias error (MBE), root mean square error (RMSE), correlation coefficient ($r$) and the Nash-Sutcliffe equation (NSE). These indices can be calculated as follows:

$$\mathrm{MAPE} = \frac{1}{n}\sum_{i=1}^{n}\left|\frac{H_{\mathrm{dci}} - H_{\mathrm{dmi}}}{H_{\mathrm{dmi}}}\right| \times 100. \tag{29}$$

$$\mathrm{MBE} = \frac{1}{n}\sum_{i=1}^{n}(H_{\mathrm{dci}} - H_{\mathrm{dmi}}). \tag{30}$$

$$\mathrm{RMSE} = \sqrt{\frac{1}{n}\sum_{i=1}^{n}(H_{\mathrm{dci}} - H_{\mathrm{dmi}})^2}. \tag{31}$$

$$r = \frac{\sum_{i=1}^{n}(H_{\mathrm{dci}} - H_{\mathrm{dca}})(H_{\mathrm{dmi}} - H_{\mathrm{dma}})}{\sqrt{\left[\sum_{i=1}^{n}(H_{dci} - H_{dca})^2\right]\left[\sum_{i=1}^{n}(H_{\mathrm{dmi}} - H_{\mathrm{dma}})^2\right]}}. \tag{32}$$

$$\mathrm{NSE} = 1 - \frac{\sum_{i=1}^{n}(H_{\mathrm{dmi}} - H_{\mathrm{dci}})^2}{\sum_{i=1}^{n}(H_{\mathrm{dmi}} - H_{\mathrm{dma}})^2}. \tag{33}$$

where $H_{\mathrm{dci}}, H_{\mathrm{dmi}}$ are the $i$-th calculated and measured values respectively, $H_{\mathrm{dca}}, H_{\mathrm{dma}}$ are the mean values of the calculated and measured values respectively, $n$ is the number of observations.

### 2.2. Models for estimating photovoltaic capacity

In addition to estimating solar power potential, there are a number of mathematical models. Designed to estimate the amount of energy produced by solar panels.

In [*Zhao et al.*, 2013], a model of photovoltaic power output is proposed. The output power of photovoltaic installations is mainly influenced by the intensity of solar illumination and the ambient temperature, which is reflected in the following expression:

$$P_{pv} = P_{\mathrm{STC}}\frac{G_c}{G_{\mathrm{STC}}}[1 + k(T_c - T_{\mathrm{STC}})] \tag{34}$$

where $P_pv$is the power output at the photocell surface temperature $T_c$ and light intensity $G_c$ , and $k$ is the temperature power factor. $G_{\mathrm{STC}}$ is 1 kW/m$^2$ and $T_{\mathrm{STC}}$ is 25 °C. The $P_{\mathrm{STC}}$ is the nominal power output of the PV cells under standard test conditions, which can usually be specified by the manufacturer.

The surface temperature $T_c$ of the PV cells is related to ambient temperature, light intensity, and wind speed and can be expressed as:

$$T_c = T_a + \alpha G_c. \tag{35}$$

Thus, the considered model allows us to determine the power output, taking into account not only meteorological factors, but also the inherent properties of the energy converter.

Another achievement of this work is the proposed optimization model, which includes the cost of battery life loss, operation and maintenance cost, fuel cost and environmental cost to obtain a set of optimal operating strategy parameters. By considering the lifetime characteristics of lead-acid batteries, a multi-objective optimization was achieved to minimize the power generation costs and maximize the lifetime of lead-acid batteries using the genetic algorithm of non-dominant sorting (NSGA-II).

The following work [*Achituev and Enebish*, 2015], proposes an approach to estimate solar radiation potential based on the following indices:

1. Environmental condition indices, which include ambient temperature, converter module temperature, average wind speed, humidity, and albedo;
2. Solar resource indices, which consist of indices such as: horizontal irradiance to the module surface, duration of sunshine, and refraction magnitude;
3. Performance indices of the photovoltaic module, which were derived from its characteristics:

$$Y_r = H_A/G_S \tag{36}$$

$$Y_A = E_{A,d}/P_{\max} \tag{37}$$

$$\mathrm{PR} = Y_A/Y_r \tag{38}$$

As a result of this integrated approach, it was possible to obtain accurate simulation results, which were verified using the experimental data obtained from the installations. This approach makes it possible to determine the most appropriate configuration of solar converter plants, based on the geographical features of the intended region of operation.

The study [*Guerra*, 2020] proposed a methodology for estimating the amount of energy produced by small photovoltaic plants based on the specific conditions of the proposed plant location region. Principal component analysis, correlation analysis and response surface method are used as basic methods, as a result of which it is possible to determine the most significant of climatic parameters in the region under study and build a characteristic equation using only them, thus reducing its complexity. The main disadvantage of such an approach is the complicated planning of the experiments and determination of the type of the supposed response surface, with complication of which the number of necessary points of experiments inevitably increases.

A number of works [*Narasimman et al.*, 2023; *Polasek and Čadík*, 2023; *Souhaila and Mohamed*, 2021] are devoted to modeling the operation of photovoltaic panels using modern intelligent technologies, due to which it is possible to build an accurate model for predicting the behavior of the energy system without using full-scale modeling and conducting a lot of physical experiments.

### 2.3. Models based on data mining techniques

There is a large number of very different models of solar radiation estimation based on machine learning using such approaches as: artificial neural network methods, fuzzy logic, radial basis functions, exponential smoothing, state space model, support vector method, Bayesian neural networks, recurrent neural networks [*Teke et al.*, 2015].

Let us consider some of the existing models presented in Table 4.

The block diagram of modeling methods based on data analysis is presented in Figure 2 [*Teke et al.*, 2015].

The use of the considered models is a necessary step in the implementation of the forecasting and planning system, because without organizing a preliminary calculation of the efficiency of the energy system functioning with the involvement of renewable energy sources it is impossible to start the process of implementation of the proposed system.

All considered models can be divided into the following categories [*Tyunkov et al.*, 2019]:

- physical models based on data on weather conditions, solar radiation obtained by numerical weather prediction;
- statistical models based on the analysis of time series of different retrospective observations obtained during observations over a certain time interval;
- adaptive models based on artificial intelligence technologies to determine the existing relationship between meteorological characteristics and solar insolation
- hybrid models based on a combination of several types of models.

It is noted that hybrid models, which combine classical static and physical models when used together with intelligent forecasting models [*Wu et al.*, 2014], have the highest accuracy, reaching small error values of the order of 5.21%.

**Table 4.** Linear and nonlinear methods used for modeling and forecasting solar radiation (time series analysis, artificial intelligence methods).

| Proposed model | Used data | Estimated indicator | Reference |
|---|---|---|---|
| Seven different models based on the Angstrom-Prescott model | Monthly average daily extraterrestrial radiation, day length, relative humidity, maximum duration of sunshine, maximum air temperature, duration of sunshine, average daily sea level pressure, average daily vapor pressure | Mean monthly global horizontal radiation | [*Robaa*, 2009] |
| The Angstrom and Heliosat model | Database of global solar irradiance and duration of solar irradiance at ground level | Global solar radiation | [*Rusen et al.*, 2013] |
| A model based on a trigonometric function that has only one independent parameter. | Number of day in the year | Daily global solar radiation | [*Bulut and Büyükalaca*, 2007] |
| Linear Regression Model | Data are presented as day-averaged maximum and minimum air temperatures and day-averaged solar radiation. | Solar radiation | [*Ibrahim et al.*, 2012] |
| ANN and Regression Analysis | Average temperature, relative humidity | Global solar radiation on the horizontal surface | [*Agbo et al.*, 2012] |
| ARIMA (autoregressive integrated moving average) and SARIMA time series prediction model | Data on solar radiation | Daily and monthly solar radiation | [*Alsharif et al.*, 2019] |
| ARMA autoregressive moving average) and ARIMA autoregressive integrated moving average) | Solar radiation data | Daily global solar radiation | [*Belmahdi et al.*, 2020] |
| AR (autoregressive moving average) and NAR (nonlinear autoregressive) | Solar radiation data | Daily global solar radiation | [*Takilalte et al.*, 2019] |

Continued on next page

**Table 4.** Linear and nonlinear methods used for modeling and forecasting solar radiation (time series analysis, artificial intelligence methods). (Continued)

| Proposed model | Used data | Estimated indicator | Reference |
|---|---|---|---|
| Naive Bayes | Dew-point, temperature, sky coverage, and relative humidity | Global solar radiation for two days ahead | [*Kwon et al.*, 2019] |
| ANN and RNS | Wind speed, dew-point temperature, dry bulb temperature, relative humidity, and wind direction | Daily global solar radiation | [*Pang et al.*, 2020] |
| SVM and C-SVM | Minimum, maximum and average temperature | Daily global solar radiation | [*Guermoui et al.*, 2020] |
| CNN | Satellite images with data on temperature, humidity, wind speed, pressure, cloud vectors | Global solar radiation | [*Yuzer and Bozkurt*, 2023] |
| Combined empirical modeling and machine learning method for estimating daily global solar radiation | daily maximum dry bulb temperature daily minimum dry bulb temperature daily mean dry bulb temperature, daytime solar duration, daily mean wind speed, daily mean relative humidity and daily air pressure | Modeling estimates of solar radiation for a specific location where no solar radiation measurement equipment can be installed | [*Zang et al.*, 2022] |
| A model that combines two machine learning models (XGB and MARS) with a covariance matrix adaptation strategy evolution (CMAES) algorithm | wind speed maximum and minimum humidity, | Prediction of daily solar radiation | [*Goliatt and Yaseen*, 2023] |
| *K*-means clustering | maximum and minimum temperatures, vapor pressure deficit, and evaporation | Maximum solar irradiance on a sloping surface | [*Yin et al.*, 2023] |
| Artificial Neural Networks | hourly solar radiation data | Estimation of solar radiation on sloping surfaces | [*Cheng et al.*, 2019] |

## 3. Results

In this work, we considered a number of existing models for estimating the solar radiation potential, necessary for constructing predictions of the theoretical values of the solar flux power arriving at the surface. Various types of models were identified, from the simplest ones, which allow calculating solar radiation under conditions of an absent region, to more complex ones, which allow taking into account such factors as atmospheric turbidity. The use of these models is a prerequisite for the implementation of a forecasting subsystem [*Simankov et al.*, 2021a, 2022] as part of a general information-analytical system for assessing renewable energy [*Simankov et al.*, 2021b] which allows assessing the efficiency of RES for a certain level of terrain scaling (local, regional). However, such a system should be based not only on classical models for assessing energy potential, but also on modern approaches based on methods of data mining and artificial intelligence, which results in

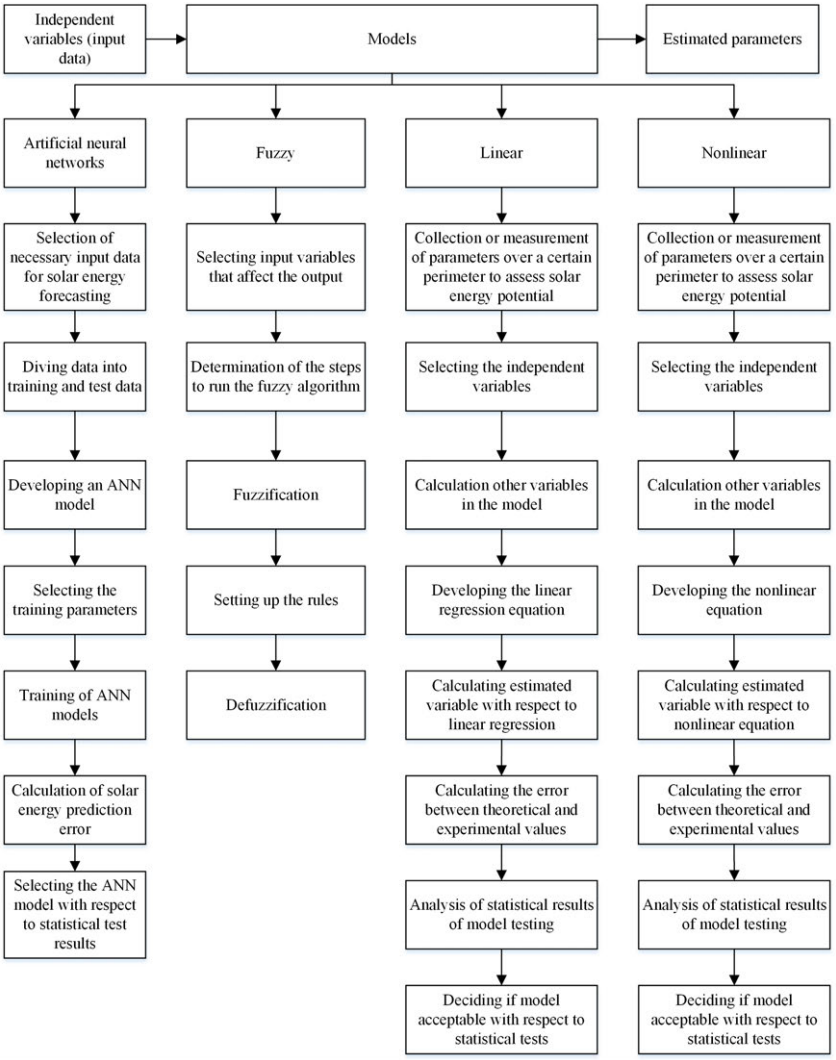


**Figure 2.** Block diagrams of models for estimating global solar radiation.

improved forecasting accuracy and the ability to determine the required level of scaling of this subsystem.

This subsystem is one of the key elements, because based on its results it is possible to start forming the structure of the energy system with the involvement of renewable energy sources.

At the same time, the considered models can be used not only as a tool for obtaining theoretical values of incoming energy, but also as a basis for implementing a subsystem based on digital twins [*Granacher et al.*, 2022; *Onishchenko et al.*, 2022], allowing the implementation of a virtual model of the projected energy system with RES to determine the most optimal structure of this system.

To obtain the highest accuracy of forecasting, it is necessary to implement the combined use of classical methods of modeling and modern methods based on artificial intelligence and data mining technologies. Such an approach will allow performing mutual verification of the models and specifying parameters to build the most optimal model based on neural networks, thereby reducing the overall error of calculations, for which existing intelligent models for assessing the energy potential of solar energy were considered.

The extensive range of models considered allows us to expand the range of input data required to implement the prediction, resulting in greater versatility due to the possibility of selecting those input parameters that are available to the potential user.

**References**

Achituev, S. A., and N. Enebish (2015), Evaluation of solar energy potential and photovoltaic (pv) module performance in the regions Buryatia, *BSU bulletin. Mathematics, Informatics*, *3*, 8–15 (in Russian).

Agbo, G. A., G. F. Ibeh, and J. E. Ekpe (2012), Estimation of global solar radiation at Onitsha with regression analysis and artificial neural network models, *Research Journal of Recent Sciences*, *1*(6), 27–31.

Akdağ, S. A., and A. Dinler (2009), A new method to estimate Weibull parameters for wind energy applications, *Energy Conversion and Management*, *50*(7), 1761–1766, https://doi.org/10.1016/j.enconman.2009.03.020.

Akdağ, S. A., and O. Güler (2015), A novel energy pattern factor method for wind speed distribution parameter estimation, *Energy Conversion and Management*, *106*, 1124–1133, https://doi.org/10.1016/j.enconman.2015.10.042.

Alsharif, M., M. Younes, and J. Kim (2019), Time series ARIMA model for prediction of daily and monthly average global solar radiation: the case study of Seoul, South Korea, *Symmetry*, *11*(2), 240, https://doi.org/10.3390/sym11020240.

An, J., D. Yan, S. Guo, Y. Gao, J. Peng, and T. Hong (2020), An improved method for direct incident solar radiation calculation from hourly solar insolation data in building energy simulation, *Energy and Buildings*, *227*, 110,425, https://doi.org/10.1016/j.enbuild.2020.110425.

Badescu, V. (2002), 3D isotropic approximation for solar diffuse irradiance on tilted surfaces, *Renewable Energy*, *26*(2), 221–233, https://doi.org/10.1016/S0960-1481(01)00123-9.

Belmahdi, B., M. Louzazni, and A. E. Bouardi (2020), One month-ahead forecasting of mean daily global solar radiation using time series models, *Optik*, *219*, 165,207, https://doi.org/10.1016/j.ijleo.2020.165207.

Besharat, F., A. A. Dehghan, and A. R. Faghih (2013), Empirical models for estimating global solar radiation: A review and case study, *Renewable and Sustainable Energy Reviews*, *21*, 798–821, https://doi.org/10.1016/j.rser.2012.12.043.

Bird, R. E., and R. L. Hulstrom (1981), *A simplified clear sky model for direct and diffuse insolation on horizontal surfaces*, 39 pp., Solar Energy Research Institute, Colorado.

Bugler, J. W. (1977), The determination of hourly insolation on an inclined plane using a diffuse irradiance model based on hourly measured global horizontal insolation, *Solar Energy*, *19*(5), 477–491, https://doi.org/10.1016/0038-092X(77)90103-7.

Bulut, H., and O. Büyükalaca (2007), Simple model for the generation of daily global solar-radiation data in Turkey, *Applied Energy*, *84*(5), 477–491, https://doi.org/10.1016/j.apenergy.2006.10.003.

Capderou, M. (1985), *Atlas solaire de l'algerie: Aspect énérgitique*, 399 pp., Office des Publications Universitaires Alger.

Cheng, H.-Y., C.-C. Yu, K.-C. Hsu, C.-C. Chan, M.-H. Tseng, and C.-L. Lin (2019), Estimating Solar Irradiance on Tilted Surface with Arbitrary Orientations and Tilt Angles, *Energies*, *12*(8), 1427, https://doi.org/10.3390/en12081427.

Cooper, P. I. (1969), The absorption of radiation in solar stills, *Solar Energy*, *12*(3), 333–346, https://doi.org/10.1016/0038-092x(69)90047-4.

Demain, C., M. Journée, and C. Bertrand (2013), Evaluation of different models to estimate the global solar radiation on inclined surfaces, *Renewable Energy*, *50*, 710–721, https://doi.org/10.1016/j.renene.2012.07.031.

Energy strategy of the Russian Federation for the period until 2035 (2020), Approved by order of the Government of the Russian Federation of June 9, 2020 N 1715-r, https://minenergo.gov.ru/node/1026 (in Russian).

EPA (2018), *Quantifying the Multiple Benefits of Energy Efficiency and Renewable Energy: A Guide for State and Local Governments*, US Environmental Protection Agency, Washington DC, USA.

George, F. (2014), A Comparison of Shape and Scale Estimators of the Two-Parameter Weibull Distribution, *Journal of Modern Applied Statistical Methods*, *13*(1), 23–35, https://doi.org/10.22237/jmasm/1398916920.

Goliatt, L., and Z. M. Yaseen (2023), Development of a hybrid computational intelligent model for daily global solar radiation prediction, *Expert Systems with Applications*, *212*, 118,295, https://doi.org/10.1016/j.eswa.2022.118295.

Granacher, J., T.-V. Nguyen, R. Castro-Amoedo, and F. Maréchal (2022), Overcoming decision paralysis - A digital twin for decision making in energy system design, *Applied Energy*, *306*, 117,954, https://doi.org/10.1016/j.apenergy.2021.117954.

Guermoui, M., R. Abdelaziz, K. Gairaa, L. Djemoui, and S. Benkaciali (2020), New temperature-based predicting model for global solar radiation using support vector regression, *International Journal of Ambient Energy*, *43*(1), 1397–1407, https://doi.org/10.1080/01430750.2019.1708792.

Guerra, D. D. (2020), Estimation by statistical methods of electric energy generation by electric technical complex with photoelectric panels, *News of the Tula state university. Technical sciences*, *12*, 369–378 (in Russian).

Hamilton, H. L., and A. Jackson (1985), A shield for obtaining diffuse sky radiation from portions of the sky, *Solar Energy*, *34*(1), 121–123, https://doi.org/10.1016/0038-092X(85)90099-4.

Ibrahim, S., I. Daut, Y. M. Irwan, M. Irwanto, N. Gomesh, and Z. Farhana (2012), Linear Regression Model in Estimating Solar Radiation in Perlis, *Energy Procedia*, *18*, 1402–1412, https://doi.org/10.1016/j.egypro.2012.05.156.

IEA (2023), Monthly Electricity Statistics, https://www.iea.org/data-and-statistics/data-tools/monthly-electricity-statistics, (date of access: 14.05.2023).

Iktisanov, V., and F. Shkrudnev (2021), Decarbonization: outside view, *Energy policy*, (8), 42–51, https://doi.org/10.46920/2409-5516_2021_8162_42.

IRENA, IEA and REN21 (2018), Renewable Energy Policies in a Time of Transition, *Tech. rep.*, IRENA, OECD/IEA and REN21.

Justus, C. G., W. R. Hargraves, A. Mikhail, and D. Graber (1978), Methods for Estimating Wind Speed Frequency Distributions, *Journal of Applied Meteorology*, *17*(3), 350–353, https://doi.org/10.1175/1520-0450(1978)017<0350:MFEWSF>2.0.CO;2.

Klucher, T. M. (1979), Evaluation of models to predict insolation on tilted surfaces, *Solar Energy*, *23*(2), 111–114, https://doi.org/10.1016/0038-092X(79)90110-5.

Koholé, Y. W., R. H. Tonsie Djiela, F. C. V. Fohagui, and T. Ghislain (2023), Comparative study of thirteen numerical methods for evaluating Weibull parameters for solar energy generation at ten selected locations in Cameroon, *Cleaner Energy Systems*, *4*, 100,047, https://doi.org/10.1016/j.cles.2022.100047.

Koronakis, P. S. (1986), On the choice of the angle of tilt for south facing solar collectors in the Athens basin area, *Solar Energy*, *36*(3), 217–225, https://doi.org/10.1016/0038-092X(86)90137-4.

Kwon, Y., A. Kwasinski, and A. Kwasinski (2019), Solar Irradiance Forecast Using Naïve Bayes Classifier Based on Publicly Available Weather Forecasting Variables, *Energies*, *12*(8), 1529, https://doi.org/10.3390/en12081529.

Li, H., W. Ma, X. Wang, and Y. Lian (2011), Estimating monthly average daily diffuse solar radiation with multiple predictors: A case study, *Renewable Energy*, *36*(7), 1944–1948, https://doi.org/10.1016/j.renene.2011.01.006.

Liu, B. Y. H., and R. C. Jordan (1962), Daily insolation on surfaces tilted towards the equator, *Ashrae Transactions*, *67*, 526–541.

Liu, Z., Z. Deng, G. He, H. Wang, X. Zhang, J. Lin, Y. Qi, and X. Liang (2021), Challenges and opportunities for carbon neutrality in China, *Nature Reviews Earth & Environment*, *3*(2), 141–155, https://doi.org/10.1038/s43017-021-00244-x.

Lysen, E. H. (1982), *Introduction to wind energy*, 309 pp., Consultancy services wind energy developing countries, Netherlands.

Ma, C. C. Y., and M. Iqbal (1983), Statistical comparison of models for estimating solar radiation on inclined surgaces, *Solar Energy*, *31*(3), 313–317, https://doi.org/10.1016/0038-092x(83)90019-1.

Mghouchi, Y. E., A. E. Bouardi, Z. Choulli, and T. Ajzoul (2016), Models for obtaining the daily direct, diffuse and global solar radiations, *Renewable and Sustainable Energy Reviews*, *56*, 87–99, https://doi.org/10.1016/j.rser.2015.11.044.

Moldovan, C. L., R. Păltănea, and I. Visa (2020), Improvement of clear sky models for direct solar irradiance considering turbidity factor variable during the day, *Renewable Energy*, *161*, 559–569, https://doi.org/10.1016/j.renene.2020.07.086.

Muneer, T., and H. Kambezidis (1997), *Solar radiation and daylight models for the energy efficient design of buildings*, Architectural press, Boston.

Narasimman, K., V. Gopalan, A. K. Bakthavatsalam, P. V. Elumalai, M. I. Shajahan, and J. J. Michael (2023), Modelling and real time performance evaluation of a 5 MW grid-connected solar photovoltaic plant using different artificial neural networks, *Energy Conversion and Management*, *279*, 116,767, https://doi.org/10.1016/j.enconman.2023.116767.

Onishchenko, S. V., K. A. Kuzmin, and T. Y. Bychkov (2022), Development of a digital twin concept for an autonomous complex for assessing the energy potential of renewable energy sources, in *Proceedings of the International Scientific and Practical Conference Applied Issues of Exact Sciences, Armavir, Armenia, 16-17 October 2022*, pp. 178–180 (in Russian).

Pang, Z., F. Niu, and Z. O'Neill (2020), Solar radiation prediction using recurrent neural network and artificial neural network: A case study with comparisons, *Renewable Energy*, *156*, 279–289, https://doi.org/10.1016/j.renene.2020.04.042.

Perez, R., R. Seals, P. Ineichen, R. Stewart, and D. Menicucci (1987), A new simplified version of the perez diffuse irradiance model for tilted surfaces, *Solar Energy*, *39*(3), 221–231, https://doi.org/10.1016/S0038-092X(87)80031-2.

Perrin de Brichambaut, C. (1975), *Estimation Des Ressources Energetiques Solaires en France. Supplement aux cahiers AFEDES*, 1, Association francaise pour l'etude et le developpement des applications de l'energie solaire.

Polasek, T., and M. Čadík (2023), Predicting photovoltaic power production using high-uncertainty weather forecasts, *Applied Energy*, *339*, 120,989, https://doi.org/10.1016/j.apenergy.2023.120989.

REN21 (2020), Renewables 2020 Global Status Report, *Tech. rep.*, REN21 Secretariat.

REN21 (2021), Renewables 2021 Global Status Report, *Tech. rep.*, REN21 Secretariat, Paris.

Rigollier, C., M. Lefèvre, S. Cros, and L. Wald (2002), Heliosat 2: an improved method for the mapping of the solarradiation from Meteosat imagery, in *Proceedings of the 2002 EUMETSAT Meteorological SatelliteConference, Dublin, Ireland, 1-6 September 2002*, pp. 585–592, EUMETSAT.

Robaa, S. M. (2009), Validation of the existing models for estimating global solar radiation over Egypt, *Energy Conversion and Management*, *50*(1), 184–193, https://doi.org/10.1016/j.enconman.2008.07.005.

Rusen, S. E., A. Hammer, and B. G. Akinoglu (2013), Coupling satellite images with surface measurements of bright sunshine hours to estimate daily solar irradiation on horizontal surface, *Renewable Energy*, *55*, 212–219, https://doi.org/10.1016/j.renene.2012.12.019.

Russia Renewable Energy Development Association (RREDA) (2022), Russian Renewable Energy Market Review, Q3 2022, https://rreda.ru/en/reports/quarter-reports/1345/ (in Russian), (date of access: 01.05.2023).

Saïghi, M. (2002), Nouveau modèle de transfert hydrique dans le système sol – plante – atmosphére continuum.

Simankov, V. S. (2002), *Automation of systems research: a monograph*, 376 pp., KubSTU, Krasnodar (in Russian).

Simankov, V. S., and P. Y. Buchatskiy (2019), Complex of mathematical models of the renewable energy for a forward-looking assesment of its potential, in *III International Scientific Conference "Autumn Mathematical Readings in Adygeya", Maykop, 15-20 October 2019*, vol. III, pp. 122–124 (in Russian).

Simankov, V. S., and P. Y. Buchatskiy (2021), Methodological foundations of innovative solutions in renewable energy engineering, *The Bulletin of the Adyghe State University, the series "Natural-Mathematical and Technical Sciences"*, (3(286)), 42–54, https://doi.org/10.53598/2410-3225-2021-3-286-42-54 (in Russian).

Simankov, V. S., P. Y. Buchatskiy, and A. V. Shopin (2000), Modelling insolation with control photowindenergy systems, *Works of the Adygheya Republic Physical Society*, (5), 67–71 (in Russian).

Simankov, V. S., A. N. Cherkasov, V. V. Buchatskaya, and S. V. Teploukhov (2021a), Situational center as an intelligent decision support system taking into account the uncertainty of the source information, in *CEUR Workshop Proceedings. 4th All-Russian Scientific and Practical Conference with International Participation "Distance Learning Technologies", DLT 2019 Yalta, Crimea, 16-21 September 2019*, pp. 404–414.

Simankov, V. S., I. G. Gorin, and A. V. Tsekhomskiy (2021b), Integration of simulation systems in a situation center, in *Modern scientific hypotheses and forecasts: from theory to practice: a collection of scientific articles based on the results of the international scientific and practical conference. August30-31, 2021. Saint-Petersburg*, pp. 20–23, Publishing House of SPbSUE, St. Petersburg (in Russian).

Simankov, V. S., P. Y. Buchatskiy, S. V. Teploukhov, and V. V. Buchatskaya (2022), Knowledge Management Subsystem of the Intellectual Situational Center, in *2022 International Conference on Quality Management, Transport and Information Security, Information Technologies (IT&QM&IS)*, IEEE, https://doi.org/10.1109/itqmis56172.2022.9976535.

Souhaila, C., and M. Mohamed (2021), Ensemble methods comparison to predict the Power produced by Photovoltaic Panels, *Procedia Computer Science*, *191*, 385–390, https://doi.org/10.1016/j.procs.2021.07.049.

Stevens, M. J. M., and P. T. Smulders (1979), The estimation of the parameters of the Weibull wind speed distribution for wind energy utilization purposes, *Wind Engineering*, *3*(2), 132–145.

Takilalte, A., S. Harrouni, and J. Mora (2019), Forecasting global solar irradiance for various resolutions using time series models - case study: Algeria, *Energy Sources, Part A: Recovery, Utilization, and Environmental Effects*, *44*(1), 1–20, https://doi.org/10.1080/15567036.2019.1649756.

Teke, A., H. B. Yıldırım, and O. Çelik (2015), Evaluation and performance comparison of different models for the estimation of solar radiation, *Renewable and Sustainable Energy Reviews*, *50*, 1097–1107, https://doi.org/10.1016/j.rser.2015.05.049.

Tonsie Djiela, R. H., P. T. Kapen, and G. Tchuen (2020), Wind energy of Cameroon by determining Weibull parameters: potential of a environmentally friendly energy, *International Journal of Environmental Science and Technology*, *18*(8), 2251–2270, https://doi.org/10.1007/s13762-020-02962-z.

Tyunkov, D. A., A. S. Gritsay, V. I. Potapov, R. N. Khamitov, A. V. Blohin, and L. K. Kondratukova (2019), Short-term forecast methods of electricity generation by solar power plants and its classification, *Journal of Physics: Conference Series*, *1260*(5), 052,033, https://doi.org/10.1088/1742-6596/1260/5/052033.

Vaskov, A. G., and A. F. Narynbaev (2020), Solar Radiation Estimation and Prediction Methods: a Review and Classification, *Vestnik MEI*, *4*(4), 49–61, https://doi.org/10.24160/1993-6982-2020-4-49-61 (in Russian).

Willmott, C. J. (1982), On the climatic optimization of the tilt and azimuth of flat-plate solar collectors, *Solar Energy*, *28*(3), 205–216, https://doi.org/10.1016/0038-092x(82)90159-1.

Wu, Y.-K., C.-R. Chen, and H. A. Rahman (2014), A Novel Hybrid Model for Short-Term Forecasting in PV Power Generation, *International Journal of Photoenergy*, *2014*, 1–9, https://doi.org/10.1155/2014/569249.

Yin, K., X. Zhang, J. Xie, Z. Hao, G. Xiao, and J. Liu (2023), Modeling hourly solar diffuse fraction on a horizontal surface based on sky conditions clustering, *Energy*, *272*, 127,008, https://doi.org/10.1016/j.energy.2023.127008.

Yuzer, E. O., and A. Bozkurt (2023), Deep learning model for regional solar radiation estimation using satellite images, *Ain Shams Engineering Journal*, *14*(8), 102,057, https://doi.org/10.1016/j.asej.2022.102057.

Zang, H., X. Jiang, L. Cheng, F. Zhang, Z. Wei, and G. Sun (2022), Combined empirical and machine learning modeling method for estimation of daily global solar radiation for general meteorological observation stations, *Renewable Energy*, *195*, 795–808, https://doi.org/10.1016/j.renene.2022.06.063.

Zhao, B., X. Zhang, J. Chen, C. Wang, and L. Guo (2013), Operation Optimization of Standalone Microgrids Considering Lifetime Characteristics of Battery Energy Storage System, *IEEE Transactions on Sustainable Energy*, *4*(4), 934–943, https://doi.org/10.1109/tste.2013.2248400.

Zhu, D., T. Hong, D. Yan, and C. Wang (2012), Comparison of Building Energy Modeling Programs: Building Loads, *Tech. rep.*, Ernest Orlando Lawrence Berkeley National Laboratory.

Zohbi, A. G., P. Hendrick, and P. Bouillard (2014), Evaluation du potentiel d'énergie éolienne au Liban, *Revue des Energies Renouvelables*, *17*(1), 83–96.

Russian Journal of Earth Sciences

Special Issue: "Fundamental and Applied Aspects of Geology, Geophysics and Geoecology"

# Software Tools for Evaluating Renewable Energy Sources

**Pavel Yu. Buchatskiy[1], Semen V. Teploukhov[1], Stefan V. Onishchenko[1], Kirill K. Kuzmin[1], Timofey Yu. Bychkov[1]**

[1] Adyghe State University, Maykop, Russia
* **Correspondence to:** Pavel Yu. Buchatskiy, butch_p99@mail.ru

**Abstract:** In this paper a review of existing software tools for the evaluating and modeling of renewable energy sources, which allow to determine various aspects, such as: the amount of incoming energy for a particular area, the economic feasibility of involving an alternative source, the impact on the environment, the cost of the projected system, the features of the terrain, etc. Programs for the evaluation of solar and wind energy, as well as solutions allowing the evaluation of several different types of renewable energy sources were considered. As a result, open-source software tools, such as: QGIS, SAGA GIS, which can be integrated into the implementation of a comprehensive assessment of renewable energy sources to perform certain functions, such as a preliminary assessment of the gross renewable energy potential in specific geographical conditions and identifying topographical features of the regions under consideration, were defined.

**Keywords:** potential assessment models, smart models, renewable energy, solar energy.

**Citation:** Buchatskiy P. Yu., Teploukhov S. V., Onishchenko S. V., Kuzmin K. K., Bychkov T. Yu. (2023), Software Tools for Evaluating Renewable Energy Sources, *Russian Journal of Earth Sciences*, Vol. 23, ES0202, https://doi.org/10.2205/2023ES02SI02

## 1. Introduction

At present, energy conversion technologies, based on renewable sources, are increasingly being developed around the world (Figure 1).

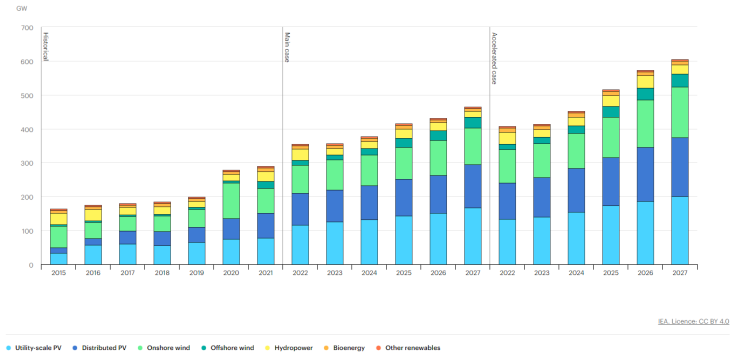


**Figure 1.** The trend of energy generation based on renewables.

In some developed countries, such as Germany, Norway, Sweden, New Zealand, the share of generation from renewable energy currently reaches about 50% of the total amount of energy produced (Figure 2) [*Enerdata*, 2009].

The use of energy systems based on renewable energy makes it possible to ensure high energy security and independence of the overall energy system and significantly reduce the amount of harmful emissions into the atmosphere arising from the use of traditional carbon resources [*Kotelenko and Ryabov*, 2018], which is an extremely urgent task in recent years.

Research Article

Received: 20 October 2023
Accepted: 27 November 2023
Published: 15 December 2023

**Copyright:** © 2023. The Authors. This article is an open access article distributed under the terms and conditions of the Creative Commons Attribution (CC BY) license (https://creativecommons.org/licenses/by/4.0/).

To solve it, many states have developed and approved policies of energy transformation, involving maximum decarbonization of the entire energy and industrial sector, for which it is proposed to produce an active involvement of all types of renewable energy sources in existing energy systems and reduce the share of traditional hydrocarbon fuels [*Simankov and Buchatskiy*, 2019].

In this case, for the effective involvement of RES in the existing energy system or to create an autonomous system based on "green" energy, it is necessary to determine the theoretical values of the amount of energy produced and the gross potential of energy sources in the area where the planned location of the energy system [*Buchatskiy et al.*, 2019a,b].

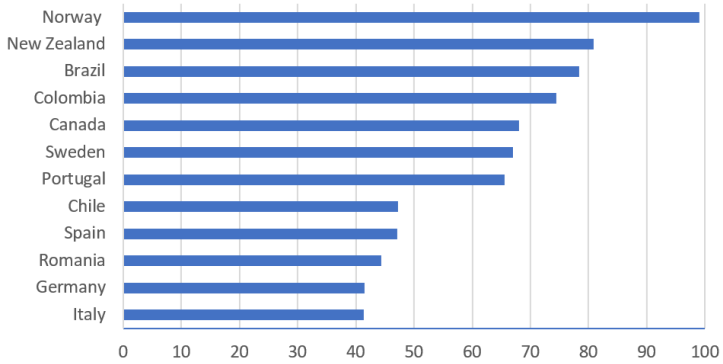


**Figure 2.** Percentage of renewable energy in electricity generation in different countries [*Enerdata*, 2009].

There is a large number of different mathematical models that allow calculating the potential of incoming energy, but their use is very difficult, especially in the presence of a large number of input data and a lot of points where it is necessary to perform modeling and forecasting [*Simankov et al.*, 2023]. For this reason, the development of automated tools that allow the user to perform such an analysis in a simplified mode, some of which allow a comprehensive assessment of the efficiency of the use of RES, not only the calculation of gross values of incoming energy.

One class of such tools are geographic information systems (GIS), which allow to analyze data on the location of solar panels, climate and other factors affecting energy production. Using GIS, it is possible to implement various models to forecast solar energy, taking into account the specific conditions of the region, as well as to integrate such solutions as part of the forecasting system. As a result, the problem of preliminary estimation of the theoretical values of renewable resources capacity can be solved.

In this connection, in this work, it is proposed to analyze the existing software tools for estimating and modeling the amount of energy obtained and to determine what functionality they can provide the user.

## 2. Materials and Methods

When implementing projects for the design and construction of energy systems involving renewable energy sources, a preliminary assessment of the energy resource potential of a particular area is of key importance [*Buchatskiy et al.*, 2020; *Simankov and Buchatskiy*, 2019], for which various software products are currently used. Since there are a large number of such software products, this paper proposes to analyze the existing software designed to assess renewable energy sources.

On the basis of this analysis, it is necessary to determine what functionality different technical solutions offer, and which of the existing solutions have the most universal application.

Thus, Table 1 presents various software products designed to assess the energy potential of solar energy and the design of solar power systems for private consumers.

As you can see, most of the reviewed systems are paid systems with the ability to provide trial access to the product to get acquainted with the features of its functionality. Some of the software products have extensive capabilities. For example, the system Aurora [*Aurora Solar*, 2023], is a universal tool for assessing and analyzing the effectiveness of the implementation of energy systems based on the use of solar energy (Figure 3).

This system allows not only to estimate the energy input and output, but also to carry out an economic analysis of the designed system and to select the most suitable composition of such a system, and to carry out a complete design of the implemented system for a particular consumer. The only disadvantage of this platform is that the system design can only be carried out for private consumers who are non-industrial energy consumers.

**Table 1**. Software tools for solar energy evaluation.

| Software | Freeware (±) | Main functions | OS |
|---|---|---|---|
| Aurora [aurorasolar.com] | – | Assessment of solar energy potential;<br>Economic analysis;<br>Report generation;<br>Data visualization;<br>Designing solar systems for the individual consumer. | Web |
| BlueSol [bluesolpv.com] | –<br>Trial version available | Economic analysis;<br>Systems modeling;<br>Writing documentation;<br>Designing a photovoltaic system. | Windows |
| Helioscope [helioscope.com] | –<br>Trial version available | Assessment of renewable energy potential;<br>Assessment of technical potential;<br>Systems modeling;<br>Report generation;<br>Data visualization. | Web |
| PV Sol Free & Premium [pvsol.software/en] | Trial version available | Systems Modeling;<br>Data visualization. | Windows |
| PVGIS [joint-research-centre.ec.europa.eu] | + | Assessment of renewable energy potential;<br>Assessment of technical potential;<br>Economic analysis;<br>Environmental impact assessment;<br>Support for autonomous, networked systems;<br>Data visualization. | Web |
| PVsyst [pvsyst.com] | – | Assessment of technical potential;<br>Economic analysis;<br>Systems modeling;<br>Systems optimization;<br>Data visualization. | Windows |
| Pylon Solar Design & CRM Software [getpylon.com] | –<br>Trial version available | Economic analysis;<br>Systems Modeling;<br>Customer relationship management. | Web |

An interesting solution is the PVGIS platform [*EU Science Hub*, 2023], which is open-source, making it possible to integrate this solution into some more universal system for assessing renewable energy potential. This platform makes it possible to assess theoretical and technical potential, assess economic aspects, and, unlike the other products considered, it also allows environmental interaction factors to be taken into account, as shown in Figure 4.

Both of these solutions allow a qualitative assessment of the amount of solar energy and an economic analysis, but the Aurora complex also allows the system to be designed

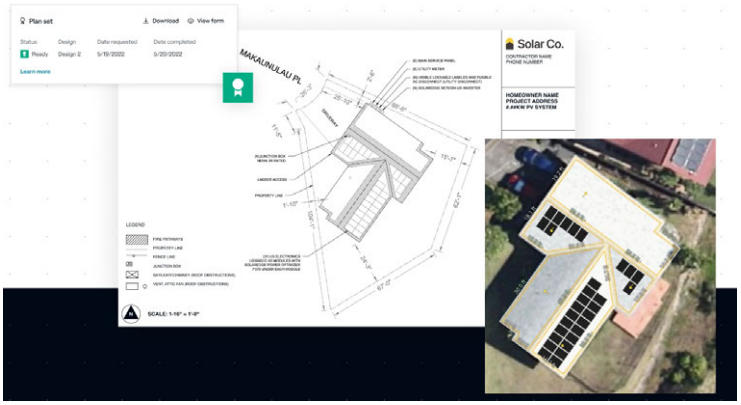


**Figure 3.** Solar power plant design feature in the Aurora app.




**Figure 4.** Functionality of the PVGIS application.

for the individual consumer. A similar solution to the PVGIS complex is PVsyst [*Photovoltaic Software*, 2023], which has similar functionality, but it is commercial and not freely available. Other software products such as BlueSol [*CadWare S.r.L. P.I.*, 2013], Helioscope [*HelioScope, an Aurora Inc. Company*, 2022], PV Sol Free & Premium [*Valentin Software*, 2023] have only some of the features of the AURORA and PVGIS tools.

Let us now look at some of the existing solutions for wind energy assessment and modeling. Table 2 presents a list of software products for wind energy assessment, with a description of the main functionalities.

Similarly, software solutions for the evaluation of solar energy, some of the presented are not available for free use. However, of the commercial solutions it is worth noting the system WindPRO [*EMD International A/S*, 2023], which allows a comprehensive assessment of the effectiveness of the implementation of wind power plants (Figure 5).

The presence of a large number of modules in this solution allows you to implement the following functionality:

- analysis of wind data;

**Table 2.** Software tools for wind energy assessment.

| Software | Freeware (±) | Main functions | OS |
|---|---|---|---|
| Openwind [ul.com] | –<br>On order only | Assessment of renewable energy potential;<br>Assessment of technical potential;<br>Economic analysis;<br>Systems Modeling;<br>Systems Optimization. | Web |
| Small Wind Economic Model Microsoft Excel [windex-change.energy.gov] | + | Assessment of technical potential;<br>Economic analysis. | Cross-platform |
| AQUA [umass.edu] | + | Evaluation of energy potential;<br>Report generation. | Windows;<br>Linux;<br>MacOS |
| WAsP [epa.gov] | + | Assessment of technical potential;<br>Economic analysis;<br>Systems Optimization. | Windows;<br>Linux;<br>MacOS |
| WindPRO [emd-international.com] | –<br>Trial version available | Assessment of renewable energy potential;<br>Assessment of technical potential;<br>Economic analysis;<br>Systems Optimization;<br>Environmental Impact Assessment;<br>Data Visualization. | Cross-platform |
| WInDS [umass.edu] | + | Data visualization;<br>Simulation of wave-induced dynamics;<br>Simulation of an offshore floating wind turbine. | |

- mapping the location of wind resources;
- evaluation of energy production;
- power plant design and optimization;
- calculation of environmental impacts;
- visualization of results;
- implementation of calculations of electrical and economic indicators.

The main distinguishing feature from complex solutions aimed at evaluating the energy potential is the ability to assess the effectiveness of the implementation of the power plant not only at the level of the individual user, but also at the level of districts and regional entities.

At the same time, freely distributed solutions for the assessment of wind energy are not comprehensive, and are usually aimed at assessing a single indicator: determination of the energy potential [*University of Massachusetts Amherst*, 2016], economic analysis [*U. S. Department of Energy*, 2023], simulation of wave dynamics [*University of Massachusetts Amherst*, 2016].

Let's consider the complex solutions that allow evaluating several types of RES at once, in the table presented in Table 3.

The Table 3 presents solutions, the distinctive feature of which is the ability to work with several types of energy resources. The most interesting solution is HOMER Energy [*HOMER Software*, 2021], which consists of three large modules: the distributed grid optimizer, the energy system designer and the module for economic analysis. This product allows to design not only the energy system based on RES, but also to organize hybrid energy systems that combine traditional and alternative energy sources.

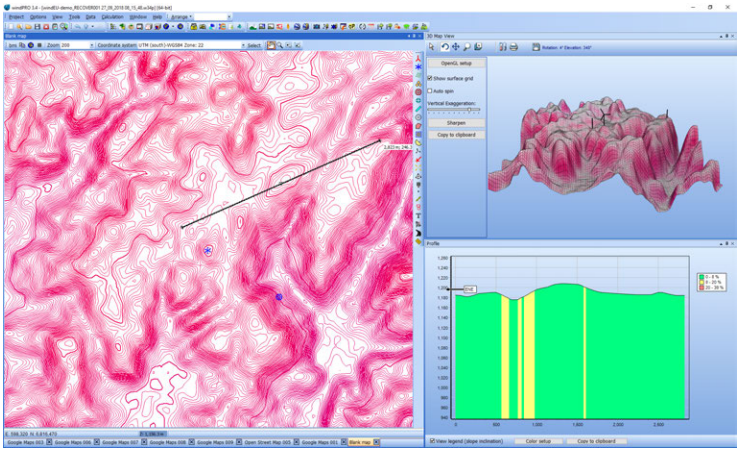

**Figure 5.** Mapping of wind resources in WindPRO software.

A distinctive feature of such solutions is their focus on the design of systems and optimization of existing energy complexes, in contrast to software tools aimed at assessing a particular energy resource.

Of the considered software products it should be noted the following solutions: SAGA GIS [*Institute of Geography Göttingen*, 2001] and QGIS [*QGIS*, 2023], which are modern geographic information systems, aimed at working with different spatial data and providing the ability to analyze the features of the topography of a particular area. These solutions are open source, which suggests the possibility of their integration in the development of more comprehensive solutions aimed at assessing renewable energy sources.

Thus, the QGIS software tool allows viewing data in different views (e. g., in the form of spatial tables in vector format, data in raster and graphical representation), as well as providing the ability to analyze the parameters required by the user. Consideration of relief features, which can be implemented through the use of this platform, is an important factor necessary for the implementation of RES forecasts, as it has a direct impact on the amount of incoming energy, and as a consequence on the power generated by power complexes used based on alternative energies. Figure 6 shows the result of the QGIS program, which resulted in a relief map for the city of Maykop and the coast near the city of Sochi.

Using the terrain map data, it is possible to determine the landscape profile, which is extremely useful for determining the existing altitude difference, which can have a significant impact on the efficiency of the operation of solar and wind energy converters.

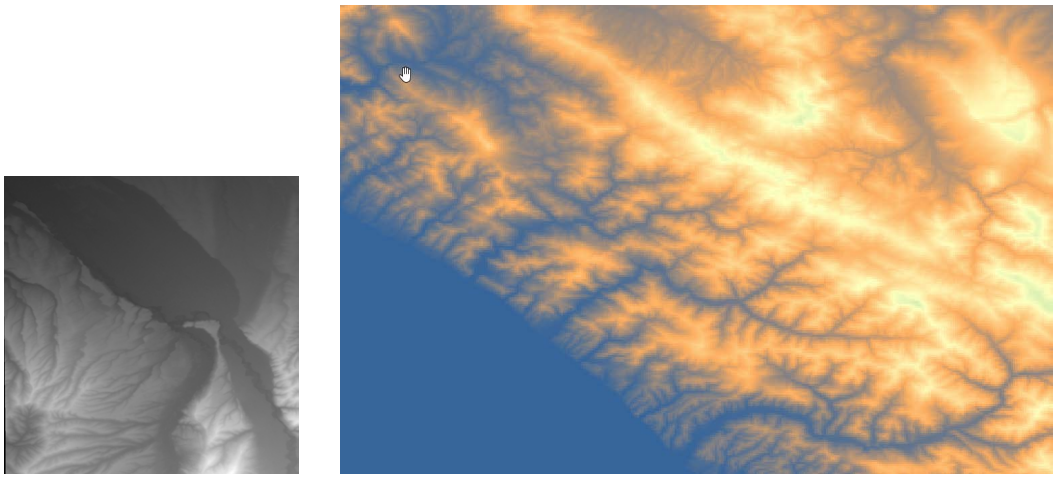

**(a)** **(b)**

**Figure 6.** Relief display in the program QGIS: a) the outskirts of the city of Maykop, b) the coast near the city of Sochi.

**Table 3**. Software tools for wind energy assessment.

| Software | Freeware (±) | Main functions | OS | Type of energy resource |
|---|---|---|---|---|
| EnergyPLAN [energyplan.eu] | + | Assessment of technical potential; Economic analysis; Systems optimization; Systems Modeling | Web; PC | Hydroresources; Petroleum fuels; Geothermal energy; Solar energy |
| Global Atlas IRENA [irena.org] | + | Assessing the potential of renewable sources; Demand forecasting; Data visualization | Web | The main types of RES; Traditional energy resources |
| HOMER Energy [homerenergy.com] | – Trial version available | Assessment of technical potential; Economic analysis; Systems modeling; Support for hybrid systems; Systems optimization; Data visualization | Windows; Web | Hydropower; Biomass; Traditional energy sources |
| RETscreen [retscreen.net] | – Trial version available | Assessment of technical potential; Economic analysis; Systems modeling; Benchmarking; Data visualization | Windows | Main types of RES |
| TRNSYS [trnsys.com] | – | Data visualization; Simulation of transient systems | Windows | Biomass; Solar energy; Hydrogen energy |

The SAGA GIS [*Institute of Geography Göttingen*, 2001] software tool is a free GIS that contains a specialized module for the evaluation of solar power production, which allows the evaluation of the theoretical values of the incoming solar radiation. Like the QGIS software environment, this solution also has the source code, which allows you to talk about the possibility of integrating this tool to implement a system for assessing and modeling the efficiency of solar power plant involvement. The results of this program are presented in Figure 7.

The results obtained in this tool allow to generate data arrays containing theoretical values of solar insolation for a specified period, which is one of the necessary parameters when building evaluation and forecasting models of the amount of incoming energy or forecasting models of power generation.

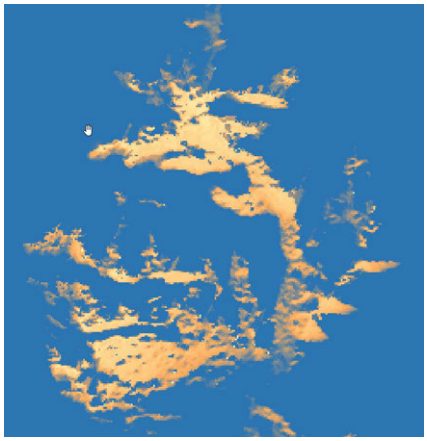

**Figure 7.** The arrival of solar insolation in the period for May 2023 near the city of Maykop.

## 3. Results

In this paper a review of some software tools for the assessment and modeling of renewable energy sources was conducted. Both commercial solutions and freely distributed products designed to evaluate wind and solar energy, as well as software that allows you to explore several types of energy resources were considered.

At the same time it was found that at the moment there are no comprehensive tools for assessing the main types of renewable energy that would not only evaluate the theoretical potential of energy, but also to determine the economic efficiency of the introduction of RES in the energy system and perform optimal energy system design, since each of the products performs only part of such functions for certain types of energy.

It was also determined that there are a number of open-source solutions, which allows the integration of such solutions when creating a more universal system for assessing renewable energy sources. The most suitable for integration are two software tools QGIS and SAGA GIS, which can be used to organize the modeling and forecasting subsystem.

The availability of such solutions allows us to talk about the possibility of creating on their basis a more advanced system for assessing the efficiency of renewable energy sources involvement, and the solutions themselves can be used when implementing one of its subsystems, namely the subsystem of forecasting and modeling of renewable energy sources.

## References

Aurora Solar (2023), Aurora Platform, http://www.aurorasolar.com/, (date of access: 09/04/2023).

Buchatskiy, P. Y., S. V. Onishchenko, and A. S. Platonov (2019a), Development of a software and hardware complex for measuring wind speed on the Arduino platform, in *Distance educational technologies: materials IV All-Russian Scientific and Practical Conference (with international participation), Yalta, September 16-21, 2019*, pp. 250–257, IT "Arial", Simferopol (in Russian).

Buchatskiy, P. Y., S. V. Teploukhov, S. V. Onishchenko, A. S. Platonov, A. A. Avdzhiyan, and V. E. Avdeev (2019b), Implementation of the power assessment appliance for renewable energy sources, *The Bulletin of the Adyghe State University,the series "Natural-Mathematical and Technical Sciences"*, *4*(251), 103–108 (in Russian).

Buchatskiy, P. Y., S. V. Teploukhov, and S. V. Onishchenko (2020), Software and Hardware Complex for Evaluating the Potential of Wind and Solar Energy, in *2020 International Conference on Industrial Engineering, Applications and Manufacturing (ICIEAM)*, IEEE, https://doi.org/10.1109/ICIEAM48468.2020.9112028.

Buchatskiy, P. Y., S. V. Onishchenko, S. V. Teploukhov, and A. N. Lisova (2023), New Renewable Energy Conversion Technologies, in *Fundamental and Applied Aspects of Geology, Geophysics and Geoecology Using Modern Information Technologies. VII International Scientific and Practical Conference. Part I*, pp. 49–57, IP Kucherenko V. O., Maykop (in Russian).

CadWare S.r.L. P.I. (2013), BlueSol. Photovoltaic design software, http://www.bluesolpv.com/, (date of access: 09/04/2023).

EMD International A/S (2023), WindPRO is the industry leading software suite for design and planning of wind farm projects, https://www.emd-international.com/windpro/, (date of access: 09/04/2023).

Enerdata (2009), The share of renewable energy in the global energy mix has increased by 10 percentage points since 2010 to almost 30%, https://energystats.enerdata.net/renewables/renewable-in-electricity-production-share.html (in Russian), (date of access: 09/04/2023).

EU Science Hub (2023), Photovoltaic Geographical Information System (PVGIS), https://joint-research-centre.ec.europa.eu/pvgis-online-tool_en, (date of access: 09/04/2023).

Government of Canada (2022), RETScreen Clean Energy Management Software platform, http://www.retscreen.net, (date of access: 09/04/2023).

HelioScope, an Aurora Inc. Company (2022), HelioScope, https://www.helioscope.com/, (date of access: 09/04/2023).

HOMER Software (2021), HOMER (Hybrid Optimization of Multiple Energy Resources), https://www.homerenergy.com/, (date of access: 09/04/2023).

Institute of Geography Göttingen (2001), SAGA - System for Automated Geoscientific Analyses, https://saga-gis.sourceforge.io/en/index.html, (date of access: 09/04/2023).

IRENA - International Renewable Energy Agency (2023), Global Atlas, https://globalatlas.irena.org/workspace, (date of access: 09/04/2023).

Kotelenko, S., and A. Ryabov (2018), The advantages and disadvantages of alternative Energy, *Izvestiya Tula State University*, (12), 84–88 (in Russian).

Photovoltaic Software (2023), A powerful software for your photovoltaic systems, (date of access: 09/04/2023).

QGIS (2023), QGIS. A Free and Open Source Geographic Information System, https://qgis.org/en/site/, (date of access: 09/04/2023).

Saru Technologies Pty (2023), Pylon. #1 Solar Design & CRM Software for fast-growing solar businesses, https://getpylon.com, (date of access: 09/04/2023).

Simankov, V. S., and P. Y. Buchatskiy (2019), Methodological Basis for Assessing Effectiveness of Involvement of Renewable Energy in Regional Energy Balance, in *2019 International Conference on Industrial Engineering, Applications and Manufacturing (ICIEAM)*, IEEE, https://doi.org/10.1109/ICIEAM.2019.8742922.

Simankov, V. S., P. Y. Buchatskiy, S. V. Onishchenko, and S. V. Teploukhov (2023), Overview of models for estimating and predicting solar energy supply, in *Fundamental and Applied Aspects of Geology, Geophysics and Geoecology Using Modern Information Technologies. VII International Scientific and Practical Conference. Part II*, pp. 167–174, IP Kucherenko V. O., Maykop (in Russian).

Sustainable Energy Planning Research Group at Aalborg University (2000), EnergyPLAN - Advanced Analysis of Smart Energy Systems, https://www.energyplan.eu/, (date of access: 09/04/2023).

TRNSYS (2019), TRNSYS Transient System Simulation Tool, https://www.trnsys.com/, (date of access: 09/04/2023).

U. S. Department of Energy (2023), Small Wind Economic Model. Wind Energy Payback Period Workbook (v1.0), https://windexchange.energy.gov/files/docs/small_wind_economic_model.xls, (date of access: 09/04/2023).

U. S. Environmental Protection Agency (2022), WASP Model Tutorials, https://www.epa.gov/ceam/wasp-model-tutorials, (date of access: 09/04/2023).

UL Solutions (2022), Openwind. Wind Farm Modeling and Layout Design Software, https://www.ul.com/services/openwind-wind-farm-modeling-and-layout-design-software, (date of access: 09/04/2023).

University of Massachusetts Amherst (2016), The Wake Induced Dynamics Simulator (WInDS), https://www.umass.edu/windenergy/research/software/WInDS, (date of access: 09/04/2023).

University of Massachusetts Amherst (2023), AQUA, https://www.umass.edu/windenergy/research/topics/tools/software/aqua, (date of access: 09/04/2023).

Valentin Software (2023), PV Sol Free & Premium, https://pvsol.software/en/, (date of access: 09/04/2023).

Russian Journal of Earth Sciences

Special Issue: "Fundamental and Applied Aspects of Geology, Geophysics and Geoecology"

# Urban Dendroflora of Dry Subtropics of the Northwestern Part of The Greater Caucasus on the Example of the City of Gelendzhik

**Yu. A. Postarnak**[1], **V. V. Zhavoronkov**[2]

[1] Kuban State University, Institute of Geography, Geology, Tourism and Service, 350018, Krasnodar, Russian Federation

[2] OOO Dorstroyengineering, Flat 182, 350088, Krasnodar, Russian Federation

* **Correspondence to:** Yu. A. Postarnak, ecopost@mail.ru

**Abstract:** The article presents the results of the analysis of the species composition of the dendroflora of the city of Gelendzhik. The research covered 20 hectares of tree plantations. The route method and the transect method were used. In total, 30 transects were laid with a width of 5-20 m and the total length was 22 km. The routes covered all biotopes of natural (natural forest plantations on the outskirts of the city) and anthropogenic habitats (boarding houses, house territories of private households, spontaneous vegetation of roadsides and wastelands). True census of all tree and shrub species was carried out on the transects. Special attention was paid to rare species for which renewal and undergrowth were taken into account. The arboreal flora of Gelendzhik is represented by 110 species, which belong to 75 genera and 35 families. The predominant part of the dendroflora is represented by angiosperms (82.7%) and gymnosperms (13.7%). The families of Rosaceae, Cupressaceae and Fabaceae are most widely represented in the dendroflora of the city's green spaces (44%). The analysis of the species composition on their share of participation showed that the native fraction of the dendroflora prevails over the cultural one, which indicates its species richness. The analysis of the geographical element of the wild-growing fraction showed the heterogeneity of the dendroflora, in the formation of which 15 geographical elements take part. The largest number of species in the studied dendroflora belongs to the ancient Mediterranean group of geoelements. The significant participation of the Mediterranean and Caucasian geoelements indicates a high degree of autochthonicity in the development of the dendroflora of the city of Gelendzhik. Phanerophytes predominate among the life forms, represented equally by mesophanerophytes, nanophanerophytes and microphanerophytes. It should also be emphasized the significant participation of adventitious tree species (15.4% of the aboriginal fraction). Most of the adventitious species are of North American origin. The leading place in the quantitative spectrum is occupied by rare Mediterranean species Pinus brutia var. pityusa (Stev) Silba) (21% of the total number of studied individuals), *Prunus mahaleb* (L.) Vassilcz.) (7%), *Pistacia atlantica* Desf. (2.1%), which reflects the specifics of the dendroflora of the city of Gelendzhik.

**Keywords:** dendroflora, species composition, rare species, urban flora, Gelendzhik resort, Krasnodar Krai, Black Sea coast of Russia, North-Western Transcaucasia.

**Citation:** Postarnak Yu. A., Zhavoronkov V. V. (2023), Urban Dendroflora of Dry Subtropics of the Northwestern Part of the Greater Caucasus on The Example of the City of Gelendzhik, *Russian Journal of Earth Sciences*, Vol. 23, ES0203, https://doi.org/10.2205/2023ES02SI03

Research Article

Received: 20 October 2023
Accepted: 27 November 2023
Published: 15 December 2023

**Copyright:** © 2023. The Authors. This article is an open access article distributed under the terms and conditions of the Creative Commons Attribution (CC BY) license (https://creativecommons.org/licenses/by/4.0/).

## 1. Introduction

Tree plantings perform an important systemic function in the urban ecosystem (dust and gas cleaning, climate control, soil protection) [*Bukharina et al.*, 2007]. The relevance of research on the dendroflora of cities is confirmed by many works [*Alikhadzhiev et al.*, 2019; *Arkuschina and Gulay*, 2010; *Bayramyan and Shekoyan*, 2021; *Boiko and Dementieva*,

2018; *Borzenkova*, 2021; *Dudyn et al.*, 2020; *Khalatyan*, 2014; *Klimko and Kaczmarek*, 2006; *Magomedova*, 2014; *Okazova et al.*, 2019; *Padutov et al.*, 2016; *Polyakova*, 2005]. This makes it possible to take into account the peculiarities of the biological diversity of urban ecosystems when making economic decisions, acquiring special significance in the presence of rare plant species [*Postarnak and Litvinskaya*, 2022]. Green spaces are of particular importance in resort towns. The city of Gelendzhik is one of the largest climatic resort towns on the Black Sea coast of Russia (Krasnodar Krai) [*Volkova et al.*, 2017]. The dendroflora of the city of Gelendzhik has not been studied specifically. There are a number of works on individual taxa [*Administration of the city of Gelendzhik: official website*, 2020; *Bondarenko*, 2020; *Ivankina et al.*, 2016].

The purpose of the work is to study the modern species composition of the tree and shrub flora on the territory of the city of Gelendzhik.

The object of the study is the cultural and spontaneous dendroflora of the city of Gelendzhik.

## 2. Characteristics of the research area

The research area belongs to the Anapa-Gelendzhik District, the North Black Sea Province occupying the northern part of the Black Sea coast of Russia from Anapa to Tuapse [*Gvozdetsky*, 1968]. The region is the most remote, northern region of dry subtropics in the North Caucasus with a characteristic Mediterranean climate regime: dry warm summers and rainy, relatively mild winters [*GOST 16350-80*, 1981]. The soil cover in the city of Gelendzhik is represented by zonal brown soils and azonal sod-carbonate (rendzins). The soils of the city's surface area are represented by lithostrats and urban quasi-soils [*V. V. Dokuchaev Soil Science Institute*, 2012].

Geobotanically, the territory of the city of Gelendzhik belongs to the Anapa-Gelendzhik district of the Northwestern Transcaucasia [*V. L. Komarov Botanical Institute of the Russian Academy of Sciences*, 2014]. It is characterized by the development of sub-Mediterranean ecosystems and upland xerophytic vegetation. The ancient Mediterranean biotic core is concentrated here, although somewhat depleted by the Mediterranean flora [*Litvinskaya*, 2020a]. It is distinguished by the presence of a number of genera not found in the area of European broad-leaved forests (*Colutea*, *Rhus*, *Vitex*, *Paliurus*, *Ruscus*, *Pistacia*, *Celtis*, *Jasminum*) [*Litvinskaya*, 2020b].

The primary plant communities were pine and oak-hornbeam forests on the territory of the city of Gelendzhik, fragments of which are now preserved in crevices and gullies located on the territory of the city. They play an important role as refugiums of natural flora. Currently, the vegetation on the territory of Gelendzhik has been changed, it is composed of anthropogenically transformed types of vegetation: artificial forest plantations of park and alley type, the species composition of which is determined by man, as well as spontaneous types of vegetation formed by the synanthropic component of flora (communities of wastelands, roadsides, construction and industrial sites). The object of research belongs to the type of urban flora according to the classification of anthropogenically transformed communities.

The specifics of the arboreal green spaces of the city of Gelendzhik is a rare endemic relict species – the Pitsunda pine, which became widespread in the landscaping of the city in the 1960s and 70s. Today, this view can be called the "calling card" of the resort. It has a ubiquitous growth in the city and performs the most important ecological functions. The species is unpretentious to soil fertility, dust- and gas-resistant. As a littoral calcifilous species, Pitsunda pine is demanding for an increased calcium content. Therefore, the species has an active renewal and forms a stable undergrowth in the territories with the outputs of the parent calcifilous rocks.

## 3. Object of study and methods

The work is based on the materials of floristic studies conducted in 2021–2022 on the territory of the city of Gelendzhik, Krasnodar Krai (Russia). The research covered

20 hectares of tree plantations. The route method and the transect method were used. In total, 30 transects were laid with a length of 0.15–2.16 km and a width of 5–20 m (Figure 1). The total length of the transect was 22 km (Figure): Primorsky Boulevard str. (4662 m), Pogranichnaya str. (500 m), Turisticheskaya str. (580 m), Solntsedarskaya str. (100 m), Konechnaya str. (200 m), Pyaty Pereulok str. (200 m), Highway 03K-555 (1780 m), Pogranichnaya str. (mkr. Blue Bay) (1600 m), Vzletnaya str. (1320 m), Gurzufskaya str. (100 m), Zheleznovodskaya str. (460 m), Severomorskaya str. (400 m), Sanatornaya str. (150 m), Sochinskaya str. (200 m), Krasnodarskaya str. (220 m), Borisovskaya str. (500 m), Kirova str. (150 m), Kurzalnaya str. (100 m), Ulyanovskaya str. (120 m), Griboyedov str. (100 m), Polevaya str. (500 m), Krasnodonskaya str. (150 m), Leselidze str. (200 m), Novorossiyskaya str. (950 m), Dekabristov str. (400 m), Mira str. (1150 m), Sadovaya str. (80 m), Revolutsionnaya str. (1450 m), Tchaikovsky str. (580 m), Ostrovsky str. (520 m), Sovetskaya str. (230 m), Sevastopolskaya str. (500 m), unnamed driveways and vacant lots (4280 m). The routes covered all biotopes of natural (natural forest plantations on the outskirts of the city limits in the Blue Bay area) and anthropogenic habitats on the territory of the city, including boarding houses, house territories of private households, spontaneous vegetation of roadsides and wastelands) (Figure 2, 3).

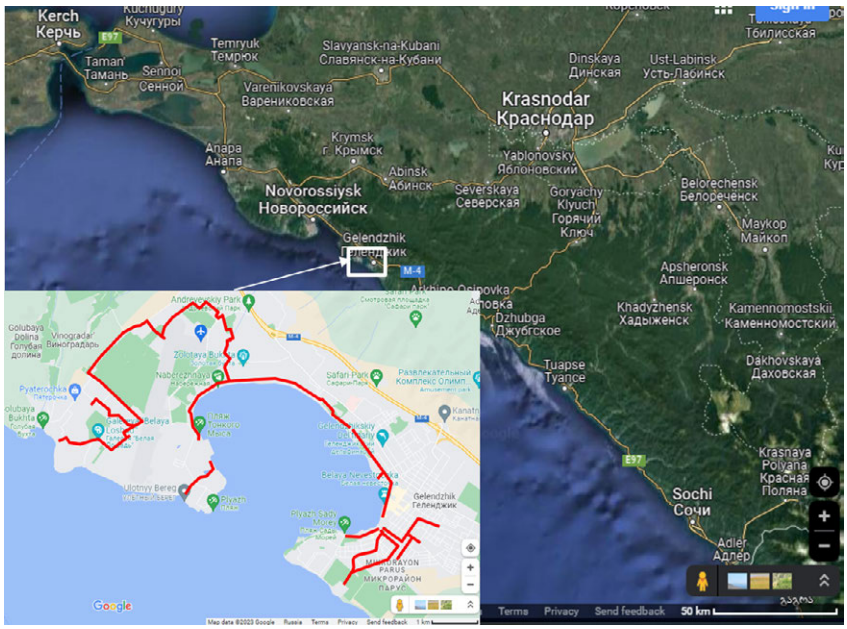


**Figure 1.** The scheme of research routes.



**(a)** Slope along the Highway 03K-555 near SNT Vinogradar-3. (11.12.2021).



**(b)** Forest belt along the Highway 03K-555 (Poeticheskaya str., 80B). (10.11.2021).



**(c)** Spontaneous vegetation of linear type, Vzletnaya str., 3. (14.11.2021).



**(d)** Zheleznovodskaya str., adjacent to the territories of the residential sector. (15.11.2021).



**(e)** Wasteland near the airport. (10.11.2021).



**(f)** The territory of a wasteland on the site of a former vineyard between Turisticheskaya str. and Solntsedarskaya str. (15.12.2021).

**Figure 2.** Slope along the Highway 03K-555 near SNT Vinogradar-3. (11.12.2021). Spontaneous dendroflora of Gelendzhik.



**(a)** Attraction area (Lunacharsky str., 129 A.)



**(b)** Turisticheskaya str., 27 A.



**(c)** Plantations *Pinus brutia* var. *pityusa* (Steven) Silba: Turisticheskaya str., 19.



**(d)** Plantations *Quercus pubescens* Willd.

**Figure 3.** Cultural dendroflora of Gelendzhik in Naberezhnaya str.

True census of all tree and shrub species was carried out on the transects. The diameter of the trunk, the height of the tree and shrub, the width of the crown projection, and the sanitary condition were evaluated. Special attention was paid to rare species evaluating renewal and undergrowth.

Based on the materials of field research, a list of the dendroflora of Gelendzhik has been compiled. Ecological and biological features and distribution areas of species are specified according to the monographs of A. S. Zernov [*Zernov*, 2013], A. L. Ivanov [*Ivanov*, 2019], S. A. Litvinskaya, R. A. Murtazaliev [*Litvinskaya*, 2006, 2019]. The analysis of the dendroflora was carried out according to the methods generally accepted in comparative floristics [*Yurtsev and Kamelin*, 1991]. The analysis of life forms was carried out using the RAUNKIAER system [*Raunkiaer*, 1934]. The analysis of geographical elements was carried out in accordance with the classification of elements of the Caucasian flora by N. N. Portenier [*Portenier*, 2000, 2012] and A. L. Ivanov [*Ivanov*, 2019]. Latin names of plants are given according to World Flora Online [*WFO*, 2023].

## 4. Results and discussion

The species composition of the identified woody plants of Gelendzhik has 110 species and hybrids. Of these, gymnosperms account for 19 species (17.3%) and angiosperms – 91 species (82.7%). The systematic composition of the taxa identified in the dendroflora of Gelendzhik is given in Table 1.

A detailed systematic analysis of the dendroflora is presented in Table 2, which shows the number of genera and species in each of the families. The leading in the number of species are the families Rosaceae, Cupressaceae and Fabaceae, which account for the third part (44 species; 40%) of the species composition of the dendroflora under consideration. The predominant role of Rosaceae is a characteristic feature of the dendroflora of the temperate climatic region of the Holarctic [*Litvinskaya*, 2019]. The high participation of Cupressaceae is explained by the high share of coniferous exotics of the dendroflora of the city. And the Salicaceae family, which is one of the three popular families of most cities, occupies only the 11th place in Gelendzhik. Also, the difference between the dendroflora of

**Table 1**. Systematic composition of the dendroflora of the city of Gelendzhik.

| | Number of families | % of the number of families | Number of genera | % of the number of genera | Number of species | % of the number of species |
|---|---|---|---|---|---|---|
| Gymnospermae | 2 | 5.7 | 8 | 10.7 | 19 | 17.3 |
| Angiosperms | 33 | 94.3 | 67 | 89.3 | 91 | 82.7 |
| Total | 35 | 100 | 75 | 100 | 110 | 100 |

Gelendzhik from similar floras of other cities is the low participation of monotypic families (16 families; 14.5%) and families represented by 2–3 species (13 families; 11.8%). In general, these families occupy 25.3% in the systematic spectrum, while in the dendroflora of most cities they reach 50–80%. This indicates the species richness of the dendroflora of the city of Gelendzhik.

**Table 2**. Systematic composition of the dendroflora of the city of Gelendzhik.

| Family | Quantity, pcs. | | Quantity, pcs. | | Family | Quantity, pcs. | | Quantity, pcs. | |
|---|---|---|---|---|---|---|---|---|---|
| | species | % | genera | % | | species | % | genera | 5 |
| Aceraceae | 2 | 1.82 | 1 | 0.91 | Magnoliaceae | 1 | 0.91 | 1 | 0.91 |
| Agavaceae | 2 | 1.82 | 1 | 0.91 | Malvaceae | 1 | 0.91 | 1 | 0.91 |
| Anacardiaceae | 3 | 2.73 | 3 | 2.73 | Moraceae | 4 | 3.64 | 3 | 2.73 |
| Araliaceae | 1 | 0.91 | 1 | 0.91 | Oleaceae | 6 | 5.45 | 6 | 5.45 |
| Berberidaceae | 2 | 1.82 | 1 | 0.91 | Pinaceae | 6 | 5.45 | 3 | 2.73 |
| Betulaceae | 4 | 3.64 | 3 | 2.73 | Platanaceae | 1 | 0.91 | 1 | 0.91 |
| Bignoniaceae | 1 | 0.91 | 1 | 0.91 | Punicaceae | 1 | 0.91 | 1 | 0.91 |
| Caprifoliaceae | 3 | 2.73 | 1 | 0.91 | Ranunculaceae | 1 | 0.91 | 1 | 0.91 |
| Celastraceae | 1 | 0.91 | 1 | 0.91 | Rhamnaceae | 2 | 1.82 | 1 | 0.91 |
| Cornaceae | 2 | 1.82 | 2 | 1.82 | Rosaceae | 24 | 21.82 | 15 | 13.64 |
| Cupressaceae | 13 | 11.82 | 5 | 4.55 | Salicaceae | 5 | 4.55 | 2 | 1.82 |
| Ebenaceae | 2 | 1.82 | 1 | 0.91 | Simaroubaceae | 1 | 0.91 | 1 | 0.91 |
| Fabaceae | 7 | 6.36 | 7 | 6.36 | Tamaricaceae | 1 | 0.91 | 1 | 0.91 |
| Fagaceae | 2 | 1.82 | 1 | 0.91 | Tiliaceae | 2 | 1.82 | 1 | 0.91 |
| Hippocastanaceae | 1 | 0.91 | 1 | 0.91 | Ulmaceae | 2 | 1.82 | 1 | 0.91 |
| Hydrangeaceae | 1 | 0.91 | 1 | 0.91 | Viburnaceae | 1 | 0.91 | 1 | 0.91 |
| Juglandaceae | 1 | 0.91 | 1 | 0.91 | Vitaceae | 3 | 2.73 | 1 | 0.91 |
| Lamiaceae | 1 | 0.91 | 1 | 0.91 | Total | 35 | 31.82 | 75 | 68.18 |

The woody vegetation of the city of Gelendzhik consists of representatives of: 1) wild flora fraction (64.2% of the total flora), including both native and naturalized cultivated species; 2) introduced – cultivated introduced and native flora species (35.8%). The wild-growing fraction of the Gelendzhik dendroflora consists of 65 species (Table 3), which is 21% of the dendroflora of the Krasnodar Krai [*Ivankina et al.*, 2016]. It includes an aboriginal (58 species; 52.7%) and a naturalizing (adventitious) component (9 species; 8.2%).

**Table 3**. Types of wild-growing fraction of the dendroflora of the city of Gelendzhik

| Species | Family | Life form | Geographical element | Number of individuals |
|---|---|---|---|---|
| Cimnosperma (Pinopsida) | | | | |
| Juniperus communis L. | Cupressaceae | Phn:sv | Caucasian.: Pan-Caucasian | 112 |
| Juniperus foetidissima Willd. | Cupressaceae | Phms:sv | Eastern Mediterranean | 1 |
| Juniperus oxycedrus L. | Cupressaceae | Phn:sv | Eastern Mediterranean | 13 |
| Juniperus sabina L. | Cupressaceae | Phn:sv | Pontic-South Siberian. | 17 |
| Pinus nigra subsp. pallasiana (Lamb.) Holmboe | Pinaceae | Phmg:sv | Crimean-Novorossiysk | 27 |
| Pinus brutia var. pityusa (Steven) Silba | Pinaceae | Phmg:sv | Caucasian.: Eucaucasian. | 2889 |
| Platycladus orientalis L. Franco | Cupressaceae | Phms:sv | Adventitious: Southeast Asia | 145 |
| Angiospermae (Magnoliopsida) | | | | |
| Acer campestre L. | Aceraceae | Phms | Euro-Caucasian | 2 |
| Acer pseudoplatanus L. | Aceraceae | Phms | European | 48 |
| Ailanthus altissima Mill. Swingle | Simaroubaceae | Phm | Adventitious China | 109 |
| Astracantha arnacanthoides (Boriss.) Boriss. | Fabaceae | Phn | Caucasian.: Eucaucasian | 12 |
| Berberis vulgaris L. | Berberidaceae | Phn | European | 1 |
| Betula pendula Roth | Betulaceae | Phms | Palearctic | 2 |
| Carpinus betulus L. | Betulaceae | Phms | Caucasian.: Pan-Caucasian | 2 |
| Carpinus orientalis Mill. | Betulaceae | Phm | Eastern Mediterranean | 1058 |
| Chrysojasminum fruticans (L.) Banfi | Oleaceae | Phn | Mediterranean | 279 |
| Clematis vitalba L. | Ranunculaceae | Ch:ll | Submediterranean *. | 78 |
| Cornus mas L. | Cornaceae | Phm | General Ancient Mediterranean | 153 |
| Cornus sanguinea subsp. australis (C.A.Mey.) Soó | Cornaceae | Phm | General Ancient Mediterranean | 237 |
| Corylus avellana L. | Betulaceae | Phn | Palearctic | 9 |
| Cotinus coggygria Scop. | Anacardiaceae | Phn | General Ancient Mediterranean | 197 |
| Crataegus monogyna Jacq. | Rosaceae | Phm | European | 731 |
| Crataegus pentagyna Waldst. & Kit. ex Willd. | Rosaceae | Phm | Western Ancient Mediterranean | 134 |
| Cydonia oblonga Mill. | Rosaceae | Phm | General Ancient Mediterranean | 1 |
| Diospyros lotus L. | Ebenaceae | Phm | Armenian-Iranian | 1 |
| Euonymus europaeus L. | Celastraceae | Phn | European | 4 |
| Ficus carica L. | Moraceae | Phm | Adventitious. Asia Minor | 29 |

Continued on next page

**Table 3**. Types of wild-growing fraction of the dendroflora of the city of Gelendzhik (Continued)

| Species | Family | Life form | Geographical element | Number of individuals |
|---|---|---|---|---|
| Fraxinus excelsior L. | Oleaceae | Phmg | European | 2408 |
| Gleditsia triacanthos L. | Fabaceae | Phm | Adventitious North America | 48 |
| Hedera helix L. | Araliaceae | Ch:ll | Euxine | 98 |
| Juglans regia L. | Juglandaceae | Phms | Adventitious Eastern Mediterranean. | 32 |
| Ligustrum vulgare L. | Oleaceae | Phn | European | 469 |
| Lonicera caprifolium L. | Caprifoliaceae | Ch:ll | Subcaucasian *. | 87 |
| Maclura pomifera Raf. C.K. Schneid. | Moraceae | Phms | Adventitious North America | 135 |
| Malus orientalis Uglitzk. | Rosaceae | Phms | Subcaucasian *. | 4 |
| Morus alba L. | Moraceae | Phms | Adventitious China | 1 |
| Morus nigra L. | Moraceae | Phms | Adventitious Western Asia | 26 |
| Paliurus spina-christi Mill. | Rhamnaceae | Phn | General Ancient Mediterranean | 2305 |
| Pistacia atlantica Desf. | Anacardiaceae | Phm | Eastern Mediterranean | 388 |
| Platanus occidentalis L. | Platanaceae | Phn | Adventitious Eastern Mediterranean. | 2 |
| Populus alba L. | Salicaceae | Phms | Palearctic | 3 |
| Populus nigra L. | Salicaceae | Phms | Palearctic | 2 |
| Prunus avium (L.)L. Moench | Rosaceae | Phms | European | 7 |
| Prunus cerasifera Ehrh. | Fabaceae | Phm | General Ancient Mediterranean | 245 |
| Prunus mahaleb L. | Rosaceae | Phm | Mediterranean | 967 |
| Prunus spinosa L. | Rosaceae | Phn | Euro-Caucasian | 640 |
| Pyracantha coccinea M. Roem. | Rosaceae | Phn | Western Ancient Mediterranean | 1 |
| Pyrus caucasica Fed. | Rosaceae | Phms | Caucasian: Pan-Caucasian | 7 |
| Quercus pubescens Willd. | Fagaceae | Phms | Submediterranean *. | 800 |
| Quercus robur L. | Fagaceae | Phms | European | 14 |
| Rhamnus cathartica L. | Rhamnaceae | Phm | Palearctic | 43 |
| Rhus coriaria L. | Anacardiaceae | Phn | General Ancient Mediterranean | 129 |
| Robinia pseudoacacia L. | Fabaceae | Phm | Adventitious North America | 44 |
| Rosa canina L. | Rosaceae | Phn | Euro-Caucasian. | 156 |
| Rubus canescens DC. | Rosaceae | Phn | Western Ancient Mediterranean | 666 |
| Salix alba L. | Salicaceae | Phm | Palearctic | 4 |

Continued on next page

**Table 3**. Types of wild-growing fraction of the dendroflora of the city of Gelendzhik (Continued)

| Species | Family | Life form | Geographical element | Number of individuals |
|---|---|---|---|---|
| Salix caprea L. | Salicaceae | Phm | Palearctic | 1 |
| Spartium junceum L. | Fabaceae | Phn | Adventitious Mediterranean region | 33 |
| Tamarix tetrandra Pall. ex M. Bieb. | Tamaricaceae | Phn | Eastern Mediterranean | 16 |
| Thymus markhotensis Maleev | Lamiaceae | Ch: | Caucasian: Eucaucasian | 1 |
| Tilia platyphyllos Scop. | Tiliaceae | Phmg | European | 2 |
| Ulmus glabra Huds. | Ulmaceae | Phms | Euro-Caucasian | 1167 |
| Ulmus minor Mill. | Ulmaceae | Phm | Euro-Caucasian | 15 |
| Viburnum opulus L. | Viburnaceae | Phn | Palearctic | 1 |
| Vitis vinifera L. | Vitaceae | Phn:ll | Submediterranean * | 10 |

The wild-growing fraction was analyzed for the correlation of life forms and geographical element.

The analysis of life forms showed the predominance of phanerophytes (Figure 4), represented equally by mesophanerophytes (25%), nanophanerophytes (26%) and microphanerophytes (28%).

Note. Phmg (Megaphanerophyton) – megaphanerophyte, Phms (Mesophanerophyton) – mesophanerophyte, Phm (Microphanerophyton) – microphanerophyte, Phn (Nanophanerophyton) – nanophanerophyte, Ch (Chamaephyton) – chamaephyte; ll (liana lignosa) – lignifying liana, sv (sempervirens) – evergreen, fl (fruticulus) – low shrub.

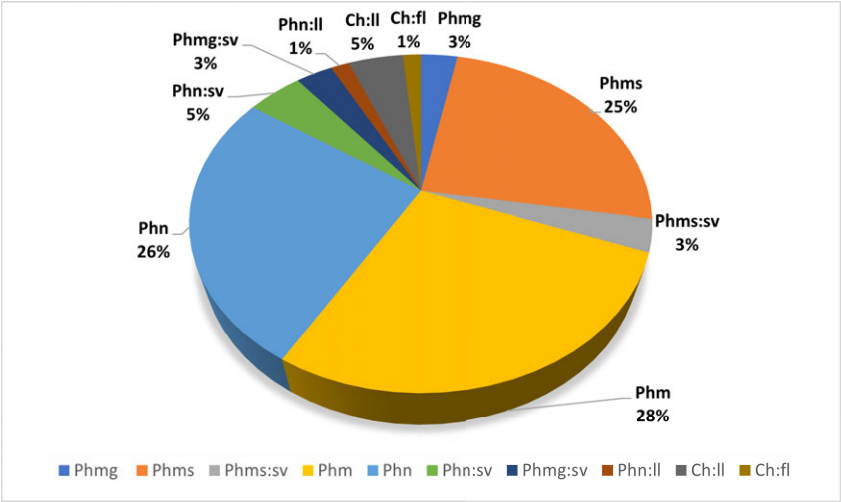


**Figure 4.** The ratio of life forms of the Gelendzhik dendroflora.

The analysis of the geographical element of the wild-growing fraction showed the heterogeneity of the dendroflora. 15 geographical elements take part in its formation (Table 4). The largest number of species in the studied dendroflora belongs to the ancient Mediterranean group of geoelements – 20 species (30.8% of the wild fraction of dendroflora). The group of widespread species included seven Common Mediterranean and Eastern Mediterranean species (12.3%). The majority of the boreal group of geoelements are Caucasian geoelements – 13 species (20%). The participation of Subcaucasian species (3 species) emphasizes the link between Caucasian species and the flora of the Mediterranean

and European forest flora. The European element is in the first place in terms of the number of species – 9 (13.8%), but quantitatively its representatives do not occupy significant positions. Palearctic (8 species) and adventitious geoelements (9 species) are of great importance in the composition of the dendroflora. Most of the adventitious species are of North American origin.

**Table 4**. Geographical spectrum of the wild-growing fraction of the dendroflora of the city of Gelendzhik

| Geographical element | Number of species | % |
|---|---|---|
| Holarctic | | |
| Palearctic | 8 | 12.3 |
| Boreal | | |
| Pontic-South Siberian | 1 | 1.5 |
| Euro-Caucasian | 5 | 7.7 |
| European | 9 | 13.8 |
| Caucasian | | |
| Pan-Caucasian | 3 | 4.6 |
| Eucaucasian | 3 | 4.6 |
| Euxine | 1 | 1.5 |
| Ancient Mediterranean | | |
| General Ancient Mediterranean | 7 | 10.8 |
| Eastern Mediterranean | 7 | 10.8 |
| Mediterranean | 2 | 3.1 |
| Western Ancient Mediterranean | 3 | 4.6 |
| Crimean-Novorossiysk | 1 | 1.5 |
| Binder | | |
| Subcaucasian* | 2 | 3.1 |
| Submediterranean* | 3 | 4.6 |
| Adventitious | | |
| North America | 3 | 4.6 |
| China | 2 | 3.1 |
| Southeast Asia | 1 | 1.5 |
| Armenian-Iranian | 1 | 1.5 |
| Mediterranean region | 1 | 1.5 |
| Western Asia | 1 | 1.5 |
| Asia Minor | 1 | 1.5 |

The analysis of the quantitative composition of woody plant species showed a clear predominance of representatives of the native dendroflora fraction. Figure 5 shows the ratio of the dominant species of dendroflora, which make up 72% of all 18,897 recorded specimens of tree and shrub plantations. The highest occurrence is from woody life forms – Pitsunda pine (*Pinus brutia* var. pityusa (Steven) Silba) and tall ash (*Fraxinus excelsior* L.) and from shrubby – hold-tree and common mahalebka (*Prunus* mahaleb (L.) Vassilcz.).

The Pitsunda pine (*Pinus brutia* var. pityusa (Stev) Silba) and the common mahaleb (*Prunus mahaleb* (L.) Vassilcz.) are rare species listed in the Red Book of the Russian Federation [*Bardunov*, 2008] and the Krasnodar Krai [*Litvinskaya*, 2017] as Mediterranean

native species. This indicates the originality and specificity of the species composition of the tree plantations of the city of Gelendzhik. Also, *Pistacia atlantica* Desf. [*Bardunov*, 2008] grows on the territory of the city of Gelendzhik, numbering 388 specimens of various age groups (2.1% of the dendroflora), some specimens of which reach a diameter of more than 60 cm.

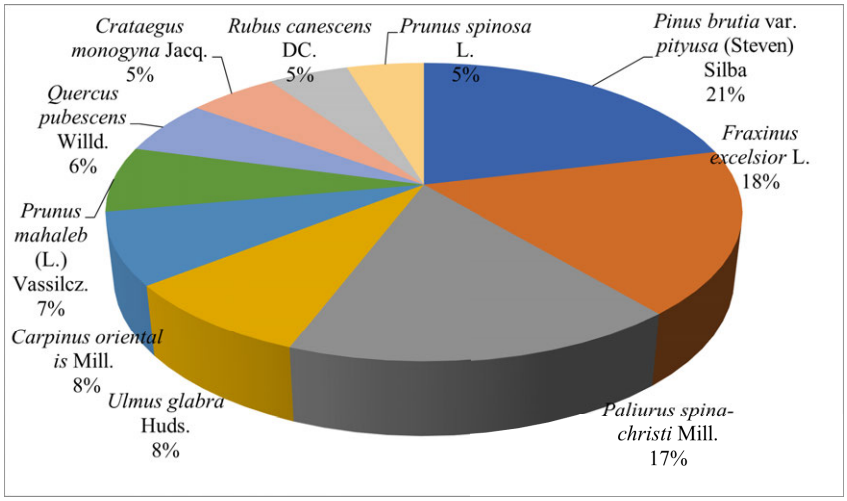


**Figure 5.** Percentage of the leading species of woody plants in the tree plantations of the city of Gelendzhik.

## 5. Conclusion

Based on the analysis of 18,897 specimens of cultural and spontaneous tree and shrub plantations of Gelendzhik, the growth of 110 species of dendroflora was established. Of these, gymnosperms account for 19 species (17.3%) and angiosperms – 91 species (82.7%). The most widely represented families are Rosaceae, Cupressaceae, Fabaceae (44%). The insignificant participation of monotypic families and families represented by 2–3 species indicates the species richness of the dendroflora of the city of Gelendzhik.

The analysis of the qualitative and quantitative composition of the dendroflora of Gelendzhik showed its original character. The predominance of representatives of the aboriginal faction over the cultural one speaks of its species richness. The wild-growing fraction of the Gelendzhik dendroflora consists of 65 species (21% of the dendroflora of the Krasnodar Krai), including an indigenous (52.7% of the Gelendzhik dendroflora) and an adventitious component (8.2%).

The significant participation of the Mediterranean and Caucasian geoelements indicates a high degree of autochthonicity in the development of the dendroflora of the city of Gelendzhik. Phanerophytes predominate among the life forms, represented equally by mesophanerophytes, nanophanerophytes and microphanerophytes.

The specifics of the dendroflora of the city of Gelendzhik is wide participation in its composition of the Mediterranean species *Pinus brutia* var. *pityusa* (Steven) Silba (21%), *Prunus* mahaleb (L.) Vassilcz. (7%), *Pistacia atlantica* Desf. (2.1%), which are rare protected species. All registered specimens of rare red Book plant species must be registered by the administrative authorities; old-aged individuals should be given a specially protected status of natural monuments.

The obtained results of the study indicate the sustainability of green spaces in the urban environment of the city of Gelendzhik and their performance of ecological functions that are of particular importance for the resort city.

## References

Administration of the city of Gelendzhik: official website (2020), Information about the green spaces of the resort city of Gelendzhik, https://admgel.ru/about/inspections/result/39730/ (in Russian), (date of access: 10.04.2023).

Alikhadzhiev, M. K., R. S. Erdzhapova, N. A. Bagrikova, and A. S. Tret'yakova (2019), Structural analysis of the tree-shrubby flora of Grozny, *Bulletin of the State Nikitsky Botanical Gardens*, (133), 115–122, https://doi.org/10.36305/0513-1634-2019-133-115-122 (in Russian).

Arkuschina, G. F., and O. V. Gulay (2010), Features of Kirovograd dendroflora and its role in optimizing the urban environment, *Scientific bulletin of UNFU*, *20*(14), 39–43 (in Russian).

Bardunov, L. V. (Ed.) (2008), *Red Book of the Russian Federation: (Plants and fungi)*, KMK Scientific Press, Moscow (in Russian).

Bayramyan, L. E., and N. G. Shekoyan (2021), The use of native and introduced species of dendroflora in landscaping the city of Vanadzor, *Universum: Chemistry and biology: electronic scientific journal*, *3*(81), 1–4 (in Russian).

Boiko, T. O., and O. I. Dementieva (2018), The tree vegetation of the Kherson State Agrarian University Arboretum, *Ukrainian journal of ecology*, *8*(2), 120–127, https://doi.org/10.15421/2018_318, (in Ukrainian).

Bondarenko, S. V. (2020), Some rare plant species of Gelendzhik, in *II All-Russian Scientific and Practical school-conference «Terrestrial and marine ecosystems of the Black Sea region and their protection»*, pp. 39–40, Institute of Natural and Technical Systems, Sevastopol (in Russian).

Borzenkova, T. G. (2021), Study of native dendroflora of Khabarovsk city, *Problems of botany of South Siberia and Mongolia*, *20*(1), 70–75, https://doi.org/10.14258/pbssm.2021015 (in Russian).

Bukharina, I. L., T. M. Povarnitsina, and K. E. Vedernikov (2007), *Ecological and biological features of woody plants in an urbanized environment: monograph*, 216 pp., FGOU VPO Izhevsk State Agricultural Academy, Izhevsk (in Russian).

Chindyaeva, L. N., M. A. Tomoshevich, A. P. Belanova, and E. V. Banaev (2018), *Woody plants in greening of Siberian cities*, 457 pp., Academic Publishing House "Geo", https://doi.org/10.21782/B978-5-9909584-3-2 (in Russian).

Dudyn, R. B., O. M. Bagatskaya, and N.-I. I. Rosul (2020), Cultivated dendroflora of Uzhhorod city, *Bioresursi i prirodokoristuvanna*, *12*(1-2), https://doi.org/10.31548/bio2020.01.007, (in Ukrainian).

GOST 16350-80 (1981), Climate of the USSR. Regionalizing and statistical parameters of climatic factors for technical purposes (in Russian).

Gvozdetsky, N. A. (Ed.) (1968), *Physico-geographical zoning of the USSR*, 578 pp., Moscow State University (in Russian).

Ivankina, N. F., T. I. Kuzmina, and E. V. Solovyova (2016), Research status pitsundsky pines in Gelendzhik, in *The potential and prospects of modern science. Materials of the All-Russian Scientific and Practical Conference of Teachers and Young Scientists. Dedicated to the 20th anniversary of the birth of the KubSU branch in Gelendzhik*, pp. 66–69 (in Russian).

Ivanov, A. L. (2019), *Conspectus florae Caucasi Rossicae (plantae vasculares)*, 341 pp., NCFU, Stavropol (in Russian).

Khalatyan, A. S. (2014), Complex floristic analysis of the dendroflora of the city of Stavropol, in *6th International Scientific and Practical Conference "Prospects for the development of scientific research in the 21st century"*, pp. 30–32, Limited Liability Company Approbation, Makhachkala (in Russian).

Klimko, M., and G. Kaczmarek (2006), Dendroflora of the town of Jarocin, *Roczniki Akademii Rolniczej w Poznaniu. Botanika-Steciana*, *10*.

Litvinskaya, S. A. (2006), *Ecological encyclopedia of trees and shrubs (ecology, geography, useful properties)*, 360 pp., Tradiziya, Krasnodar (in Russian).

Litvinskaya, S. A. (Ed.) (2017), *Red Book of the Krasnodar Region. Plants and fungi*, iii ed., 850 pp., Administration of the Krasnodar territory, Krasnodar (in Russian).

Litvinskaya, S. A. (2019), *The Caucasus element within the flora of the Russian Caucasus: geography, sozology, ecology*, 439 pp., Prosveshenie-Yg, Krasnodar (in Russian).

Litvinskaya, S. A. (2020a), Sub-mediterranean of the Black Sea coast of the Caucasus - hot spot for biodiversity conservation in Russia, in *International scientific and practical conference "Ecology and Nature management"*, pp. 399–406, LLC "KEP", Nazran (in Russian).

Litvinskaya, S. A. (2020b), Environmental problems of the Azov-Black Sea coastal zones, *Astrakhan Bulletin of Environmental Education*, *19*(1), 38–44, https://doi.org/10.36698/2304-5957-2020-19-1-38-44.

Magomedova, M. A. (2014), On the diversity of the dendroflora of the city of Makhachkala and its significance for landscaping, *Bulletin of the Socio-Pedagogical Institute*, (2(10)), 27–33 (in Russian).

Molganova, N. A., and S. A. Ovesnov (2018), Analysis of the arboretum of the city of Perm, *Vestnik Permskogo universiteta*, pp. 16–23, https://doi.org/10.17072/1994-9952-2018-1-16-23 (in Russian).

Okazova, Z., N. Kusova, F. Agaeva, and I. Bigaeva (2019), Analysis of dendroflora of urbanized territories using the city of Vladikavkaz as an example, *IOP Conference Series: Earth and Environmental Science*, *316*(1), 012,046, https://doi.org/10.1088/1755-1315/316/1/012046.

Padutov, A. E., V. S. Isakov, and N. V. Maltseva (2016), The Dendroflora of the city of Gomel Dendroflora of Gomel city, *Problems of forestry and forestry*, *76*, 445–449 (in Russian).

Polyakova, E. V. (2005), Dendroflora of the city of Vladivostok, *V. L. Komarov Memorial Lectures*, *51*, 154–175 (in Russian).

Portenier, N. N. (2000), The system of geographical elements of the flora of the Caucasus, *Botanicheskii Zhurnal*, *85*(9), 26–33 (in Russian).

Portenier, N. N. (2012), *Flora and botanical geography of the North Caucasus: Selected Works*, 294 pp., KMK Scientific Press, Moscow (in Russian).

Postarnak, Y., and S. Litvinskaya (2022), A new association of Trachomitetum sarmatiensea of Phragmiti-Magnocaricetea Klika in Klika et Novak 1941 class on the territory of Krasnodar Krai, *Russian Journal of Earth Sciences*, *22*(5), 1–8, https://doi.org/10.2205/2022es01si06.

Raunkiaer, C. (1934), *The life forms of plants and statisticae plant geography*, 632 pp., Clarendon press, Oxford.

V. L. Komarov Botanical Institute of the Russian Academy of Sciences (2014), Botanical and geographical zoning of the Caucasus. Maps of the areas of the flora of the Caucasus and indications of the general distribution of species, https://www.binran.ru/resursy/informatsionnyye-resursy/tekuschie-proekty/caucasian-flora/contentkav/departments.php (in Russian), (date of access: 15.04.2023).

V. V. Dokuchaev Soil Science Institute (2012), Information and reference system for classification of soils of Russia v1.0, http://infosoil.ru/index.php?pageID=opr-77 (in Russian), (date of access: 15.04.2023).

Volkova, T. A., A. A. Mishchenko, Y. O. Antiptseva, and D. A. Lipilin (2017), *Coastal geosystems in space and time: based on the materials of the Krasnodar Territory: monograph*, 275 pp., Prosveshenie-Yg (in Russian).

WFO (2023), World Flora Online. Royal Botanic Gardens, Kew, https://wfo.kew.org/, (date of access: 22.10.2023).

Yurtsev, B. A., and R. V. Kamelin (1991), *Basic concepts and terms of floristry*, 80 pp., Perm State University, Perm (in Russian).

Zernov, A. S. (2013), *Illustrated flora of the South of the Russian Black Sea region*, 588 pp., KMK Scientific Press, Moscow (in Russian).

Russian Journal of Earth Sciences

Special Issue: "Fundamental and Applied Aspects of Geology, Geophysics and Geoecology"

# Investigation of the Cyclicity and Trend of the Surface Air Temperature According to the Weather Station Mayak of Sukhum

**I. S. Afanasyev[1,2], L. V. Khintuba[3,4], Y. A. Ekba[3,4], R. G. Zakinyan[1,2]**

[1] North Caucasus Federal University, Stavropol, Russia
[2] North Caucasus Center for Mathematical Research, Stavropol, Russia
[3] Institute of Ecology of the Academy of Sciences of Abkhazia, Sukhum, Abkhazia
[4] Abkhaz State University, Sukhum, Abkhazia
* **Correspondence to:** I. S. Afanasyev, afanasevigor278@gmail.com

**Abstract:** This paper analyzes the surface air temperature data for the city of Sukhum for the period 1961–2022. These values are presented as time series of average annual temperatures. As a result, we get 2 main components: trend, spectrum (including cycles). In general, the average annual temperature has a predominantly positive trend, i. e. over the entire period the temperature has increased by 1.31 degrees, which may occur against the background of global warming. Accordingly, another task of the current work was to identify cyclic components and determine their physical nature. A quasi-two-year, 5–6-year, solar activity cycle and a multi-year cycle (2–3 decades) are observed.

**Keywords:** surface air temperature, time series, trend, moving average, average annual temperature, cycles, solar activity, spectral analysis.

**Citation:** Afanasyev I. S., Khintuba L. V., Ekba Y. A., Zakinyan R. G. (2023), Investigation of the Cyclicity and Trend of the Surface Air Temperature According to the Weather Station Mayak of Sukhum, *Russian Journal of Earth Sciences*, Vol. 23, ES0204, https://doi.org/10.2205/2023ES02SI04

One of the most important environmental factors determining the state of the biosphere is the climate, which has a significant impact on human activity, agriculture, the economy and the environment as a whole [*Ekba et al.*, 2020]. The climate changes occurring in the last century are subject to the most attention, a significant increase in the average global air temperature at the earth's surface by 0.5 °C / 100 years has been recorded. There is an increase in the negative impact of natural phenomena on the economic and social life of the world community. Total losses in the world directly related to natural disasters have increased 40 times since the 1960s and amount to an average of hundreds of billions of US dollars per year [*Khintuba and Ekba*, 2018].

In our work, we analyze the surface air temperature data for the city of Sukhum for the period 1961–2022. The time series (TS) is investigated in order to assess the dynamics of changes in atmospheric air temperature by decomposing TS into trend and cycles. The trend is found by smoothing, i. e. a moving average is obtained [*Kendall and Stuart*, 1976].

Sukhum is located in the central part of the Republic of Abkhazia and is located 107 km from the border with Russia on the Black Sea coast (Figure 1). There are 3 rivers on the territory of Sukhum: Basla, Sukhumka and Kyalasur, the latter is the border of the city in the south.

The climate in Sukhum is humid subtropical. Average annual temperature: +14.8 °C, sea water warms up to +28–30 °C. Winters in Sukhum are warm and mild: from +8 °C to +14 °C, summers are hot and humid: from +24 °C to +30 °C.

Research Article

Received: 20 October 2023
Accepted: 27 November 2023
Published: 15 December 2023

**Copyright:** © 2023. The Authors. This article is an open access article distributed under the terms and conditions of the Creative Commons Attribution (CC BY) license (https://creativecommons.org/licenses/by/4.0/).

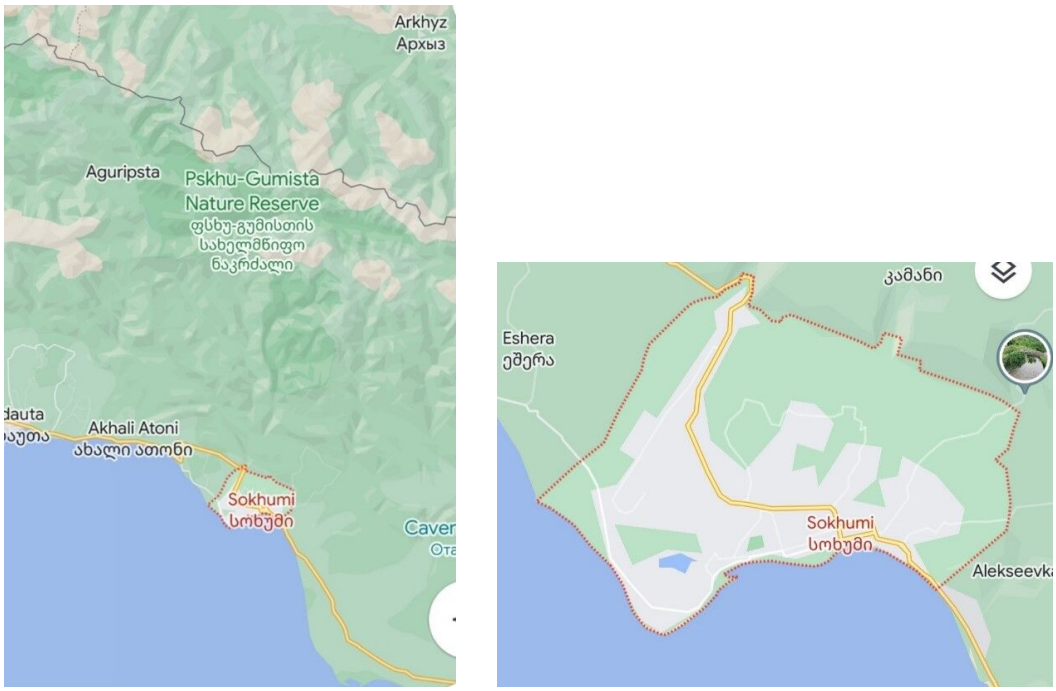


**(a)** **(b)**

**Figure 1.** Sukhum on the map (at different scales).

The lighthouse (Mayak station) is located on a sandy promontory washed by the Gumista River (Figure 2). The height of the lighthouse is 37 m, the lighting horizon is 24 km. The lighthouse overlooks the cities of New Athos and Sukhum.

According to Ya. A. Ekba and R. S. Dbar, the long-term variability of the average annual temperature of sea water in the water area of Sukhum is in the range of 15.2–17.6 °C [*Akhsalba et al.*, 2013]. With a general positive trend in the temperature of the upper horizon of the sea, amounting to 0.4–0.5 °C / 100 years, from the beginning of the XX century until the 90s. it decreased. Since 1994, the water temperature has been rising synchronously with the increase in air temperature, and in recent decades the temperature of the upper horizon of the Sukhumi water area has increased by 1.1 °C.

In this paper, we consider the time series of air temperature for the Mayak station in Sukhum, which also has a positive trend, although there are some temporary temperature drops over several decades, as well as for the temperature of seawater.

Using both a simple moving average and an exponential one allows for the most detailed analysis of temperature time series. For example, a simple moving average over 10 years makes it possible to estimate the temperature change on average for each cycle of solar activity, trace the temperature trend and identify cycles with periods of several decades [*Melnikova et al.*, 2020].

As a result, we get a graph that can be represented as sets of polynomials. Let's start by considering the trend line, making a simple smoothing, and only then we will select the degrees of the polynomials. When smoothing, a moving average of 10 and 30 years was given.

The final trend line is not growing monotonously. It grows and falls. The presence of highs and lows suggests the existence of fluctuations, the frequency of which is 30–40 years. In Figure 3, the picture of global warming is not so obvious, but the value of the moving average temperature has increased.

Figure 4 shows a moving average and a linear trend, where the following peak values of the simple moving average temperature (10 years) are visible: +14.52 °C (1970 y.), +13.95 °C (1994 y.), +16.25 °C (2010 y.), +15.73 °C (2020 y.), with the most pronounced the growth was up to 1994–2010 (by 2.3 degrees, from +13.95 °C to +16.25 °C. Over the entire




**Figure 2.** Mayak station in Sukhum on the map.

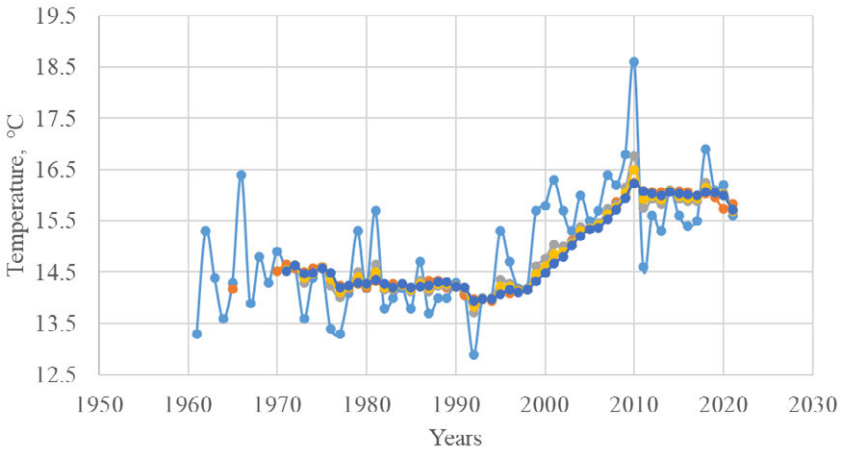


**Figure 3.** Average annual temperature and moving average for 10 years.

period, the temperature increased by 1.31 degrees, i. e. the areas of growth of the trend temperature were more pronounced than its fall.

After deducting a simple moving average and a linear trend, we do get some long–period fluctuations (with a period of about 30 years), the highs in 1970 and 2010, the minimum in 1994 (Figure 5).

To get rid of long-period fluctuations, we will find a moving average for 30 years. This will also make it possible to determine the change in the climatic norm, compare its characteristics for 1961–1990 and 1991–2020.

From Figure 6 it can be seen that the moving average has predominantly positive dynamics, growing smoothly. The climatic norm also increased by 1.31 degrees, and this was most pronounced in the new century. Accordingly, the talk about global warming is not groundless. This issue has become particularly acute in recent decades. Since 1900, the average temperature of the surface layer of air has increased by about 0.8° (1.4° F), and most of the temperature increase occurred in the period from the mid-70s of the twentieth century up to the present time [*Afanasyev et al.*, 2022]. It is generally believed that the problem of global warming is related to anthropogenic impact (i. e. human emissions into the air), while referring to the fact that the concentration of greenhouse gases has increased in the atmosphere, especially $CO_2$ [*Semenov and Popov*, 2011]. It is also interesting that the 11-year moving average of the solar constant has been decreasing over the past 2–3 decades, while the global temperature, on the contrary, has been growing rapidly, which

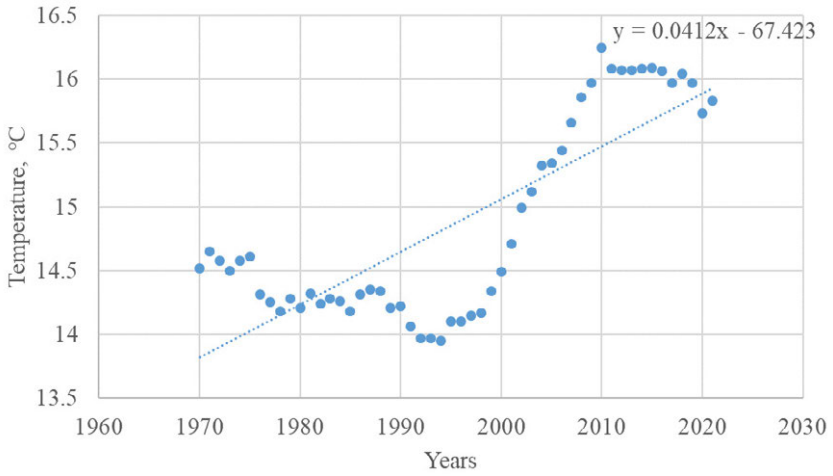


**Figure 4.** Moving average and trend.

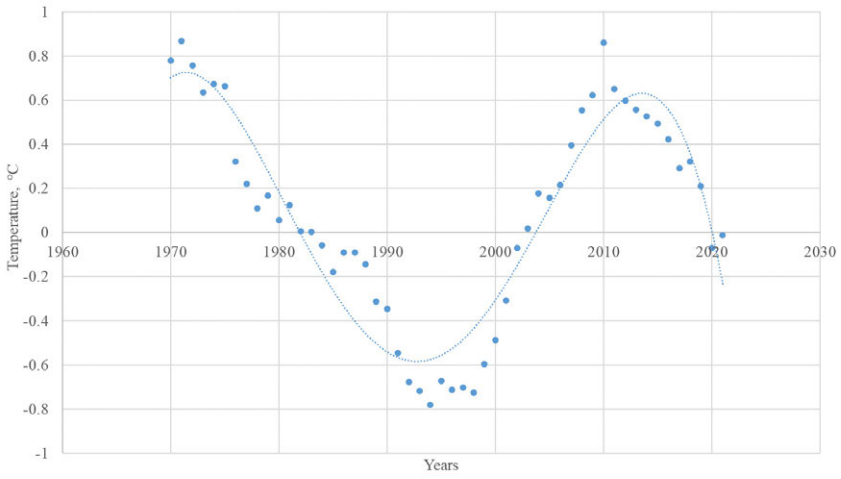


**Figure 5.** The difference between the actual values and the moving average over 10 years.

was an additional argument in favor of strengthening the greenhouse effect [*Melnikova et al.*, 2020].

However, the mechanism of the greenhouse effect itself is much more complicated. In addition to the anthropogenic factor, the change in the concentration of greenhouse gases may also be due to natural causes, for example, volcanic activity. A significant part of carbon dioxide is in the ocean. Accordingly, the growth of greenhouse gases can be both the cause of an increase in temperature (anthropogenic activity, volcanic activity) and a consequence (during evaporation, water vapor and carbon dioxide contained in the oceans enter the atmosphere).

It is worth noting that there is a significant difference between water vapor and carbon dioxide in the mechanism of the greenhouse effect. Thus, the concentration of saturated water vapor directly depends on temperature, i. e., with an increase in global temperature, the moisture capacity of the air increases. However, carbon dioxide spreads evenly on the planet, and we observe this against the background of the fact that the temperature increase differs in different latitudes. Accordingly, global warming is more pronounced in the circumpolar zones than in moderate, and even more subequatorial ones [*Melnikova et al.*, 2020]. An increase in temperature at the poles leads to the melting of glaciers, which also contain greenhouse gases. Thus, the problem of increasing the concentration of greenhouse gases is quite acute.

Exponential smoothing can also be performed for a time series of average annual temperatures. After all, in addition to cyclical factors associated with solar activity (and

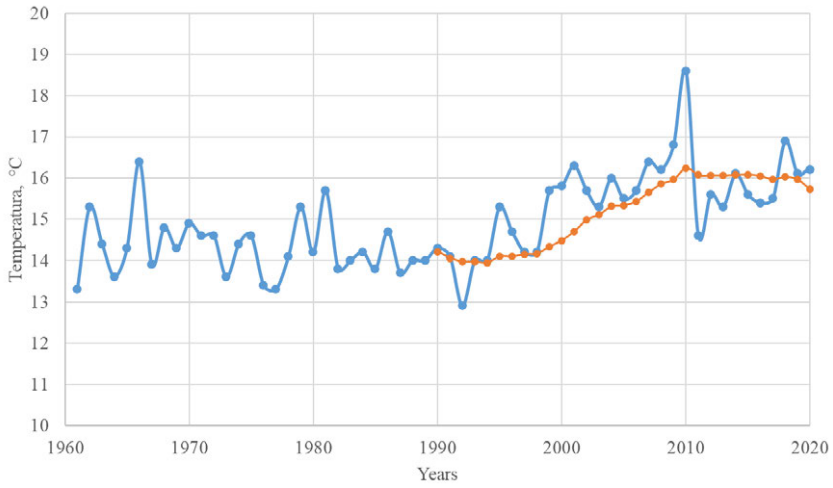


**Figure 6.** Average annual temperature and moving average for 30 years.

other harmonics), [*Semenov and Popov*, 2011] there are also random events, for example, the eruption of powerful volcanoes whose tephra height reaches the stratosphere [*Eliseev and Mokhov*, 2008]. Their role can be revealed when considering exponential moving averages (Figure 7).

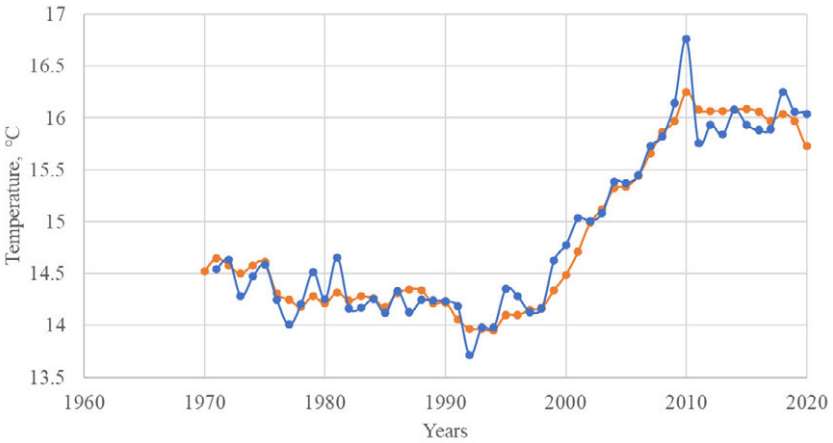


**Figure 7.** Simple and exponential smoothing with alpha equal to 0.3 (10-year moving average).

At the same time, "jumps" are clearly visible on the charts that are not related to seasonal factors. First of all, we can pay attention to the nature of temperature changes and its moving averages in 1990–1995 and 2010–2012. This is due to the eruptions of the volcanoes Pinatubo (1991) and Eyjafjallajekul (2010). In addition, on the graphs of the exponential moving average temperature, we see other peaks that may also be associated with volcanic eruptions:

- 1980 – St. Helens;
- 1982 – El Chichon;

### 1. Spectral analysis. Fourier Analysis

To consider cycles, it is advisable to pay attention to the time series of average annual temperatures [*Vityazev*, 2001].

**The periodogram** is a function of frequency, which shows an estimate of the spectral density of the signal.

To carry out spectral analysis, it is necessary to take away the trend line from the actual values of average annual temperatures. It can be seen from the figure that the trend line can be represented as a polynomial of the 4th degree, or as 2 polynomials of the 2nd

degree, where the transition point will be 2010 (the eruption of the Icelandic volcano and the achievement of the maximum of the 30-year cycle, the trend change to the opposite). The use of a polynomial of the 4th degree is impractical, therefore, we will consider the TS spectrum, limiting ourselves to the data before the eruption of the Eyjafjallajekull volcano.

For a 48-year period of time (1961 – 2008), we will construct a periodogram of the average annual temperature.

It is possible to note several harmonics of the time series period (Figure 8), which are presented in the form of pointed ends. The most pronounced are 16-year, 5–6-year and quasi-two-year cycles. The graph shows that the arrival function is monotonically decreasing, i. e. we cannot consider fluctuations of a large period. Considering the 48-year range, we cannot talk about the presence of cycles in it, the period of which is greater than or equal to 24 years (a consequence of Kotelnikov's theorem). Another disadvantage of the FFT is that the considered harmonic periods depend on the sample, i. e. the presence of a 16-year cycle is questionable. Also, the FFT excludes the possibility of the existence of cycles with a variable period, which is characteristic of solar activity [*Tarasov*, 2004]. However, the latter problem is solved by wavelet analysis.

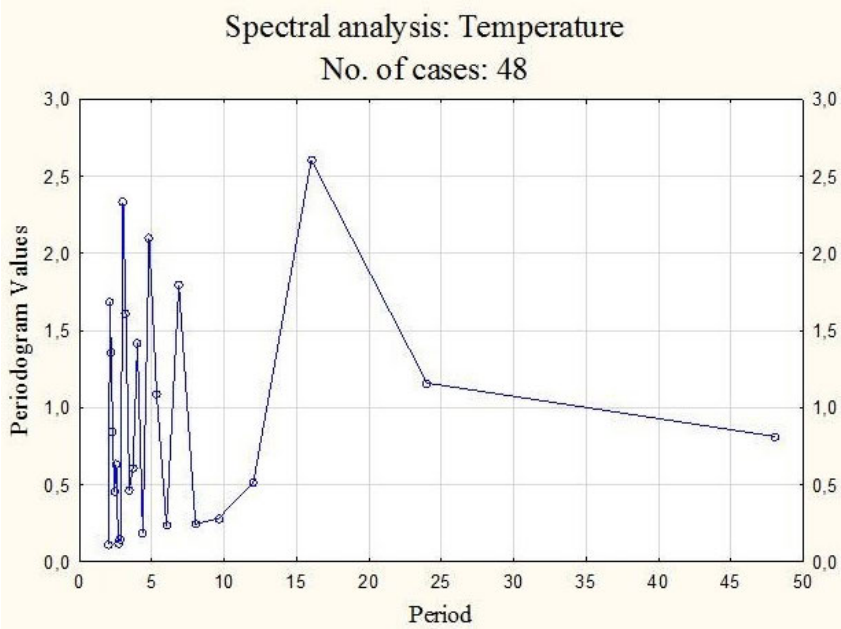


**Figure 8.** FFT periodogram of average annual air temperatures for Sukhum (1961 -2008), minus the polynomial trend line.

## 2. Wavelet analysis. Scalogram

When performing a wavelet analysis, a scalogram is constructed that estimates the distribution of energy (which is represented as the square of the amplitude) on the scales. The time is set on the axis, and the period scale is set on the axis. The result is a color graph that shows the amplitude spectrum of the continuous wavelet transform. It allows us to estimate harmonics that can manifest in different time ranges [*Vityazev*, 2001].

In Python, it was possible to build a scalogram for this series, which made it possible to identify cycles, including variables.

Figure 9 shows that there are variable periods of 4–6 years and 8–13 years (the second of them may be associated with an 11-year cycle, which actually varies from about 9 to 13 years), and a weak cycle with a period of 2–3 years is also visible (possibly quasi-two-year).

## 3. Conclusions

The time series of average annual temperatures for the city of Sukhum were considered on the basis of data for the period 1961–2022. The cyclical components and the trend were

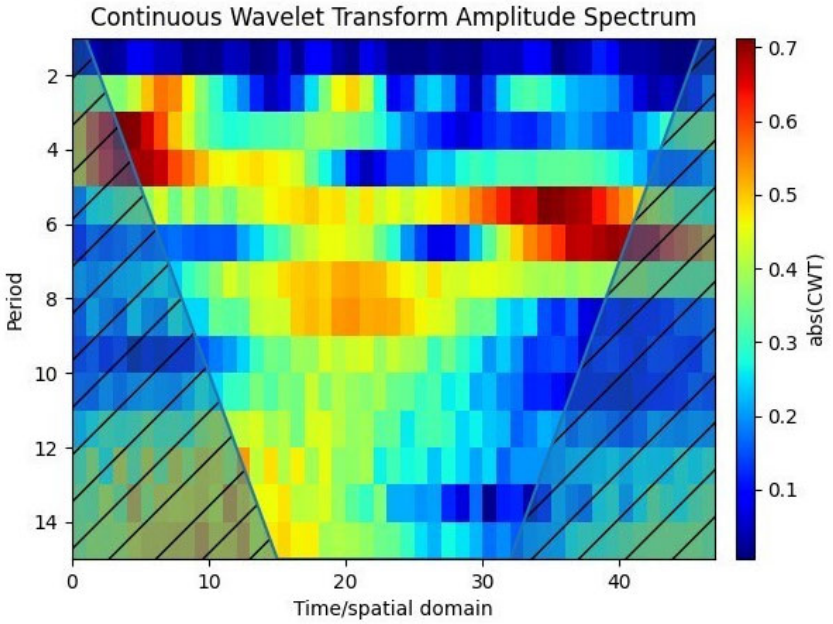


**Figure 9.** Wavelet analysis of BP average annual temperature values for Sukhum (1961–2008).

analyzed, which allowed us to draw the following conclusions. Over the entire period, the temperature increased by 1.31 degrees, i. e. the areas of growth of the trend temperature (a simple moving average for 10 years) were more pronounced than its fall. And the difference between the moving average and the straight trend line showed the presence of highs and lows of the trend temperature, which suggests the existence of fluctuations, with a periodicity of about 30 years. In the Fourier analysis and wavelet analysis, a periodogram of the FFT and a scalogram of average annual temperatures were obtained, which showed 5–6-year, quasi-two-year and solar cycles.

Attention was also paid to non-periodic deviations. The average annual temperature and the moving average for 10 years showed changes in temperature and its moving averages in 1990–1995 and 2010–2012. This is due to the eruptions of volcanoes Pinatubo (1992) and Eyjafjallajökull (2010). If we talk about the exponential moving average temperature, it showed other peaks that are associated with volcanic eruptions in 1980 – St. Helens and in 1982 – El Chichon.

## References

Afanasyev, I. S., A. R. Komarova, R. G. Zakinyan, and A. I. Shevchenko (2022), Greenhouse effect, in *Problems of Atmospheric Physics, Climatology and Environmental Monitoring: Reports of the IV International Scientific Conference (Stavropol, May 23-25, 2022)*, p. 256, North-Caucasus Federal University (in Russian).

Akhsalba, A. K., Y. A. Ekba, and S. I. Marandidi (2013), The influence of gas composition of atmospheric air of the seashore of Abkhazia, *Izvestiya SFEDU. Engineering sciences*, *9*(146), 30–34 (in Russian).

Ekba, Y. A., A. K. Akhsalba, L. V. Khintuba, and K. A. Nachkebia (2020), Variability of major climate-forming factors in the territory of Abkhazia for the global warming period, *Bulletin of the Academy of Sciences of Abkhazia. A series of natural sciences*, pp. 172–182 (in Russian).

Eliseev, A. V., and I. I. Mokhov (2008), Influence of volcanic activity on climate change in the past several centuries: Assessments with a climate model of intermediate complexity, *Izvestiya, Atmospheric and Oceanic Physics*, *44*(6), 723–736 (in Russian).

Kendall, M., and A. Stuart (1976), *Multivariate statistical analysis and time series*, 736 pp., Nauka, Moscow (in Russian).

Khintuba, L. V., and Y. V. Ekba (2018), The impact of volcanoes on the climate, in *International Scientific and Practical Conference "Open Physical Readings" Abstracts of Reports Youth Section*, pp. 29–30, LNU named after V. Dahl, Lugansk (in Russian).

Melnikova, M., A. Perdero, and E. Zalyubovsky (2020), *Global climate threat and Russia's economy in search of a special path*, 69 pp., Energy Center of the Moscow School of Management SKOLKOVO, Moscow (in Russian).

Semenov, S. M., and I. O. Popov (2011), Comparative estimates of influence of changes in carbon dioxide, methane, nitrous oxide, and water vapor concentrations on radiation-equilibrium temperature of Earth's surface, *Russian Meteorology and Hydrology*, (8), 33–34 (in Russian).

Tarasov, B. G. (2004), On the nature of cycles of geodynamic activity and the method of their forecast, Bulletin of the Kuzbass State Technical University, *Bulletin of the Kuzbass State Technical University*, (6-2(44)), 3–13 (in Russian).

Vityazev, V. V. (2001), *Wavelet analysis of time series*, 58 pp., St. Petersburg State University, St. Petersburg (in Russian).

Russian Journal of Earth Sciences

Special Issue: "Fundamental and Applied Aspects of Geology, Geophysics and Geoecology"

# Chemoecological Monitoring of Water Quality in the Ham Luong River (Mekong Delta, Vietnam)

**Nataliya N. Tereshchenko[1], Vladislav Yu. Proskurnin[1], Olga V. Soloveva[1], Elena A. Tikhonova[1], Nguyen Trong Hiep[2], Olga D. Chuzhikova-Proskurnina[1], Ilya G. Sidorov[1]**

[1] A. O. Kovalevsky Institute of Biology of the Southern Seas, Russian Academy of Sciences, Sevastopol, Russia
[2] Southern Branch of Joint Vietnam-Russia Tropical Science and Technology Research Center, Ho Chi Minh City, Vietnam
* **Correspondence to:** Nataliya N. Tereshchenko, ntereshchenko@yandex.ru

**Abstract:** Investigation of concentrations of organic and inorganic pollutants (hydrocarbons, including oil hydrocarbons, and trace elements – heavy metals and metalloids) in the Ham Luong River in the Mekong Delta was carried out and water quality was assessed by comparing the obtained levels of values with the regulatory limits of concentration. The determination of the total content of hydrocarbons and oil hydrocarbons was made by gas chromatography method; the trace elements were measured by ICP-MS technique after chemical treatment of samples. The content of oil hydrocarbons in the Ham Luong River water ranged from 0.042 to 0.076 mg/l. These values were quite high, exceeding the sanitary standard (0.05 mg/l) for fishery reservoirs, or approaching it, but they were lower compared to Vietnam national standard for domestic supply water (0.1 mg/l). The content of hydrocarbons in suspended matter was in the range of 0.011–0.37 mg/l. The concentrations of 15 trace elements were studied, nine of them (Ni, Fe, V, As, Se, Be, Cd, Sb, Tl) did not exceed any of the established regulatory limits of concentration for surface water. However, concentrations of six trace elements (Pb, Zn, Cu, Co, Ag, Mo) were found to exceed the standard regulatory limits. Among the studied 15 trace elements, critical and potentially critical elements were identified, which are subject to primary monitoring control. Chemoecological studies of water quality are important for monitoring of the ecological and sanitary water state for ensure the quality of consumed natural resources and to preserve the biological diversity of the Mekong Delta ecosystems.

**Keywords:** water quality, oil hydrocarbons, heavy metals, metalloids, pollution, Ham Luong River, Mekong Delta, Vietnam.

**Citation:** Tereshchenko N. N., Proskurnin V. Yu., Soloveva O. V., Tikhonova E. A., Nguyen Trong Hiep, Chuzhikova-Proskurnina O. D., Sidorov I. G. (2023), Chemoecological Monitoring of Water Quality in the Ham Luong River (Mekong Delta, Vietnam), *Russian Journal of Earth Sciences*, Vol. 23, ES0205, https://doi.org/10.2205/2023ES02SI05

Research Article

Received: 20 October 2023
Accepted: 27 November 2023
Published: 15 December 2023

**Copyright:** © 2023. The Authors. This article is an open access article distributed under the terms and conditions of the Creative Commons Attribution (CC BY) license (https://creativecommons.org/licenses/by/4.0/).

## 1. Introduction

The Mekong Delta is one of the most important river systems in Vietnam. The area of the Mekong Delta is about 39,000 km$^2$, which is 13% of the country's territory. The population living in the Mekong Delta is about 18 million people (19% of the country's population). It contributes to 75% of Vietnam's total agricultural-fishery-forestry production, over 50% of agricultural exports, and 90% of rice exports [*Dinh et al.*, 2019]. However, indiscriminately disposed waste and sewage discharge along the river's length has turned the Mekong into one of the world's ten most polluted rivers. The waste includes pollutants coming from land, such as untreated waste and waste water, hazardous substances, heavy metals, oil and oil products – a result of domestic, agricultural and industrial activities. The Ministry of Natural Resources and Environment reports the total annual discharge of

all rivers of the country to be 880 $km^3$ of water and about 270–330 million tons of alluvium, carrying pollutants to the ocean [*Viet Nam News*, 2016].

The oil pollution is becoming more and more serious. In theory, the 0.1 mg per liter concentration is large enough to kill plankton species and affect larvae of benthic organisms. In addition, one of the most toxic technogenic substances are heavy metals and metalloids, which, being trace elements, and depending on the toxicity class they can have a toxic effect on living organisms in micrograms and smaller amounts [*Kostyleva and Racheva*, 2016]. These substances are subject to monitoring observations in aquatic ecosystems, and especially in rivers, whose waters often bring substances from vast catchment basin of the river system.

The Mekong is a trans-boundary river that runs through China, Myanmar, Laos, Thailand, Cambodia, and finally Vietnam before discharging into sea. It moves 475 $km^3$ of water annually and supports over 70 million people who rely on it as their main source of water. The Mekong River enters the territory of Vietnam in the form of 2 branches (the Hau River and the Tien River) each 200–250 km long. Both rivers are further divided into a vast general delta, the arms of which flow into the East Sea. The Tien River (R.) is divided into 6 branches (My Tho R., Ba Lai R., Cua Dai R. (forks at the sea into Cua Dai R. and Cua Tieu R.), Ham Luong R. and Co Chien R.) [*Phung*, 2015]. The Ham Luong R. was chosen as the object of research as the largest and the most full-flowing branch of the Tien R. Ham Luong R. is about 70 km long, with a width of up to 2800 m and an average depth of 11.3 m [*Phung*, 2015].

The Ham Luong R., like all branches of the Mekong Delta, serves as a source of fish, shrimp, shellfish, as well as a source of drinking water and for water supply of irrigated agricultural lands for growing rice and fruits. The food products obtained are used both to satisfy the country's internal needs and to make up a significant part of the state's exports. At the same time, its riverbed serves as a transport system in the region and a recipient of wastewater from industrial, agricultural and domestic sources. Studies conducted in the rivers of Vietnam indicate the presence of elevated concentrations of certain heavy metals in river ecosystems [*Ngo*, 2018; *Pham*, 2011; *Savichev and Phung*, 2014; *Tereshchenko et al.*, 2023]. Therefore, the assessment of the ecological state of the waters in the Ham Luong R. is relevant in the modern period – the time of accelerating development of the country's economy. In this regard, the purpose of this work was to determine the water concentrations of pollutants of organic and inorganic nature (hydrocarbons, including oil hydrocarbons, and trace elements, including heavy metals and metalloids) throughout the entire riverbed of the Ham Luong R. in the Mekong Delta and to assess the water quality on the basis of accepted values of the regulatory limits of concentration.

## 2. Material and methods

Water samples were taken along the entire course of the Ham Luong R. from the sea to the Tien R. at stations 1–6 (Figure 1) in November–December 2022. Samples at each station were taken on the cross section of the channel at 3 points (near each bank and in the center of the river channel) in 2 replicates. Thus, for each station, the average value of the concentration of trace elements in surface water was determined from three sampling points. Bottom water was sampled only in the center of the riverbed. Sampling was carried out at high tide as a rule. At station 1, samples were taken at low tide and high tide. The results of the analysis of water samples for the determination of hydrocarbons, including oil hydrocarbons, are presented for st. 1–5. The location of the stations was chosen in order to study possible zones of salinization of the waters of the Ham Luong R. (seaward part) and freshwater areas, as well as taking into account the location of large industrial and urban facilities along its banks (Figure 1).

### 2.1. Hydrocarbon determination method

The determination of the total content of hydrocarbons in suspended matter and the concentration of oil hydrocarbons in filtered river water was performed. To obtain

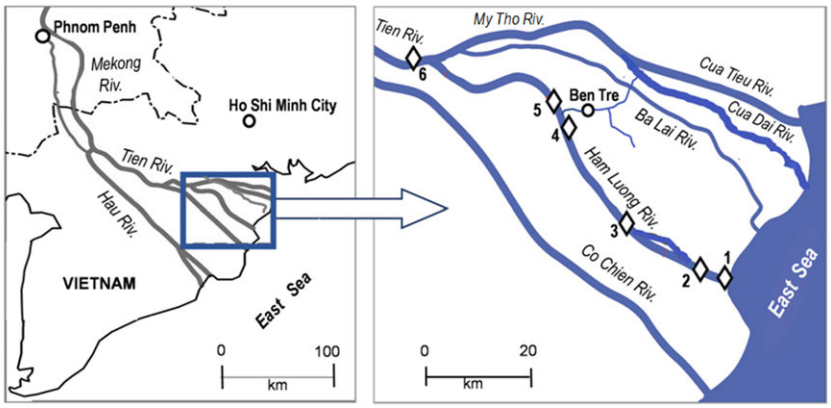


**Figure 1.** Study areas. Location of sampling sites on the Ham Luong River in the Mekong Delta, where the stations are marked with rhombs (the location of cross sections from three points on the riverbed).

a suspended matter, vacuum filtration was carried out using a vacuum pump, a Bunsen flask, a filter unit, and nitrocellulose membrane filters with a pore size of 0.45 μm. The volume of filtered river water varied depending on the concentration of suspended matter in water and was taken into account when recalculating the content of hydrocarbons in suspended matter. The filters were dried in natural conditions and stored in a desiccator and transported in sealed zip-lock bags.

Pretreatment of water samples was fulfilled under laboratory conditions by extraction with n-hexane according to the procedure [*Barabashin*, 2018].

Determination of hydrocarbons was made by chromatography on a chromatograph "Crystal 5000.2". Quantitative determination of their content was carried out by absolute calibration of the FID with a hydrocarbon's mixture (standard sample ASTMD2887 Reference Gas Oil (SUPELCO, USA). To process the results of determining the hydrocarbons concentrations, the Chromatek Analytic 3.0 software was used (the method of absolute calibration and percentage normalization). Correlation analysis ($p = 0.05$) was performed using the Microsoft Excel 2010 analysis package.

### 2.2. Heavy metals and metalloids determination method in water

In surface and near-bottom water, 15 trace elements were determined – heavy metals and metalloids (Be, V, Fe, Co, Ni, Cu, Zn, As, Se, Mo, Ag, Cd, Sb, Tl, Pb) in dissolved form. They included some of the most toxic elements recommended for monitoring in natural waters, as well as a list of elements determined by the capabilities of the analytical method used for the chemical quantitative determination of the trace element composition of waters [*Gidrometeoizdat*, 1993; *Mirzoeva et al.*, 2020]. To define the dissolved form of trace elements in water, the samples of river water were filtered through nitrocellulose membrane filters with a pore size of 0.45 μm. Filtered water was processed in the laboratory according to the guidance document [*Gidrometeoizdat*, 1993], with subsequent measurement of trace elements in the prepared acid extracts from samples on a mass spectrometer with inductively coupled plasma (ICP-MS) PlasmaQuant MS Elite (Analytik Jena AG) in accordance with [*Analytik Jena AG*, 2014; *Mirzoeva et al.*, 2020; *SS R 56219-2014*, 2015]. The mass spectrometer was calibrated using the standard solution "Multi-element calibration standard IV-28, HNO3/HF, 125 ml" (Inorganic Ventures). The calculation and presentation of the measurement results were performed in accordance with the regulatory documents [*Gidrometeoizdat*, 1993; *SS R 56219-2014*, 2015]. The average relative error in the determination of trace elements was no more than ±10% for all studied heavy metals and metalloids in samples of natural river water.

Measurement of hydrocarbons and trace elements was made on equipment of the Scientific and Educational Center for Collective Use "Spectrometry and Chromatography" of the IBSS.

The assessment of the chemoecological state of the river water was fulfilled by comparing the obtained levels of trace element concentrations with the standard regulatory limits – maximum permissible concentration (MPC) and target value for surface water (TV). National standard values – $MPC_V$ – from the National Technical Regulation for Surface Water Quality in Vietnam (NTR) [*NTR-2015*, 2015] were used as well. For comparative analysis, the standard values of concentrations accepted in other countries were also used: $MPC_{FP}$ – for waters of reservoirs for fishery purposes (Russian Federation) [*Kostyleva and Racheva*, 2016], as well as $TV_N$ (the limit of safe concentration, the non-exceeding of which ensures the absence of a negative impact on biota) and $MPC_N$ (the limit of permissible concentration, the excess of which leads to a significant negative impact of pollutants on biota) (Netherlands) [*Warmer and van Dokkum*, 2002]. According to the Regulations of Vietnam, standard values were used for surface water sources of category A1 – sources for household use and conservation of flora and fauna [*NTR-2015*, 2015].

The obtained concentrations of oil hydrocarbons in water were compared with the sanitary standard for fishery reservoirs (MPC = 0.05 mg/l) in Russia [*SanPIN 1.2.3685-21*, 2021] and Vietnam national standard for domestic supply water (0.1 mg/l). [*TCVN5502:2003*, 2003] as well as MPC for surface water of category A – 0.3–0.5 mg/l [*NTR-2015*, 2015].

Determination of station metadata and measurement of some physical and chemical characteristics of water (temperature, salinity S, pH, Eh, TDS, concentration of dissolved oxygen) were performed using a ProDSS–Professional Digital Sampling System (YSI, USA) multi-parameter measuring instrument (measurement errors did not exceed: pH ± 0.01; Eh ± 0.5 mV; TDS ± 1 mg/l; S ± 0.01 PES, DO ± 0.001 mg/l; T ± 0.15 °C) with built-in GPS navigator to determine the location of sampling stations – equipment of the Environmental Analysis Laboratory of Southern Branch of Joint Vietnam-Russia Tropical Science and Technology Research Center, Ho Chi Minh City.

## 3. Results and discussion

### 3.1. Physicochemical parameters of water in the Ham Luong River in rainy season

Measurement of the physicochemical parameters of the river water was carried out to characterize them as independent indicators of water quality, the deviation of which from the standard regulatory limits can lead to negative consequences for hydrobionts and affect the quality of water and other natural resources of rivers. In addition, these measurements were performed in order to study the degree of water salinization, its magnitude and distance of spreading along the riverbed of the Ham Luong R., as well as possible impact of salinization on the levels of technogenic substances concentrations.

Average values of measured physicochemical parameters of water in investigated areas of the Ham Luong R. present in Table 1.

Bold type in the Table 1 indicates the values of the studied parameters that did not comply with the NTR of Vietnam for surface water of category A1.

One of the normalized water quality parameters is the concentration of dissolved oxygen in water (DO). During the rainy season in November-December 2022 in the Mekong Delta, the concentrations of DO in surface water of Ham Luong R. were below the standard for water of category A1 (≥6 mg/l) at almost all stations. Only at the st. 1 – the closest station to the sea – concentrations of DO higher than 6 mg/l were observed during a high tide (Table 1). The hydrogen index (pH) in the water at all the stations studied did not go beyond the range of standard values, according to the NTR. Water salinization was observed during high tide at all points of st. 1. It changed from 6 PSU in surface water to 14 PSU in bottom water. At low tide, salinity increased much less than at high tide: from 0.4 PSU in surface water to 0.8 PSU in bottom water. With distance from the sea, increased water salinity was noted only at st. 2 in bottom water in a high tide, at other stations in Ham Luong R. the levels of salinity values corresponded to fresh water (Table 1). The DO

**Table 1**. Average values of physicochemical characteristics in November-December 2022 in surface and measured values in near-bottom (B) waters in the Ham Luong River in Mekong Delta where: LT is a low tide period; HT – a high tide period, DO – dissolved oxygen.

| Station no | DO, mg/l | S, PSU | TDS, mg/l | T, °C | Eh, mV | pH |
|---|---|---|---|---|---|---|
| 1-LT | 5.8 | 0.41 | 540 | 28.8 | 10.2 | 7.58 |
| 1-LT-B | —* | 0.80 | — | 29.0 | — | 6.90 |
| 1-HT | 6.38 | 6.25 | 9117 | 28.9 | 10.1 | 7.66 |
| 1-HT- B | — | 13.90 | — | — | — | 6.40 |
| 2-HT | 5.58 | 0.15 | 203 | 29.0 | 12.2 | 7.57 |
| 2-HT-B | — | 5.40 | — | 29.0 | — | 6.20 |
| 3-HT | 5.14 | 0.08 | 122 | 28.9 | 15.7 | 7.49 |
| 3-HT-B | — | 0.0 | — | 29.0 | — | 6.08 |
| 4-HT | 5.27 | 0.08 | 109 | 29.0 | 11.1 | 7.42 |
| 4-HT-B | — | 0.0 | — | 29.2 | — | 6.80 |
| 5-LT | 5.19 | 0.08 | 108 | 29.3 | 9.9 | 7.38 |
| 5-LT-B | — | 0.0 | — | 29.6 | — | 6.80 |
| 6-LT | 4.78 | 0.07 | 97 | 29.4 | 21.2 | 7.22 |
| 6-LT-B | — | 0.0 | — | 29.5 | — | 7.00 |

* no data.

concentrations were higher and salinity values – lower in the rainy season in 2022 in Ham Luong R. compared to those in the dry season in May 2021. In the dry season at station 4, the DO concentration was below 4 mg/l, and a salinity of 13 PSU was observed even at station 3 [*Russian-Vietnamese Tropical Center*, 2023].

### 3.2. Hydrocarbons in the Ham Luong River water and suspended matter

Oil hydrocarbon's content in the water of the investigated branch – the Ham Luong R. – ranged from 0.042 to 0.076 mg/l, averaging 0.061 ± 0.019 mg/l (Figure 2). These concentrations were quite high, in some cases they exceeded the sanitary standard for fishery reservoirs (MPC = 0.05 mg/l) [*SanPIN 1.2.3685-21*, 2021], in other cases they approached its value. Since the river studied is used both for fishing and for aquaculture, these values of concentrations characterize the state of its waters as unsatisfactory. On the other hand, the level of oil hydrocarbon concentration in water of the Ham Luong R. from this study was significantly lower compared to values reported in some regions including Buffalo R. of South Africa [*Abdullah et al.*, 1996; *Adeniji et al.*, 2017; *Li et al.*, 2010]. The observed levels were also lower than Vietnam Quality requirements for domestic supply water – 0.1 mg/l [*TCVN5502:2003*, 2003] as well as than MPC for surface water of category A – 0.3–0.5 mg/l [*NTR-2015*, 2015].

The obtained concentrations of hydrocarbons depended on the presence of the source of their input. Near the settlements and when approaching the seawater area, the values increased and corresponded to a similar pattern of concentration changing in other water bodies. For example, in Don R., where concentrations in the range of 0.03–0.04 mg/l were recorded in its waters far from settlements, near the large settlements content in water increased to 0.10 mg/l. In Don R. water in the area of the port of Ust-Donetsk, the highest concentrations were noted – up to 0.122 mg/l [*Stepanyan and Kharkovsky*, 2020].

The hydrocarbons content in suspended matter was in the range of 0.011–0.37 mg/l, averaging 0.019 ± 0.009 mg/l (Figure 2). The hydrocarbons total content in suspended

matter was in the range of 0.011–0.037 mg/l, averaging 0.019 ± 0.009 mg/l (Figure 2). It should be noted the increase in the content of hydrocarbons in the suspended phase in the water at area of st. 1 compared to upstream sections of the river. This fact may be associated with the transition of substances from a dissolved to a suspended state with an increase of water salinity in the river-sea mixing zone (Table 1), as it was observed earlier in the zone of geochemical barriers in other regions of the oceans [*Nemirovskaya*, 2004].

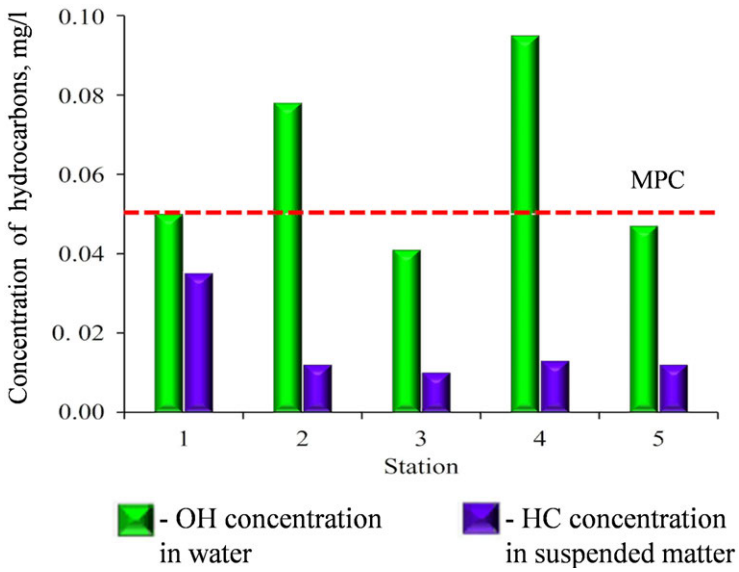


**Figure 2.** Concentrations of hydrocarbons at stations of the Ham Luong River in Delta Mekong, where OH – oil hydrocarbons in water; HC – hydrocarbons total content in suspended matter and MPC – maximum permissible concentration for fishery reservoirs [*SanPIN 1.2.3685-21*, 2021].

The share of hydrocarbons in suspended matter accounted from 20 to 75% (average 34±21%) from the total content of hydrocarbons in water. That is, the range of values was quite wide.

### 3.3. Heavy metals and metalloids

The obtained results on the determination of the dissolved form of trace elements concentration in the surface water of the Ham Luong R. are presented in Table 2, which shows the mean concentrations of trace elements at the stations.

Analysis of the elements concentrations presented in Table 2 showed that in general for most trace elements (Ni, Co, V, Cu, Se, Ag, Be, Sb) their concentrations were characterized by limited variability, differing from each other at the studied stations by 2–3 times within the same order of magnitude. For another group of the investigated trace elements (Fe, Pb, As, Zn, Cd, As, Tl), the variability was more pronounced and the concentration values at individual stations exceeded those at other stations by an order of magnitude. It was noted that for Fe, Cd, Tl, Pb, and Zn, the highest concentrations were found at station 6 in the riverbed of the Tien R. This indicated the inflow of an increased amount of these elements from the upstream sections of the catchment basin of the Mekong R. Comparison of the heavy metals and metalloids concentrations at stations 3 and 4, showed that significant trace element pollution of the surface waters of the Ham Luong R. did not flow from the city of Ben Tre.

This is obviously, because the agricultural sector of the economy is mainly developed in the province and industry in it occupies about 30% of the city's economy. In addition, the confectionery and clothing industries are predominantly developed there [*Map of Vietnam*, 2008].

As well, the bottom waters were examined for the content of trace elements. The results of determining the trace elements concentration in the bottom water layer of the Ham Luong R. are presented in Table 3.

**Table 2.** Levels of heavy metals and metalloids concentrations in the surface water of the Ham Luong R. in November-December 2022 mainly at high tide during the wet season, where DL – detection limit.

| Station no | Concentrations of trace elements in the surface water, μg/l | | | | |
|---|---|---|---|---|---|
| | V | Fe | Co | Ni | Cu |
| | DL = 0.01 | DL = 0.1 | DL = 0.001 | DL = 0.01 | DL = 0.01 |
| 1 | 0.37 ± 0.03 | 2.6 ± 0.5 | 0.013 ± 0.003 | 0.60 ± 0.06 | 0.91 ± 0.08 |
| 2 | 0.28 ± 0.02 | 7.7 ± 1.0 | 0.285 ± 0.028 | 0.58 ± 0.06 | 0.86 ± 0.07 |
| 3 | 0.23 ± 0.02 | 11.8 ± 1.5 | 0.053 ± 0.006 | 0.68 ± 0.07 | 0.77 ± 0.08 |
| 4 | 0.29 ± 0.02 | 14.7 ± 1.6 | 0.049 ± 0.005 | 0.43 ± 0.04 | 0.75 ± 0.07 |
| 5 | 0.26 ± 0.02 | 16.4 ± 1.8 | 0.021 ± 0.003 | 0.51 ± 0.05 | 0.79 ± 0.06 |
| 6 | 0.18 ± 0.02 | 30.0 ± 2.3 | 0.011 ± 0.003 | 1.31 ± 0.09 | 0.72 ± 0.05 |
| Station no | Zn | As | Se | Mo | Ag |
| | DL = 0.1 | DL = 0.001 | DL = 0.01 | DL = 0.01 | DL = 0.001 |
| 1 | 1.71 ± 0.29 | 0.135 ± 0.016 | 0.032 ± 0.028 | 0.100 ± 0.012 | 0.027 ± 0.020 |
| 2 | 2.86 ± 0.33 | 0.075 ± 0.011 | <0.01 | 0.026 ± 0.004 | <0.001 |
| 3 | 6.67 ± 0.57 | 0.053 ± 0.010 | 0.027 ± 0.017 | 0.068 ± 0.008 | 0.006 ± 0.004 |
| 4 | 3.08 ± 0.37 | 0.125 ± 0.014 | 0.031 ± 0.026 | 0.071 ± 0.008 | 0.021 ± 0.006 |
| 5 | 1.64 ± 0.20 | 0.129 ± 0.013 | <0.01 | 0.068 ± 0.008 | 0.012 ± 0.004 |
| 6 | 17.71 ± 0.96 | 0.057 ± 0.009 | 0.021 ± 0.011 | 0.053 ± 0.007 | 0.005 ± 0.003 |
| Station no | Cd | Sb | Tl | Pb | Be |
| | DL = 0.001 | DL = 0.0001 | DL = 0.0001 | DL = 0.01 | DL = 0.003 |
| 1 | 0.012 ± 0.003 | 0.004 ± 0.001 | 0.0036 ± 0.0012 | 0.03 ± 0.02 | <0.003 |
| 2 | 0.007 ± 0.004 | 0.004 ± 0.001 | 0.0028 ± 0.0006 | 0.07 ± 0.02 | <0.003 |
| 3 | 0.005 ± 0.002 | 0.006 ± 0.001 | 0.0031 ± 0.0005 | 0.04 ± 0.01 | <0.003 |
| 4 | 0.007 ± 0.001 | 0.004 ± 0.001 | 0.0036 ± 0.0008 | 0.04 ± 0.01 | <0.003 |
| 5 | 0.004 ± 0.003 | 0.003 ± 0.001 | 0.0038 ± 0.0009 | 0.04 ± 0.01 | <0.003 |
| 6 | 0.022 ± 0.004 | 0.005 ± 0.001 | 0.0126 ± 0.0017 | 0.53 ± 0.10 | <0.003 |

In general, the concentrations of trace elements in the bottom layer between stations varied within a narrower range than the concentrations in surface water, with the exception of Fe, whose concentration at st. 6 was an order of magnitude higher than that at st. 1.

At the same time, the concentrations in the bottom water layer exceeded the concentrations in the surface layer for such elements as Zn, Cd, Ni, Co, Mo, Tl, and vice versa for As and Pb, higher concentrations were determined in the surface water layer (Table 2, 3).

Consideration of the levels of trace elements concentrations at st. 1 during high and low tide indicates that the concentration of a number of elements (V, Co, Pb, Tl, Sb, Mo) was higher during the high tide, especially in the bottom layer, which indicates salty seawaters, moving along the bottom of the riverbed during high tide. Therefore, seawater can be considered as the source of introduction of these elements into the Ham Luong R. water (Figure 3).

**Table 3**. Levels of trace elements concentrations in the bottom water of the Ham Luong R. in November-December 2022 during the rainy season mainly at high tide, where DL – detection limit.

| Station no | Concentrations of trace elements in the bottom water, μg/l | | | | |
|---|---|---|---|---|---|
| | V | Fe | Co | Ni | Cu |
| | DL = 0.01 | DL = 0.1 | DL = 0.001 | DL = 0.01 | DL = 0.01 |
| 1 | 0.32 ± 0.01 | 2.5 ± 0.3 | 0.003 ± 0.002 | 0.98 ± 0.05 | 0.95 ± 0.04 |
| 2 | 0.21 ± 0.01 | 2.4 ± 0.3 | 0.013 ± 0.002 | 0.75 ± 0.04 | 0.78 ± 0.03 |
| 3 | 0.22 ± 0.01 | 5.1 ± 0.5 | 0.013 ± 0.002 | 0.89 ± 0.04 | 0.79 ± 0.04 |
| 4 | 0.30 ± 0.01 | 16.0 ± 1.1 | 0.016 ± 0.002 | 0.77 ± 0.04 | 1.03 ± 0.05 |
| 5 | 0.29 ± 0.01 | 14.4 ± 0.9 | < 0.001 | 0.98 ± 0.04 | 0.80 ± 0.04 |
| 6 | 0.13 ± 0.01 | 27.0 ± 1.2 | 0.007 ± 0.001 | 1.28 ± 0.05 | 1.17 ± 0.05 |
| Station no | Zn | As | Se | Mo | Ag |
| | DL = 0.1 | DL = 0.001 | DL = 0.01 | DL = 0.01 | DL = 0.001 |
| 1 | 3.01 ± 0.17 | 0.033 ± 0.006 | 0.039 ± 0.003 | 0.160 ± 0.008 | 0.018 ± 0.008 |
| 2 | 2.57 ± 0.19 | 0.011 ± 0.006 | <0.01 | 0.267 ± 0.014 | 0.012 ± 0.004 |
| 3 | 11.00 ± 0.52 | 0.043 ± 0.005 | <0.01 | 0.074 ± 0.003 | <0.001 |
| 4 | 3.40 ± 0.18 | 0.073 ± 0.007 | <0.01 | 0.059 ± 0.003 | <0.001 |
| 5 | 2.16 ± 0.10 | 0.239 ± 0.012 | <0.01 | 0.077 ± 0.004 | <0.001 |
| 6 | 16.40 ± 0.62 | 0.042 ± 0.005 | <0.01 | 0.040 ± 0.003 | 0.006 ± 0.003 |
| Station no | Cd | Sb | Tl | Pb | Be |
| | DL = 0.001 | DL = 0.0001 | DL = 0.0001 | DL = 0.01 | DL = 0.003 |
| 1 | 0.006 ± 0.002 | 0.0037 ± 0.0009 | 0.0053 ± 0.0006 | 0.018 ± 0.006 | <0.003 |
| 2 | 0.013 ± 0.002 | 0.0030 ± 0.0007 | 0.0041 ± 0.0005 | 0.022 ± 0.006 | <0.003 |
| 3 | <0.001 | 0.0062 ± 0.0008 | 0.0024 ± 0.0002 | 0.010 ± 0.005 | <0.003 |
| 4 | <0.001 | 0.0037 ± 0.0006 | 0.0038 ± 0.0005 | 0.045 ± 0.008 | <0.003 |
| 5 | <0.001 | 0.0035 ± 0.0006 | 0.0039 ± 0.0004 | 0.014 ± 0.006 | <0.003 |
| 6 | 0.016 ± 0.002 | 0.0041 ± 0.0007 | 0.0029 ± 0.0004 | 0.054 ± 0.007 | <0.003 |

For Zn and As at high tide, higher concentrations were observed only in the bottom layer.

For Be and Se, the concentrations at high and low tide were the same, and for Fe, Ni, Cd, Cu, Ag, the concentrations were lower at high tide (Figure 4).

The obtained levels of trace elements concentrations showed that according to the NTR, which regulates 6 elements: Pb, Zn, Cu, As, Cd, Ni, Fe in the surface water of the Ham Luong R., the established normative values ($MPC_V$) of concentrations for water sources of category A1 were not exceeded. It should be noted that the normative values of NTR are from 2 to 10 times higher than the standards adopted in other countries. Moreover, for the eight studied trace elements, the standard regulatory limit values in the NTR of Vietnam have not been established. In this regard, a comparison of the results obtained with the accepted regulatory limits of concentration in other countries was carried out. It was found that these standards ($TV_N$, $MPC_N$ and $MPC_{FP}$) were exceeded for individual trace elements. The concentrations of nine trace elements among the studied ones (Ni, Fe, V, As, Se, Be, Cd, Sb, Tl) did not exceed any of the considered normative indicators. But for six elements, the found concentrations were above the normative values (Table 4).

The highest excess of the $MPC_N$ was determined for Zn. Its concentration at station 6 was more than 3 time higher the $MPC_N$ and more than 10 times the $TV_N$. In addition to

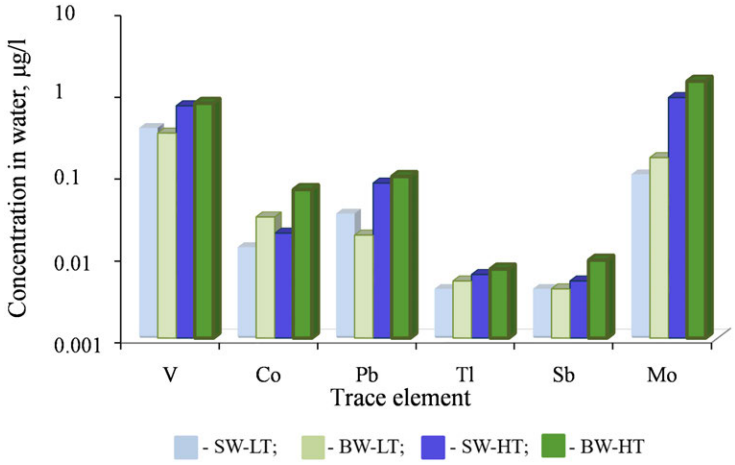


**Figure 3.** Concentrations of trace elements in the surface and bottom water at station 1 of the Ham Luong River during low tide and high tide, where SW – surface water, BW – bottom water, LT – low tide, HT – high tide.

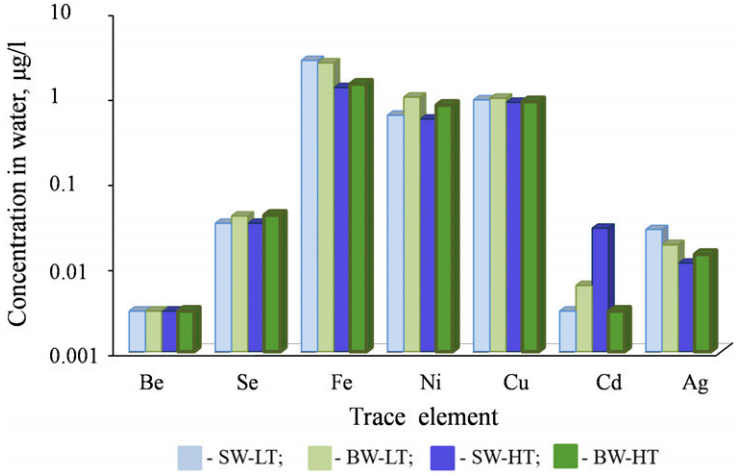


**Figure 4.** Concentrations of trace elements in the surface and bottom water at station 1 of the Ham Luong River during low tide and high tide, where SW – surface water, BW – bottom water, LT – low tide, HT – high tide.

Zn, at station 6, the $TV_N$ exceeded the concentrations of Cu and Pb. Exceeding the $TV_N$ for Zn and Cu was noted at all six stations studied. The excess of $TV_N$ for Ag was recorded at four stations (st. 1, 2, 4, 5), and for Co – only at one station – 3 (Table 4). Exceeding the permissible concentration for fishery reservoirs – $MPC_{FP}$ – was observed only in relation to Mo.

## 4. Conclusion

The use of modern techniques of mass spectrometry and chromatography has made it possible to obtain new data on the concentrations of a wider range of heavy metals and metalloids in water than previously studied, as well as oil hydrocarbons in water and total hydrocarbon content in suspended matter in the Ham Luong River. Based on the results obtained, a chemoecological reconnaissance analysis of the state of the quality of waters was carried out in one of the most full-flowing branches in the lower part of the Mekong Delta – the Ham Luong River.

The results obtained indicate that the levels of concentrations of some pollutants were more related to the inflow from the catchment basin of the river, while others enter the water of the river with seawater and suspended matter during high tides. The level of water salinity, as well as the deficiency of dissolved oxygen in the Ham Luong water, is much

**Table 4**. Range of trace elements concentrations in water (Cw) in the Ham Luong R. compared to the standard regulatory limits of concentration in surface waters (the bold type indicates the data exceeding one of the regulatory limits and the standard values being exceeded); n.d. – no data.

| Element Trace | Range of Cw Value for 6 station, μg/l | $MPC_{FP}$, μg/l (station number with increased concentration Cw) | $MPC_N$, μg/l (station number with increased concentration Cw) | $TV_N$, μg/l (station number with increased concentration Cw) | $MPC_V$ for sources of category A1, μg/l |
|---|---|---|---|---|---|
| Pb | 0.10–1.333 | 10 | 11 | 0.3 (st. 6) | 20 |
| Cu | 0.68–1.17 | 5 | 1.5 | 0.5 (st. 1–6) | 100 |
| Zn | 1.01–8.07–31.61 | 50 | 9.4 (st. 6) | 2.9 (st. 1-5) | 500 |
| Ni | 0.39–1.28 | 10 | 5.1 | 3.3 | 100 |
| Co | 0.002–0.482 | 10 | 2.8 | 0.2 (st. 3) | n.d. |
| V | 0.13–0.87 | 1 | 4.3 | 0.9 | n.d. |
| As | 0.007–0.255 | 10 | 25 | 1.0 | 10 |
| Ag | 0.012–0.043 | n.d. | 1.2 | 0.01 (st. 1,2,4,5) | n.d. |
| Mo | 0.014–1.383 | 1 | 290 | 4.3 | n.d. |
| Cd | < 0.002–0.061 | 10 | 0.4 | 0.08 | 5 |
| Se | < 0.002–0.042 | 2 | 5.3 | 0.09 | n.d. |
| Sb | 0.0024–0.0088 | n.d. | 6.5 | 0.4 | n.d. |
| Fe | 0.46–32.35 | 100 | n.d. | n.d. | 500 |
| Be | <0.003 | 0.3 | 0.2 | 0.02 | n.d. |
| Tl | 0.0024–0.0070 | n.d. | 1.6 | 0.06 | n.d. |

higher in the dry season of the year compared to the rainy season. Therefore, monitoring studies of river water quality should cover different seasons of the year.

It is shown that the excess of the installed regulatory limits of concentration was observed only in relation to a part of trace elements and oil hydrocarbons in the water, and the concentration of dissolved oxygen was below the standard value at all stations of the river, with the exception of the seaward st. 1 in rainy season.

Critical pollutants include Zn, Mo and oil hydrocarbons, the concentrations of which exceed the established MPCs, can have a significant negative impact on living organisms and therefore they are subject to priority attention. Potentially critical substances include trace elements (*Pb*, *Co*, *Cu*, *Ag)*, whose concentrations exceeded the safe concentration limit ($TV_N$), the non-exceeding of which ensures the absence of a negative impact on biota, and therefore they are subject to monitoring as well.

With regard to critical pollutants, it is necessary to carry out primary regular monitoring and take measures to identify the main sources of pollutant entry and reduce their entry into the riverbed of Ham Luong R. to reduce the levels of modern concentrations of these substances. Potentially critical elements require periodic monitoring to track further changes in their concentration levels in river waters. It is important to take timely measures to improve the chemoecological state of the waters to ensure the proper quality of the river water itself and the biological resources of the river, which are widely used as food and food raw materials both to meet the country's domestic needs and to export products.

## 5. Acknowledgments

The study was carried out on the theme of Southern Branch of the Joint Vietnam-Russia Tropical Scientific and Technology Research Center "Ecolan E-3.4: Ecosystem of the Mekong River in the context of global climate change and anthropogenic impact" and on the theme of the state assignment of the A.O. Kovalevsky Institute of Biology of the

Southern Seas of the Russian Academy of Sciences "Molismological and biogeochemical foundations of homeostasis of marine ecosystems" (state registration no.121031500515-8).

**References**

Abdullah, A. R., W. C. Woon, and R. A. Bakar (1996), Distribution of Oil and Grease and Petroleum Hydrocarbons in the Straits of Johor, Peninsular Malaysia, *Bulletin of Environmental Contamination and Toxicology*, *57*(1), 155–162, https://doi.org/10.1007/s001289900169.

Adeniji, A. O., O. O. Okoh, and A. I. Okoh (2017), Petroleum Hydrocarbon Fingerprints of Water and Sediment Samples of Buffalo River Estuary in the Eastern Cape Province, South Africa, *Journal of Analytical Methods in Chemistry*, *2017*, 1–13, https://doi.org/10.1155/2017/2629365.

Analytik Jena AG (2014), *PlasmaQuant MS Elite Mass-spectrometers With Inductively Coupled Plasma (ICP-MS)*.

Barabashin, T. O. (Ed.) (2018), *Practical guide to chemical analysis of elements of aquatic ecosystems. Priority toxicants in water, sediments, hydrobionts*, 436 pp., Mini Type, Rostov n/Don (in Russian).

Dinh, D. A., B. Elmahrad, P. Leinenkugel, and A. Newton (2019), Time series of flood mapping in the Mekong Delta using high resolution satellite images, *IOP Conference Series: Earth and Environmental Science*, *266*, 012,011, https://doi.org/10.1088/1755-1315/266/1/012011.

Gidrometeoizdat (1993), RD 52.10.243-92. Guide to the chemical analysis of marine waters (in Russian).

Kostyleva, N. V., and N. L. Racheva (2016), *Characteristics of pollutants from section "II. For water bodies" of the "List of pollutants to which government regulation measures apply in the field of environmental protection", approved by order of the government of the Russian Federation dated 07/08/2015 No. 1316-R*, 296 pp., FGBU UralNII "Ecology" (in Russian).

Li, Y., Y. Zhao, S. Peng, Q. Zhou, and L. Q. Ma (2010), Temporal and spatial trends of total petroleum hydrocarbons in the seawater of Bohai Bay, China from 1996 to 2005, *Marine Pollution Bulletin*, *60*(2), 238–243, https://doi.org/10.1016/j.marpolbul.2009.09.020.

Map of Vietnam (2008), City and province Ben Tre in Vietnam, http://www.map-vietnam.ru (in Russian), (accessed 17.04.2023).

Mirzoeva, N. Y., N. N. Tereshchenko, A. A. Paraskiv, V. Y. Proskurnin, and E. G. Morozov (2020), Heavy metals in surface water of the Atlantic sector of the Antarctic during the 79th cruise of the research vessel "Akademik Mstislav Keldysh", *Marine Biological Journal*, *5*(4), 56–68, https://doi.org/10.21072/mbj.2020.05.4.05 (in Russian).

Nemirovskaya, I. A. (Ed.) (2004), *Hydrocarbons in the ocean (snow-ice-water-suspended sediments)*, 328 pp., Nauchny Mir, Moscow (in Russian).

Ngo, T. K. (2018), Content and regularities of distribution of heavy metals and arsenic in river ecosystems of industrialized regions of Vietnam (on the example of the Sherepok River, Dak Lak Province), Ph.D. thesis, RUDN University, Moscow (in Russian).

NTR-2015 (2015), National Technical Regulation on Surface Water Quality, (in Vietnamese).

Pham, V. N. (2011), (As) Pollution in the Mekong Delta, *Agricultural Journal and development of rural areas*, (2), 15–21.

Phung, T. D. (2015), Ecological and geochemical state of the Mekong river delta (Republic of Vietnam) according to the results of the study of bottom sediments, Ph.D. thesis, National Research Tomsk Polytechnic University (in Russian).

Russian-Vietnamese Tropical Center (2023), Bioindication studies - assessment of the radiochemical state of the ecosystem of the lower reaches of the Mekong River. Ecolan e-3.4: The ecosystem of the Mekong River under the conditions of global climate change and anthropogenic impact (in Russian).

SanPIN 1.2.3685-21 (2021), Maximum permissible concentrations (MPC) of chemical substances in drinking water of centralized, including hot, and non-centralized water supply systems, water of underground and surface water bodies for domestic, drinking and cultural water use, water of swimming pools, water parks. Hygienic standards and requirements for ensuring the safety and (or) harmlessness of environmental factors for humans. III. Water quality and safety standards, approved by the Decree of the Chief State Sanitary Doctor of the Russian Federation (in Russian).

Savichev, O. G., and T. D. Phung (2014), Ecological and geochemical state of surface waters and bottom sediments in the Mekong Delta (Vietnam), *Bulletin of Tomsk State University*, (388), 246–252 (in Russian).

SS R 56219-2014 (2015), Determination of the content of 62 elements by inductively coupled plasma mass spectrometry (in Russian).

Stepanyan, O. V., and V. M. Kharkovsky (2020), Oil pollution in the Sea of Azov and the Black Sea (2012-2017), *Studies of the Southern Scientific Centre of the Russian Academy of Sciences*, *8*, 213–224, https://doi.org/10.23885/1993-6621-2020-8-213-224 (in Russian).

TCVN5502:2003 (2003), Domestic supply water Quality Requirements, (in Vietnamese).

Tereshchenko, N. N., O. D. Chuzhikova-Proskurnina, V. Y. Proskurnin, and N. T. Hiep (2023), Heavy Metals and Metalloids in Water and Bottom Sediments in the Rivers in the Can Gio Biospheric Reserve, Vietnam, *Water Resources*, *50*(2), 330–343, https://doi.org/10.1134/S009780782302015X.

Viet Nam News (2016), Pollution threat for VN marine life, https://vietnamnews.vn/environment/301480/Pollution-threat-for-vn-marine-life.html, (accessed 20.03.2023).

Warmer, H., and R. van Dokkum (2002), *Water pollution control in the Netherlands. Policy and practice the Netherlands*, 76 pp., RIZA, Lelystad.

Russian Journal of Earth Sciences

Special Issue: "Fundamental and Applied Aspects of Geology, Geophysics and Geoecology"

# Variations of Organic and Inorganic Atmospheric Boundary Layer Gaseous Species by Observations in Moscow and Zvenigorod

**V. A. Belousov[1], I. B. Belikov[1], K. B. Moiseenko[1], A. I. Skorokhod[1,2]**

[1] A. M. Obukhov Institute of Atmospheric Physics, Russian Academy of Sciences, Moscow, Russia
[2] University of Vienna, Vienna, Austria
* **Correspondence to:** V. A. Belousov, belousov@ifaran.ru

**Abstract:** Anthropogenic pollution of the atmosphere with organic and inorganic gaseous species has been studied using constant high-quality monitoring of the atmosphere composition both in megacity of Moscow and in its countryside. The article considers continuous measurements of the main climatically and chemically active atmospheric gaseous species concentrations, including volatile organic compounds. The main attention is paid to the comparative analysis, mainly between the megacity and its suburban area, by average species concentrations and some quality features of their seasonal and diurnal variations. The obtained results confirmed the previously studied features of the daily variations of inorganic gaseous species in Moscow and showed such features for organic compounds in the countryside.

**Keywords:** minor gaseous species of the atmospheric boundary layer, volatile organic compounds, seasonal and daily variations of concentrations.

**Citation:** Belousov V. A., Belikov I. B., Moiseenko K. B., Skorokhod A. I. (2023), Variations of Organic and Inorganic Atmospheric Boundary Layer Gaseous Species by Observations in Moscow and Zvenigorod, *Russian Journal of Earth Sciences*, Vol. 23, ES0206, https://doi.org/10.2205/2023ES02SI06

## 1. Introduction

Currently, in the course of human production activities, a significant amount of various chemical compounds is emitted into the atmosphere. New compounds appear in the atmosphere that were previously either absent on Earth at all, or were present in insignificant quantities. This leads to changes in the composition of the Earth's atmosphere and its radiative and dynamic properties. As a result of these processes, the climate of the Earth is changing [*GAW WMO*, 2012].

Numerous adverse consequences of the impact of atmospheric pollution on the human environment require a thorough study of the processes leading to global shifts in the concentrations balance of atmospheric species. One of the main research methods for this is the constant monitoring of the main air pollutants concentrations.

At the national level in the Russian Federation, such monitoring is carried out by Roshydromet. In addition, monitoring of the atmospheric air composition is carried out in Moscow by BEPI "Mosecomonitoring", and in St. Petersburg – by SBU "Mineral". Also, the monitoring of atmospheric air composition parameters is carried out by observation stations, created on the initiative of some academic and branch scientific institutions. Among them, the Institute of Experimental Meteorology RPA "Typhoon" (Obninsk), the Institute of Atmospheric Optics of the Siberian Branch of the Russian Academy of Sciences (Tomsk), and some others should be mentioned. Similar stations for observing the composition of the atmosphere also operate at the A. M. Obukhov Institute of Atmospheric Physics, Russian Academy of Sciences (hereinafter – IAP RAS).

Research Article

Received: 20 October 2023
Accepted: 27 November 2023
Published: 15 December 2023

**Copyright:** © 2023. The Authors. This article is an open access article distributed under the terms and conditions of the Creative Commons Attribution (CC BY) license (https://creativecommons.org/licenses/by/4.0/).

## 2. Equipment and observation technique

Observations in Moscow were carried out on the territory of the IAP RAS at Pyzhevsky per., 3, (Central administrative okrug, Yakimanka district), in the courtyard of the building. In the vicinity of the observation site there are streets with fairly heavy traffic, residential buildings and offices of institutions. In the countryside, the observations were carried out on the territory of the Zvenigorod Scientific Station (hereinafter – ZSS) of the IAP RAS (Moscow region, Odintsovsky city okrug, village Novoshikhovo). This observation site is placed more than 1 km away from highways and rural residential areas. There are no industrial enterprises and other sources of air pollution in the vicinity.

Measurements of the concentrations of minor gaseous species in the atmospheric surface layer were carried out using automated integrated hardware and software systems developed and manufactured at the IAP RAS (hereinafter – complexes) [*Berezina et al.*, 2020, 2022]. The complexes are built on the basis of a set of measuring instruments manufactured by leading foreign and domestic manufacturing companies.

Table 1 shows the main parameters of the instruments used for observations in Moscow, and Table 2 shows the instruments used for observations at the ZSS. As can be seen from the tables, the instruments used make it possible to determine impurity concentrations in a very wide range, from values significantly exceeding the maximum permissible concentrations to values typical of an unpolluted atmosphere.

**Table 1**. Equipment used for observations in Moscow.

| No. | Instrument type | Manufacturer | Measured parameter | Measurement range | Accuracy | Response time |
|---|---|---|---|---|---|---|
| 1 | 1008AH | Dasibi Inc. (USA) | $O_3$ concentration | 1–1000 ppb | ±1 ppb | 60 s |
| 2 | TE48S | Thermo Inc. (UAS) | CO concentration | 0.05–10 ppm | ±1% | 60 s |
| 3 | AC32e | ENVEA Inc. (France) | NO, $NO_2$ and $NH_3$ concentrations | 0.2–1000 ppb | ±1% | 40 s |
| 4 | AF22e | ENVEA Inc. (France) | $SO_2$ concentration | 0.4–1000 ppb | ±1% | 60 s |
| 5 | G2132-i | Picarro Inc. (USA) | CH4 concentration<br>$CO_2$ concentration<br>$H_2O$ concentration<br>$\sigma^{13}C$ | 1.8–12 ppm<br>200–2000 ppm<br>0–2.4%<br>— | ±5 ppb<br>±1 ppm<br>±0.01%<br>±0.8‰ | 30 s |
| 6 | HC51M | ENVEA Inc. (France) | CH4 and NMHC concentrations | 0.05–10 ppm | ±1% | 60 s |
| 7 | MTP-5 | LLC RPO ATTEX (Russia) | Vertical temperature profile in 0–600 meters layer | −30–+30 °C | ±1.0 °C | 5 min |
| 8 | ACAT-3M | RPA "Typhoon" (Russia) | Atmospherics pressure<br>Air temperature<br>Air relative humidity<br>Wind direction<br>Wind speed | 800–1080 hPa<br>−40–+50 °C<br>10–100%<br>0–360 deg.<br>0–40 m/s | ±0.5 hPa<br>±0.5 °C<br>±5%<br>±5 deg.<br>±0.2 m/s | 0.08 s |
| 9 | HMP-233 | Vaisala Oyj (Finland) | Air temperature | −40–+50 °C | ±0.1 °C | 15 s |

The complex for observations at the ZSS included a unique (according to some information, the only one at Russia territory) device for measuring the concentrations of a number of volatile organic compounds (VOCs) in the surface air, the Compact PTR-MS proton mass spectrometer manufactured by Ionicon Inc. (Austria). The device is based on the so-called method of proton mass spectrometry. This method was first developed

in 1995 at the Institute of Ion Physics of the University of Innsbruck (Austria) [*de Gouw and Warneke*, 2006]. In recent years, instruments of this type have become widely used for observing VOCs concentrations in the atmosphere [*Belousov et al.*, 2018; *Berezina et al.*, 2020, 2022; *Jordan et al.*, 2009; *Taipale et al.*, 2008].

A feature of the complexes is location of all their components not in laboratory rooms, but in the so-called all-weather racks installed outdoors at the observation sites. Such a technical solution ensures fire safety of continuous and round-the-clock operation of the devices of the complexes, and also eliminates interference with the work of personnel from significant noise generated by operating devices. To accommodate the equipment of the complexes, rack of the ShKK-42U and ShKK-24U models manufactured by the Telecom Group company (Russia, Belgorod) were used.

Figure 1 shows an internal view of racks with open doors in Moscow and at the ZSS, as well as a general view of the placement of racks at the observation site at the ZSS.

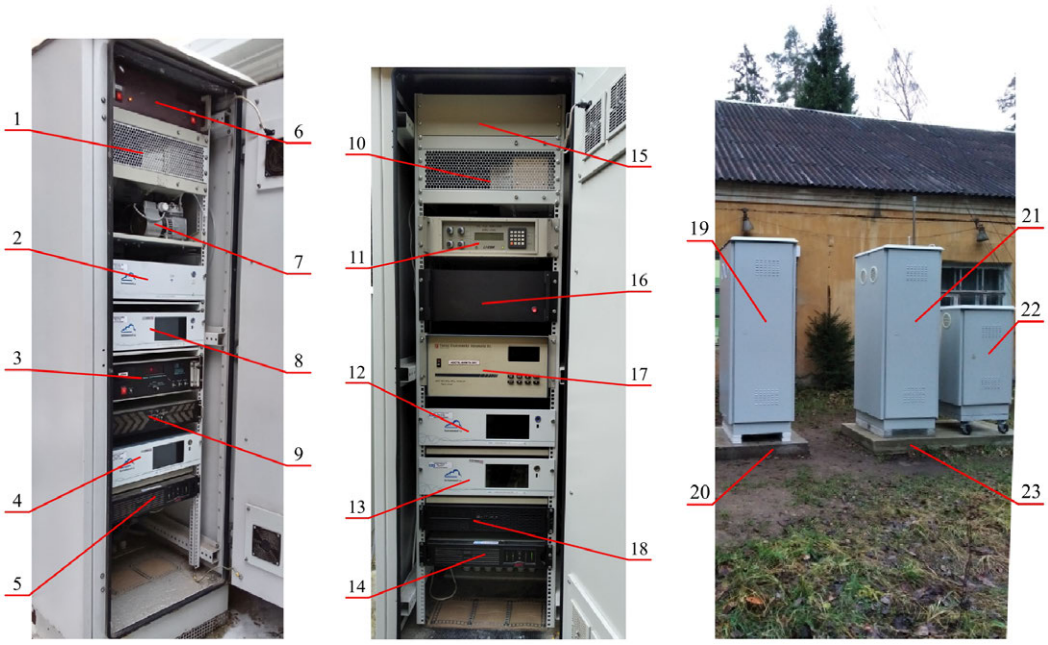


**(a)** **(b)** **(c)**

**Figure 1.** Internal views of all-weather racks in Moscow (a) and at the ZSS (b) and a general view of the location of all-weather racks at the ZSS territory (c).
1, 10 – ventilation grille; 2 – converter for measurement of ammonia ENVEA CNH3; 3 - ozone gas analyzer Dasibi 1008-AH; 4 – $SO_2$ gas analyzer ENVEA AF22e; 5, 14 – uninterruptible power supply; 6 - power supply unit of the meteorological complex; 7 - compressor unit for ENVEA AC32e instrument; 8 – NOx gas analyzer ENVEA AC32e; 9, 18 – registering computer; 11 – $CO_2$ gas analyzer Li-Cor LI6262; 12 – ozone gas analyzer ENVEA O342e; 13 – CO gas analyzer ENVEA CO12e; 15 – plug of the power supply socket; 16 – compressor unit for Thermo TE-42CTL instrument; 17 – NOx gas analyzer Thermo TE-42CTL; 19, 21 – all-weather racks ShKK-42U; 20, 23 – ferroconcrete pedestal; 22 – all-weather rack ShKK-24U.

The PTR-MS instrument was periodically calibrated using permeation tubes. The calibration procedure was in detail described in [*Berezina et al.*, 2022]. Functioning checking and calibration of other instruments is carried out out at least quarterly, using calibration gas mixtures manufactured by the company "Linde Gas Rus" (Russia, Balashikha), with accuracy of about 4%. Zero shift checking and correction of most instruments was carried out automatically, using built-in scrubbers, at least daily or even more often.

A specialized part of the software of the complexes is used for primary processing of observational data in order to remove data classified as unreliable. First of all, automated software processing is performed, and then all data is viewed by a specialist. As a result,

data series of concentrations of all measured gas and aerosol species and meteorological parameters are formed, with averaging over intervals of 1 minute, 20 minutes, 3 hours (corresponding to the standard period of meteorological observations) and 1 day.

**Table 2.** Equipment used for observations at ZSS.

| No. | Instrumen type | Manufacturer | Measured parameter | Measurement range | Accuracy | Response time |
|---|---|---|---|---|---|---|
| 1 | O342e | ENVEA Inc. (France) | $O_3$ concentration | 0.2–10,000 ppb | ±1 ppb | 20 s |
| 2 | CO12e | ENVEA Inc. (France) | CO concentration | 1–300 ppm | ±1% | 35 s |
| 3 | TE42C-TL | Thermo Inc. (USA) | NO and $NO_2$ concentrations | 0.05–200 ppb | ±1% | 60 s |
| 4 | LI6262 | LI-COR Inc. (USA) | $CO_2$ concentration | 1–3000 ppm | ±1 ppm | 1 s |
| 5 | HC51M | ENVEA Inc. (France) | $CH_4$ and NMHC concentrations | 0.05–10 ppm | ±1% | 60 s |
| 6 | Compact PTR-MS | Ionicon Inc. (Austria) | Acetylene, methanol, acetonitrile, acetaldehyde, ethanol, 1,3-butadiene, butenes, acetone, acetic acid, isoprene, methyl vinyl ketone, peroxyacetyl nitrate, benzene, monoterpenes, toluene, phenol, styrene xylenes, propylbenzene and trichloroacetic acid concentrations. | 0.5–1000 ppb | ±0.5 ppb | 0.5 s |
| 7 | Vantage Pro 2 | Davis Inc. (USA) | Atmospherics pressure | 880–1080 hPa | ±0.1 hPa | 2.5 s |
| | | | Air temperature | −40–+65 °C | ±0.5 °C | 10 s |
| | | | Air relative humidity | 1–100% | ±3 % | 2.5 s |
| | | | Wind direction | 0–360 deg. | ±7 deg. | 2.5 s |
| | | | Wind speed | 1–67 m/s m/s | ±1 m/s | 2.5 s |
| | | | Precipitation amount | 0–9999 mm | ±0.25 mm | 10 s |
| 8 | WXT536 | Vaisala Oyj (Finland) | Atmospherics pressure | 6001100 hPa | ±0.5 hPa | 15 s |
| | | | Air temperature | −52–+60 °C | ±0.3 °C | |
| | | | Air relative humidity | 0–100% | ±3% | |
| | | | Wind direction | 0–360 deg. | ±3 deg. | |
| | | | Wind speed | 1–60 m/s | ±3 % | |
| | | | Precipitation amount | 0–200 mm/h | ±0.01 mm | |

## 3. Analysis of results

One of the significant parameters characterizing the patterns of variations of gaseous boundary concentrations in the atmospheric surface layer is their monthly averaged concentrations. Figure 2 shows diagrams of monthly averaged concentrations obtained from observational data in Moscow and at the ZSS during 2022 and part of 2023.

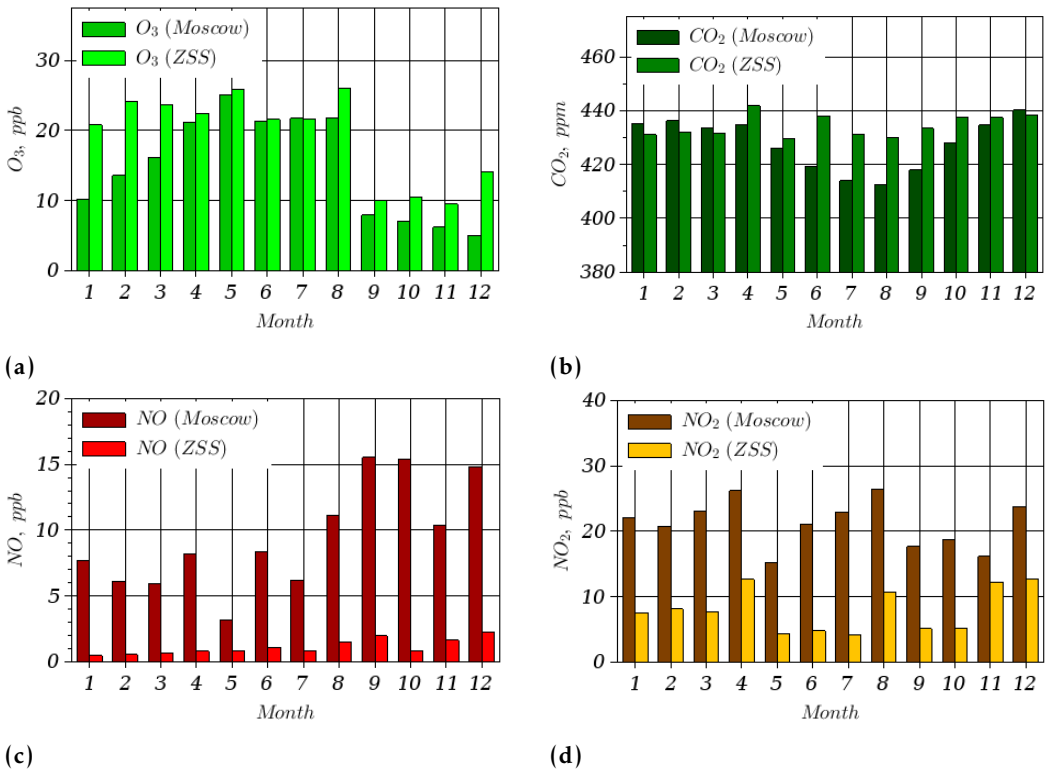


**Figure 2.** Monthly averaged concentrations of gaseous species in Moscow and at the ZSS.

The performed analysis confirms the previously studied [*Elansky et al.*, 2007, 2015] features of the seasonal course of the ozone concentration with a pronounced maximum in the spring. In winter, solar illumination is low, and ozone depletion on the underlying surface in the presence of snow cover is also small. With the onset of spring, the illumination increases, and ozone generation increases, but the ozone sink does not increase, since the snow cover has already disappeared, and green vegetation has not yet appeared. This leads to an increase in average ozone concentrations in the spring period. In summer, when there is green vegetation, the ozone sink increases and the average ozone concentration decreases.

A similar character of seasonal variations in ozone concentration is also observed for the countryside. The decrease in the ozone concentration in the winter period is less pronounced, which may be due to the overall lower atmospheric pollution in the suburban area with species that react with ozone, which will be discussed below.

The seasonal course of the concentration of nitrogen dioxide and monoxide, in general, does not show pronounced variations during the year. As is known [*Elansky et al.*, 2015], the main source of air pollution in cities is motor transport, the intensity of which in winter is now decreasing slightly [*Elansky et al.*, 2018]. Attention is drawn to significantly (more than an order of magnitude) lower values of nitrogen oxide concentrations in the countryside than in the metropolis of Moscow, which is explained by significantly lower emissions of these species.

The seasonal course of carbon dioxide is characterized by a slight decrease in average monthly concentrations in summer, which is usually associated with plant respiration processes, as well as with a decrease in the intensity of urban heating systems [*Elansky et al.*, 2015]. In the countryside, the anthropogenic contribution to the growth of $CO_2$ concentration is significantly less than in the metropolis, which, apparently, leads to smaller seasonal variations in $CO_2$ concentration.

The seasonal variations in VOCs concentrations in the countryside are of significant interest. According to available information, at the moment there are no publications of the results of observations by the PTR-MS instrument in Russia outside megacities in the

scientific periodical press. Figure 3 shows graphs of monthly averaged concentrations of some VOCs. Seasonal variations of the same VOCs in the metropolis were previously studied using the same instrument and published in [*Belikov et al.*, 2019]. In particular, it was found that the concentrations of acetone and acetic acid increase in summer, which can be explained by an increase in the volatility of these substances with an increase in air temperature. As can be seen from the above diagrams, in the suburban area, these substances show a similar pattern of seasonal variations.

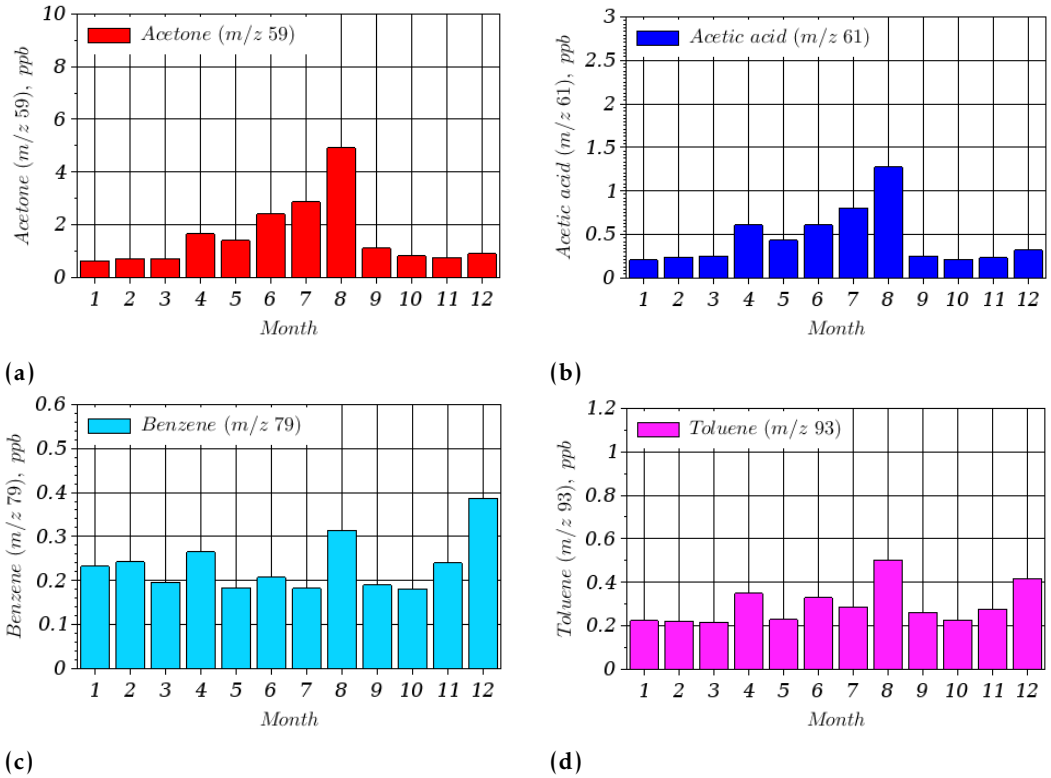


**Figure 3.** Monthly averaged concentrations of VOCs at the ZSS.

The significance of the detected seasonal variations can only be determined after accumulation of sufficient (several years or even more) observation statistics. In the above diagrams, a significant peak of impurity concentrations in August 2022 attracts attention. Figure 4 shows a diagram of the monthly averaged air temperature in 2022 and for 2019–2021. As can be seen from the diagram, in August 2022 there was a clear excess of the average monthly temperature over the average over the past 3 years by more than 5 °C. Apparently, this anomaly was the reason for the significant increase in impurity concentrations.

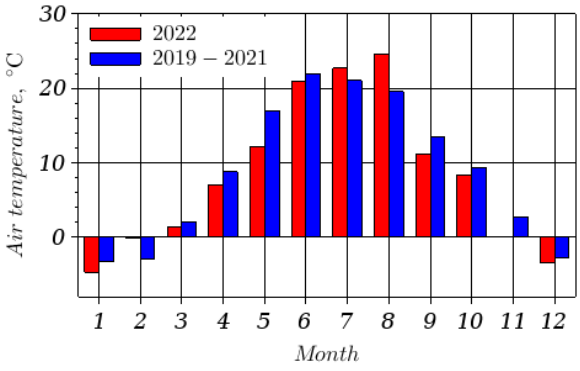


**Figure 4.** Monthly averaged air temperatures in 2022 year and for 2019–2021 years.

Another significant parameter that characterizes the patterns of variations in the concentrations of gaseous boundary in the atmospheric surface layer is their diurnal variations in different seasons of the year.

Figures 5 and 6 show diagrams of diurnal variations (relative to Moscow local time UTC +3) obtained from observations in Moscow and at the ZSS in winter (December to February) and summer (June to August) periods of the year. In order to exclude the effect of daily variations in the concentration of these species, we analyzed the ratio of a single concentration Ci (for 20 min) to the daily averaged concentration Cc for a given day.

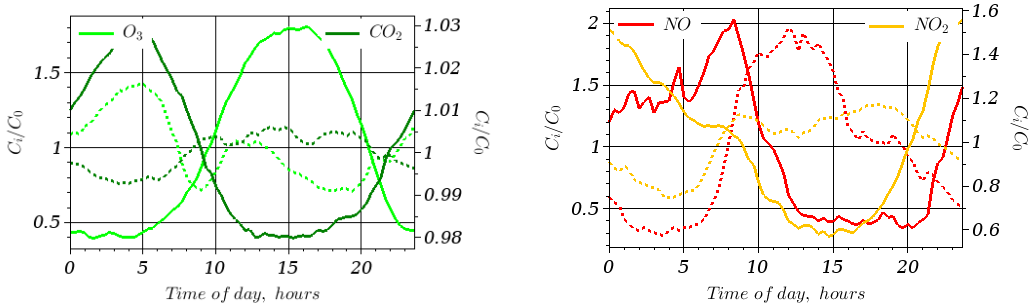


**(a)** **(b)**

**Figure 5.** Diurnal variations of species in Moscow in summer (solid lines) and winter (dotted line) periods.

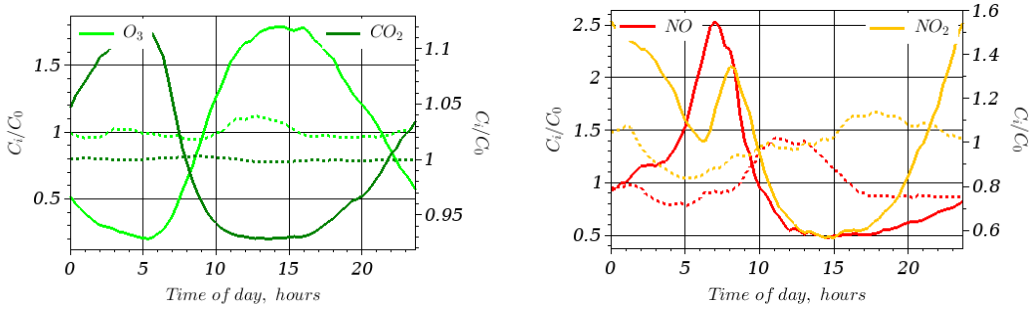


**(a)** **(b)**

**Figure 6.** Diurnal variations of species at ZSS in summer (solid lines) and winter (dotted lines) periods.

For diurnal variations, confidence intervals were also calculated for the probability of 0.95, which turned out to be equal to 0.05–0.10 of the ratio of Ci to Cc. Confidence intervals are not shown in the graphs given to preserve the clarity of the display.

The analysis performed also confirms the features of diurnal variations in surface concentrations of nitrogen monoxide and nitrogen dioxide previously studied [*Elansky et al.*, 2007, 2015]. In summer, these variations are characterized by the presence of two pronounced maxima in the morning and evening, and periods separating them with lower values in the middle of the day and in the early morning. During the cold period, in the daytime, the temperature inversion, as a rule, persists, and does not collapse, as in the warm period, which leads to the formation of an extended period of high impurity values throughout the day. Diurnal variations in ozone concentration in winter are characterized by daytime and nighttime maxima and morning and evening minima, which are explained by an increase in car traffic in the metropolis, leading to an increase in nitrogen oxide emissions and a decrease in ozone concentration. During the warm period, the diurnal variation of ozone is characterized by a pronounced maximum in the daytime, when the photochemical generation of this gas in the atmosphere is most intense [*Elansky et al.*, 2007, 2015, 2022].

In the countryside (Figure 6), the nature of the daily variations of the considered species is preserved, but much less pronounced, which can be explained by less anthropogenic pollution of the atmosphere.

The nitrogen monoxide concentrations peaks at Figure 5 between 0:00 and 5:00 o'clock could be explained by complex pollutant emission sources at the densely built area surrounding the measuring site [*Berezina et al.*, 2022]. Measurements at the ZSS (Figure 6), where there are no such emission sources, don't show such peaks, as well as measurements at the site in Moscow, but located far from local emission sources [*Elansky et al.*, 2007].

The patterns of diurnal variations in VOCs in the countryside area are of great interest. Figure 7 shows the diurnal variations obtained from the PTR-MS observations on the ZSS.

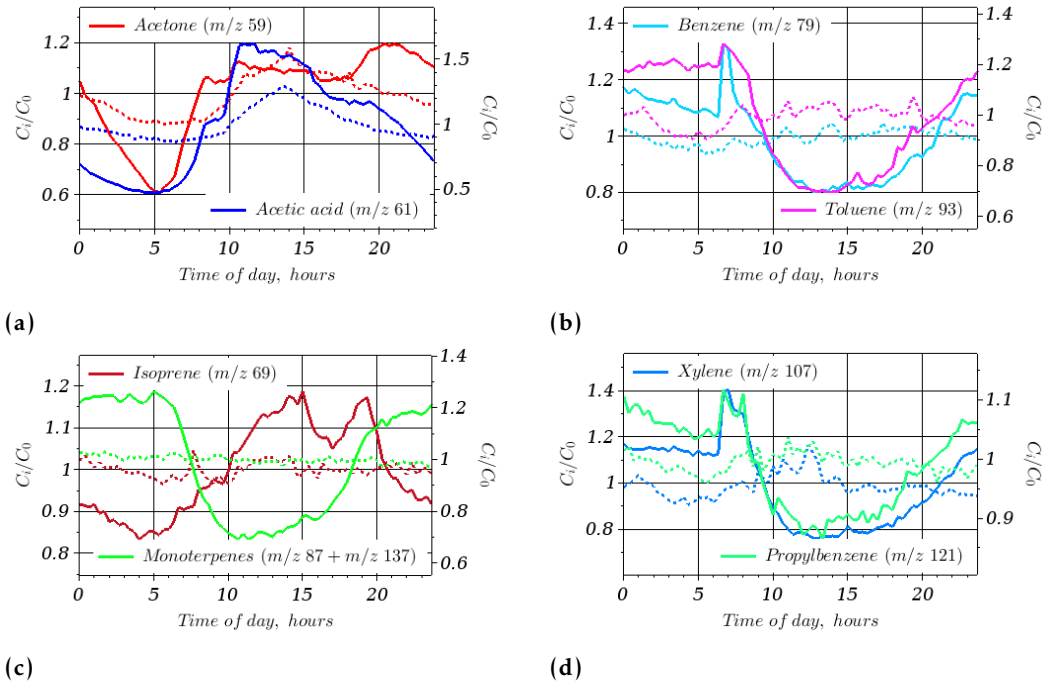


**Figure 7.** Diurnal variations in VOCs at ZSS in summer (solid lines) and winter (dashed lines).

The diurnal variations of such VOCs as acetone and acetic acid are completely similar to those for observations in a metropolis [*Belikov et al.*, 2019; *Berezina et al.*, 2020, 2022; *Jordan et al.*, 2009]. The concentrations of these VOCs, both in the metropolis and in the countryside, have a pronounced maximum in the daytime, and a minimum - at night. Variations in the concentrations of anthropogenic VOCs, in particular, benzene and toluene, on the contrary, are characterized by their increase at night due to accumulation under the inversion layer. Similar results were previously obtained for the same VOCs for observations in a metropolis [*Belikov et al.*, 2019]. The diurnal variation of isoprene concentration is similar to that of acetone and acetic acid, while the diurnal variation of monoterpenes concentration is similar to that of benzene and toluene, i.e. characterized by their accumulation under the inversion layer.

The results of data analysis are generally in good agreement with previous observations [*Belikov et al.*, 2019; *Berezina et al.*, 2020, 2022; *Elansky et al.*, 2007, 2015; *Gubanova et al.*, 2018; *Jordan et al.*, 2009], which indicates the representativeness of the data obtained.

## 4. Conclusions

The performed analysis of the data shows the following characteristic features of variations in surface concentrations of gaseous species, as well as volatile organic compounds in both the metropolis and countryside:

- significantly lower concentrations of nitrogen oxides in the countryside than in the metropolis, which is explained by a significantly smaller number of sources of their emissions (mainly vehicles) in the suburban area;
- low concentrations of almost all measured VOCs in the surface air, much lower than their maximum allowable concentrations;
- pronounced diurnal variations in anthropogenic VOCs: benzene and toluene, with their accumulation in the boundary layer during the nighttime temperature inversion;
- an increase in the concentrations of almost all VOCs, especially acetone and acetic acid vapors, with an increase in air temperature during the transition from spring to summer seasons.

With the accumulation of data series of continuous observations of gaseous species concentrations in the atmospheric boundary layer in Moscow and at the ZSS, their analysis will be continued in the future. The data obtained will also be used to estimate emissions of atmospheric pollutants, in particular, according to the methods described in [*Berezina et al.*, 2022; *Elansky et al.*, 2018, 2022].

**Acknowledgments.** Measurements carrying out in Moscow were supported by the Russian Science Foundation, project no. 21-17-00021. Measurements at ZSS and all data statistical analysis were supported by the Russian Foundation for Basic Research, project no. 19-05-50088.

## References

Belikov, I. B., V. A. Belousov, D. P. Gubanova, and A. I. Skorokhod (2019), Variations of concentrations of volatile organic compounds and aerosol particles PM2.5 in the surface layer of the atmosphere of Moscow, in *Fundamental and applied aspects of geology, geophysics and geoecology using modern information technologies. V International Scientific and Practical Conference. Part 1*, pp. 80–89, IP Kucherenko V. O., Maykop (in Russian).

Belousov, V. A., I. B. Belikov, and A. I. Skorokhod (2018), Volatile organic compounds in the surface air according to observations by a proton mass spectrometer, in *TURBULENCE, ATMOSPHERE AND CLIMATE DYNAMICS. The International Conference dedicated to the centenary of the birth of Academician Alexander Mikhailovich Obukhov. 16–18 May 2018. Abstracts*, p. 116, Fizmatkniga, Moscow (in Russian).

Berezina, E., K. Moiseenko, A. Skorokhod, N. V. Pankratova, I. Belikov, V. Belousov, and N. F. Elansky (2020), Impact of VOCs and NOx on Ozone Formation in Moscow, *Atmosphere*, *11*(11), 1262, https://doi.org/10.3390/atmos11111262.

Berezina, E., K. Moiseenko, A. Vasileva, N. Pankratova, A. Skorokhod, I. Belikov, and V. Belousov (2022), Emission Ratios and Source Identification of VOCs in Moscow in 2019-2020, *Atmosphere*, *13*(2), 257, https://doi.org/10.3390/atmos13020257.

de Gouw, J., and C. Warneke (2006), Measurements of volatile organic compounds in the earth's atmosphere using proton-transfer-reaction mass spectrometry, *Mass Spectrometry Reviews*, *26*(2), 223–257, https://doi.org/10.1002/mas.20119.

Elansky, N. F., M. A. Lokoshchenko, I. B. Belikov, A. I. Skorokhod, and R. A. Shumskii (2007), Variability of trace gases in the atmospheric surface layer from observations in the city of Moscow, *Izvestiya, Atmospheric and Oceanic Physics*, *43*(2), 219–231, https://doi.org/10.1134/s0001433807020089.

Elansky, N. F., M. A. Lokoshchenko, A. V. Trifanova, I. B. Belikov, and A. I. Ckorokhod (2015), On Contents of Trace Gases in the Atmospheric Surface Layer over Moscow, *Izvestiya, Atmospheric and Oceanic Physics*, *51*(1), 39–51, https://doi.org/10.7868/s0002351515010034 (in Russian).

Elansky, N. F., N. A. Ponomarev, and Y. M. Verevkin (2018), Air quality and pollutant emissions in the Moscow megacity in 2005-2014, *Atmospheric Environment*, *175*, 54–64, https://doi.org/10.1016/j.atmosenv.2017.11.057.

Elansky, N. F., A. V. Shilkin, N. A. Ponomarev, P. V. Zakharova, M. D. Kachko, and T. I. Poliakov (2022), Spatiotemporal Variations in the Content of Pollutants in the Moscow Air Basin and Their Emissions, *Izvestiya, Atmospheric and Oceanic Physics*, *58*(1), 80–94, https://doi.org/10.1134/s0001433822010029.

GAW WMO (2012), *WMO/IGAC Impacts of Megacities onAir Pollution and Climate*, 304 pp., World Meteorological Organization.

Gubanova, D. P., I. B. Belikov, N. F. Elansky, A. I. Skorokhod, and N. E. Chubarova (2018), Variations in PM2.5 Surface Concentration in Moscow according to Observations at MSU Meteorological Observatory, *Atmospheric and Oceanic Optics*, *31*(3), 290–299, https://doi.org/10.1134/s1024856018030065.

Jordan, C., E. Fitz, T. Hagan, B. Sive, E. Frinak, K. Haase, L. Cottrell, S. Buckley, and R. Talbot (2009), Long-term study of VOCs measured with PTR-MS at a rural site in New Hampshire with urban influences, *Atmospheric Chemistry and Physics*, *9*(14), 4677–4697, https://doi.org/10.5194/acp-9-4677-2009.

Taipale, R., T. M. Ruuskanen, J. Rinne, M. K. Kajos, H. Hakola, T. Pohja, and M. Kulmala (2008), Technical Note: Quantitative long-term measurements of VOC concentrations by PTR-MS - measurement, calibration, and volume mixing ratio calculation methods, *Atmospheric Chemistry and Physics*, *8*(22), 6681–6698, https://doi.org/10.5194/acp-8-6681-2008.

Russian Journal of Earth Sciences

Special Issue: "Fundamental and Applied Aspects of Geology, Geophysics and Geoecology"

# Evaluation of Changes in the Scale and Direction of Thermal Pollution Flows in the Kalinin NPP Cooling Lakes From 1985 to 2020

**Alexandr V. Bocharov[1], Sergey A. Lebedev[2,3,4], Pavel N. Kravchenko[1,5]**

[1]Tver State University, Tver, Russia
[2]Geophysical Center of the Russian Academy of Sciences, Moscow, Russia
[3]Maikop State Technological University, Maikop, Russia
[4]National Research University Moscow Institute of Electronic Technology, Moscow, Russia
[5]S. Yu. Witte Moscow University, Moscow, Russia
* **Correspondence to:** Alexandr V. Bocharov, bochalex@bk.ru

**Abstract:** The article evaluates the change in the scale and direction of thermal pollution flows of the cooling lakes of the Kalinin NPP from 1985 to 2020 based on the use of Earth remote sensing data. A retrospective analysis was carried out using satellite images obtained by the sensors of the Landsat series satellites. An analysis of the distribution of surface water temperature over the water area of NPP cooling lakes has been carried out. The change in the structure of thermal pollution after the increase in the capacity of the Kalinin NPP is determined. The temperature of the cooling lakes of the Kalinin NPP was estimated relative to the background indicators in the lakes-analogues, which were used as nearby Lake Navolok and Lake Kezadra. The study identified five stages of transformation of the water mass circulation system in the cooling lakes of the Kalinin NPP.

**Keywords:** remote sensing, water temperature, thermal pollution, Kalinin NPP, Landsat.

**Citation:** Bocharov A. V., Lebedev S. A., Kravchenko P. N. (2023), Evaluation of Changes in the Scale and Direction of Thermal Pollution Flows in the Kalinin NPP Cooling Lakes From 1985 to 2020, *Russian Journal of Earth Sciences*, Vol. 23, ES0207, https://doi.org/10.2205/2023ES02SI07

## 1. Introduction

Provision of the territory with sufficient power capacity is a necessary condition for economic development. The most advanced way to generate electricity is nuclear power. The advantages of nuclear energy are: huge energy intensity, stability of generation, reduction of carbon emissions, the possibility of reusing fuel. About 10% of the world's electricity is generated by more than 440 operating nuclear reactors [*International Atomic Energy Agency*, 2021]. In Russia, about 20% of electricity is generated by 38 reactors located at 11 operating nuclear power plants, one of which is the Kalinin Nuclear Power Plant.

To cool the nuclear power plant, a circulation system of circulating water supply with a cooling pond is used. Cooling of the heated water flow in cooling ponds occurs due to heat transfer from the water surface. Efficient cooling is a necessary condition for the operation of nuclear power plants. Artificial or natural reservoirs are used as reservoirs-coolers. The Udomelskoye reservoir acts as a cooling reservoir for the Kalinin NPP. It is formed on the basis of the natural lakes Udomlya and Pesvo, which are regulated by a dam on the Syezha River flowing from them.

The history of its appearance begins in the 70s of the XX century, at that time, a powerful source of electricity was required to provide the energy system of the center and north of the USSR. In 1970, a commission was established to select a site for the construction of a nuclear power plant. Of all the possible options, a site was chosen on the southeastern shore of Lake Udomlya, 3 km from the village of Udomlya (Figure 1). In the

Research Article

Received: 20 October 2023
Accepted: 27 November 2023
Published: 15 December 2023

**Copyright:** © 2023. The Authors. This article is an open access article distributed under the terms and conditions of the Creative Commons Attribution (CC BY) license (https://creativecommons.org/licenses/by/4.0/).

production cycle of the Kalinin NPP, it was supposed to use the waters of the Pesvo and Udomlya lakes as a coolant.

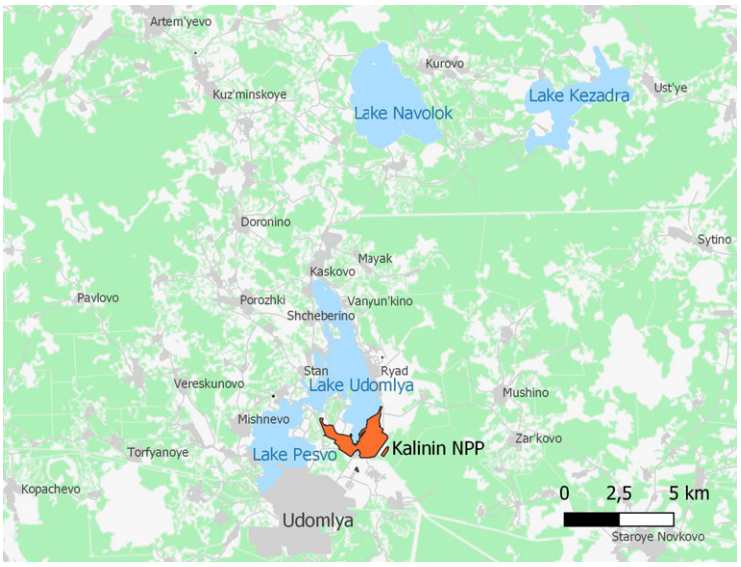


**Figure 1.** Overview map of the study area.

Three years were spent on the design of the nuclear power plant. Construction work began in 1973 [*Myasnikov and Scriabin*, 1994]. The first stage involved the construction of two power units with a capacity of 1000 MW. Power unit 1 was launched in 1984, and in 1986 it was brought to its design capacity. Power unit 2 was launched in 1986 and brought to full capacity in 1987.

In 1984, the construction of the second stage of the Kalinin nuclear power plant began. For a number of reasons, the construction of power unit 3 was greatly delayed; it was launched and brought to its design capacity only in 2004. In 2007, the final project for increasing the capacity of the KNPP to 4000 MW was adopted, and in 2011, power unit 4 was commissioned and connected to the power grid.

The construction of such a large-scale facility as a nuclear power plant inevitably leads to anthropogenic transformation of the surrounding natural complexes. During construction, the landscape undergoes complex changes. Significant changes in the natural environment during construction are associated with the need to create hydraulic structures that allow efficient cooling of nuclear power plants.

After the start-up of the power plant, one of the main factors affecting the ecosystems of cooling ponds is heat emission. The issues of thermal pollution of water bodies are always an important part of the environmental impact assessment in the regions of operating NPPs [*Beznosov and Suzdaleva*, 2001].

Thermal pollution of reservoirs is an increase in water temperature compared to the usual for a given reservoir due to the discharge of warm wastewater into it [*Ilshinsky*, 2004]. An increase in water temperature affects both directly the physiology of hydrobionts and the nature of the course of chemical processes in the aquatic environment [*Suzdaleva and Beznosov*, 1999].

According to the temperature distribution of the surface layer, «heated» and «non-heated» zones are distinguished, which was used in most works on cooling ponds. Usually, with such an approach, several zones of different degrees of heating are distinguished: strong, moderate, and weak [*Mordukhai-Boltovskoy*, 1975].

The area of the zone where the increase in temperature is observed is largely determined by the difference between the temperature of waste water and the natural temperature of the surface water of the reservoir at a given particular moment in time. In winter, the heated zone can be reduced due to the rapid cooling of the waters.

Quite often, in the cold season, the boundaries of the entire water mass of the circulation flow from the discharge to the NPP water intake are clearly visible, visually, from the steam above the water and the nature of the formation of the ice cover. In remote areas of the circulation flow, ice forms at a much lower air temperature than in areas occupied by peripheral water masses. In the warm season, it is difficult to visually establish the boundaries of water masses.

The use of remote sensing data greatly simplifies the assessment of thermal pollution of cooling lakes, allows us to evaluate its dynamics, visualize the circulation flows of the distribution of heated waters, while studies using traditional methods do not provide such a spatial picture, and they are more economically costly and laborious.

The purpose of this study is to assess the change in the scale and direction of thermal pollution flows of the cooling lakes of the Kalinin NPP from 1985 to 2020 based on the use of Earth remote sensing data.

Studies of the thermal regime on lakes Pesvo and Udomlya began in 1972. Prior to the commissioning of the station, observations were carried out at a fairly limited number of points; since 1985, the observation system has been expanded. Detailed and surface thermal surveys were carried out on the lakes, which alternated with surveys of currents, carried out on a limited number of verticals. Standard equipment was used to measure water temperature, current velocities and hydrometeorological characteristics [*Institute FSUE NIAEP*, 2002].

Technical water supply of the Kalinin NPP is carried out according to the reverse scheme using a lake-type cooling reservoir formed on the basis of the natural lakes Udomlya and Pesvo, regulated by a dam on the Syezha River. With the start of the nuclear power plant, the temperature regime of the lakes has changed. The water, heated by the condensers of the turbines by 8–10 degrees, enters the waste channels and then into the lakes. As a result, the water temperature rises, reaching critical values at the mixing points of waste and lake waters. Further, as the circulation flow spreads, as a result of the mixing of lake and waste waters, the water temperature decreases. In the peripheral parts of the lakes, water heating is less pronounced.

Since the start of operation of the Kalinin NPP, several more reactors have been put into operation, the circulating water supply system has gradually undergone a significant transformation, and thermal pollution flows have increased significantly. The main main hydraulic structures in the cooling lakes of the Kalinin NPP as of 2020 are shown in Figure 2.

Water is taken from Lake Udomlya, discharged into Lake Pesvo and Lake Udomlya. After a multi-stage transformation, the system of outlets of heated water used for cooling the systems of the Kalinin NPP, as of 2020, includes: a discharge channel in the lake. Pesvo, a diverting channel in the lake. Udomlya, outlet channel from cooling towers 1 and 2, outlet channel from cooling towers 3 and 4 (Figure 3).

The dam directing the flow of water prevents the direct ingress of heated water into the source of the Syezha River, flowing from the lake. Udomlya. The volume of withdrawn water resources is spent to compensate for irretrievable losses due to natural and additional evaporation from the cooling reservoir; for evaporation and droplet entrainment from cooling towers and spray ponds. Lakes are fed by rivers and streams flowing into them [*ROSATOM*, 2006].

## 2. Data and methods

In this study, a retrospective analysis of the transformation of the circulation system of water masses and an assessment of the thermal regime of the cooling lakes of the Kalinin NPP were carried out according to the data of remote sensing of the Earth.

The study used images from Landsat series satellite sensors from 1985 to 2020 [*United States Geological Survey*, 2023]. To determine the water surface, in order to identify the boundaries and retrospective analysis of the appearance of hydraulic structures, remote sensing data in the near infrared range obtained by sensors were used:

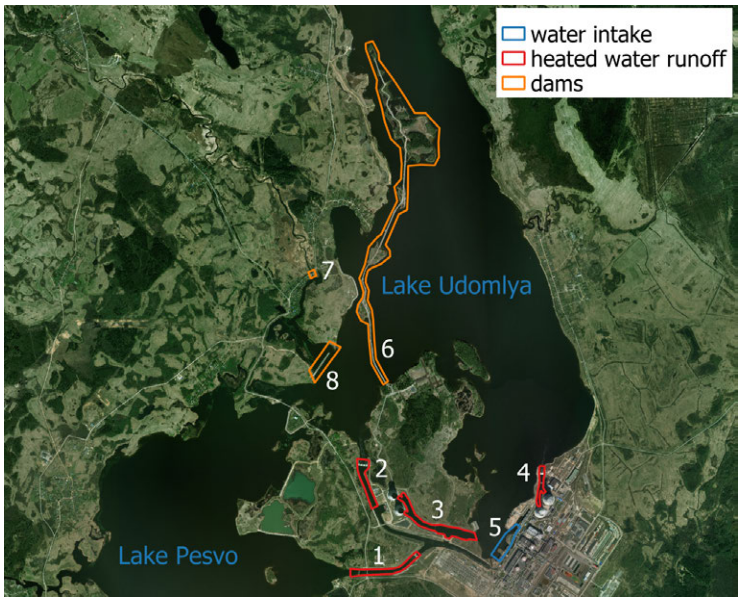


**Figure 2.** Location of the main hydraulic structures in the cooling lakes of the Kalinin NPP: 1 – water discharge through the canal into the lake Pesvo; 2 – water discharge through the canal into the lake Udomlya; 3 – outlet channel of cooling towers 1,2; 4 – outlet channel of cooling towers 3,4; 5 - water intake; 6 – dam directing the flow of heated waters in Lake Udomlya; 7 – dam on the river Syezha; 8 – dam directing the flow of water at the source of the river Syezha.

- TM of the Landsat-5 satellite (4th image channel (0.76–0.9 μm));
- ETM+ of the Landsat 7 satellite (4th image channels (0.77–0.9 μm));
- TIRS of the Landsat-8 satellite (5th channel of images (0.85–0.88 μm)).

To obtain the temperature values of the radiating surface, we used remote sensing data in the infrared range obtained by sensors:

- TM of the Landsat-5 satellite (6th image channel (10.40–12.50 μm));
- ETM+ of the Landsat 7 satellite (61st and 62nd image channels (10.40–12.50 μm));
- TIRS of the Landsat-8 satellite (10th and 11th image channels (10.30–12.50 μm)).

The brightness of satellite imagery pixels was converted into the brightness temperature of the water surface using standard formulas [*Chander and Markham*, 2003]. For pure water, the emissivity is close to unity; therefore, the brightness temperature of the water surface has values close to the actual temperature.

## 3. Results

To correlate thermal pollution flows with the transformation of hydraulic structures in the Udomelskoe reservoir, an analysis was made of changes in the water mass circulation system from 1985 to 2020. According to satellite images, the increase in bulk objects in the water area of the reservoir was recorded, and areas were identified where the increase in the area of the water surface was determined. It should be noted that during the construction of bulk hydraulic structures, the identification of these objects was carried out using satellite images with a resolution of 30 m / pixel, it was also associated with fluctuations in the water level in the reservoir, and water erosion, so sometimes the outlines of the object may appear, but then be absent on later pictures.

The satellite image of 1985 shows that after the launch of the station, the flow of heated water emission was carried out only through the outlet channel to Lake Pesvo. From 1987 to 1991, the construction of separate sections of the jet-directing dam in the western part of Udomlya Lake was observed.

According to satellite images of the 1990s, permanent changes in the configuration of the outlet channels to the Pesvo and Udomlya lakes are observed, but the scale of the

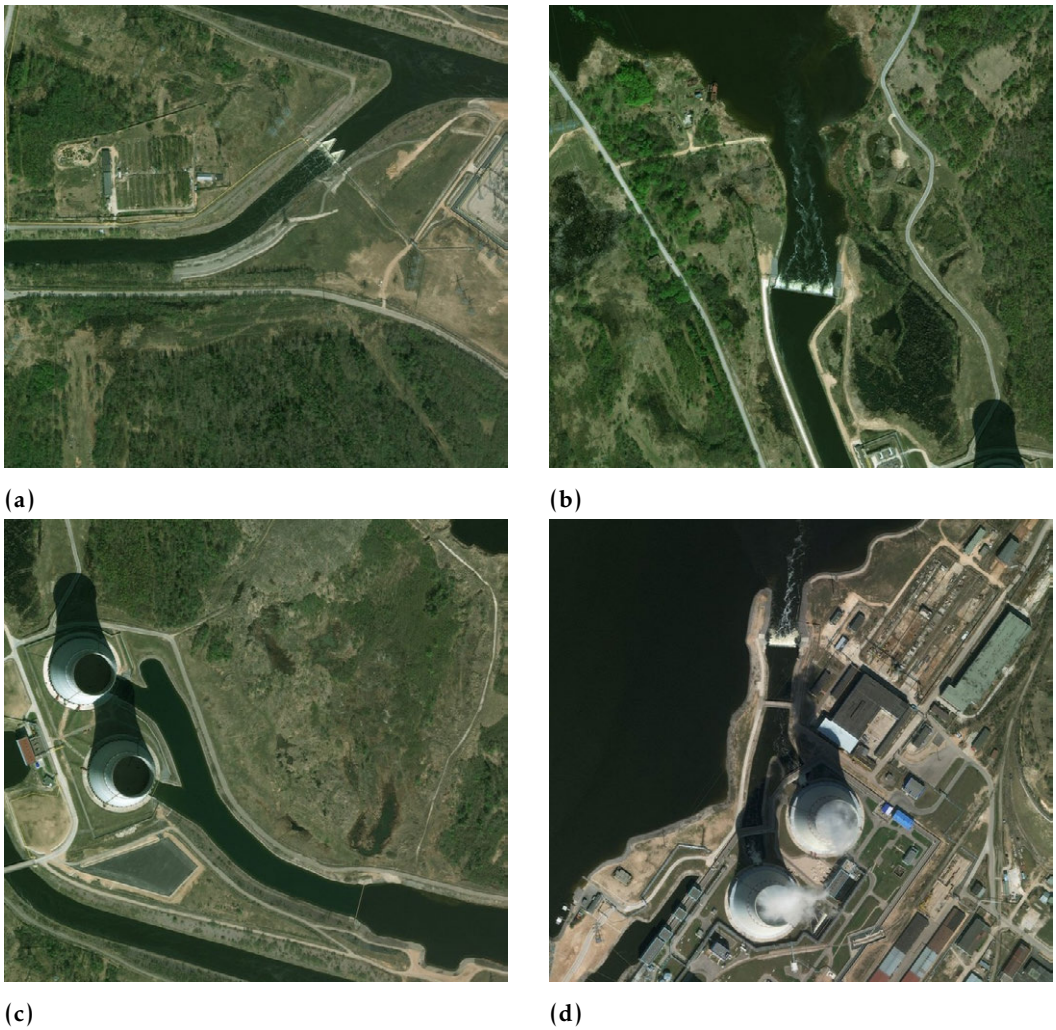

**Figure 3.** (a) Discharge of water through the canal into Lake Pesvo. b) Discharge of water through the canal into Lake Udomlya. c) Outlet channel of cooling towers 1,2. d) Outlet channel of cooling towers 3,4.

data used does not allow a detailed assessment of these transformations. But at the same time, the used remote sensing data allow us to establish that the construction of the canal to Lake Udomlya began after 1993. By 1997, the contours of the channel on the satellite image become more visible. From 1997 to 2005, no strong changes were found in the water area of the Udomelskoye reservoir.

On the satellite image of 2005, the outlines of a jet-directing dam at the source of the Syezha River appear, and a discharge channel from cooling towers 1 and 2 appears. In 2008 in Lake Udomlya, the construction of a jet-directing dam to the north is observed, and in 2009 another large section of the dam is added. In 2010, in the northern part of Lake Udomlya, near the village of Shcheberino, work began on creating a continuation of the canal to divert the heated waters of the jet-directing dam to the northernmost part of the lake, which, according to satellite imagery, were completed in 2011. Since that time, significant changes in the configuration of hydraulic structures have not been determined.

It should be noted that from 1985 to 1991 in the southwestern part of the lake. Udomlya, east of cooling towers 1 and 2, there is an intensive increase in the area of the water surface. This is probably a consequence of the withdrawal of materials for the construction of hydraulic structures and other infrastructure of the nuclear power plant, as well as an increase in the water level due to the construction in 1987 of a hydroelectric complex on the Syezha River [*Obyazov et al.*, 2019], flowing from cooling lakes. As a result of this, the area of Lake Udomlya increased by 1.9%. The increase in the area of the lake

has increased evaporation from the water surface. This makes a small contribution to the hydrothermal regime of the reservoir.

All major changes in the water area of the Udomelskoye reservoir, obtained from the analysis of remote sensing data, are shown in Figure 4.

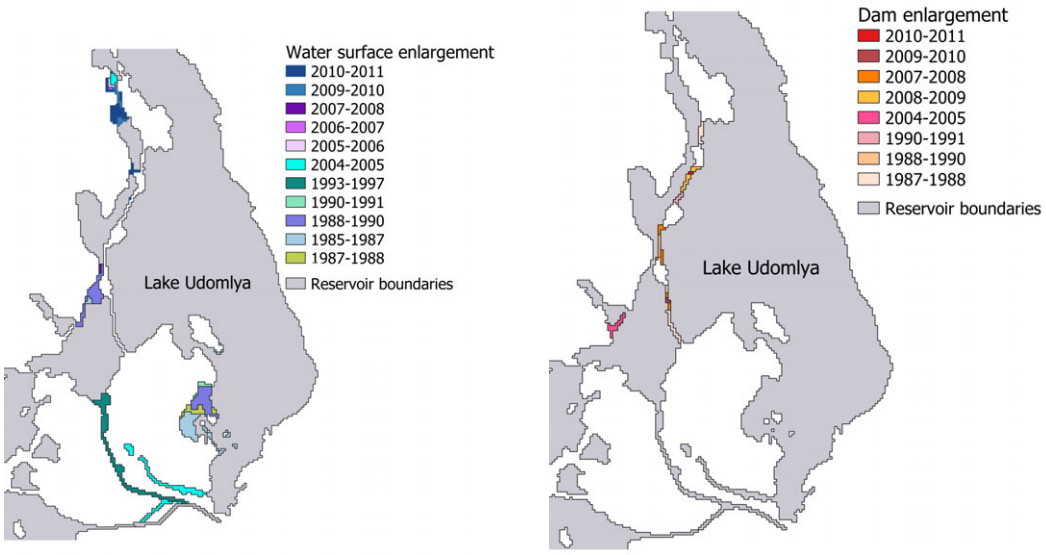


**(a)** **(b)**

**Figure 4.** (a) Retrospective analysis of the increase in the area of the water surface of the Lake. Udomlya according to sensors of Landsat series satellites. b) Retrospective analysis of the construction of hydraulic structures in Lake Udomlya according to the data of sensors of Landsat series satellites.

To study the thermal pollution of the Udomelskoye reservoir from 1985 to 2020, 33 satellite images were selected, from which the rasters of the water surface temperature distribution were constructed (Figure 5). The obtained data allow: to study the spatial and temporal distribution of the temperature of water masses in lakes; highlight overheated and stagnant areas; evaluate the input characteristics of thermal conditions for the river Syezha flowing from Lake Udomlya; find solutions to other problems.

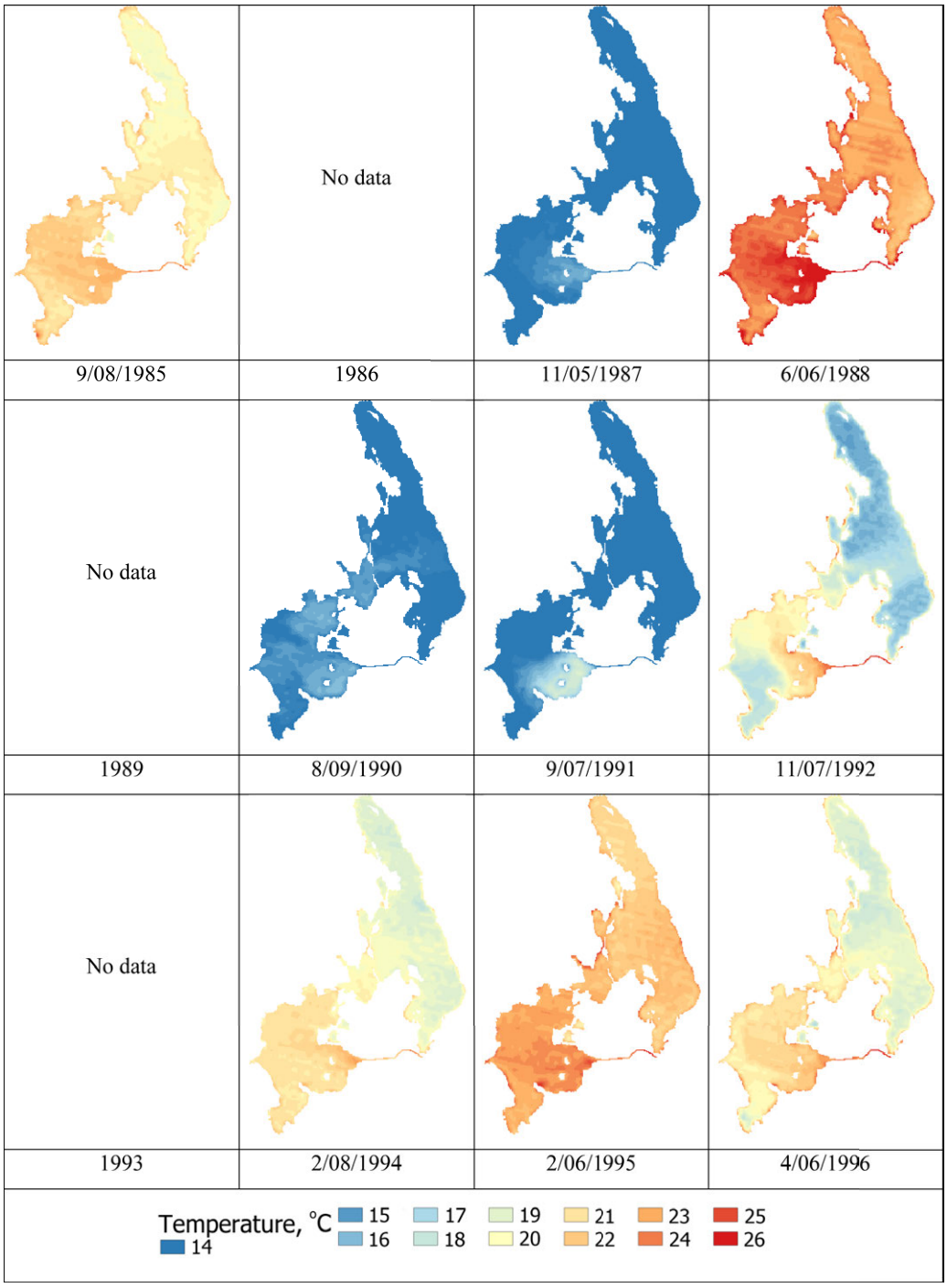
No data
9/08/1985
1986
11/05/1987
6/06/1988
No data
1989
8/09/1990
9/07/1991
11/07/1992
No data
1993
2/08/1994
2/06/1995
4/06/1996
Temperature, °C
14
15
16
17
18
19
20
21
22
23
24
25
26

**(a)**

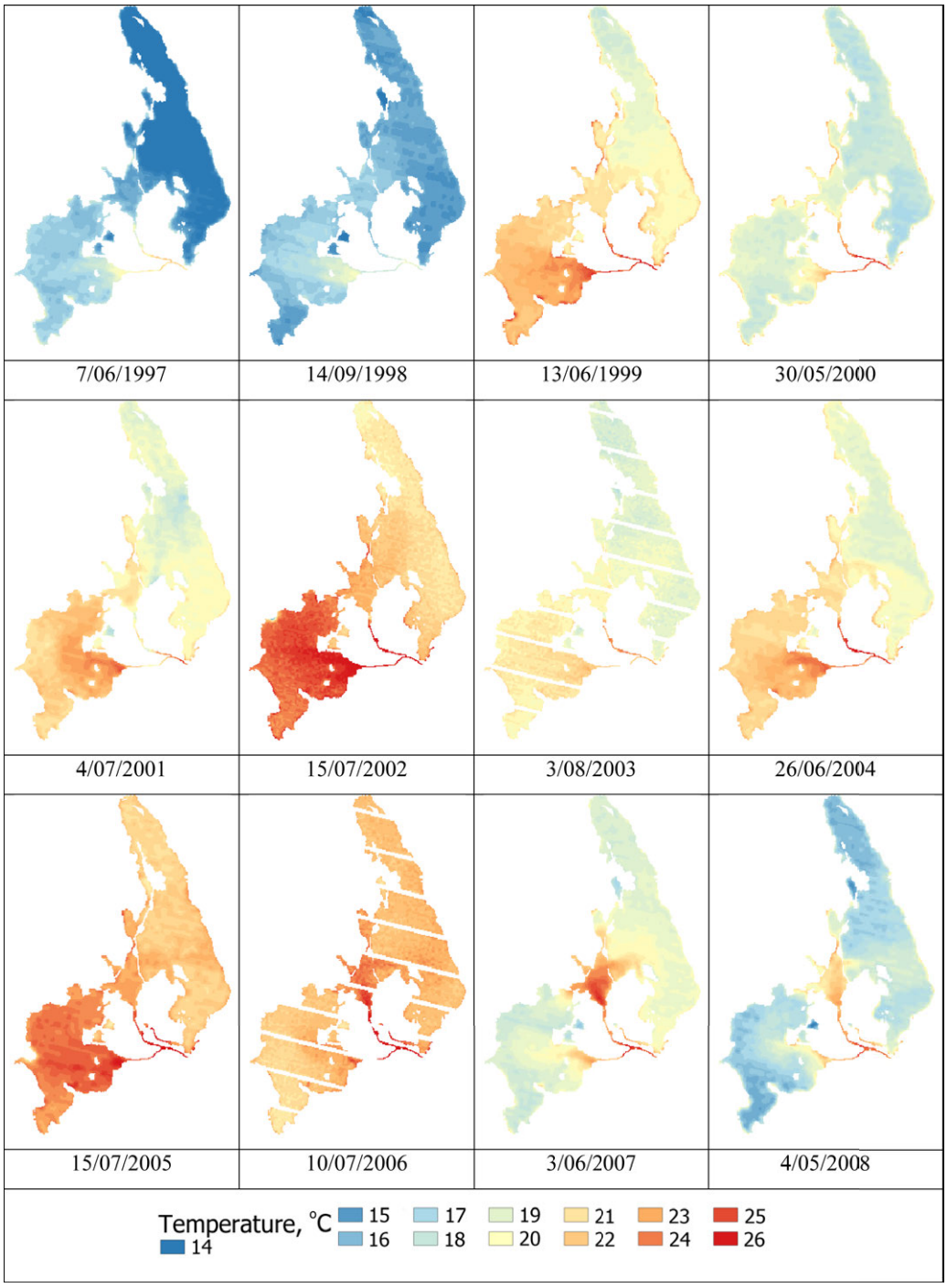
7/06/1997
14/09/1998
13/06/1999
30/05/2000
4/07/2001
15/07/2002
3/08/2003
26/06/2004
15/07/2005
10/07/2006
3/06/2007
4/05/2008
Temperature, °C
14
15
16
17
18
19
20
21
22
23
24
25
26

**(b)**

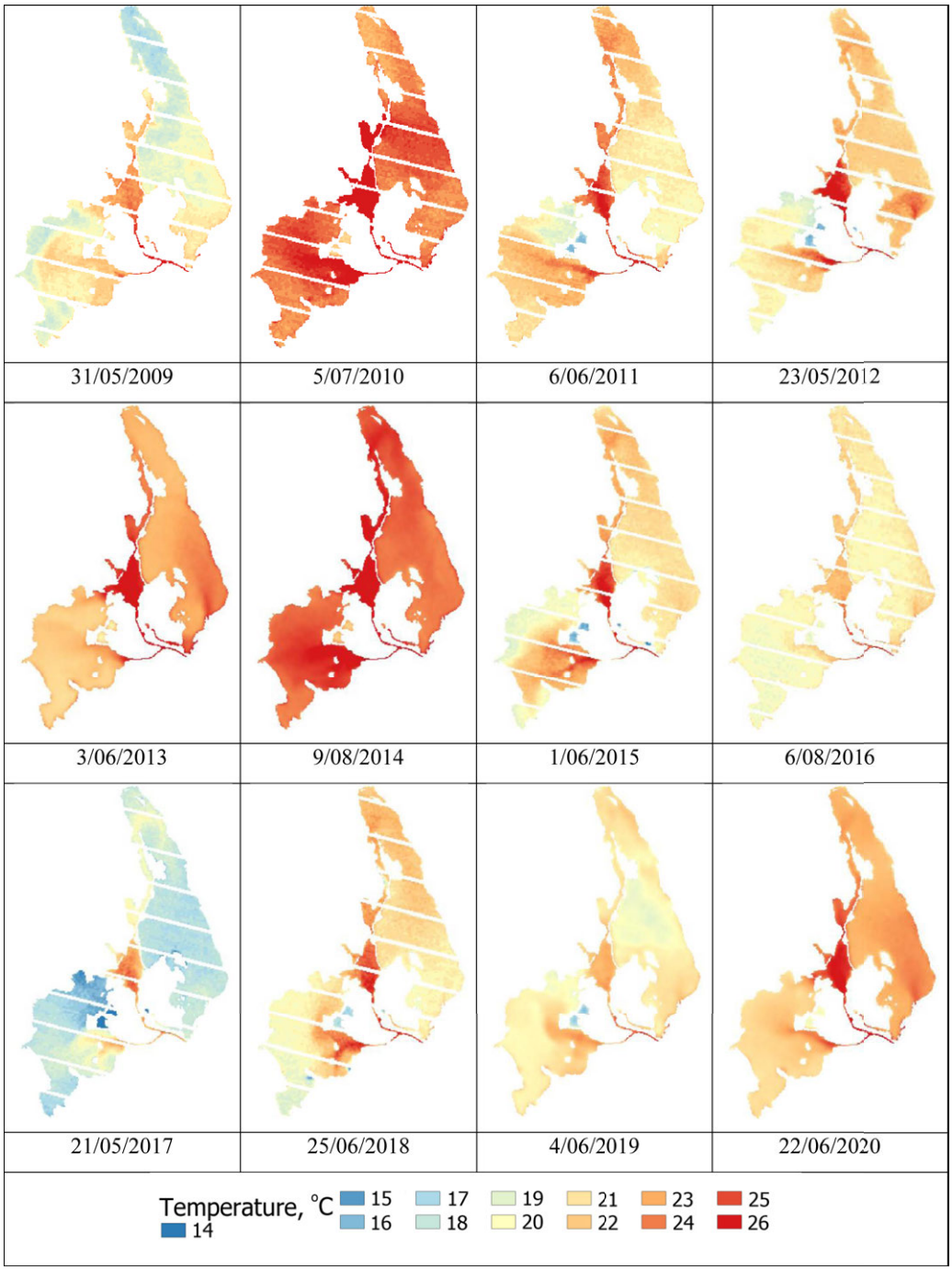


(c)

**Figure 5.** Water surface temperature of the cooling lakes of the Kalinin NPP according to the sensors of the Landsat series satellites for 1985–2020.

An analysis of remote sensing data showed that until 2005, the used space images almost always showed an excess of the average water surface temperature in Lake Pesvo over Lake Udomlya. In 2004, power unit 3 of the Kalinin NPP was put into operation. After 2004, there is a change in the structure of thermal pollution in the cooling water bodies of the Kalinin NPP, and the average water surface temperatures in Lake Udomlya become predominantly higher than in Lake Pesvo (Figure 6). In 2011, power unit 4 of the Kalinin NPP began to operate. Also in 2011, the water circulation scheme changed significantly and took on a modern look. This caused an even greater increase in water temperature in Lake Udomlya.

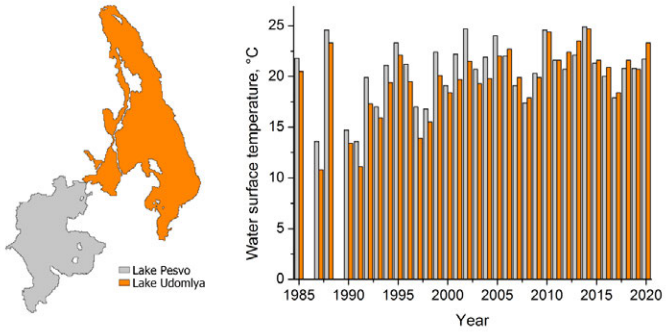


**Figure 6.** Change in the average temperature of the water surface in the cooling reservoirs of the Kalinin NPP according to the data of sensors of the Landsat series satellites.

In 2011, the construction of jet-directing dams was completed, as a result of which "hot" and "cold" areas began to be clearly observed in Lake Udomlya (Figure 7). The analysis of remote sensing data after 2011 showed that the average water surface temperature in the "hot" area exceeded the "cold" area by 1.3–3.3 °C.

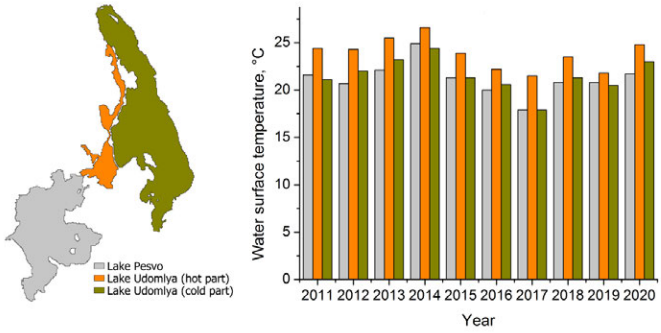


**Figure 7.** Analysis of temperature differentiation in the "hot" and "cold" areas of Lake Udomlya according to the data of sensors of Landsat series satellites.

To assess the temperature of the cooling lakes of the Kalinin NPP relative to the background indicators, a comparison was made with analogous lakes, which were used as nearby Lake Navolok and Lake Kezadra (Figure 1). An analysis of space images obtained by the sensors of the Landsat satellites showed that from 1985 to 2020. The Udomelskoye reservoir has always had an excess of surface water temperature over the background values within 1.3–7.7 °C (Figure 8). On average, over the period under study, the temperature of the cooling lakes of the Kalinin NPP was higher than that of the analogue lakes by 3.1 °C. At the same time, there is an increase in water temperature relative to the background values after the completion of work to increase the power of the station. From 1985 to 2010 the temperature rise relative to analogue lakes was 3.3 °C, after 2011 it is 4.8 °C.

According to the rasters of the temperature distribution of the water surface of the cooling lakes of the Kalinin NPP, the direction of heat flows can be traced. A comparison of heat flows and a retrospective analysis of the time of the appearance of hydraulic structures provides good opportunities for analyzing the changes that have occurred from 1985 to 2020. The use of remote sensing data made it possible to trace the main stages of the transformation of the water mass circulation system. Based on a retrospective analysis of space images, five main stages of the transformations that took place were identified (Figure 9).

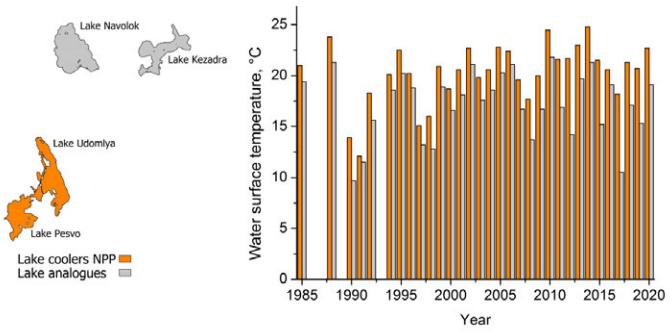


**Figure 8.** Analysis of temperature differentiation in the Udomelskoye reservoir and lakes of analogues according to data from sensors of Landsat series satellites.

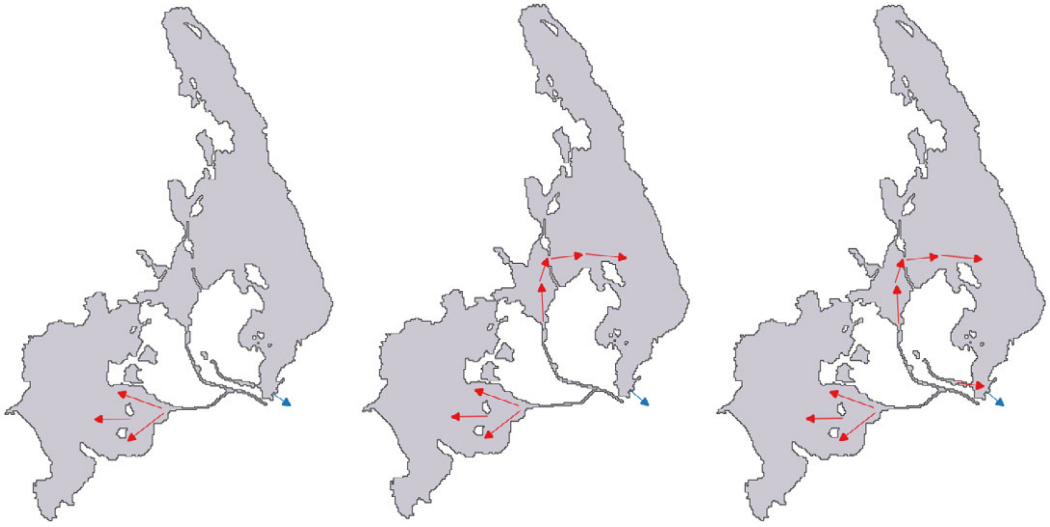

**(a)** 1985 **(b)** 1997 **(c)** 2004

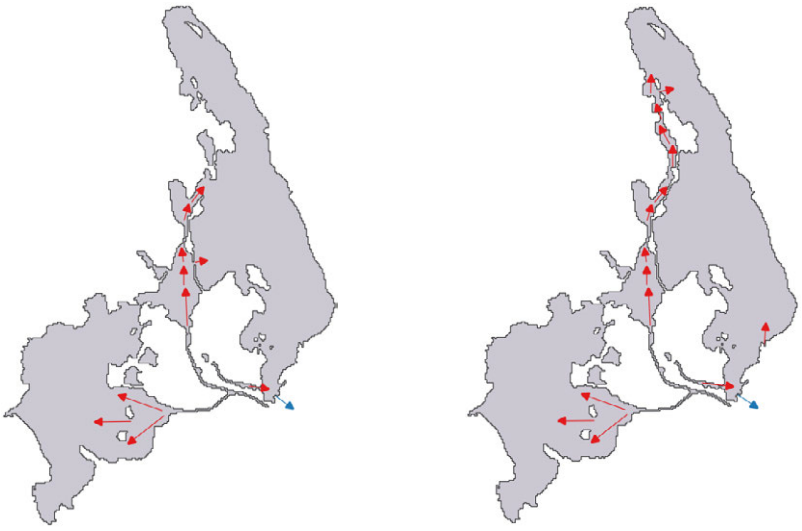

**(d)** 2008 **(e)** 2011

**Figure 9.** The main stages of changes in the sources of thermal pollution emission and its circulation in the cooling lakes of the Kalinin NPP according to the data of the sensors of the Landsat series satellites.

## 4. Conclusion

The analysis of the temperature distribution of the water surface of the cooling lakes of the Kalinin NPP based on Landsat satellite images confirms the promise of using remote sensing data to assess the magnitude and direction of thermal pollution of the cooling lakes of the NPP. The application of these methods made it possible to study the spatial distribution of water temperature in lakes, identify overheated and stagnant areas, evaluate circulation flows in cooling lakes, and compare with background values in analogue lakes.

The study showed that, after 2004, there is a change in the structure of thermal pollution of the cooling reservoirs of the Kalinin NPP, and the average water surface temperatures in Lake Udomlya become predominantly higher than in Lake Pesvo.

The construction of jet-directing dams caused the division of Lake Udomlya into a "hot" and "cold" area. The analysis of remote sensing data showed that the average temperature of the water surface in the "hot" area exceeds the "cold" one by 1.3–3.3 °C.

The assessment of the temperature of the cooling lakes of the Kalinin NPP relative to the background values in the lakes-analogues, which were used as nearby Lake Navolok and Lake Kezadra, showed an excess in the range of 1.3–7.7 °C.

When comparing a retrospective analysis of the appearance of hydraulic structures and rasters of the distribution of water surface temperature, five stages of the transformation of the circulation system of water masses in the cooling lakes of the Kalinin NPP were identified. As a result of the increase in the capacity of the Kalinin NPP in the Udomelskoye reservoir, there was an increase in thermal pollution of the environment. At the same time, there was an increase in the efficiency of the use of existing cooling reservoirs. After the completion of the last stage of the construction of hydraulic structures, a more uniform distribution of water temperature in the main water areas of the cooling lakes is observed.

## Acknowledgements

This work was conducted in the framework of budgetary funding of the Geophysical Center of RAS, adopted by the Ministry of Science and Higher Education of the Russian Federation.

## References

Beznosov, V. N., and A. L. Suzdaleva (2001), Exotic species of the phytobenthos and the zoobenthos living into cooling-ponds of NPS as a bioindicators of the thermal pollution, *Moscow University Bulletin. Series 16 Biology*, (3), 27–31 (in Russian).

Chander, G., and B. Markham (2003), Revised landsat-5 tm radiometric calibration procedures and postcalibration dynamic ranges, *IEEE Transactions on Geoscience and Remote Sensing*, *41*(11), 2674–2677, https://doi.org/10.1109/tgrs.2003.818464.

Ilshinsky, A. Y. (Ed.) (2004), *Big encyclopedic polytechnical dictionary*, Multitrade (in Russian).

Institute FSUE NIAEP (2002), Environmental Impact Assessment (EIA). Part 3. The state of ecosystems and their elements. Kalinin NPP. Expansion up to 4000 MW (in Russian).

International Atomic Energy Agency (2021), Nuclear Technology Review 2021. Report by the Director General, *Tech. rep.*, Vienna, Austria.

Mordukhai-Boltovskoy, F. D. (1975), Thermal power plants and life of reservoirs, *Priroda*, (1), 68–77 (in Russian).

Myasnikov, V., and B. Scriabin (1994), Kalinin NPP - 10 years, in *Atomic Energy Bulletin*, pp. 5–6, CNIIatominform, Moscow (in Russian).

Obyazov, V. A., A. Y. Vinogradov, and A. V. Kuchmin (2019), Assessment of the impact of the Kalinin NPP on the thermal regime of the cooling pond and the climate of coastal areas, *Atomic Energy*, *127*(3), 158–163 (in Russian).

ROSATOM (2006), Water use at nuclear power plants. Classification of cooling water supply systems. STO 1.1.1.02.006.0689-2006.

Suzdaleva, A. L., and V. N. Beznosov (1999), Ecological Consequences of Changes in the Udomlya Lake Stratification Regime (Reservoir-Cooler of the Kalinin NPP), *Problems of regional ecology*, pp. 46–47 (in Russian).

United States Geological Survey (2023), Earth Explorer, https://earthexplorer.usgs.gov, (accessed 2023/05/13).

Russian Journal of Earth Sciences

Special Issue: "Fundamental and Applied Aspects of Geology, Geophysics and Geoecology"

# E-Waste: a Concise Update on Global Movement, Impacts, Management, and Site Remediation

**Ming Hung Wong**[1,2]

[1] Soil Health Laboratory, Southern Federal University, Rostov-on-Don, Russia
[2] Consortium on Health, Environment, Education, and Research (CHEER), The Education University of Hong Kong, Tai Po, Hong Kong, China
* **Correspondence to:** Ming H. Wong, minghwong@eduhk.hk

**Abstract:** The rapid rise of electronic waste (e-waste) worldwide has become a public health concern. Wealthy countries are disposing of their e-waste to other countries taking advantage of their less stringent environmental laws and regulations. China used to receive large amounts of e-waste through Hong Kong (a free port) but banned the entry of e-waste in 2013. Salvaging or recycling different parts of the e-waste using primitive and uncontrolled techniques generated a wide range of toxic chemicals (mainly heavy metals and persistent organic pollutants). Most studies concerning the environmental and health impacts of the emitted toxic chemicals were conducted in China. The principal aim of this short article is to review the various environmental problems and health impacts of e-waste recycling, policies, management, and remediation of contaminated sites. Out of the primitive methods used for recycling, the two most destructive ones causing harm to the environment and human health are (1) Open-burning of e-waste for disposing of the salvaged e-waste and (2) Acid-stripping of electronic boards for collecting precious metals (gold, silver, platinum). There is sufficient evidence showing the associations between the toxic chemicals in different media (i.e., water, soil/sediment, air) and local food items (i.e., fish, meat, vegetables), linking with body burdens (hair, milk, placenta) of workers and residents. The epidemiological data further demonstrated the abrupt rise of several significant diseases (i.e., respiratory disease, cardiovascular disease, malignant tumors) in Taizhou (China), one of the two e-waste recycling sites. Effective policies and vigorous enforcement in managing e-waste are essential. International cooperation is necessary to prohibit the transboundary movement of e-waste. Sites contaminated by e-waste recycling contain incredibly high concentrations of toxic pollutants, which should be removed using excavation, degradation (via microbes, nanoparticles, biochar), soil washing, etc. Planting appropriate plants with associated rhizospheric microbes would achieve longer-term stability.

**Keywords:** ecological and human health, open burning, persistent toxic substances, primitive recycling techniques.

**Citation:** Wong M. H. (2023), E-Waste: a Concise Update On Global Movement, Impacts, Management, and Site Remediation, *Russian Journal of Earth Sciences*, Vol. 23, ES0208, https://doi.org/10.2205/2023ES02SI08

Research Article

Received: 20 October 2023
Accepted: 27 November 2023
Published: 15 December 2023

**Copyright:** © 2023. The Authors. This article is an open access article distributed under the terms and conditions of the Creative Commons Attribution (CC BY) license (https://creativecommons.org/licenses/by/4.0/).

## 1. Introduction

End-of-life electrical and electronic equipment (EEE) is called waste electrical, electronic equipment, WEEE, or simply electronic waste (e-waste). E-waste contained personal computers, mobile phones, and entertainment electronics made of plastic, metals, glass, and other materials. The total annual global e-waste generation rose from 44.4 metric tonnes (Mt) in 2014 to 57.4 Mt in 2021, expected to reach 74.7 Mt in 2030, growing by 2 Mt yearly. One primary reason for the rapid rise of e-waste is various products' shorter lifespans. The ever-growing number of new models for attracting buyers, especially in more

affluent countries, has aggravated the problem. The Europeans produced the most e-waste per person (16.2 kg), followed by Oceania (16.1 kg) and the Americas (13.3 kg). In terms of the amount of e-waste by countries, China tops the list (10,129 kilo tonnes [Kt]), followed by the USA (6918 kt) and India (3230 kt). Less than one-fifth of e-waste is recycled globally, although the amount varies by region. About 17.4% of the total e-waste has been collected and properly recycled, but the figure has decreased in the past 5 years due to more e-waste generated [*Roundup.com*, 2022]. Table 1 indicates the top 10 e-waste-producing countries with the total volumes of e-waste produced in Kt and the recycling rates.

**Table 1**. The amounts of e-waste and recycling rates of the world's top 10 e-waste-producing countries [*Roundup.com*, 2022].

| Rank | Country | E-Waste Produced (Kt) | Recycling Rate |
|---|---|---|---|
| 1 | China | 10129 | 16% |
| 2 | USA | 6918 | 15% |
| 3 | India | 3230 | 1% |
| 4 | Japan | 2569 | 22% |
| 5 | Brazil | 2143 | 0% |
| 6 | Russia | 1631 | 6% |
| 7 | Indonesia | 1618 | Not Available |
| 8 | Germany | 1607 | 52% |
| 9 | UK | 1598 | 57% |
| 10 | France | 1362 | 56% |

This fast-growing waste stream imposes severe environmental issues, especially in China in the past. In addition to many domestically produced and discarded products, China received about 70% of worldwide e-waste illegally imported from developed countries. As a free port, Hong Kong Self Administrative Region (HKSAR) received a large amount of e-waste from the USA, EU, Japan, and Korea and smuggled to mainland China from the 1990s to 2010s, ending up in two mega e-waste recycling sites: Guiyu (Guangdong Province) and Taizhou (Zhejiang Province). The disposal, recycling, and part salvaging of discarded electronic devices (computers, printers, televisions, and toys) using primitive techniques severely impacted the environment and human health around the recycling sites for almost three decades [*Lin et al.*, 2019].

A food consumption survey was conducted to find out the consumption pattern of workers and residents in Guiyu and Taizhou. This was followed by the food basket analyses, quantifying the toxic chemicals entering human bodies through oral intake. There were significant correlations between poisonous substances (Hg, PCDD/Fs, PCBs, PBDEs, etc.) in the food items they consumed daily and the high body burdens (i.e., different human tissues such as milk, placenta, and hair) of these toxic chemicals. The human health impacts were further demonstrated by a local hospital's higher morbidities of several significant diseases [*Chan et al.*, 2007; *Lin et al.*, 2022a].

China exerted stringent border control in 2012, prohibiting the entry of e-waste. As such, e-waste has been stored in Hong Kong or diverted to other countries. Placing trackers on e-waste by the Basal Action Convention Network on various e-waste items revealed that e-waste originating from the USA is illegally transferred to Hong Kong SAR and other places [*Lin et al.*, 2019; *Purchase et al.*, 2020].

The principal objective of this presentation is to update the recent status of the international movement of e-waste, the environmental and health impacts of uncontrolled e-waste recycling, the management and policy of e-waste, and the remediation strategies of contaminated sites. This article focused on the two mega e-waste recycling sites (i.e., Guiyu and Taizhou, China), where most environmental and human health impact studies

were conducted. Now that the e-waste is diverted to other countries due to the entry ban imposed by China, it is hoped that these receiving countries of e-waste will not repeat the same mistakes made in these two sites and also learn from the achievements made towards solving the problem.

## 2. Transboundary Movement of E-waste

### 2.1. 2.1 China Received Large Amounts of E-waste Before 2010

China was the world's major country receiving incredibly high quantities of e-waste from abroad for over two decades in the 2000s, mainly through Hong Kong. Most of this imported e-waste was sent to two mega e-waste sites for uncontrolled recycling. China started to amend and enforce import regulations in 2010 and has achieved positive outcomes, with the quantities of illegal importation gradually decreasing since the 2020s. The import quantities will sharply shrink and disappear in the coming decades if China keeps tightening import regulations. Substantial amounts of displaced e-waste divert to other countries due to China's entry ban on e-waste.

Hong Kong is China's Self Administrative Region (SAR) with an independent judiciary, the rule of law, and a free trading policy. A substantial amount of e-waste has entered Hong Kong. Based on the e-trash transparency project conducted by The Basel Action Network (BAN), a watchdog of the Basel Convention, it has been noted that most exported tracked devices from the USA (57%), Canada (50%) and Australia (67%) ended up in Hong Kong in 2016/17, adding up to about 335,084 t e-waste entering Hong Kong. Therefore, Hong Kong's role as an entry pot for mainland China's ewaste has now changed to an alternative e-waste receiving center [*Lin et al.*, 2019].

### 2.2. The Consequences After China Banned E-waste Entry

This large quantity of e-waste has been stored and even recycled in the northern part (the New Territories) of Hong Kong at about 70 sites, mainly abandoned farm soils, with some close to the RAMSAR site (Tai Po) [*Lin et al.*, 2019]. These areas had active agricultural activities in the past (before the 1980s), mainly producing vegetables and fruits for local consumption. However, due to socio-economic development and the change in land use, large stretches of farmland have been converted to car repairing workshops and e-waste storage. Some simple disassembling and recycling are also carried out on-site, leading to severe soil pollution with high concentrations of heavy metals (HMs): cadmium (Cd), chromium (Cr), copper (Cu), lead (Pb), zinc (Zn), mercury (Hg), and nickel (Ni), and persistent organic pollutants (POPs): polychlorinated biphenyls (PCBs), aromatic hydrocarbons (PAHs), dioxins/furans: polychlorinated dibenzo-p-dioxins and dibenzofurans (PCDD/Fs), and flame retardants: polybrominated diphenyl ethers (PBDEs) in abandoned farm soils, incredibly open burning sites [*Lopez et al.*, 2010].

It was demonstrated that the high concentrations of HMs of air particulates and floor dust inside e-waste recycling workshops posed potential health risks linked to the workers' elevated blood Pb levels [*Lau et al.*, 2013]. In addition, POPs such as PAHs and PCDD/Fs in open burning sites of these abandoned farm soils may also pose detrimental health effects: mutagenicity and genotoxicity to the general public [*Man et al.*, 2014].

As some of the e-waste storage and recycling sites are close to the RAMSAR site (Tai Po), there are concerns about whether the water birds have been safely protected. These included the endangered species: black-face spoonbills visiting the sites every winter from Siberia [*Man et al.*, 2021]. Ecological risk assessments were conducted based on Cd, Cu, Hg, Pb, Zn, and arsenic (As) concentrations in biota (two fish and one shrimp species), water, and sediment. Results showed that the common sandpiper (*Actitis hypoleucos*) was at risk as the small-sized bird sought food from the sediments, reflecting that other juvenile birds with similar ecological and feeding habits may also be at risk.

## 3. Two Mega E-Waste Sites and the Primitive Techniques Used for Recycling

Most of the e-waste shipped to Hong Kong ended up in two e-waste recycling sites in China through smuggling through the China and Hong Kong border in the past. As most of the studies were conducted in these two sites, understanding more about the two mega sites for e-waste recycling and the techniques employed for dismantling, salvaging, and recycling various parts of end-of-life electronic products is essential.

### 3.1. Two Mega E-Waste Recycling Sites in China

Guiyu town (N23° E116°), located in the south-eastern part of Guangdong Province, with a population of 150,000 and a land area of 52.4 $km^2$, has been a significant e-waste dumping site for e-waste exported from North America since the 1980s. E-waste recycling was also conducted in Luqiao City, in the southern part of Taizhou (N28° E112°), along the central coastal section of Zhejiang Province, with a population of 400,000 and a land area of 274 $km^2$. The city has handled e-waste, especially those containing PCBs, generated domestically since the 1970s and started to process different kinds of e-waste imported from other countries since the 1990s. It was China's largest center for dismantling obsolete transformers and capacitors [*Lin et al.*, 2022a].

### 3.2. Primitive Techniques Used in Recycling E-Waste

In general, the primitive and unsafe techniques used included: (1) Manual separation of different products of the e-waste; (2) Stripping of metals in open-pit acid baths to collect precious metals (gold, silver, and platinum); (3) Removing electronic components from a circuit board by heating it over a grill, and chipping and melting plastics indoor, without proper ventilation; (4) Burning electronic cables to collect copper; and (4) Open burning all unsalvageable materials in the field, to reduce the waste volume and dispose of the waste (with ash flushed into nearby waterways) [*Wong et al.*, 2007].

## 4. Toxic Chemicals Emitted During Uncontrolled E-waste Recycling

Our recent review [*Lin et al.*, 2022a] summarized the published results on sources and types of various heavy metals and POPs derived from uncontrolled e-waste recycling obtained in Guiyu and Taizhou (China), compared with studies carried out in other countries. There is no intention to repeat the detailed discussion in the current article. Listed below highlighted the sources and extent of pollution derived from e-waste recycling linking to the next section on health implications.

The primary sources of toxic chemicals were the incomplete combustion (open burning) of various components of e-waste (e.g., plastic chips, wire insulations, PVC materials, and metal scraps), acid treatment of printed circuit boards and uncontrolled disposal of processed materials (including the acid baths after stripping electronic boards). All the environmental media (i.e., air, soil/sediment, water) are highly contaminated with extremely toxic chemicals, including HMs: Hg, Cu, Zn, and Pb and POPs: PBDEs, PCDD/Fs, PCBs, and PAHs in air, soil/sediment, water, and fish. In general, the concentrations of these toxic chemicals were extremely high compared with guidelines adopted in different countries [*Lin et al.*, 2022b].

### 4.1. Heavy Metals (HMs)

Printed circuit boards are heated on top of an open fire indoors to remove different components more efficiently, and they are also treated with strong acids to collect more precious metals like gold, silver, and platinum. Leung et al. [*Leung et al.*, 2008] investigated heavy metal pollution inside and close to these workshops in Guiyu. They noted high mean concentrations of HMs in the workshop dust and roadside dust near the workshops: Pb (110,000, 22,600 mg/kg), Cu (8360, 6170 mg/kg), Zn (4420, 2370 mg/kg), and Ni (1500, 304 mg/kg). Schoolyards and food markets were also affected though to a lesser extent.

Printed circuit boards were also treated with strong acids for collecting precious metals, and the acid residues were disposed of along river banks. The river sediments in Guiyu

were contaminated with Pb (28.6–590 mg/kg), Cu (17.0–4540 mg/kg), Zn (51.3–324 mg/kg), Ni (12.4–543 mg/kg) and Cd (ND–10.3 mg/kg). The local and downstream aquatic and terrestrial environment is expected to be severely impacted.

### 4.2. Persistent Organic Pollutants (POPs)

The combustion of e-waste generated a relatively high concentration of PCDD/Fs (0.65 pg WHO-TEQ/$m^3$) (TEQ = the toxic equivalent) in air particles (PM2.5) at Guiyu, slightly exceeding the Japanese guideline of 0.6 pg TEQ/$m^3$. However, the concentration of the most toxic congener: 2,3,7,8-TCDD (54 fg/$m^3$) (TCDD=2,3,7,8-tetrachlorodibenzo-p-dioxin, the most toxic congener of PCDDs) was substantially higher than the USA (Indiana, Kansas, and Washington) guideline (of 30 fg/$m^3$). The air particles also contained extremely high concentrations of total PBDEs (11,226 pg/$m^3$), 100 times higher than any published data. The particles also had predominately lower brominated PBDEs (1-5 bromine atoms contributed to over 94% of the PBDEs generated), which are known to adversely affect hormonal (thyroid gland), reproductive, and neurological systems [*Leung et al.*, 2007].

Opening burning sites also contained the highest concentrations of PCDD/Fs (14,500 pg WHO-TEQ/g) and PBDEs (883,000 pg/g) ever recorded in soil/sediment, which greatly exceeded various guidelines for agriculture imposed by different countries (Canada: 4 pg TEQ/g, New Zealand, and Sweden: 10 pg-TEQ/g, Japan: 1000 pg WHO-TEQ/g). Deca-BDE (BDE-209) was the most dominant congener (35–82% of total PBDEs) found in combusted residues at the open burning site as well as the dumpsites (at riverbanks). PBDEs are commonly found in various parts of e-waste. It was alarming to note that the monthly concentration of 22 PBDE congeners of 16.8 ng $m^{-3}$ contained in the air particulates PM2.5 at Guiyu was 100 times higher than any published data [*Leung et al.*, 2007].

## 5. Ecological Effects

The e-waste recycling sites also serve as toxic transformers. An example is the burning of cables to extract the embedded copper. Burning PVC (cable casing) can emit dioxins, and Cu will catalyze to enhance the generation of more dioxins. Furthermore, various toxic chemicals emitted interact, forming new poisonous chemicals that our equipment cannot detect. Due to air and water movement, toxic chemicals from open-burning and acid treatment residues will be diverted to the surrounding environment. They will affect local living organisms such as fish and ducks in rivers, ponds, vegetables, and rice cultivated in local small farms. Some toxic elements, especially POPs (e.g., PBDEs), are expected to enter living organisms by bioaccumulation. Their concentrations will be biomagnified along food chains, posing health hazards to residents.

### 5.1. Toxic Effects on Different Trophic Organisms

Bioassay tests using different living organisms can indicate the toxicity of various environmental pollutants. Our early study [*Wang et al.*, 2009] employed organisms of three trophic levels: a bacterium *Vibrio fishceri*, a microalga *Selenastrum capricornutum* (elutriate toxicity tests), and a crustacean *Heterocypris incongruens* (whole sediment toxicity test) to characterize the sediment toxicity of the Guiyu site. The sediment received ashes from the open-burning of e-waste and acid residues after acid-tripping metals from electronic boards. Therefore, it is acidic and highly contaminated by HMs and POPs. Results revealed that most sediments exhibited acute toxicity on various trophic organisms due to elevated Cu, Zn, Pb, PAHs, and low pH caused by uncontrolled acid discharge.

### 5.2. Toxic Chemicals Entering into Food Chains and Biomagnified

It was revealed that rice (*Oryza sativa*) grown (in six areas) near e-waste recycling sites at Taizhou was contaminated with various HMs [*Fu et al.*, 2008]. The daily uptake of Pb through rice consumption of 3.7 µg/day/kg body wt exceeded the FAO Tolerable Daily Intake (TDI). In comparison, the Cd daily uptake of 0.7 µg/day/kg body wt had taken up 70% of the TDI of 1 µg/day/kg body wt. Therefore, long-term locally-produced rice

consumption may pose health hazards. Recently, Wu et al. [*Wu et al.*, 2016] carried out a similar study at Guiyu and noted that rice plants could absorb some metals, such as molybdenum (Mo), Cr, and Mn, more efficiently (bioconcentration factor [BCF>1]) than POPs, such as PBDEs and alternative halogenated flame retardants (AHFRs) (BCF<0.15). Rice is the staple diet in South China. A stringent monitoring program of farmland near e-waste sites should be in place to safeguard public health.

Furthermore, POPs are generally lipophilic and can be stored in the lipid of biota efficiently. Therefore, the tissues with high lipid content had higher concentrations of PBDEs in several fish species (e.g., common carp, *Cyprinus carpio*) collected from the local rivers in Guiyu [*Luo et al.*, 2007a]. The distributions of different PBDE congeners in various sampling locations reflected the predominant commercial PBDE products and their subsequent degradation. A significant correlation of concentration of each PBDE conger between sediment and fish muscle was also demonstrated. It was alarming that the total PBDEs in tilapia (*Oreochromis* spp.) collected from local rivers were 600 times and 15,000 times higher than those from Canadian (0.18 ng/g wet wt) and US markets (0.0085 ng/g wet wt), accordingly [*Luo et al.*, 2007b]. Based on the above results, there is an urgent need for a more comprehensive investigation into everyday food items consumed locally.

## 6. Health Impacts

Lin et al. [*Lin et al.*, 2022a] reviewed the toxic chemicals emitted from uncontrolled e-waste recycling related to the wide range of harmful substances, their transfer to various ecological compartments, and subsequent environmental and health impacts. It was observed that the local biota was grossly polluted, which included food items with vegetables, rice, fish, and seafood contaminated by HMs and livestock by POPs.

### 6.1. Case Studies (Food Intake, Body Loadings of POPs, and Disease Morbidities)

The workers and residents of e-waste recycling sites are exposed to various toxic chemicals emitted during recycling processes: (1) Oral intake of contaminated food and water, and also contaminated soil and dust unintentionally, (2) Inhalation of aerosol gases and particles, and (3) Dermal contact. In addition, fetuses and children can be exposed through ingesting human milk and placental transfer. The residents of Guiyu and Taizhou drink bottled water to minimize intake of toxic chemicals, but it is expected that some food items they consume daily may be highly contaminated.

The current review focuses on the associations of toxic chemicals entering into human bodies through oral ingestion of locally produced food, linking with body burdens of workers and residents, by analyzing various tissues as bioindicators. Several studies were conducted in the two Mega sites [*Chan and Wong*, 2013; *Man et al.*, 2017; *Xing et al.*, 2010] using exact sampling and chemical analysis protocols. Therefore, they are used as examples to show the adverse health impacts on workers/residents and infants residing in these two mega sites for e-waste recycling.

After gaining information on the food consumption patterns of workers and residents, a food basket analysis was conducted by analyzing POPs (PCDD/Fs, PCBs, and PBDEs) contained in their food items. The oral intake of toxic chemicals was quantified based on the food consumed in these two areas compared with the control site: Lin'an, without any e-waste recycling activities. In general, results showed that over 90% of POPs were through oral intake of contaminated food. The toxic chemicals in local food items were linked with workers' and residents' high body loadings (milk, placenta, hair).

#### *6.1.1. PCDD/Fs (Guiyu and Taizhou)*

PCDD/Fs are generated from waste combustion, especially burning materials containing plastics under relatively low temperatures. Heating electronic boards on an open fire indoor and open-burning of savaged e-waste to reduce its volume will undoubtedly generate PCDD/Fs. The ashes and residues derived from these operations were disposed

of around burned sites and flushed into waterways spreading the highly toxic substances around [*Lin et al.*, 2019].

The data on PCDD/Fs generated from the uncontrolled operations on the environmental fate, body burdens, and human health risk assessments and detected levels in environmental compartments: air, soil/sediment, dust, and biota (including food) and the human body (milk, placenta and hair of workers/residents) demonstrated extreme environmental and health hazards of the e-waste site. The Estimated Daily Intakes (EDIs) via oral intake, inhalation, soil/dust ingestion, and dermal contacts estimated for adults, children, and breastfed infants ranged from 5.59 to 105.16 pg WHO-TEQ/kg bw/day. All values well-exceeded the TDIs recommended by WHO (1–4 pg WHO-TEQ/kg bw/day). Dietary intake and inhalation are the most critical exposure pathways for infants, children, and adults, with 60–99% and 12–30% of the total exposure doses of intakes [*Chan and Wong*, 2013].

#### *6.1.2. PCBs (Taizhou)*

Taizhou has been the primary site for recycling transforms; therefore, PCBs emitted from recycling are a significant public health concern. Results showed a high EDI of PCBs of lactating mothers of 12.9 pg WHO-PCB-TEQ/kg bw/day). This reflected that the PCB-contaminated food (primarily PCB-216 derived from transformers) resulted in high total PCBs detected in these mothers: milk, placenta, and hair of 363, 224, and 386 ng/g dry wt., three times higher than samples of the control site (Lin'an).

Compared with the 3$^{rd}$ round WHO-coordinated study on POPs in human milk, in terms of TEQ levels in human milk, Taizhou topped the list in terms of TEQ levels. If these mothers breastfeed, the infants will lead an extraordinarily high EDI of PCBs of 438 pg WHO-PCB-TEQ/kg. The EDIs of PCBs of 12.9 and 438 pg WHO-PCB-TEQ/kg were higher than the DTI stipulated by WHO of 1–4 pg WHO-PCB-TEQ/kg by 3 and 110 times, respectively, for mothers and infants. This raised a severe health concern as the extremely high body burdens reflected the e-waste recycling activities (mainly recycling transformers) imposed on workers, residents, and the second generation in Taizhou [*Man et al.*, 2017; *Xing et al.*, 2010].

#### *6.1.3. PBDEs (Taizhou)*

The pregnant mothers from the e-waste site contained high PBDEs in their tissues (milk 117±191, 8.89–457 ng/g fat, placenta 19.5±29.9, 1.28–72.1 ng/g fat, hair 110±210, 8.47–486 ng/g dry wt.) which were significantly higher than those from the control site (milk 2.06±0.94, 1.0–3.56 ng/g fat, placenta 1.02±0.36, 0.59–1.42 ng/g fat, hair 3.57±2.03, 1.56–5.61 ng/g dry wt.). The following trend was observed in terms of dry weight basis: hair>milk>placenta. A 6-month-old breastfed baby would be exposed to PBDEs orally (572±839 ng/kg body wt/day), 57 times higher than infants from the control site (Lin'an). The maximum calculated value (2240 ng/kg body wt/day) exceeded US EPA's chronic oral reference dose for penta-BDE (2000 ng/kg/day) [*Leung et al.*, 2010].

#### *6.1.4. Lessons Learned From These Cases*

Though the long-term health effects are unknown, the 3-year data provided by the Centre for Disease Control in Taizhou showed an abrupt increase in morbidity of a few major diseases (cancer, respiratory, and cardiovascular) [*Lin et al.*, 2022a]. This reflected the seriousness of the problem showing that e-waste recycling activities severely affected human health and the second generation. These and associated socio-economic loss can better convince policymakers to formulate and enforce control policies.

These studies indicated that local food items: vegetables, rice, livestock, seafood, and in particular, fish, were heavily polluted by HMs and POPs. Dietary exposure is the most important exposure pathway. The associations between exposure to e-waste and high body burdens of these pollutants were evident. Furthermore, the exceedance of national and international standards showed the seriousness of PCDD/Fs, PCBs, and PBDEs on

their adverse impacts on the environment and human health. It seems apparent that toxic chemicals emitted from e-waste activities are causing several major illnesses mentioned above.

There are potential dangers of toxic chemicals passing on to the next generation via placental transfer and lactation. Following the development and health status of infants and children born and brought up in the e-waste sites is essential. Knowledge gaps exist, including more comprehensive and accurate dietary exposure data, body burdens (mothers, infants, and children), and kinetics about POPs partitions among different human tissues. More epidemiological and clinical studies are essential to address all these problems and make them available to the general public.

### 6.2. Modes of Action and Effects of Toxic Chemicals

According to experimental and human studies, Table 2 [*Frazzoli et al.*, 2019] provides a more comprehensive of all the toxic chemicals emitted during various recycling processes and their long-term toxicological impacts. The mixtures of poisonous substances cover both chemicals present in multiple e-waste, i.e., HMs and POPs: brominated flame retardants (BFRs) and non-dioxin-like polychlorinated biphenyls (NDL PCBs) and chemicals emitted during e-waste combustion: PAHs, PCDD/Fs, and dioxin-like polychlorinated biphenyls (DL PCBs).

HMs enter the human body through oral ingestion, dermal contact, and inhalation. They pose severe health threats due to membrane and DNA damage, protein function, and enzyme activity disturbance. They interfere with normal protein functions by binding to free thiols or other functional groups. They also catalyze the oxidation of amino acid side chains, disturb protein folding, and/or substitute essential metal ions in enzymes. Accumulating these heavy metals in various tissues and organs may lead to critical diseases like cancer.

POPs like PCDD/Fs, PBDEs, and PCBs can be bioaccumulated and biomagnified in the food chains. Furthermore, they are considered silent killers because of their persistent and highly toxic nature. Once emitted, they enter into different ecological compartments and biota, including plants, animals, and humans, imposing severe ecological and human health impacts. The lethal diseases include diabetes, obesity, endocrine disturbance, cancer, and cardiovascular and reproductive problems [*Alharbi et al.*, 2018].

**Table 2.** Summary of long-term toxicological effects of e-waste-related chemicals by nonoccupational exposure; evidence collected from experimental and human studies [*Frazzoli et al.*, 2019].

| Chemical | Mode(s) of action | Effects |
|---|---|---|
| PCDD/Fs | Interaction with the aryl hydrocarbon receptor. Significant bioaccumulation related to lipid solubility | Chloracne at high exposure levels. Disruption of reproductive, neurobehavioral, and immune development. Increased risk of chronic diseases, including cancer |
| PBDEs | Interaction with thyroid hormones, retinoic acid, and several nuclear receptors (e.g., pregnane-X). Significant bioaccumulation related to lipid solubility | Lower thyroid function. Impaired reproductive and neurobehavioral development |
| PCBs | Significant bioaccumulation related to lipid solubility. Many congeners with different modes of action: dioxin-like PCBs are similar to PCDDs/PCDFs, though generally less potent; non-dioxin-like PCB: interference with the metabolism of thyroid and estrogens, oxidative stress | Disruption of reproductive, neurobehavioral, and immune development. Increased risk of chronic diseases, including cancer |

Continued on next page

**Table 2.** Summary of long-term toxicological effects of e-waste-related chemicals by nonoccupational exposure; evidence collected from experimental and human studies [*Frazzoli et al.*, 2019]. (Continued)

| Chemical | Mode(s) of action | Effects |
|---|---|---|
| PAHs (high molecular wt) | Genotoxic damage, oxidative stress, and interaction with aryl hydrocarbon receptor | Carcinogenicity, mutagenicity, and teratogenicity |
| Al | Interaction with calcium and cell-cell communication | Skeletal development and metabolism, neurotoxicity, and fetal toxicity |
| Inorganic As | Oxidative stress and interaction with glucocorticoid receptor | Skin alterations, decreased nerve conduction, increased risk of diabetes and skin and other cancers |
| Cd | Oxidative stress and interaction with other elements (Ca and Se), the agonist of estrogen receptor alpha | Kidney damage, bone disease (osteomalacia and osteoporosis), possibly reproductive damage, and lung emphysema |
| Cu | An essential element at high-dose levels may cause liver damage and interfere with Zn | Liver damage |
| Hexavalent Cr | Cytotoxicity and oxidative DNA damage | Carcinogenicity |
| Fe | An essential element that may cause liver damage at high-dose levels | Liver damage |
| Pb | Interaction with sulfur amino acids, disturbed cell proliferation/ differentiation/communication | Impaired neurobehavioral development of children; anemia, kidney damage, and chronic neurotoxicity |
| Hg | Interaction with sulfur amino acids, disturbed cell proliferation/ differentiation/communication; interaction with Se. Organic methylmercury can bioaccumulate | Impaired neurobehavioral development of children (especially methylmercury). Anemia, kidney damage, and chronic neurotoxicity |
| Se | An essential element that may interact with sulfur amino acids at supernormal dose levels | Hair loss; nail brittleness; cardiovascular, renal, and neurological abnormalities |
| Zn | An essential element that may impair copper metabolism at high-dose levels | Increased risk of copper deficiency (anemia and neurological abnormalities) |

### 6.3. Overall Health Impacts with Emphasis on Children and Pregnant Women

Grant et al. [*Grant et al.*, 2013] conducted the 1st review on the health impacts of e-waste recycling based on 23 epidemiological studies between Jan 1965 and Dec 2012. Residents of e-waste sites are exposed to elevated levels of HMs and POPs, with children and pregnant women more susceptible to the adverse effects on biological systems and organs. The neonatal growth indices and hormone levels were detrimentally affected. There were possible associations between chronic exposure to toxic chemicals and DNA lesions, telomere attrition, elevated oxidative stress, etc. A more recent follow-up review [*Parvez et al.*, 2021] based on 70 (66 in China, 2 in Vietnam, 1 in India, 1 in Ghana) studies conducted between Dec 2012 to Jan 2020 showed more detailed analyses disclosing the following adverse health impacts: (1) Growth and neurodevelopment effects, (2) Hormonal and immunological function, (3) Genetic and oxidative changes, (4) Respiratory, cardiovascular, and hematological changes, (5) Vaccine, olfactory, reproductive, and other health effects.

WHO [*WHO*, 2021] stated substances detected in e-waste recycling sites that are of significant public health concern: Pb, Cd, Hg, PCDDs, PM2.5, PCBs, PBDEs, per- and polyfluoroalkyl substances (PFAS), phthalate esters, organophosphate flame retardants (PFRs), and bisphenols. Based on various studies primarily conducted in China, it was

concluded that prenatal and childhood exposure to e-waste toxic chemicals are significantly correlated with (1) impaired neurodevelopment and behavior (Pb, Hg, and some organic chemicals such as PCBs), (2) adverse birth outcomes (PAHs, Pb, Cd, Ni, and Cr), (3) damaged lung function and respiratory systems (cough, wheezing, and asthma) (Cr, Mn, and Pb), (4) impaired thyroid function (PCBs and PBDEs), (5) impaired cardiovascular system function (Pb and PAHs), (6) DNA damage (Pb, Cr, Cd, and Ni), (7) weakened immune system functions (to common infections such as from hepatitis B, ear and respiratory infections), reduced response to immunization (some organics), more susceptible to allergies and autoimmune diseases (some HMs), and suppression of immune system (Pb and Cd), and (8) increased chronic diseases (cancer and cardiovascular disease) at a later stage in life (various toxic chemicals).

Because of their hand-to-mouth activities and spending more time contacting the floor coated with dust and dirt, children are more susceptible to exposure through oral intake and dermal contact with contaminated soil/dust. Furthermore, due to their smaller size, less developed organs and immune systems, and rapid growth and development, they tend to absorb higher proportions of pollutants. They are less able to metabolize and eliminate toxic substances from their bodies than adults. For pregnant women working or residing close to e-waste sites, there are dangers of fetal exposure to various toxic chemicals, leading to short-term impacts on the pregnancy and long-term effects on the health of new-borns in childhood or adult life [*WHO*, 2021].

## 7. Policy and Management

Some countries, such as Australia, dispose of e-waste in landfills, generating leachates containing high concentrations of toxic metals and flame retardants [*Kiddee et al.*, 2013a]. The leached toxic chemicals may find their way into the waterways. Through bioaccumulation and biomagnification in food chains, some of our crops and aquatic products accumulate incredibly high concentrations of poisonous chemicals, posing health threats. A more effective collection, disposal, and recycling strategy should be established.

### 7.1. Responsibilities of Manufacturers and Recyclers

It is critical to follow the EU Regulations on Waste Electrical and Electronic Equipment (WEEE) and the Restriction of Hazardous Substances Directive (RoHS) not to use certain harmful materials (such as Hg and Cd) to manufacture the products and for recycling e-waste [*Kiddee et al.*, 2013a]. The Extended Producer Responsibility (EPR) should be in place to regulate the manufacturers' responsibilities for appropriate management. Some regions/countries, such as Hong Kong (China) and Taiwan (China), the USA, Switzerland, Japan, etc., implemented the EPR to regulate the responsibilities of various sectors: manufacturers, retailers, and relevant administrations to properly manage e-waste. Unfortunately, these policies tend to focus on pre-contamination rather than post-contamination management.

Receiving countries of e-waste should establish and implement regulations and policies to avoid illegal imports and recycling. Techniques for e-waste recycling should be improved. Centralized dismantling and treatment of e-waste using more sophisticated equipment and methods are also needed. National strategies for managing e-waste should include (1) Effective environmental education, (2) Prohibiting illegal import/transaction, (3) Forbidding illegal recycling activities, (4) Reinforcing regulations and laws, (5) Centralizing and encouraging legal recycling activities, and (6) Continuous monitoring [*Lin et al.*, 2022b].

### 7.2. International Conventions Should Be Revisited

The loopholes of the e-waste movement from more wealthy countries to other countries possess less stringent environmental laws, and less prosperous economies should be plugged. Unfortunately, the USA, the largest e-waste exporter, has not signed the convention. It is vital to check the effectiveness of the Basel Convention on the Control of

Transboundary Movements of Hazardous Wastes and their Disposal (entered into force in 1998). The Basel Convention intended to protect human and environmental health from hazardous wastes (including e-waste) by restricting its transboundary movement. It comprises a three-step approach: (1) minimize waste generation, (2) treat waste near where it is produced, and (3) reduce its international movement.

Under the Basel Convention, a legal loophole exists that the export of whole products is allowed to other countries if they are not purposed for recycling, e.g., for donation for reuse. As such, a substantial amount of waste is being exported as reusable equipment other than waste. One solution to close this legal loophole is only to allow the export of materials that could be used as raw materials, such as crushed glass, shredded plastic, aggregated metal, etc. [*Wong et al.*, 2012]

### 7.3. Tracking the Global Movement of E-waste is Essential

The global movement across international borders should be discouraged. The Basal Network has done an excellent job of tracking illegal activity, with more wealthy countries sending their trash to other countries with less developed environmental laws and regulations. Some efforts have been made to address the problem since 2010. The initiative related to 'Solving the E-waste Problem Initiative (STEP)' was jointly launched by the US Environmental Protection Agency and the United Nations University (UNU). Projects included the 'Person-in-the-Port' for tracking e-waste movements in Nigeria and dismantling facility improvement in Ethiopia. The EPA also made attempts in 2020, collaborating with various environmental authorities in Asia, Africa, Latin America, North America, and the Caribbean to manage e-waste more effectively. Nevertheless, the Basel Network's recent finding on tracking the global movement of e-waste has pointed out the deficiencies [*Lin et al.*, 2019].

## 8. Site Remediation

There are techniques successfully developed to decontaminate soil/sediment/water contaminated by mixtures of toxic metals and POPs that we can adopt to clean up contaminated sites derived from e-waste activities. The environmental behavior of toxic chemicals derived from uncontrolled e-waste recycling should be better understood. Different contaminated environmental compartments should be remediated using various techniques [*Lin et al.*, 2022b].

### 8.1. Remediation of air

In-workshop air treatment facility should be installed for cleaning the e-waste processing air before discharging it into the ambient environment. The gas treatment reactor consists of a spray tower, electrostatic precipitation, and photocatalysis. It can effectively remove almost 70% of volatile organic compounds (VOC) (i.e., halogenated hydrocarbons, aromatic hydrocarbons, and ethyl acetate) after 60 days. In addition, particles of different sizes and water-soluble gaseous pollutants from the polluted air could be efficiently removed by electrostatic precipitation. The powerful and nonselective oxidants could oxidize the levels of POPs via photocatalysis [*Zhang et al.*, 2019].

### 8.2. Remediation of water

Low-cost permeable reactive barriers supplemented by waste materials such as coal fly ash and wood-derived biochar can prevent the leaching of toxic metals from e-waste-contaminated soils. Low-cost adsorbents, such as coal fly ash (CFA) and food waste compost (FWC), can effectively adsorb toxic metals in water. POPs in water could be degraded via integrated chemical and biological approaches [*Beiyuan et al.*, 2017].

Chelating agents can remove HMs for ex-situ wastewater treatment, while wetland plants can stabilize toxic metals for in-situ treatment. Wetland plants: water hyacinth (*Eichhornia crassipes*), common reed (*Phragmites australis*), bulrush (*Typha* sp.), and vetiver

grass (*Chrysopogon zizanioides*) are potential candidates to achieve the purpose [*Deng et al.*, 2016].

### 8.3. Remediation of sediment/soil

#### *8.3.1. Dredging and excavation – for removing most toxic soils*

Soils/sediments serve as sinks of pollutants. POPs such as PBDEs are readily adsorbed by sediment or soil particles instead of accumulated in water. Therefore, they should be excavated and treated by stabilization (mixing with a binding agent) and reused or disposed of in landfills. For example, part of the contaminated sediment/soil (about 77,000 $m^2$) in Guiyu was either excavated, replaced by clean soil, or washed [*Gdut SII*, 2020].

#### *8.3.2. 8.3.1 Soil washing – for extracting and degrading pollutants*

Generally, soil washing using extractants or solvents can enhance pollutant extraction and degradation. Chemicals extract, degrade, or fix pollutants; oxidation and/or degradation could be used simultaneously. Vegetable oil and inexpensive chelants can serve the purpose. A study using hydroxypropyl-$\beta$-cyclodextrin (HPCD), citric acid (CA), and sodium persulfate (SP) achieved satisfactory results in treating e-waste contaminated soils (HPCD was effective for extraction of POPs, CA for extraction of metals, and SP for further oxidation of POPs) [*Chen et al.*, 2017]. Environmentally friendly and biodegradable solvents, e.g., sunflower and peanut oil, effectively removed HMs and POPs. The pollutant removal efficiency of soil washing can be further enhanced by different means, e.g., ultrasonication-assisted soil washing. It can strengthen the mobilization of pollutants and reduce the washing time. Soil washing and assisted/enhanced phytoremediation are effective methods for site remediation as they are cost-effective and sustainable, with more significant economic benefits in the long term. However, higher plants and associated microbes are critical components in restoring the normal soil function of the highly disturbed environment, which may require long-term stabilization after soil washing (please refer to the below section on phytoremediation).

#### *8.3.3. Nanoparticle and biochar – for effective pollutant degradation*

Nanoscale zero-valent iron (nZVI) and Pd/Fe bimetallic nanoparticles were effective in degrading PCBs (i.e., hydrodechlorination) soils from Taizhou (removal efficiencies: 50–80%) [*Chen et al.*, 2014]. A study also showed that Ni/Fe bimetallic nanoparticles can degrade PBDEs (i.e., debromination), removing PBDEs spiked into clean soil [*Xie et al.*, 2014]. Adding biochar could disperse the nanoparticles, thereby adsorbing metal ions more effectively with negatively charged carboxyl and hydroxyl groups. Debromination of PBDEs was greatly enhanced due to the closer contact between nanoparticles and PBDEs, achieving a removal efficiency of 90% in 72 h. Furthermore, biochar can effectively adsorb and immobilize degradation products and metal ions (such as Ni) investigated in the study to avoid secondary pollution [*Wu et al.*, 2016].

#### *8.3.4. Chelates – for enhancing plant metal uptake and microbial degradation*

It is a common practice to use chelates such as S,S-ethylenediamine disuccinic acid (EDDS), and ethylenediamine tetraacetic acid (EDTA) to form metal complexes to lower their toxicity and availability. EDDS is more sustainable because it is more biodegradable and less toxic to biota when compared with EDTA. Soils from a past e-waste-opening site were extracted with EDDS (1:10 ratio of soil: extractant, w/v) observed that a high concentration of EDDS solution can remove more metals, pending on soil pH and target metal. Combining organic acid with EDDS was also valuable in removing toxic metals in the highly contaminated soil with removal efficiencies between 2.7 to 78% pending on metal, acid type, and acid dosage [*Yang et al.*, 2012].

*8.3.5. Bioremediation*

Bioremediation and phytoremediation are biological processes that can maintain soil health during and after remediation, though they are slower than physical, chemical, and/or thermal approaches. Bacteria are vital to degrade and detoxify pollutants, enhancing pollutant uptake and site stabilization using higher plants. Deep tillage was employed with bioremediation, phytoremediation, or chemical remediation to clean up the contaminated farm soils (64,000 $m^2$) in Guiyu, significantly reducing Cu and Ni [*Gdut SII*, 2020]. The local government (Guiyu Town) launched active soil remediation projects in 2010 (via soil treatment companies) adopting the following methods: (1) Bioremediation- biopiles added with organic materials to assist microbial degradation of pollutants, (2) Phyto-microbial remediation – e.g., the use of a wetland plant (*Canna indica*) and associated microbes to degrade and detoxify PCBs, (3) Phytochemical remediation – chemical agents are added to assist the wetland pant (*Aeschynomene indica*) for removing Pb, Mn, Cr, and Zn. After the treatment, the soil quality complied with the national standard for construction lands (GB36600-2018) [*MEE (The Ministry of Ecology and Environment of the People's Republic of China)*, 2019].

*8.3.6. Phytoremediation*

Field observation and screening tests must identify suitable plant and microbial species. Plant species that are not invasive, such as infertile vetiver grass, can be used directly. Combining plant species and associated microbes can enhance plants' pollutant uptake, stabilize the contaminated sites, and degrade and detoxify toxic chemicals. Metal hyperaccumulator plants can extract toxic metals and deposit them in their above-ground tissues. The metals can be removed from the sites upon harvest. Although some plants do not take up and accumulate substantial metals in their upper plant tissues, they can stabilize and degrade pollutants when interacting with rhizospheric microbes (bacteria and fungi). Therefore, they can restore soil functions and health. As such, some residual organic pollutants can be degraded, pending on the plant species and types of pollutants.

It is essential to select suitable and native plant species before remediation. Ideally, the plants should be able to deal with multiple pollutants simultaneously. The soil collected from Taizhou was planted with five upland plants: pumpkin (*Cucurbita pepo*), tall fescue (*Festuca arundinacea*, milk vetch (*Astragalus sinicus*), alfalfa (*Medicago sativa*), and ryegrass (*Lolium perenne*), and two wetland plants: rice (*Oryza sativa*) cultivars Huanghuazhan and Xiushui 1. Results indicated that rice cv. Xiushui 134, rice cv. Huanghuazhan and ryegrass were more effective in removing BDE-209 (with removal efficiencies of 52.9, 41.9, and 38.7%, respectively) [*He et al.*, 2015]. Another study also revealed that rice was relatively efficient in removing PCBs (35–45%) [*Chen et al.*, 2010].

Vetiver grass (*C. zizanioides*), with its high tolerance to environmental stress, relatively large biomass, and extensive root system, is an excellent candidate for stabilizing riverbanks, mine tailings, and contaminated sites containing mixtures of HMs and POPs [*Chen et al.*, 2020]. Planting vetiver grass in soils (from an e-waste site after soil washing) can degrade PBDEs, PCBs, and PAHs (35–45% removal for these POP residues. The root-associated microbes enhanced the plant, subsequently reactivated microbial activities with higher microbial biomass and biodiversity, and restored soil health [*Ye et al.*, 2015].

Suitable microbes associated with higher plants can improve remediation efficiency, involving plant-regulated degradation/detoxification and direct uptake of organic pollutants and toxic metals, notably mycorrhizal fungi. Some bacteria associated with specific plant species can degrade POPs, such as PAHs, PCBs, and PBDEs. Mycorrhizal fungus-induced bacteria significantly degrade organic pollutants such as PAHs. Species combination (plants and microbes) and removal efficiency of contaminants should be tested before field application [*Chen et al.*, 2020; *Lin et al.*, 2022b].

Remediating e-waste-contaminated soils containing mixtures of POPs and HMs poses a severe challenge. Table 3 shows limited information about laboratory experiments on e-waste soils collected with e-waste sites dealing with complex pollution. In general, soil

washing using cyclodextrin and tea saponin could desorb pollutants. Adding chelates could enable higher plants to take up metals. Microbes alone can degrade pollutants, notably POPs. However, higher plants associated with rhizospheric microbes (fungi and bacteria) are necessary for removing and degrading POPs and HMs for long-term sustainability. Remediating e-waste-contaminated soils using different combinations according to specific site conditions seems effective.

**Table 3**. Remediation of e-waste soils contaminated with mixtures of POPs and HMs.

| Reference | Pollutants | Treatments | Mechanisms | Remarks |
|---|---|---|---|---|
| Chen et al. [2017] | PAHs, PCBs, PBDEs/Cu, Pb, Ni | HPCD, CA, SP | Extraction and oxidation | 280-240 min |
| Ye et al. [2015a] | PBDEs/Pb, Cd | Carboxymethyl chitosan in the oil-water solvent; bacteria | Extraction and degradation | 2 h |
| Ye et al. [2015b] | PBDEs, PCBs, PAHs/Cu, Pb, Ni | Ultrasound, cyclodextrin, tea saponin | Desorption of pollutants during soil washing | 60 min |
| Shen et al. [2009] | PBDEs, PCBs, PAHs/Pb, Ni | Tea saponin in a peanut oil–water solvent; vetiver grass (C. zizanioides) | Extraction and degradation | Soil washing: 1 h, plant growth: 4 months |
| Wang et al. [2015] | PBDEs, PCBs/Cu | EDDS and corn (Zea mays) | EDDS-triggered pollutant uptake by plants | 42 days |
| Luo et al. [2015] | PCBs/Cu, Zn | EDDS and plant growth-promoting bacterium with corn (Z mays) | Chelant- and PGPR-assisted phytoextraction and phytodegradation | 1 month |
| Sun et al. [2016] | PAH (phenanthrene)/Cd | EDTA, ethyl lactate, willow (Salix sp.) | EDTA and ethyl lactate enhanced PAH and Cd uptake by willow | 30-45 days |
| Li et al. [2021] | PAH (pyrene)/Cd | Urea, willow (Salix sp.) | Urea enhanced the uptake of PAH and Cd by willow | 60 days |

Successful strategies have been implemented since 2000 in Guiyu: (1) Biopiles incorporated with organic materials to promote the degradation of pollutants; (2) A constructed wetland consisting of *Canna indica* (an emergent wetland plant) with root-associated microbes to degrade PCB; (3) Chelates added to decontaminate Pb, Mn, Cr, and Zn by another wetland plant *Aeschynomene indica*. The soil quality complied with the national standard for construction land after treatments [*MEE (The Ministry of Ecology and Environment of the People's Republic of China)*, 2019].

The intercropping system could be employed for contaminated farm soils by planting a plant species dealing with pollutants and a crop for human consumption. Taizhou successfully used this system to treat contaminated farm soils using legume-grass cropping to remove phthalic acid esters (PAEs) [*Ma et al.*, 2013]. Including metal hyperaccumulating plants with crops could remove toxic metals from the soil, resulting in lower metal uptake in crops and simultaneously producing crops for safer consumption. A substantial amount of soil metals could be removed upon harvest. Alfred stonecrop (*Sedum alfredii*, a Cd/Zn hyperaccumulator) was planted with vegetable upland Kangkong (*Ipomoea aquatica*) in an artificial Cd/Zn contaminated soil. The vegetable contained higher biomass and lower Cd content in the intercropping system assisted with symbiotic fungi than in the monoculture [*Hu et al.*, 2013].

Other successful phytoremediation approaches on sites contaminated with complex pollutants similar to e-waste recycling sites can serve as valuable references. It is expected that the remediation techniques can apply to emerging e-waste sites in other countries/regions as the basic principle of environmental remediation is universal. In e-waste-

receiving countries, confronting challenges to decontaminate such complex contamination could be a significant socioeconomic concern. It is best to start with pilot-scale remediation trials (greenhouse trials), selecting the most appropriate technique(s) at larger scales (field trials), using the above successful strategies obtained in China and elsewhere.

## 9. Conclusion

There is an enormous data gap between exposure quantification and possible health effects. However, we possess enough evidence that e-waste contains various toxic chemicals that cause adverse environmental impact and toxicity to the biota, including humans. Different toxic chemicals exert various negative health impacts. Using bioindicators (hair, serum, urine, blood, human milk) to indicate the extent of health damage is recommended as it can help to obtain proper knowledge of various exposure pathways. This will help design mitigation plans. Detailed toxicological and epidemiological evidence is still insufficient. Therefore, more studies are essential to elucidate and provide comprehensive information on environmental and public health risks that e-waste constituents pose. It is also vital that these studies can cover the acute and chronic health risks of toxic chemicals to set their updated reference doses. Monitoring the development and health status of infants and children born and brought up in the e-waste sites is critical.

Manufacturers should fulfill their 'Extended Producer Responsibility' and polluters pay concept. They should also follow EU Directive to stop using toxic chemicals (such as Hg) in their products. The international movement of e-waste should be solved via national and international cooperation. Wealthier countries must stop exploiting poorer countries with less stringent environmental laws and poorer economies. Imposing tighter control of e-waste movement across international borders is a top priority. The loophole of the Basel Convention should be closed by having a better definition of e-waste. The USA should ratify the conventions not to export e-waste.

Each country/region should establish its strategy for dealing with the e-waste problem. Formulating new and strengthening existing laws would greatly help. Centralized sophisticated treatment facilities for recycling e-waste should be installed in various areas to minimize extensive impacts. Environmental protection and education should be strengthened in receiving countries. China has been the primary destination. As such, the policy, management, and remediation strategies adopted in China's two e-waste mega sites could serve as valuable references for other countries receiving e-waste.

## Acknowledgments

The study was carried out in the laboratory "Soil Health" of the Southern Federal University with the financial support of the Ministry of Science and Higher Education of the Russian Federation, agreement no. 075-15-2022-1122.

## References

Alharbi, O. M. L., A. A. Basheer, R. A. Khattab, and I. Ali (2018), Health and environmental effects of persistent organic pollutants, *Journal of Molecular Liquids*, *263*, 442–453, https://doi.org/10.1016/j.molliq.2018.05.029.

Beiyuan, J., D. C. W. Tsang, M. Valix, W. Zhang, X. Yang, Y. S. Ok, and X.-D. Li (2017), Selective dissolution followed by EDDS washing of an e-waste contaminated soil: Extraction efficiency, fate of residual metals, and impact on soil environment, *Chemosphere*, *166*, 489–496, https://doi.org/10.1016/j.chemosphere.2016.09.110.

Chan, J. K. Y., and M. H. Wong (2013), A review of environmental fate, body burdens, and human health risk assessment of PCDD/Fs at two typical electronic waste recycling sites in China, *Science of The Total Environment*, *463-464*, 1111–1123, https://doi.org/10.1016/j.scitotenv.2012.07.098.

Chan, J. K. Y., G. H. Xing, Y. Xu, Y. Liang, L. X. Chen, S. C. Wu, C. K. C. Wong, C. K. M. Leung, and M. H. Wong (2007), Body Loadings and Health Risk Assessment of Polychlorinated Dibenzo-p-dioxins and Dibenzofurans at an Intensive Electronic Waste Recycling Site in China, *Environmental Science & Technology*, *41*(22), 7668–7674, https://doi.org/10.1021/es071492j.

Chen, F., Z. Luo, G. Liu, Y. Yang, S. Zhang, and J. Ma (2017), Remediation of electronic waste polluted soil using a combination of persulfate oxidation and chemical washing, *Journal of Environmental Management*, *204*, 170–178, https://doi.org/10.1016/j.jenvman.2017.08.050.

Chen, X., X. Yao, C. Yu, X. Su, C. Shen, C. Chen, R. Huang, and X. Xu (2014), Hydrodechlorination of polychlorinated biphenyls in contaminated soil from an e-waste recycling area, using nanoscale zerovalent iron and Pd/Fe bimetallic nanoparticles, *Environmental Science and Pollution Research*, *21*(7), 5201–5210, https://doi.org/10.1007/s11356-013-2089-8.

Chen, X. W., J. T. F. Wong, J.-J. Wang, and M. H. Wong (2020), Vetiver grass-microbe interactions for soil remediation, *Critical Reviews in Environmental Science and Technology*, *51*(9), 897–938, https://doi.org/10.1080/10643389.2020.1738193.

Chen, Y., X. Tang, S. A. Cheema, W. Liu, and C. Shen (2010), $\beta$-cyclodextrin enhanced phytoremediation of aged PCBs-contaminated soil from e-waste recycling area, *Journal of Environmental Monitoring*, *12*(7), 1482, https://doi.org/10.1039/c0em00029a.

Deng, D., J. Liu, M. Xu, G. Zheng, J. Guo, and G. Sun (2016), Uptake, translocation and metabolism of decabromodiphenyl ether (BDE-209) in seven aquatic plants, *Chemosphere*, *152*, 360–368, https://doi.org/10.1016/j.chemosphere.2016.03.013.

Frazzoli, C., O. E. Orisakwe, and E. C. Ilo (2019), Electronic Waste and Human Health, in *Encyclopedia of Environmental Health*, pp. 315–323, Elsevier, https://doi.org/10.1016/b978-0-12-409548-9.02170-9.

Fu, J., Q. Zhou, J. Liu, W. Liu, T. Wang, Q. Zhang, and G. Jiang (2008), High levels of heavy metals in rice (Oryzasativa L.) from a typical E-waste recycling area in southeast China and its potential risk to human health, *Chemosphere*, *71*(7), 1269–1275, https://doi.org/10.1016/j.chemosphere.2007.11.065.

Gdut SII (2020), Evaluation of the environmental status of Guiyu Circular Economy Industrial Park in Chaoyang District of Shantou City.

Grant, K., F. C. Goldizen, P. D. Sly, M.-N. Brune, M. Neira, M. van den Berg, and R. E. Norman (2013), Health consequences of exposure to e-waste: a systematic review, *The Lancet Global Health*, *1*(6), e350–e361, https://doi.org/10.1016/s2214-109x(13)70101-3.

He, Y., X. Li, X. Shen, Q. Jiang, J. Chen, J. Shi, X. Tang, and J. Xu (2015), Plant-assisted rhizoremediation of decabromodiphenyl ether for e-waste recycling area soil of Taizhou, China, *Environmental Science and Pollution Research*, *22*(13), 9976–9988, https://doi.org/10.1007/s11356-015-4179-2.

Hu, J., J. Li, F. Wu, S. Wu, Z. Ye, X. Lin, and M. H. Wong (2013), Arbuscular mycorrhizal fungi induced differential Cd and P phytoavailability via intercropping of upland kangkong (Ipomoea aquatica Forsk.) with Alfred stonecrop (Sedum alfredii Hance): post-harvest study, *Environmental Science and Pollution Research*, *20*(12), 8457–8463, https://doi.org/10.1007/s11356-013-1903-7.

Kiddee, P., R. Naidu, and M. H. Wong (2013a), Metals and polybrominated diphenyl ethers leaching from electronic waste in simulated landfills, *Journal of Hazardous Materials*, *252-253*, 243–249, https://doi.org/10.1016/j.jhazmat.2013.03.015.

Kiddee, P., R. Naidu, and M. H. Wong (2013b), Electronic waste management approaches: An overview, *Waste Management*, *33*(5), 1237–1250, https://doi.org/10.1016/j.wasman.2013.01.006.

Lau, W. K. Y., P. Liang, Y. B. Man, S. S. Chung, and M. H. Wong (2013), Human health risk assessment based on trace metals in suspended air particulates, surface dust, and floor dust from e-waste recycling workshops in Hong Kong, China, *Environmental Science and Pollution Research*, *21*(5), 3813–3825, https://doi.org/10.1007/s11356-013-2372-8.

Leung, A. O. W., W. J. Luksemburg, A. S. Wong, and M. H. Wong (2007), Spatial Distribution of Polybrominated Diphenyl Ethers and Polychlorinated Dibenzo-p-dioxins and Dibenzofurans in Soil and Combusted Residue at Guiyu, an Electronic Waste Recycling Site in Southeast China, *Environmental Science & Technology*, *41*(8), 2730–2737, https://doi.org/10.1021/es0625935.

Leung, A. O. W., N. S. Duzgoren-Aydin, K. C. Cheung, and M. H. Wong (2008), Heavy Metals Concentrations of Surface Dust from e-Waste Recycling and Its Human Health Implications in Southeast China, *Environmental Science & Technology*, *42*(7), 2674–2680, https://doi.org/10.1021/es071873x.

Leung, A. O. W., J. K. Y. Chan, G. H. Xing, Y. Xu, S. C. Wu, C. K. C. Wong, C. K. M. Leung, and M. H. Wong (2010), Body burdens of polybrominated diphenyl ethers in childbearing-aged women at an intensive electronic-waste recycling site in China, *Environmental Science and Pollution Research*, *17*(7), 1300–1313, https://doi.org/10.1007/s11356-010-0310-6.

Li, W., A. Fishman, and V. Achal (2021), Ureolytic bacteria from electronic waste area, their biological robustness against potentially toxic elements and underlying mechanisms, *Journal of Environmental Management*, *289*, 112,517, https://doi.org/10.1016/j.jenvman.2021.112517.

Lin, S., Y. B. Man, K. L. Chow, C. Zheng, and M. H. Wong (2019), Impacts of the influx of e-waste into Hong Kong after China has tightened up entry regulations, *Critical Reviews in Environmental Science and Technology*, *50*(2), 105–134, https://doi.org/10.1080/10643389.2019.1619377.

Lin, S., M. U. Ali, C. Zheng, Z. Cai, and M. H. Wong (2022a), Toxic chemicals from uncontrolled e-waste recycling: Exposure, body burden, health impact, *Journal of Hazardous Materials*, *426*, 127,792, https://doi.org/10.1016/j.jhazmat.2021.127792.

Lin, S., X. W. Chen, Z. Cai, J. Shi, J. Fu, G. Jiang, and M. H. Wong (2022b), Remediation of emerging contaminated sites due to uncontrolled e-waste recycling, *Chemical Engineering Journal*, *430*, 133,169, https://doi.org/10.1016/j.cej.2021.133169.

Lopez, B. N., Y. B. Man, Y. G. Zhao, J. S. Zheng, A. O. W. Leung, J. Yao, and M. H. Wong (2010), Major Pollutants in Soils of Abandoned Agricultural Land Contaminated by e-Waste Activities in Hong Kong, *Archives of Environmental Contamination and Toxicology*, *61*(1), 101–114, https://doi.org/10.1007/s00244-010-9590-6.

Luo, C., S. Wang, Y. Wang, R. Yang, G. Zhang, and Z. Shen (2015), Effects of EDDS and plant-growth-promoting bacteria on plant uptake of trace metals and PCBs from e-waste-contaminated soil, *Journal of Hazardous Materials*, *286*, 379–385, https://doi.org/10.1016/j.jhazmat.2015.01.010.

Luo, Q., Z. W. Cai, and M. H. Wong (2007a), Polybrominated diphenyl ethers in fish and sediment from river polluted by electronic waste, *Science of The Total Environment*, *383*(1-3), 115–127, https://doi.org/10.1016/j.scitotenv.2007.05.009.

Luo, Q., M. Wong, and Z. Cai (2007b), Determination of polybrominated diphenyl ethers in freshwater fishes from a river polluted by e-wastes, *Talanta*, *72*(5), 1644–1649, https://doi.org/10.1016/j.talanta.2007.03.012.

Ma, T. T., Y. Teng, Y. M. Luo, and P. Christie (2013), Legume-grass intercropping phytoremediation of phthalic acid esters in soil near an electronic waste recycling site: a field study, *International Journal of Phytoremediation*, *15*(2), 154–167, https://doi.org/10.1080/15226514.2012.687016.

Man, Y. B., K. L. Chow, H. S. Wang, X. L. Sun, S. C. Wu, Z. W. Cai, Y. Kang, H. Li, J. S. Zheng, J. P. Giesy, and M. H. Wong (2014), Human health risk assessment of soil dioxin/furans contamination and dioxin-like activity determined by ethoxyresorufin-O-deethylase bioassay, *Environmental Science and Pollution Research*, *22*(7), 5218–5227, https://doi.org/10.1007/s11356-014-3909-1.

Man, Y. B., K. L. Chow, G. H. Xing, J. K. Y. Chan, S. C. Wu, and M. H. Wong (2017), A pilot study on health risk assessment based on body loadings of PCBs of lactating mothers at Taizhou, China, the world's major site for recycling transformers, *Environmental Pollution*, *227*, 364–371, https://doi.org/10.1016/j.envpol.2017.04.069.

Man, Y. B., K. L. Chow, F. Zhang, K. M. Lei, A. O. W. Leung, W. Y. Mo, and M. H. Wong (2021), Protecting water birds of wetlands: Using toxicological tests and ecological risk assessment, based on metal/loid (s) of water, sediment and biota samples, *Science of The Total Environment*, *778*, 146,317, https://doi.org/10.1016/j.scitotenv.2021.146317.

MEE (The Ministry of Ecology and Environment of the People's Republic of China) (2019), Dig up and Combine "Electronic Waste City" Transformation and Crossing – Comprehensive Treatment Practice of "Dispersion and Pollution" in Guiyu Town, Shantou City, Guangdong Province, (date of access: 16.05.2023).

Parvez, S. M., F. Jahan, M.-N. Brune, J. F. Gorman, M. J. Rahman, D. Carpenter, Z. Islam, M. Rahman, N. Aich, L. D. Knibbs, and P. D. Sly (2021), Health consequences of exposure to e-waste: an updated systematic review, *The Lancet Planetary Health*, *5*(12), e905–e920, https://doi.org/10.1016/S2542-5196(21)00263-1.

Purchase, D., G. Abbasi, L. Bisschop, D. Chatterjee, C. Ekberg, M. Ermolin, P. Fedotov, H. Garelick, K. Isimekhai, N. G. Kandile, M. Lundström, A. Matharu, B. W. Miller, A. Pineda, O. E. Popoola, T. Retegan, H. Ruedel, A. Serpe, Y. Sheva, K. R. Surati, F. Walsh, B. P. Wilson, and M. H. Wong (2020), Global occurrence, chemical properties, and ecological impacts of e-wastes (IUPAC Technical Report), *Pure and Applied Chemistry*, *92*(11), 1733–1767, https://doi.org/10.1515/pac-2019-0502.

Roundup.com (2022), Latest global e-waste statistics and what they tell us, https://theroundup.org/global-e-waste-statistics/, (date of access: 16.05.2023).

Shen, C., X. Tang, S. A. Cheema, C. Zhang, M. I. Khan, F. Liang, X. Chen, Y. Zhu, Q. Lin, and Y. Chen (2009), Enhanced phytoremediation potential of polychlorinated biphenyl contaminated soil from e-waste recycling area in the presence of randomly methylated-$\beta$-cyclodextrins, *Journal of Hazardous Materials*, *172*(2-3), 1671–1676, https://doi.org/10.1016/j.jhazmat.2009.08.064.

Sun, Y. Y., H. X. Xu, J. H. Li, X. Q. Shi, J. C. Wu, R. Ji, and H. Y. Guo (2015), Phytoremediation of soils contaminated with phenanthrene and cadmium by growing willow (Salix × Aureo-Pendula CL 'j1011'), *International Journal of Phytoremediation*, *18*(2), 150–156, https://doi.org/10.1080/15226514.2015.1073668.

Wang, F., A. O. W. Leung, S. C. Wu, M. S. Yang, and M. H. Wong (2009), Chemical and ecotoxicological analyses of sediments and elutriates of contaminated rivers due to e-waste recycling activities using a diverse battery of bioassays, *Environmental Pollution*, *157*(7), 2082–2090, https://doi.org/10.1016/j.envpol.2009.02.015.

Wang, S., Y. Wang, W. Lei, Y. Sun, Y. Wang, C. Luo, and G. Zhang (2015), Simultaneous enhanced removal of Cu, PCBs, and PBDEs by corn from e-waste-contaminated soil using the biodegradable chelant EDDS, *Environmental Science and Pollution Research*, *22*(22), 18,203–18,210, https://doi.org/10.1007/s11356-015-5045-y.

WHO (2021), Children and digital dumpsites: e-waste exposure and child health: web annex: literature review on the health effects of exposure to e-waste, https://www.who.int/publications/i/item/9789240024106, (date of access: 16.05.2023).

Wong, M. H., S. C. Wu, W. J. Deng, X. Z. Yu, Q. Luo, A. O. W. Leung, C. S. C. Wong, W. J. Luksemburg, and A. S. Wong (2007), Export of toxic chemicals - A review of the case of uncontrolled electronic-waste recycling, *Environmental Pollution*, *149*(2), 131–140, https://doi.org/10.1016/j.envpol.2007.01.044.

Wong, M. H., A. O. Leung, S. Wu, C. K. Leung, and R. Naidu (2012), Mitigating environmental and health risks associated with uncontrolled recycling of electronic waste: Are international and national regulations effective?, in *Environmental Contamination*, pp. 214–229, CRC Press, https://doi.org/10.1201/b12531-14.

Wu, J., Y. Q. Yi, Y. Q. Li, Z. Fang, and E. P. Tsang (2016), Excellently reactive Ni/Fe bimetallic catalyst supported by biochar for the remediation of decabromodiphenyl contaminated soil: Reactivity, mechanism, pathways and reducing secondary risks, *Journal of Hazardous Materials*, *320*, 341–349, https://doi.org/10.1016/j.jhazmat.2016.08.049.

Xie, Y., Z. Fang, W. Cheng, P. E. Tsang, and D. Zhao (2014), Remediation of polybrominated diphenyl ethers in soil using Ni/Fe bimetallic nanoparticles: Influencing factors, kinetics and mechanism, *Science of The Total Environment*, *485-486*, 363–370, https://doi.org/10.1016/j.scitotenv.2014.03.039.

Xing, G. H., S. C. Wu, and M. H. Wong (2010), Dietary exposure to PCBs based on food consumption survey and food basket analysis at Taizhou, China - The World's major site for recycling transformers, *Chemosphere*, *81*(10), 1239–1244, https://doi.org/10.1016/j.chemosphere.2010.09.032.

Yang, R., C. Luo, G. Zhang, X. Li, and Z. Shen (2012), Extraction of heavy metals from e-waste contaminated soils using EDDS, *Journal of Environmental Sciences*, *24*(11), 1985–1994, https://doi.org/10.1016/s1001-0742(11)61036-x.

Ye, M., M. Sun, J. Wan, G. Fang, H. Li, F. Hu, X. Jiang, and F. O. Kengara (2014), Evaluation of enhanced soil washing process with tea saponin in a peanut oil-water solvent system for the extraction of PBDEs/PCBs/PAHs and heavy metals from an electronic waste site followed by vetiver grass phytoremediation, *Journal of Chemical Technology & Biotechnology*, *90*(11), 2027–2035, https://doi.org/10.1002/jctb.4512.

Ye, M., M. Sun, J. Wan, G. Fang, H. Li, F. Hu, X. Jiang, and F. O. Kengara (2015), Enhanced soil washing process for the remediation of PBDEs/Pb/Cd-contaminated electronic waste site with carboxymethyl chitosan in a sunflower oil-water solvent system and microbial augmentation, *Environmental Science and Pollution Research*, *22*(4), 2687–2698, https://doi.org/10.1007/s11356-014-3518-z.

Zhang, W., G. Li, H. Liu, J. Chen, S. Ma, and T. An (2019), Micro/nano-bubble assisted synthesis of Au/TiO2@CNTs composite photocatalyst for photocatalytic degradation of gaseous styrene and its enhanced catalytic mechanism, *Environmental Science: Nano*, *6*(3), 948–958, https://doi.org/10.1039/c8en01375f.

Russian Journal of Earth Sciences

Special Issue: "Fundamental and Applied Aspects of Geology, Geophysics and Geoecology"

# Monitoring the Content of Polycyclic Aromatic Hydrocarbons in Soils and Natural Herbal Vegetation of Technogeneously Polluted Territory

**Andrey Barbashev[1], Svetlana Sushkova[1], Tamara Dudnikova[1], Tatiana Minkina[1], Vladislav Popov[1]**

[1]Southern Federal University, Rostov-on-Don, Russia

* **Correspondence to:** Andrey Barbashev, Barbashev_andrei@mail.ru

**Abstract:** Currently, one of the most important problems is the pollution of natural systems by polycyclic aromatic hydrocarbons (PAHs) as a result of human industrial activity. In this connection, it is necessary to carry out monitoring of territories subjected to the anthropogenic impact. As a result of the monitoring study of the impact zone of the fuel and energy complex enterprises, it was found that polycyclic aromatic hydrocarbons (PAHs) in the soil of the impact zone accumulate mainly up to 2 km along the line of the prevailing wind rose from the enterprise. The group composition of PAHs is dominated by 4-ring compounds, exceeding the background values by 23 times. At the same time, plants growing on the territory of the impact zone mainly accumulate such compounds as fluoranthene, pyrene, benzo[a]anthracene and phenanthrene, which is 70–82% of the total content of polyarenes in various parts of plants.

**Keywords:** PAHs, benzo[a]pyrene, monitoring, soil-plants.

**Citation:** Barbashev A., Sushkova S., Dudnikova T., Minkina T., Popov V. (2023), Monitoring the Content of Polycyclic Aromatic Hydrocarbons in Soils and Natural Herbal Vegetation of Technogeneously Polluted Territory, *Russian Journal of Earth Sciences*, Vol. 23, ES0209, https://doi.org/10.2205/2023ES02SI09

## 1. Introduction

Studies of soil and vegetation cover through monitoring studies are primary in assessing food security and carcinogenic risk, and also serve as the basis for engineering and survey work [*Cristale et al.*, 2012; *Tobiszewski and Namieśnik*, 2012]. Polycyclic aromatic hydrocarbons (PAHs) are a class of widespread pollutants, many of which exhibit mutagenic, teratogenic, and carcinogenic effects on living organisms. Their prevalence in environmental objects is associated with the pyrolysis of hydrocarbon materials [*Tsibart and Gennadiev*, 2013; *Yunker et al.*, 2012]. The sources of formation and entry of these compounds into the environment are high-temperature and microbiological processes, as well as anthropogenic factors, which are mainly associated with the extraction, transportation and processing of fossil fuels, the impact of road and rail transport, energy, petrochemistry, and the production of building materials [*Kuppusamy et al.*, 2017; *Tsibart and Gennadiev*, 2013; *Yunker et al.*, 2012]. Emissions of pollutants into the atmosphere create technogenic halos around the emission source with an anomalous content of the pollutant for natural areas. Often, research on PAHs is focused on the study of 16 representatives of this group, included in the list of priority pollutants of the US Environmental Protection Agency [*US Environmental Protection Agency*, 2020]. In Russia, only benzo[a]pyrene (BaP) is subject to regulation for soils, the maximum permissible concentration (MPC) of which in soils is 20 µg/kg [*GN 2.1.7.2041-06*, 2006].

Since soils and plants are and function in close relationship, an integral system is formed that links the processes of accumulation and transformation of PAHs [*Yakovleva*

Research Article

Received: 20 October 2023
Accepted: 27 November 2023
Published: 15 December 2023

**Copyright:** © 2023. The Authors. This article is an open access article distributed under the terms and conditions of the Creative Commons Attribution (CC BY) license (https://creativecommons.org/licenses/by/4.0/).

*et al.*, 2008]. Therefore, one of the main tasks is to monitor the content of PAHs not only in the soils of impact zones, but also in wild vegetation. The aim of the work was to monitor the content of polycyclic aromatic hydrocarbons in soils and natural herbaceous vegetation of a technogenically polluted area.

## 2. Objects and methods

To conduct the study, 5 monitoring sites were laid and sampling was carried out [*GOST 17.4.3.01-2017*, 2019] on the territory of the Novocherkassk Power Station (NPS) impact zone, the largest enterprise of the fuel and energy complex and the main polluting enterprise in the south of Russia. Monitoring sites are located in the northwest (NW) direction from the enterprise (1n – 1.6 km NW, 2n – 6.9 km NW, 3n – 15.0 km NW, 4n – 20.0 km NW) are represented by Haplic chernozem and Gleyic Chernozems (site 2n) with similar physicochemical properties (Figure 1, Table 1). In the course of geobotanical expeditions, it was established that representatives of herbaceous plants, perennials, predominate on the monitoring sites of the NPS impact zone. Dominant species of natural herbaceous vegetation are represented by bluegrass (*Poa pratensis L.*), couch grass (*Elytrigia repens L.*) and sagebrush (*Artemisia austriaca Jacq.*). As a background, a monitoring site was laid on the territory of a specially protected natural area (SPNA) of the "Persianovsky reserved steppe" (Table 1).

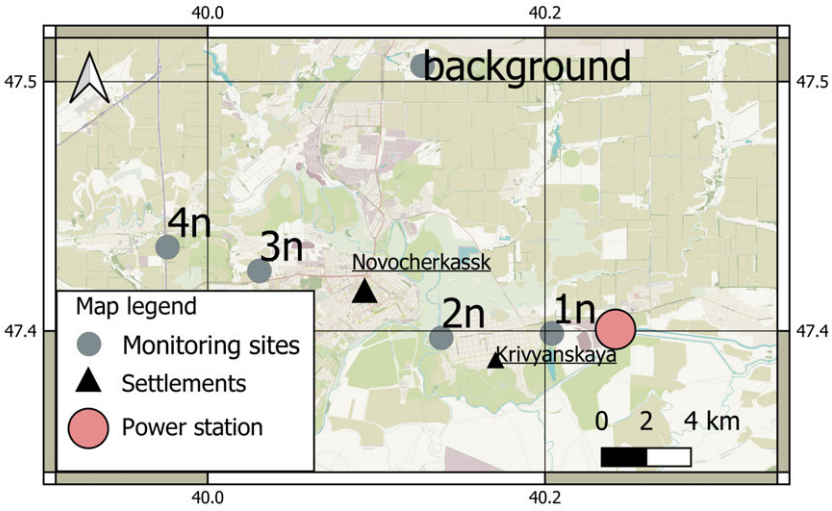


**Figure 1.** Location of monitoring sites.

**Table 1**. Soil properties of the monitoring sites of the study areas.

| Site number | Physical clay, % | Silt, % | Humus content, % | pH | CaCO3, % | Soil texture | Soil type |
|---|---|---|---|---|---|---|---|
| Persianovsky reserved steppe | | | | | | | |
| Background | 57.4 | 31.3 | 4.4 | 7.8 | 0.9 | Heavy loamy | Haplic Chernozem |
| Impact zone NAS | | | | | | | |
| 1n | 58.4 | 31.2 | 4.4 | 7.4 | 0.9 | Heavy loamy | Haplic Chernozem |
| 2n | 56.2 | 32.9 | 4.7 | 7.9 | 0.9 | | Gleyic Chernozems |
| 3n | 55.3 | 26.5 | 3.9 | 7.9 | 0.8 | | Haplic Chernozem |
| 4n | 53.5 | 26.7 | 3.9 | 7.7 | 0.7 | | Haplic Chernozem |

Extraction of PAHs in soil and plant samples was performed using subcritical water [*Sushkova et al.*, 2014, 2015]. A portion of a specially prepared soil or plant sample weighing

1 g, sifted through a 1 mm sieve, was placed in a stainless-steel extraction cartridge and hermetically screwed on both sides. The cartridge was installed in a thermostat and heated to 250 °C and a pressure of 100 atm within 30 min. After cooling the system, the cartridge was unscrewed, the contents were filtered two or three times until the solution was transparent. The resulting aqueous extract was mixed with 5 ml of n-hexane (analytical grade) and placed on a mechanical shaker for 15 minutes. The layers were separated on a separating funnel with a volume of 50 ml sequentially in three stages with the next portion of hexane. The combined hexane extract was passed through a funnel with anhydrous sodium sulfate into a clean dry round bottom flask, evaporated on a rotary evaporator at a water bath temperature of 40 °C to dry residue. The obtained dry residue was dissolved in 1 ml of acetonitrile with stirring for 30 minutes. Quantitative determination of PAHs in extracts was carried out by high performance liquid chromatography (HPLC) on an AGILENT 1260 instrument.

## 3. Results and discussions

The total content of PAHs in the background soil, located at a distance from the impact zone, was 188 µg/kg (Table 2). At the same time, more than 50% of the total PAH content is accounted for by low molecular weight 2 and 3 ring compounds, mainly naphthalene and phenanthrene, which indicates the natural origin of PAHs in the soil of this area [*Abdel-Shafy and Mansour*, 2016; *Chai et al.*, 2017]. We can distinguish the following decreasing series according to the content of PAHs of different annularity in the studied soil: 3-x > 4-x > 2-x > 5-> 6-annular (Figure 2). Exceeding the MPC of BaP in the soil of the site was not detected, and, in general, the content of the most dangerous 5- and 6-ring PAH compounds does not exceed 20–25 µg/kg (Table 2).

The total content of PAHs in soils of the NPS impact zone is 6–20 times higher than in the soil of protected areas and forms the following decreasing series: 3840 µg/kg (1n 1.6 km NW) > 1729 µg/kg (2n 6.9 km NW) > 1515 µg/kg (3n 15.0 km NW) > 1056 µg/kg (4n 20.0 km NW) (Table 2). The distribution pattern of PAHs in soils corresponds to the pyrogen-coal association of pollutants, since compounds with 4 benzene rings predominate in the composition of PAHs – 409–1355 µg/kg, the content of which decreases with distance from NPS (Figure 2) [*Kołtowski et al.*, 2016; *Medunić et al.*, 2016]. In addition to 4-ring PAH compounds, benzo[b]fluoranthene, benzo[g,h,i]perylene, and phenanthrene make a significant contribution to the total content of polyarenes (Table 2). The content of other PAH compounds does not exceed 80 µg/kg. An exception was BaP, the content of which in the soil of the monitoring site 1n is 355 µg/kg, which exceeds the MPC by 18 times. With the distance from the source of pollution, the content of BaP in the soil decreases and corresponds to 7.7, 3.5, and 2.5 MPC of BaP, respectively (Table 2).

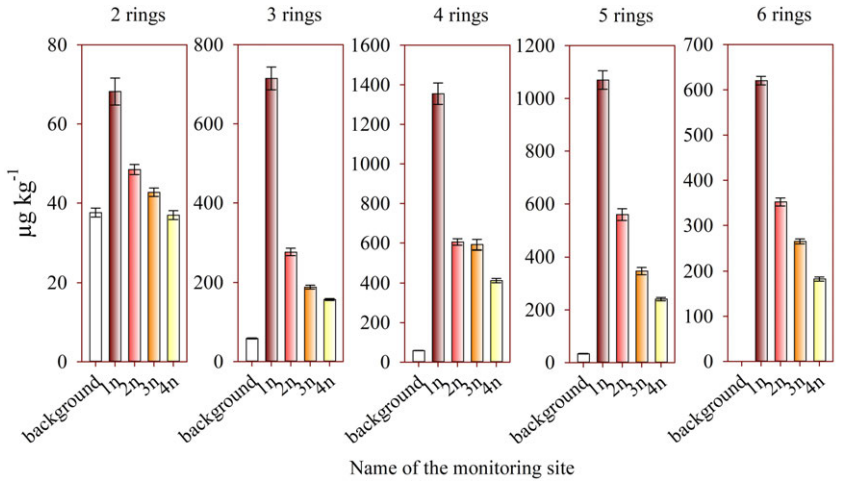


**Figure 2.** The total content of PAHs with the same number of rings in the soils of the monitoring sites of the NPS impact zone.

**Table 2.** Content of individual PAH compounds in the soils of the monitoring sites of the NchGRES impact zone.

| Number of benzene rings | PAH representative | Name of the monitoring site | | | | |
|---|---|---|---|---|---|---|
| | | Background | 1n | 2n | 3n | 4n |
| 2 | Naphthalene | 24.0±0.7 | 25.0±1.3 | 30.0±1.2 | 26.0±1.8 | 25.7±1.5 |
| | Anthracene | 0.4±0.03 | 28.9±1.7 | 32.7±1.6 | 22.6±0.9 | 24.5±1.2 |
| 3 | Fluorene | 8.8±0.4 | 13.7±0.6 | 23.0±1.4 | 15.9±0.6 | 8.5±0.5 |
| | Phenanthrene | 49.4±1.9 | 667.4±40.0 | 217.4±13.0 | 150.5±9.0 | 123.5±6.2 |
| | Benzo[a]anthracene | 3.6±0,2 | 311.2±18.7 | 164.7±11.5 | 91.3±5.4 | 63.2±4.1 |
| 4 | Pyrene | 30.3±1.2 | 470.4±23.5 | 198.6±14.7 | 253.0±19.2 | 175.2±9.9 |
| | Fluoranthene | 24.3±1.2 | 573.4±37.4 | 248.2±16.2 | 245.8±13.3 | 170.2±9.2 |
| | Benzo[b]fluoranthene | 10.2±0.6 | 401.6±21.9 | 263.8±14.4 | 181.6±11.8 | 125.7±7.8 |
| 5 | Benzo[k]fluoranthene | 5.7±0.5 | 138.4±7.5 | 70.9±4,6 | 56.1±3.0 | 38.8±1.9 |
| | Benzo[a]pyrene | 17.6±1.5 | 354.9±20.6 | 154.1±9.1 | 69.9±6.1 | 48.4±2.3 |
| | Dibenzo[a,h]anthracene | 0.2±0.02 | 189.2±12.9 | 70.5±4.8 | 37.0±2.6 | 25.6±1.9 |
| 6 | Benzo[g,h,i]perylene | 0.3±0.03 | 622.3±47.7 | 353.2±26.4 | 264.6±17.8 | 183.2±8.8 |

The content of pollutants in plants growing on the background plot is observed mainly in their root part. Accumulation of 2-ring PAHs, mainly naphthalene (20–23 μg/kg), and 3-ring polyarenes, mainly phenanthrene (5–18 μg/kg) is typical for various parts of plants. The content of 4-ring PAHs did not exceed 7 μg/kg, while that of 5- and 6-ring PAHs did not exceed 1 μg/kg (Figure 3).

The content of PAHs in plants growing on the territory of the impact zone is higher than in plants of the background territory. In general, under the condition of a similar level of soil pollution, according to the ability to accumulate pollutants, plants are located in the following descending order: sagebrush > wheatgrass > bluegrass.

The total content of PAHs in the root part of the plants of the impact zone of the NAS is 3.1–7.0 times higher than in the plants of the background territory and varies from 256–429 μg/kg for sagebrush, 167–255 μg/kg for cereals (bluegrass and wheatgrass) (Figure 3). The content of pollutants in the aerial parts of plants is lower than in the root part, it is 157–300 μg/kg for sagebrush, 48–115 μg/kg for bluegrass and wheatgrass (Figure 3). The highest values of PAH content were established for plants from monitoring site 1n (1.6 km NW), and the minimum values were found for site 4n (20.0 km NW). In general, for all plant species of the impact zone of the NAS, the nature of the accumulation of polyarenes corresponds to the following decreasing series: 4-x > 3-x > 2-x > 5-> 6-annulate (Figure 3). At the same time, 70–82% of the total content of polyarenes in various parts of plants falls on fluoranthene, pyrene, benzo[a]anthracene, and phenanthrene. The accumulation of other PAHs in the root part of plants does not reach 30 μg/kg, and in the aerial part it is less than 10 μg/kg (Figure 3).

Among all the studied species of steppe plants, the lowest content of PAHs in the root part is noted for bluegrass. Most likely, this is due to the physiological characteristics of its root system. The presence of a knotty rhizome and numerous adventitious roots contributes to a greater formation of root exudates compared to other species, which stimulates the growth in the number of PAH-degrading microorganisms in the rhizosphere [*Kumar et al.*, 2017; *Sasse et al.*, 2018; *Wood et al.*, 2016].

## 4. Conclusion

Thus, it was established that in the soils and plants of the background territory of the protected area, mainly low-molecular compounds accumulate, among which 2-ring naphthalene and 3-ring phenanthrene predominate. With pollution, an increase in the content of pollutants in soils and plants, especially high-molecular 4-ring PAHs, is

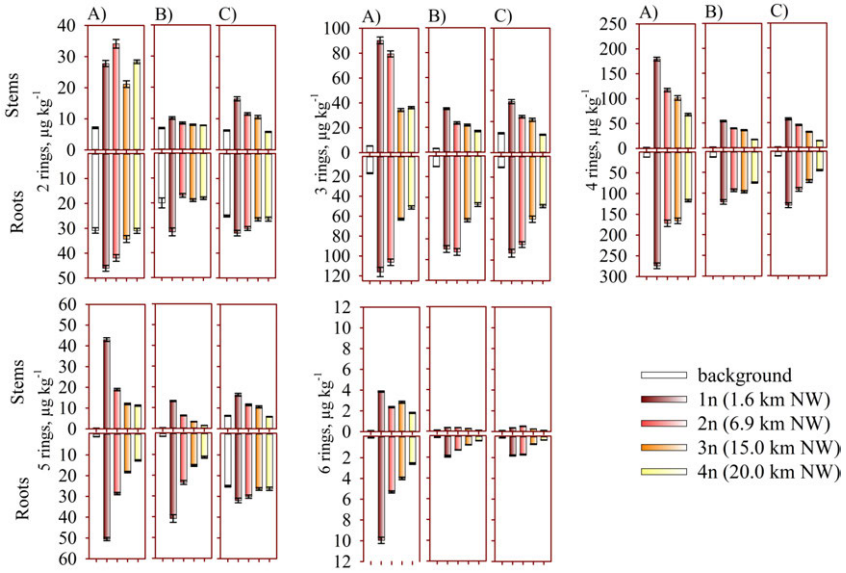


**Figure 3.** The content of PAHs with the same number of rings in different parts of herbaceous plants on the monitoring sites of the NAS impact zone.

observed. MPC BaP in the most polluted soil of monitoring site 1n, located 1.6 km in the NW direction, reaches a value of 18. An increase in the content of pollutants in the soil increases their accumulation in plants, which is especially pronounced for fluoranthene, pyrene, benzo[a]anthracene and phenanthrene, especially for bluegrass. At the same time, pollutants in the soil and plants of the impact zone accumulate mainly up to 2 km from the enterprise.

**Acknowledgments**

The study was carried out in the laboratory "Soil Health" of the Southern Federal University with the financial support of the Ministry of Science and Higher Education of the Russian Federation, agreement no. 075-15-2022-1122.

## References

Abdel-Shafy, H. I., and M. S. M. Mansour (2016), A review on polycyclic aromatic hydrocarbons: Source, environmental impact, effect on human health and remediation, *Egyptian Journal of Petroleum*, *25*(1), 107–123, https://doi.org/10.1016/j.ejpe.2015.03.011.

Chai, C., Q. Cheng, J. Wu, L. Zeng, Q. Chen, X. Zhu, D. Ma, and W. Ge (2017), Contamination, source identification, and risk assessment of polycyclic aromatic hydrocarbons in the soils of vegetable greenhouses in Shandong, China, *Ecotoxicology and Environmental Safety*, *142*, 181–188, https://doi.org/10.1016/j.ecoenv.2017.04.014.

Cristale, J., F. S. Silva, G. J. Zocolo, and M. R. R. Marchi (2012), Influence of sugarcane burning on indoor/outdoor PAH air pollution in Brazil, *Environmental Pollution*, *169*, 210–216, https://doi.org/10.1016/j.envpol.2012.03.045.

GN 2.1.7.2041-06 (2006), Maximum Permissible Concentrations (MPC) and Estimated Permissible Concentrations (APC) of chemicals in soil: Hygienic standards (in Russian).

GOST 17.4.3.01-2017 (2019), Nature protection. Soils. General requirement for sampling (in Russian).

Kołtowski, M., I. Hilber, T. D. Bucheli, and P. Oleszczuk (2016), Effect of activated carbon and biochars on the bioavailability of polycyclic aromatic hydrocarbons in different industrially contaminated soils, *Environmental Science and Pollution Research*, *23*(11), 11,058–11,068, https://doi.org/10.1007/s11356-016-6196-1.

Kotoky, R., and P. Pandey (2018), Plant-microbe Symbiosis as an Instrument for the Mobilization and Removal of Heavy Metals from Contaminated Soils - A Realistic Approach, *Current Biotechnology*, *7*(2), 71–79, https://doi.org/10.2174/2211550106666170321104354.

Kumar, S. S., A. Kadier, S. K. Malyan, A. Ahmad, and N. R. Bishnoi (2017), Phytoremediation and Rhizoremediation: Uptake, Mobilization and Sequestration of Heavy Metals by Plants, in *Plant-Microbe Interactions in Agro-Ecological Perspectives*, pp. 367–394, Springer Singapore, https://doi.org/10.1007/978-981-10-6593-4_15.

Kuppusamy, S., P. Thavamani, K. Venkateswarlu, Y. B. Lee, R. Naidu, and M. Megharaj (2017), Remediation approaches for polycyclic aromatic hydrocarbons (PAHs) contaminated soils: Technological constraints, emerging trends and future directions, *Chemosphere*, *168*, 944–968, https://doi.org/10.1016/j.chemosphere.2016.10.115.

Medunić, G., M. Ahel, I. B. Mihalić, V. G. Srček, N. Kopjar, Ž. Fiket, T. Bituh, and I. Mikac (2016), Toxic airborne S, PAH, and trace element legacy of the superhigh-organic-sulphur Raša coal combustion: Cytotoxicity and genotoxicity assessment of soil and ash, *Science of The Total Environment*, *566-567*, 306–319, https://doi.org/10.1016/j.scitotenv.2016.05.096.

Sasse, J., E. Martinoia, and T. Northen (2018), Feed Your Friends: Do Plant Exudates Shape the Root Microbiome?, *Trends in Plant Science*, *23*(1), 25–41, https://doi.org/10.1016/j.tplants.2017.09.003.

Sushkova, S. N., G. K. Vasilyeva, T. M. Minkina, S. S. Mandzhieva, I. G. Tjurina, S. I. Kolesnikov, R. Kizilkaya, and T. Askin (2014), New method for benzo[a]pyrene analysis in plant material using subcritical water extraction, *Journal of Geochemical Exploration*, *144*, 267–272, https://doi.org/10.1016/j.gexplo.2014.02.018.

Sushkova, S. N., T. M. Minkina, S. S. Mandzhieva, G. K. Vasilyeva, N. I. Borisenko, I. G. Turina, O. V. Bolotova, T. V. Varduni, and R. Kızılkaya (2015), New alternative method of benzo[a]pyrene extractionfrom soils and its approbation in soil under technogenic pressure, *Journal of Soils and Sediments*, *16*(4), 1323–1329, https://doi.org/10.1007/s11368-015-1104-8.

Tobiszewski, M., and J. Namieśnik (2012), PAH diagnostic ratios for the identification of pollution emission sources, *Environmental Pollution*, *162*, 110–119, https://doi.org/10.1016/j.envpol.2011.10.025.

Tsibart, A. S., and A. N. Gennadiev (2013), Polycyclic Aromatic Hydrocarbons in Soils: Sources, Behavior, Indicative Value (A Review), *Pochvovedenie*, *7*, 788–802, https://doi.org/10.7868/S0032180X13070125 (in Russian).

US Environmental Protection Agency (2020), Integrated Risk Information System (IRIS), https://cfpub.epa.gov/ncea/iris_drafts/AtoZ.cfm, (date of access 10.07.2023).

Wood, J. L., C. Tang, and A. E. Franks (2016), Microbial associated plant growth and heavy metal accumulation to improve phytoextraction of contaminated soils, *Soil Biology and Biochemistry*, *103*, 131–137, https://doi.org/10.1016/j.soilbio.2016.08.021.

Yakovleva, E. V., V. A. Beznosikov, B. M. Kondratenok, D. N. Gabov, and M. I. Vasilevich (2008), Bioaccumulation of polycyclic aromatic hydrocarbons in the soil-plant system, *Agrochemistry*, *9*, 66–74 (in Russian).

Yunker, M. B., A. Perreault, and C. J. Lowe (2012), Source apportionment of elevated PAH concentrations in sediments near deep marine outfalls in Esquimalt and Victoria, BC, Canada: Is coal from an 1891 shipwreck the source?, *Organic Geochemistry*, *46*, 12–37, https://doi.org/10.1016/j.orggeochem.2012.01.006.

Russian Journal of Earth Sciences

Special Issue: "Fundamental and Applied Aspects of Geology, Geophysics and Geoecology"

# Properties of Short-Period Internal Waves in the Kara Gates Strait Revealed from Spaceborne SAR Data

**I. O. Kopyshov[1,2], I. E. Kozlov[1], A. I. Shiryborova[3,5], S. A. Myslenkov[3,4,5]**

[1]Marine Hydrophysical Institute of RAS, Sevastopol, Russia;
[2]Moscow Institute of Physics and Technology, Dolgoprudny, Russia;
[3]Lomonosov Moscow State University, Moscow, Russia;
[4]Hydrometcenter of Russia, Moscow, Russia;
[5]Shirshov Institute of Oceanology RAS, Moscow, Russia
* **Correspondence to:** I. Kopyshov, kopyshov.io@phystech.edu

**Abstract:** This paper presents the results of identification of surface manifestations (SM) of short-period internal waves (SIW) in Sentinel-1 A/B synthetic aperture radar (SAR) images of the Kara Gates Strait in August–September 2021. 44 SM of SIW trains were detected in 47 SAR images. Statistics of occurrence, propagation direction and spatial characteristics of SIWs in the study area are given. During two months, satellite observations cover almost all phases of spring-neap tidal cycle. The use of a detailed topography of the study area made it possible to identify certain regions with a more frequent presence of the SIW leading crests with a particular focus made on the shallow (< 100 m) part of the strait. Each identified region is then described in terms of water depth, dimensionless slope, amplitudes of tidal current velocity and properties of SIWs. The obtained results were then compared with the results of previous studies.

**Keywords:** short-period internal waves, SAR imaging of sea surface, barotropic tide, spring-neap cycle, Kara Gates Strait, Arctic Ocean.

**Citation:** Kopyshov I., Kozlov I., Shiryborova A., Myslenkov S. (2023), Properties of Short-Period Internal Waves in the Kara Gates Strait Revealed from Spaceborne SAR Data, *Russian Journal of Earth Sciences*, Vol. 23, ES0210, https://doi.org/10.2205/2023ES02SI10

## 1. Introduction

The problem of studying internal waves (IWs) in the Arctic region has been raised many times and is still relevant today, because it has an important practical application. The formation and further collapse of internal waves can lead to intensive mixing of water masses [*D'Asaro*, 2022; *Fer et al.*, 2020; *Phillips*, 1980; *Sabinin et al.*, 2004], vertical transport of heat and nutrients [*Boegman and Stastna*, 2019; *Edge et al.*, 2021; *Garwood et al.*, 2020; *Moum et al.*, 2003, 2007; *Pineda*, 1991]. In addition, IWs in the Arctic region can directly affect the characteristics of sea ice [*Carr et al.*, 2019; *Czipott et al.*, 1991] and the formation of polynyas [*Morozov and Pisarev*, 2004].

A peculiar feature of IWs in the Arctic Ocean is their formation and propagation near the critical latitude [*Kagan et al.*, 2018; *Konyaev*, 2000; *Morozov and Paka*, 2010; *Morozov and Pisarev*, 2002]. When approaching it, the internal tide (IT) at the main tidal frequency $M_2$ becomes unstable and cannot freely propagate far from the generation area. The final stage of the evolution of the IT is its destruction and generation of packets of short-period internal waves (SIWs). Due to the stability of wave packets as a separate structure, they can spread over long distances. This was confirmed by the analysis of satellite synthetic aperture radar (SAR) data [*Kozlov et al.*, 2015a,b], on which surface manifestations (SM) of SIWs are visible in the form of alternating light and dark bands associated with the amplification and attenuation of the radar backscattering in surface current convergence and divergence zones [*Kudryavtsev et al.*, 2014].

Research Article

Received: 20 October 2023
Accepted: 27 November 2023
Published: 15 December 2023

**Copyright:** © 2023. The Authors. This article is an open access article distributed under the terms and conditions of the Creative Commons Attribution (CC BY) license (https://creativecommons.org/licenses/by/4.0/).

The transformation of IT into SIW packets is associated with the instability of the former at high depth gradients. In simple linear two-dimensional case, the impingement of the IT on the underwater inhomogeneity generates a series of packets of SIWs running in the opposite direction [*Jackson et al.*, 2012; *Li et al.*, 2019; *Morozov et al.*, 2002]. In the real case, underwater inhomogeneities can have a very complex structure so that the direction of SIW propagation might change underway. Narrow ocean areas with fairly intense tidal dynamics are exactly such regions. One such example is the Kara Gates Strait (KGS) characterized by a complex bottom relief [*Li et al.*, 2019; *Morozov and Frey*, 2023; *Morozov et al.*, 2017] and a variety of directions for the distribution of SIW packages [*Kozlov et al.*, 2015a; *Morozov et al.*, 2017].

Considering the process of SIW generation, it is important to remind that the current flow regime is characterized by a dimensionless Froude number $Fr = u/c$, where $u$ is the total vector of the flow velocity, and $c$ is the phase velocity of long linear internal waves determined by background stratification. The formation of SIW packets occurs during the transition of Fr from subcritical ($Fr < 1$) to the supercritical flow mode ($Fr > 1$) [*Maxworthy*, 1979]. The flow velocity includes the background current velocity and the tidal current velocity. Hence, the second term changing its magnitude and direction several times per day, can change the flow mode and affect the generation of SIWs. In the KGS, the flow velocity averages 0.06–0.26 m/s and reaches 0.5 m/s at the peak [*Morozov et al.*, 2003]. At the same time, the velocities of tidal currents vary in the range up to 0.5 m/s, which can potentially create a total magnitude of the flow velocity vector up to 1 m/s.

The active use of methods of satellite oceanography, in particular measurements of spaceborne SARs, the quantity and quality of information about the areas of formation and spatial characteristics of SIWs has significantly increased [*Dubina and Mitnik*, 2007; *Jackson*, 2004; *Kozlov et al.*, 2015a; *Kozlov and Kuzmin*, 2022; *Lavrova et al.*, 2009, 2011]. A large volume of satellite data allows to use statistical methods to determine the areas of regular formation of SIWs and to study their distribution and evolution.

This paper presents the analysis results of the SIW properties in the KGS obtained based on the processing of Sentinel-1 SAR data in August-September 2021. The obtained results are compared with the detailed bottom topography of the area and the characteristics of tidal currents from the Arc5km2018 model [*Erofeeva and Egbert*, 2020].

## 2. Data and methods

To analyze the characteristics of the SIW field in the KGS, Sentinel-1 A/B SAR data were used in the IW (Interferometric Wide Swath) and EW (ExtraWide) modes with a spatial resolution of 20 m and 40 m, respectively. SAR images were obtained from the archives of the Copernicus Marine Open Access Hub (https://scihub.copernicus.eu). A total of 47 SAR images were processed, 11 of which possessed clear surface manifestations of SIWs. Table 1 presents summary data on the number of processed images in August–September 2021. Earlier studies of this region have shown that the largest number of SIW trains is observed in September [*Kozlov et al.*, 2015a], so special attention was paid to the analysis of the data in late summer – early autumn.

**Table 1**. Main characteristics of satellite radar observations in the Kara Gates Strait.

| Month, 2021 | Count of RI | Count of packet of SIW |
|---|---|---|
| August | 23 | 10 |
| September | 24 | 34 |

Satellite radar monitoring of the sea surface can be complicated at strong winds. According to the modeling results in the Kara Gates Strait, the maximum wave height can reach 6–7 m at a wind speed of 15 m/s [*Myslenkov et al.*, 2021a,b]. At such wind speeds, SMs of SIWs become indistinguishable in SAR images. The optimal range of wind speeds for observing the SMs of SIWs is 3–10 m/s. A data set of ASCAT METOP-A/B/C satellite scatterometer was used to assess the background wind conditions. The time interval

between the ASCAT and Sentinel-1 flights ranged from 1.5 to 8 hours. In total, the wind speed went beyond the optimal range for 15 days during the research period (Figure 1), while for two days wind conditions were stormy (wind speed >25 m/s).

To analyze the background tidal conditions, data from the Arc5km2018 model with a horizontal resolution of 5 km were used. The strait has relatively small horizontal dimensions (no more than 50 km), and the maximum difference in the tidal phase across the strait is 22 minutes. Hence, the analysis of the model data was carried out only for the central point of the strait (70.4688°N, 57.9513°E). The exception was the spatial distribution of the tidal ellipses for the lunar semidiurnal tide $M_2$.

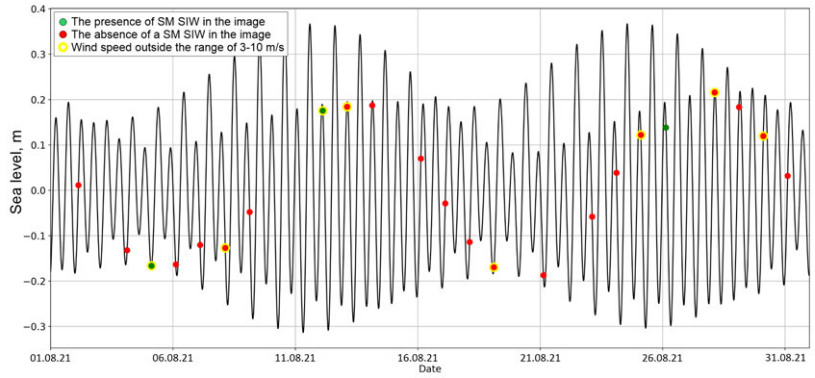


**(a)**

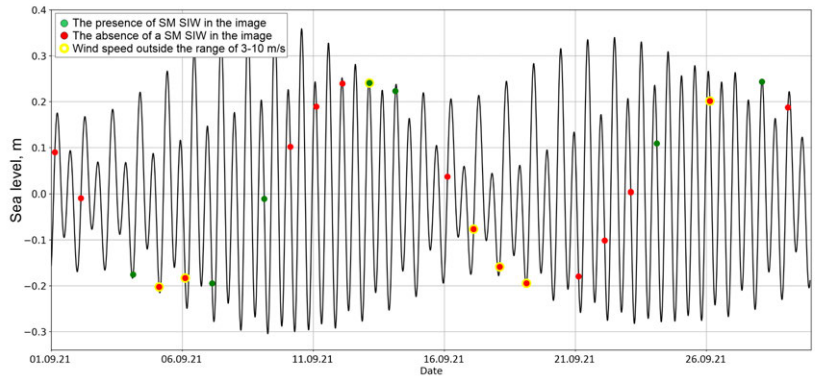


**(b)**

**Figure 1.** Tidal fluctuations of sea level [m] in a) August and b) September 2021 according to the Arc5km2018 model with points marking the time of satellite observations. Green (red) markers show the time when SIW signatures were present (absent) in satellite images

The coverage of the strait by satellite data in August 2021 was very uneven in time, most of the images were obtained in the second half of the month (Figure 1a). In September 2021, the coverage was more uniform (Figure 1b) and, on average, there was one SAR snapshot every second day. The acquisition time of satellite data was nearly the same, around 03:00 UTC. Since an $M_2$ tidal period (12.4 hours) slightly exceeds half a day, satellite imagery enabled to observe the characteristics of the SIWs at different phases of spring-neap cycle (Figure 1).

To assess the impact of bottom topography inhomogeneities on SIW propagation, ocean bathymetry data digitized from the 1:500000 scale navigation map of the DNaO MD RF were used. This map was published in 1995 with the last correction in 2016. The distance between adjacent marks on the navigation map is about 5 km. For further analysis, digitized data were transformed into a regular grid with a step of 1′ using linear interpolation. Bathymetry map (Figure 2a) and the dimensionless slope of the bottom relief (Figure 2b) are constructed on the basis of the resulting array. The dimensionless slope of

the bottom relief was calculated as the ratio of the depth difference to the distance between adjacent grid nodes.

### 3. Analysis of background conditions

The Kara Gates Strait has a complex heterogeneous bottom (Figure 2a). The area can be divided into deep-water (>100 m) and shallow-water (<100 m) parts. The first is a broken depression, which, twisting, passes through the strait. According to [*Morozov et al.*, 2017] and [*Kopyshov et al.*, 2021], a large number of small-scale topographic inhomogeneities are observed in the strait. These features are often smoothed out by standard bottom topography data sets, such as IBCAO [*Jakobsson et al.*, 2012], etc. Analyzing the dimensionless slope data (Figure 2b), its elevated values are found in the southeastern part of the strait and in its central part. Also, strong heterogeneities are observed at the exit of the strait from the Kara Sea, as well as at the entrance of the strait from the Barents Sea, as well as in its central part. There is also a pronounced slope off the east coast of Vaygach Island, however, this region was not considered in our work.

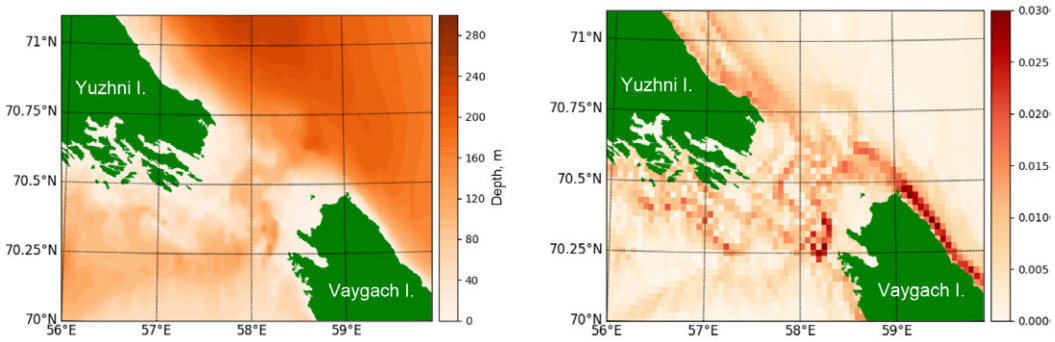


**(a)** **(b)**

**Figure 2.** Bottom topography of the Kara Gates Strait: a) total depths and b) dimensionless slope

To study the objects of the internal tide evolution, it is important to know its characteristics. As already mentioned before, the tidal harmonic $M_2$ prevails in the study area [*Kagan and Timofeev*, 2015; *Morozov et al.*, 2008, 2017]. Figure 3 shows $M_2$ tidal ellipses from the Arc5km2018 model.

The tidal ellipses in the strait differ very much from each other both in magnitude and in their geometry. In the eastern part of the strait, large values of the maximum tidal flow velocity of 0.4 m/s are observed. In the southeastern part of the strait, they are very elongated and play a key role during the peak moments of the tidal cycle. In the northeastern part, on the contrary, the ellipses have a more rounded shape meaning the tidal flow is more uniform in time in this subregion.

In the central part of the strait, especially at the entrance and exit from it, tidal ellipses have very small sizes (magnitude < 0.01 m/s), which indicates their reduced influence on the overall picture of currents. In the southwestern part of the district, near the southern part of Novaya Zemlya, tidal ellipses also have an elongated shape and reach 0.15 m/s at the peak of the tidal flow velocity.

It is worth paying attention to the fact that due to the different geometry and orientation of tidal ellipses, the maximum values of tidal velocities are not achieved synchronously. It means that the tidal conditions favorable for the SIW generation occur at different times in different parts of the strait. Moreover, the maximum value of the tidal velocity can vary greatly during spring-neap cycle. In such case, the maximum deviation of the instant flow velocity from its average value will also vary significantly, which in turn would affect the transition of the flow to supercritical mode.

The superposition of the intense tidal dynamics and the complex bottom relief with a large number of underwater elevations near the critical latitude should naturally lead to the formation of multidirectional packets of SIWs [*Li et al.*, 2019; *Morozov et al.*, 2017],

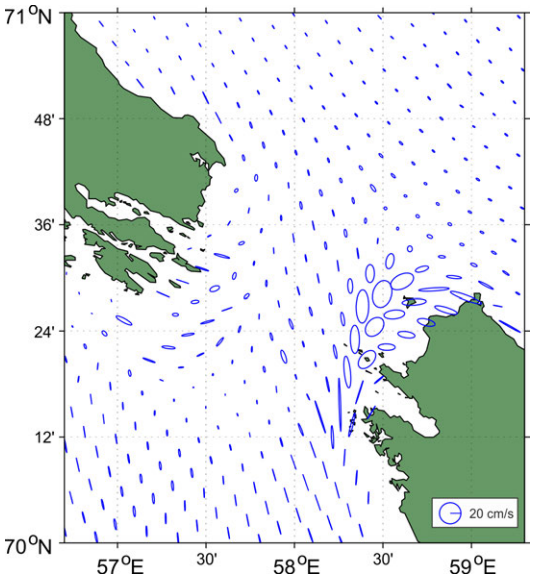


**Figure 3.** $M_2$ tidal ellipses obtained from the Arc5km2018 model for August 2021.

as confirmed both by full-scale *in situ* measurements [*Morozov et al.*, 2017] and satellite observations [*Kozlov et al.*, 2015a].

### 3.1. Results of satellite observations

In total, during the analysis of 47 SAR images, 10 SIW packets were identified in August 2021 and 37 – in September 2021. Such ratios of the number of recorded SIW manifestations by month were also observed in earlier studies [*Kozlov et al.*, 2015a,b].

An overall map showing leading waves of all identified SIWs in the KGS is shown in Figure 4. About 40% of all observed SIWs were recorded over the deep-water part of the strait, which makes up ~23% of the total area of the strait. The geographic areas where SIW trains were observed over the shallow part of the strait can be divided into three regions (Figure 4).

In region 1, 7 manifestations of SIWs were registered on ~120 $km^2$. Most packets of SIWs are directed across the strait and across isobaths to the northwest, which is a very interesting feature rarely described in the literature. The only wave train directed to the southwest is characterized by a much longer leading wave. It is located approximately in the center of an elongated shoal/hill with depths of about 30–40 m, oriented across the strait and surrounded by deep-water areas on three sides.

The smallest number of SIW trains was detected in the region 2 (5 packets per ~400 $km^2$), where large amplitudes of the tidal current are observed (up to 0.5 m/s), while the bottom is fairly uniform (dimensionless slope is less than 0.001). The SIWs registered in this area were directed to the south, east and west, thus spreading primarily across the strait, while having very short lengths of the leading wave ~ 1 km. Some of the waves, in the northwestern part of the area, were most likely generated either over a sloping bottom or over the deeper parts of the strait. These waves have a much longer length of the leading wave than those found to the east.

The largest number of SIWs was registered in the region 3. Here, 12 manifestations of SIWs per ~100 $km^2$ were registered. The directions of wave propagation in this region were more diverse compared to other areas. Yet, most waves were predominantly directed to the southwest. The values of the dimensionless slope here are rather average, around 0.015. An interesting feature is the fact that in the northwestern sector of this region the waves are directed across the strait towards Vaygach Island, while in the central sector – along the strait, towards the Barents Sea.

The main difference between the regions 1, 3 and the region 2 is the availability of steeper area where slope values exceed 0.015. The amplitudes of tidal currents in regions 1

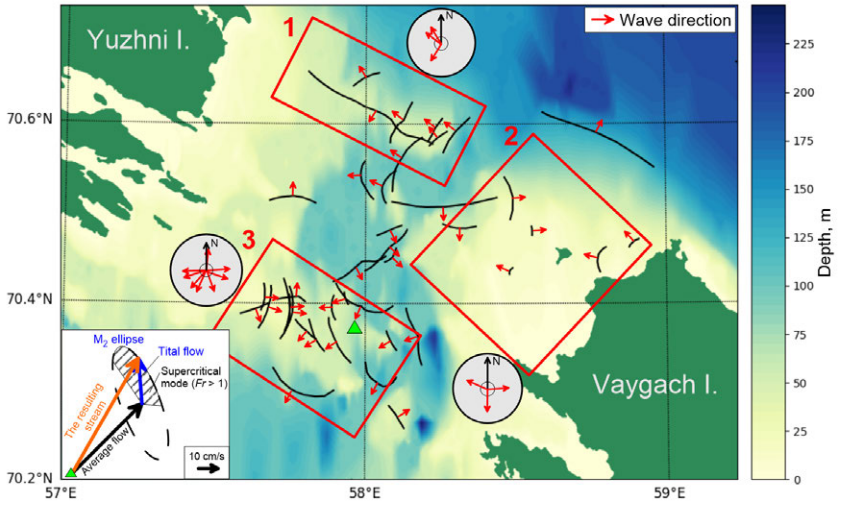


**Figure 4.** The position of the surface manifestations of the leading waves in the packets of SIWs in August-September 2021. The main shallow water regions where the SIW registration took place are highlighted with red frames and numbered. Each region has a diagram of SIW propagation direction shown by red arrows in grey circles. The graph in the lower left corner schematically shows the formation of resulting supercritical flow ($c_0$ = 0.5 m/s, the average flow velocity of 0.3 m/s, the magnitude of the tidal current fluctuations of 0.3 m/s) in the place marked by a green triangle.

and 3 are slightly lower than 0.15–0.20 m/s, however, due to the heterogeneous topography, the conditions for the destruction of the IT are favorable. Moreover, the region 3 is also characterized by a large number of secluded seamounts [*Kopyshov et al.*, 2021; *Morozov et al.*, 2017], explaining the variety of SIW propagation directions in this region.

As already mentioned above, generation of SIWs should occur near the critical flow regime (Fr ~ 1). In the strait, the total current velocity consists of the mean flow from the Barents Sea to the Kara Sea, and the tidal current. The latter term is variable in time, which leads to a change in the resulting flow velocity vector from subcritical to supercritical Fr values, and vice versa. This process is illustrated by the vector diagram in the lower left corner shown in Figure 4. It is constructed for a single point in the strait marked with a green triangle. The schematic shown in Figure 4 was produced by assuming the mean flow of 0.3 m/s, the amplitude of the tidal current velocity of 0.3 m/s, and the phase speed of linear internal wave of 0.5 m/s obtained for the background stratification conditions in the strait.

Let us now consider some features of the spatial characteristics of the SIWs. Figure 5 shows histogram distribution of the length of the leading front (Figure 5a) and the SIW packet width (Figure 5b) characterizing the horizontal dimensions of these structures. The most common were SIW packets with a leading front length of about 5 km. The maximum values of this property reached 26 km and were observed in the region 1 at the exit of the strait. For packet widths, the peak value is 2 km while the maximum width of the SIW packets is 6.5 km. The widest structures were recorded over the deep-water regions and in the northern part of region 3.

The spatial differences noted above directly depend on the characteristics of the slope, since the generation of packets with a longer length of the leading front should occur on longer slopes, which are observed at the exit of the strait from the Kara Sea side. The width of the packet is determined by the number of waves in the packet and their wavelength. The first is determined by the lifetime of the wave packet, while the second largely depends on the horizontal size of the obstacle [*Kozlov and Kuzmin*, 2022]. The horizontal lengths of obstacles in the strait are very different from each other and, usually, they have a relatively small scale of 0.1–1 km. The available bathymetric data are not enough detailed to perform

a more complete analysis of the relationship of the spatial properties of the observed SIW trains with the geometric characteristics of the bottom topography.

Lastly, it is also important to accent here that satellite imagery covers different phases of the spring-neap tidal cycle, allowing to observe 5–7 different episodes of this cycle (Figure 1). Surface manifestations of SIWs were recorded equally often both during the spring and the neap tides. As obtained, the registration of many SIW packets occurred a few hours after the onset of low/high water.

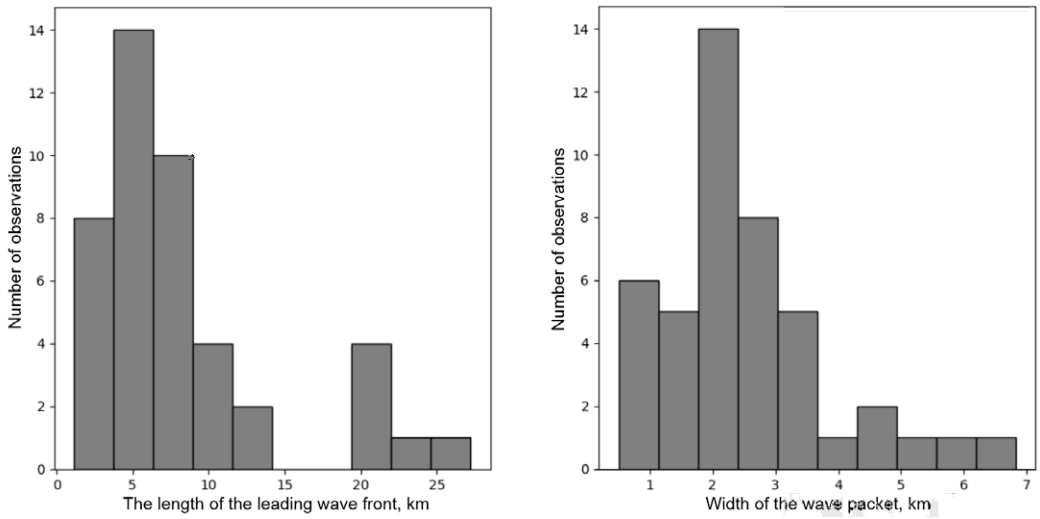


**(a)** **(b)**

**Figure 5.** Histograms a) the length of the front of the leading waves in packets of SIW, and b) their width.

## 4. Discussion

In this paper, the peculiarities of SIW generation and propagations in the Kara Gates Strait were considered. As shown, most of the SIW trains were registered at the entrance to the strait in regions 1 and 3, as well as in the central deep-water part. Most often the packets of SIWs were found near pronounced inhomogeneities of the bottom topography where amplitudes of tidal velocity exhibited relatively high values. In such areas, SIWs could be generated either via the lee wave mechanism when the total current flow exceeds critical value (Fr>1), or in the transcritical regime when the Froude number passes over a critical value [*da Silva, J. C. B. and Helfrich*, 2008]. In any case, we presume that modulation of the resulting current flow by the changing tidal current velocity is the key factor governing the generation of NIWs in the study region.

An interesting fact is that with a certain ratio of the intensity of the mean flow, the tidal flow, the IW phase velocity, as well as the orientation of the tidal ellipse, the "permitted zone", where the supercritical flow regime is observed (Figure 4, the dashed fill in the diagram of the resulting flow formation) may appear in the opposite direction. This means that the generation of SIW packets will occur not once per semidiurnal tidal period, but at least twice – at high and low tide. Also, the $M_2$ tidal harmonic is dominant, but not the only one in the study area. When additional ellipses of other harmonics are superimposed, the resulting tidal velocity can change in a rather complicated way within both a semidiurnal period and a spring-neap cycle. This may lead to an increase in the number of "permitted zones" of SIW generation, as well as their overlap with each other at nearby locations.

Also, the question of the particular tidal phase at which SIWs are generated remains poorly understood. It is known from theory that this begins at the moment of the onset of the supercritical flow (Fr ~ 1) and occurs until the value of the flow velocity decreases to the subcritical regime [*Jackson et al.*, 2012; *Maxworthy*, 1979]. It is assumed that at this moment there is an intensive pumping of energy, while the flow of the jet onto the

topographic inhomogeneity causes the shape of the isopycnic surfaces to change. The further the stream is in the supercritical state, the more intense the SIWs packet should be. If the passage of the "permitted zone" occurs very quickly, for example, when the tidal ellipses are very elongated, the generated internal waves should be less intense, but experimental confirmation of the latter fact is not known to us.

The Kara Gates Strait is also interesting because it has a strong frontal zone. It separates the flow of the relatively warm Barents Sea water, which usually occupies the central part of the strait, and the cold counter-current from the Kara Sea, which spreads along the southern coast of Novaya Zemlya to the southwest. Their interaction is complex, which generates a quasi-stable vertical inhomogeneity of velocities [*McClimans et al.*, 2000; *Morozov et al.*, 2017]. However, we do not consider SIW generation in the KGS owing to existence of the frontal zone in this work.

## 5. Conclusions

The paper presents the results of spaceborne SAR data processing to investigate properties of short-period internal waves in the Kara Gates Strait. Analysis of 47 Sentinel-1A/B SAR images for August-September 2021 allowed to identify 44 surface manifestations of SIWs. It was shown that a large number of SIW packets was observed near sloping bottom with relatively high values of dimensionless slope and moderate amplitudes of tidal current velocities in the shallow areas of the strait.

Manifestations of SIW were recorded in large numbers both over the deep-water parts of the strait (>100 m) and over its shallow areas (from 30 to 100 m). Analysis of satellite data showed that SIW was actively registered both during spring (about half of all packets) and neap tides. As suggested, spring-neap variability of tidal current intensity mainly affects the intensity of the initial pycnocline disturbance from which SIW are generated later. As such, the locations of SIW generation could be more or less constant within a spring-neap cycle, but the horizontal and vertical properties of SIW should be enhanced during spring tide. Nevertheless, spatial properties of SIWs such as their wavelength and the length of the leading front should also depend on the horizontal dimensions of the obstacles.

Analysis of the satellite data in conjunction with tidal model predictions of sea level fluctuations showed that SIW packets in the strait are recorded equally frequent at different phases of the semidiurnal tide.

## Acknowledgements

The study was carried out within the framework of the state task No. FNNN-2021-0010. Sentinel-1A/B satellite data were obtained from the Copernicus Marine Open Access Hub (https://scihub.copernicus.eu). Wind speed data of ASCAT METOP-A/B/C scatterometers were obtained from the National Environmental Satellite, Data, and Information Service (NESDIS) Satellite Application and Research Center from (https://manati.star.nesdis.noaa.gov).

The part of the study related to the calculation of tidal conditions was funded by the state task FMWE-2021-0015.

## References

Boegman, L., and M. Stastna (2019), Sediment Resuspension and Transport by Internal Solitary Waves, *Annual Review of Fluid Mechanics*, *51*(1), 129–154, https://doi.org/10.1146/annurev-fluid-122316-045049.

Carr, M., P. Sutherland, A. Haase, K.-U. Evers, I. Fer, A. Jensen, H. Kalisch, J. Berntsen, E. Părău, Ø. Thiem, and P. A. Davies (2019), Laboratory Experiments on Internal Solitary Waves in Ice-Covered Waters, *Geophysical Research Letters*, *46*(21), 12,230–12,238, https://doi.org/10.1029/2019GL084710.

Czipott, P. V., M. D. Levine, C. A. Paulson, D. Menemenlis, D. M. Farmer, and R. G. Williams (1991), Ice Flexure Forced by Internal Wave Packets in the Arctic Ocean, *Science*, *254*(5033), 832–835, https://doi.org/10.1126/science.254.5033.832.

da Silva, J. C. B., and K. R. Helfrich (2008), Synthetic Aperture Radar observations of resonantly generated internal solitary waves at Race Point Channel (Cape Cod), *Journal of Geophysical Research: Oceans*, *113*(C11), https://doi.org/10.1029/2008JC005004.

D'Asaro, E. A. (2022), How do Internal Waves Create Turbulence and Mixing in the Ocean?, *ESS Open Archive*, https://doi.org/10.1002/essoar.10511843.1, (Preprint).

Dubina, V. A., and L. M. Mitnik (2007), Internal waves in the Sea of Japan: spatial-temporal distribution and characteristics according to satellite remote sensing data, *Issledovanie Zemli iz Kosmosa*, *3*, 37–46 (in Russian).

Edge, W. C., N. L. Jones, M. D. Rayson, and G. N. Ivey (2021), Calibrated Suspended Sediment Observations Beneath Large Amplitude Non-Linear Internal Waves, *Journal of Geophysical Research: Oceans*, *126*(12), https://doi.org/10.1029/2021jc017538.

Erofeeva, S., and G. Egbert (2020), Arc5km2018: Arctic Ocean Inverse Tide Model on a 5 kilometer grid, 2018, https://doi.org/10.18739/A21R6N14K.

Fer, I., Z. Koenig, I. E. Kozlov, M. Ostrowski, T. P. Rippeth, L. Padman, A. Bosse, and E. Kolås (2020), Tidally Forced Lee Waves Drive Turbulent Mixing Along the Arctic Ocean Margins, *Geophysical Research Letters*, *47*(16), https://doi.org/10.1029/2020gl088083.

Garwood, J., R. Musgrave, and A. Lucas (2020), Life in Internal Waves, *Oceanography*, *33*(3), 38–49, https://doi.org/10.5670/oceanog.2020.313.

Jackson, C., J. da Silva, and G. Jeans (2012), The Generation of Nonlinear Internal Waves, *Oceanography*, *25*(2), 108–123, https://doi.org/10.5670/oceanog.2012.46.

Jackson, C. R. (2004), *An atlas of internal solitary-like waves and their properties*, 2nd ed., Global Ocean Associates, Alexandria.

Jakobsson, M., L. Mayer, B. Coakley, J. A. Dowdeswell, S. Forbes, B. Fridman, H. Hodnesdal, R. Noormets, R. Pedersen, M. Rebesco, H. W. Schenke, Y. Zarayskaya, D. Accettella, A. Armstrong, R. M. Anderson, P. Bienhoff, A. Camerlenghi, I. Church, M. Edwards, J. V. Gardner, J. K. Hall, B. Hell, O. Hestvik, Y. Kristoffersen, C. Marcussen, R. Mohammad, D. Mosher, S. V. Nghiem, M. T. Pedrosa, P. G. Travaglini, and P. Weatherall (2012), The International Bathymetric Chart of the Arctic Ocean (IBCAO) Version 3.0, *Geophysical Research Letters*, *39*(12), https://doi.org/10.1029/2012GL052219.

Kagan, B. A., and A. A. Timofeev (2015), Spatial variability in the drag coefficient and its role in tidal dynamics and energetics, a case study: The surface M 2 tide in the subsystem of the Barents and Kara Seas, *Izvestiya, Atmospheric and Oceanic Physics*, *51*(1), 98–111, https://doi.org/10.1134/s0001433814060103.

Kagan, B. A., E. V. Sofina, and A. A. Timofeev (2018), Critical Latitude in Tidal Dynamics Using the Kara Sea as an Example, *Izvestiya, Atmospheric and Oceanic Physics*, *54*(2), 206–212, https://doi.org/10.1134/s000143381802010x.

Konyaev, K. V. (2000), Internal tide at the critical latitude, *Izvestiya. Atmospheric and Oceanic Physics*, *36*(3), 363–375 (in Russian).

Kopyshov, I. O., I. E. Kozlov, V. R. Zhuk, A. V. Artamonova, K. P. Silvestrova, O. S. Mekhova, A. I. Korzhenovskaya, D. I. Frey, A. G. Jamalova, P. V. Gaisky, A. A. Osadchiev, and N. B. Stepanova (2021), Study of high-amplitude internal waves in The Kara Gate Straitin August 2021, in *X International conference «Marine Research and Education» MARESEDU-2021*, vol. 1, pp. 238–241, PoliPRESS, Tver (in Russian).

Kozlov, I., V. Kudryavtsev, E. Zubkova, O. Atadzhanova, A. Zimin, D. Romanenkov, A. Myasoedov, and B. Chapron (2015a), SAR observations of internal waves in the Russian Arctic seas, in *2015 IEEE International Geoscience and Remote Sensing Symposium (IGARSS)*, IEEE, https://doi.org/10.1109/IGARSS.2015.7325923.

Kozlov, I. E., and A. V. Kuzmin (2022), New regions of short-period internal wave generation in the Laptev Sea revealed from Sentinel-1 data, *Sovremennye problemy distantsionnogo zondirovaniya Zemli iz kosmosa*, *19*(4), 280–290, https://doi.org/10.21046/2070-7401-2022-19-4-280-290.

Kozlov, I. E., V. N. Kudryavtsev, E. V. Zubkova, A. V. Zimin, and B. Chapron (2015b), Characteristics of short-period internal waves in the Kara Sea inferred from satellite SAR data, *Izvestiya, Atmospheric and Oceanic Physics*, *51*(9), 1073–1087, https://doi.org/10.1134/s0001433815090121.

Kudryavtsev, V., I. Kozlov, B. Chapron, and J. A. Johannessen (2014), Quad-polarization SAR features of ocean currents, *Journal of Geophysical Research: Oceans*, *119*(9), 6046–6065, https://doi.org/10.1002/2014jc010173.

Lavrova, O. Y., M. I. Mityagina, and K. D. Sabinin (2009), Manifestation of internal waves on the sea surface in the northeastern part of the Black Sea, *Issledovanie Zemli iz Kosmosa*, (6), 49–55 (in Russian).

Lavrova, O. Y., M. I. Mityagina, and K. D. Sabinin (2011), Study of internal wave generation and propagation features in non-tidal seas based on satellite synthetic aperture radar data, *Doklady Earth Sciences*, *436*(3), 165–169 (in Russian).

Li, Q., H. Wu, H. Yang, and Z. Zhang (2019), A numerical simulation of the generation and evolution of nonlinear internal waves across the Kara Strait, *Acta Oceanologica Sinica*, *38*(5), 1–9, https://doi.org/10.1007/s13131-019-1437-z.

Maxworthy, T. (1979), A note on the internal solitary waves produced by tidal flow over a three-dimensional ridge, *Journal of Geophysical Research: Oceans*, *84*(C1), 338–346, https://doi.org/10.1029/jc084ic01p00338.

McClimans, T. A., D. R. Johnson, M. Krosshavn, S. E. King, J. Carroll, and Ø. Grenness (2000), Transport processes in the Kara Sea, *Journal of Geophysical Research: Oceans*, *105*(C6), 14,121–14,139, https://doi.org/10.1029/1999jc000012.

Morozov, E., and D. Frey (2023), Strait of Kara Gates: A Region of Strong Internal Tides in the Arctic Seas, *Russian Journal of Earth Sciences*, *23*(3), 1–7, https://doi.org/10.2205/2023es000860.

Morozov, E. G., and V. T. Paka (2010), Internal waves in a high-latitude region, *Oceanology*, *50*(5), 668–674, https://doi.org/10.1134/s0001437010050048.

Morozov, E. G., and S. V. Pisarev (2002), Internal tides at the Arctic latitudes (numerical experiments), *Oceanology*, *42*(2), 165–173.

Morozov, E. G., and S. V. Pisarev (2004), Internal waves and polynya formation in the Laptev Sea, *Doklady Earth Sciences*, *397*(3), 1–4 (in Russian).

Morozov, E. G., S. V. Pisarev, and S. Y. Erofeeva (2002), Internal tidal waves in the Arctic seas of Russia, in *Surface and internal waves in Arctic seas. Part II. Internal waves in the Arctic seas of Russia*, pp. 214–234, Gidrometeoizdat, Saint Petersburg (in Russian).

Morozov, E. G., V. G. Neiman, and A. D. Shcherbinin (2003), Internal tide in the Kara Strait, *Doklady Earth Sciences*, *393*(9), 1312–1314.

Morozov, E. G., V. T. Paka, and V. V. Bakhanov (2008), Strong internal tides in the Kara Gates Strait, *Geophysical Research Letters*, *35*(16), https://doi.org/10.1029/2008GL033804.

Morozov, E. G., I. E. Kozlov, S. A. Shchuka, and D. I. Frey (2017), Internal tide in the Kara Gates Strait, *Oceanology*, *57*(1), 8–18, https://doi.org/10.1134/s0001437017010106.

Moum, J. N., D. M. Farmer, W. D. Smyth, L. Armi, and S. Vagle (2003), Structure and Generation of Turbulence at Interfaces Strained by Internal Solitary Waves Propagating Shoreward over the Continental Shelf, *Journal of Physical Oceanography*, *33*(10), 2093–2112, https://doi.org/10.1175/1520-0485(2003)033<2093:sagota>2.0.co;2.

Moum, J. N., J. M. Klymak, J. D. Nash, A. Perlin, and W. D. Smyth (2007), Energy Transport by Nonlinear Internal Waves, *Journal of Physical Oceanography*, *37*(7), 1968–1988, https://doi.org/10.1175/jpo3094.1.

Myslenkov, S., V. Platonov, A. Kislov, K. Silvestrova, and I. Medvedev (2021a), Thirty-Nine-Year Wave Hindcast, Storm Activity, and Probability Analysis of Storm Waves in the Kara Sea, Russia, *Water*, *13*(5), 648, https://doi.org/10.3390/w13050648.

Myslenkov, S. A., V. S. Platonov, K. P. Silvestrova, and S. A. Dobrolyubov (2021b), Increase in Storm Activity in the Kara Sea from 1979 to 2019: Numerical Simulation Data, *Doklady Earth Sciences*, *498*(2), 502–508, https://doi.org/10.1134/s1028334x2106012x.

Phillips, O. M. (1980), *The Dynamics of the Upper Ocean (Cambridge Monographs on Mechanics)*, 344 pp., Cambridge University Press.

Pineda, J. (1991), Predictable Upwelling and the Shoreward Transport of Planktonic Larvae by Internal Tidal Bores, *Science*, *253*(5019), 548–549, https://doi.org/10.1126/science.253.5019.548.

Sabinin, K. D., A. N. Serebryanyi, and A. A. Nazarov (2004), Intensive internal waves in the World Ocean, *Oceanology*, *44*(6), 753–758 (in Russian).

Russian Journal of Earth Sciences

Special Issue: "Fundamental and Applied Aspects of Geology, Geophysics and Geoecology"

# Histograms of the Caspian Sea Hydrometeorological Parameters

**Andrey G. Kostianoy[1,2,3], Sergey A. Lebedev[4,3,5], Alexandr V. Bocharov[1,6], Ilya A. Kosolapov[1], Ilya D. Tretiyak[1], Daniil S. Volkov[7], Dmitry A. Grebenikov[1,8], Pavel N. Kravchenko[1,2,6]**

[1]Shirshov Institute of Oceanology of RAS, Moscow, Russia
[2]S. Yu. Witte Moscow University, Moscow, Russia
[3]Maykop State Technological University, Maykop, Russia
[4]Geophysical Center of RAS, Moscow, Russia
[5]National Research University of Electronic Technology (MIET), Moscow, Zelenograd, Russia
[6]Tver State University, Tver, Russia
[7]Skolkovo Institute of Science and Technology (Skoltech), Moscow, Russia
[8]Sirius University of Science and Technology, Sochi, Sirius, Russia
* **Correspondence to:** Andrey Kostianoy, Kostianoy@gmail.com

**Abstract:** The article analyzes histograms of the distribution of the main hydrometeorological parameters of the Caspian Sea for 1980–2021 – air temperature, atmospheric pressure, absolute humidity, atmospheric precipitation and wind speed according to the MERRA-2 atmospheric reanalysis. Histograms were constructed for the entire study region of the Caspian Sea (36°–48°N, 45.625°–55°E), as well as separately for land and sea areas. The extremeness criteria were calculated based on the normal distribution and the real histogram for all 5 main meteorological parameters. A comparison was made of histograms obtained from MERRA-2 data and from weather station at Derbent located on the coast of the Caspian Sea. Distributions of average monthly wind speed, integral water vapor content and water vapor content in clouds over the Caspian Sea were also constructed according to microwave radiometry (SMMR, SSM/I) data for the time interval 1980–2021.

**Keywords:** Caspian Sea, climate, extreme weather events, meteo parameters, weather stations, MERRA-2, SMMR, SSM/I.

**Citation:** Kostianoy A., Lebedev S., Bocharov A., Kosolapov I., Tretiyak I., Volkov D., Grebenikov D., Kravchenko P. (2023), Histograms of the Caspian Sea Hydrometeorological Parameters, *Russian Journal of Earth Sciences*, Vol. 23, ES0211, https://doi.org/10.2205/2023ES02SI11

## 1. Introduction

The Intergovernmental Panel on Climate Change (IPCC) assessment reports [*IPCC*, 2007, 2014, 2021] indicate that in the 21st century, climate change will be accompanied by an increase in the frequency, intensity and duration of extreme natural events such as extreme precipitation and extremely high and low air temperatures. All this will lead to floods, droughts, fires, shallowing of rivers, lakes and reservoirs, desertification, dust storms, melting of glaciers and permafrost, blooming of seas and freshwater bodies. In turn, these phenomena will lead to chemical and biological pollution of water, land and air. The end result of these events is a deterioration in the quality of life of the population, significant financial losses associated with damage to housing, businesses, roads, agriculture and forestry, tourism, and in many cases they result in loss of life.

The same forecasts are confirmed by the results of studies presented in the Roshydromet Assessment Reports on climate change and its consequences on the territory of the Russian Federation [*Roshydromet*, 2008, 2014, 2022]. Scientists' forecasts have been repeatedly confirmed over the past 20 years – these are floods, droughts, fires, heat and cold waves in various regions of the Russian Federation.

Research Article

Received: 20 October 2023
Accepted: 27 November 2023
Published: 15 December 2023

**Copyright:** © 2023. The Authors. This article is an open access article distributed under the terms and conditions of the Creative Commons Attribution (CC BY) license (https://creativecommons.org/licenses/by/4.0/).

Climate change leads to changes in the frequency, intensity, spatial extent, and duration of extreme weather and climate events, leading to the occurrence of hazardous hydrometeorological events. More than 30 types of dangerous hydrometeorological phenomena are observed in Russia. Their total number per year increased on average at the end of the 20th and beginning of the 21st centuries. Of these, 52% were observed in the European territory of Russia. The North Caucasus and Southern Federal districts are most susceptible to various extreme weather and climate phenomena. In this regard, the analysis and forecasting of extreme climatic events associated with regional climate change on the coast of the Caspian Sea and its waters is an extremely important task.

The state of the ecosystems of the Caspian Sea and its coast is of serious concern, due not only to anthropogenic, but also natural causes (climate changes, extreme meteorological and hydrological phenomena, dangerous natural phenomena, as well as the frequency of their recurrence, etc.). In this regard, there is a need for a comprehensive analysis of both climate change and all phenomena associated with them [*Kostianoy and Kosarev*, 2005; *Lavrova et al.*, 2011, 2016, 2022; *Zonn et al.*, 2010].

The Caspian Sea has important economic (fishing, shipping, offshore production and transportation of oil and gas, international transportation, and tourism) and military-strategic significance, especially in connection with the real narrowing of the boundaries of Russian influence in the Caspian Sea after the collapse of the USSR. Characteristic features of the Caspian Sea are the absence of water exchange with other seas and World Ocean, the reduced salt content (compared to the ocean), and the fact that its water balance is largely determined by the runoff of the rivers flowing into the sea and evaporation. The lack of water exchange makes it extremely sensitive to both changes in global and regional climate, as well as to anthropogenic impacts caused by river flow and its regulation, waste from resort areas and industrial centers on the shore, offshore oil and gas production and transportation, etc., which can lead to changes at the ecosystem level. The consequence of climate change is changes in sea surface temperature, its salinity and sea level, the onset of formation and duration of ice cover, associated with climate-related changes in air temperature, wind speed and direction, runoff of rivers flowing into the sea, atmospheric precipitation and evaporation from the sea surface. Environmental objectives and the maintenance of coastal infrastructure require constant monitoring of changes in these hydrological and meteorological parameters.

From April 2023 at the Shirshov Institute of Oceanology of Russian Academy of Sciences (Moscow), with the support of the Russian Science Foundation Grant N 23-77-00027, the project «Investigation of the climate variability of thermo-hydrodynamic regime of the Caspian Sea based on remote sensing data» (https://rscf.ru/en/project/23-77-00027) is being carried out. The main fundamental objectives of the project are:

1. Analysis of climatic variability of the main physical parameters of the sea state (sea surface temperature, sea level, wind waves, sea ice, etc.) and meteorological parameters (air temperature, atmospheric pressure, surface wind speed, humidity, integral water vapor content, water vapor content in clouds, atmospheric precipitation) over the waters of the Caspian Sea;
2. Application of the analysis of "extremeness" (i.e., phenomena that stand out sharply against the background of the "norm") to the study of the variability of the main parameters of the state of the Caspian Sea and the atmosphere over its water area. Analysis of extreme hydrological and meteorological events will be carried out using remote sensing data and reanalysis data. This will make it possible to give scientifically based recommendations for the implementation of the "Strategy for the development of Russian sea ports in the Caspian Basin, railway and road approaches to them in the period until 2030", adopted by Order of the Government of the Russian Federation of November 8, 2017 No. 2469-r.

The aim of this paper is: (1) to analyze histograms of the distribution of the main hydrometeorological parameters of the Caspian Sea for 1980–2021 – air temperature, atmospheric pressure, absolute humidity, atmospheric precipitation and wind speed according

to the MERRA-2 atmospheric reanalysis; (2) to construct and compare histograms for the entire study region of the Caspian Sea (36°–48°N, 45.625°–55°E), as well as separately for land and sea areas; (3) to calculate the extremeness criteria based on the normal distribution and the real histogram for all 5 main meteorological parameters; (4) to compare the histograms obtained from MERRA-2 data and from Derbent weather station located on the Caspian Sea coast; and (5) to analyze histograms of average monthly wind speed, integral water vapor content and water vapor content in clouds over the Caspian Sea constructed according to microwave radiometry (SMMR, SSM/I) data for the time interval 1980–2021.

## 2. Extreme and dangerous events, emergency situations

Extreme hydrological and meteorological phenomena are usually understood as those phenomena that stand out sharply in their characteristics against the background of "normal" phenomena in the climate system. As a rule, such phenomena have a special, often negative impact on natural systems and lead to the emergence of dangerous natural consequences, which should be understood as a spontaneous event of natural origin, which, in its intensity, scale of distribution and duration, can cause negative consequences for the life of people, as well as economy and natural environment. Depending on the mechanism and nature of origin, hazardous natural phenomena are divided into the following groups (classes):

1. Geophysical hazards: earthquakes; volcanic eruptions; tsunami.
2. Geological hazards (exogenous geological phenomena): landslides, mudflows, screes, avalanches, subsidence of the earth's surface, abrasion, erosion, dust storms, etc.
3. Meteorological and agrometeorological hazards: storms, hurricanes, tornadoes, squalls, vertical vortices (flows), large hail, heavy rain, heavy snowfall, heavy ice, severe frost, severe snowstorm, heat wave, cold wave, heavy fog, drought, dry wind, frosts.
4. Marine hydrological hazards: tropical cyclones (typhoons), strong waves, strong fluctuations in sea level, strong currents in ports, early ice cover or fast ice, ice pressure, intense ice drift, impassable (difficult to pass) ice, icing of ships, detachment of coastal ice.
5. Hydrological hazards: high water level, flood, rain floods, wind surge, low water level, early freeze-up and appearance of ice on navigable reservoirs and rivers, rising groundwater levels (flooding).
6. Natural fires: extreme fire danger, forest fires, fires of steppe and grain massifs, peat fires, underground fossil fuel fires.

Not every dangerous natural phenomenon leads to an emergency situation, especially if there is no threat to human life at the place of its occurrence. For example, an annual flood is not counted as a flood if it does not threaten anyone. There is no reason to consider storms, avalanches, freeze-ups, and volcanic eruptions as emergencies in places where people do not live or do any work. An emergency occurs only when, as a result of a dangerous natural phenomenon, a real threat arises to people and their environment. Many dangerous natural phenomena are closely related to each other. An earthquake can cause landslides, mudflows, floods, tsunamis, avalanches, and increased volcanic activity. Many storms, hurricanes, and tornadoes are accompanied by showers, thunderstorms, and hail. Extreme heat waves are accompanied by drought, low groundwater, fires, epidemics, and pest infestations.

## 3. Norm and extremeness

Climatic norms can be calculated for a wide range of parameters. While some parameters, such as temperature and precipitation, have significance for all parts of the world, others, such as snowfall or the exceedance of certain thresholds (for example, maximum temperatures below 0°C in the tropics), have little or no significance. meanings for some parts of the world.

According to [*WMO*, 2007], the period from 1961 to 1990 was adopted as the standard reference period for long-term climate change assessment. The Seventeenth World

Meteorological Congress [*WMO*, 2015] approved a number of changes that are reflected in the "*WMO Guidelines on the Calculation of Climate Normals*" in the definitions relating to climate norms [*WMO*, 2017]. The most significant of these changes was the redefinition of climatological standard normals so that they now apply to the most recent 30-year period ending with a year ending in 0 (for example, periods 1901–1930, 1931–1960, 1961–1990, and 1991–2020).

With the development of methods for remote sensing of the Earth from space at the end of the 20$^{th}$ century, the time interval 1961–1990 as the standard reference period or "norm" for long-term climate change assessments cannot be applied due to lack of data. Since the 1980s, active monitoring of the characteristics of the land and atmosphere (air and surface temperature, wind speed, humidity, atmospheric precipitation, integral content of water vapor, water in clouds, etc.) and the World Ocean (sea surface temperature, ocean color, sea level anomaly, sea surface state) has been carried out in the infrared, optical, and microwave ranges [*Kopelevich and Kostianoy*, 2018; *Kostianoy*, 2017a,b; *Kostianoy et al.*, 2018]. This makes it possible to determine the time intervals 1991–2020 as a reference period for long-term assessment of climate change in both the atmosphere, ocean and inland seas and calculate the "norm" of the state of individual parameters, relative to which "extreme" values will be determined.

Extreme meteorological phenomena are usually understood as statistics of "extreme", i.e., phenomena in the climate system that stand out sharply against the background of the "norm". As a rule, such phenomena have a special (usually negative) impact on natural systems, which are therefore especially sensitive to changes in their frequency and intensity [*IPCC*, 2007, 2014, 2021; *Roshydromet*, 2008, 2014, 2022; *Shkol'nik et al.*, 2012]. Various types of extreme events can be distinguished:

1. Values of meteorological parameters that differ greatly from the norm at points of regular observation (meteorological stations): anomalies exceeding certain threshold values (extreme heat/cold, rain, etc.); for this group the most reliable statistics can be obtained from observational data;
2. Long-term episodes during which a meteorological variable or set of variables exceeds a given level: heat and cold waves, droughts (it should be noted that in this case the levels are not necessarily "extreme": drought can be the result of a prolonged combination of above-normal temperature and precipitation below normal);
3. Large-scale phenomena associated with atmospheric circulation: the most intense cyclones/anticyclones, blockings, tropical hurricanes (typhoons); for these phenomena (at least for repeatability) fairly reliable statistics can also be obtained;
4. Dangerous or unfavorable natural phenomena of a local nature; this includes tornadoes, floods, severe ice, etc.: the peculiarity of this group is that, according to the observation network, it is difficult to obtain sufficiently adequate statistics for them; however, a qualitative analysis of regional generalizations on a fairly large scale is possible for them.

Definitions of extreme events in the first two groups depend on the choice of threshold values. One approach to the selection of threshold values is directly related to the understanding of extreme events as rare: in other words, belonging to the extreme regions of the distribution of a meteorological parameter, the probability of occurrence in which is low. Many researchers a priori accept the distribution of hydrometeorological parameters to correspond to the Gaussian distribution or normal distribution, and take the three-sigma law as threshold values, for example, [*Coumou and Robinson*, 2013].

A more reasonable criterion for determining "extremeness" is whether a value falls into a given percentile of the distribution function, for example, 10, 5, or 1 percentile for extreme negative anomalies (respectively, 90, 95, 99 percentile for positive ones).

Another approach is based on critical values, determined based on the thresholds of a certain (usually adverse) impact on natural or technical systems. The simplest example is frosts during the growing season; a more complex example is the adverse impact of

prolonged heat on people's health (here 2 thresholds must be assigned simultaneously, for example, temperatures above 30 °C for 5 days or more).

Changes in the statistics of extreme values inevitably occur with climate change, which for a given meteorological parameter is described by a change in the distribution function. In the simplest case, when the distribution is close to Gaussian, these changes are completely described by changes in the mean value and standard deviation. Changes in extremes can be described as changes in the probability (recurrence) of values exceeding a fixed threshold, or as changes in threshold values (if they are assigned according to the percentile of the distribution).

Thus, for example, if the average value increases and the overall variability remains constant, the frequency of positive extremes increases and the frequency of negative extremes decreases (Figure 1a). In terms of changes in the quantiles of the distribution, this means an increase in the threshold quantile in both cases (as the average decreases, the changes in the extrema are the opposite of those described). An increase in the variability of standard deviations with a constant average value leads to an increase in the frequency of both positive and negative extremes, or to an increase in the "upper" ($P_e^+$) thresholds and a decrease in the "lower" ($P_e^-$) (Figure 1b). Simultaneous changes in the mean value and standard deviation can lead to different results depending on the ratio of the magnitudes of these changes (Figure 1c). In the case of multimodal distribution, the picture becomes more complex (Figure 1d).

To describe extremes, the WMO Joint Working Group on Climate Change proposed a set of 27 extremeness indices [*Karl et al.*, 1999]. Most indices refer to the number of days on which the values of a meteorological parameter fall outside some specified threshold. Initially, the indices were defined for the whole year, but such definitions in many cases did not make much sense for the extratropical zone, where the seasonal variation of meteorological variables is large, so they were reformulated for seasons or months. The threshold for various locations may be fixed or variable (e.g., a specific percentile). The most commonly used extremity indices are:

1. FD – total number of days with frost (days). The indicator is important for agriculture. It is calculated as the number of days in a calendar year (season) with a daily minimum air temperature below 0 °C. In extratropical latitudes, the index in annual generalization is one of the possible characteristics of the duration of the cold period of the year.
2. R10 – number of days with precipitation of at least 10 mm (days). On the territory of Russia, the index mainly characterizes the frequency of significant precipitation, since in mid-latitudes a daily amount of 10 mm corresponds mainly to heavy precipitation.
3. CDD – maximum duration of the "dry" period per year (days). A "dry" period is defined as a sequence of days without precipitation or with traces of precipitation (<1 mm); can serve as an indicator of droughts. Changing the duration of such a phenomenon and shifting its boundaries affects vegetation and ecosystems as a whole.
4. TXx, TNn – annual maximum of maximum daily air temperature and annual minimum of minimum daily air temperature. Naturally, on the territory of Russia, the first of the indices characterizes the summer season, and the second - the winter season.
5. TX95p, TN5p – number of days per season (year) with extreme (above the 95th percentile/below the 5th percentile) values of maximum/minimum daily temperature.
6. RR95p – number of days per season (year) with extreme (above 95th percentile/below 5th percentile) precipitation.
7. Indices of "moderate" extremes (TX90p, TN10p, etc.)
8. Duration of stable frosty and frost-free periods, number of days with thaws, etc.

The disadvantage of the ongoing research is the averaging of the studied parameters and the generalization of the findings for very large territories and water areas comparable to the size of individual countries. This project proposes to detail the variability of various hydrometeorological parameters and characteristics of extreme climatic events with a

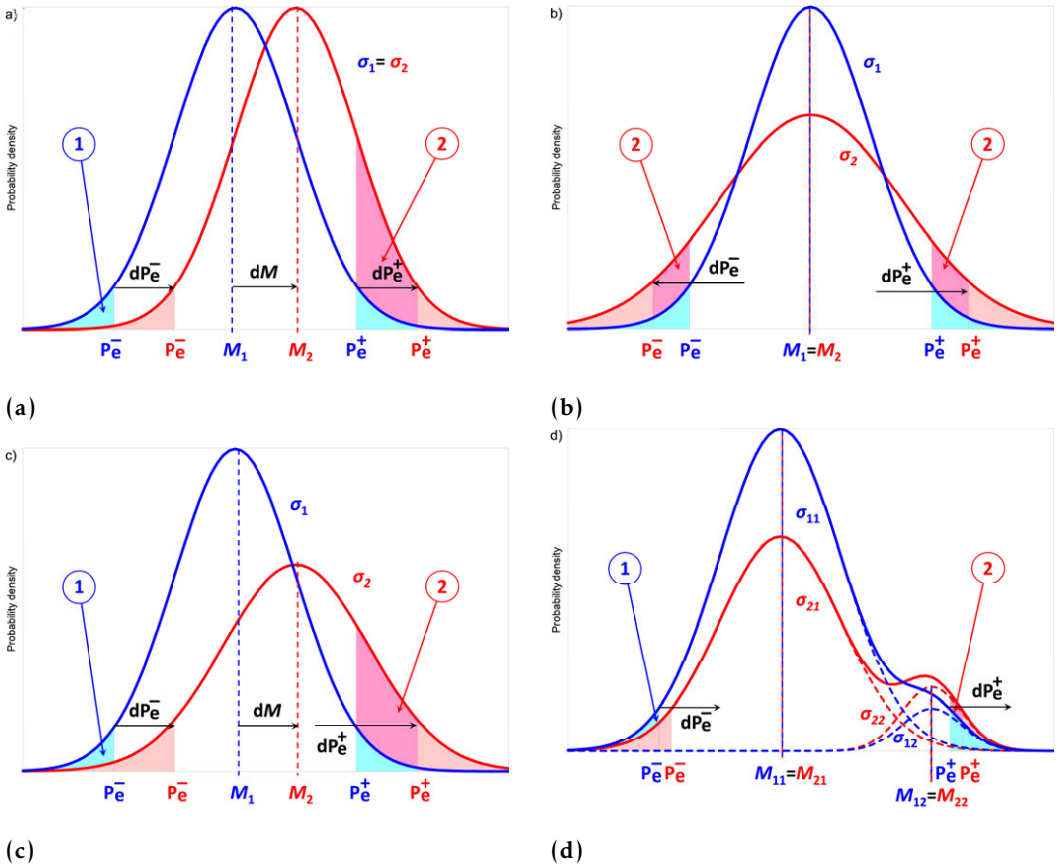


**Figure 1.** Scheme of possible changes in the frequency of extrema relative to unchanged percentiles of the distribution when changing the mean (a), dispersion (b), mean and dispersion (c), dispersion in the case of a multimodal distribution (d). The distribution of the previous climate is shown in blue, and the distribution of the new climate in red. $P_e^-$ and $P_e^+$ are threshold values for minimum and maximum values. $M_i$ and $M_{ij}$ are the mean, and $\sigma_i$ and $\sigma_{ij}$ are the standard deviation of the distributions. Numbers 1 and 2 show areas of decrease and increase in the frequency of events while maintaining threshold values.

spatial scale of about 0.5 degrees (and for some hydrological parameters of the state of the water surface – a quarter of a degree) in the Caspian Sea and its coast.

For the coast of the Caspian Sea and its waters, there is not enough data from field measurements to statistically describe the main parameters of the state of the atmosphere and sea water and identify extreme meteorological and/or hydrological phenomena. This is also true for mountainous or foothill areas, where instrumental measurements of meteorological parameters are clearly insufficient.

## 4. Data

For the study, regional databases of basic meteorological parameters for 1980–2021 were created:

1. Atmospheric pressure at sea level, atmospheric pressure at station level, air temperature, relative air humidity, water vapor pressure, amount of cloud cover, precipitation amounts, number of days with precipitation more than 1 mm, etc. according to data from coastal weather stations located on the coast of the Caspian Sea (Makhachkala, Baku, Fort Shevchenko, Turkmenbashi (formerly Krasnovodsk), etc.) [*Volkov et al.*, 2023a];
2. Air temperature, water temperature, atmospheric pressure at sea level, wind speed, humidity, precipitation, sea ice, state of vegetation cover – based on the global at-

mospheric reanalysis database MERRA-2 (Modern-Era Retrospective analysis for Research and Applications) [*Kostianoy and Lebedev*, 2023];

3. Surface wind speed, integral water vapor content and water vapor content in clouds according to microwave radiometers SMMR (Scanning Multichannel Microwave Radiometer) and SSM/I (Special Sensor Microwave Imager) [*Volkov et al.*, 2023b].

There are a huge number of databases on weather stations included in the network of the World Meteorological Organization, which exchanges data between its members. Thus, the All-Russian Scientific Research Institute of Hydrometeorological Information – World Data Center (VNIIGMI-MCD) provides urgent, daily and average monthly data from 521 meteorological stations in the territory of the former USSR from the moment the stations were founded to present, in some places with breaks for wars, etc. [*Bulygina et al.*, 2014; *Kuznetsova et al.*, 2019; *Shvets et al.*, 2018]. The main parameters of these data are: the number of days with precipitation more than 1 mm, air temperature, water vapor pressure, atmospheric pressure at the station level, average monthly cloudiness, precipitation amounts, relative air humidity, atmospheric pressure at sea level, etc.

Among the foreign sources of information on weather stations is the GSOD (Global Surface Summary of the Day) average daily data base [*NCDC NESDIS NOAA*, 2021; *Sparks et al.*, 2017] of the National Centers for Environmental Information. This database contains average daily data for the following parameters: average dew point, average sea level pressure, average wind speed (in knots), maximum sustained wind speed, snow depth (in inches). Historical data is generally available from 1929 to the present, with data from 1973 being the most complete. Since the data is converted to constant units (such as nodes), there may be a slight rounding error from the original data [*Lavigne and Liu*, 2022].

MERRA-2 (US National Aeronautics and Space Administration, NASA) is a global atmospheric reanalysis covering the era of satellite observations from 1980 to the present. It provides an organized, regularly referenced record of global atmospheric parameters and includes additional information about the climate system: trace gases (stratospheric ozone), an improved representation of the Earth's surface, and cryosphere processes. MERRA-2 is the first global reanalysis of the satellite era, assimilating space-based observations of aerosols and representing their interaction with other physical processes in the climate system [*Gelaro et al.*, 2017].

Application of microwave radiometry for climate studies of surface wind speed [*Atlas et al.*, 1996; *Chang and Li*, 1998], integral water vapor content [*Jackson and Stephens*, 1995; *Tjemkes et al.*, 1991] and cloud water vapor content [*Greenwald et al.*, 1993] became possible after the launch of the SMMR multichannel scanning radiometer on the Nimbus-7 satellite in 1978, which operated for about 9 years. With a short break, since 1987, operational meteorological satellites DMSP (Defense Meteorological Satellite Program) with microwave radiometers SSM/I have been constantly operating. The SSM/I multichannel scanning radiometer is the most prominent representative of satellite microwave radiometric systems operated in recent years as part of the US Department of Defense meteorological program designed for long-term monitoring of the Earth in order to provide global meteorological, oceanographic and solar geophysical operational information. In December 1992 the data was declassified and became available to the civil and scientific community. In the future, this series of observations may be expanded both by DMSP satellites and by satellites planned for launch. Thus, at present, a unique opportunity has arisen to assess changes in climate-significant parameters of the state of the atmosphere using satellite microwave radiometry methods.

## 5. Methods

To analyze extremality, at the first stage, distributions (probability density) were constructed for all parameters included in the created databases. For the parameters of the atmospheric state of the MERRA-2 reanalysis, the data of which exist both over land and over the sea: atmospheric pressure at sea level, air temperature (at a height of 2 m), absolute humidity (at a height of 2 m), precipitation and wind speed (at a height of

10 m) – three distributions were constructed for data over land, over the sea and over the whole Caspian Sea region (36°–48°N, 45.625°–55°E) for the time interval 1980–2021. A significant difference in distributions over land, over sea and over the region as a whole is observed for air temperature at a height of 2 m according to the MERRA-2 reanalysis data (Figure 2).

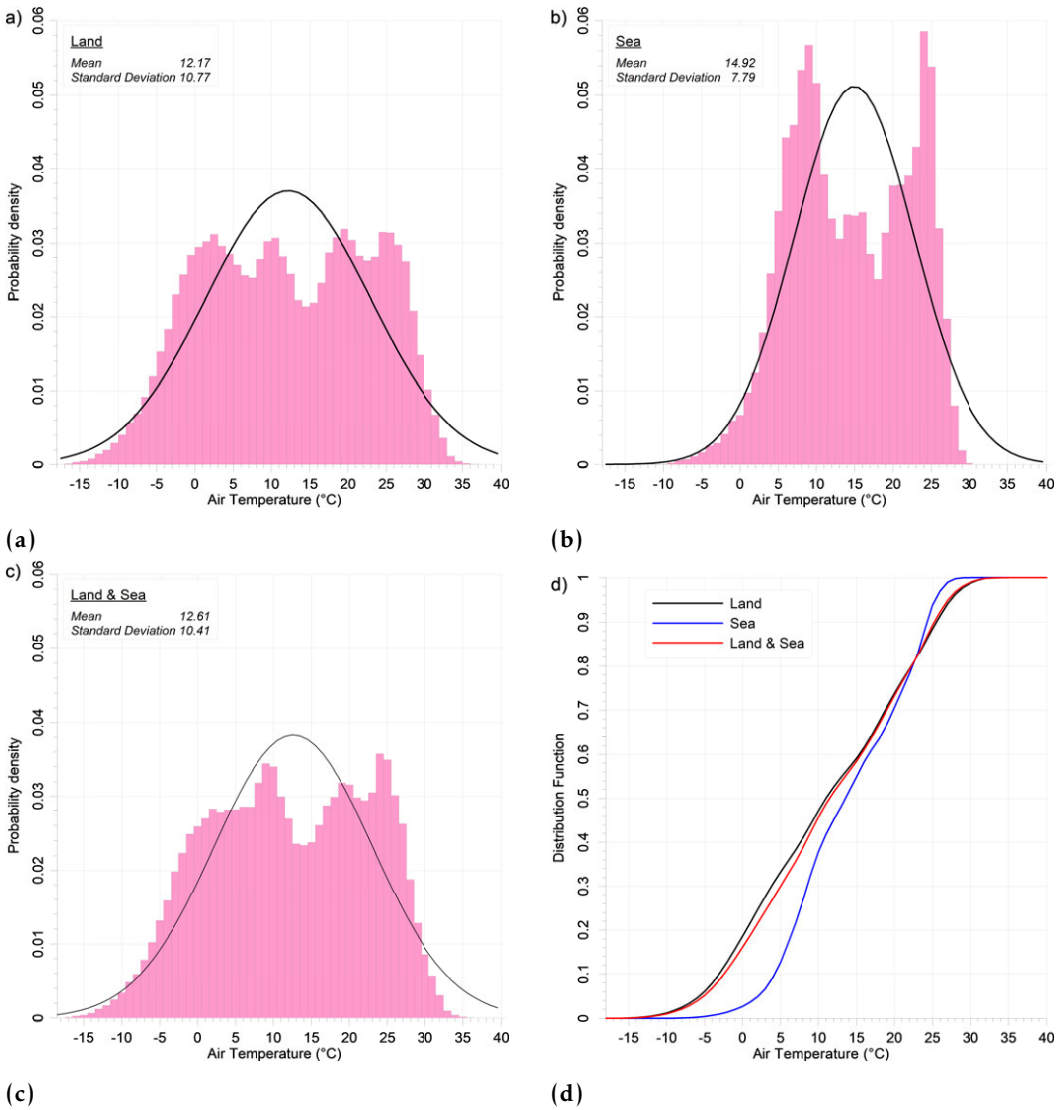


**Figure 2.** Probability density of air temperature at a height of 2 m above land (a), over the sea (b) and over the Caspian Sea region (36°–48°N, 45.625°–55°E) as a whole (c) and distribution function (d) according to MERRA-2 reanalysis data for 1980–2021. The solid line shows the corresponding Gaussian distributions. Each figure shows the mean value and standard deviation.

According to the MERRA-2 reanalysis, the probability density distribution of not a single parameter corresponds to a normal distribution (Figure 3). The distribution of atmospheric pressure at sea level is closest to it (Figure 3a). To analyze the probability density of wind speed (at a height of 10 m), the most optimal is the Rayleigh distribution (Figure 3e), and for atmospheric precipitation, the exponential distribution (Figure 3d).

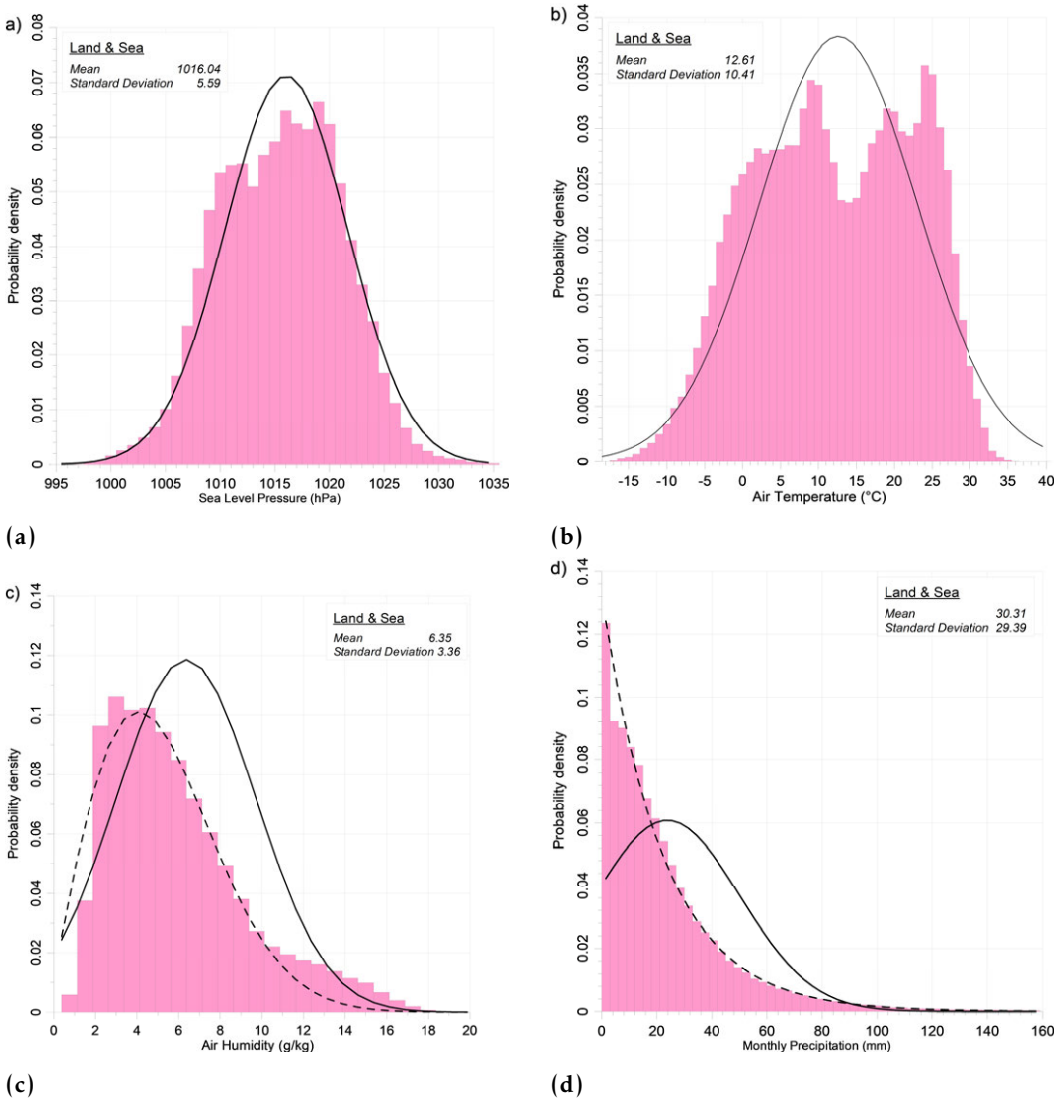
a)
Land & Sea
Mean 1016.04
Standard Deviation 5.59
Probability density
Sea Level Pressure (hPa)
(a)
b)
Land & Sea
Mean 12.61
Standard Deviation 10.41
Probability density
Air Temperature (°C)
(b)
c)
Land & Sea
Mean 6.35
Standard Deviation 3.36
Probability density
Air Humidity (g/kg)
(c)
d)
Land & Sea
Mean 30.31
Standard Deviation 29.39
Probability density
Monthly Precipitation (mm)
(d)

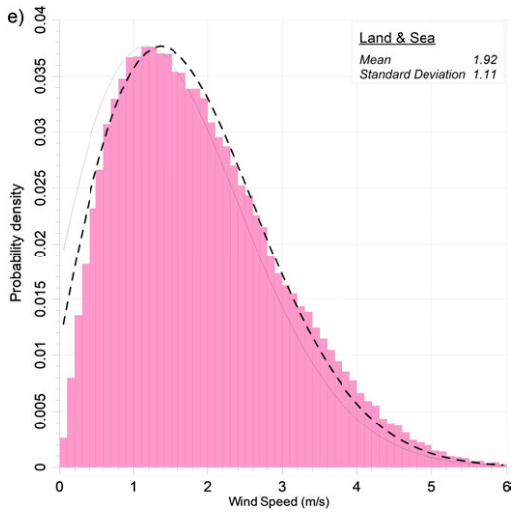


(e)

**Figure 3.** Probability density distribution of atmospheric pressure at sea level (a), air temperature (at a height of 2 m) (b), absolute humidity (at a height of 2 m) (c), atmospheric precipitation (d) and wind speed (at a height of 10 m) (e) over the Caspian Sea region (36°–48°N, 45.625°–55°E) according to MERRA-2 reanalysis data for the time interval 1980–2021. The solid line shows the corresponding Gaussian distributions (a–e), the dashed line shows exponential distribution (d) and Rayleigh distribution (c, e). Each figure shows the mean value and standard deviation.

## 6. Results and Discussion

The distributions of air temperature and absolute humidity at a height of 2 m can be considered multimodal or a combination of several Gaussian distributions (Figure 3b) or Gaussian and Rayleigh distributions (Figure 3c). Assuming that these probability densities of these values correspond to the Gaussian distribution, we compare the limits of extremity based on the 2 and 3 sigma rule with the limits determined from the 1, 5 and 10 percentiles for the minimum values and 99, 95 and 90 percentiles for the maximum values (Table 1).

**Table 1.** Extremeness criteria calculated from the normal distribution and a real histogram for five main meteorological parameters according to the MERRA-2 reanalysis data for 1980–2021.

| Criteria | Land | | Sea | | Land & Sea | |
|---|---|---|---|---|---|---|
| Sea level pressure (hPa) | | | | | | |
| 2 sigma (4.56%) | < 1010.25 | > 1021.62 | < 1011.43 | > 1021.52 | < 1010.44 | > 1021.64 |
| 3 sigma (0.28%) | < 1007.41 | > 1024.46 | < 1008.91 | > 1024.04 | < 1007.65 | > 1024.44 |
| 1 and 99 percentile (2%) | < 1002.49 | > 1027.92 | < 1006.30 | > 1026.57 | < 1002.79 | > 1027.76 |
| 5 and 95 percentile (10%) | < 1006.35 | > 1024.41 | < 1007.93 | > 1023.81 | < 1006.64 | > 1024.33 |
| 10 and 90 percentile (20%) | < 1008.10 | > 1022.68 | < 1009.06 | > 1022.42 | < 1008.28 | > 1022.64 |
| Air temperature (°C) | | | | | | |
| 2 sigma (4.56%) | < 1.41 | > 22.94 | < 7.12 | > 22.71 | < 2.20 | > 23.01 |
| 3 sigma (0.28%) | < −3.98 | > 28.33 | < 3.23 | > 26.61 | < −3.01 | > 28.22 |
| 1 and 99 percentile (2%) | < −10.00 | > 30.81 | < −2.45 | > 27.50 | < −9.55 | > 30.53 |
| 5 and 95 percentile (10%) | < −5.22 | > 27.88 | < 2.57 | > 25.86 | < −4.66 | > 27.52 |

Continued on next page

**Table 1**. Extremeness criteria calculated from the normal distribution and a real histogram for five main meteorological parameters according to the MERRA-2 reanalysis data for 1980–2021. (Continued)

| Criteria | Land | | Sea | | Land & Sea | |
|---|---|---|---|---|---|---|
| 10 and 90 percentile (20%) | < −2.60 | > 26.01 | < 4.72 | > 24.79 | < −1.95 | > 25.72 |
| Air humidity (g/kg) | | | | | | |
| 2 sigma (4.56%) | < 2.88 | > 8.86 | < 4.93 | > 12.95 | < 2.90 | > 9.72 |
| 3 sigma (0.28%) | < 1.39 | > 10.36 | < 2.93 | > 14.95 | < 1.31 | > 11.40 |
| 1 and 99 percentile (2%) | < 1.18 | > 14.55 | < 2.31 | > 17.13 | < 1.21 | > 13.97 |
| 5 and 95 percentile (10%) | < 1.86 | > 11.50 | < 3.44 | > 15.63 | < 1.93 | > 13.67 |
| 10 and 90 percentile (20%) | < 2.20 | > 9.58 | < 4.03 | > 14.60 | < 2.31 | > 10.94 |
| Monthly Precipitation (mm) | | | | | | |
| 2 sigma (4.56%) | | > 48.02 | | > 59.70 | | > 50.05 |
| 3 sigma (0.28%) | | > 60.74 | < 0.92 | > 74.40 | | > 63.17 |
| 1 and 99 percentile (2%) | < 22.59 | > 105.12 | < 30.31 | > 118.33 | < 23.81 | > 107.73 |
| 5 and 95 percentile (10%) | < 47.66 | > 79.87 | < 62.29 | > 93.77 | < 50.52 | > 137.24 |
| 10 and 90 percentile (20%) | < 54.52 | > 64.62 | < 73.45 | > 79.31 | < 57.49 | > 67.53 |
| Wind speed (m/s) | | | | | | |
| 2 sigma (4.56%) | < 0.76 | >2.88 | <1.32 | > 3.68 | < 0.81 | > 3.03 |
| 3 sigma (0.28%) | < 0.22 | >3.41 | < 0.72 | > 4.27 | < 0.26 | > 3.58 |
| 1 and 99 percentile (2%) | <0.36 | >4.80 | < 0.24 | > 5.39 | < 0.58 | > 4.92 |
| 5 and 95 percentile (10%) | < 0.55 | >3.79 | < 0.61 | > 4.45 | < 0.38 | > 3.94 |
| 10 and 90 percentile (20%) | < 1.82 | >3.25 | < 0.91 | > 4.00 | < 1.92 | > 3.43 |

For sea level pressure at land 3 sigma approximately corresponds to a value between 5 and 10 percentile for minimum values and 95 percentile for maximum values. For air temperature at land 3 sigma approximately corresponds to a value between 5–10 percentile for minimum values and between 95–99 percentile for maximum values. For air humidity at land 3 sigma approximately corresponds to a value between 1–5 percentile for minimum values and between 90–95 percentile for maximum values. For atmospheric precipitation at land 3 sigma approximately corresponds to a value of 90 percentile for maximum values. For wind speed at land 3 sigma approximately corresponds to values less than 1 percentile for minimum values and between 90–95 percentile for maximum values. For all five parameters the same relationships are valid for the sea area only as well as for the whole region of investigation.

Many real histograms are multimodal (Figure 3a, 3b). To develop an extremeness criterion, we present them as a superposition of several Gaussian distributions. For example, let's solve this problem for a histogram of air temperature over land (Figure 4a), which is decomposed into 4 Gaussian distributions. The probability density $p(x,I)$ in this case is written as:

$$p(x,I) = \frac{1}{\sum_{i=1}^{4} k_i} \sum_{i=1}^{I=4} \frac{k_i}{\sigma_i \sqrt{2\pi}} \exp\left(-\frac{(x-m_i)^2}{2\sigma_i^2}\right), \quad (1)$$

where $m_i$ is a mean value of a parameter $x$, $\sigma_i$ is a standard deviation, $k_i$ is a proportionality factor, $i = 1, 2, 3, 4$ is an index of the corresponding Gaussian distribution. Values of coefficients $m_i, \sigma_i$ and $k_i$ were calculated by minimizing the error functional

$$J(x, k_i, m_i, \sigma_i) = p(x, k_i, m_i, \sigma_i) - P(x),$$

where $P(x)$ – is a real histogram of distribution of parameter $x$.

The resulting system of linear equations was solved by the gradient descent method [*Korn and Korn*, 2000]. The resulting coefficient values for the air temperature histogram over land are presented in Table 2, and the corresponding distributions and their superposition in Figure 4b.

**Table 2**. Values of Gaussian distributions for air temperature over land are presented according to MERRA-2 reanalysis data for 1980–2021 time period.

| Distribution | Mean value of the parameter ($m$), °C | Standard deviation ($\sigma$), °C | Proportionality factor ($k$) |
|---|---|---|---|
| One distribution | 12.17 | 10.71 | 1.00 |
| Distribution 1 from 4 | 1.43 | 5.27 | 0.41 |
| Distribution 2 from 4 | 11.27 | 2.70 | 0.17 |
| Distribution 3 from 4 | 18.90 | 2.51 | 0.19 |
| Distribution 4 from 4 | 26.07 | 2.97 | 0.23 |

To identify the boundaries of extremity according to the 2 and 3 sigma rule, the average air temperature values and standard deviations of the first distribution for minimum values and the fourth distribution for maximum values were used according to Table 2. The results obtained are presented in Table 3.

Figure 4 shows that a superposition of four Gaussian distributions perfectly describes a real histogram of air temperature above land in the Caspian Sea region based on MERRA-2 data. The complexity of the real shape of the histogram of air temperature over land suggests that deviations from the norm calculated for 1980–2021 can be observed not only at the "tails" of the distribution, but also inside the distribution. Thus, Figure 5 shows the deviations of the annual distribution density from the climate norm.

**Table 3**. Extremeness criteria calculated from the normal distribution and a real histogram for air temperature over land (°C) according to the MERRA-2 reanalysis data for 1980–2021 time period.

| Criteria | Land | |
|---|---|---|
| One distribution | | |
| 2 sigma (4.56%) | < 1.41 | > 22.94 |
| 3 sigma (0.28%) | < −3.98 | > 28.33 |
| Distribution 1 and 4 from 4 | | |
| 2 sigma (4.56%) | < −2,43 | > 29.04 |
| 3 sigma (0.28%) | < −3.84 | > 30.53 |
| Histogram | | |
| 1 and 99 percentile (2%) | < −10.00 | > 30.81 |
| 5 and 95 percentile (10%) | < −5.22 | > 27.88 |
| 10 and 90 percentile (20%) | < −2.60 | > 26.01 |

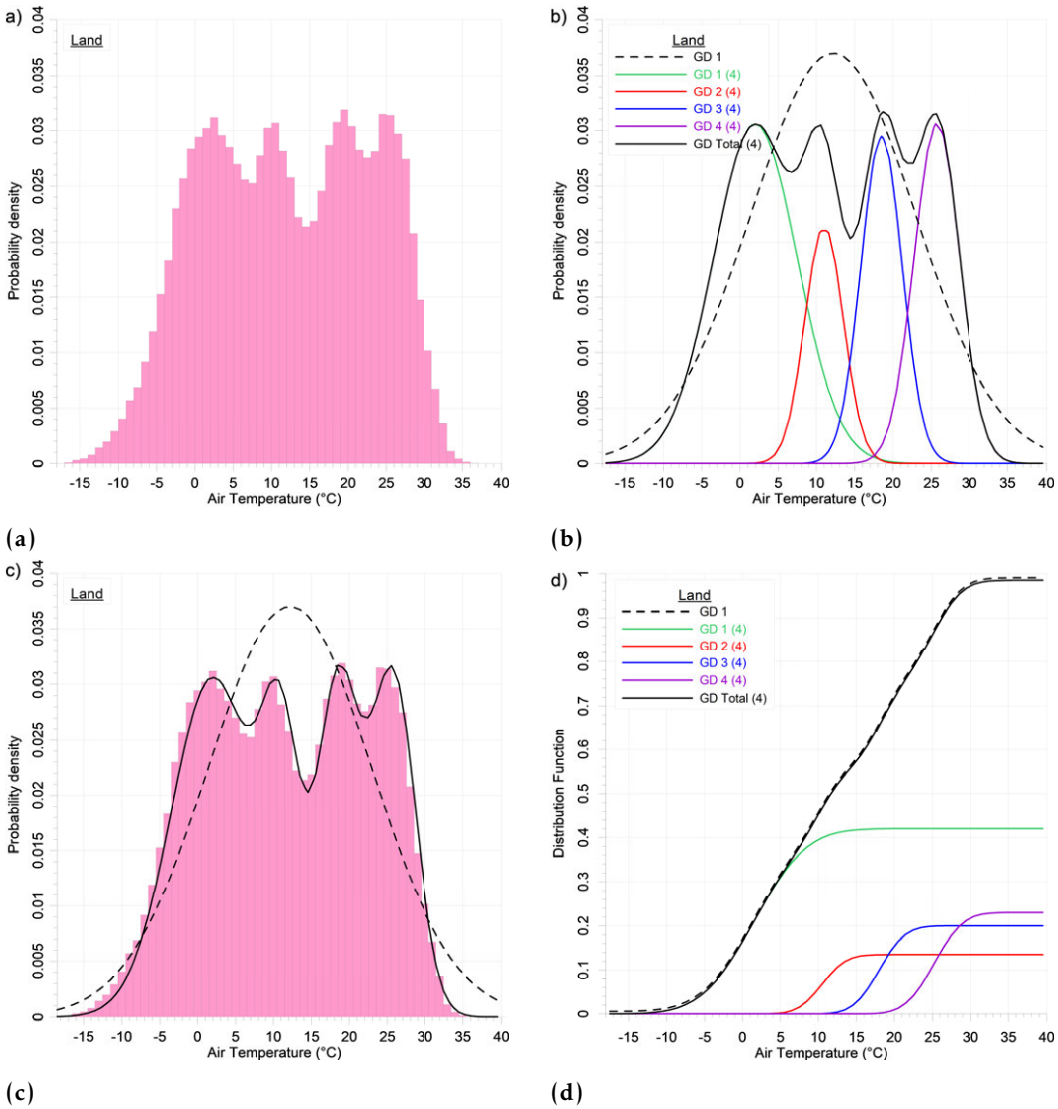


**Figure 4.** Probability density of air temperature at a height of 2 m above land (a), decomposition of the histogram into four Gaussian distributions (GD) (b), combined results (c) and distribution functions for each distribution (d) according to MERRA-2 reanalysis data for 1980–2021.

Analysis of the distribution of the main parameters according to data from weather stations located on the coast of the Caspian Sea (Figure 6) showed a relatively good agreement with the MERRA-2 reanalysis data at least for atmospheric pressure, air temperature and precipitation. The distribution of air temperature is considered multimodal or a combination of several Gaussian distributions (Figure 6b).

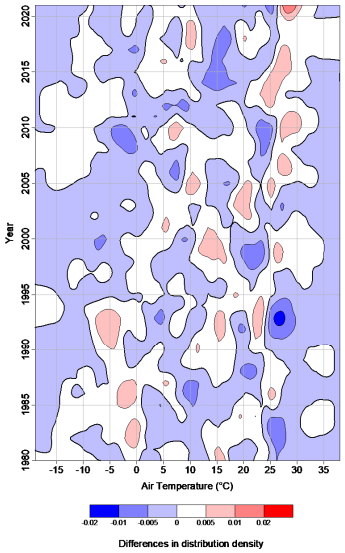


**Figure 5.** Deviations of the annual air temperature distribution density according to the MERRA-2 reanalysis data from the climate norm calculated for the time interval 1980–2021. The zero isoline is highlighted with a thick line.

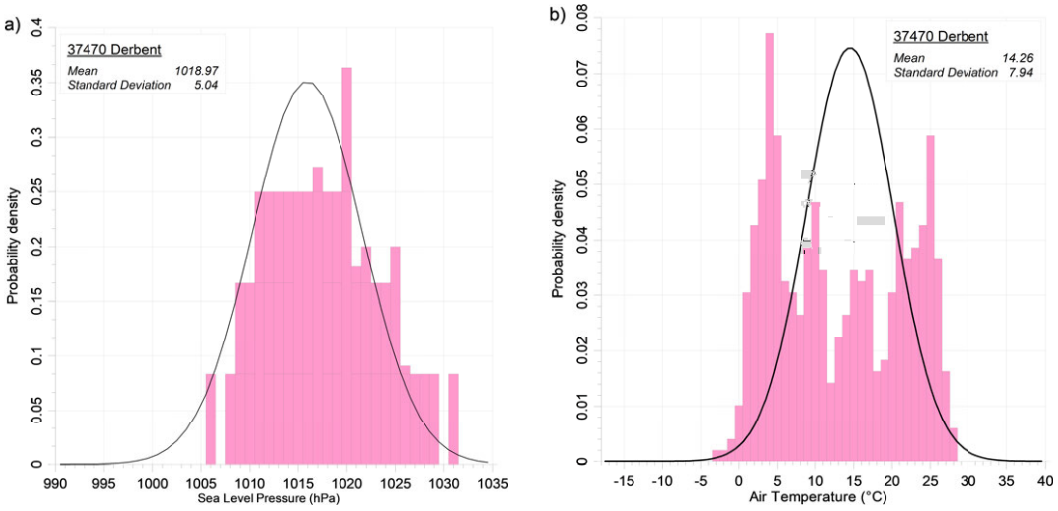


**(a)** **(b)**

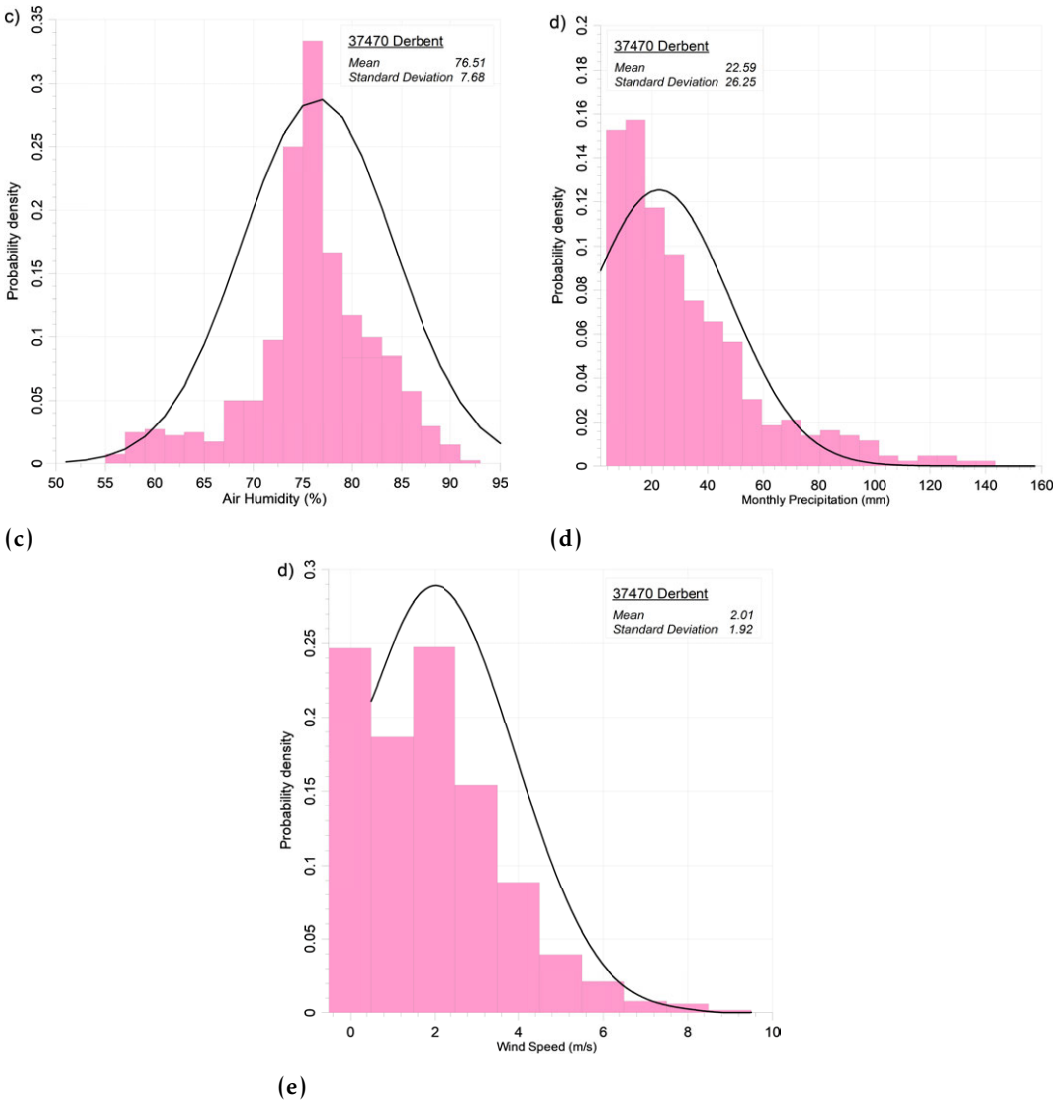


**Figure 6.** Probability density distribution of atmospheric pressure at sea level (a), air temperature (b), relative humidity (c), atmospheric precipitation (d) and wind speed (e) according to the Derbent weather station (WMO No. 37470) for the time interval 1980–2021. The solid line shows the corresponding Gaussian distributions. Each figure shows the mean value and standard deviation.

The distributions of average monthly wind speed (Figure 7a), integral water vapor content (Figure 7b) and water vapor content in clouds (Figure 7c) over the Caspian Sea were also constructed according to microwave radiometry data for the time interval 1980–2021.

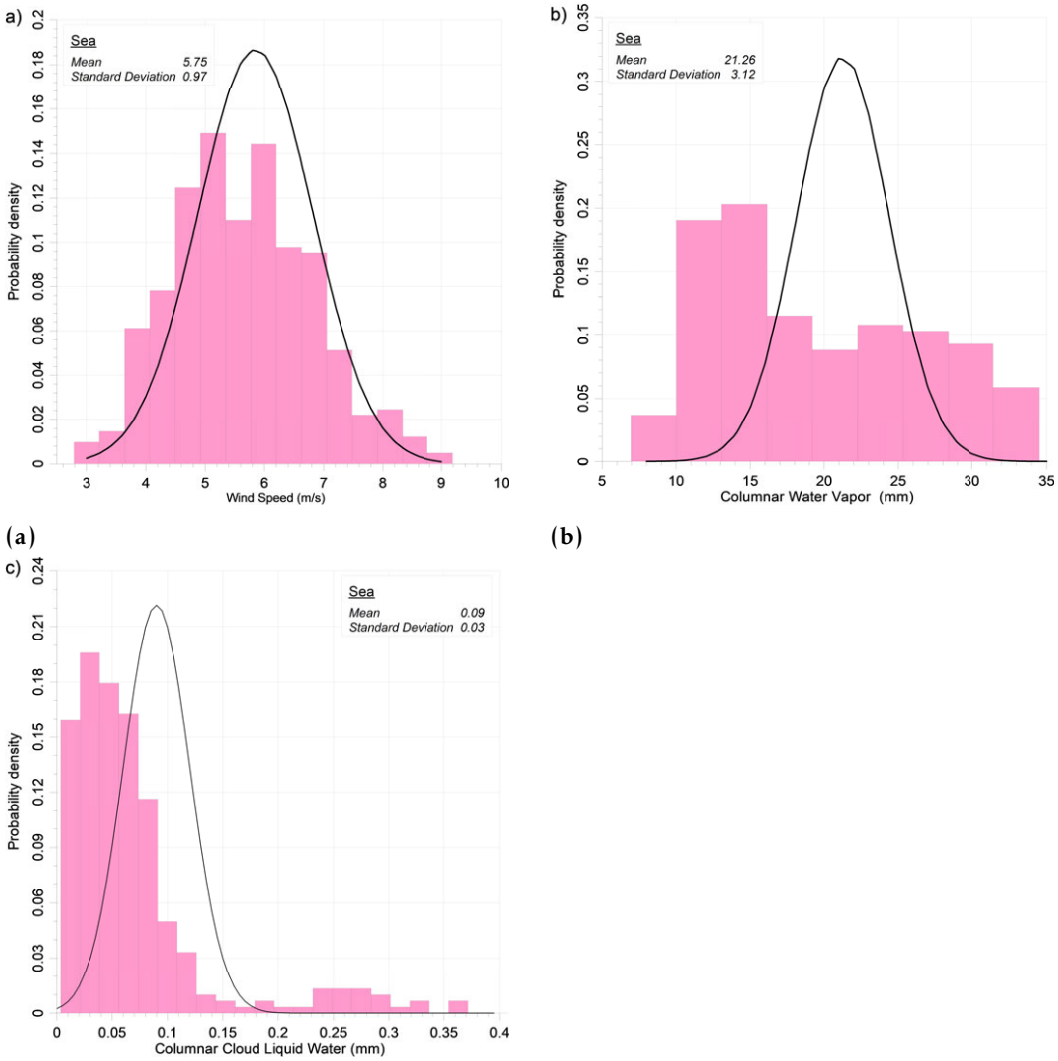


**Figure 7.** Probability density of average monthly wind speed (a), integral water vapor content (b) and water vapor content in clouds (c) over the Caspian Sea according to microwave radiometry data for the time interval 1980–2021. The solid line shows the corresponding Gaussian distributions. Each figure shows the mean value and standard deviation.

## 7. Conclusions

We have examined histograms of the main hydrometeorological parameters of the Caspian Sea Region in the boundaries between 36°–48°N, 45.625°–55°E based on the MERRA-2 atmospheric reanalysis for 1980–2021. The histograms of air temperature, atmospheric pressure, absolute humidity, atmospheric precipitation and wind speed have been built based on monthly averaged data. The histograms were constructed for the whole area of investigation mentioned above, as well as separately for land and sea areas. All these three types of histograms have been used to calculate extreme values of the above mentioned meteo parameters based on two and three sigma criteria, and 1 and 99, 5 and 95, 10 and 90 percentiles for minimum and maximum values accordingly.

All histograms turned out to be far from normal (Gaussian) distribution. The distribution of atmospheric pressure at sea level was closest to the normal distribution. The histogram of air temperature showed a multimodal distribution which has four distinct peaks (local maxima) in the probability density function. The Rayleigh distribution is the most optimal do describe the probability density of wind speed and humidity. In case of atmospheric precipitation, the exponential distribution has the best fit. In this respect, we

found that two and three sigma criteria do not work well for establishment of thresholds for extreme values, instead it is better to use a percentiles approach.

We could calculate a superposition of four Gaussian distributions which perfectly describes a real histogram of air temperature above land in the Caspian Sea region, as an example. This is a very promising methodology which can be used to understand the reasons of such a complex structure of the probability density function for air temperature. This will be one of the tasks for our future research – to understand the physical nature of this four-mode distribution. Potentially, we could expect three modes according to division of the Caspian Sea on the Northern, Middle and Southern Caspian.

A significant difference in distributions over land, over sea and over the region as a whole is observed for air temperature at a height of 2 m according to the MERRA-2 reanalysis data. For instance, for the land this is a four-mode distribution, and for the sea – two-mode distribution, as well as for the whole region where the sea plays the major role as a surface area.

Another interesting task is to follow interannual changes in thresholds of extreme values for different meteo parameters which will be displayed in the form of histograms. How will the tails change in the probability distributions, will they become longer or shorter, fat or thin?

A comparison was made of histograms obtained from MERRA-2 data and from weather station at Derbent located on the coast of the Caspian Sea. We found evident differences in the form of the obtained histograms for all five meteo parameters which is not surprising taking in mind a huge area of the Caspian Sea Region. Distributions of average monthly wind speed, integral water vapor content and water vapor content in clouds over the Caspian Sea were also constructed according to microwave radiometry (SMMR, SSM/I) data for the same time interval 1980–2021. If we compare histograms for wind speed constructed from MERRA-2, microwave radiometry and Derbent weather station, we also find significant discrepancies.

Finally, we have to note that we have analyzed general probability distributions constructed on the base of monthly averaged data for the 1980–2021 time period. Thus, the obtained characteristics of the extremes are seriously smoothed. This will be improved in the future research by using daily data. In case of air temperature the obtained characteristics of the negative and positive extremes correspond to minimal temperature in winter and maximal temperature in summer accordingly. But air temperature extremes can be observed at any point in the region under study on any day of the year, they will vary greatly and need to be calculated, which is of great importance for natural and socio-economic systems in the Caspian Sea Region.

**Acknowledgements**

The research was done with the support of the RSF Grant N 23-77-00027 "Investigation of the climate variability of thermo-hydrodynamic regime of the Caspian Sea based on remote sensing data", https://rscf.ru/en/project/23-77-00027.

## References

Atlas, R., R. N. Hoffman, S. C. Bloom, J. C. Jusem, and J. Ardizzone (1996), A Multiyear Global Surface Wind Velocity Dataset Using SSM/I Wind Observations, *Bulletin of the American Meteorological Society*, *77*(5), 869–882, https://doi.org/10.1175/1520-0477(1996)077<0869:AMGSWV>2.0.CO;2.

Bulygina, O. N., V. M. Veselov, V. N. Razuvaev, and T. M. Aleksandrova (2014), Description of an array of urgent data on the main meteorological parameters at Russian stations. Certificate of state registration of the database No 2014620549, http://meteo.ru/data/163-basic-parameters#%D0%BE%D0%BF%D0%B8%D1%81%D0%B0%D0%BD%D0%B8%D0%B5-%D0%BC%D0%B0%D1%81%D1%81%D0%B8%D0%B2%D0%B0-%D0%B4%D0%B0%D0%BD%D0%BD%D1%8B%D1%85 (in Russian).

Chang, P. S., and L. Li (1998), Ocean surface wind speed and direction retrievals from the SSM/I, *IEEE Transactions on Geoscience and Remote Sensing*, *36*(6), 1866–1871, https://doi.org/10.1109/36.729357.

Coumou, D., and A. Robinson (2013), Historic and future increase in the global land area affected by monthly heat extremes, *Environmental Research Letters*, *8*(3), 034,018, https://doi.org/10.1088/1748-9326/8/3/034018.

Gelaro, R., W. McCarty, M. J. Suárez, R. Todling, A. Molod, L. Takacs, C. A. Randles, A. Darmenov, M. G. Bosilovich, R. Reichle, K. Wargan, L. Coy, R. Cullather, C. Draper, S. Akella, V. Buchard, A. Conaty, A. M. da Silva, W. Gu, G.-K. Kim, R. Koster, R. Lucchesi, D. Merkova, J. E. Nielsen, G. Partyka, S. Pawson, W. Putman, M. Rienecker, S. D. Schubert, M. Sienkiewicz, and B. Zhao (2017), The Modern-Era Retrospective Analysis for Research and Applications, Version 2 (MERRA-2), *Journal of Climate*, *30*(14), 5419–5454, https://doi.org/10.1175/JCLI-D-16-0758.1.

Greenwald, T. J., G. L. Stephens, T. H. V. Haar, and D. L. Jackson (1993), A physical retrieval of cloud liquid water over the global oceans using special sensor microwave/imager (SSM/I) observations, *Journal of Geophysical Research: Atmospheres*, *98*(D10), 18,471–18,488, https://doi.org/10.1029/93JD00339.

IPCC (2007), *Climate Change 2007: The Physical Science Basis. Contribution of Working Group I to the Fourth Assessment Report of the Intergovernmental Panel on Climate Change*, 996 pp., Cambridge University Press, Cambridge, United Kingdom and New York, NY, USA.

IPCC (2014), *Climate Change 2014: Impacts, Adaptation, and Vulnerability. Part A: Global and Sectoral Aspects. Contribution of Working Group II to the Fifth Assessment Report of the Intergovernmental Panel on Climate Change*, 1132 pp., Cambridge University Press, Cambridge, United Kingdom and New York, NY, USA.

IPCC (2021), *Climate Change 2021 – The Physical Science Basis: Working Group I Contribution to the Sixth Assessment Report of the Intergovernmental Panel on Climate Change*, 1132 pp., Cambridge University Press, Cambridge, United Kingdom and New York, NY, USA, https://doi.org/10.1017/9781009157896.

Jackson, D. L., and G. L. Stephens (1995), A Study of SSM/I-Derived Columnar Water Vapor over the Global Oceans, *Journal of Climate*, *8*(8), 2025–2038, https://doi.org/10.1175/1520-0442(1995)008<2025:ASOSDC>2.0.CO;2.

Karl, T. R., N. Nicholls, and A. Ghazi (1999), CLIVAR/GCOS/WMO Workshop on Indices and Indicators for Climate Extremes Workshop Summary, in *Weather and Climate Extremes*, pp. 3–7, Springer Netherlands, https://doi.org/10.1007/978-94-015-9265-9_2.

Kopelevich, O. V., and A. G. Kostianoy (2018), The use of bio-optical parameters of the ocean, derived from satellite data as essential climate variables, *Fundamental and Applied Climatology*, *3*, 8–29, https://doi.org/10.21513/2410-8758-2018-3-8-29 (in Russian).

Korn, G., and T. Korn (2000), *Mathematical Handbook for Scientists and Engineers: Definitions, Theorems, and Formulas for Reference and Review*, 1152 pp., Dover Publications.

Kostianoy, A. G. (2017a), Satellite monitoring of the ocean climate parameters. Part 1, *Fundamental and Applied Climatology*, *2*, 63–85, https://doi.org/10.21513/2410-8758-2017-2-63-85 (in Russian).

Kostianoy, A. G. (2017b), Satellite monitoring of the ocean climate parameters. Part 2, *Fundamental and Applied Climatology*, *3*, 57–64, https://doi.org/10.21513/2410-8758-2017-3-57-64 (in Russian).

Kostianoy, A. G., and A. N. Kosarev (Eds.) (2005), *The Caspian Sea Environment*, Springer Berlin Heidelberg, https://doi.org/10.1007/b138238.

Kostianoy, A. G., and S. A. Lebedev (2023), Creation of a regional database of main meteorological parameters of the Caspian Sea for 1980–2022. according to the data of atmospheric reanalysis, in *Fundamental and applied aspects of geology, geophysics and geoecology using modern information technologies. VII International Scientific and Practical Conference. Part 1*, pp. 196–206, Maykop State Technological University, Republic of Adygeya, Maykop (in Russian).

Kostianoy, A. G., A. I. Ginzburg, O. V. Kopelevich, V. N. Kudryavtsev, O. Y. Lavrova, S. A. Lebedev, L. M. Mitnik, M. I. Mityagina, V. G. Smirnov, S. V. Stanichny, and Y. I. Troitskaya (2018), Ocean Remote Sensing in Russia, in *Comprehensive Remote Sensing*, pp. 284–325, Elsevier, https://doi.org/10.1016/B978-0-12-409548-9.10412-9.

Kuznetsova, V. N., S. G. Davletshin, and N. V. Shvets (2019), Description of the database "Average monthly relative air humidity at meteorological stations in Russia", Certificate of state registration of the database No 2019621537, http://meteo.ru/data/790-srednemesyachnaya-otnositelnaya-vlazhnost-vozdukha#%D0%BE%D0%BF%D0%B8%D1%81%D0%B0%D0%BD%D0%B8%D0%B5-%D0%BC%D0%B0%D1%81%D1%81%D0%B8%D0%B2%D0%B0-%D0%B4%D0%B0%D0%BD%D0%BD%D1%8B%D1%85 (in Russian).

Lavigne, T., and C. Liu (2022), Validity of Global Fog-Day Trends Indicated by the Global Surface Summary of the Day (GSOD) Data Set, *Journal of Geophysical Research: Atmospheres*, *127*(10), https://doi.org/10.1029/2021jd035881.

Lavrova, O. Y., A. G. Kostianoy, S. A. Lebedev, V. I. Mityagina, A. I. Ginzburg, and N. A. Sheremet (2011), *Complex Satellite Monitoring of the Russian Seas*, 470 pp., IKI RAS, Moscow (in Russian).

Lavrova, O. Y., M. I. Mityagina, and A. G. Kostianoy (2016), *Satellite Methods for Detecting and Monitoring Marine Zones of Ecological Risk*, 336 pp., IKI RAS, Moscow (in Russian).

Lavrova, O. Y., M. I. Mityagina, and A. G. Kostianoy (2022), *Satellite methods in the study of the Caspian Sea variability*, 250 pp., IKI RAS, Moscow (in Russian).

NCDC NESDIS NOAA (2021), Global Surface Summary of the Day (GSOD), https://www.ncei.noaa.gov/access/metadata/landing-page/bin/iso?id=gov.noaa.ncdc:C00516, (date of access: 20.08.2023).

Roshydromet (2008), *Assessment Report on Climate Change and its Consequences on the Territory of the Russian Federation. V. 1. Climate Change*, 227 pp., Roshydromet, Moscow (in Russian).

Roshydromet (2014), *Second Roshydromet Assessment Report on Climate Change and its Consequences in Russian Federation*, 1008 pp., Roshydromet, Moscow (in Russian).

Roshydromet (2022), *The Third Assessment Report on Climate Change and its Consequences on the Territory of the Russian Federation*, 227 pp., Roshydromet, St.-Petersburg (in Russian).

Shkol'nik, I. M., V. P. Meleshko, S. V. Efimov, and E. N. Stafeeva (2012), Changes in climate extremes on the territory of Siberia by the middle of the 21st century: An ensemble forecast based on the MGO regional climate model, *Russian Meteorology and Hydrology*, (2), 5–23 (in Russian).

Shvets, N. V., V. N. Razuvaev, and L. T. Trofimenko (2018), Description of the data array "Average monthly air pressure at sea level at meteorological stations in Russia", Certificate of state registration of the database No 2018621521, http://meteo.ru/data/746-srednemesyachnoe-davlenie-vozdukha-na-urovne-morya#%D0%BE%D0%BF%D0%B8%D1%81%D0%B0%D0%BD%D0%B8%D0%B5-%D0%BC%D0%B0%D1%81%D1%81%D0%B8%D0%B2%D0%B0-%D0%B4%D0%B0%D0%BD%D0%BD%D1%8B%D1%85 (in Russian).

Sparks, A. H., T. Hengl, and A. Nelson (2017), GSODR: Global Summary Daily Weather Data in R, *The Journal of Open Source Software*, *2*(10), 177, https://doi.org/10.21105/joss.00177.

Tjemkes, S. A., G. L. Stephens, and D. L. Jackson (1991), Spaceborne observation of columnar water vapor: SSMI observations and algorithm, *Journal of Geophysical Research: Atmospheres*, *96*(D6), 10,941–10,954, https://doi.org/10.1029/91JD00272.

Volkov, D. S., I. A. Kosolapov, D. A. Grebenikov, and S. A. Lebedev (2023a), Creation of the main meteorological parameters Caspian Sea regional database based on weather station data, in *Fundamental and applied aspects of geology, geophysics and geoecology using modern information technologies. VII International Scientific and Practical Conference. Part 1*, pp. 58–62, Maykop State Technological University, Republic of Adygeya, Maykop (in Russian).

Volkov, D. S., I. A. Kosolapov, D. A. Grebenikov, and S. A. Lebedev (2023b), Creation of the main meteorological parameters Caspian Sea regional database based on satellite microwave radiometry data, in *Fundamental and applied aspects of geology, geophysics and geoecology using modern information technologies. VII International Scientific and Practical Conference. Part 1*, pp. 63–68, Maykop State Technological University, Republic of Adygeya, Maykop (in Russian).

WMO (2007), *The role of Climatological Normals in a Changing Climate. WCDMP-No. 61. WMO-TD No. 1377*, 130 pp., World Meteorological Organization, Geneva.

WMO (2015), *Cg-17 Seventeenth World Meteorological Congress. Abridged final report with resolutions. Geneva. 25 May–12 June 2015. WMO-No. 1157*, 1171 pp., World Meteorological Organization, Geneva.

WMO (2017), *WMO Guidelines on the Calculation of Climate Normals. WMO-No. 1203*, 29 pp., World Meteorological Organization, Geneva.

Zonn, I. S., A. G. Kostianoy, A. N. Kosarev, and M. H. Glantz (2010), *The Caspian Sea Encyclopedia*, Springer Berlin Heidelberg, https://doi.org/10.1007/978-3-642-11524-0.

Russian Journal of Earth Sciences

Special Issue: "Fundamental and Applied Aspects of Geology, Geophysics and Geoecology"

# Temporal Variability of Soil Temperature in the North-West Arctic Zone of Russia. Part I: Interannual Linear Trends Based on Thermometer Measurements and Reanalysis Data

**Sergey A. Lebedev[1,2,3], Andrey G. Kostianoy[1,3,4,5], Ilya D. Tretiyak[1,6]**

[1]Geophysical Center of RAS, Moscow, Russia
[2]National Research University of Electronic Technology (MIET), Moscow, Zelenograd, Russia
[3]Maykop State Technological University, Maykop, Russia
[4]Shirshov Institute of Oceanology of RAS, Moscow, Russia
[5]S. Yu. Witte Moscow University, Moscow, Russia
[6]Phystech School of Applied Mathematics and Informatics of Moscow Institute of Physics and Technology, Dolgoprudny, Russia
* **Correspondence to:** Sergey A. Lebedev, lebedev@wdcb.ru

**Abstract:** In this article we investigate near-surface air temperature (NSAT) and soil temperature variability at four depths in the region of the White Sea, Murmansk and Arkhangelsk Regions, and Republic of Karelia. For the analysis we used NOAA-CIRES-DOE 20th Century Reanalysis (Version 3) reanalysis data for the 1980–2015 time period and data of bent-stem thermometers at 5, 10, 15, 20 cm depths and extraction thermometers at 20, 60, 80, 120, 240 and 320 cm depths for 1985-2021 time period. Average variability of NSAT is estimated using linear trend as +0.028 °C/year. For soil temperature a linear trend is of +0.0137 °C/year on surface (0 cm), +0.0136 °C/year at 10 cm depth, +0.0142 °C/year at 40 cm depth and +0.0133 °C/year at 100 cm depth.

**Keywords:** Air temperature, soil temperature, bent-stem thermometer, extraction thermometer, NOAA-CIRES-DOE 20th Century Reanalysis V3, climate change, North-West Arctic Zone of Russia.

**Citation:** Lebedev S. A., Kostianoy A. G., Tretiyak I. D. (2023), Temporal Variability of Soil Temperature in the North-West Arctic Zone of Russia. Part I: Interannual Linear Trends Based on Thermometer Measurements and Reanalysis Data, *Russian Journal of Earth Sciences*, Vol. 23, ES0212, https://doi.org/10.2205/2023ES02SI12

## 1. Introduction

Most climate change scenarios are based on studies of air temperature fluctuations. However, for many theoretical and applied problems, the response of the earth's surface to these changes is important. For the territory of Russia, more than half of which is occupied by the most sensitive shell to climate change – permafrost, this is of paramount importance, determining sudden changes in natural conditions and, as a consequence, infrastructure risks. As a result of climate warming, the depth of thawing in soils increases, but unevenly in different regions of the permafrost zone, including due to the action of processes with negative and positive feedbacks.

When solving many problems in the construction of buildings and technical structures, in the operation of roads and railways and underground communications, data on soil temperature (ST) at depths are used. The most important characteristic is the minimum annual temperature, which is necessary to determine the depth of seasonal soil freezing, and the interannual variability of ST at different horizons for scientifically based forecasts.

Research Article

Received: 22 September 2023
Accepted: 24 November 2023
Published: 15 December 2023

**Copyright:** © 2023. The Authors. This article is an open access article distributed under the terms and conditions of the Creative Commons Attribution (CC BY) license (https://creativecommons.org/licenses/by/4.0/).

## 2. Research area

According to observational data since the mid-1970s, average temperatures in the subarctic zone of Russia are growing 2.5 times faster than on the planet as a whole [*Intergovernmental Panel on Climate Change (IPCC)*, 2023; *IPCC*, 2007, 2013; *Roshydromet*, 2008, 2014, 2022]. This region of Russia is particularly vulnerable to climate change because hundreds of billions of dollars worth of infrastructure is located in the permafrost zone. If thawing of frozen strata occurs, then due to the significant ice content in them, the average soil settlement can be 10 meters or more.

Railway infrastructure in subarctic regions is operated in extremely difficult engineering-geological and landscape-climatic conditions, subject to continuous exposure to various external influences leading to deformations of the track and artificial structures [*Kostianaia and Kostianoy*, 2023; *Kostianaia et al.*, 2021]. Examples include coastal abrasion, mudflows, floods, erosion, landslides and drifts, karst failures, suffusion subsidence, ice dams, thermokarst, thermal erosion and solifluction, rupture deformations, snow avalanches, etc.

The Arctic zone of northwestern Russia (Murmansk, Arkhangelsk regions, Republic of Karelia) is characterized by the presence of island permafrost zones. The infrastructure of Russian Railways in this region is especially vulnerable to the negative factors of regional climate change, since the main problem of the Volkhovstroy - Murmansk section is the fact that out of 1.320 kilometers of its length, more than 340 kilometers are single-track sections, which limits its capacity and makes it vulnerable. In addition, on April 30, 2020, the Russian Government set the goal of increasing transportation from 28 to 44 million tons per year on the Murmansk branch of the Oktyabrskaya Railway by 2023, and not by 2035, as previously planned.

In this regard, studies of climate changes in the region under consideration (61°–70° N, 28°–45° E) are extremely important for Russian Railways. This study is a continuation of work begun in [*Gvishiani et al.*, 2023; *Serykh et al.*, 2022].

## 3. Data and Methods

To analyze the interannual variability of the state of the atmosphere and soil in the Arctic zone of northwestern Russia, the following data were selected: soil temperature (ST) observation data at 13 meteorological stations (Figure 1) of the Roshydromet network [*Bykhovets et al.*, 2007]. The data array contains daily ST values measured with bent-stem thermometers at 4 depths (5, 10, 15, 20 cm) under areas bare (cultivated) of vegetation, as well as daily ST values measured with extraction thermometers at 6 depths up to 320 cm (20, 60, 80, 120, 240, 320 cm). Typically, measurements with bent-stem thermometers are carried out from late spring to early autumn (May–October).

ST time intervals observation data at meteorological stations of Roshydromet network are presented in Table 1.

Observations contain gaps in data at individual depths or at all depths simultaneously. Sometimes these omissions coincide with various historical events and transitional moments in the development of the country. To assess the spatial variability of climate trends, the study area was divided into three subregions: (1) – Northern subregion (NSR): 65.5°–70° N, 28°–45° E; (2) – Central subregion (CSR): 63.5°–65.5° N, 28°–45° E; (3) – Southern subregion (SSR): 61°–62.5° N, 28°–45° E.

The density of these stations in the study region (Figure 1), unfortunately, does not allow us to assess climate variability for the entire region as a whole. For this reason, data from the NOAA-CIRES-DOE 20th Century Reanalysis (Version 3) [*Slivinski et al.*, 2019] for the period 1980–2015 were additionally used. with a spatial resolution of 1° in longitude and latitude at four horizons (0, 10, 40 and 100 cm). Calculations of the linear trend were carried out using average monthly near surface air temperature (NSAT) and ST data.

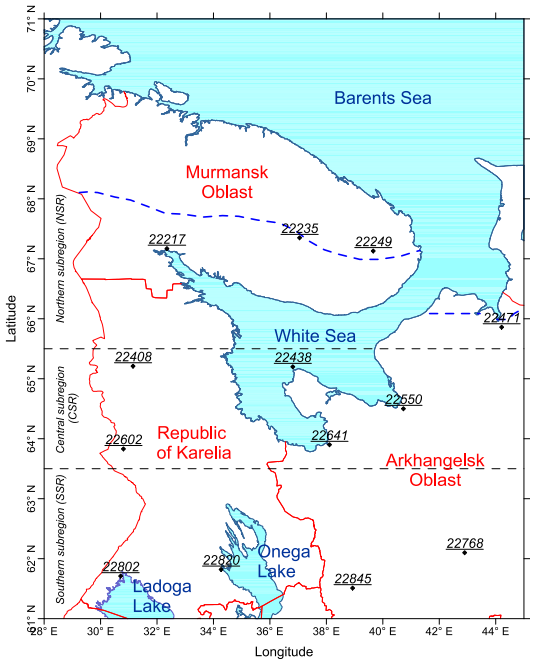


**Figure 1.** The location of weather stations in Arctic zone of northwest Russia, where ST observations are carried out at different depths. Blue dashed line is permafrost boundary. Gray dashed line is boundaries of subregions.

## 4. Results and their discussion

### 4.1. Results according to weather stations

Based on bent-stem thermometer ST measurements at weather stations, linear trends (°C/year) were calculated for the time interval 1985–2012. for each month when measurements were taken, at 4 depths. The maximum average positive climatic trends in ST changes across subregions according to bent-stem thermometer measurements for the period 1985–2012 are observed at all depths in July. The minimum trend in NSR is 0.085 °C/year and the maximum in SSR is 0.115 °C/year at a depth of 10 cm. In CSR this value in July is 0.081 °C/year. Below 10 cm depth, climate trends decrease with increasing depth in all subregions. Thus, we can say that the maximum contribution to the climate trend of ST changes is made in the summer months.

The average seasonal changes in TP climate trends across subregions at all depths exceeds 0.05 °C/year (Table 2). The maximum values are observed in CSR, the minimum – in NSR.

Since there are no ST measurements from the bent-stem thermometer in other months except for the period June–October, the contribution of other months can only be judged from the measurement data of extraction thermometers. Results of calculations of seasonal variability of climate trends at different depths for these measurements for the time interval 1985–2021. are presented in Figures 2–3 and Table 3.

In the seasonal course of depth-averaged linear trends in ST changes for all subregions, two maxima are observed: in spring-summer (May–June) and in autumn (September–October), and two minima – in spring (April) and in summer (July–August) (Figure 4).

For NSR and CSR, the values of the June maxima are almost the same and amount to 0.055 and 0.056 °C/year, respectively, and for SSR this value is 0.044 °C/year (Figure 4). This can be explained by the fact that in NSR in June at depths up to 140 cm there is an area of high ST trends of more than 0.06 °C/year with a local maximum of 0.083 °C/year at a depth of 120 cm (Figure 5a). In June, in the CSR at depths of 65–175 cm, an area of high ST trends of more than 0.06 °C/year is observed (Figure 5b). In May in SSR, the area of increased ST trends of more than 0.08 °C/year is localized at depths up to 55 cm. With increasing depth, the trend sharply decreases to 0.025 °C/year (at 320 cm). The large trend

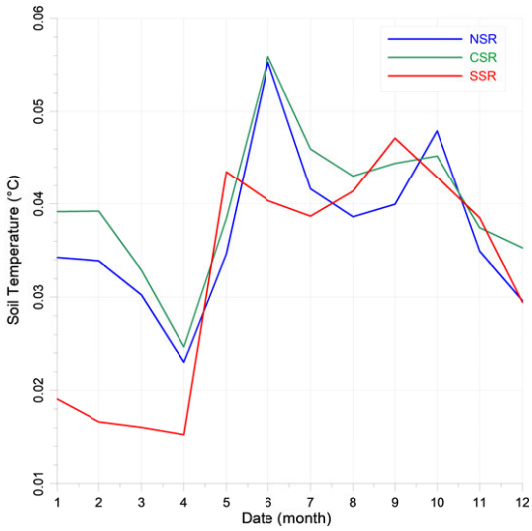


**Figure 2.** Seasonal variability of depth-averaged linear trends (°C/year) in subregions according to ST observations at meteorological stations of the Roshydromet network for extraction thermometer for the time interval (1985–2021).

gradient reduces the depth-average value to 0.044 °C/year (Figure 5c). A similar monthly shift between SSR and CSR/NSR is also observed in autumn maxima, the values of which lie in the range of 0.045–0.048 °C/year. This is explained by slower changes in the ST trend with depth (Figure 5).

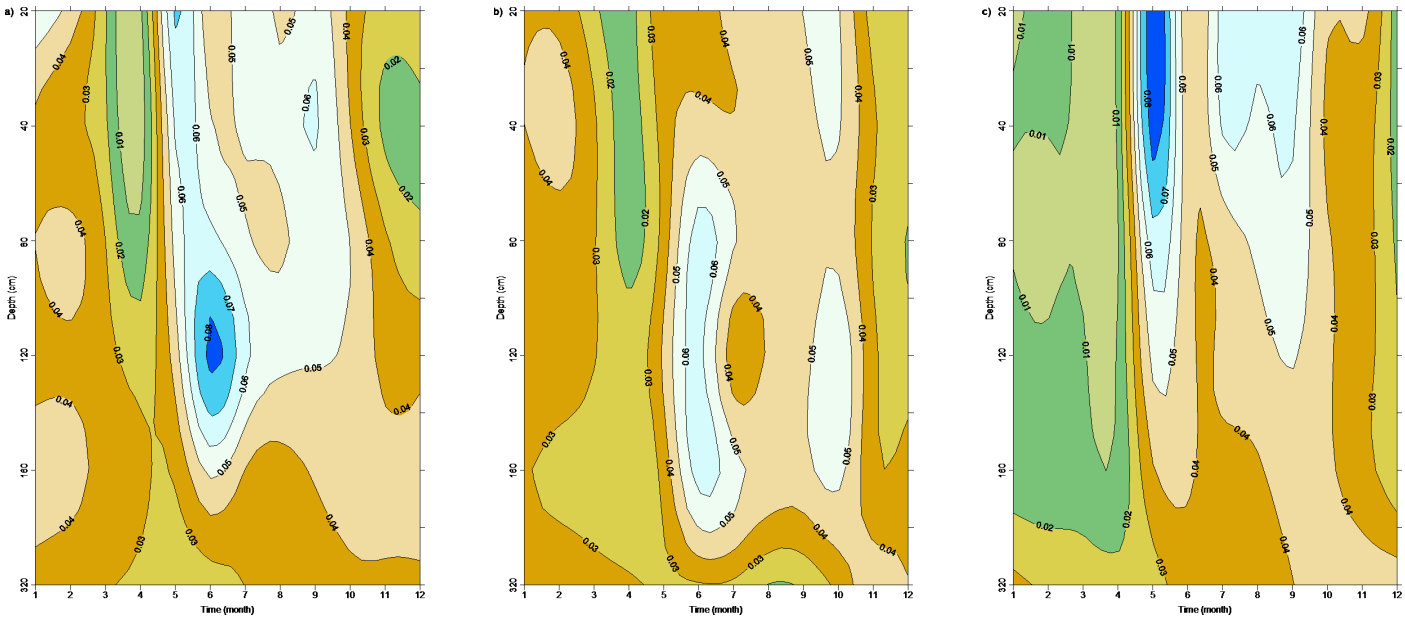


**(a)** **(b)** **(c)**

**Figure 3.** Seasonal and deep linear trends variability (°C/year) for NSR (a), CSR (b) and SSR (c) according to ST observations at meteorological stations of Roshydromet network for extraction thermometer for time interval (1985–2021).

The April minimum of the depth-averaged TP climate trend according to extraction thermometer data for NSR and CSR are also close to each other: 0.023 and 0.025 °C/year, respectively, and for SSR this value is 0.015 °C/year (Figure 2). As well as for the June maximum of ST trends, changes in depth are observed to include a vast area of less than 0.02 °C/year, which extends from the surface to 100 cm in the NSR and CSR (Figure 3a, 3b). In SSR, this area is observed down to a depth of 240 cm (Figure 3c).

**Table 1**. Time intervals of ST data observation data observation at meteorological stations of Roshydromet network for various thermometers types.

| # WMO | Name of station | Bent-stem thermometers | Extraction thermometers |
|---|---|---|---|
| NSR: 28°–45°E – 65.5°–70°N | | | |
| 22217 | Kandalaksha | 1985–2012 | 1963–2022 |
| 22235 | Krasnoshchelye | 1985–2012 | 1977–2022 |
| 22249 | Kanevka | 1984–2012 | 1977–2022 |
| 22471 | Mezen | 1984–2012 | 1977–2022 |
| CSR: 28°–45°E – 63.5°–65.5°N | | | |
| 22408 | Kalevala | 1984–2012 | 1977–2022 |
| 22438 | Zhizhgin Island | – | 1977–2022 |
| 22550 | Arkhangelsk | – | 1965–2022 |
| 22602 | Reboly | 1984–2012 | 1963–2022 |
| 22641 | Onega | 1984–2012 | 1963–2022 |
| SSR: 28°–45°E – 61°–63.5°N | | | |
| 22768 | Shenkursk | 1984–2012 | 1977–2022 |
| 22802 | Sortavala | 1984–2012 | 1963–2022 |
| 22820 | Petrozavodsk | 1984–2012 | 1963–2022 |
| 22845 | Kargopol | 1984–2012 | 1963–2022 |

As in local maxima, a monthly shift between SSR and CSR/NSR is also observed in summer minima, the values of which lie in the range of 0.040–0.046 °C/year. This is explained by the presence of a large area of less than 0.05 °C/year in August to depths of 170 cm (NSR) and 240 cm (CSR) (Figures 3a, 3b). In the SSR, this area is located at depths of 120–320 cm (Figure 3c)

The average seasonal changes in TP climate trends across subregions at all depths exceeds 0.03 °C/year (Table 3). The maximum value of 0.0459 °C/year is observed in CSR at a depth of 120 cm, and minimum value is of 0.0296 °C/year is observed at depth of 160 cm in SSR.

## 5. Results according to reanalysis data

In the study region, according to [*Serykh et al.*, 2022], according to the NCEP/NCAR reanalysis data, in the last 2 decades (1999–2020), NSAT increased from 0.9 to 1.5 °C compared to previous years (1977–1998), and the increase in NST was 0.04–0.1 °C. This led to a shift of the +2 °C isotherm by 550 km to the north up to the southern part of the White Sea and to the complete disappearance of average negative temperatures. According to the NOAA-CIRES-DOE 20th Century Reanalysis (Version 3) for the period 1980–2015, a linear trend for NSAT at a height of 2 m for the region as a whole was 0.024 °C/year. The maximum trend was observed in NSR – 0.031 °C/year, and the minimum in CSR – 0.023 °C/year. In SSR, the climate trend was 0.024 °C/year, which is slightly higher than in CSR (Table 4).

Analysis of the spatial distribution of interannual trends (Figure 4) shows. that the linear NSAT trend begins to increase from +0.005 °C/year from north to south till the Onega Bay of the White Sea. Further, the growth of the interannual trend increases in the northeast direction.

The climatic increase in ST for the entire region was: 0.0095 °C/year at the surface (0 cm), 0.0096 °C/year at a depth of 10 cm, 0.0102 °C/year at a depth of 40 cm and 0.0097 °C/year at a depth of 100 cm (Table 4). In NSR, the maximum climate trend was

**Table 2.** Average linear trends in the sub-regions (°C/year) according to ST observations at meteorological stations of Roshydromet network for bent-stem thermometer over a time interval 1985–2012.

| Value | Depth | | | |
|---|---|---|---|---|
| | 5 cm | 10 cm | 15 cm | 20 cm |
| NSR: 28°–45°E – 65.5°–70°N | | | | |
| Average value | 0.0522 | 0.0558 | 0.0518 | 0.0510 |
| Standard deviation | 0.0156 | 0.0138 | 0.0070 | 0.0112 |
| CSR: 28°–45°E – 63.5°–65.5°N | | | | |
| Average value | 0.0632 | 0.0652 | 0.0589 | 0.0561 |
| Standard deviation | 0.0220 | 0.0209 | 0.0189 | 0.0158 |
| SSR: 28°–45°E – 61°–63.5°N | | | | |
| Average value | 0.0577 | 0.0564 | 0.0561 | 0.0552 |
| Standard deviation | 0.0391 | 0.0372 | 0.0334 | 0.0162 |

**Table 3.** Sub-regions average linear trends (°C/year) according to ST observations at meteorological stations of Roshydromet network for extraction thermometers for time interval 1985–2021.

| Value | Soil depth | | | | | |
|---|---|---|---|---|---|---|
| | 20 cm | 40 cm | 80 cm | 120 cm | 160 cm | 320 cm |
| NSR: 28°–45°E – 65.5°–70°N | | | | | | |
| Average value | 0.0356 | 0.0375 | 0.0378 | 0.0388 | 0.0393 | 0.0321 |
| Standard deviation | 0.0095 | 0.0083 | 0.0110 | 0.0094 | 0.0116 | 0.0058 |
| CSR: 28°–45°E – 63.5°–65.5°N | | | | | | |
| Average value | 0.0417 | 0.0373 | 0.0418 | 0.0459 | 0.0409 | 0.0320 |
| Standard deviation | 0.0148 | 0.0158 | 0.0119 | 0.0113 | 0.0047 | 0.0040 |
| SSR: 28°–45°E – 61°–63.5°N | | | | | | |
| Average value | 0.0385 | 0.0363 | 0.0326 | 0.0311 | 0.0296 | 0.0350 |
| Standard deviation | 0.0233 | 0.0215 | 0.0183 | 0.0150 | 0.0117 | 0.0070 |

0.0166 °C/year at a depth of 40 cm, in CSR – 0.0072 °C/year and SSR – 0.0018 °C/year at the same depth (Table 4). In general, the same picture is observed as according to measurement data at weather stations only relative to a depth of 10 cm. This difference is apparently associated with the parameterization of heat and moisture exchange processes in the soil, which is used in the atmospheric circulation model when calculating reanalysis fields [*Arzhanov and Mokhov*, 2013; *Slivinski et al.*, 2019].

On the Kola Peninsula and the eastern coast of the White Sea (Zimny and Kaninsky coasts and Mezen Bay) value of ST linear trends exceeds +0.025 °C/year (Figure 5a). The linear trend of ST behaves the same at all depths. In the southern part of the region (south of latitude 61.5°) it has negative values. On the territory of the Republic of Karelia there is an area of negative values elongated in a northeast direction towards the Pechersk coast (Figures 5a–5d). For the Kola Peninsula, the interannual ST trend is more than +0.01 °C/year at all 4 depths. A similar picture is observed on the eastern coast of the White Sea north of the Northern Dvina Delta.

More informative is the ratio of the linear trend of ST at a depth of 100 cm to the linear trend of NSAT [*Pavlov*, 2008]. For the Kola Peninsula and the eastern coast of the White Sea north of the Northern Dvina Delta, its value is more than 0.4. At the same time, in the area of the Rybachy and Teriberka Peninsulas (northern coast of the Kola Peninsula) and

**Table 4.** Average linear trends for air and soil temperature in the sub-regions (°C/year) according to NOAA-CIRES-DOE 20th Century Reanalysis for time period 1980–2015.

| Value | Air | Soil Depth | | | |
|---|---|---|---|---|---|
| | | 0 cm | 10 cm | 40 cm | 100 cm |
| NSR: 28°–45°E – 65.5°–70°N | | | | | |
| Average value | 0.0312 | 0.0154 | 0.0161 | 0.0166 | 0.0155 |
| Standard deviation | 0.0050 | 0.0033 | 0.0037 | 0.0036 | 0.0035 |
| CSR: 28°–45°E – 63.5°–65.5°N | | | | | |
| Average value | 0.0231 | 0.0068 | 0.0065 | 0.0072 | 0.0069 |
| Standard deviation | 0.0032 | 0.0053 | 0.0059 | 0.0059 | 0.0055 |
| SSR: 28°–45°E – 61°–63.5°N | | | | | |
| Average value | 0.0108 | 0.0013 | 0.0008 | 0.0018 | 0.0017 |
| Standard deviation | 0.0046 | 0.0019 | 0.0019 | 0.0019 | 0.0019 |
| Total region: 28°–45°E – 61°–70°N | | | | | |
| Average value | 0.0235 | 0.0095 | 0.0096 | 0.0102 | 0.0097 |
| Standard deviation | 0.0084 | 0.0070 | 0.0076 | 0.0075 | 0.0069 |

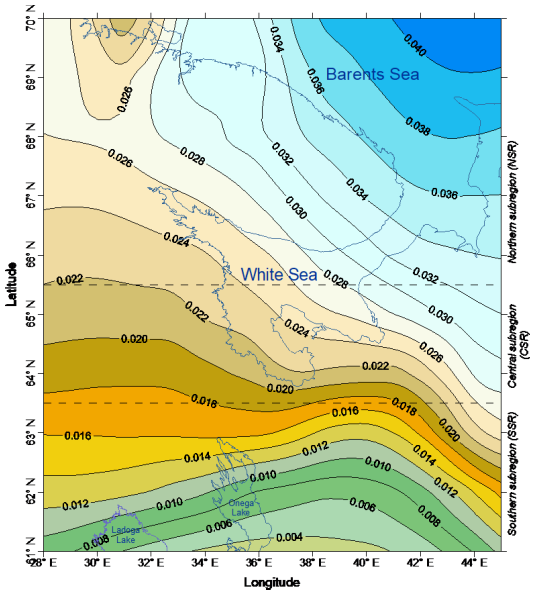


**Figure 4.** NSAT climatic trends (°C/year) changes according to NOAA-CIRES-DOE 20th Century Reanalysis data for time period 1980–2015.

north of the White Sea – Kuloi Plateau (eastern coast of the White Sea), areas of maximum values of this ratio of more than 0.6 are observed. It is in these areas that island permafrost zones are observed. which are at high risk of destruction (Figure 6).

## 6. Conclusions

Analysis of ST climatic variability according to bent-stem thermometer measurements at weather stations for time period 1985–2012 shows positive trend values at all 4 depths exceeding 0.05 °C/year. Maximum values of 0.0561–0.0652 °C/year are observed for CSR, the minimum 0.0510–0.0558 °C/year – for NSR. According to extraction thermometers for time interval 1985–2021, ST linear trends for all depths exceeds 0.03 °C/year. Maximum value is 0.0459 °C/year is observed in CSR at a depth of 120 cm, and minimum value is 0.0296 °C/year at a depth 160 cm in SSR.

According to NOAA-CIRES-DOE 20th Century Reanalysis for time period 1980–2015, ST climatic growth in whole region was 0.0095 °C/year at surface (0 cm), 0.0096 °C/year at a depth of 10 cm, 0.0102 °C/year at a depth of 40 cm and 0.0097 °C/year at a depth of 100 cm. In NSR, maximum climatic trend was 0.0166 °C/year at a depth of 40 cm, in CSR −0.0072 °C/year and SSR – 0.0018 °C/year at same depth.

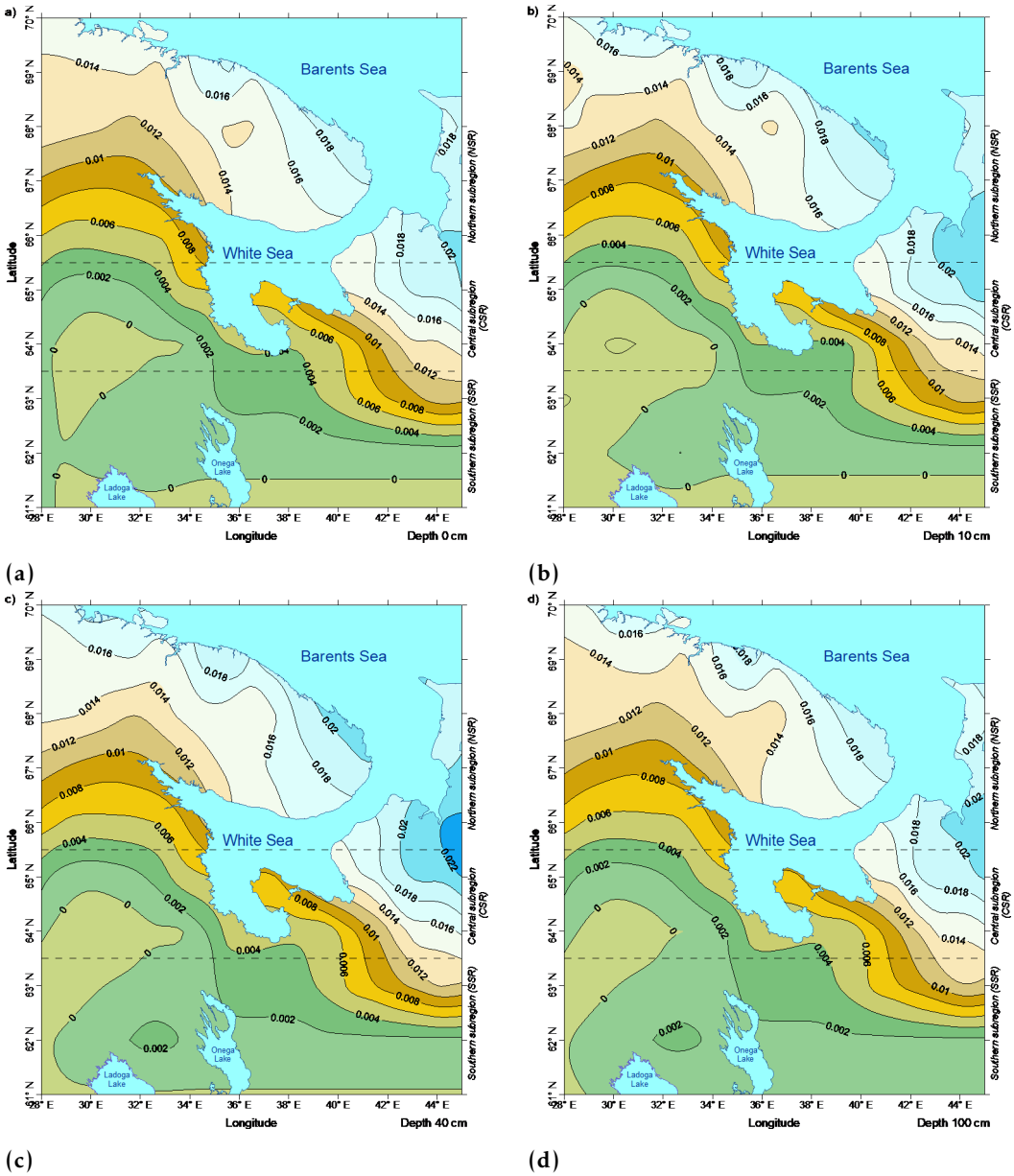


**Figure 5.** Climatic trends (°C/year) in ST changes at depths of 0 cm (a). 10 cm (b). 40 cm (c) and 100 cm (d) according to NOAA-CIRES-DOE 20th Century Reanalysis for the period 1980–2015.

These data are in a good agreement with values calculated according to the data for permafrost thermal monitoring for the past 25–35 years. According to work [*Pavlov*, 2008] linear trends of NSAT and ST for 1961–2003 in the north of the European part of Russia were +0.026 °C/year and +0.018 °C/year, respectively. Time interval for interannual trends in the Second Assessment Report of Roshydromet on climate change and its consequences on Russian Federation territory [*Roshydromet*, 2014] was expanded to 1961–2010. Linear trens presented in the Report become higher: +0.033 °C/year and +0.024 °C/year, respectively. The ratio of the linear trend of ST to the linear trend of NSAT was 0.69 in [*Pavlov*, 2008] and 0.73 in [*Roshydromet*, 2014]. According to our data, this ratio was

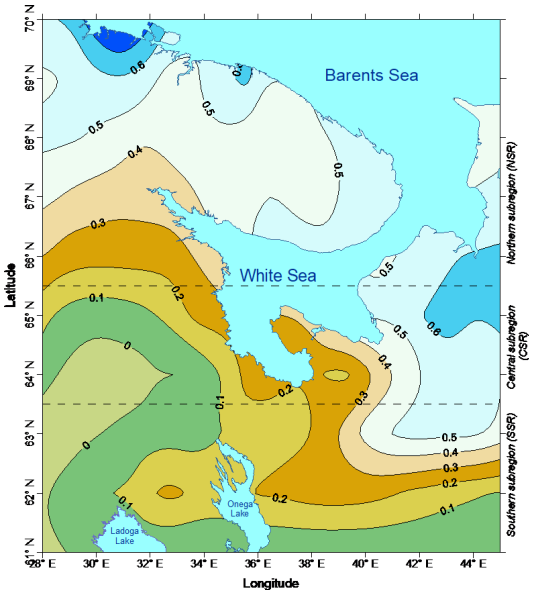


**Figure 6.** The ratio of the linear trend of ST at a depth of 100 cm to the linear trend of NSAT

$0.49 \pm 0.01$. This difference is due to the fact, that a maximum depth for soil temperature in NOAA-CIRES-DOE 20th Century Reanalysis is of 1 m and in-situ thermal monitoring of permafrost involves measuring soil temperature at a depth of 10 m.

**Acknowledgments.** The work was carried out within the framework of the RSF grant N 21-77-30010 (2021–2024) "System analysis of geophysical process dynamics in the Russian Arctic and their impact on the development and operation of the railway infrastructure"

## References

Arzhanov, M. M., and I. I. Mokhov (2013), Temperature trends in the permafrost of the Northern Hemisphere: Comparison of model calculations with observations, *Doklady Earth Sciences*, *449*(1), 319–323, https://doi.org/10.1134/s1028334x1303001x.

Bykhovets, S. S., V. A. Sorokovikov, R. A. Martuganov, V. G. Mamykin, and D. A. Gilichinsky (2007), History of soil temperature measurements at the network of meteorological stations in Russia, *Kriosfera Zemli*, *11*(1), 7–21 (in Russian).

Gvishiani, A. D., I. N. Rozenberg, A. A. Soloviev, A. G. Kostianoy, S. A. Gvozdik, I. V. Serykh, R. I. Krasnoperov, N. V. Sazonov, I. A. Dubchak, A. B. Popov, E. A. Kostianaia, and G. A. Gvozdik (2023), Electronic Atlas of Climatic Changes in the Western Russian Arctic in 1950-2021 as Geoinformatic Support of Railway Development, *Applied Sciences*, *13*(9), 5278, https://doi.org/10.3390/app13095278.

Intergovernmental Panel on Climate Change (IPCC) (2023), *Climate Change 2022 - Impacts, Adaptation and Vulnerability*, Cambridge University Press, https://doi.org/10.1017/9781009325844.

IPCC (2007), *Climate Change. The Physical Science Basis. Contribution of Working Group I to the Fourth Assessment Report of the Intergovernmental Panel on Climate Change*, 1206 pp., Cambridge University Press, Cambridge, United Kingdom and New York, NY, USA.

IPCC (2013), *Climate Change 2013: The Physical Science Basis. Contribution of Working Group I to the Fifth Assessment Report of the Intergovernmental Panel on Climate Change*, 1535 pp., Cambridge University Press, Cambridge, United Kingdom and New York, NY, USA.

Kostianaia, E. A., and A. G. Kostianoy (2023), Railway Transport Adaptation Strategies to Climate Change at High Latitudes: A Review of Experience from Canada, Sweden and China, *Transport and Telecommunication Journal*, *24*(2), 180–194, https://doi.org/10.2478/ttj-2023-0016.

Kostianaia, E. A., A. G. Kostianoy, M. A. Scheglov, A. I. Karelov, and A. S. Vasileisky (2021), Impact of Regional Climate Change on the Infrastructure and Operability of Railway Transport, *Transport and Telecommunication Journal*, *22*(2), 183–195, https://doi.org/10.2478/ttj-2021-0014.

Pavlov, A. V. (2008), Trends of contemporary changes of soil temperature in northern Russia, *Kriosfera Zemli*, *12*(3), 22–27 (in Russian).

Roshydromet (2008), Assessment report on climate change and its consequences on the territory of the Russian Federation. T. 1. Climate change, *Tech. rep.* (in Russian).

Roshydromet (2014), Second assessment report of Roshydromet on climate change and its consequences on the territory of the Russian Federation, *Tech. rep.* (in Russian).

Roshydromet (2022), Third assessment report on climate change and its consequences on the territory of the Russian Federation, *Tech. rep.* (in Russian).

Serykh, I. V., A. G. Kostianoy, S. A. Lebedev, and E. A. Kostianaia (2022), On the transition of temperature regime of the White Sea Region to a new phase state, *Fundamental and Applied Hydrophysics*, *15*(1), 98–111, https://doi.org/10.59887/fpg/k9x4-p8fz-5kz6.

Slivinski, L. C., G. P. Compo, J. S. Whitaker, P. D. Sardeshmukh, B. S. Giese, C. McColl, R. Allan, X. Yin, R. Vose, H. Titchner, J. Kennedy, L. J. Spencer, L. Ashcroft, S. Brönnimann, M. Brunet, D. Camuffo, R. Cornes, T. A. Cram, R. Crouthamel, F. Domínguez-Castro, J. E. Freeman, J. Gergis, E. Hawkins, P. D. Jones, S. Jourdain, A. Kaplan, H. Kubota, F. L. Blancq, T.-C. Lee, A. Lorrey, J. Luterbacher, M. Maugeri, C. J. Mock, G. W. K. Moore, R. Przybylak, C. Pudmenzky, C. Reason, V. C. Slonosky, C. A. Smith, B. Tinz, B. Trewin, M. A. Valente, X. L. Wang, C. Wilkinson, K. Wood, and P. Wyszyński (2019), Towards a more reliable historical reanalysis: Improvements for version 3 of the Twentieth Century Reanalysis system, *Quarterly Journal of the Royal Meteorological Society*, *145*(724), 2876–2908, https://doi.org/10.1002/qj.3598.

Russian Journal of Earth Sciences

Special Issue: "Fundamental and Applied Aspects of Geology, Geophysics and Geoecology"

# Using the Strategy of Multi-Cloud Solutions for Environmental Protection

**Vitaly A. Dovgal**[1], **Saida K. Kuizheva**[1]

[1] Maykop State Technological University, Maykop, Russia
* **Correspondence to:** Vitaly Dovgal, vdovgal @mkgtu.ru

**Abstract:** This paper discusses several extremely promising applications of multi-cloud solutions that can help achieve environmental protection and sustainability goals, provide ecological benefits, and aid wildlife research, conservation and protection. The widespread adoption of multi-cloud strategies helps illustrate the range of initiatives and approaches to reduce environmental burdens employed by government agencies, non-governmental organizations, and private companies.

**Keywords:** environmental protection; multi-cloud computing; multi-cloud platforms.

**Citation:** Dovgal V., Kuizheva S. (2023), Using the Strategy of Multi-Cloud Solutions for Environmental Protection, *Russian Journal of Earth Sciences*, Vol. 23, ES0213, https://doi.org/10.2205/2023ES02SI13

## 1. The concept of multi-cloud environment

Cloud computing (CC) is a paradigm for providing customers with networked access capabilities to a scalable and elastic pool of shared physical or virtual resources on a self-service and on-demand administration basis [*Dovgal and Dovgal*, 2019a]. Through the network, the customer obtains from more than one cloud service provider the cloud computing services they need to process and analyze datasets. According to GOST ISO/IEC 17788-2016 [*GOST ISO/IEC 17788-2016*, 2016] cloud computing services are categorized into seven cloud computing services called categories: Communications as a Service (CaaS), Compute as a Service (CompaaS), Data Storage as a Service (DSaaS), Infrastructure as a Service (IaaS), Software as a Service (SaaS), Platform as a Service (PaaS) and Network as a Service (NaaS). The main purpose of such categories is to provide services via the Internet to cloud clients on a paid basis.

A multi–cloud solution is the execution of cloud computing, allowing the client to deploy applications and services in multiple cloud infrastructures regardless of the provider. The multi-cloud paradigm for most businesses and organizations means using solutions from multiple cloud providers such as Amazon Web Services (AWS), Microsoft Azure, and Google Cloud Platform (GCP). Multi-cloud solutions are usually built on the basis of open-source cloud technologies (for example, Kubernetes), which allow you to run workloads in any cloud without being tied to a specific platform.

Organizations choosing a multi-cloud architecture can use any combination of public clouds along with private cloud deployments and traditional on-premises infrastructure – and these environments do not necessarily need to be integrated [*Dovgal and Dovgal*, 2019b].

With a multi-cloud strategy, customers can choose their preferred services from each cloud provider based on cost, technical requirements, geographic availability, and other factors. For example, a company may use GCP for development/testing environments, AWS for disaster recovery, and Microsoft Azure for business intelligence workloads.

Traditionally, experts distinguish between a multi-cloud solution and a hybrid cloud. The primary difference between the two is that a hybrid cloud approach utilizes a combination of public cloud, private cloud and/or on-premises platforms with some form

Research Article

Received: 20 October 2023
Accepted: 27 November 2023
Published: 15 December 2023

**Copyright:** © 2023. The Authors. This article is an open access article distributed under the terms and conditions of the Creative Commons Attribution (CC BY) license (https://creativecommons.org/licenses/by/4.0/).

of integration or orchestration between these environments. In contrast, a multi-cloud approach involves deploying systems on cloud platforms delivered by several different vendors. This does not necessarily require coordinated operations or integration between different cloud environments.

Figure 1 shows a diagram of a multi-cloud technology.

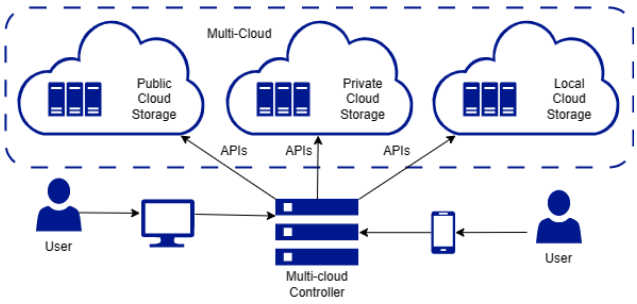


**Figure 1.** Schematic diagram of multi-cloud technology.

## 2. Prospective advantages of using multi-cloud environment

Let's consider the advantages of using multiple clouds by clients, which have an impact, among other things, on the level of environmental protection [*Al-Bdairi*, 2022].

1. The greater flexibility of multi-cloud strategy gives environmental protection companies the freedom to choose where and how to deploy workloads, which prevents the client from being tied to a monopoly vendor. Thus, the customer reduces the risk or unnecessary costs that may result from using only one vendor. In addition, the customer is not limited to the offerings or functionality offered by a single cloud provider at the current point in time. Instead, the customer, by going to different providers, can choose only the services they need based on specific pricing preferences, required levels of performance, security and compliance.
2. Increased information security protection resulting from deploying customer business services across multiple clouds and reducing the likelihood of being hit by distributed denial of service (DDoS) and single point of failure (SPoF) attacks, and therefore increasing the continuity and availability of data. Many enterprises also utilize distributed and redundant deployments across multiple clouds to provide seamless failover and disaster recovery. Distributing workloads across multiple clouds avoids the risk of key applications and data being unavailable in the event of a failure in one of the clouds.
3. Better performance of multi-cloud strategy due to the ability to choose a cloud service provider with data centers geographically close to their business users or customers. By doing so, latency and other performance issues can be minimized.

However, multi-cloud also has some drawbacks, especially from an identity management perspective. Potential problems include:

1. More clouds, more complexity – increased complexity in managing access to applications and environments, and security as the number of service and application providers expands. The use of a single cloud platform allows you to solve these problems quite safely and consistently.
2. The need for several groups of highly skilled professionals maintaining services deployed in multiple clouds. In addition, the use of multiple cloud service providers requires the use of overlapping teams with specialized skills at these providers. Given the ongoing shortage of IT professionals, recruiting and retaining professionals with the required level of cloud security expertise can be challenging.
3. Difficulty managing costs. The primary reason many companies choose to move to the cloud in the first place is to reduce costs, but without careful planning and management, dealing with multiple clouds can be costly. Flexible charging models

can make it difficult to predict costs, especially the customer does not have a clear idea of which users will access which systems and resources.

4. Increased concerns about the secure use of data residing in multi-cloud architectures due to the need to enforce multiple access control policies. Any deviations in security mechanisms, strict adherence to a centralized approach to identity management opens up a wider range of security vulnerabilities, leading to an increased risk of data protection issues and security breaches.

## 3. Examples of the use of multi-cloud architecture in conservation and sustainable development

It is clear that multi-cloud environments can be useful in the field of environmental research, enabling conservation organizations to efficiently and cost-effectively identify key conditions and trends in the environmental state of specific regions, countries, and the planet as a whole. The application of multi-cloud architecture has the potential to bring great benefits when backed by ongoing sustainability efforts.

Multicloud technologies can also play a significant role in protecting natural resources. The use of multiple cloud providers by environmental organizations can reduce the risk of data loss or downtime in the event of a disaster or cyberattack, which can be especially important for those environmental organizations that rely on data to monitor and protect natural resources.

There are many examples of proactive use of a multi-cloud strategy to protect the environment. Let us consider those that are most significant and popular on the Internet.

### 3.1. Cloud environment for the Advanced Multi-risk Management (SIGMA) sensor-integrated environmental information processing system

Such a system utilizes multi-cloud technologies to store data provided by sensors monitoring water quality or air pollution levels [*Stecca et al.*, 2016]. By using multiple cloud providers, organizations can ensure that their critical data is always available, even if one provider experiences an outage. In addition, multi-cloud architectures can be designed with built-in redundancy and failover mechanisms to further reduce the risk of data loss.

A similar data processing scheme is used, for example, by the Italian National Operative Program project (PON), aimed at collecting, integrating and calculating heterogeneous data from different sensor networks (weather, seismic, volcanic, water, rain, road and sea traffic, environment, etc.), and allows the management of hazardous situations both in the industrial production process and in the national territory [*PON Ricerca*, 2021].

### 3.2. Specialized services provided by various cloud providers.

Their use is one of the advantages of companies that use multi-cloud technologies to protect natural resources. For example, a company that monitors water quality may use one cloud provider to store raw sensor data, another provider that offers advanced analytics capabilities to process and analyze large amounts of environmental data and visualize it, and yet another provider for data backup and disaster recovery. That way, if one cloud provider experiences downtime or data loss, a cloud client company could still access its data from the other provider. In addition, these companies could use specialized services provided by different cloud providers, such as machine learning algorithms to identify patterns in environmental data or geospatial tools to visualize and analyze data from remote sensors.

Examples of companies that monitor water quality and utilize cloud-based solutions include:

- The company Aquatic Informatics (Vancouver, Canada), which provides water management software solutions for government agencies, utilities and consulting firms [*Aquatic Informatics ULC*, 2023]. The software, which uses multi-cloud solutions, helps analyze water quality data and water management decisions;

- The analytical company for the water market Bluefield Research (Boston) provides data, analysis, and analytical information to water companies and investors [*Bluefield*, 2023]. The company uses cloud-based platforms to monitor water quality, helping customers make informed decisions about water investments;
- The company Echologics, which has offices not only in Toronto, Canada, but also in the Free Zone of Dubai Airport (United Arab Emirates), London, Singapore, and Atlanta (Georgia, USA), provides acoustic leak detection and pipe condition assessment services to water utilities around the world [*Echologics a Mueller brand*, 2023]. Several cloud-based platforms used by the company allow real-time monitoring of water quality and distribution networks.

### 3.3. Disaster forecasting using multi-cloud technologies

This is another example of using multiple providers to store and analyze data from different sources (such as satellite imagery, weather reports, and seismic activity). Using machine learning algorithms and predictive analytics, organizations can identify patterns and predict natural disasters such as volcanic eruptions, earthquakes, hurricanes, floods, avalanches, tsunamis, and fires.

Examples of companies using multi-cloud technology to predict natural disasters include both large and smaller companies. Among the former are:

- The company IBM, which provides various cloud-based disaster management solutions. The IBM Weather for Emergency Management artificial intelligence platform includes cloud-based industry packages that can analyze data from various sources including social media, news feeds, and sensors to provide real-time information and forecasts [*IBM*, 2015]. IBM cloud solutions can also help first responders in resource allocation and logistics planning;
- The company Google, which provides its Google Cloud solution with tools for disaster response, including Earth Engine [*Google Earth Engine*, 2023] and Google Maps satellite imagery analysis platforms that can be used to visualize disaster data and create custom maps. Google Cloud services also offer machine learning tools for predictive modeling and data analysis.

Similar solutions are offered by other large companies, such as Amazon (Amazon Web Services solution, AWS) [*Amazon Web Services*, 2023] or Microsoft (Microsoft Azure solution) [*Descartes Labs*, 2023], which offer various cloud-based tools for disaster response, including real-time data analytics, machine learning, and geographic information systems (GIS).

Some of the less well-known companies that use multi-cloud technologies for disaster forecasting include:

- Everstream analytics, a software company that provides predictive analytics solutions for supply chain risk management [*Everstream Analytics*, 2023]. Their cloud-based platform uses machine learning algorithms to analyze data from multiple sources such as weather forecasts, traffic patterns, and operator throughput to help businesses anticipate and mitigate supply chain disruptions caused by natural disasters such as hurricanes, floods, and wildfires;
- The Planetary Computer project is a Microsoft initiative that provides cloud-based tools and infrastructure for environmental science and conservation [*Microsoft*, 2023]. The platform integrates data from various sources such as satellite imagery, climate models, and ground observations to help researchers and governments monitor and respond to natural disasters such as droughts, floods, and wildfires;
- One Concern startup offers a digital twin of the world around us that uses artificial intelligence and machine learning to predict and prevent hidden risks in artificial and natural environments associated with natural disasters, extreme weather and climate change by analyzing data from various sources, including satellite imagery, social media and historical records [*Climate FieldView*, 2023]. The project provides cloud

technologies to help emergency managers and municipal officials make data-driven decisions and allocate resources more efficiently during disasters.

### 3.4. Environmental organizations utilizing multi-cloud technologies

Examples of companies using multiple clouds to store and analyze data from remote sensors, cameras to monitor wildlife and animal habitats [*Dovgal and Kuizheva*, 2022]:

- WildTrack is a non-profit organization that uses artificial intelligence and machine learning to monitor endangered species and their habitats [*WildTrack*, 2023]. The company uses multi-cloud technology to monitor wildlife non-invasively, analyzing data from remote sensors and camera traps, as well as local communities and indigenous knowledge. The platform used by the company can help conservationists identify individual animals, track their movements and assess the health of their populations;
- TrailGuard AI is a tool to facilitate wildlife protection and monitoring, the result of a collaboration between Intel and the nonprofit organization Resolve [*Resolve TrailGuard AI*, 2023]. The artificial intelligence platform, using multi-cloud technology to analyze data from camera traps and motion sensors to monitor endangered species such as elephants and tigers, can detect poachers in real time and alert rangers or law enforcement officers to prevent illegal hunting and wildlife trafficking;
- Wildlife Insights is a platform developed by the non-profit organization Conservation International that uses multi-cloud technology to monitor wildlife and their habitats, helping researchers and conservationists identify and track endangered species, assess ecosystem health, and develop conservation strategies [*Wildlife Insights*, 2023].

Climate change research can also utilize multi-cloud technologies. Here are examples of companies using machine learning algorithms and predictive analytics to identify patterns and make predictions about the future of the environment:

- Climate Corporation is a subsidiary of the Bayer concern, has developed a multi-cloud technology platform to help farmers optimize their crop yields, reduce water consumption, and mitigate climate change on their farms [*Climate FieldView*, 2023];
- Climate Group is an international non-profit organization that uses multi-cloud technologies as well as data from various sources such as energy consumption models, emissions data and policy frameworks to advise businesses and governments on the transition to a low-carbon economy [*Climate Group*, 2023]. To do so, the platform sets emission reduction targets, tracks their progress and shares best practices with other stakeholders;
- Jupiter Intelligence is a multi-cloud startup that assesses risks associated with climate change [*Jupiter*, 2023]. The platform offers businesses and governments to identify areas vulnerable to flooding, extreme heat or other climate-related hazards and develop strategies to adapt to these risks.

### 3.5. Wildfire prevention

This type of human activity to protect the environment can also utilize multi-cloud technologies. Some examples are:

- Descartes Labs is a startup that identifies areas at risk of wildfires based on processing satellite data, forest health and wildfire risk information using artificial intelligence and machine learning. The platform can help foresters to take preventive measures to reduce the risk of forest fires [*GOST ISO/IEC 17788-2016*, 2016];
- Exci is a company that offers multi-cloud platforms for early emergency response, effective coordination of efforts, and better allocation of resources in real time [*EXCI*, 2023];
- Descartes Laboratories is a project that uses artificial intelligence and machine learning techniques to analyze data related to wildfires based on vegetation density, temperature, and humidity [*ESRI*, 2023];

- Forest Fire Analyst is a software that provides real-time analysis of wildfire behavior and simulates the spread of wildfires to enable timely and effective decision making [*Descartes Labs*, 2023].

Thus, we are on the threshold of widespread implementation of multi-cloud architecture technologies in the protection of the world around us, conservation and sustainable development of nature. Currently, the services provided by the tools described in this article can be used for environmental forecasting of decision-making processes in both public and private sectors. It should be emphasized that, in order to solve sustainable development problems, it is important to maintain close links between decision makers and those affected by them. The application of artificial intelligence tools and machine learning techniques can only provide environmental authorities with detailed evidence of the rapid changes in nature, from documenting the greenness of our planet to identifying where resources are being illegally extracted. Ultimately, there must be a strong link between the data collected and processed by cloud platforms and the sustainability agenda to ensure that humanity still has the time and space to save not only our environment, but humanity itself.

**References**

Al-Bdairi, G. A. H. (2022), "Multicloud" as a key to the benefits, in *Modern trends in the development of science and the world community in the era of digitalization: Proceedings of the V International Scientific and Practical Conference Moscow, March 11, 2022*, pp. 82–91, Alef Printing House, Moscow (in Russian).

Amazon Web Services (2023), AWS Disaster Response, https://aws.amazon.com/ru/government-education/nonprofits/disaster-response/, (date of access: 04/04/2023).

Aquatic Informatics ULC (2023), Aquatic Informatics, https://aquaticinformatics.com, (date of access: 04/04/2023).

Bluefield (2023), We believe that water is the most pressing issue facing our generation, https://www.bluefieldresearch.com, (date of access: 04/04/2023).

Climate FieldView (2023), Digital Farming's Leading Software Platform, https://climate.com, (date of access: 06/04/2023).

Climate Group (2023), Driving climate action, https://www.theclimategroup.org, (date of access: 06/04/2023).

Descartes Labs (2023), Natural Disaster Prediction and Monitoring. Wildfires, https://descarteslabs.com/climate-solutions/natural-disaster, (date of access: 08/04/2023).

Dovgal, V., and S. Kuizheva (2022), Using Big Data Technology to Protect the Environment, *Russian Journal of Earth Sciences*, pp. 1–5, https://doi.org/10.2205/2022ES01SI02.

Dovgal, V. A., and D. V. Dovgal (2019a), A survey of the integration possibilities of cloud computing and Internet of things, *Vestnik of Adygeya State University. Series 4: Natural-mathematical and technical sciences*, *4*(251), 81–86 (in Russian).

Dovgal, V. A., and D. V. Dovgal (2019b), The use of the Internet of Things for environmental protection, in *Fundamental and applied aspects of geology, geophysics and geoecology using modern information technologies. Proceedings of the V International Scientific and Practical Conference*, pp. 152–157, Maykop State Technological University, Maykop (in Russian).

Echologics a Mueller brand (2023), Built to protect water networks, https://www.echologics.com, (date of access: 04/04/2023).

ESRI (2023), Geospatial Intelligence. Thrive in an Ever-Shifting World, https://www.esri.com/content/dam/esrisites/en-us/media/ebooks/geospatial-intelligence.pdf, (date of access: 08/04/2023).

Everstream Analytics (2023), Risk Center, https://www.everstream.ai/risk-center/, (date of access: 05/04/2023).

EXCI (2023), Smoke alarm for the bush, https://www.exci.ai, (date of access: 08/04/2023).

Google Earth Engine (2023), A planetary-scale platform for Earth science data & analysis, https://earthengine.google.com, (date of access: 08/04/2023).

GOST ISO/IEC 17788-2016 (2016), Information technology. Cloud computing. Overview and vocabulary (in Russian).

IBM (2015), Weather for Emergency Management, a cloud-based weather data service, enables Smarter Cities Emergency Management users to enrich their emergency management solutions with weather-based insights, https://www.ibm.com/docs/en/announcements/archive/ENUSZP15-0071, (date of access: 05/04/2023).

Jupiter (2023), The Trusted Leader In Climate Risk Analytics, https://www.jupiterintel.com, (date of access: 06/04/2023).

Microsoft (2023), A Planetary Computer for a Sustainable Future, https://planetarycomputer.microsoft.com, (date of access: 05/04/2023).

One Concern (2023), Digital Infrastructure of the Physical World, https://www.oneconcern.com/en/, (date of access: 05/04/2023).

PON Ricerca (2021), The National Operational Programme on Research and Innovation 2014-2020, http://www.ponricerca.gov.it/pon-ricerca/programme/, (date of access: 04/04/2023).

Resolve TrailGuard AI (2023), Stopping poachers and protecting parks and communities, https://www.resolve.ngo/trailguard.htm, (date of access: 05/04/2023).

Seto, J. (2018), Using AI and IoT for disaster management, https://azure.microsoft.com/es-es/blog/using-ai-and-iot-for-disaster-management/, (date of access: 04/04/2023).

Stecca, G., A. Puliafito, M. Simonetti, G. Mariotta, and P. Sciuto (2016), A Cloud-based System to Protect Against Industrial Multi-risk Events, *Procedia CIRP*, *41*, 650–654, https://doi.org/10.1016/j.procir.2015.12.093.

Wildlife Insights (2023), Bringing Cutting-Edge Technology to Wildlife Conservation, https://www.wildlifeinsights.org, (date of access: 06/04/2023).

WildTrack (2023), Non-Invasive Wildlife Monitoring, https://wildtrack.org, (date of access: 05/04/2023).

Russian Journal of Earth Sciences

Special Issue: "Fundamental and Applied Aspects of Geology, Geophysics and Geoecology"

# Activation of Dangerous Natural Processes on the Territory of the Kabardino-Balkarian and Karachay-Cherkess Republics

**Elena V. Kyul[1], Maryana M. Gedueva[1], Natalia V. Kondratyeva[2], Anton L. Drozdov[1], Zuleikha R. Baidaeva[3]**

[1] Federal Scientific Federal Scientific Center "Kabardino-Balkarian Scientific Center of the Russian Academy of Sciences", Nalchik, Russia
[2] Federal State Budgetary Institution "High-Mountain Geophysical Institute of Roshydromet", Nalchik, Russia
[3] Elbrus National Park, Russia, v. Elbrus
* **Correspondence to:** Elena Kyul, elenakyul@mail.ru

**Abstract:** The paper considers the manifestations of dangerous natural processes and their consequences in the territories of two republics – the Kabardino-Balkarian and Karachay-Cherkess Republics for the period from 2015 to 2022. On the basis of the collected material, an analysis of the manifestations of hazardous natural processes was carried out and maps-schemes were compiled.

**Keywords:** hazardous natural processes, monitoring, floods, mudslides, atmospheric (stormwater) precipitation, GPS-survey, schematic map.

**Citation:** Kyul E., Gedueva M., Kondratyeva N., Drozdov A., Baidaeva Z. (2023), Activation of Dangerous Natural Processes on the Territory of The Kabardino-Balkarian and Karachay-Cherkess Republics, *Russian Journal of Earth Sciences*, Vol. 23, ES0214, https://doi.org/10.2205/2023ES02SI14

## 1. Introduction

Currently, on the northern slope of the Greater Caucasus, especially in the Kabardino-Balkarian (KBR) and Karachay-Cherkess (KChR) Republics, the activity of hazardous natural processes is observed [*Kyul et al.*, 2019b]. Therefore, the assessment of the impact of hazardous natural processes on the transformation of geosystems becomes an urgent and priority task.

At the same time, large-scale and long-term work in the study area in recent years has practically not been carried out on this problem. A number of works on mudflow issues published during this period, in most cases, were largely based on data from the 80s–90s of the 20th century, incl. and Cadastre of Mudflow Hazard in the South of the European Part of Russia [*Kondratieva et al.*, 2015]. Therefore, the Center for Geographical Research of the Kabardino-Balkarian Scientific Center of the Russian Academy of Sciences (KBSC RAS), starting from 2011, along with fundamental research into the dynamics of geosystems, resumed geoecological monitoring of hazardous natural processes, in particular, mudflows and nanowater floods, which was almost completely stopped in the 1990s. years of the XX century. A number of similar articles were published on some selected geosystems of the northern slope of the Greater Caucasus [*Kyul et al.*, 2022, 2021a].

## 2. Materials and methods

The article presents data both from the analysis of the descent of hazardous natural processes, taken from electronic sources, and data obtained in the course of field research. At the same time, the collection and analysis of data during the monitoring of hazardous natural processes was carried out according to the methodology developed by the authors [*Kyul et al.*, 2019a; *Kyul and Borisova*, 2015].

Research Article

Received: 20 October 2023
Accepted: 27 November 2023
Published: 15 December 2023

**Copyright:** © 2023. The Authors. This article is an open access article distributed under the terms and conditions of the Creative Commons Attribution (CC BY) license (https://creativecommons.org/licenses/by/4.0/).

## 3. Results

The need to conduct field work to monitor the manifestations of hazardous natural processes is confirmed by the news about them constantly coming to the media. The most serious consequences caused by heavy rainfall were observed in 2015, 2018–2022 (Table 1).

**Table 1**. Mudslides and floods on the territory of the KChR for the period from 2015 to 2022.

| Administrative district | Highway | River basin | Hazardous natural processes (HNP) | Date of manifestation HNP | Consequences of the descent HNP [Kyul et al., 2021b] |
|---|---|---|---|---|---|
| Malokarachaevsky | | | Flood | 07.06.2022 | 50 yard plots were flooded, water entered 19 houses |
| Malokarachaevsky | "Pyatigorsk – Karachayevsk" | Podkumok | Mudflow | 07.06.2022 | A section of the road on the 71st kilometer "Pyatigorsk-Karachayevsk" was damaged |
| Karachay city district | "Cherkessk – Dombay" | | Mudflow | 05.06.2019 | Skidding of the highway on 77 km of the Cherkessk-Dombay highway. The volume of the mudflow is about 30 $m^3$ |
| Zelenchuk | | Bejgon | Flood | 18.06.2018 | The bridge over the Bejgon River was washed away by a flood of water |
| Karachay city district | | Amanauz | Flood | 05.07.2017 | The children's camp "Adel" was flooded, 80 people were evacuated |
| | | | | | |
| Zelenchuk | Kuban – Khudes – Bichesyn | Podorvanka | Flood | 18.06.2016 | The bridge over the river was destroyed Podorvanka |
| Zelenchuk | | | Mudflow | 01.07.2015 | Roads are washed out, household plots are flooded. One person was killed, two were injured |
| | | | | | |
| Urupsky | | | Mudflow | 01.07.2015 | |

For example, on the territory of the Karachay-Cherkess Republic, on July 1, 2015, numerous mudflows occurred in the Zelenchuksky and Urupsky districts, caused by heavy rains. The elements dealt a powerful blow to settlements as well. Roads were washed out, household plots were flooded. One person died, two were injured (Figure 1) [*Kyul et al.*, 2019a, 2021b].

Mudflows descended in Urupsky, Zelenchuksky and Karachaevsky districts on June 16–17, 2018. In the village of Kurdzhinovo, 110 farmsteads were flooded, mud flows blocked the Karachaevsk-Uchkulan road. The dam on the Khusa River in the village of Zelenchukskaya and the approach to the pedestrian crossing over the Bezhgon River in the village of Storozhevaya are washed out. Mudflow descended in the village of Khasaut-Greek. More than 500 households, a school and a kindergarten were flooded in the village of Pregradnaya. The mudflow that came down between the villages of Upper Teberda and Lower Teberda blocked about 100 m of the road (Figure 2).

Dangerous natural processes make land plots unsuitable for national economy. In this regard, in the summer of 2019, after the passage of heavy rainfall in the study areas, we examined some river basins and adjacent settlements in the territories of the KBR and KChR. Based on the results of field trips, a table of hazardous natural processes was compiled with photographic material and their binding by coordinates, which makes it possible for us to monitor these areas (a part is given) (Table 2).



**Figure 1.** Consequences of mudflows in Zelenchuksky and Urupsky districts of the KChR on July 1, 2015 [*Kyul et al.*, 2021b].



**Figure 2.** Mudflow descent along the left tributary of the Teberda River to the federal highway "Cherkessk-Dombai" on 06/16/2018 [*Kyul et al.*, 2021b].

Also, based on the results of field trips, schematic maps have been compiled, with GPS points applied (for example, Figure 3).

All the places where the road intersects with streams (waterways), drifts and erosion of the highway are recorded. The wooden bridge over the Zagedanka River is in disrepair – the bridge supports are clogged with karch, the banks are washed away. The floodplain forest is flooded. Traces of mudflows of small volumes are visible. The dirt road on the left side of the Bolshaya Laba River from the village of Damkhurts to the village of Rozhkao suffered more from the rains. Mudflows of 50,000 $m^3$ were observed in the Damkhurts River basin (a wooden bridge was destroyed). Below the Karapyr cordon in the area of the stream, the left tributary of the Bolshaya Laba River, there is a drift and erosion of the road. On the entire left side, as a result of surface washout, the roadbed was damaged (2 landslide massifs). Fresh mudflow deposits are visible in the Zakan river basin. The bridge across the Zakan River is in disrepair. At the intersections of the road with streams (observation points 1110, 1114, 1127), the canvas is completely washed out (traces of backfilling are visible). Above the village of Rozhkao, opposite the bridge, there is a mudflow cone with fresh mudflow deposits at the mouth of the right tributary of the Bolshaya Laba River. The bridge is in disrepair (washed out river banks). The basin of the Rozhkao River, the left tributary of the Bolshaya Laba River, is also mud-bearing: traces of microflows (washout and bank collapse). Below the village of Rozhkao, a mudflow fan is observed at the mouth of the right tributary of the Bolshaya Laba River. The riverbed is divided into 3 branches

**Table 2.** Areas of manifestation of hazardous natural processes on the territory of the KChR according to the data of the Central Geological Survey.

| № points | Binding | Coordinates N | Coordinates E | Marks | Height |
|---|---|---|---|---|---|
| | Karachay-Cherkess Republic | | | | |
| | Teberda. The exit point of the mudflow to the road. | | | | |
| 564 |  | 43° 38.814' | 41° 53.041' | ±4 m | 1036 m |
| | Uchkulan. The collapsed bridge. | | | | |
| 930 |  | 43° 27.571' | 42° 05.878' | ±2 m | 1362 m |

(under the road bed there are mudflow trays clogged with fresh mudflow deposits, the possible volume is more than 50,000 $m^3$). As a result of the mudflow along the right slope (observation point 1161), a mudflow was formed. Throughout the entire length of the road on the starboard side (observation points 1162–1172) traces of floods are observed (the road is partially at the level of the river, it was flooded in places). Clearing traces are visible, the floodplain forest is flooded. As a result, a number of landslide massifs formed along the right slope.

The left side of the Bolshaya Laba river. Below (observation points 1173–1179), the road crosses the mudflow fan at the mouth of the right tributary of the Bolshaya Laba River and goes to the left side. In the Asian village (above the village, in the village itself and below the village), there were thin mudflows along the right tributaries. In the area of the village of Kurdzhinovo, the right-bank part (observation point 1195), due to the low level of the road, a section 50 m long was flooded. In the area of the village of Psemen (the Psemenka River, the right tributary of the Bolshaya Laba River), traces of the flood are visible (erosion of the banks and undermining of the bridge supports). In the left-bank part of the village of Kurdzhinovo in the basin of the Beskes River, the left tributary of the Bolshaya Laba River, there are fresh mudflow deposits in the estuarine part (a landslide zone was formed along the left slope, within which residential buildings and part of the road turned out to be).

In general, it can be concluded that many dangerous natural processes take place in the Bolshaya Laba river basin. Nival-glacial processes are developed in the upper reaches of the mountains. Mudflows are the main process. Almost all major tributaries of the Bolshaya Laba are mud-bearing. Mudflows are recharged not only because of avalanches, but because of the widespread development of landslide-scree and less often landslide processes, which are often of an anthropogenic nature. The peak of mudflow activity falls on summer time (July). Mudflows and floods, mainly of rain genesis. Due to the good development of the territory, almost all areal and linear economic objects fall into the zone of action of hazardous natural processes.

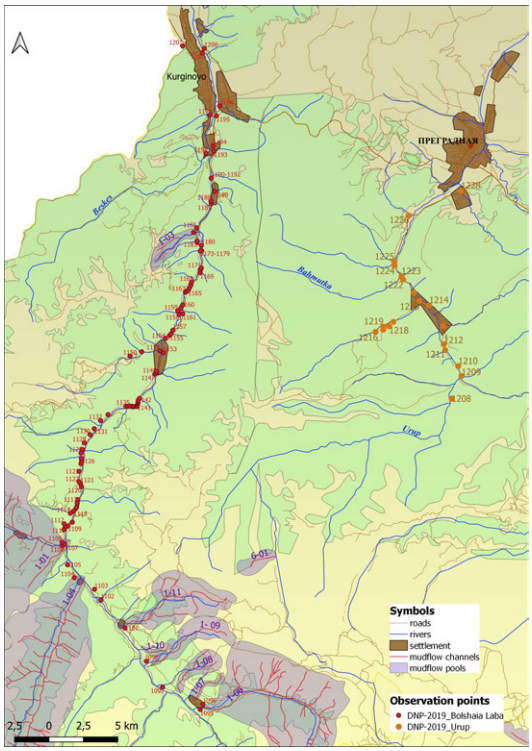


**Figure 3.** Map-scheme of the actual exposure to natural hazards of linear facilities in the Bolshaya Laba and Urup river basins (KCR).

*Urup river basin.* In the area of the Trout farm, along the right tributary of the Urup River, erosion of the banks and flooding of the floodplain forest are recorded. Below the Sebeldinka River, the right tributary of the Urup River, on the old alluvial cone at the mouth of the river, fresh mudflow deposits are visible (the dirt road is covered and washed out). The bridge across the Urup River is in disrepair (bank erosion and undermining of the bridge supports). On the left side of the Urup River, in the zone of action of hazardous natural processes, in addition to the road, there is the building of the Urup plant (mine) and a mining village. In the basin of the Vlasenchikha River, the left tributary of the Urup River, (adits and treatment facilities with an industrial site), as a result of mining activities, an anthropogenic zone (a number of tenogenic landscapes) was formed with the development of subsidence processes. On all left tributaries, traces of floods are observed (bank erosion, motorway skidding). The bridge over the Urup River (observation point 1226) is in disrepair. Fresh mudflow deposits are noted in the riverbed. Fresh mudflow deposits are observed on the Urup River and its right tributary, the Seroshtanka River. There is an activation of coastal erosion (bank erosion). Floodplain forests are flooded due to rising water levels in the river. On the left side of the Urup River, below the village of Mednogorsky, an anthropogenic zone has been formed, namely: a tailing dump is located, which is at the stage of reclamation.

It can be concluded that the mudflow process is the leading process in the Urup river basin. Mudflows – rain and less often anthropogenic genesis (within anthropogenic zones). Mudflows are fed by numerous anthropogenic landslide and landslide-scree massifs formed by mining activities. Activation and is often associated with subsidence processes, which manifest themselves in the locations of the facilities of the Urup plant.

On the territory of the Kabardino-Balkarian Republic for the period under review, as well as in the KChR, various types of manifestations of hazardous natural processes were observed (Table 3).

**Table 3**. Mudflows and floods in the territory of the KBR for the period from 2015 to 2022

| Adminis dis-trict | Highway | River basin | DNP | Date of manifesta-tion DNP | Consequences of the descent DNP. [ Kyul et al., 2021b ] |
|---|---|---|---|---|---|
| Zolsky | "Kislovodsk – Dolina Narzanov – Dzhilysu-Elbrus" | Malka | Mudflow | 05.10.2022 | At the 59th kilometer, the road is skidding "Kislovodsk – Dolina Narzanov – Dzhilysu-Elbrus" |
| Elbrus | "Prohladnyj – Baksan – Elbrus" | Baksan | Mudflow | 05.08.2022 | There is no damage |
| Chereksky | | Cherek-Bezengiysky | Mudflow | 01.08.2021 | Skidding of the road to the alpine camp "Bezengi" |
| Chereksk | "Urvan' – Verhnyaya Balkariya - Ushtulu" | | Mudflow | 24.07.2019 | Mudflow on the road at the 65th kilometer |
| Urvansky | "Nizhnij CHerek - Staryj CHerek" | New Cherek | Flood | 18.06.2019 | The road was washed away between the villages of Nizhny and Old Cherek. In the village of Psykod, the bridge over the Novy Cherek River was damaged. Residential buildings and more than 100 hectares of farmland were flooded. The threat of destruction of the dam. |
| Elbrus | A-158 "Prohladnyj-Azau" | Baksan | Flood | 05.07.2018 | 12 sections of the road were washed away, four bridges and several power transmission towers collapsed. A section of the gas pipeline is damaged |
| Urvansky | "Nartkala – Ozrek – Staryj Uruh" | | Flood | 13.01.2017 | A section of the road between Nartkala and Old Urukh and a dam on the Cherek River were destroyed |
| Elbrus | A-158 "Prohladnyj-Azau" | Adylsu, Baksan | Mudflow | 01.09.2017 | Breakthrough of Lake Bashkara. Destruction of highways. There are human casualties |
| Chereksky | "Kara-Su – Bezengi" | | Mudflow | 24.06.2016 | Skidding of the road between the villages of Karasu and Bezengi and the homesteads of the village of Karasu |
| Elbrus | "Baksan-Azau" | | Mudflow | 25.06.2015 | A mudslide in the Suu-kosh tract blocked the road. The volume of mudflows - 100-120 thousand m3 |
| Zolsky | | Zolka | Flood | 30.05.2015 | The villages of Shordakovo and Kichmalka were flooded, 2 bridges were damaged. There are several private households in the flood zone. |

In the Cherek Bezengisky gorge in the spring of 2016, during field surveys, mudflows of small and medium volumes were recorded, first of all, the left tributary of the Karasu River near the village of the same name (Figure 4).



**(a)** **(b)**

**Figure 4.** The left tributary of the Karasu River without a name near the village of Karasu (photo on the left – March 2016), (photo on the right – after the mudflow descent on 06/24/2016). Photo Gedueva M. M.

Surveys with instrumental measurements show that the mudflow was formed as a result of showers the day before, due to the sliding of the slope along the right bank downstream 1000 m above the village of Karasu. The volume of deposited material is 120,000–150,000 $m^3$. Mudflows covered household plots, partially destroyed outbuildings. After the mudflow descent, it was planned to build a mudflow flume along this channel.

Also, several sections of the Baksan-Azau highway are periodically covered and washed out by mudflows. Micro-mudflows descend along temporary streams and almost every year and enter the Baksan-Azau federal highway (for example, Figure 5).



**(a)** **(b)**

**Figure 5.** Sediments after microflow flows along a temporary watercourse of storm origin above the gas station in the Tegenekli settlement. Photo by Kyul E. V. 2017

On September 1, 2017, a catastrophic mudflow formed along the Adylsu and Baksan rivers as a result of the outburst of Lake Bashkara. The breakthrough was caused by anomalous heavy rains that took place the day before and on the night of August 31 to September 1 in the gorge of the Adylsu River, which eroded the ice-moraine bridge. Up to 1 million $m^3$ of water was discharged from the lake. The drop in the water level in the lake is 22–25 meters. According to the automatic weather station installed at the Dzhankuat Moscow State University, from August 28 to September 1, 200 mm of precipitation fell, of which more than 100 mm fell after 20:00 on August 31 (the monthly norm in August is about 80 mm). This mudflow can be attributed to a mixed or glacial-storm type.

As a result, 3 sections of the road were destroyed in the Adylsu gorge and on the very territory of the Dzhantugan base, where eight residential premises were demolished - the so-called "barrels" (for example, Figure 6). The mudflow washed away seven sections of the A-158 Prokhladny-Azau road, with a total length of 3.3 km. Four bridges across the Baksan River were destroyed, supports were washed away and gabions of the bridge were cut above the village of Neutrino and near the village of Verkhniy Baksan. Three people died.



**Figure 6.** Consequences of the breakthrough of the lake and the descent of the mudflow in the gorge of the river Adylsu. Photo by Dzhappuev D. R.

## 4. Conclusions

Mudflow and flood processes in the territories of the KChR and KBR differ in their characteristics, namely, the conditions of formation, volumes of flows, etc. In contrast to the KBR, in the territory of the KChR, for example, the absolute heights are lower, there is also a greater gentleness of the slopes and their good forest cover, and, secondly, a much smaller scale of modern glaciation of the Kuban basin compared to the Terek basin. It is also important to note that in the mountainous regions of the KBR, outburst glacial lakes pose a great danger, often being an impetus for the formation of a mudflow or flood flow of catastrophic force, while for the territory of the KChR, these processes have a rain, torrential genesis to a greater extent. One of the most mudflow-active regions of the Karachay-Cherkess Republic is the Teberda River basin, including its sources. In the upper reaches of the Teberda there are: the famous resort village of Dombay, the Alibek alpine camp, cable cars and other recreational facilities, some of which are located in the mudflow impact zone. For the territory of the KBR, the most catastrophic and frequent manifestations of hazardous natural processes are recorded in the Baksan river basin.

## References

Kondratieva, N. V., A. K. Adzhiev, M. Y. Bekkiev, M. M. Gedueva (Gyaurgieva), V. F. Perov, V. V. Razumov, I. B. Seinova, and L. V. Khuchunaeva (2015), *Cadastre of mudflow hazard the South of the European part of Russia*, 148 pp., KBSC RAS, Nal'chik (in Russian).

Kyul, E., L. Kankulova, and A. Ezaov (2019a), The theoretical basis of geo-environmental monitoring of the mountain geosystems, *Sustainable Development of Mountain Territories*, *11*(1), 36–43, https://doi.org/10.21177/1998-4502-2019-11-1-36-43 (in Russian).

Kyul, E., N. Kondratyeva, M. Gedueva, and D. Dzhappuev (2022), Results of monitoring of hazardous natural processes in the Belaya river basin, *Russian Journal of Earth Sciences*, pp. 1–6, https://doi.org/10.2205/2022ES01SI05.

Kyul, E. V., and N. A. Borisova (2015), Geoecological monitoring: creation of a monitoring network based on the results of inventory and certification, in *Ecology, economics, computer science: Collection of articles: in 3 volumes*, vol. 1, pp. 145–149, Southern Federal University, Rostov-on-Don (in Russian).

Kyul, E. V., E. A. Korchagina, and D. R. Dzhappuev (Eds.) (2019b), *Geoecological studies on the territory of the Kabardino-Balkarian Republic in the period from 2012 to 2018. Vol. 1. Spatial patterns of the formation of dangerous exogenous processes*, 173 pp., KBSC RAS, Nal'chik (in Russian).

Kyul, E. V., M. M. Gedueva, D. R. Dzhappuev, A. M. Hutuev, and A. L. Drozdov (2021a), Monitoring of mudflow processes in the Samur River basin, in *III International scientific and practical conference "Modern problems of biology and ecology" dedicated to the 80th anniversary of the birth of Sh. I. Ismailov*, pp. 304–308, Dagestan State Pedagogical University, Makhachkala (in Russian).

Kyul, E. V., E. A. Korchagina, M. M. Gedueva, Z. V. Ataev, D. R. Dzhappuev, A. M. Hutuev, and A. L. Drozdov (2021b), Investigation of the natural hazard of selected geosystems of the northern slope of the Greater Caucasus on the basis of geoinformation technology, *Tech. rep.*, KBSC RAS (in Russian).

Russian Journal of Earth Sciences

Special Issue: "Fundamental and Applied Aspects of Geology, Geophysics and Geoecology"

# Impact of Nano-fertilizers and Nutrient Management on Growth and Yield of Strawberry

**Lakhwinder Singh[1], Ramesh Kumar Sadawarti[1], Shaifali[1], Sandeep Menon[1], Tatiana Minkina[2], Svetlana Sushkova[2], Vishnu D. Rajput[2]**

[1]Lovely Professional University, Jalandhar, Punjab, India
[2]Southern Federal University, Rostov-on-Don, Russia
* **Correspondence to:** L. Singh, lakhwindersingh60478@gmail.com; V. D. Rajput, rajput.vishnu@gmail.com

**Abstract:** In the pursuit of enhancing agricultural practices, this research delves into the intricate interplay between nano-fertilizers, nutrient management strategies, and their collective impact on the growth and yield metrics of strawberries. The present research was carried out to ascertain the impact of nano-fertilizers (ZnO and FeO) and integrated nutrients management (Phosphate solubilizing bacteria (PSB) & *Azotobacter*) on strawberry (Fragaria x ananassa Duch.) Cv. Winter Dawn. The results of present work showed different treatments of nano fertilizers and nutrients management has variable impact on strawberry growth such as treatment 7 ($T_7$: 50% Recommended dose of fertilizer) + FYM + vermicompost + *Azotobacter* + 150 ppm nano-ZnO + 150 ppm nano-FeO) showed highest growth parameters regarding number of leaves (14), plant height (11.24 cm), leaf area (74.86 $cm^2$) and chlorophyll content (52.41 µmol/$m^2$) etc. compared with other treatments. However, treatment ($T_9$: 50% RDF + FYM + vermicompost + *Azotobacter* + PSB + nano-ZnO + nano-FeO) indicated bit similar regarding number of leaves (13.33), plant height (11.96 cm), leaf area (74.08 $cm^2$) and chlorophyll content (53.06 µmol/$m^2$) etc. The biochemical parameters were also observed higher in treatment ($T_9$). Considering above results, it can be concluded that the dose, i. e., 50% RDF along with FYM, vermicompost and *Azotobactor* + ZnO + FeO (150 ppm) could enhance growth and yield of strawberry.

**Keywords:** Winter Dawn, FYM, Vermicompost, PSB, Azotobacter, ZnO, FeO.

**Citation:** Singh L., Sadawarti R. K., Shaifali, Menon S., Minkina T., Sushkova S., Rajput V. D. (2023), Impact of Nano-fertilizers and Nutrient Management on Growth and Yield of Strawberry, *Russian Journal of Earth Sciences*, Vol. 23, ES0215, https://doi.org/10.2205/2023ES02SI15

## 1. Introduction

Nano-fertilizers have been identified as a potential tool to achieve sustainable intensification in agricultural. This is a reason being their ability to synchronize the release of nutrients, such as nitrogen and phosphorus, with increases in yield and production of crops, while simultaneously decline the amount of fertilization inputs [*El-Bialy et al.*, 2023]. Due to the ability of consistent and slow release of nutrients, nanofertilizers can enhance nutrient use efficiency (NUE) and help plants to uptake nutrients easily [*Reddy and Chhabra*, 2022]. Recent studies have reported significant improvements in crop production with 30% increases crop yield compared with conventional fertilizers input [*Mandal et al.*, 2021; *Weber et al.*, 2021].

Integrated nutrient management (INM) is another strategy which can serves as a safe and effective approach for managing crop residues and producing high-quality compost [*Kumar et al.*, 2018]. It involves the integration and management of both chemical and organic fertilizers to maintain fertility of the soil by providing the necessary nutrients to plants. INM focuses on timely nutrient application to optimize crop yields and minimize

Research Article

Received: 20 October 2023
Accepted: 27 November 2023
Published: 15 December 2023

**Copyright:** © 2023. The Authors. This article is an open access article distributed under the terms and conditions of the Creative Commons Attribution (CC BY) license (https://creativecommons.org/licenses/by/4.0/).

environmental impacts. It offers economic options for meeting crop nutrient requirements, reducing costs, improving soil physiochemical conditions, preserving soil nutrients, and promoting better physiological functions in plants [*Mandal et al.*, 2021]. Additionally, INM provides sustainable solutions for managing agricultural waste while safeguarding the environment.

Strawberry (*Fragaria* × *ananassa* Duch.) is a highly nutritious soft fruit that is globally favoured and cultivated worldwide nearly 75 countries. China is leading producer of strawberries, with an estimated production of approximately 3,336,690 tons during the 2020–2021 period, whereas USA follows with a production of around 1,055,963 tons of strawberries [*Food and Agriculture Organization of the United Nations*, 2023]. Strawberry is an herbaceous crop having prostrate growth habit, fleshy fruit contains small seeds on the exterior, and enriched with vitamins and minerals, making it a popular choice among consumers [*Kumar et al.*, 2018]. The preferred pH range for soil cultivation of strawberries is approximately 4.5–6.5.

Recently, breeding of new varieties that is suitable for subtropical regions and research on different combinations for its nutrients requirements has as a result to boosting the cultivation of strawberry even some of the non-traditional regions [*Usenik et al.*, 2005]. Cultivation of strawberry is profitable under subtropical regions due to the development of some cultivars that are suitable for such areas [*Saini et al.*, 2021]. Quality of fruits is found excellent in hilly areas as compared with plain regions. Similarly, the colour and flavour development are not proper in plains as compared to hilly varieties. To overcome from such challenges appropriate nutrient balance is required. Thus, the series of experiments are needed to standardize the appropriate dose or combination of nutrients. Considering the importance of strawberry and role of nanofertilizers in crop improvement, the present study was aimed to evaluate integrated use of nano fertilizers and nutrient management to improving crop yield and quality produce.

## 2. Materials and Methods

### 2.1. Experimental setup and treatment details

The experiment was carried out at "Lovely Professional University" (Phagwara) Punjab, India during the 2022–23. Experimental plot is located at 31.2242° N latitude and 75.77° E longitude, is situated approximately 768 ft (237 meters) above mean sea level. The region experiences an average annual rainfall of 816 mm. In the study, uniform-sized strawberry's runners carefully transplanted in the first week of November (2022–23) season.

The experiment consisted of following treatments such as

$T_0$: Control 100% RDF,

$T_1$: 50 % RDF+ FYM + ZnO + FeO,

$T_2$: 50% RDF + FYM + *Azotobacter* + ZnO + FeO,

$T_3$: 50% RDF + FYM + Phosphate solubilizing bacteria + ZnO + FeO,

$T_4$: 50% RDF + Vermicompost + ZnO + FeO,

$T_5$: 50% RDF+ Vermicompost + *Azotobacter* + ZnO + FeO,

$T_6$: 50% RDF+ Vermicompost + PSB + ZnO + FeO,

$T_7$: 50% RDF+ FYM + Vermicompost + *Azotobacter* + ZnO + FeO,

$T_8$: 50% RDF + FYM + Vermicompost + PSB + ZnO + FeO,

$T_9$: 50% RDF+ FYM + *Azotobacter* + PSB + ZnO + FeO.

*Note: RDF: Recommended dose of fertilizer, FYM: Farm Yard Manure, PSB: Phosphate solubilizing bacteria*

### 2.2. Observation of Plant Growth, Sample Collection and Analysis

Urea was applied in two splits at the concentration of 23.9 g per square meter and DAP was applied at the amount of 21.7 g and MOP was applied at the amount of 20 g per square meter, before transplanting of runners and after that on flowering while phosphorus and potash were applied prior to planting. The solutions of *Azotobacter* and PSB were prepared by dissolving 50 ml of these bio-fertilizers into 20 liters of water. Nanoparticles of ZnO and FeO were prepared at concentration of 150 ppm. Commercial nano Zinc oxide and Iron oxide fertilizers were used in the form of foliar application on plants of Strawberry Cv. Winter Dawn. Nano-ZnO and FeO were obtained from ad-nano Technologies Pvt Ltd prepared by the chemical precipitation method containing the purity rate 99.9%, average particle size 30–80 nm and bulk density 0.58 g/cm$^3$.

At the initial stage, black polythene mulching (thickness 200 gauges) was used. Plant's growths were noted at a day's interval of 15 initially. Biochemical observations were recorded after the harvesting of the fruits. After the physiological maturity of the fruits per hectare yield of crop and yield of crop per plant was recorded.

Leaves (fully opened) counted (randomly) and the average was calculated. The plant's height was individually measured using a measuring scale, leaf area meter is used to measure leaf area. SPAD 502 (m) was used to measure the chlorophyll content in the leaves. Weight of fruits was noted using an electric weighing machine (g). The length of fully developed berries was measured using a vernier calliper and expressed in centimetres. TSS in the fruits was calculated using a refractometer (digital) and expressed in degrees Brix.

Ascorbic acid content in the fruit was estimated titrimetrically using 2,6-dichlorophenolindophenol dye following a modify procedure from A.O.A.C. Value of ascorbic acid was expressed as mg per 100 g of fruit pulp of fresh fruits. Titratable acidity (% citric acid) was determined by extracting and filtering the juice of fresh fruits. The 5 ml of the juice were taken and diluted with water (distilled) to a total volume of 50 ml. The diluted juice was titrated over 0.1N NaOH with the help of phenolphthalein used as an indicator. The endpoint was indicated by a light pink color, and the observed values were defined as citric acid/100 ml of juice. At the time of harvest, the amount of fruit per plot was calculated, and the ratio of fruit per plant was determined.

### 2.3. Statistical analysis

Statistical analysis of on plant's growth, yield and quality parameters was done significantly and the results were interpreted accordingly. To assess the performance of the different treatments, the data were analysed using analysis of variance (ANOVA). Significance tests were conducted at a 5% significance level. The analysis was performed using OPSTAT, which calculates measures such as the standard error of means SE(m), standard error of differences SE(d), and critical difference (CD) among all treatments.

## 3. Results

### 3.1. Impact of Nano-fertilizer and INM on Plant's Growth Indices

With the growth phase of the crop, significant variations were found between all the treatments such as total number of leaves, plant's height, spreading of plants as well as area of leaves. There was a steady rise of these morphometric indices. The rate of increase in these growth parameters were diminished in the later stages of plant growth (Figure 1). The treatment $T_7$:– 50% RDF + FYM + Vermicompost + *Azotobacter* + ZnO + FeO*)* showed the Maximum number of leaves (14), while the control (T0, 100% RDF) had the lowest number of leaves (12) as shown in in Figure 2. Maximum plant height (12.32 cm) was observed in treatment $T_5$:- 50% RDF + Vermicompost + *Azotobacter* + ZnO + FeO) as comparison with T0 (9.88 cm) (Figure 3).

The maximum leaf area (74.86 cm$^2$) was recorded in $T_7$ treatment compared to the untreated (T0) plants (72.12 cm$^2$). The chlorophyll content was highest in $T_5$: 50 % RDF + Vermicompost + *Azotobacter* + ZnO + FeO) with a value of 53.06, followed by $T_9$: – 50% RDF+ FYM + *Azotobacter* + PSB + ZnO + FeO) at different intervals of 30, 60, 90,



(a) (b) (c)

**Figure 1.** a) Vegetative growth stage, b) Phase of flowering, c) Fruiting phase of crop.

and 110 days. The best results were observed in $T_7$ (Figure 4) and $T_5$ after following the other treatments. It was observed that the simultaneous application of ZnO and FeO nanoparticles at a concentration of 150 ppm each led to enhanced growth and increased yield in strawberry.

### 3.2. Effect on Quality and Yield Parameters

The quality parameters e. g., weight of fruits, fruit length, TSS of fruits, ascorbic acid content, total sugars, fruits per plant significant variations were observed. The maximum fruit weight (10.59 g) was recorded in $T_5$ (Figure 5). The maximum (5.01 cm) fruit length was under the treatment of $T_9$ plants. The plants treated with $T_9$, shows variations as compared with control (3.05 cm) in case of length of fruits.

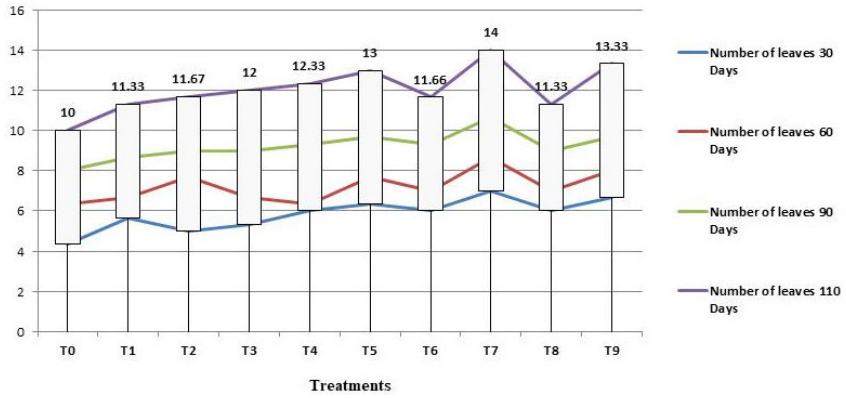


**Figure 2.** Role of nano-fertilizers and integrated nutrient management on number of leaves of plants of crop strawberry (*Fragaria* × *ananassa Duch.*) Cv. Winter Dawn.

Maximum fruit TSS 6.95° brix was noted down in $T_7$ treatment followed by the $T_9$, 6.55° brix as compared with the control 5.53° brix. Increased TSS (° brix) levels in high nitrogen-related levels are likely to be because of the certainty that nitrogen absorption may play a role in the regulation during fruit ripe stage, the carbohydrate conserves of roots along with stems are heavily absorbed by the fruit which may result in higher TSS fruit set. Maximum value of ascorbic acid (mg/100 gm pulp) 52.29 mg/100 gm was noted in the treatment $T_7$ after following the treatment $T_9$ that is 50.79 (mg/100 gm pulp) as compared to control 48.63 (mg/100 gm pulp).

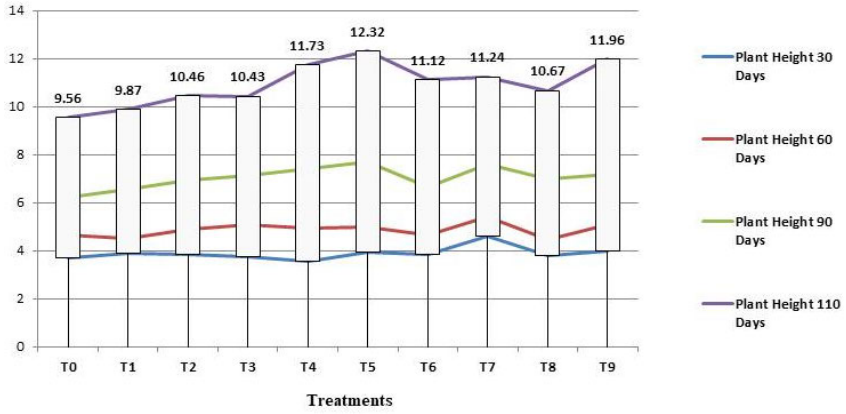


**Figure 3.** Role of nano-fertilizers and integrated nutrient management on plant height of crop strawberry (*Fragaria* × *ananassa Duch.*) Cv. Winter Dawn.

Total sugar was recorded maximum in treatment $T_9$ (7.50%) followed by $T_7$ (7.45%) as compared with the control (6.54%) (Figure 6). Harvested fruits from the plants which were treated with the vermicompost, were found producing fruits with higher total sugars (%) in higher amount. Maximum fruit yield/plant 116.78 g was noted in the $T_7$ followed by 100.69 g in $T_9$ respectively. Minimum fruit yield per plant 57.48 g was recorded in $T_0$ (Figure 6).



**(a)** **(b)**

**Figure 4.** Comparison of total number of fruits per plant RDF with $T_7$.

## 4. Discussion

Application of manures such as vermicompost, farmyard manure and poultry manures along with nano-fertilizers e.g., Zinc oxide and Iron oxide, and bio-fertilizers like *Azotobacter*, *Beijerinkia*, and *Azospirillum*, has been found to enhance vegetative growth parameters in strawberry crop. When *Azotobacter* is applied in combination with farmyard manure, it enhances the vegetative growth due to improved nutrient uptake by the plants at a slower pace [*Usenik et al.*, 2005]. Significant role of *Azotobacter* is attributed to its ability to fix atmospheric nitrogen, while FYM enhances the soil's water and nutrient holding capacity. A*zotobacter*, has been demonstrated to elevate the mobilization of nutrients within the soil

matrix. This, in turn, establishes a continuum of nutrient accessibility, thereby ensuring an enduring nutrient reservoir to fuel the botanical maturation process [*Sharma et al.*, 2018].

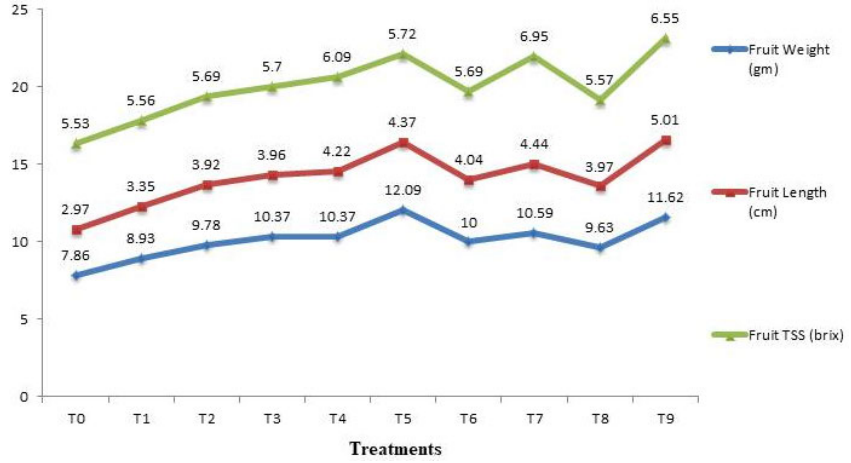


**Figure 5.** Role of Nano-fertilizers and Integrated Nutrient Management on TSS of fruits, length of fruits, weight of fruits of strawberry.

According to a study conducted in a region of northern India (semi-arid), different levels of vermicompost were applied with bio-fertilizer to maintain the fertilizer requirements of strawberries. Results showed that increasing dose of vermicompost consequently, improve the growth (No. of leaves, leaf length, plant height and plant spreading etc.) of Strawberry plants. Vermicompost applied at the concentration of 10 t/h along with free-living bio-fertilizers enhance the spreading of the plants (16.1%), total area of leaf (31%), and dry matter (17.8%) [*Singh et al.*, 2010].

The application of zinc oxide can positively influence growth of plant and development. For instance, same findings were demonstrated by Laware (2014) in onions [*Laware and Raskar*, 2014]. They reported that lower concentrations of zinc oxide NPs had a significant impact on germination of seeds. However, higher doses of ZnO were found to impair seed germination. Furthermore, the impact of nanoparticles on germination can vary depending on the specific concentrations & plant species involved [*de la Rosa et al.*, 2013]. In a study by [*Raliya and Tarafdar*, 2013], different concentrations of NPs were applied to cucumber, tomato, alfalfa, and it was observed that seed germination of cucumber was enhanced [*Raliya and Tarafdar*, 2013].

In the present study, the combination of vermicompost and farmyard manure with nanofertilizers has shown promising results in increasing flower production and overall yield in strawberry plants. Vermicompost has the potential to produce enzymes, growth hormones, antifungals, and antibacterial compounds, which contribute to improved commercial yields [*Zargar et al.*, 2008]. When these organic manures are applied along with bio-fertilizers and nano-fertilizers, they aid in the decomposition of harmful elements, improve soil structure, promote root development, enhance soil water availability, and increase soil microbial biomass, ultimately leading to better plant growth in terms of height, spreading, leaf area, etc. So, it was observed when vermicompost and neem cake were applied with different doses of free-living bio-fertilizers in strawberries [*Arancon et al.*, 2004].

[*Naidu et al.*, 2001] claimed that the effect of various doses of organic manure and bio-fertilizers (symbiotic) was significant in case of tomato crop growth. They showed maximum number of flowers/plant and early flowering with good yield as compared to non-treated plants. Increase in soil-microbial biomass, vermicompost, along with FYM, having direct role in the production of hormones and humus in the soil [*Naidu et al.*, 2001]. Combined application of FYM, vermicompost, and PSB (bio-fertilizer) resulted in a higher no. of flowers per plant and increased yield compared to non-treated guava plant [*Sharma et al.*, 2018].

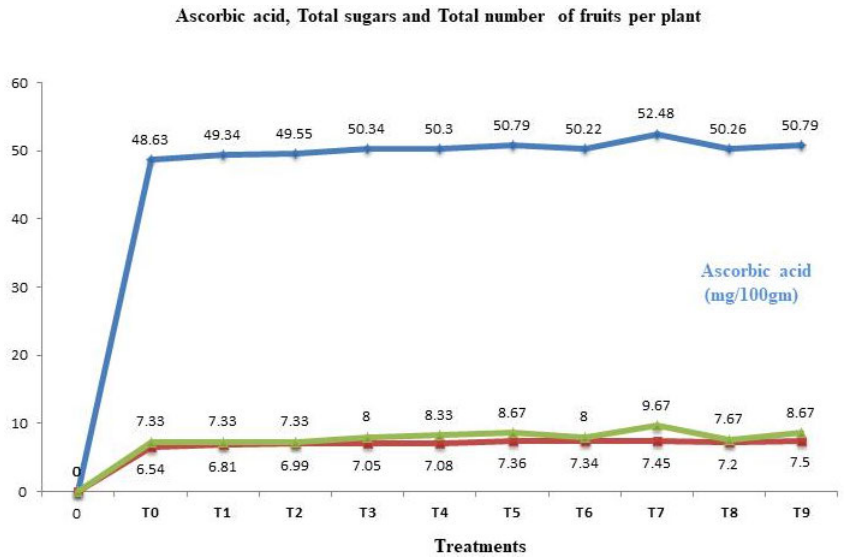


**Figure 6.** Role of Nano-fertilizers and Integrated Nutrient Management on Vitamin 'C' content (mg/100gm) and total no. of fruits per plant of crop strawberry (*Fragaria* × *ananassa Duch.*) Cv. Winter Dawn.

*Azotobacter* (biofertilizer) along with FYM and vermicompost in strawberry results in good fruit length, maximum number of fruits per plant but combination of PSB (phosphate solubilizing bacteria) with press mud and poultry manure improves the weight and shape of fruits [*Nazir et al.*, 2006]. These results indicate that the combination of farm waste manures, bio-fertilizers and nano-fertilizers positively influences nitrogen fixation, phytohormone production, and nutrient uptake, leading to improvements in fruit quality characteristics [*Sajjadi et al.*, 2017]. Nano-fertilizers boost nutrient use efficiency by enabling a slow and constant release of nutrients, thus assisting nutrient uptake by plant.

## 5. Conclusion

Based on the meticulous research study conducted within the timeframe of 2022–23, a consecutive series of conclusions can be derived, highlighting the pre-eminence of treatments $T_7$ and $T_9$. These treatments, denoted as $T_7$ comprising 50% of the recommended dosage of fertilizers in conjunction with farmyard manure, vermicompost, *Azotobacter*, ZnO, and FeO, and $T_9$ encompassing an analogous composition but incorporating phosphate solubilizing bacteria, ZnO, and FeO, have distinctly emerged as the most optimal. Their superiority is evidenced in terms of augmenting the growth dynamics, enhancing the intrinsic quality, and amplifying the overall yield parameters of the esteemed Strawberry Cv. Winter Dawn. In summation, it is unequivocally affirmed that the judicious amalgamation of farmyard manure and vermicompost fortified with *Azotobacter*, bolstered further by the incorporation of ZnO and FeO at a concentration of 150 ppm, bestows momentous and noteworthy outcomes upon the cultivation of Strawberry Cv. Winter Dawn.

**Acknowledgments.** We greatly acknowledge lovely professional university (school of agriculture) for providing their facilities to conduct this research experiments. T. M., S. S. and V. D. R. acknowledge support by the laboratory "Soil Health" of the Southern Federal University and the financial support of the Ministry of Science and Higher Education of the Russian Federation (agreement No. 075-15-2022-1122).

**Conflict of Interest.** Authors declared that they have no conflict of interest.

## References

Arancon, N. Q., C. A. Edwards, P. Bierman, C. Welch, and J. D. Metzger (2004), Influences of vermicomposts on field strawberries: 1. Effects on growth and yields, *Bioresource Technology*, *93*(2), 145–153, https://doi.org/10.1016/j.biortech.2003.10.014.

de la Rosa, G., M. L. López-Moreno, D. de Haro, C. E. Botez, J. R. Peralta-Videa, and J. L. Gardea-Torresdey (2013), Effects of ZnO nanoparticles in alfalfa, tomato, and cucumber at the germination stage: Root development and X-ray absorption spectroscopy studies, *Pure and Applied Chemistry*, *85*(12), 2161–2174, https://doi.org/10.1351/pac-con-12-09-05.

El-Bialy, S. M., M. E. El-Mahrouk, T. Elesawy, A. E.-D. Omara, F. Elbehiry, H. El-Ramady, B. Áron, J. Prokisch, E. C. Brevik, and S. Ø. Solberg (2023), Biological Nanofertilizers to Enhance Growth Potential of Strawberry Seedlings by Boosting Photosynthetic Pigments, Plant Enzymatic Antioxidants, and Nutritional Status, *Plants*, *12*(2), 302, https://doi.org/10.3390/plants12020302.

Food and Agriculture Organization of the United Nations (2023), Crops and livestock products, http://www.fao.org/faostat/en/#data/QC, (date of access: 06.07.2023).

Kumar, A., N. Sharma, and C. L. Sharma (2017), Studies on nutrient management in apple cv. Oregon Spur-II under the cold desert region of Himachal Pradesh in India, *Indian Journal Of Agricultural Research*, *51*(2), 161–166, https://doi.org/10.18805/ijare.v0iof.7633.

Kumar, R., P. Bakshi, M. Singh, A. K. Singh, V. Vikas, J. N. Srivatava, V. Kumar, and V. Gupta (2018), Organic production of strawberry: A review, *International Journal of Chemical Sciences*, *6*(3), 1231–1236.

Laware, S. L., and S. Raskar (2014), Influence of Zinc Oxide Nanoparticles on Growth, Floweringand Seed Productivity in Onion, *International Journal of Current Microbiology Science*, *3*(7), 874–881.

Mandal, K., V. Bahadur, and A. B. Ekka (2021), Effect of different organic media on growth andestablishment of strawberry (Fragaria ananassa) cv.winter dawn under East-Singhbhum (Jharkhand) agro - climatic conditions, *The Pharma Innovation Journal*, *10*(9), 1603–1608.

Naidu, A. K., S. S.Kushwah, A. K. Mehta, and P. K. Jain (2001), Study of organic, inorganic and biofertilizers in relation to growth and yield of tomato, *JNKVV RESEARCH JOURNAL*.

Nazir, N., S. R. Singh, A. Khalil, M. Jabeen, and S. Majeed (2006), Yield and growth of strawberry cv Senga Sengana as influenced by integrated organic nutrient management system, *Environment and Ecology*, *24*(3), 651.

Raliya, R., and J. C. Tarafdar (2013), ZnO Nanoparticle Biosynthesis and Its Effect on Phosphorous-Mobilizing Enzyme Secretion and Gum Contents in Clusterbean (Cyamopsis tetragonoloba L.), *Agricultural Research*, *2*(1), 48–57, https://doi.org/10.1007/s40003-012-0049-z.

Reddy, S. S., and V. Chhabra (2022), Nanotechnology: its scope in agriculture, *Journal of Physics: Conference Series*, *2267*(1), 012,112, https://doi.org/10.1088/1742-6596/2267/1/012112.

Saini, S., P. Kumar, N. C. Sharma, N. Sharma, and D. Balachandar (2021), Nano-enabled Zn fertilization against conventional Zn analogues in strawberry (Fragaria × ananassa Duch.), *Scientia Horticulturae*, *282*, 110,016, https://doi.org/10.1016/j.scienta.2021.110016.

Sajjadi, M., M. Nasrollahzadeh, and S. M. Sajadi (2017), Green synthesis of Ag/Fe3O4 nanocomposite using Euphorbia peplus Linn leaf extract and evaluation of its catalytic activity, *Journal of Colloid and Interface Science*, *497*, 1–13, https://doi.org/10.1016/j.jcis.2017.02.037.

Sharma, J. R., S. Baloda, R. Kumar, V. Sheoran, and H. Saini (2018), Response of organic amendments and biofertilizerson growth and yield of guava during rainy season, *Journal of Pharmacognosy and Phytochemistry*, *7*(6), 2692–2695.

Sharma, S., V. S. Rana, R. Pawar, J. Lakra, and V. K. Racchapannavar (2020), Nanofertilizers for sustainable fruit production: a review, *Environmental Chemistry Letters*, *19*(2), 1693–1714, https://doi.org/10.1007/s10311-020-01125-3.

Singh, G., and A. Kalia (2019), Nano-Enabled Technological Interventions for Sustainable Production, Protection, and Storage of Fruit Crops, in *Nanoscience for Sustainable Agriculture*, pp. 299–322, Springer International Publishing, https://doi.org/10.1007/978-3-319-97852-9_14.

Singh, R., R. R. Sharma, and D. B. Singh (2010), Effect of vermicompost on plant growth, fruit yield and quality of strawberries in irrigated arid region of northern plains, *Indian journal of Horticulture*, *67*(3), 318–321.

Usenik, V., D. Kastelec, and F. Štampar (2005), Physicochemical changes of sweet cherry fruits related to application of gibberellic acid, *Food Chemistry*, *90*(4), 663–671, https://doi.org/10.1016/j.foodchem.2004.04.027.

Weber, N. C., D. Koron, J. Jakopič, R. Veberič, M. Hudina, and H. B. Česnik (2021), Influence of Nitrogen, Calcium and Nano-Fertilizer on Strawberry (Fragaria × ananassa Duch.) Fruit Inner and Outer Quality, *Agronomy*, *11*(5), 997, https://doi.org/10.3390/agronomy11050997.

Zargar, M. Y., Z. A. Baba, and P. A. Sofi (2008), Effect of N, P and biofertilizers on yield and physiochemical attributes of strawberry, *Agro Thesis*, *6*(1), 3–8.

Russian Journal of Earth Sciences

Special Issue: "Fundamental and Applied Aspects of Geology, Geophysics and Geoecology"

# Rare Flora of the Khadzhokh Recreational Area of the Republic Of Adygea

**E. A. Sirotyuk[1], G. N. Gunina[1], I. G. Gergia[2]**

[1] Maykop State Technological University, Maykop, Russian Federation
[2] Abkhazian State University, Sukhum, Republic of Abkhazia
* **Correspondence to:** E. A. Sirotyuk, emiliya09@yandex.ru

**Abstract:** The problem of preserving the diversity of the Earth's flora is extremely relevant due to the increasing impact of economic and other human activities on the natural environment. The most fragile and very significant part of the flora in need of protection are rare, endangered and threatened with extinction species. From a biological point of view, these categories include: species that are not threatened with extinction, but their number on the planet is very small; species that are dying out as a result of evolutionary processes; species that are potentially vulnerable due to their biological characteristics; widespread species that reduce their range and numbers as a result of anthropogenic influences. The article shows that the Khadzhokh recreational area of the Republic of Adygea includes three settlements: the villages of Dakhovskaya, Kamennomostsky and Pobeda, which are the most attractive for the local population and tourists from all the regions of Russia and abroad. Based on the survey of the territory of the area in 2017–2022, we studied landscape and botanical monuments of nature and identified rare plants. The rare flora of the area includes a large proportion of relict and endemic species. The rarest plant species are recommended for inclusion in the third edition of the Red Book of the Republic of Adygea, which will be published in 2023. The limiting factors of the rare flora of the area are revealed. The aim of the work is to study the Khadjokh recreational zone of the Republic of Adygea, identify the species composition of plants in this territory and identify rare species, assess the current state of their populations and determine the category of rarity status for the third edition of the Red Book of the Republic.

**Keywords:** Republic of Adygea, Khadzhokh recreational area, natural monuments, rare plants, endemics, relics, Red Book of the Republic of Adygea.

**Citation:** Sirotyuk E. A., Gunina G. N., Gergia I. G. (2023), Rare Flora of the Khadzhokh Recreational Area of the Republic Of Adygea, *Russian Journal of Earth Sciences*, Vol. 23, ES0216, https://doi.org/10.2205/2023ES02SI16

Research Article

Received: 20 October 2023
Accepted: 27 November 2023
Published: 15 December 2023

**Copyright:** © 2023. The Authors. This article is an open access article distributed under the terms and conditions of the Creative Commons Attribution (CC BY) license (https://creativecommons.org/licenses/by/4.0/).

## 1. Introduction

The reduction of plant diversity affects the stability of natural ecosystem functioning, that is, their productivity and resistance to the introduction of invasive species decrease while the pest activity increases. At the same time, it should be noted that each species makes a certain contribution to ensuring the stability not only of its local ecosystem, but also of the biosphere as a whole, participating in biogeochemical, climatic and other planetary processes. Changes in the plant world caused by human activity have a number of consequences for the process of evolution: intraspecific genetic diversity decreases, populations are divided into a number of isolated fragments, previously separated taxa hybridize, endemics of technogenic substrates and polluted territories appear, etc. [*Gorchakovsky and Shchurova*, 1982]. Also, the extinction of plants leads to the loss of potential sources of economically useful resources for humanity: food, medicinal, decorative, construction and other resources. All this makes the preservation of the diversity of flora one of the most significant problems of our time.

## 2. Research methods

The study used literary sources and herbarium collections of the Caucasian State Natural Biosphere Reserve named after H. G. Shaposhnikov (CSR), Adygea State University (MAY) and the National Museum of the Republic of Adygea. The collection of factual material was carried out in 2017–2022 during expeditionary surveys of the area. The determinants of A. A. Grossheim [*Grossheim*, 1949], I. S. Kosenko [*Kosenko*, 1970] and A. A. Galushko [*Galushko*, 1980], "Flora of the Northwest Caucasus" [*Zernov*, 2006] were used to determine the plants. Latin names of species are given according to Cherepanov [*Cherepanov*, 1995]. The research included the development of proposals on the status of rare species in order to include them in the third edition of the Red Book of the Republic of Adygea.

## 3. Study area

The Republic of Adygea (RA) is the only region in the Russian Federation (RF) surrounded on all sides by another region (Krasnodar Krai) (Figure 1). The republic is located in the northwestern part of the Caucasus on the left bank of the Kuban and Laba rivers. The area of Adygea is 7792 km$^2$. The northern part of the Republic is a slightly undulating Pre-Kuban inclined plain, the southern part is composed of the foothills (up to 300 m above sea level) and mountains (Mount Chugush, up to 3238 m above sea level) of the Greater Caucasus. The climate is moderately warm and humid. The average temperature in January in the capital (Maykop) is −1.6 °C, in July is 22.2 °C. Precipitation falls about 700 mm per year. The frost-free period lasts 180 days. Chernozems are common in most of the territory. The massifs of plavnevo-meadow, meadow-marsh and mountain forest soils are significant.




**Figure 1.** Map of the Republic of Adygea.

Several geographical zones and vertical vegetation belts is replaced from the north to the south on the territory of the Republic: forest–steppe – up to 500 (600) m above sea level; oak and hornbeam forests – 500 (600)–900 (1000) m above sea level; beech forests – 900 (1000) – 1400 m above m.; dark coniferous forests of Caucasian fir with "islands" of pine forests 1200 (1400)–2220 m above sea level; subalpine belt of a complex of crooked forests, woodlands, rhododendron thickets and tall grass meadows – 1800–2300 (2500) m above sea level. m.; the alpine belt consists of a complex of shrubs, low-grass meadows, carpets and rock communities – 2500 (2600)–2800 (3200) m above sea level; the nival belt of "eternal" snows and glaciers.

A distinctive feature of Adygea is a significant landscape and biological diversity and a high level of endemism and relict flora. About 14% of the territory of the republic are UNESCO World Natural Heritage Sites "Western Caucasus" [*Zhane*, 1999] and more than 30% of the Republic's area is occupied by specially protected natural areas (protected areas) [*Kozmenko*, 2007]. Currently, there are 20 protected areas on the territory of the republic: two of them are of federal significance (the Northern Department of the Caucasian State Natural Biosphere Reserve named after H. G. Shaposhnikov (KGPPZ) and the Arboretum of the Adygea State University), 18 – of regional subordination. The protected areas of regional subordination are comprised of 3 natural parks, 2 nature reserves and 13 natural monuments. They are as follows: the nature parks "Bolshoy Tkhach", "Gornaya Adygea" and "Upper Reaches of the Tsitsa River", botanical reserves of Maykop and Kuzhorsky; natural monuments: "Bujny Ridge", "Waterfalls of Rufabgo Creek", "Granite Gorge", "Monk Mountain", "Syuk River Valley", "Ammonite Valley", "Natural plantings of chestnut", "Canyon of the Aminovka River", "Canyon of the Meshoko Creek", "Maiden Stone", "Canyon of the Sakhray River", "Colchis boxwood massif" and "Khadjokh gorge" [*Official Internet site of the executive bodies of state power of the Republic of Adygea*, 2000].

Currently, the species diversity of the higher plants of the republic is estimated at about 2000 species: about 1500 species of vascular plants and 400 species of mossy. A significant number of relics, endemics, rare and endangered plants have been noted in the flora. In our opinion, the presence of 133 species of relict plants belonging to 99 genera from 48 families in the flora of Adygea should be considered reliable [*Sirotyuk et al.*, 2013]. According to M. D. Altukhov, about 350 Caucasian endemic species grow in the North-Western Caucasus. of these, more than 150 species grow in Adygea [*Altukhov*, 1985], including 33 species of rare orchids [*Sirotyuk and Zhemadukova*, 2020]. Rare and endangered plants of Adygea are more than 300 species of higher spore and seed plants, of which 140 species are included in the Red Book of the Republic of Adygea [*The Red Book of the Republic of Adygea*, 2012], including 27 endemic Caucasian species and 21 relicts, 55 species (39.2%) are listed in the Red Book of the Russian Federation [*Bardunov*, 2008].

The local centers of speciation in Adygea are the Fisht-Oshten massif and the Bolshoy Tkhach Mountain. The subalpine and alpine vegetation of these mountain systems contains approximately 36% of the endemic species of the republic. It should be noted that all modern forest-forming rocks of Adygea are relics of the tertiary period.

A high degree of economic development of the territory of the republic, intensive development of recreation and tourism can jeopardize the stability of natural ecosystems and existence of many unique habitats and rare species of flora. However, the main danger is the intensive development of the territory for the needs of the national economy, during which there is not only a violation of the locations of rare flora species, but also the destruction of the soil cover [*Lebedev et al.*, 2021].

## 4. Research results

The Republic of Adygea is a tourist and recreational region. 13 places of concentration of tourist and recreational facilities have been identified at the recreational area level in the Republic, where natural resources are supplemented by historical, cultural and infrastructural ones. The most attractive for the local population and tourists from the regions of Russia is the Khadzhokh recreational area, which covers the village of Dakhovskaya and the villages of Kamennomostsky and Pobeda. There are 23 tourist routes in the area. The number of natural objects is 97 pcs., historical and cultural – 11 pcs., hospitality – 43 pcs. There are regional branches of road and rail transport in the village of Kamennomostsky [*Sviridova*, 2022].

The largest river of Adygea, the Belaya, flows in the Khadzhokh recreational area and it has many tributaries (more than 3000): Pshekh, Kurdzhips, Kisha, Dakh, Aminovka, Bolshoy Rufabgo, etc. The Belaya forms two large canyons: on the southwestern outskirts of the village is Kamennomostsky – Khadzhokhsky (Figure 2) and in the Dakhovsky gorge is Granite (Figure 3), as well as many waterfalls, gorges, caves and rock formations.



**Figure 2.** Khadzhokh Canyon.



**Figure 3.** Granite Canyon.

The village of Dakhovskaya is the administrative center of the Dakhovsky rural settlement and the center of tourism in Adygea [goryuga.ru/dahovskaya.php]. The village is located at the foot of Mount Gut at an altitude of 480 m above sea level, on the right bank of the Belaya River at the confluence of the Dakh tributary (Figure 4).



**Figure 4.** The village of Dakhovskaya.

Ridges with oak, beech and fir forests on both sides surround Dakhovskaya: on the left, it is Una-Koz, which is a part of the Rocky Ridge; on the right – Azish-Tau. The village is located 7 km south of the village Kamennomostsky, where the nearest railway station Khadzhokh is located. The highway to the village of Guzeripl passes through the village along the gorge of the Belaya River. A little to the north there is a bridge over which there is a road to the Azish pass and the Lagonak Highlands.

The villages of Kamennomostsky and Pobeda have a rich tourist history and are widely known in the countries of the former USSR. Numerous and diverse recreational resources have been developed on their territory such as dolmens, waterfalls, grottos, canyons, and caves. Tourist flows are formed in the village of Kamennomostsky, heading throughout the mountainous Adygea. There is a tourist camp "Gornaya", built in 1935, from which

the thirtieth All-Union hiking tourist route "Along Adygea to the Black Sea", the oldest in Russia, began. It should also be mentioned the sanatorium "Lesnaya Skazka", which is located 5 km from the village of Kamennomostsky and operates on the basis of hydrogen sulfide waters. Diseases of the musculoskeletal and central nervous systems are treated here.

The village of Pobeda, so named in May 1945, is the highest mountainous settlement of the Maykop district. It has a wide range of historical, cultural and natural monuments. There is a male Orthodox monastery (St. Michael-Athos Zakubanskaya male cenobitic monastery), founded in 1877, on the territory of which there is a holy spring, an underground temple, caves and monastic cells, which attract numerous pilgrims and tourists.

Natural monuments of various types are concentrated on the territory of the Khadzhokh recreational area of the republic: "Maiden Stone" (geological); "Waterfalls of Rufabgo creek" (landscape-geological); "Canyon of the Aminovka River" (landscape-botanical), "Canyon of the Meshoko creek" (landscape-botanical), "Khadzhokhskaya gorge" (landscape-botanical), which are visited by tourists from all the regions of Russia all year round. Intensive development of recreation and a high degree of economic development of the territory of natural monuments lead to changes and destruction of species habitats.

The forestry and mining industry of the republic is concentrated in the village of Kamennomostsky. The village has been developing and as a large industrial center for many years. Its further development is also connected with industry. New mining and sand pits, workshops for processing wood and natural stone are being opened. Concentration of recreational and industrial centers of the mountainous region of the mountainous region on the same industrial zone of the village of Kamennomostsky is at least irrational in terms of environmental and aesthetic parameters [*Popov*, 2020].

In addition, an industrial complex has been built in the village of Kamennomostsky, which includes: a plant for the production of gypsum and gypsum-binding mixtures with a capacity of 240 thousand tons per year, a plant for the production of cellular concrete blocks with a capacity of 450 thousand tons per year, a plant for the production of hyperpressed bricks with a capacity of 24 million pieces per year, a lime plant with a capacity of 80 thousand tons per year, as well as a railway terminal for transshipment of non-metallic and construction materials, crushing and sorting units, a carpool for the placement of equipment intended for the transportation of non-metallic raw materials from quarries to the industrial zone [zavodfoto.livejournal.com].

The soils of the district are polluted with toxic chemicals coming from industrial emissions into the atmosphere and exhaust gases of motor vehicles, sewage, industrial and household waste, as well as agrochemicals (in particular, pesticides) used for plant treatment [*Lebedev et al.*, 2021]. Data have been obtained that the soils are contaminated with petroleum products and destructive processes have begun. There are no diatoms in soil cyano-algosinusions, which are the main indicators of oil pollution of soils, and cyanobacteria resistant to soil contamination with petroleum products and heavy metals predominate [*Sirotyuk and Zhemadukova*, 2020].

The area is dominated by a broad-leaved forest mid-mountain landscape. However, the flora of the area has not been studied enough and the information about its composition and rare species is fragmentary. The deterioration of the state of natural monuments in the form of weakening of stands due to anthropogenic impact and the introduction of alien landscape elements reduces the recreational attractiveness of these tourist sites [*Varzareva*, 2009].

The rare plants growing in the Khadzhokh recreational area have the following threats:

- construction of roads, economic and tourist facilities;
- creation of recreation areas on the banks of rivers with remnants of primary natural vegetation, fragments of which have survived on the floodplain terraces;
- massive deforestation in the mountains;
- collecting plants for bouquets by the population of adjacent villages and tourists;
- the highest recreational load on ecosystems, including protected areas;

- long-term natural factors caused by cyclical climate changes leading to habitat isolation and fragmentation of regional plant ranges;
- the introduction of foreign species with significant tolerance to many environmental factors that can displace stenotopic relict and ancient endemic plants from their habitats.

As a result of the conducted research, 42 rare species of plants growing in the area were identified. All of them are recommended for inclusion in the third edition of the Red Book of the Republic of Adygea. The list of flowering plant species from two classes are Magnoliopsida Brongn., 1843 and Liliopsida Batsch, 1760, includes 20 orders and 23 families, including the Magnoliopsida class – 16 orders and 16 families, the Liliopsida class – four orders and 7 families. The most widely represented species will be the family Orchidaceae Juss. (14 species).

The share of relict (15 species – 36%) and endemic species (8 species – 20%) is significant in the composition of the rare flora of the Khadzhokh recreational area. The degree of threat of species extinction varies (Figure 5). The majority of species (30 species, or 71.4%) are recommended to be classified in the third edition of the Red Book of the Republic of Adygea as "Vulnerable", seven species (16.7%) – as "Endangered", four species (9.5%) – as "Critically endangered". The orchid *Dactylorhiza urvilleana* (Steud.) H. Baumann & Kunkele (2.4%) is classified as "Specially controlled".

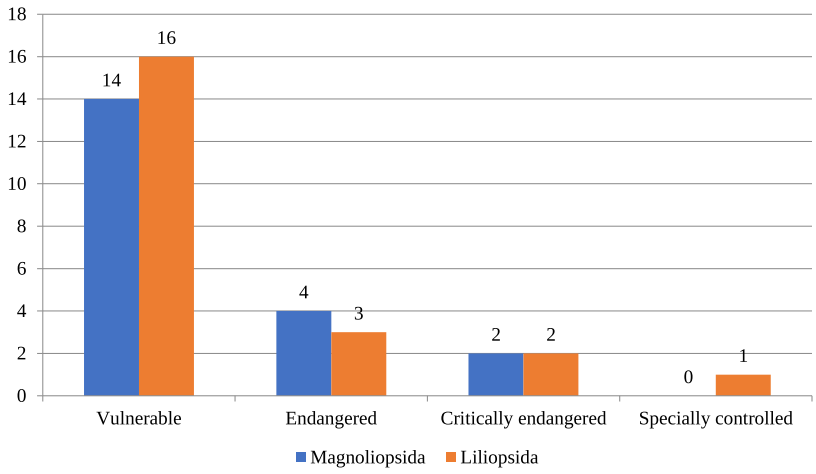


**Figure 5.** The degree of threat of extinction of plant species in the Khadzhokh recreational area of Adygea.

The following plant species are recommended to be included in the third edition of the Red Book of the Republic of Adygea with the category of the rarity status of V (Vulnerable): *Helleborus caucasicus* A. Braun, *Berberis vulgaris* L., *Paeonia caucasica* (Schipcz.) Schipcz., *Ilex colchica* Pojark., *Euonymus leiophloea* (Stev.) Prokh., *Cyclamen coum* Mill. subsp. *caucasicum* (C. Koch) O. Schwarz, *Genista albida* Willd., *Astragalus demetrii* Kharadze, *Staphylea pinnata* L., *Gentianopsis blepharophora* (Bordz.) Galushko, *Scopolia caucasica* Kolesn. ex Kreyer, *Solenanthus biebersteinii* DC., *Digitalis ferruginea* subsp. *schischkinii* (Ivanina) K. Werner, *Campanula pendula* Bieb., *Lilium monadelphum* Bieb., *Colchicum umbrosum* Steven, *Crocus speciosus* Bieb., *Gladiolus tenuis* Bieb., *Muscari neglectum* Guss., *Ornithogalum ponticum* Zahar., *Anacamptis pyramidalis* (L.) Rich., *Cephalanthera damasonium* (Mill.) Druce, *Cephalanthera longifolia* (L.) Fritsch, *Neottia ovata* Bluff & Fingerh., *Neotinea tridentata* (Scop.) R.M. Bateman, Pridgeon & M.W. Chase, *Orchis mascula* (L.) L., *Orchis militaris* L., *Orchis purpurea* Huds., *Platanthera chlorantha* (Cust.) Rchb., *Carex elata* Bell. ex All.

The following plant species are recommended to be included in the third edition of the Red Book of the Republic of Adygea with the category of the rarity status of E (Endangered): *Anemone blanda* Schott et Kotschy, *Corylus colurna* L., *Ostrya carpinifolia* Scop., *Genista angustifolia* Schischk., *Cephalanthera rubra* (L.) Rich., *Spiranthes spiralis* (L.) Chevall. and

*Stipa pennata* L. *Anemone blanda* – a rare Caucasian-Asian species. *Corylus colurna* – an ancient Eastern Mediterranean relict species that reduces the area of growth and abundance due to the violation of growing conditions and weak natural renewal. *Ostrya carpinifolia* – a Mediterranean relict species with a declining number of plants as a result of anthropogenic impact. *Genista angustifolia* – a limited-spread Western Caucasian endemic with a low population, facing a high risk of extinction in the wild life. *Cephalanthera rubra* – European-Mediterranean-Near-Asian species with low population density and declining numbers. In the conditions of Adygea, the species was recorded in a wide altitude range, that is, at altitudes of 209–1724 m above sea level. It occurs in single instances, rarely in small groups [*Sirotyuk et al.*, 2022]. *Spiranthes spiralis* – European-Mediterranean-Near-Asian species. It is very rare in Adygea, only three localities are known in meadows in the belt of broad-leaved forests. *Stipa pennata* – a rare Eurasian steppe species with declining numbers and isolated locations.

The following plant species are recommended to be included in the third edition of the Red Book of the Republic of Adygea with the category of the rarity status of C (Critically endangered): *Buxus colchica* Pojark., *Pyracantha coccinea* (L.) M. Roem., *Orchis pallens* L. and *Orchis spitzelii* Saut. ex Koch. *Buxus colchica* – a tertiary relic of the ancient Colchian forests that survived the ice Age. The species could have completely disappeared from the face of the earth in 2013 due to human negligence. Volunteers and environmentalists of Adygea have been restoring an ancient relic for several years. The seedlings of Colchis boxwood were planted in 2018. The results of the inspection in 2021 showed a satisfactory condition of the relic. There were no characteristic traces of the presence of boxwood firewebs, nests and gnawing, as well as traces of other possible pests. *Pyracantha coccinea* – a rare species, a representative of the post-glacial xerothermal period, a South European-Anteroasiatic species. *Orchis pallens* – a rare European-Asian relict species. *Orchis spitzelii* – a South European-Caucasian-Asia Minor endemic species with declining numbers, in critical condition.

The third edition of the Red Book of the Republic of Adygea defines the priority of protection III for the majority of rare and endangered plant species (29 species, or 69%), because their conservation does not require the implementation of additional environmental measures [*Sirotyuk et al.*, 2022]. Separate special measures (priority II) are required for the conservation of 12 plant species (28.6%): *Anemone blanda*, *Corylus colurna*, *Ostrya carpinifolia*, *Pyracantha coccinea*, *Genista angustifolia*, *Scopolia caucasica*, *Crocus speciosus*, *Cephalanthera rubra*, *Orchis pallens*, *Orchis spitzelii*, *Spiranthes spiralis*, *Stipa pennata*. Priority I has been determined for *Buxus colchica*, because the species is in critical condition and special comprehensive measures are being taken to preserve it in the Republic of Adygea.

## 5. Conclusion

The limiting factors and threats to the rare flora of the Khadzhokh recreational area are anthropogenic impacts such as: economic development of territories, changing their hydrological regime; trampling due to recreation and tourism; burning stubble and weeds; fires; collecting plants for bouquets; digging up plants, picking up plants by the population for food, etc. Natural factors also limit the existence of species: narrow or fragmentary range; stenotopy; relict; endemicity; low competitive capacity; low population size; method of reproduction; low seed productivity; low number of pollinators, etc.

In connection with global climate change, intensive economic use of land, habitat destruction, activation of various types of recreation and tourism, increasing collection of plants by the population for various purposes, one should probably expect a deterioration in the populations of the most vulnerable species. The negative impacts of anthropogenic and natural nature create a decrease in the living condition of species and the threat of their extinction in some localities. The population sizes of some species have significantly decreased compared to earlier descriptions and have a regressive type of succession dynamics. All of the above requires an objective scientific analysis that would allow us to

assess the current state of the populations of rare plants of the Khadzhokh recreational area, study the mechanisms of self-support and develop conservation measures.

**Acknowledgements**

This study was carried out with the financial support of the Cabinet of Ministers of the Republic of Adygea.

**References**

Altukhov, M. D. (1985), Vegetation cover of the highlands of the North-Western Caucasus, its rational use and protection, phdthesis, Moscow (in Russian).

Bardunov, L. V. (Ed.) (2008), *Red Book of the Russian Federation: (Plants and mushrooms)*, KMK Scientific Press, Moscow (in Russian).

Cherepanov, S. K. (1995), *Vascular plants of Russia and neighboring states (within the former USSR)*, 990 pp., Peace and family – 95, St. Petersburg (in Russian).

Galushko, A. I. (1980), *Flora of The North Caucasus: Determinant*, vol. 3, 328 pp., Rostov University, Rostov n/D (in Russian).

Gorchakovsky, P. L., and E. A. Shchurova (1982), *Rare and endangered plants of the Urals and the Urals*, 208 pp., Nauka, Moscow (in Russian).

goryuga.ru (2013), The village of Dakhovskaya, https://goryuga.ru/dahovskaya.php (in Russian).

Grossheim, A. A. (1949), *Determinant of plants of the Caucasus*, 749 pp., Sovetskaya Nauka, Moscow (in Russian).

Kosenko, A. S. (1970), *The determinant of higher plants of the North-Western Caucasus and Ciscaucasia*, 613 pp., Kolos, Moscow (in Russian).

Kozmenko, G. G. (2007), System of specially protected natural territories and its role in the preservation and restoration of biological and soil diversity of the Republic of Adygea, phdthesis, Moscow (in Russian).

Lebedev, S. A., G. N. Gunina, Y. N. Ashinov, and P. N. Kravchenko (2020), Ecological Conditions of Soils in the Republic of Adygea, in *The Handbook of Environmental Chemistry*, pp. 145–166, Springer International Publishing, https://doi.org/10.1007/698_2020_640.

Lebedev, S. A., E. A. Sirotyuk, A. K. Shkhapatsev, and P. N. Kravchenko (2021), Ecological State of Soils of the Republic of Adygea Under High Anthropogenic Load, in *The Handbook of Environmental Chemistry*, pp. 185–216, Springer International Publishing, https://doi.org/10.1007/698_2021_741.

livejournal (2016), VOLMA with an Adygea accent. Report from the opening of a gypsum plant in Kamennomostsky (Khadzhokh), https://dmitriy.livejournal.com/717127.html (in Russian).

Official Internet site of the executive bodies of state power of the Republic of Adygea (2000), List of operating specially protected natural territories of regional significance as of January 1, 2023, http://www.adygheya.ru (in Russian).

Popov, A. V. (2020), On the question of the main recreational centers of the Republic of Adygea, https://pandia.ru/text/79/118/75271.php (in Russian).

Sirotyuk, E., G. Gunina, and V. Khiryanov (2022), Distribution, ecological and biological features and the state of cenopopulations of species of the genus Cephalanthera Rich. (Republic of Adygea), *Russian Journal of Earth Sciences*, pp. 1–8, https://doi.org/10.2205/2022es01si10.

Sirotyuk, E. A., and S. R. Zhemadukova (2020), Maykop City Soil Quality Determination Based on the Analyses of Soil Algae and Cyanobacteria Content, in *The Handbook of Environmental Chemistry*, pp. 217–235, Springer International Publishing, https://doi.org/10.1007/698_2020_498.

Sirotyuk, E. A., O. A. Panesh, S. I. Chitao, and D. A. Kuasheva (2013), Condition and prospects of studying relic, endemic, rare and disappearing plants of Adyghea, *The Bulletin of the Adyghe State University*, (3(122)), 28–35 (in Russian).

Sirotyuk, E. A., A. E. Shadzhe, and G. N. Gunina (2020a), Plants and Fungi Species Listed in the Red Book of the Republic of Adyge (2017-2019), in *The Handbook of Environmental Chemistry*, pp. 633–652, Springer International Publishing, https://doi.org/10.1007/698_2020_559.

Sirotyuk, E. A., A. E. Shadzhe, and G. N. Gunina (2020b), New data on the distribution and populations of rare species of the family Orchidaceae Juss. in the flora of the Republic of Adygea, *Herald of Tver State University. Series: Biology and Ecology*, (1(57)), 187–198, https://doi.org/10.26456/vtbio140.

Sviridova, E. P. (2022), Geoecological assessment of tourist and recreational development of a mountainous region (on the example of the republic of adygea) (in Russian).

The Red Book of the Republic of Adygea (2012), *Rare and under threat of disappearance objects of the animal and plant world. Part 1.Introduction: Plants and mushrooms*, 2nd ed., Environmental Protection and Natural Resources of the Republic of Adygea, Maykop (in Russian).

Varzareva, V. G. (2009), About the condition of nature monuments in Adyghea, *The Bulletin of Adyghe State University: Internet Scientific Journal*, (3), 156–158 (in Russian).

Zernov, A. S. (2006), *Flora of the North-Western Caucasus*, KMK Scientific Press, Moscow (in Russian).

Zhane, Z. K. (1999), Analysis of the possibilities of sustainable development of the mountainous regions of the Republic of Adygea, *News of the Center for System Research MGTI*, (2), 24–37 (in Russian).

Russian Journal of Earth Sciences

Special Issue: "Fundamental and Applied Aspects of Geology, Geophysics and Geoecology"

# Geological Filtration Model of the Layers of Nizovsky Field of Volga-Ural Oil and Gas Province

**M. A. Meretukov[1], R. A. Toroyan[1], M. K. Bedanokov[1], R. B. Kokhuzheva[1], A. M. Artamonov [1]**

[1] Maykop State Technological University, Maykop, Russian Federation
* **Correspondence to:** R. A. Toroyan, rubenet@mail.ru

**Abstract:** The article presents the results of modeling a three-dimensional digital geological filtration model. The substantiation of the volumetric grids of the model is given and the analysis of the distribution of filtration-capacitance properties of layers and models of reservoir saturation with fluids is carried out. Based on the constructed three-dimensional model of Nizovsky field, the reliability of revealing hydrocarbon reserves at the field has been confirmed.

**Keywords:** Digital three-dimensional geological model, filtration and capacitance properties, porosity coefficient, reservoir thickness, well logging.

**Citation:** Meretukov M. A., Toroyan R. A., Bedanokov M. K., Kokhuzheva R. B., Artamonov A. M. (2023), Geological Filtration Model of the Layers of Nizovsky Field of Volga-Ural Oil and Gas Province, *Russian Journal of Earth Sciences*, Vol. 23, ES0217, https://doi.org/10.2205/2023ES02SI17

## 1. Introduction

Nizovsky oil field is located in Kinelsky district of Samara region, 5 km east of Domashka village, in the aisles of Nizovsky license area. In tectonic terms, the deposit is confined to the southwestern side of the Buzuluk depression (the structure of the I order) and in the zone of its gradual transition to the Zhiguli vault (the structure of the I order).

The industrial oil content of the field is set in four productive layers: A-4 - the Bashkir tier of the middle carboniferous (C2b), B-2 – the Bobrikov horizon of the Visei tier (C1v), C-1 – the Tournaisian tier (C1t) of the lower carboniferous and D-I' – the Pashian horizon of the Fransk tier of the Upper Devonian, containing four oil deposits.

The deposit is considered to be small according to the size of the initial recoverable hydrocarbon reserves and complex according to the complexity of the geological structure.

The deposit of the A4 formation of the Bashkir tier (C 2b) is massive, arched. The size of the deposit is 1.7×1.1 km and the height is 14.7 m. 6–10 permeable dense layers of carbonates 0.4–0.6 m thick represent the formation, separated by dense layers 0.4–0.11 m thick. The oil-water contact was defined at absolute mark of 1564.2 m.

The C1v formation of the Visean tier is a reservoir, arched. The size of the deposit is 1.6×1.2 km and the height is 38 m. The oil-water contact was defined at absolute mark of 2143.3 m.

C1t Tournaisian, formation C-1. The deposit is massive, arched. The size of the deposit is 1.3×0.8 km and the height is 32.5 m. Conventionally, the calculated level of the deposit was taken at absolute mark of 2168.2 m along the sole of the oil-saturated interlayer.

D3f Fransk, layer D-I'. The reservoir is a vaulted reservoir, lithologically limited from the north. The dimensions are 2.0×0.3 km and the height is 34.3 m. The oil-water contact is conditionally defined at absolute mark of 3038.8 m along the sole of the oil–saturated reservoir [*Expert commission of the Volga-Ural branch of the FBU GKZ*, 2019; *Toroyan and Meretukov*, 2023].

The technical and economic advantages of setting and operating three-dimensional geological and technological models with existing operational facilities of gas and oil

Research Article

Received: 20 October 2023
Accepted: 27 November 2023
Published: 15 December 2023

**Copyright:** © 2023. The Authors. This article is an open access article distributed under the terms and conditions of the Creative Commons Attribution (CC BY) license (https://creativecommons.org/licenses/by/4.0/).

fields are undeniable. The efficiency consists in increasing the oil recovery coefficient to 10% from low-yielding deposits, reducing associated water production. Thus, the setting and the use of geological and technical models of oil and gas and oil deposits, as well as permanent operational facilities, makes it possible to solve topical issues of current and future hydrocarbon production planning [*Baturin*, 2007].

## 2. Object of research and methods

The objects of geological modeling of the Nizovsky deposit are A-4 layers of the Bashkir tier, B-2 of the Bobrikov horizon, C-1 of the Tournaisian tier of the lower Carboniferous and the formation D-I' of the Pashian horizon of the Upper Devonian. The justification of the geological model consists in constructing a model in the form of a three-dimensional grid [*Raspopov and Mordvinov*, 2010], in which each cell is represented by a hexagon with quadrangular faces, tied in space using a coordinate system. The number of grid cells is usually from several million to about a billion.

To create a three-dimensional digital model of the formations of the deposit in question, a grid with the geometry of a corner point was used [*Gaisina*, 2010], with a horizontal cell size of 25×25 m [*Zakrevsky*, 2009]. The vertical pitch of the grid varies in the interval:

- 0.04–0.34 m with an average estimate of 0.19 m for deposits of the A-4 formation of the Bashkir tier;
- 0.03–0.38 m with an average estimate of 0.16 m for the deposits of the B-2 formation of the Bobrikov horizon;
- 0.04–0.35 m with an average estimate of 0.21 m for the deposits of the C-1 formation of the Tournaisian tier;
- 0.04–0.34 m with an average estimate of 0.14 m for the deposits of the D-1 formation of the Pashian horizon.

The chosen grid scheme takes into account the vertical (internal) and lateral heterogeneity of the deposits of the Nizovsky deposit [*Gladkov and Gladkova*, 2011].

The size of the grid objects is as follows:

$160 \times 149 = 3814400$ cells (A4 formation model);

$160 \times 118 = 3020800$ cells (B-2 reservoir model);

$160 \times 113 = 2892800$ cells (C-1 formation model);

$160 \times 152 \times 75 = 1824000$ cells (D-I' reservoir model).

The spatial distribution of the reservoirs of the Nizovsky deposit was performed using the deterministic Geomod model of the IRAP RMS complex [*Tikhomirova*, 2020]. The deterministic modeling technology includes 3-dimensional stratigraphic interpolation taking into account a priori given 2-dimensional distribution of sandiness.

The result of constructing a lithology cube of productive layers of the Nizovsky deposit is the spatial distribution of reservoirs, describing their geological heterogeneity in section and area.

## 3. Results and discussion

The constructed lithological model is satisfactorily consistent with the concept of the structure of deposits, at the level of maps of effective and initial oil-saturated thicknesses. Based on the constructed lithological models for all productive formations, the volume of oil-saturated rocks was estimated. When estimating the volumes of oil-saturated rocks, the lithological model does not exceed 5% according to these deposits, which indirectly confirms the validity of estimates of the volumes of these rocks by counting objects.

The proportion of reservoirs of the simulated objects for wells and for the reservoir as a whole is shown in histograms on Figures 1–4.

The porosity cube for all productive layers is constructed by interpolating the value of the porosity coefficient calculated from the results of well logging along the borehole. The

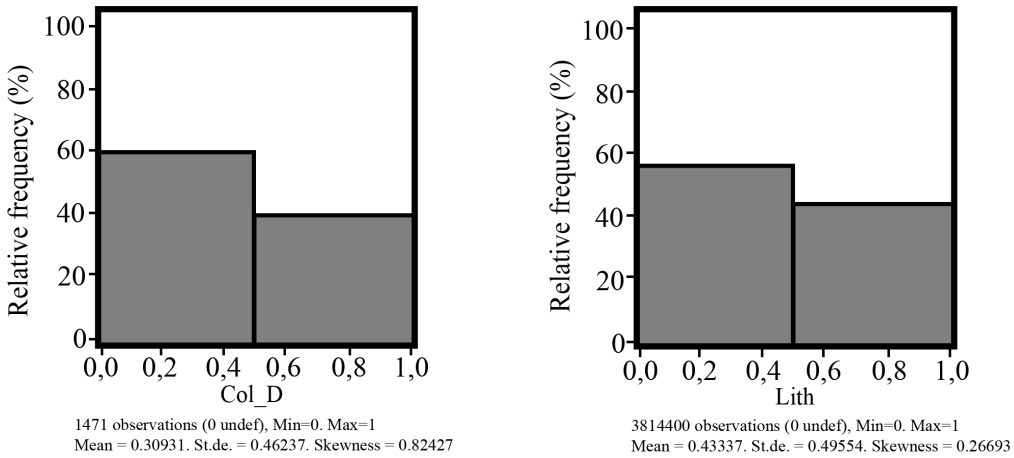


**(a)** **(b)**

**Figure 1.** Comparison of the proportion of the collector and non-collector of A4 formation in wells (a) and in the reservoir as a whole (b).

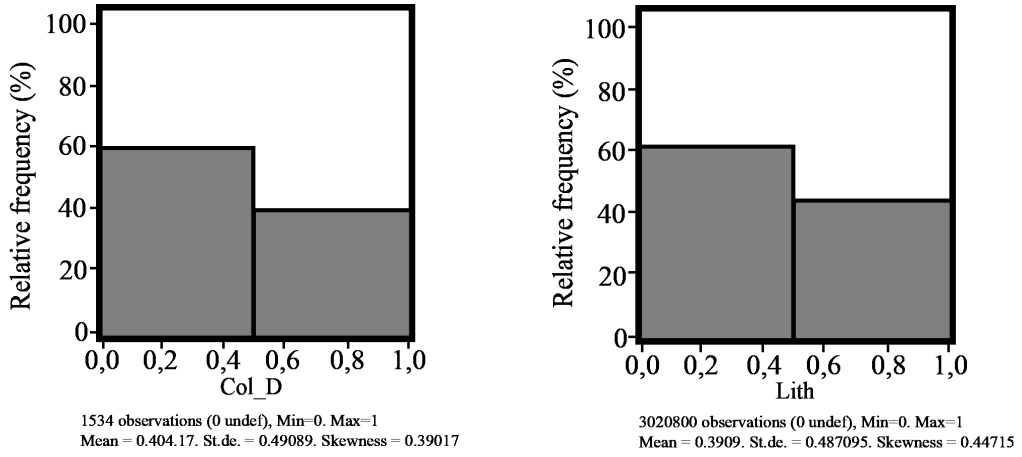


**(a)** **(b)**

**Figure 2.** Comparison of the reservoir and non-reservoir shares of B-2 formation in wells (a) and in the reservoir as a whole (b).

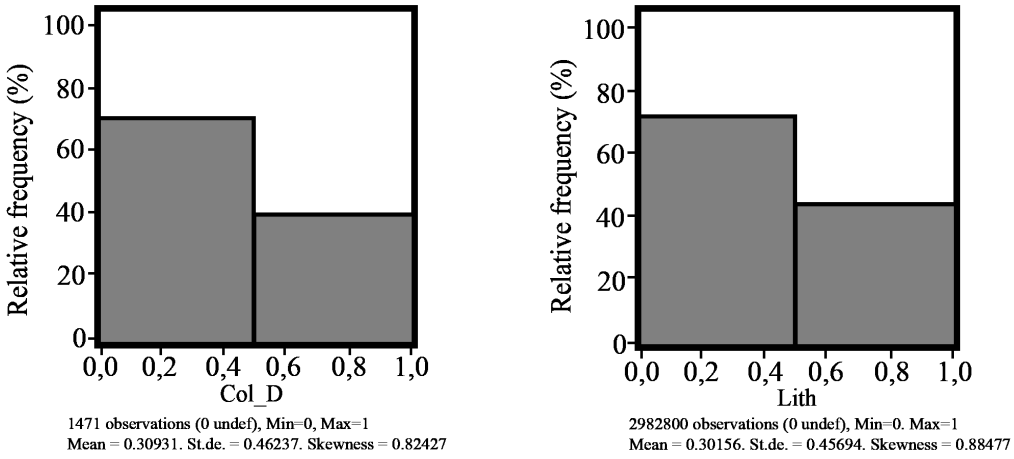


**(a)** **(b)**

**Figure 3.** Comparison of the share of collector and non-collector C-1 in wells (a) and in the reservoir as a whole (b).

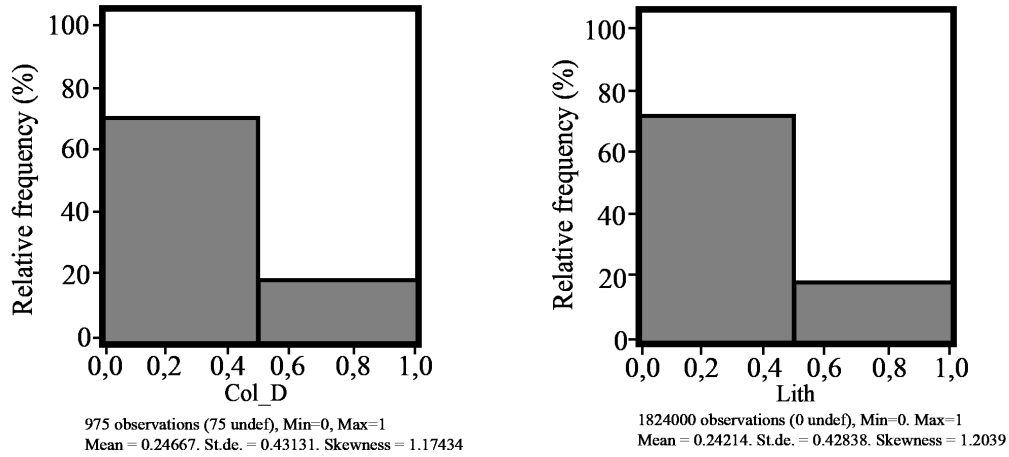


**(a)** **(b)**

**Figure 4.** Comparison of the proportion of the collector and non-collector D-I' in wells (a) and in the reservoir as a whole (b).

distribution of porosity values in the reservoirs of productive formations according to the initial data and for the reservoir as a whole are shown in histograms on Figures 5–8.

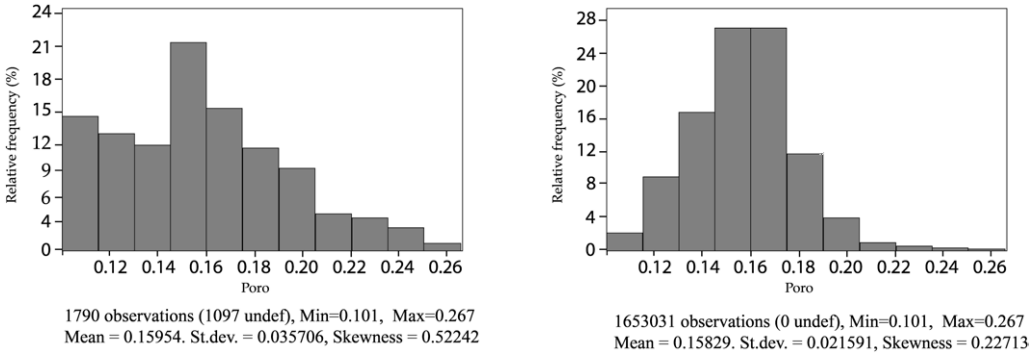


**(a)** **(b)**

**Figure 5.** Porosity distribution of A-4 formation in wells (a) and in the formation as a whole (b).

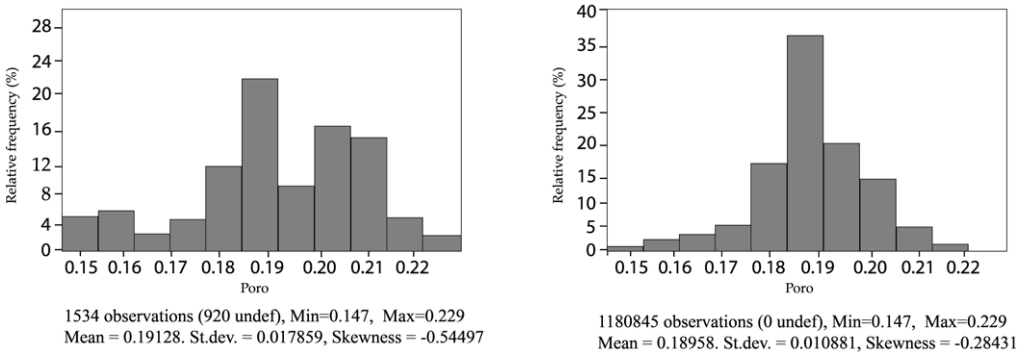


**(a)** **(b)**

**Figure 6.** Porosity distribution of B-2 formation in wells (a) and in the formation as a whole (b).

The average porosity estimates in the model for all deposits (with an accuracy from 0% to 3.1%) are consistent with the proposed values of the parameter under consideration.

To restore the permeability fields, information on the filtration-capacitance properties of the core material was used in the form of correlations between porosity and permeability parallel to the Kp–Kpr stratification, given below. The permeability cubes are calculated by recalculating the 3D distribution of Kp according to the Kp – Kpr correlation dependencies.

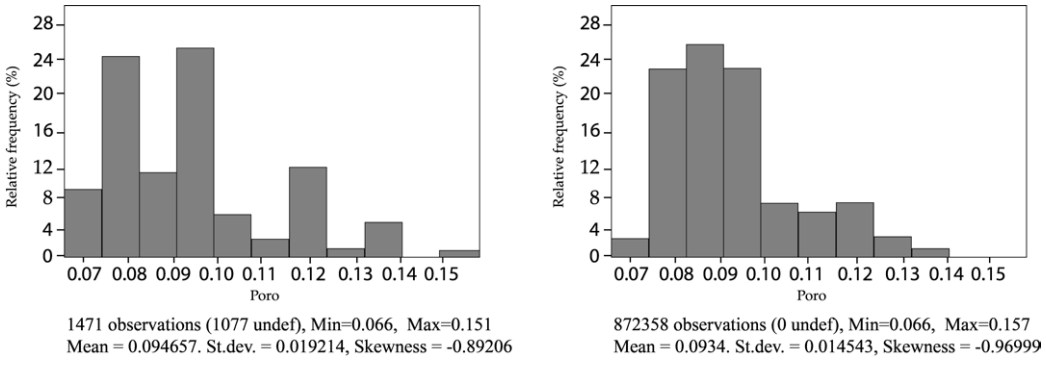


**(a)** **(b)**

**Figure 7.** Porosity distribution of C-1 formation in wells (a) and in the formation as a whole (b).

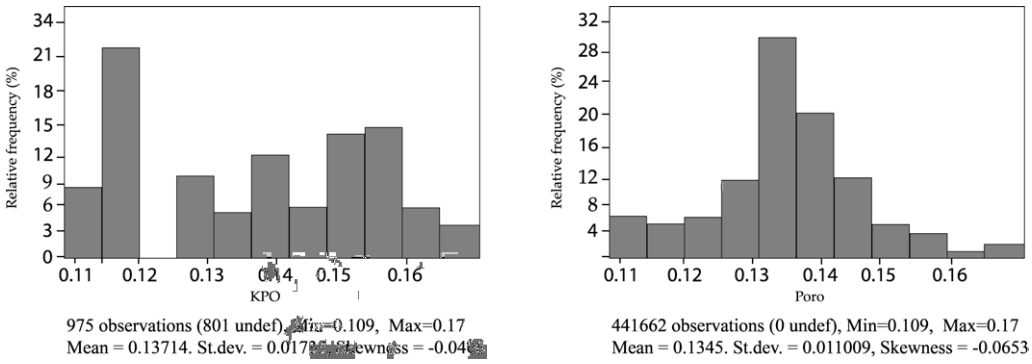


**(a)** **(b)**

**Figure 8.** Distribution of the porosity of D-I' formation in wells (a) and in the formation as a whole (b).

$Kpr = 9225.7 \times Kp - 6.3951$ – for A-4 formation;;

$Kpr = 101794 \times Kp - 7.2317$ – for B-2 formation;

$lgKpr = 29.301 \times Kp - 5.5686$ – for C-1 formation;

$Kpr = 5754.4 \times Kp - 5.783$ – for D-I formation'.

The distribution of oil saturation values in the reservoir of productive formations by source and by formations as a whole is shown in histograms on Figures 9–11.

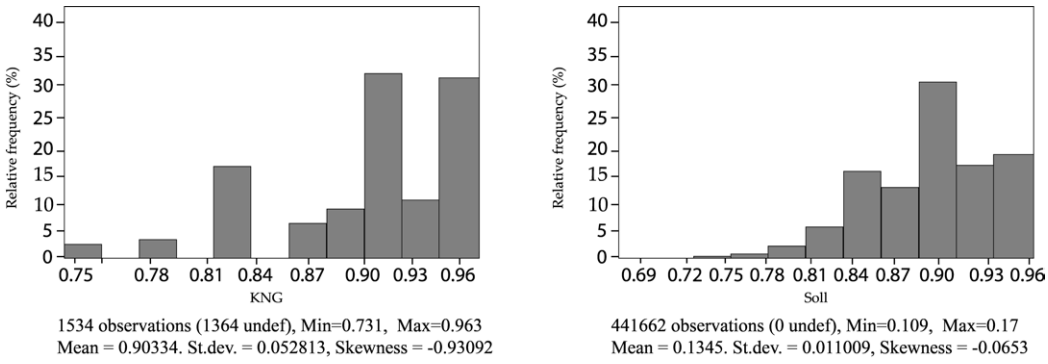


**(a)** **(b)**

**Figure 9.** Distribution of oil saturation of B-2 formation in wells (a) and in the reservoir as a whole (b).

The results of geological hydrocarbon reserves were obtained based on the constructed three-dimensional geological model of the Nizovsky field [*Expert commission of the Volga-Ural branch of the FBU GKZ*, 2019].

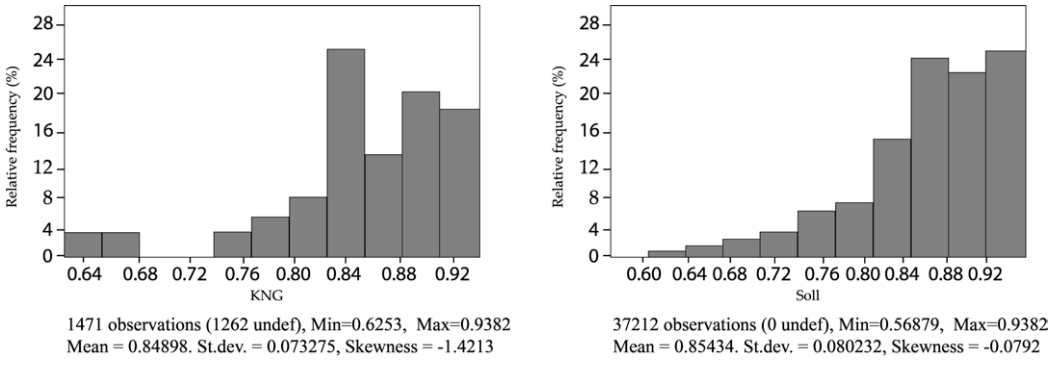


**(a)** **(b)**

**Figure 10.** Distribution of oil saturation of C-1 formation in wells (a) and in the reservoir as a whole (b).

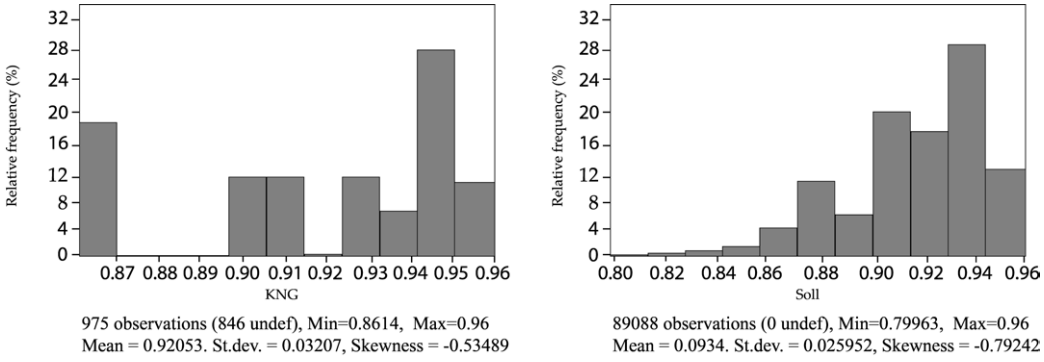


**(a)** **(b)**

**Figure 11.** Distribution of oil saturation of D-I' formation in wells (a) and in the reservoir as a whole (b).

Table 1 shows an assessment of the reliability of the created geological model by comparing the initial geological reserves of hydrocarbons, the volume of oil-saturated rocks, the area of oil-bearing capacity, the average effective thickness, the average porosity coefficient and the average coefficient of initial oil saturation.

Based on the authors' statement [*Davydov et al.*, 2017], terrigenous layer with increased porosity and having differences in lithological structure can be easily identified in the seismic field.

There are fewer terrigenous formations at the Nuzovsky deposit and they are heterogeneous in their composition and are often replaced. These layers can be barely identified.

There are similar problems with the identifying of carbonate formations and less powerful formations. This is because the layers have a large dissection and are located in the thickness of the same carbonate rocks with the same properties, which leads to difficulties in their identification.

Thus, geological models have been constructed for all the objects of calculation listed on the state balance sheet. The reserves deviation does not exceed 5%, which meets the requirements. Deviations of the calculated parameters from the approved ones are also within the framework of the regulations.

Digital geological models (GM) [*Meretukov et al.*, 2023] were used as the basis for a filtration model of the studied productive layers and were created by TRAP RMS software package, while digital hydrodynamic models (GDM) and modeling of the filtration process of the deposit layers were made by Eclipse software calculation complex.

The grids of filtration models were created using the procedure of rescaling the grid of geological models. The linear dimensions of the grid cells along the direction of the X and Y axes were chosen 50×50 m. Horizontal layers are variable power layers. The main

**Table 1**. Comparison of calculated parameters and oil reserves listed on the state balance sheet with those calculated in the geological model.

| Layer | Oil-bearing area | Average oil-saturated thickness | Volume of oil-saturated rocks | Coefficients | | Recalculated | Oil density | Initial geological oil reserves |
|---|---|---|---|---|---|---|---|---|
| | | | | Open porosity | Oil saturation | | | |
| **A-4** | thousand $m^2$ | metre | thousand $m^3$ | decimal fraction | decimal fraction | decimal fraction | $g/cm^3$ | thousand tons |
| State balance | 1395 | 3.8 | 5347 | 0.16 | 0.77 | | | 649 |
| Geomodel | 1414 | 3.9 | 54.51 | 0.165 | 0.764 | 0.926 | 0.839 | 648.2 |
| % discrepancies | 1.4 | 1.5 | 1.9 | 3.1 | −0.8 | | | 0.12 |
| **B-2** | | | | | | | | |
| State balance | 1246 | 5.9 | 7352 | 0.19 | 0.9 | | | 993 |
| Geomodel | 1249 | 6.1 | 7568.8 | 0.1903 | 0.899 | 0.937 | 0.843 | 1022.9 |
| % discrepancies | 0.2 | 2.7 | 2.9 | 0.2 | −0.1 | | | 3.0 |
| **C-1** | | | | | | | | |
| State balance | 788 | 7.8 | 6158 | 0.1 | 0.86 | | | 413 |
| Geomodel | 799 | 7.8 | 6208.5 | 0.1 | 0.862 | 0.942 | 0.827 | 417.8 |
| % discrepancies | 1.4 | −0.4 | 0.8 | 0.0 | 0.2 | | | 1.3 |
| **D-I'** | | | | | | | | |
| State balance | 2806 | 2.6 | 7398 | 0.14 | 0.92 | | | 655 |
| Geomodel | 2818 | 2.7 | 7518.8 | 0.14 | 0.92 | 0.81 | 0.849 | 667.8 |
| % discrepancies | 0.4 | 2.6 | 1.6 | 0.0 | 0.0 | | | 1.9 |

characteristics of filtration models of productive layers of the deposit are presented in Table 2.

The procedure for transferring data from geological models (GM) to filtration models (FM) was carried out correctly, as evidenced by the satisfactory convergence of the calculated parameters and oil reserves to the parameters of geological models and oil reserves listed on the state balance sheet (Table 3).

As can be seen from Table 1, deviations do not exceed the limits of 5% allowed by the regulations.

Since there is no gas cap at objects A-4, B-2, C-1, D-I', the development of deposits is assumed at a reservoir pressure above the saturation pressure. Therefore, the creation of filtration models is carried out within the framework of the theory of isothermal two-phase filtration [*Basniev et al.*, 1993; *Buckley and Leverett*, 1942].

The initial distribution of oil saturation of reservoirs was calculated according to digital geological models. The pressure in the formation was distributed depending on the depth and the known initial reservoir pressure at the reduction boundary (OWC).

The volumetric representation of the filtration models is shown in Figure 12.

**Table 2.** The main characteristics of filtration models of productive layers of the field.

| Model | Number of grid blocks by direction | | | Horizontal dimensions of the grid block, m | Vertical dimensions of the grid block, m | Total number of blocks | Number of active model blocks |
|---|---|---|---|---|---|---|---|
| | NX | NY | NZ | | | | |
| 1 | 2 | 3 | 4 | 5 | 6 | 7 | 8 |
| | | | | Layer A-4 | | | |
| GDM | 33 | 47 | 20 | 50×50 | 0.13–1.3 | 31020 | 23883 |
| | | | | Layer B-2 | | | |
| GDM | 34 | 43 | 27 | 50×50 | 0.11–1.26 | 39474 | 26032 |
| | | | | Layer C-I | | | |
| GDM | 28 | 36 | 23 | 50×50 | 0.33–2.71 | 23184 | 13172 |
| | | | | Layer D-I' | | | |
| GDM | | | | 50×50 | 0.18–1 | 29700 | 21464 |

**Table 3.** Comparison of initial geological reserves of hydrocarbons listed on the state balance sheet and calculated on the basis of three-dimensional GM and FM.

| Layer | Initial geological oil reserves, thousand tons | | | Discrepancy, % | |
|---|---|---|---|---|---|
| | State balance | GM | GDM | State balance – GDM | GM-GDM |
| A–4 | 649 | 648.2 | 647.3 | −0.26 | −0.14 |
| B–2 | 993 | 1022.9 | 1013.2 | +2.03 | −0.95 |
| C–1 | 413 | 417.8 | 418.5 | +1.34 | +0.18 |
| D–I' | 655 | 667.8 | 658.0 | +0.46 | −1.46 |

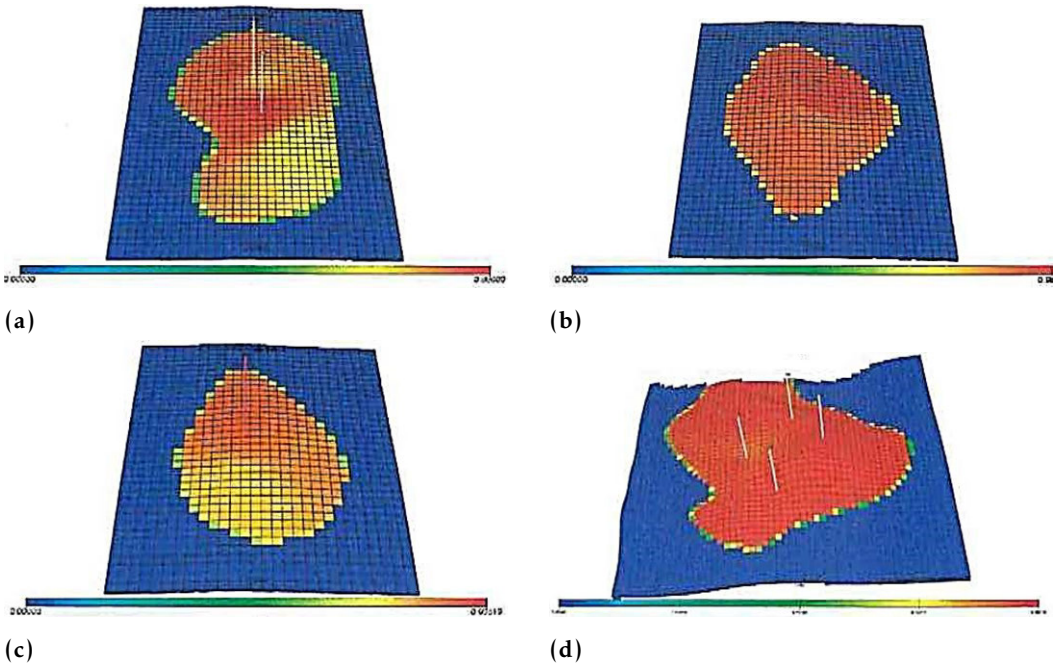

**Figure 12.** Volumetric representation of filtration models of the Nizovsky field: a) A-4 formation; b) B-2 formation; c) C-1 formation; d) D-I' formation, Oil saturation as of 01.01.2019.

The modeling of the water-pressure system of the modeling objects of the Nizovsky field was carried out by connecting the Fetkovich analytical aquifer [*Yagafarov et al.*, 2011; *Yu et al.*, 2021].

The diagrams of the relative permeability were used for the layers similar to Zapadno-Kommunarskoye field such as the deposits of Bashkir, Turiyeysky tiers and Pashiysky horizon. As for Bobrikovsky horizon deposits the research data on a composite model of 10 core samples of B-2 formation from well 25 Sovetsky field was used.

The graphs of relative permeability used in the models of the Nizovsky field are shown in Figure 13.

The option of scaling the end points of the tables from saturation was used in the models.

The values of displacement coefficients for deposits of A-4, B-2, C-1, D-I' formations of Nizovsky field were calculated using correlation petrophysical dependences of residual oil saturation on permeability, established according to the data of the core of analog formations.

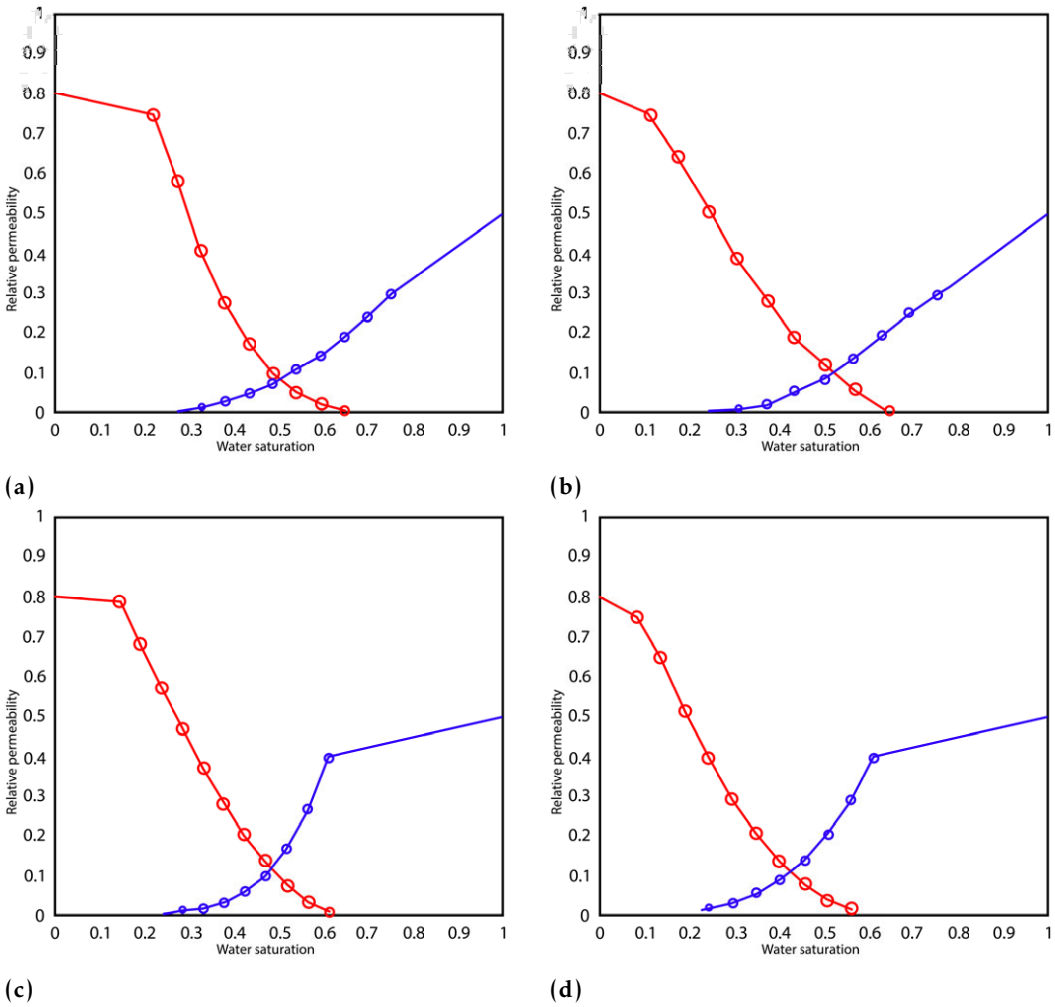


**Figure 13.** Relative permeability of the layers of Nizovsky deposit.

The displacement coefficients obtained by modeling layers A-4, B- 2, C-1, D-I' correspond to reasonable values (Table 4).

The adaptation of the history of the field development was carried out as of 01.01.2019 for all simulated objects with a history of the development.

The results of predictive calculations of technological indicators of development are presented in Figures 14–15. The figures show comparisons of oil, liquid and injection production levels according to models and those presented in state balance sheets according to the recommended option.

**Table 4.** Comparison of displacement coefficients for layers A-4, B-2, C-1, D-I' of Nizovsky deposit.

| Layer | Accepted displacement coefficient | FM | Discrepancy, % |
|---|---|---|---|
| A-4 | 0.674 | 0.674 | 0.0 |
| B-2 | 0.724 | 0.724 | 0.0 |
| C-1 | 0.543 | 0.543 | 0.0 |
| D-I' | 0.572 | 0.572 | 0.0 |

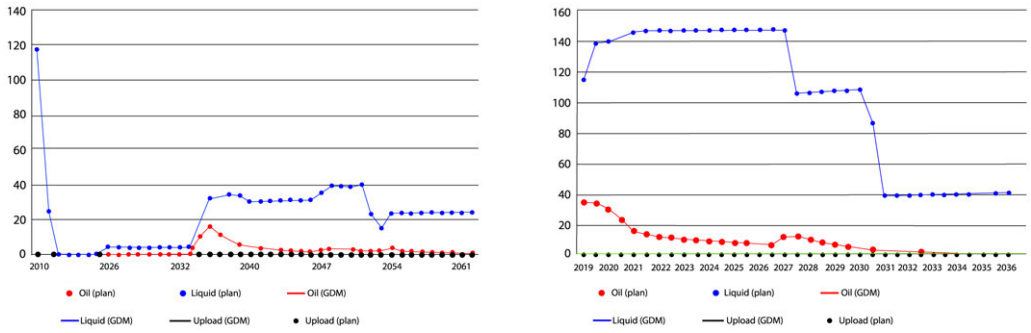


**(a)** **(b)**

**Figure 14.** The graph of compliance of model calculations and state plan tables for A-4 and B-2 layers.

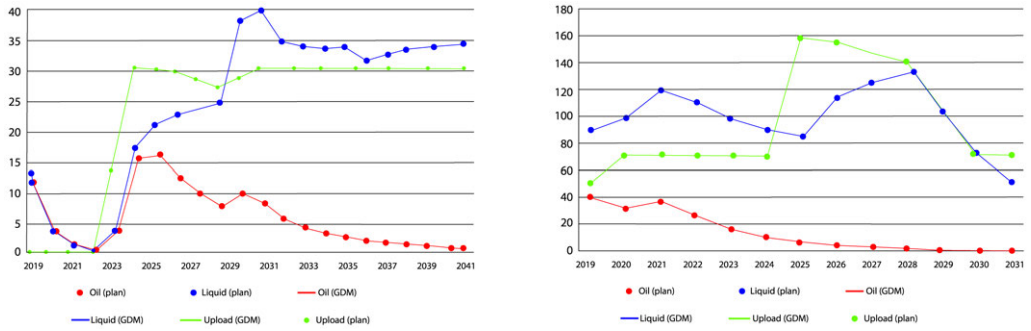


**(a)** **(b)**

**Figure 15.** The graph of compliance of model calculations and state plan tables for C-1 and D-I' formations.

## 4. Conclusions

1. The presented filtration model of A-4, B-2, C-1, D-I' formations allows predicting the behavior of productive formations and tracking the dynamics of changes in the production indicators of project wells under a given operating mode.
2. The results obtained and their correspondence with the expected parameters confirmed the realism of the forecast, which is ensured by using exclusively physical tools for model adaptation.
3. The basic properties of reservoir fluids and the values of initial reservoir pressures set in the GDM correspond to the basic parameters for Nizovsky field.
4. The forecast indicators of oil, liquid and injection production correspond to the indicators obtained using hydrodynamic models.

## References

Basniev, K. S., I. N. Kochina, and V. M. Maksimov (1993), *Underground hydromechanics: textbook for universities*, 416 pp., Nedra, Moscow (in Russian).

Baturin, A. Y. (2007), Geological and technological justification of the design of the development of oil and gas-oil fields, candthesis, Tyumen (in Russian).

Buckley, S. E., and M. C. Leverett (1942), Mechanism of Fluid Displacement in Sands, *Transactions of the AIME*, *146*(01), 107–116, https://doi.org/10.2118/942107-g.

Davydov, A. A., A. M. Pligin, I. A. Levin, and M. A. Istomova (2017), Accuracy estimation of the dynamic analysis of oil and gas-bearing complex in Samara region, *International Research Journal*, (08(62)), https://doi.org/10.23670/IRJ.2017.62.077 (in Russian).

Expert commission of the Volga-Ural branch of the FBU GKZ (2019), Technological project for the development of the Nizovsky oil field in the Samara region. The user of the subsoil of Samaraneftegaz JSC (in Russian).

Gaisina, G. F. (2010), Geologic modeling the Malyshev field oil pool with using the Norway program RMS 9.0.7, *Neftegasovaâ geologiâ. Teoriâ i practika*, *5* (in Russian).

Gladkov, E. A., and E. E. Gladkova (2011), Methodology for creating a three-dimensional geological model of technology in the fields with a history of the development over 50 years, *Bureniye i neft'*, (1), 32–35 (in Russian).

Meretukov, M. A., R. A. Toroyan, M. K. Bedanokov, R. B. Kohuzheva, and A. M. Artamonov (2023), Assessment of the quality of constructing a geological filtration model of the Nizovsky deposit formation of the Samara region, in *FUNDAMENTAL AND APPLIED ASPECTSOF GEOLOGY, GEOPHYSICS AND GEOECOLOGY USING MODERN INFORMATION TECHNOLOGIES. VII International Scientific and Practical Conference. Part 2*, pp. 66–73, Kucherenko V.O., Maykop (in Russian).

Raspopov, A. V., and V. A. Mordvinov (2010), *Designing the development of oil and gas fields: a textbook*, 87 pp., Perm State Technical University, Perm (in Russian).

Tikhomirova, E. A. (2020), Methods of oil saturation modeling and their application in IRAP RMS, *Herald of Tver State University. Series: Geography and Geoecology*, (1(29)), 69–78, https://doi.org/10.26456/2226-7719-1-2020-69-78 (in Russian).

Toroyan, R. A., and M. A. Meretukov (2023), Analysis of Circulation Losses Behavior during Wells Drilling at the Nizovskoye Field in the Samara Region, *Science and Technology in the Gas Industry*, *1*(93), 22–29 (in Russian).

Yagafarov, A. K., I. I. Kleshchenko, and V. A. Korotenko (2011), *Geology and development of oil and gas fields in Western Siberia*, TSOGU, Tyumen (in Russian).

Yu, J., L. Zhuo, Y. Chen, W. Sun, and Y. Liu (2021), Production Performance Analysis of Class II Hydrate-Bearing Layers Based on an Analytic Aquifer Model, *Frontiers in Energy Research*, *9*, https://doi.org/10.3389/fenrg.2021.702456.

Zakrevsky, K. E. (2009), *Geological 3D modeling textbook*, 376 pp., Maska, Moscow (in Russian).

Russian Journal of Earth Sciences

Special Issue: "Fundamental and Applied Aspects of Geology, Geophysics and Geoecology"

# Transformation and Features of Plant Successions of the Taman Peninsula in Case of Technogenic Impact

**S. A. Litvinskaya**[1,2]

[1]Kuban State University, Krasnodar, Russia
[2]Southern Federal University, Rostov-on-Don, Russia
* **Correspondence to:** S. A. Litvinskaya, Litvinsky@yandex.ru

**Abstract:** The impact of technogenic objects on the plant communities of the Taman Peninsula is considered. Technogenic transformations lead to destabilization of the balance in plant communities and landscapes of the Taman Peninsula. Anthropogenic successions are manifested differently in different types of ecosystems. The speed and nature of these processes usually determine the resistance of individual populations to the action of new environmental factors on them. When the vegetation cover is destroyed, the succession will focus on the formation of a ruderal community. When the sand-shell substrate was replaced with cement blocks in the littoral zone, the succession began to form linear synanthropic communities.

**Keywords:** Taman peninsula, steppe communities, littoral communities, technogenic impact.

**Citation:** Litvinskaya S. A. (2023), Transformation and Features of Plant Successions of the Taman Peninsula in Case of Technogenic Impact, *Russian Journal of Earth Sciences*, Vol. 23, ES0218, https://doi.org/10.2205/2023ES02SI18

Ecological, botanical and landscape studies are carried out in the area of anthropogenic impact in order to obtain reliable information that could adequately reflect the current state of ecosystems and the anthropogenic impact on the state of the plant component of ecosystems and the abiotic environment. The Taman Peninsula is a young formation. The study of historical documents shows that it was a system of islands with mud volcanoes, there is an abundance of water channels, straits, lakes, the shores of which were covered with forest floodplain communities. There are forests in the form of "khmerechs" that have been preserved to this day: on the Duboviy Rynok Mountain, on the hills near the village of Golubitskaya, Ilyich khutor, to the south of the ancient settlement of Fanagoria, along the old Kuban riverbed, on the hills along the shore of the Vityazevsky estuary and near the village of Dzhighinka, etc. [*Litvinskaya*, 2021]

The vegetation of the Taman Peninsula of the pre-agricultural period is considered as herb bunchgrass steppe with copses of tree species, grass bunchgrass steppe and grass bunchgrass shrub steppe. Currently, the steppes of the Taman Peninsula belong to a special provincial subzone of the Azov-Black Sea, grass bunchgrass shrub steppe with elements of the Mediterranean flora [*Litvinskaya*, 2018]. Stable communities have been preserved in some beam and coastal areas. The steppes of the Taman Peninsula have experienced prolonged anthropogenic pressure [*Litvinskaya*, 2020].

The main historical environmental management associated with agriculture [*Litvinskaya and Bochko*, 2019], viticulture, pasture animal husbandry contributed to the destruction of tree and shrubbery renewal. Constant military operations and domestic needs required the use of wood. All this gradually led to the change of the climax community of the shrub steppe by herb bunchgrass steppe. Moreover, the sod base was formed very quickly by feather-grasses due to the features of growth.

The object of research is a plant component. Steppe (Taman port) and littoral (Verbnaya Spit) plant communities were studied. Generally accepted geobotanical research

Research Article

Received: 20 October 2023
Accepted: 27 November 2023
Published: 15 December 2023

**Copyright:** © 2023. The Authors. This article is an open access article distributed under the terms and conditions of the Creative Commons Attribution (CC BY) license (https://creativecommons.org/licenses/by/4.0/).

methods were used in our studies such as: the method of sample areas, cenotic description according to geobotanical forms for meadow communities, the method of analysis and the method of mapping communities.

The territory of the Taman Peninsula is characterized by increased environmental sensitivity as a territory marked by the occurrence of dangerous natural processes and phenomena. An increased seismicity of the area and mud volcanism of the endogenous dangerous geological processes should be noted. Currently, technological impact has increased on the ecosystems of the Taman Peninsula, which is accompanied by certain environmental risks. First of all, there is ecological risk of habitat disturbance for biota, which leads to the loss and degradation of natural steppe ecosystems.

Grass bunchgrass steppe communities are widespread on the territory of the surroundings of the technogenic facility "Port Taman". Presumably, the steppe communities between the capes of Panagia and the Iron Horn are secondary, but long-existing, having formed stable more or less stable biogeocenoses corresponding to specific abiotic environmental conditions of the Pre-Caucasian steppe zone [*Litvinskaya*, 2018].

The steppe ecosystem had been developing for a long time in relatively stable climatic and soil conditions, which led to the development of stability of their structure and saturation with floral components of a close ecology and to the development of stenobiont in steppe species, including assemblers. But it is also characterized by the abundance of steppe grasses, the presence of species of different ecology, in particular steppe-meadow (*Medicago romanica* Prodan, *Filipendula vulgaris* Moench, *Fragaria viridis* Duch., *Inula culus-christi* L., *Achillea setacea* Waldst.et Kit., *Salvia tesquicola* Klok. et Pobed.et al.), an insufficiently strong sod base, but they had been developing in relatively stable conditions for a long time (Figure 1).

The technogenic impact of the Port of Taman and the occurrence of an unfavorable environmental background (air pollution, dust emissions, etc.) will cause disturbances of the existing equilibrium in the formed steppe ecosystem. These disturbances may exceed the regenerative capacity of the steppe ecosystem. If the intensity of the impact goes beyond these possibilities, the initially stable, species-rich community of the forb feather-grass steppe will gradually degrade.



**(a)** Crimean-wormwood monodominant



**(b)** Solonechnikov-forb



**(c)** Fescue – solonechnikov



**(d)** Forb-fescue-feather grass

**Figure 1.** The formed stable steppe ecosystems of the Port of Taman.

The steppe ecosystem disturbance leads to disruption of the normal functioning of many organisms. *Festuca sulcata* L. and *Artemisia taurica* Willd have the greatest resilience and tolerance in extreme conditions due to their ecological individuality. They can survive a period of unfavorable conditions and produce seeds and then the edifiers will gradually but slowly recover under favorable conditions, and the succession will gradually lead to the filling of the cenosis in quantitative terms. The succession will strive for a sustainable ecosystem but this process is long. Most likely, the Crimean-wormwood monodominant community, which has a wider area of tolerance, will be restored.

The smallest range of tolerance has forb-fescue-feather grass community. It is characterized by high floral saturation, a complex vertical structure, the presence of rare species belonging to stenobiont organisms that exist only with small deviations of the factor from the optimal value, which makes these communities sensitive to disturbance. *Stipa capillata* is the most tolerant from feather grasses. Feather grass prefers well-drained, loose, non-acidic soils, which indicates a fairly low diversity of possible habitats by the factor of soil moisture.

The most important environmental factors for normal functioning are light, temperature, and water. The disturbance of the coherence of the action of abiotic factors occurs upon technogenic impact and the edaphotope, the regime of water and mineral nutrition change and pollution is introduced into the environment. First of all, during the construction of facilities, the main impact falls on the edaphic factor and then on plants. In case of soil disturbance, the nutrients become physiologically inaccessible. The least tolerant species (ephemera and ephemeroids, juveniles) will drop out of the community. When the vegetation cover is destroyed, the succession will be directed to the formation of a ruderal community. The first species to appear will be those whose seeds are carried by the wind, some of them will fall with moving transport (on wheels, in building material). The nature of the developing vegetation will depend on the properties of the substrate, the degree of its disturbance, the remoteness of the territories from which the soil or construction material is taken. Populations of synanthropic species more resistant to the changed environment such as: *Elytrigia repens* (L.) Nevski, *Cynodon dactylon* (L.) Pers., *Hordeum leporinum* Link, *Echinochloa crus-galli* (L.) Beauv., species of the genus *Amaranthus*, *Xanthium srumarium* L., etc. will be expanded. Some plants will expand the ecological niche and will use the slightest opportunities for germination in places of soil accumulation.

A reduction in the species richness of plants will lead to a reduction in insects, whose food base has decreased. Insect life will occur in a disturbed environment (Figure 2).



**Figure 2.** Insect life in a disturbed environment.

Herpetofauna stations will be reduced. Lizards and steppe vipers are characterized by the principle of station loyalty. With the territorial reduction of the steppe ecosystem among the herpetofauna, the effect of crowding from overpopulation may manifest itself. With overpopulation of the environment, its quality deteriorates sharply: excrement, metabolic products are accumulated, growth and development of organisms are delayed, the timing of puberty, the rate of reproduction, cannibalism may take place. In the presence of competition, none of the populations can achieve such a number and density that would be possible in its absence. As a result of interspecific competition, ecological successions are manifested: the change of less competitive species to more competitive ones, as well as the narrowing of the ecological niche of the species. Thus, *Elaphe sauromates* prefer open steppe landscapes, often adhere to colonies of small rodents whose burrows are used as shelters. The species is characterized by two-peak daily activity. The species is rare for the steppes of the Taman Peninsula and with anthropogenic disturbance of the steppe ecosystem, the species will not withstand the competition of the steppe viper. New cenoses are being formed that are completely different from the original ones. At the same time, a significant part of the native flora and fauna is lost due to accidental or intentional acclimatization of new plant and animal species, pathogenic, parasites and predators. Seeds, bulbs, rhizomes and native species can remain in the substrate and even go through the full stages of vegetation with reduced vitality during the first 1-2 years. They will completely leave the environment later. Secondary succession will not lead to the restoration of the natural steppe cenosis. Along with the change in vegetation, the fauna of the territory subject to succession will also change. The animal population largely changes its composition. Due to the fact that all changes are related to human activity, we deal with ecological successions that occur under the influence of human activity. In this case, it is a constantly acting external factor, and we deal with an anthropogenically altered landscape. Usually, allogeneic successions manifest themselves in gradual destruction (digression) ecosystems. As a result, some group of eurytopic species, maximally adapted to specific conditions, will remain on the territory of the Port of Taman. In these conditions, the study of the vital state of plants as structural units of cenopopulations is of great importance for assessing the impact of the complex on the natural environment. With the repetition of technogenic disturbances, the further development of anthropogenic successions is suspended for an indefinite period of time and the stages of relatively stable low-component secondary "communities" are formed. It is difficult to call them communities but it is a complex of species of a monotonous set of biomorphs with the structure of a derived ruderal community with insignificant floral saturation, limited composition of dominants, changing abundance and mosaic. Seed sources cease to supply diasporas with further irreversible changes in environmental conditions, and succession stops at the stage of community death. Moreover, the main "blow" is inflicted on the plant component, animals can leave this habitat or switch to a more favorable biotope. Nevertheless, there will be fragmentation of habitats of terrestrial, especially small animals, migration routes to forage resources, mating and breeding sites will change and new anthropogenic biotopes will appear, which may lead to a change in the composition and abundance of animal species. Rare species are particularly sensitive. In the area of Cape Panaghia, there are pied wheatear, little grebe, collared bushchat (first recorded in 2003 [*Belik et al.*, 2009]) and crows, blue pigeon and green cormorant nest.

Anthropogenic successions have the most unexpected nature, they are difficult to predict and manifest themselves in different ways in different types of ecosystems. The speed and nature of these processes usually determine the resistance of individual populations to the action of new unexpected factors for them.

The studies of successions under technogenic impact (construction of the drilling station site) on littoral communities were carried out during the studies of the Azov coastal zone. Plant communities not affected by anthropogenic disturbances were distinguished by the presence of characteristic species, higher projective coverage, pronounced structure, as evidenced by the mapped transect (area 8 × 20 m) (Figure 3)

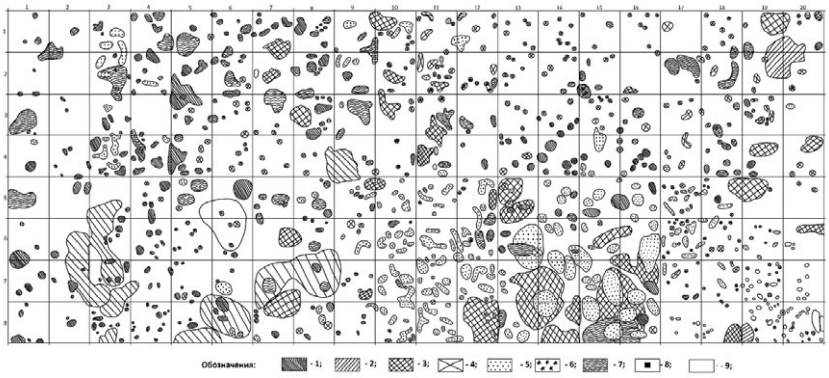

**Figure 3.** A projection of a community unaffected by anthropogenic impacts.
Notation keys: 1 – *Plantago maritima*; 2 – *Verdascum pinnatifidum*; 3 – *Tribulus terrestris*; 4 – *Plantago arenaria*; 5 – *Cynodon dactylon*; 6 – *Erodium cicutarium*; 7 – *Astragalus onobrychis*; 8 – *Leymus sabulosus*; 9 – *Carex colchica*

During the construction of the technogenic facility, the natural vegetation was completely destroyed and the new substrate was cemented blocks. At the first stages, there was a massive reproduction of the invasive species *Cenchrus longispinus*, which had not previously grown in these biotopes. *Cenchrus longispinus* is an invasive annual species of the *Poaceae* family, spread by prickly fruit systems containing 1–3 spikelets with grain fruits. The fruit systems are easily attached to the wool and skin of animals, clothing, shoes and human skin, by the wheels of cars and spread over long distances from the mother plant. *Cenchrus longispinus* was introduced, apparently, during the construction of a road with transport and was quickly spread. Its new ecological niche is an interplate biotope with soil accumulation. The monodominant communities were formed extremely quickly during two years. Two years later, *Echinochloa crus-galli* began to be introduced. 10 species have been recorded in a community dominated by *Echinochloa crus-galli* with no species from natural littoral communities. Sandbur was only occasionally found in the derived cenoses of the drilling site five years later. *Euphorbia maculata* L., a new invasive species whose homeland is North America, appeared that had not previously grown within the littoral area of the Verbnaya Spit. As a result, the dominance passed to *Euphorbia maculata*.

There was a clear shift in succession towards the dominance of annual and weed species over the years of observations. Littoral species, having mainly powerful root systems, could not grow in conditions covered with cement blocks of the substrate. In the future, the succession followed a more powerful overgrowth of linear ecotopes. The number of species increased slightly but individuals of some species moved from the vegetative state to the flowering and fruiting phase (*Phalacroloma septentrionale* (Fern. et Wiegand) Tzvelev, *Crepis rhoeadifolia* M. Bieb.). The anthropogenic ecological niche was completely populated not only by synanthropic species (*Hordeum geniculatum* All., *Digitaria sanguinalis* (L.) Scop., *Setaria pumila* (Poir.) Roem. et Schult., *Conyza canadensis* (L.) Cronquist, *Ambrosia artemisiifolia* L., *Anthemis ruthenica* M. Bieb.) (Figure 4) but species of natural communities (*Medicago romanica*, *Cacile euxina*) also grew in interplate substrates.

The Taman Peninsula is one of the few territories that has concentrated in its landscapes an unprecedented number of species of biogeocenotic complexes, as well as rare, endangered and protected species. Studies have shown that technogenic transformations lead to destabilization of the balance in plant communities and landscapes of the Taman Peninsula. These impacts belong to the direct category, i.e. there will be a direct destruction of vegetation in different landscapes and a reduction in the number of rare species. The construction of technogenic facilities affects the entire complex of natural landscapes. From the point of view of the impact on the geological environment, the impact is associated with the redevelopment of the relief and the terracing of steep slopes, an increase in the intensity of the development of the processes of planar and linear erosion. The process of



**Figure 4.** Formation of linear interplate communities on an anthropogenic substrate.

anthropogenic changes in natural complexes is accompanied by many undesirable consequences: reduction of habitats of a number of plant and animal species, general depletion of biota, reduction of genetic diversity of individual species, etc. The most vulnerable elements are usually protected plant species and steppe ecosystems.

## References

Belik, V. P., V. V. Vetrov, and Y. V. Milobog (2009), Data on avifauna of Taman' Peninsula, *"Branta": Transactions of the Azov-Black Sea Ornithological Station*, *12*, 7–26 (in Russian).

Litvinskaya, S. A. (2018), Tamansky steppe refugium, in *Steppes of Northern Eurasia: Proceedings of the 8th International Symposium*, Institute of Steppe, UB RAS, Orenburg (in Russian).

Litvinskaya, S. A. (2020), Nineteenth century as beginning of social upheavals and transformations of steppe landscapes in West Ciscaucasia, in *Bulletin of the Krasnodar Regional Branch of the Russian Geographical Society*, pp. 274–281, Platonov Publishing House (in Russian).

Litvinskaya, S. A. (2021), *The Red Book of the Kuban Steppe*, 256 pp., Tradition (in Russian).

Litvinskaya, S. A., and T. F. Bochko (2019), Agrarian development as the main cause of the steppe biome degradation of the Western Ciscaucasia, *Proceedings of the Kuban State Agrarian University*, *1*(76), 116–123, https://doi.org/10.21515/1999-1703-76-116-123 (in Russian).